Investigating the Early Phases of Aerosol Particle Nucleation: A Broadband Rotational Spectroscopic and Computational Study

by

Arsh S. Hazrah

A thesis submitted in partial fulfillment of the requirements for the degree of

Doctor of Philosophy

Department of Chemistry
University of Alberta

Abstract

Atmospheric aerosols consist of solid or liquid particles suspended in air with sizes ranging from a few nanometers to several micrometers. Aerosols have the ability to both scatter and absorb incoming solar radiation, directly influencing Earth's energy budget and resulting in either cooling or warming effects on our climate. Aerosol formation consists of two phases: nucleation and growth. In the nucleation phase, gaseous molecular species aggregate to form molecular clusters that contain only a few molecules. These clusters are held together by non-covalent interactions such as van der Waals forces and hydrogen bonds. However, these small molecular clusters, and in general, the early stages of nucleation remain poorly understood due to the high degree of compositional and structural variability and the complex network of non-covalent interactions present within the clusters. As a result, these molecular clusters in the early phases of nucleation may adopt many different conformations making it challenging to elucidate their structure. To study the initial stages of nucleation a molecular beam expansion is used to produce and stabilize the clusters. Broadband rotational spectra of the species are recorded using a chirped pulse Fourier transform microwave spectrometer, and several computational techniques are then used to help in the spectroscopic assignments and further characterize the molecular species.

In this thesis, I describe my work studying the conformational landscapes of molecules and molecular clusters found in the early phases of nucleation and the non-covalent interactions within them. It is quite challenging to create and analyze molecular complexes containing multiple molecular species simultaneously. To simplify this problem, I focus on oxygenated hydrocarbon monomers and their aggregates with water, one of the most abundant molecular species in the atmosphere. Using a combination of experimental and theoretical techniques, I investigated different isomers of naphthol, an oxygenated polycyclic aromatic hydrocarbon, to gain new

insights into a controversial non-covalent interaction between two hydrogen atoms. The structural and thermodynamic data obtained from the monomer study was then used to investigate the 1-naphthol dimer, which revealed new insights into a complex intermolecular interplay between two molecules. Next, the conformational flexibility of (-)-carveol, a photo-oxidation product of a common biogenic volatile organic compound, limonene, was investigated. The results revealed a complicated conformational landscape which plays a significant role in the aggregation of (-)-carveol with atmospheric species such as water. The α-pinene-water complex was studied to investigate internal dynamics, such as water tunnelling and large amplitude motions, which occur in the molecular clusters found in the early stages of nucleation. Finally, to examine the early phases of aggregation, the 3-methylcatechol monomer and 3-methylcatechol hydrated with up to five water molecules were investigated. The study compared two different aggregation mechanisms and revealed a preference for dispersion assisted aggregation over the more common hydrogen bond dominated mechanism, or droplet aggregation. By studying the fundamental molecular properties of molecular clusters found in the early stages of nucleation, I hope to provide further insights into the initial steps of aerosol particle formation and ultimately bridge the gap between the molecular and macroscopic regimes.

Preface

This thesis is a partial collection of my research completed during my doctoral studies at the University of Alberta, from September 2018 to March 2023. The contributions of each author to the research described in this thesis are summarized below.

The study described in Chapter 3 has been published as "Structural study of 1-and 2-naphthol: new insights into the non-covalent H–H interaction in cis-1-naphthol" by A. S. Hazrah, S. Nanayakkara, N. A. Seifert, E. Kraka and W. Jäger, *Phys. Chem. Chem. Phys*., 2022, **24**, 3722–3732. I was responsible for the project conception, calculations, measurements, data analysis, and manuscript preparation. S. Nanayakkara performed the local mode analysis calculations. N.A. Seifert participated in measurements and data analysis. E. Kraka and W. Jäger are the supervisory authors and were involved with concept formation and manuscript composition.

The study described in Chapter 4 has been published as "The 1-naphthol dimer and its surprising preference for π–π stacking over hydrogen bonding" by N. A. Seifert, A. S. Hazrah and W. Jäger, *J. Phys. Chem. Lett.*, 2019, **10**, 2836–2841. I was responsible for the project conception, calculations, measurements, data analysis, and manuscript preparation. N. A. Seifert was responsible for project conception, calculations, measurements, data analysis, and manuscript preparation. W. Jäger was the supervisory author and was involved with concept formation and manuscript composition.

The study described in Chapter 5 is in the final stage of manuscript edits and will be submitted for publication as "Examining intermolecular interactions between hydrocarbons and water: A broadband rotational spectroscopic study of the α-pinene – water complex" by A. S. Hazrah, C.D. Carlson, M. H. Al-Jabiri, Y. Xu and W. Jäger. I was responsible for the project conception, calculations, measurements, data analysis, and manuscript preparation. C.D. Carlson and M. H. Al-Jabiri performed calculations and participated in project discussions. Y. Xu and W. Jäger are the supervisory authors and were involved with concept formation and manuscript composition.

The study described in Chapter 6 has been published as "A rotational spectroscopic and *ab initio* study of *cis*- and *trans*-(−)-carveol: further insights into conformational dynamics in monoterpenes and monoterpenoids" by A. S. Hazrah, M. H. Al-Jabiri, R. Speelman and W. Jäger, *Phys. Chem. Chem. Phys.*, 2021, **23**, 15159–15168. I was responsible for the project conception,

calculations, measurements, data analysis, and manuscript preparation. M. H. Al-Jabiri and R. Speelman participated in measurements, data analysis, and project discussions. W. Jäger was the supervisory author and was involved with concept formation and manuscript composition.

The study described in Chapter 7 has been published as "Structure and conformations of 3-methylcatechol: A rotational spectroscopic and theoretical study" by A. S. Hazrah, M. H. Al-Jabiri and W. Jäger, *J. Mol. Spectrosc*., 2022, **390**, 111715. I was responsible for the project conception, calculations, measurements, data analysis, and manuscript preparation. M. H. Al-Jabiri participated in data analysis, project discussions and manuscript edits. W. Jäger was the supervisory author and was involved with concept formation and manuscript composition.

The study described in Chapter 8 is in the final stage of manuscript edits and will be submitted for publication as "Wetting vs droplet aggregation: a broadband rotational spectroscopic study of 3-methylcatechol ⋯ water Clusters" by A. S. Hazrah, A. Insausti, J. Ma, M. H. Al-Jabiri, Y. Xu and W. Jäger. I was responsible for the project conception, calculations, measurements, data analysis, and manuscript preparation. A. Insausti and J. Ma were responsible for measurements and data analysis. M. H. Al-Jabiri participated in data analysis, project discussions and manuscript edits. Y. Xu and W. Jäger are the supervisory authors and were involved with concept formation and manuscript composition.

For my parents

Acknowledgements

Like many endeavors in life, success in science and research are never solely achieved by an individual, but rather a direct product of the efforts and contributions of the community of people they choose to surround themselves with. Here I express my gratitude and appreciation for the support and guidance I have received from my friends, family, colleagues, and mentors throughout the years. From the bottom of my heart, I thank you all.

I would like to express my deepest gratitude to my supervisor, Prof. Wolfgang Jäger, for his mentorship and unwavering support throughout my studies. His passion for science and his commitment to my development as both a scientist and a professional has made my research experience enjoyable and inspiring. I am grateful for the time and effort he has invested in me. The skills I have acquired under his guidance are invaluable and will continue to benefit me for years to come, regardless of where my future ventures take me. Thank you, Wolfgang.

I am grateful to Prof. Yunjie Xu for her guidance and discussions about molecular symmetry and spectroscopy, as well as introducing me to various chiroptical techniques. I thank Prof. Gabe Hanna and Prof. Ran Zhao for not only agreeing to be on my supervisory committee, but also providing me with advice and guidance over the years. I also thank Prof. Alex Brown for the many useful career and scientific discussions. I thank Prof. Arthur Mar, Prof. Lingzi Sang, Prof. Rod Wasylishen, and Prof. Sonia Melandri for being on my examining committee. I thank Dr. Reza Poopari for making my teaching assistant responsibilities so enjoyable. I thank the technical staff in the department, especially Dieter Starke, Dirk Kelm, Farhat Emhemed, Paul Crothers, and Vincent Bizon for their assistance during this research. I thank Alex, Amanda, Aran, Bowei, Colton, Craig, Eddie, Guojie, Haolu, Jiarui, Juliette, Matthias, Moe, Mutasem, Raiden, Sam, Qian, and Yangqing for their friendship and support. A special thank you to Fan and Nate, for not only their friendship, but for their teachings in rotational spectroscopy.

Funding from the Alberta Graduate Excellence Scholarship, Dr. R. Norman and Magda Kemeny Jones Travel Award, J Gordin Kaplan Graduate Student Award, Marshall Syska Chemistry Graduate Scholarship, Gunning Research Associate Award, Natural Sciences and Engineering Research Council, and the University of Alberta is gratefully acknowledged.

I am grateful to my brother, Kaveer, as well as my family members in Edmonton, Ottawa, Toronto, and Welland for their relentless encouragement and endless support. Thank you. While words cannot fully express my appreciation for all that you have done for me, I would like to thank my parents for their never-ending support and inspiration. This thesis not only represents the culmination of the past five years of hard work but also serves as a tribute to the 27 years of your support and guidance that have enabled me to pursue my dreams and aspirations. Finally, I am grateful to my future wife, Kelli, who has never stopped supporting me through all the stressful and tumultuous times in graduate school. You not only celebrate my successes but also provide guidance and support to steer me back on the right path when I have gone astray. You continuously motivate me to not only become a better scientist, but also a better person.

Table of Contents

Chapter 1. Introduction 1
1.1. Atmospheric Aerosol and Secondary Organic Aerosol Particles 1
1.2. Initial Stages of Nucleation 2
1.3. Conformational Flexibility 3
1.4. Rotational Spectroscopy and Computational Chemistry 5
1.5. Thesis Structure 6
1.6. References 7
Chapter 2. Experimental and Theoretical Methods 10
2.1. Introduction 10
2.2. Rotational Spectroscopy 12
2.2.1. Rotational Energy Levels and Rotational Constants 13
2.2.2. Centrifugal Distortion Effect 17
2.3. Molecular Beam Technique 17
2.4. Chirped Pulse Fourier Transform Microwave Spectroscopy 19
2.4.1. Excitation and Detection 20
2.4.2. Transistor-Transistor Logic (TTL) Pulses and Timing 21
2.5. Theoretical Techniques 22
2.5.1. Conformational Ensemble Search 23
2.5.2. Electronic Structure Calculations 23
2.6. Assignment Process 24
2.7. Non-covalent Interactions Analyses 25
2.8. References 26
Chapter 3. Structural Study of 1- and 2-Naphthol: New Insights into the Non-Covalent H–H Interaction in C*is*-1-Naphthol 29
3.1. Introduction 29
3.2. Methods 31
3.2.1. Theoretical Methods 31
3.2.2. Experimental Methods 33
3.3. Results and Discussion 33
3.3.1. Experimental Results 33
3.3.2. Electronic Structure Calculations 36
3.3.3. Structures 38
3.3.4. Interpretation of the Close Contact in *Cis*-1-Naphthol 42
3.3.5. Biphenyl: A Related System 52
3.4. Conclusions 54

3.5. References 55
Chapter 4. The 1-Naphthol Dimer and its Surprising Preference for π–π Stacking Over Hydrogen Bonding 60
4.1. Introduction 60
4.2. Methods 61
4.2.1. Experimental Methods 61
4.2.2. Theoretical Methods 62
4.3. Results and Discussion 63
4.3.1. Spectroscopic Assignment 63
4.3.2. Theoretical Discussion 65
4.3.3. Non-Covalent Interactions Analyses 67
4.4. Conclusions 70
4.5. References 70
Chapter 5. Examining Intermolecular Interactions Between Hydrocarbons and Water: A Broadband Rotational Spectroscopic Study of the α-pinene – Water Complex 74
5.1. Introduction 74
5.2. Methods 76
5.2.1. Experimental Methods 76
5.2.2. Theoretical Methods 76
5.3. Results and Discussion 78
5.3.1. Theoretical Results 78
5.3.2. Experimental Results 83
5.3.3. Conformer Assignment 85
5.3.4. Water Tunneling 87
5.3.5. NCI/QTAIM/IGM Analyses 88
5.3.6. NBO Analyses 92
5.3.7. Theoretical Discussion 94
5.3.8. Atmospheric Implications – Thermodynamics 96
5.3.9. Atmospheric Implications – Kinetics 98
5.4. Conclusions 102
5.5. References 102
Chapter 6. A Rotational Spectroscopic and *Ab Initio* Study of *Cis*- and *Trans*-(−)-Carveol: Further Insights into Conformational Dynamics in Monoterpenes and Monoterpenoids 107
6.1. Introduction 107
6.2. Methods 110
6.2.1. Configuration and Conformer Nomenclature 110
6.2.2. Theoretical Methods 111
6.2.3. Experimental Methods 114

6.3. Results and Discussion 114
6.3.1. Theoretical Results 114
6.3.2. Experimental Results and Conformational Cooling 117
6.3.3. Spectroscopic Assignments 120
6.3.4. Experimental Intensities and Relative Energy Ordering 122
6.3.5. Axial Isopropenyl Conformation 124
6.4. Conclusions 126
6.5. References 127
Chapter 7. Structure and Conformations of 3-Methylcatechol: A Rotational Spectroscopic and Theoretical Study 130
7.1. Introduction 130
7.2. Methods 131
7.2.1. Experimental Methods 131
7.2.2. Theoretical Methods 132
7.3. Results and Discussion 134
7.3.1. Theoretical Results 134
7.3.2. Experimental Results 135
7.3.3. Interconversion Pathways 137
7.3.4. Spectroscopic Parameters 139
7.3.5. Structures 139
7.4. Conclusions 141
7.5. References 141
Chapter 8. Wetting vs Droplet Aggregation: A Broadband Rotational Spectroscopic Study of 3-Methylcatechol ··· Water Clusters 144
8.1. Introduction 144
8.2. Methods 146
8.2.1. Experimental Methods 146
8.2.2. Theoretical Methods 146
8.3. Results and Discussion 147
8.3.1. Experimental Results 147
8.3.2. Theoretical Results 148
8.3.3. Spectroscopic Assignment 150
8.3.4. Wetting vs Droplet Aggregation 153
8.3.5. Transition Splittings 157
8.4. Conclusions 159
8.5. References 159
Chapter 9. Conclusions 163
9.1. Conclusions and Future Work 163

9.2. References 168
Bibliography 170
Appendix A 186
Appendix B 215
Appendix C 224
Appendix D 236
Appendix E 250
Appendix F 257

List of Tables

Table 2.1.	Effects of centrifugal distortion on bond lengths	17
Table 3.1.	Spectroscopic parameters for the conformers of 1- and 2-naphthol from theory and from fits of experimental data	34
Table 3.2.	Experimental, semi-experimental, and theoretical rotational constants of *cis*-1-naphthol	40
Table 4.1.	Experimental spectroscopic parameters for the detected 1-naphthol dimer	64
Table 4.2.	Calculated properties of seven isomers of the 1-naphthol dimer, predicted using different levels of theory	66
Table 5.1.	Rotational constants and dipole moment components at six different levels of theory for the anti- and syn-complexes	80
Table 5.2.	Rotational constants and dipole moment components for the experimental, uncorrected, and corrected anharmonic results	82
Table 5.3.	Relative zero-point corrected energies between the anti- and syn-conformer at different levels of theory	83
Table 5.4.	Electron density topology parameters obtained from QTAIM analyses	90
Table 5.5.	Decomposition of the two intermolecular interactions into donor and acceptor Natural Bond Orbitals	93
Table 5.6.	Stabilization energies and bond orders obtained from NBO analyses	94
Table 5.7.	Theoretical rate constants for the anti- and syn- conformers at 298.15 K	100
Table 6.1.	Theoretical results for *trans* and *cis* (-)-carveol conformers obtained from the 2D PES scan and CREST searches	113
Table 6.2.	Relative zero-point corrected interconversion barrier heights of *trans* and *cis* (-)-carveol	115
Table 6.3.	Spectroscopic parameters for the five experimentally assigned conformers of (-)-carveol	119

Table 6.4.	Abundances of *cis* and t*rans* (-)-carveol conformers at 298K and 353K (source temperature)	121
Table 6.5.	Results from NBO analyses for H_2O-H_2O, carveol and carveol-H_2O	124
Table 7.1.	Theoretical results for the three conformers of 3-methylcatechol	134
Table 7.2.	Spectroscopic parameters for the two experimentally assigned conformers of 3-methylcatechol	137
Table 7.3.	Effective (r_0), substitution (r_s), semi-experimental (r_{se}), and theoretical structure parameters for Conformer 1	139
Table 7.4.	Effective (r_0), substitution (r_s), semi-experimental (r_{se}), and theoretical structure parameters for Conformer 2	140
Table 8.1.	Spectroscopic parameters for the five experimentally assigned hydrates	149
Table A.1.	Assigned rotational transitions for *cis*-1-naphthol	188
Table A.2.	Assigned rotational transitions for *trans*-1-naphthol	188
Table A.3.	Assigned rotational transitions for *cis*-2-naphthol	189
Table A.4.	Assigned rotational transitions for *trans*-2-naphthol	191
Table A.5.	Assigned rotational transitions for *cis*-1-naphthol ^{13}C isotopologues	192
Table A.6.	Assigned rotational transitions for *trans*-1-naphthol ^{13}C isotopologues	193
Table A.7.	Assigned rotational transitions for *cis*-2-naphthol ^{13}C isotopologues	195
Table A.8.	Assigned rotational transitions for *trans*-2-naphthol ^{13}C isotopologues	196
Table A.9.	Rotational transitions for ^{13}C isotopologues of *cis*-1-naphthol	198
Table A.10.	Rotational transitions for ^{13}C isotopologues of *trans*-1-naphthol	198
Table A.11.	Rotational transitions for ^{13}C isotopologues of *cis*-2-naphthol	199
Table A.12.	Rotational transitions for ^{13}C isotopologues of *trans*-2-naphthol	199
Table A.13.	Structural parameters for *cis*-1-naphthol	200
Table A.14.	Structural parameters for *trans*-1-naphthol	200

Table A.15.	Structural parameters for *cis*-2-naphthol	200
Table A.16.	Structural parameters for *trans*-2-naphthol	201
Table A.17.	Data from AIMA11 QTAIM calculations	201
Table A.18.	*Cis*-1-naphthol theoretical method comparison	201
Table A.19.	Semi-experimental rotational constants for parent species	202
Table A.20.	Semi-experimental rotational constants for *cis*-1-naphthol ^{13}C isotopologues	202
Table A.21.	Semi-experimental rotational constants for *trans*-1-naphthol ^{13}C isotopologues	202
Table A.22.	Semi-experimental rotational constants for *cis*-2-naphthol ^{13}C isotopologues	203
Table A.23.	Semi-experimental rotational constants for *trans*-2-naphthol ^{13}C isotopologues	203
Table A.24.	Local Mode Force Constants and Local Mode Frequencies	207
Table A.25.	Moment of inertia and Inertial defect values for calculated and experimental results	208
Table A.26.	Calculated inertial defect values obtained from Oka's equation	208
Table A.27.	Inertial defect differences between calculated and experimental defect values	208
Table A.28.	Lowest out-of-plane modes for naphthol isomers and previous work	208
Table A.29.	Net CM5 charge change for naphthol and biphenyl	212
Table A.30.	Bonding and antibonding orbital occupancy	212
Table A.31.	Interaction Energies between bonding and antibonding orbitals for *trans*-1-naphthol	213
Table A.32.	Interaction Energies between bonding and antibonding orbitals for *cis*-1-naphthol	213
Table A.33.	Interaction Energies between bonding and antibonding orbitals for *trans*-2-naphthol	213
Table A.34.	Interaction Energies between bonding and antibonding orbitals for *cis*-2-naphthol	213

Table A.35.	*Cis*-1-naphthol theoretical method comparison	214
Table B.1.	Assigned rotational transitions for the 1-naphthol dimer	215
Table B.2.	Cartesian coordinates for the B3LYP-D3(BJ) optimized structure of the V-shape isomer	219
Table B.3.	Cartesian coordinates for the B3LYP-D3(BJ) optimized structure of the Saeki-a isomer	219
Table B.4.	Cartesian coordinates for the B3LYP-D3(BJ) optimized structure of the Saeki-b isomer	220
Table B.5.	Cartesian coordinates for the B3LYP-D3(BJ) optimized structure of the Saeki-c isomer	220
Table B.6.	Cartesian coordinates for the B3LYP-D3(BJ) optimized structure of the Saeki-d isomer	221
Table B.7.	Cartesian coordinates for the B3LYP-D3(BJ) optimized structure of the Saeki-e isomer	222
Table B.8.	Cartesian coordinates for the B3LYP-D3(BJ) optimized structure of the Hinge isomer	222
Table C.1.	Conformers obtained from the CREST searches at the B3LYP-D3(BJ)/Jun-cc-pVTZ level of theory	225
Table C.2.	Raw and zero-point energy corrected barrier heights for the rotation of the water unit about the O-H---π bond.	227
Table C.3.	A full NBO analysis of the anti- and syn-complex	231
Table C.4.	Intermolecular bond characterization obtained from an NBO analysis	231
Table C.5.	Measured frequencies of assigned rotational transitions with their quantum number assignments of the ortho spin isomer of the anti-water complex	233
Table C.6.	Measured frequencies of assigned rotational transitions with their quantum number assignments of the para spin isomer of the anti-water complex	234

Table C.7.	Measured frequencies of assigned rotational transitions with their quantum number assignments of the ortho spin isomer of the syn-water complex	235
Table C.8.	Measured frequencies of assigned rotational transitions with their quantum number assignments of the para spin isomer of the anti-water complex	235
Table D.1.	Theoretical conformers for *trans* (-)-carveol	238
Table D.2.	Theoretical conformers for *cis* (-)-carveol	239
Table D.3.	*cis* (-)-carveol, Experiment vs. Theory	240
Table D.4.	*trans* (-)-carveol, Experiment vs. Theory	240
Table D.5.	Assigned rotational transitions for E1	241
Table D.6.	Assigned rotational transitions for E2	242
Table D.7.	Assigned rotational transitions for E3	243
Table D.8.	Assigned rotational transitions for E4	244
Table D.9.	Assigned rotational transitions for E5	245
Table D.10.	Geometry for E1	247
Table D.11.	Geometry for E2	247
Table D.12.	Geometry for E3	248
Table D.13.	Geometry for E4	248
Table D.14.	Geometry for E5	249
Table E.1.	Cartesian coordinates for all three conformers	251
Table E.2.	Assigned rotational transitions of Conformer 1	525
Table E.3.	Assigned rotational transitions of Conformer 2	253
Table E.4.	Spectroscopic parameters for ^{13}C isotopologues of Conformer 1	254
Table E.5.	Spectroscopic parameters for ^{13}C isotopologues of Conformer 2	254
Table E.6.	Assigned rotational constants of the ^{13}C isotopologues of Conformer 1	255
Table E.7.	Assigned rotational constants of the ^{13}C isotopologues of Conformer 2	256
Table E.8.	C-atom coordinates for Conformer 1 and Conformer 2	256

Table F.1.	ωB97XD/Jun-cc-pVTZ level of theory refined CREST results of each hydrate within 5.0 kJ mol^{-1}	258
Table F.2.	B3LYP-D3BJ/def2-TZVP level of theory refined CREST results of each hydrate within 5.0 kJ mol^{-1}	259
Table F.3.	Spectroscopic Parameters of the ^{13}C and ^{18}O isotopologues of MC1-1W I	263
Table F.4.	Spectroscopic Parameters of the ^{18}O isotopologues of the MC2-1W II	264
Table F.5.	Spectroscopic Parameters of the ^{18}O isotopologues of the dihydrate	264
Table F.6.	Spectroscopic Parameters of the ^{18}O isotopologues of the trihydrate	265
Table F.7.	Structural parameters for the mono-, di-, and trihydrate species	265
Table F.8.	Geometries for monohydrates	266
Table F.9.	Geometry for Dihydrate species	266
Table F.10.	Geometry for Trihydrate species	267
Table F.11.	Geometry for Tetrahydrate species	267
Table F.12.	Geometry for Pentahydrate species	268
Table F.13.	Assigned rotational transitions for Monohydrate 1	269
Table F.14.	Assigned rotational transitions for Monohydrate 2	270
Table F.15.	Assigned rotational transitions for Dihydrate	271
Table F.16.	Assigned rotational transitions for Trihydrate	272
Table F.17.	Assigned rotational transitions for Tetrahydrate	273
Table F.18.	Assigned rotational transitions for Pentahydrate	274
Table F.19.	Assigned rotational transitions for MC1-1W I ^{18}O and ^{13}C isotopologues	275
Table F.20.	Assigned rotational transitions for MC2-1W II ^{18}O isotopologues	280
Table F.21.	Assigned rotational transitions for dihydrate ^{18}O isotopologues	280
Table F.22.	Assigned rotational transitions for trihydrate ^{18}O isotopologues	283
Table F.23.	ωB97XD/Jun-cc-pVTZ level of theory refined CREST results of monohydrate	288

Table F.24.	ωB97XD/Jun-cc-pVTZ level of theory refined CREST results of dihydrate	288
Table F.25.	ωB97XD/Jun-cc-pVTZ level of theory refined CREST results of trihydrate	289
Table F.26.	ωB97XD/Jun-cc-pVTZ level of theory refined CREST results tetrahydrate	290
Table F.27.	ωB97XD/Jun-cc-pVTZ level of theory refined CREST results of pentahydrate	292
Table F.28.	B3LYP-D3BJ/def2-TZVP level of theory refined CREST results of monohydrate	296
Table F.29.	B3LYP-D3BJ/def2-TZVP level of theory refined CREST results of dihydrate	296
Table F.30.	B3LYP-D3BJ/def2-TZVP level of theory refined CREST results of trihydrate	297
Table F.31.	B3LYP-D3BJ/def2-TZVP level of theory refined CREST results of tetrahydrate	299
Table F.32.	B3LYP-D3BJ/def2-TZVP level of theory refined CREST results of pentahydrate	301

List of Figures

Figure 1.1.	A schematic of the formation process of secondary organic aerosol particles	2
Figure 1.2.	Two examples of sources of conformational flexibility	4
Figure 2.1.	My experimental/theoretical workflow used to study the conformational landscapes of nucleation precursors and the non-covalent interactions within them	12
Figure 2.2.	A comparison of an energy level diagram and rotational spectrum of a linear top molecule and linear top molecule distorted by centrifugal distortion	13
Figure 2.3.	An energy level diagram and rotational spectrum of an asymmetric top molecule	14
Figure 2.4.	A section of the broadband rotational spectrum of *trans*-1-naphthol with all ten singly substituted ^{13}C isotopologues shown	15
Figure 2.5.	The simulated rotational spectrum of two different conformations of (-)-carveol where the conformations differ only by their orientation of their isopropenyl group	16
Figure 2.6.	An overview of the chirped pulse Fourier transform microwave spectrometer used in my research	19
Figure 2.7.	A schematic of the chirped pulse Fourier transform microwave spectrometer, with the pathways of the microwave radiation, transistor-transistor logic (TTL) pulses, and 10 MHz rubidium frequency standard	21
Figure 2.8.	An example of a non-covalent interactions analysis	25
Figure 3.1.	Broadband rotational spectra of 1-naphthol and 2-naphthol	35
Figure 3.2.	Atom number labelling for all four isomers of naphthol	37
Figure 3.3.	Potential energy curves and zero-pointed corrected *cis*-*trans* barriers for 1-naphthol and 2-naphthol	38
Figure 3.4.	Results from QTAIM analyses for the four experimentally observed isomers of naphthol	43

Figure 3.5.	Intrinsic bond strength indexes (IBSI) for the sum of the bonds in the heavy atom frame and bonds participating in the close-contact H-H interaction as a function of dihedral angle	45
Figure 3.6.	Power relationship between bond strength order (BSO) n and k^a of O-H bonds in naphthol isomers and reference molecules for B3LYP-D3(BJ) and MP2 calculations	48
Figure 3.7.	Atom labelling used in the descriptions of the H-H interactions	49
Figure 3.8.	Charge Model 5 (CM5) charges for atoms involved in the H-H interaction for all four naphthol isomers	50
Figure 3.9.	Natural Bond Orbital Analysis of naphthol isomers and biphenyl	52
Figure 3.10.	Results from non-covalent interactions (NCI) analyses of biphenyl	53
Figure 4.1.	Seven predicted 1-naphthol dimer structures optimized at the B3LYP-D3(BJ)/6-311++g(d,p) level of theory	63
Figure 4.2.	Experimental spectrum and simulated transitions for 1-naphthol dimer.	65
Figure 4.3.	Non-covalent interactions (NCI) analysis of the observed V-shape 1-naphthol dimer	69
Figure 4.4.	Experimental IR dip spectrum of the naphthol dimer from Saeki et al., in comparison to the B3LYP-D3(BJ)/6-311++g(d,p) harmonic vibrational spectra for the observed V-shape isomer	69
Figure 5.1.	Optimized structures for the anti-conformer and syn-conformer	79
Figure 5.2.	One-dimensional relaxed potential energy scans corresponding to rotation about the O-H---π intermolecular bond	81
Figure 5.3.	A potential energy curve for the anti-conformer water tunneling motion	84
Figure 5.4.	Two different potential energy curves for the syn-conformer water tunneling motion, obtained from the NEB-TS calculation at the B3LYP-D3(BJ)/Jun-cc-pVTZ level of theory	85
Figure 5.5.	The broadband rotational spectrum of the α-pinene water complex	86

Figure 5.6.	Results from non-covalent interactions (NCI) analyses of the syn- and anti-conformers	89
Figure 5.7.	Equilibrium constants and relative abundance plots for the syn- and anti-conformers	97
Figure 5.8.	Reaction pathway for ozonolysis of α-pinene, for ozone attacking from the anti- and syn-positions	99
Figure 5.9.	Reaction pathway for ozonolysis of α-pinene, with a water molecule non-covalently bound, for ozone attacking from the anti- and syn-positions	101
Figure 6.1.	*Cis* and *trans* configuration of (-)-carveol	108
Figure 6.2.	Carbon atom numbering of (-)-carveol with the Newman projections of the antiperiplanar, gauche -, and gauche + conformations of the isopropenyl group	110
Figure 6.3.	Graphical representation of a two-dimensional potential energy scan of the half-chair conformation of *trans* and *cis* (-)-carveol along the isopropenyl dihedral angle and the hydroxyl dihedral angle	112
Figure 6.4.	Broadband rotational spectrum of *cis* and *trans* (-)-carveol	118
Figure 6.5.	Isosurfaces of the reduced electron density gradient from NCI analyses of the five experimentally assigned conformers	123
Figure 7.1.	The three possible conformers of 3-methylcatechol	132
Figure 7.2.	A two-dimensional relaxed potential energy scan of the rotation of the two hydroxyl groups	133
Figure 7.3.	Isosurfaces of the reduced electron density gradient (s=0.7) from NCI analyses of the three conformers 3-methylcatechol	135
Figure 7.4.	Broad-band rotational spectrum of 3-methylcatechol	136
Figure 8.1.	A 2-6 GHz broadband rotational spectrum of 3-methylcatechol and water	148
Figure 8.2.	Potential energy scans of the water wagging motion for the water molecules in the tetrahydrate species	152

Figure 8.3.	Atom numbering of the tetrahydrate species for the atoms involved the dihedral energy scans	153
Figure 8.4	Four different conformations of the tetrahydrate species at the ωB97XD/Jun-cc-pVTZ level of theory.	153
Figure 8.5.	Two possible solvation pathways for 3-methylcatechol based on the conformer searches and electronic structure calculations	154
Figure 8.6.	Example transitions with characteristic tunneling splittings of the six hydrates assigned their respective NCI analyses	156
Figure 8.7.	A comparison of the 3-methylcatechol trihydrate and tetrahydrate to the corresponding pure water clusters	157
Figure A.1.	Non-covalent interactions plot of naphthol conformers	204
Figure A.2.	Decomposition plot for all normal modes of *cis*-1-naphthol	205
Figure A.3.	Decomposition plot for all normal modes of *trans*-1-naphthol	206
Figure A.4.	Vibrational displacement vectors for the O-H stretching motion	206
Figure A.5.	Lowest out-of-plane vibrational modes for *cis*-1-naphthol	209
Figure A.6.	Lowest out-of-plane vibrational modes for *trans*-1-naphthol	209
Figure A.7.	Lowest out-of-plane vibrational modes for *cis*-2-naphthol	210
Figure A.8.	Lowest out-of-plane vibrational modes for *trans*-2-naphthol	210
Figure A.9.	Inertial defect differences for the four isomers of naphthol compared to the results of Jahn et al.	211
Figure A.10.	CM5 charges for atoms involved in the biphenyl H-H interaction	212
Figure A.11.	Heavy atom steric exchange and donor-acceptor interaction energies	214
Figure B.1.	NCI plots and diagram for the V-shape isomer	217
Figure B.2.	NCI plots and diagram for the Saeki-a isomer	217
Figure B.3.	NCI plots and diagram for the Saeki-d isomer	218
Figure B.4.	NCI plots and diagram for the phenol dimer	218
Figure C.1.	An electrostatic plot of the α-pinene monomer	225
Figure C.2.	Inertial axis system for anti- and syn-conformer and the atom labelling for α-pinene and water	226

Figure C.3.	Potential energy scans for rotation about the O-H---π intermolecular bond of the anti-conformer at various levels of theory	228
Figure C.4.	Potential energy scans for rotation about the O-H---π intermolecular bond of the syn-conformer at various levels of theory	229
Figure C.5.	QTAIM analyses of syn- and anti- complexes	230
Figure C.6.	NCI analysis of the transition state for the C_2 motion	230
Figure C.7.	Scheme of an ozonolysis reaction with α-pinene	232
Figure D.1.	Boat and half-chair conformations of cyclohexane	237
Figure D.2.	QTAIM analyses of the five experimentally assigned conformers	238
Figure D.3.	Three hydrogen bond containing systems used for the NBO analyses	249
Figure F.1.	Examples of different types of aggregation	260
Figure F.2.	NCI analyses of the droplet aggregation conformers	261
Figure F.3.	QTAIM analyses of the five experimentally assigned hydrates	262
Figure F.4.	Carbon atom numbering	263

List of Symbols

A	Antiperiplanar conformation
$Ax_{I(H)}$	Axial conformation of isopropenyl (hydroxyl) group
A, B, C	Rotational Constants
(B)	Boat ring conformation of cyclohexene
BD	Bonding natural bond orbital
BD^*	Anti-bonding natural bond orbital
$BSO\ n$	Bond strength orders index
(C)	Chair ring conformation of cyclohexene
D_0	Dissociation energy
E_a	Activation energy
$E_{I(H)}$	Equiatorial conformation of isopropenyl (hydroxyl) group
E_J	Rotational energy levels of a linear top molecule
$G+$	Gauche + conformation
$G-$	Gauche - conformation
h	Planck's constant
$\hbar$	Reduced Planck's constant
$I_{a,\,b,\,c}$	Moments of inertia about principal axes
J	Rotational angular momentum quantum number
$K_{a(c)}$	Quantum number at the oblate (prolate) limit
K_p	Equilibrium constant
k	Rate constant
k^a	Local stretching force constant
k_b	Boltzmann constant
LP	Lonepair natural bond orbital
m_i	Mass of atom i

$\|P\|$	Magnitude of the polarization response
p_a	Ambient atmospheric pressure
$p(H_2O)$	Partial pressure of water
Q_X	Partition function for species X
R	Gas constant
r_e	Equilibrium structure
r_i	The distance between atom i and the $a, b,$ or c principal inertial axis.
r_0	Effective structure
r_s	Substitution structure
r_{se}	Semi-experimental strcuture
$s(r)$	Reduced density gradient
T	Temperature
V_3	The height of the three-fold barrier of internal rotation
Δ	Inertial defect
Δ_J, Δ_{JK}, Δ_K, δ_J, and δ_K	Quartic centrifugal distortion constants
ΔE	Relative Energy
ΔE_0	Relative zero-point corrected energy
ΔN_0	Initial population difference of a two-level system
δ	The angle between the internal rotor axis and the a-axis
ε	Electric field (Chapter 2)
ε	Bond ellipticity (Chapters 3/5)
ε	The angle between the *b*-principal inertial axis and the projection of the internal rotor axis onto the *bc*-inertial plane (Chapters 7/8)
$\mu_{a,b,c}$	Dipole moment components
μ_{ab}	Transition dipole moment
$\rho(r)$	Electron density

$\nabla\rho$	Gradient of the electron density
σ	Root mean square error of fit
χ	Relative hydrate abundance

List of Abbreviations

AWG	Arbitrary waveform generator
BCP	Bond critical point
BSSE	Basis set superposition error
B3LYP	Becke, 3-parameter, Lee-Yang-Parr
CC	Coupled cluster
CP	Chirped pulse
CP-FTMW	Chipred pulse Fourier transform microwave
CMO	Canonical molecular orbital
CM5	Charge Model 5
CNM	Characterization of normal modes
CREST	Conformer-rotamer ensemble sampling tool
DFT	Density functional theory
D3BJ	Dispersion correction and Becke-Johnson damping function
FID	Free induction decay
FTMW	Fourier transform microwave
GFN2-xTB	Geometry, Frequency, Noncovalent, eXtended Tight binding
GVPT2	Generalized second order vibrational perturbation theory
IBSI	Intrinsic Bond Strength Index
IGM	Independent Gradient Model
LNA	Low noise amplifier
MC	3-methylcatechol
MP2	Møller-Plesset second order perturbation theory
NBO	Natural bond orbitals
NCI	Non-covalent interactions
NRT	Natural resonance theory

OSC	Oscilloscope
PL	Power limiter
QTAIM	Quantum theory of atoms-in-molecules
RCP	Ring critical point
SMA	Subminiature version A
SOA	Secondary Organic Aerosol
SPST	Single-pull single-throw
STP	Standard Temperture and Pressure
STQN	The synchronous transit quasi-newton method
TTL	Transistor-transistor logic
TWTA	Travelling wave tube amplifier
VOC	Volatile Organic Compound
ZPE	Zero-point energy
3MC	3-methylcatechol

1

Introduction

Contents

1.1. Atmospheric Aerosol and Secondary Organic Aerosol Particles · · · · · · · · · 1
1.2. Initial Stages of Nucleation · 2
1.3. Conformational Flexibility · 3
1.4. Rotational Spectroscopy and Computational Chemistry · · · · · · · · · · · · 5
1.5. Thesis Structure · 6
1.6. References · 7

1.1. Atmospheric Aerosol and Secondary Organic Aerosol Particles

Atmospheric aerosol consists of solid or liquid particles suspended in air, with sizes ranging from a few nanometers to several micrometers. Atmospheric aerosol particles can, among other things, have detrimental effects on human physiology and the environment. For example, when inhaled, aerosol particles can have damaging effects throughout the human respiratory tract, and can lead to pulmonary disease, lung cancer, and cardiovascular disease.[1] When in the atmosphere, aerosol particles have the ability to both scatter and absorb incoming solar radiation and can thus directly influence Earth's energy budget,[2] ultimately leading to net cooling or warming effects on our climate. Aerosol particles can also indirectly influence Earth's energy budget, as they can serve as nuclei for the condensation of water droplets. These hydrated particles, or cloud condensation nuclei, are the starting points for the formation of clouds.[3] Clouds possess a high albedo, and thus reflect a significant portion of solar radiation back into space.[4]

Atmospheric aerosol particles can be directly released into the air, or formed in the atmosphere via photochemical reactions between emitted gaseous molecules and other atmospherically relevant molecules.[5] The initial gaseous species can either be biogenic, such as terpenes released from forests,[6] or anthropogenic, such as polycyclic aromatic hydrocarbons released from industrial processes.[7] In many instances, the initial source of different types of particles are known, but the exact chemical makeup of atmospheric aerosol particles is difficult to

decipher as they can be, for instance, comprised of sulfates, organic carbon, black carbon, nitrates, mineral dust, and sea salt.[8] The chemical composition of aerosol particles can drastically change their physical properties, such as morphology and optical properties.[9] For example, sea-spray particles, which are predominately composed of sodium chloride, adopt a cubic-like morphology[10] and possess extremely high single scattering albedo values,[11] while soot particles, which are composed predominantly of black carbon, adopt a grape-like cluster morphology[12] and possess low single scattering albedo values.[13] In the atmosphere, these particles are often mixed together to form compositionally complex hybrid particles, drastically changing their physical properties relative to their initial state.[9] For example, soot particles are often coated with particles known as secondary organic aerosol (SOA), which changes both the morphology[14] and optical properties[15] of the new particle. SOA particles are formed when volatile organic compounds (VOCs) are photo-oxidized by various species, such as nitrous oxides, ozone, and oxygenated radicals, to form low volatile species or oxygenated hydrocarbons, which aggregate with other atmospheric molecules, such as sulfuric acid, ammonia, and water to form SOA particles.[16–18] Despite their significance, several aspects of aerosol particles, such as ageing in the atmosphere, optical properties, and more pertinent to my work, the initial stages of formation, are still not fully understood.

1.2. Initial Stages of Nucleation

Generally, SOA formation consists of two phases: nucleation and growth.[19] In the nucleation process, gaseous molecular species, such as oxygenated hydrocarbons, begin to cluster with other species, water for example, forming molecular clusters containing only a few molecules, where they begin to further aggregate as part of the growth phase to form SOA particles (Figure 1.1). These small molecular clusters involved in the early stages of nucleation are held together by intermolecular or non-covalent interactions, such as hydrogen bonds or van der Waals

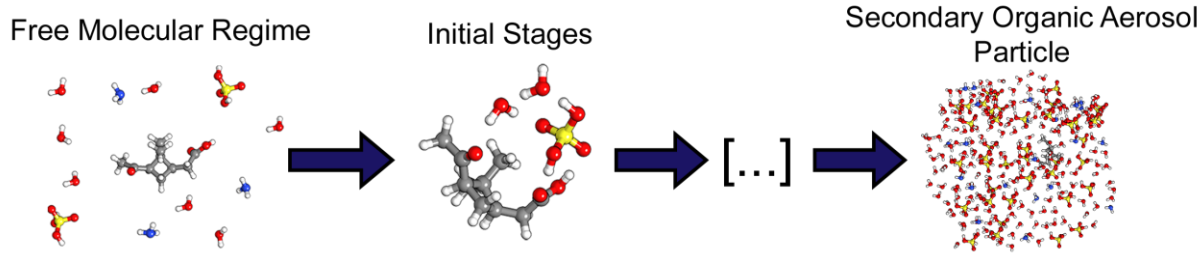

Figure 1.1. A schematic of the formation process of secondary organic aerosol particles. No interactions are present between molecules in the free molecular regime, while the molecules within the proposed intermediate are held together by intermolecular interactions.

interactions,[20] and are a pivotal step in the formation of SOA particles. Possessing a deeper understanding of these molecular cluster can provide insights into the transition from the free molecular regime to macroscopic particles.[21] Several techniques have already been developed to theoretically model this transition, such as classical nucleation theory,[22] but struggle with the modelling of clusters with only a few molecules aggregated together.[23] This is because the non-covalent interactions which hold these clusters together, as well as the tunnelling processes occurring within the clusters, are inherently quantum mechanical, and classical approaches cannot model these phenomena with sufficient accuracy. As the thermodynamics and kinetics of classical nucleation theory is based on the free energies of the cluster/particle,[24] it is imperative that accurate energetic data is available to better benchmark these methods for the initial stages of nucleation. More refined theoretical methods can in turn be used to better model aerosol particle formation both in the laboratory and atmospheric setting. However, obtaining accurate energetic data is extremely challenging, as it is not only difficult to elucidate the structure of the molecular clusters involved in the initial stages of nucleation, but also difficult to determine which of the many possible structures are abundant enough to be atmospherically relevant. These difficulties arise from the high compositional and conformational variability of the clusters, which are often accompanied by a complex network of intermolecular interactions.[19]

1.3. Conformational Flexibility

Conformations are a type of stereoisomer (same molecular formula and atom connectivity) which differ by the spatial positioning of atoms. Conformations which correspond to a minimum on a potential energy surface are known as conformers. Different conformers can interconvert between each other through movement along a particular reaction coordinate. For example, different conformers of a monomer may interconvert between each other through a dihedral angle rotation, a rink puckering movement, or a combination of both movements. Different conformers of a molecular cluster may not only vary by the conformation of their monomer subunits, but also the spatial position of each subunit relative to each other. The spatial positioning of each subunit is dictated by the non-covalent interactions within the system. For example, a water molecule interacting with a methanol molecule may serve as a hydrogen bond donor or acceptor species resulting in different conformers. In the case of molecular clusters, although the different non-covalent interactions may change the atom connectivity between molecules, the covalent bonds

within each monomer subunit remain unchanged. The different spatial positioning of monomer subunits in a cluster are therefore still considered conformers because the atom connectivity within each monomer does not change. If a molecule or molecular cluster possesses several different conformers, it can be described as being conformationally flexible. This is the case for the majority of molecular clusters in the initial stages of nucleation, especially for clusters containing oxygenated hydrocarbons, as they often possess several flexible dihedral angles, multiple hydrogen bond donor/acceptor sites, and π-systems that can be involved in dispersion interactions (Figure 1.2). Carveol (Chapter 6), for example, is an oxygenated hydrocarbon and has four different chiral configurations, two different ring conformations, and two flexible substituents, which may be either equatorial or axial, and can be in the antiperiplanar, gauche +/- conformers. This results in approximately 150 different conformers of the monomer alone. The number of conformers increases when monomers aggregate to form molecular clusters. For example, in a cluster of 3-methylcatechol (3MC) aggregated with five water molecules (Chapter 8), over 200 theoretical conformers within a 40 kJ mol^{-1} energetic window were generated. As the monomer subunits of the cluster are not conformationally flexible (three conformers for 3MC and one conformer for water) the number of conformers in this instance is a result of the non-covalent

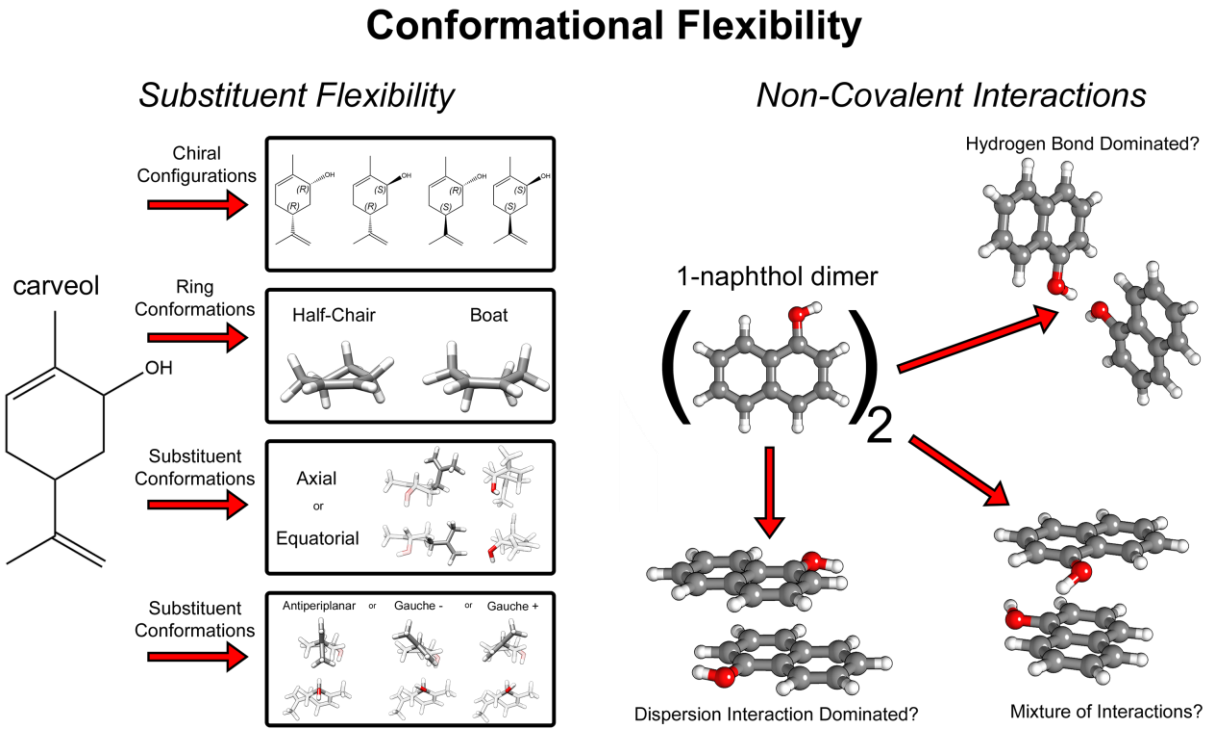

Figure 1.2. Two examples of sources of conformational flexibility. Carveol is an example of how substituents can be responsible for conformational flexibility and 1-naphthol dimer is an example of how non-covalent interactions can be responsible for conformational flexibility.

interactions present, and the many ways the monomers can orientate themselves within the cluster. Determining how the non-covalent interactions influence the structure can be difficult as oftentimes there is a competition between different intermolecular interactions, for example, between hydrogen bonding and dispersion interactions.[25] One can imagine how complicated these clusters can become if in addition to the network of non-covalent interactions, conformationally flexible monomer subunits are included in the complex. Therefore, elucidating the structures of conformers can be a daunting task, where each one of these conformers will have an impact on the energetics of the system, and will thus have direct effects on the nucleation process.

1.4. Rotational Spectroscopy and Computational Chemistry

To properly characterize these structurally complex clusters, a technique with high resolution and selectivity is needed. Rotational spectroscopy is well suited to deal with molecular structure studies because the geometric distribution for a polyatomic molecule is encoded within the respective spectrum. The incredible resolving power allows one to easily and unambiguously identify chemical species in a complex mixture, and in no other spectroscopy is the relationship between the spectrum and geometric structure so precise. This makes rotational spectroscopy well suited to identify and determine the structures of different conformers of molecular clusters involved in the initial stages of nucleation.[26,27] Just as a figure skater increases or decreases the frequency of rotation by contracting or extending their arms (altering their structure), the structure of a molecule or molecular cluster can be derived, with high precision, by studying the respective rotational frequencies. Where previous studies have failed in structure identification,[28] rotational spectroscopy has correctly identified the structure and intermolecular interplay within complexes, for example, in the dimer of naphthol,[25] a polycyclic aromatic hydrocarbon (see Figure 1.2). This high resolving power derives in part from cooling of the molecular system of interest, such that only the lower rotational states are populated. This is achieved by a pulsed molecular expansion into vacuum, which cools the sample to a rotational temperature of about 1 K.[29] This allows for effective probing of structures that would otherwise be difficult or impossible to observe at STP conditions. In addition to the experimental techniques, I have also utilized high level electronic structure calculations, such as density functional theory,[30] perturbation theory,[31] and coupled cluster methods,[32] to predict structures and conformer energies to support the experimental

identification of the molecular clusters involved in the initial stages of nucleation, as well as further study other physical properties of the clusters such as interaction energies.

1.5. Thesis Structure

In this thesis, I describe my work studying the conformational landscapes of molecules and molecular clusters involved in the initial stages of nucleation and the non-covalent interactions within them, using rotational spectroscopy and computational chemistry. These molecular clusters involved in the initial stages of nucleation can be composed of several different molecules, *e.g.* water,[33] ammonia,[34] sulfuric acid,[20] oxygenated hydrocarbons,[19] metals,[35] and/or inorganic compounds.[36] However, to create and study precursors with these molecules simultaneously is extremely challenging. To simplify this problem, I not only study oxygenated hydrocarbon monomers, but also their aggregates with water, one of the most abundant molecular species in the atmosphere. In addition to enabling the removal of the monomer transitions from the spectrum, allowing for a more clear identification of the cluster transitions, studying the monomers prior to the clusters is advantageous as possessing knowledge of the thermodynamic abundances of different monomer conformers will provide insights into the structure of the molecular cluster.

In Chapter 2 I describe the principles of rotational spectroscopy, and how I measure the rotational spectrum of monomers and molecular aggregates using a chirped pulse Fourier transform microwave (CP-FTMW) spectrometer. I also outline some of the theoretical techniques used throughout my work to assign the rotational quantum numbers of molecular aggregates and monomers to the measured transitions in the rotational spectrum. In Chapter 3 I describe a CP-FTMW spectroscopic and computational study of two different isomers of naphthol,[37] a polycyclic aromatic hydrocarbon, which is a known SOA precursor[38] and also used commonly in the insecticide industry.[39] Here I show that even in its monomeric form, it can be challenging to correctly characterize non-covalent interactions. The data obtained from this study is then used to investigate the 1-naphthol dimer (Chapter 4), where a competition between π-π stacking and hydrogen bonding interactions is present.[25] In Chapter 5 I describe the investigation of α-pinene, one of the most abundant biogenic VOCs released into the atmosphere,[40] complexed with one water molecule using CP-FTMW spectroscopy and computational chemistry. Here I not only show that this complex has an interesting network of intermolecular interactions, but also how various internal dynamics, such as a large amplitude motion, can influence the structure of the complex.

In Chapter 6, I discuss my CP-FTMW spectroscopic and computational study of (-)-carveol,[41] a photooxidation product of limonene,[42,43] which, in addition to providing insights into the complexity of the conformational dynamics within monoterpenes and monoterpenoids, also lays a foundation for future studies examining carveol containing molecular clusters involved in the initial stages of nucleation. In Chapter 7, I investigate the different conformers of 3-methylcatechol monomer,[44] a molecule released by vegetation during biomass burning,[45–47] using CP-FTMW spectroscopy and computational chemistry. I then use the structural and conformational data obtained from the monomer study in Chapter 8, where I investigate the microsolvation pathway of 3-methylcatechol. Finally, in Chapter 9, I summarize some of the key results from each chapter and describe their impact on the field of aerosol science.

1.6 References

1 U. Pöschl, *Angew. Chem. Int. Ed.*, 2005, **44**, 7520–7540.

2 D. Rosenfeld, S. Sherwood, R. Wood and L. Donner, *Science*, 2014, **343**, 379–380.

3 J. Sun and P. A. Ariya, *Atmos. Environ.*, 2006, **40**, 795–820.

4 R. J. Charlson, J. E. Lovelock, M. O. Andreae and S. G. Warren, *Nature*, 1987, **326**, 655–661.

5 C. Tomasi and A. Lupi, *Atmospheric Aerosols Life Cycles Eff. Air Qual. Clim.*, 2017, 1–86.

6 V. A. Isidorov, I. G. Zenkevich and B. V. Ioffe, *Atmospheric Environ. 1967*, 1985, **19**, 1–8.

7 K. Nikolaou, P. Masclet and G. Mouvier, *Sci. Total Environ.*, 1984, **32**, 103–132.

8 V. A. Lanz, A. S. H. Prévôt, M. R. Alfarra, S. Weimer, C. Mohr, P. F. DeCarlo, M. F. D. Gianini, C. Hueglin, J. Schneider and O. Favez, *Atmospheric Chem. Phys.*, 2010, **10**, 10453–10471.

9 R. Zhang, A. F. Khalizov, J. Pagels, D. Zhang, H. Xue and P. H. McMurry, *Proc. Natl. Acad. Sci.*, 2008, **105**, 10291–10296.

10 W. Li, L. Shao, D. Zhang, C.-U. Ro, M. Hu, X. Bi, H. Geng, A. Matsuki, H. Niu and J. Chen, *J. Clean. Prod.*, 2016, **112**, 1330–1349.

11 E. Andrews, P. J. Sheridan, J. A. Ogren, D. Hageman, A. Jefferson, J. Wendell, A. Alástuey, L. Alados-Arboledas, M. Bergin and M. Ealo, *Bull. Am. Meteorol. Soc.*, 2019, **100**, 123–135.

12 K. Adachi, S. H. Chung and P. R. Buseck, *J. Geophys. Res. Atmospheres*., 2010, 115, D15206

13 Y. F. Cheng, M. Berghof, R. M. Garland, A. Wiedensohler, B. Wehner, T. Müller, H. Su, Y. H. Zhang, P. Achtert and A. Nowak, *J. Geophys. Res. Atmospheres*., 2009, 225, D00G10.

14 E. G. Schnitzler, A. Dutt, A. M. Charbonneau, J. S. Olfert and W. Jäger, *Environ. Sci. Technol.*, 2014, **48**, 14309–14316.

15 G. Saliba, R. Subramanian, R. Saleh, A. T. Ahern, E. M. Lipsky, A. Tasoglou, R. C. Sullivan, J. Bhandari, C. Mazzoleni and A. L. Robinson, *Aerosol Sci. Technol.*, 2016, **50**, 1264–1276.

16 J. H. Kroll, N. L. Ng, S. M. Murphy, R. C. Flagan and J. H. Seinfeld, *Environ. Sci. Technol.*, 2006, **40**, 1869–1877.

17 J. H. Kroll and J. H. Seinfeld, *Atmos. Environ.*, 2008, **42**, 3593–3624.

18 S. N. Pandis, R. A. Harley, G. R. Cass and J. H. Seinfeld, *Atmospheric Environ. Part Gen. Top.*, 1992, **26**, 2269–2282.

19 R. Zhang, *Science*, 2010, **328**, 1366–1367.

20 J. Zhao, A. Khalizov, R. Zhang and R. McGraw, *J. Phys. Chem. A*, 2009, **113**, 680–689.

21 C. Li and R. Signorell, *J. Aerosol Sci.*, 2021, **153**, 105676.

22 V. I. Kalikmanov, in *Nucleation theory*, Springer, 2012, 17–41.

23 A. B. Nadykto, A. Al Natsheh, F. Yu, K. V. Mikkelsen and J. Herb, *Adv. Quantum Chem.*, 2008, **55**, 449–478.

24 A. Afzalifar, G. C. Shields, V. R. Fowler and R. H. Ras, *J. Phys. Chem. Lett.*, 2022, **13**, 8038–8046.

25 N. A. Seifert, A. S. Hazrah and W. Jäger, *J. Phys. Chem. Lett.*, 2019, **10**, 2836–2841.

26 G. B. Park and R. W. Field, *J. Chem. Phys.*, 2016, **144**, 200901.

27 T. Shou-Yuan, X. Zhi-Ning, F. Yu-Jie and G. Qian, *Chin. J. Anal. Chem.*, 2008, **36**, 1145–1151.

28 M. Saeki, S. Ishiuchi, M. Sakai, and M. Fujii, *J. Phys. Chem. A*, 2007, **111**, 1001–1005.

29 N. Dam, C. Liedenbaum, S. Stolte and J. Reuss, *Chem. Phys. Lett.*, 1987, **136**, 73–80.

30 W. Kohn, A. D. Becke and R. G. Parr, *J. Phys. Chem.*, 1996, **100**, 12974–12980.

31 Chr. Møller and M. S. Plesset, *Phys. Rev.*, 1934, **46**, 618–622.

32 R. J. Bartlett and M. Musiał, *Rev. Mod. Phys.*, 2007, **79**, 291.

33 E. G. Schnitzler and W. Jäger, *Phys. Chem. Chem. Phys.*, 2014, **16**, 2305–2314.

34 M. E. Erupe, D. R. Benson, J. Li, L.-H. Young, B. Verheggen, M. Al-Refai, O. Tahboub, V. Cunningham, F. Frimpong and A. A. Viggiano, *J. Geophys. Res. Atmospheres*., 2010, 115, D23216

35 E. G. Moody and L. R. Collins, *Aerosol Sci. Technol.*, 2003, **37**, 403–424.

36 S. Zhang, S. Li, A. Ning, L. Liu and X. Zhang, *Phys. Chem. Chem. Phys.*, 2022, **24**, 13651–13660.

37 A. S. Hazrah, S. Nanayakkara, N. A. Seifert, E. Kraka and W. Jäger, *Phys. Chem. Chem. Phys.*, 2022, **24**, 3722–3732.

38 A. W. H. Chan, K. E. Kautzman, P. S. Chhabra, J. D. Surratt, M. N. Chan, J. D. Crounse, A. Kürten, P. O. Wennberg, R. C. Flagan and J. H. Seinfeld, *Atmospheric Chem. Phys.*, 2009, **9**, 3049–3060.

39 N. E. Stewart, R. E. Millemann and W. P. Breese, *Trans. Am. Fish. Soc.*, 1967, **96**, 25–30.

40 A. Zare, J. H. Christensen, A. Gross, P. Irannejad, M. Glasius and J. Brandt, *Atmospheric Chem. Phys.*, 2014, **14**, 2735–2756.

41 A. S. Hazrah, M. Al-Jabiri, R. Speelman and W. Jäger, *Phys. Chem. Chem. Phys.*, 2021, **23**, 15159–15168.

42 F. M. N. Nunes, M. C. C. Veloso, P. A. de P. Pereira and J. B. de Andrade, *Atmos. Environ.*, 2005, **39**, 7715–7730.

43 T. E. Graedel, *Rev. Geophys.*, 1979, **17**, 937–947.

44 A. S. Hazrah, M. H. Al-Jabiri and W. Jäger, *J. Mol. Spectrosc.*, 2022, **390**, 111715.

45 M. S. Ganewatta, H. N. Lokupitiya and C. Tang, *Polymers*, 2019, **11**, 1176.

46 M. Asmadi, H. Kawamoto and S. Saka, *J. Anal. Appl. Pyrolysis*, 2011, **92**, 88–98.

47 A. N. Glazer and H. Nikaido, *Microbial biotechnology: fundamentals of applied microbiology*, Cambridge University Press, 2007.

2

Experimental and Theoretical Methods

Contents

2.1. Introduction · · · · · 10
2.2. Rotational spectroscopy · · · · · 12
2.2.1. Rotational Energy Levels and Rotational Constants · · · · · 13
2.2.2. Centrifugal Distortion Effect · · · · · 17
2.3. Molecular Beam Technique · · · · · 17
2.4. Chirped Pulse Fourier Transform Microwave Spectroscopy · · · · · 19
2.4.1. Excitation and Detection · · · · · 20
2.4.2. Transistor-Transistor Logic (TTL) Pulses and Timing · · · · · 21
2.5. Theoretical Techniques · · · · · 22
2.5.1. Conformational Ensemble Search · · · · · 23
2.5.2. Electronic Structure Calculations · · · · · 23
2.6. Assignment Process · · · · · 24
2.7. Non-covalent Interactions Analyses · · · · · 25
2.8. References · · · · · 26

2.1. Introduction

Rotational spectroscopy is a field that is nearly a century old and, in its infancy, was restricted to the measurement of a few rotational transitions of small molecules.[1] In the 1980s, the development of the Balle-Flygare microwave spectrometer,[2] more commonly known as the cavity Fourier transform microwave spectrometer (FTMW), greatly improved the ability to measure numerous rotational transitions for not only large polyatomic molecules, but also molecular clusters. The cavity FTMW technique utilizes a Fabry-Perot cavity to amplify a single frequency of microwave radiation, resulting in drastic improvements in sensitivity and spectral resolution. However, the narrowband nature of the technique makes it tedious when studying a wide frequency range of rotational transitions. The systems studied in Chapters 3-8, for example, possess hundreds of transitions across several GHz, which may take days to weeks to measure with the cavity FTMW spectrometer. Made possible by the technological advancements in radio wave/microwave

electronics, such as amplifiers, arbitrary waveform generators, and high-speed digitizers, the invention of chirped-pulse Fourier transform microwave (CP-FTMW)[3] spectroscopy has allowed us to overcome this problem of slow acquisition time. In the CP-FTMW technique, the molecular ensemble is irradiated with a broadband of frequencies in a single excitation pulse, turning what would take several months to acquire into a single overnight average. The development of CP-FTMW spectroscopy has also expanded the size range of systems we can study, for example, molecular clusters containing several molecules or different molecular conformers of a conformationally flexible molecule.

As a molecule and molecular cluster may adopt several different conformers, the broadband rotational spectra obtained from CP-FTMW spectroscopy are dense with rotational transitions from different conformers of monomers and molecular clusters. For example, (-)-carveol (Chapter 6) has two chiral centers, two different ring conformers, and two flexible substituents, which may be either equatorial or axial, and can be in the antiperiplanar, gauche +/- conformers, resulting in 72 potentially detectable conformers. The number of conformers one has to consider increases when monomer subunits aggregate to form molecular clusters. To aid in the spectroscopic assignment of the many potential conformers detectable in a rotational spectrum, I utilize computational chemistry to generate an array of trial structures.

In general, with the improvements of experimental techniques and technology, it has now become quicker and easier to obtain spectra, resulting in experimental spectroscopists relying more on theory to help decipher the vast quantity of measured data. As a consequence, the notion of experimental spectroscopy remaining purely experimental is changing, as the field is now transforming itself into a hybrid of experimental and theoretical techniques.

In this chapter, I describe how I use a hybrid approach of experimental and theoretical techniques to study the conformational landscapes of the molecular clusters involved in the initial stages of nucleation and the non-covalent interactions within them. Figure 2.1 outlines the workflow of a research project. In Section 2.2, I provide a brief overview of rotational spectroscopy. In Section 2.3, I describe how a molecular beam expansion is used to prepare and introduce the sample into the spectrometer prior to the irradiation process. In Section 2.4, I briefly describe the CP-FTMW spectrometer used in my work, and how it is utilized to obtain a broadband rotational spectrum. In Section 2.5, I describe how I used several computational techniques, such as the conformer-rotamer ensemble sampling tool (CREST)[4] and electronic structure calculations, to

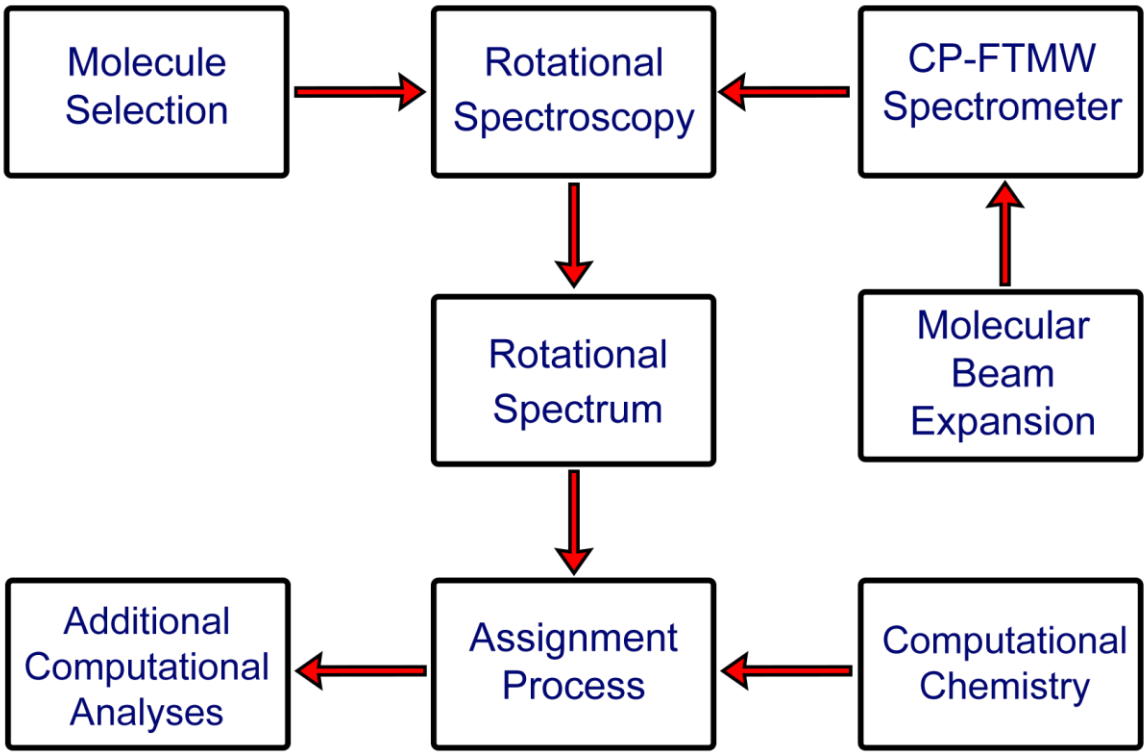

Figure 2.1. My experimental/theoretical workflow used to study the conformational landscapes of the molecular clusters involved in the initial stages of nucleation, and the non-covalent interactions within them.

assist me in the assignment of the rotational quantum numbers to the experimentally measured transition frequencies. This assignment process is discussed in Section 2.6. Once the assignment process is complete, additional computational analyses are carried out to further characterize the molecular system of interest. In Section 2.7, I briefly describe the non-covalent interactions (NCI) analyses,[5,6] one of the most prevalent computational analyses used in my work.

2.2. Rotational Spectroscopy

Rotational spectroscopy is used to study the structure of gas phase molecules and molecular clusters. Conceptually, rotational spectroscopy probes the spatial mass distribution of molecules by directly measuring transition frequencies between quantized rotational states of the molecular system. Here, I will briefly discuss the derivation of rotational constants, their relevance to a rotational spectrum, and how they are determined experimentally.

2.2.1. Rotational Energy Levels and Rotational Constants

Rotational constants describe the spatial mass distribution along each principal inertial axis, and are related to the respective moments of inertia by Equation (2.1):

$$A = \frac{h^2}{8\pi I_a};\ B = \frac{h^2}{8\pi I_b};\ C = \frac{h^2}{8\pi I_c} \tag{2.1}$$

where h is Planck's constant, A, B, and C are the rotational constants along the a, b, and c axis, respectively, of the principal inertial axis system. The principal moments of inertia along each axis (I_a, I_b, and I_c) are given by the following equation:

$$I_{a,b,c} = \sum_i m_i r_i^2 \tag{2.2}$$

where m_i is the mass of atom i, and r_i is the distance between atom i and the a, b, or c principal inertial axis.

Using the rotational constants, all molecules can be classified under one of five different rotor categories: linear top, spherical top, oblate top, prolate top, and asymmetric top. The categorization of a molecule is important as each rotor type will have its own unique energy level diagram and quantum numbers. For example, the rotational energy levels of a linear top molecule ($I_a = 0, I_b = I_c$) are given by:

$$E_J = BJ(J+1) = \frac{h^2}{8\pi I} J(J+1) \tag{2.3}$$

where J is the rotational angular momentum quantum number. The energy level diagram and resulting rotational spectrum for a linear top molecule is shown in Figure 2.2. As one can see, the energies of the rotational levels and rotational transition frequencies are multiples of the rotational

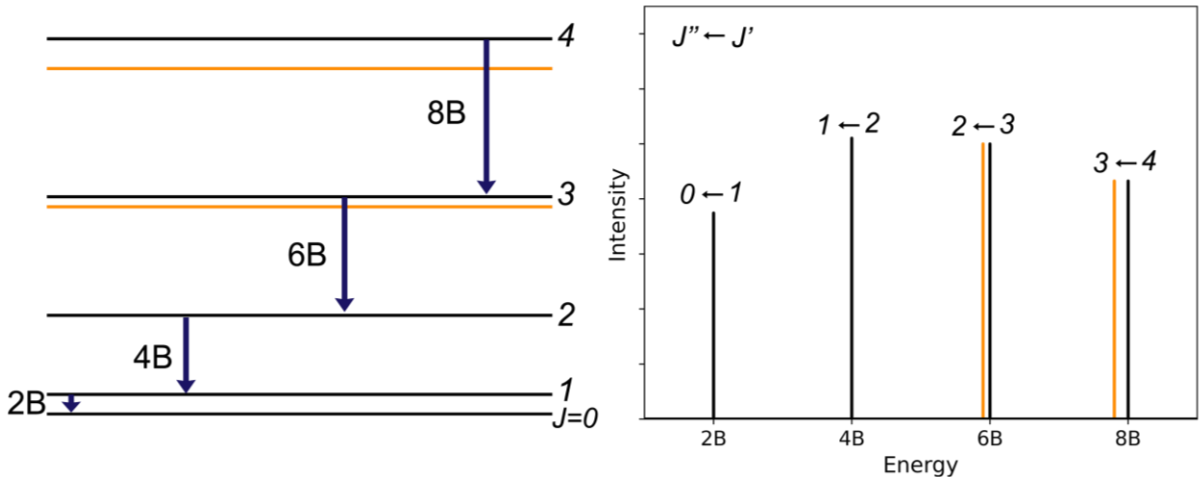

Figure 2.2. A comparison of an energy level diagram and rotational spectrum of a linear top molecule (black) and linear top molecule distorted by centrifugal distortion (orange).

constant B. Therefore, by measuring rotational transitions and then assigning quantum numbers to them, one can directly determine rotational constants from experiment. However, the energy level diagram and rotational spectrum can be more complicated than in the linear top case. Most molecules are asymmetric top molecules, where each rotational constant is unique from each other ($A > B > C$). This is the case for every molecular system studied in Chapters 3-8. In the asymmetric top molecule case the determination of the rotational energy levels is a more involved process, which is shown in great detail in Gordy and Cook.[7] For an asymmetric top molecule, the resulting energy levels are labelled with J, and two new quantum numbers, K_a and K_c, which correlate to the limits of a prolate and oblate symmetric top molecule, respectively. In symmetric top molecules K is a good quantum number as the projection of the total angular momentum vector onto the symmetry axis of the molecule is conserved. In asymmetric top molecules K is not a good quantum number as its projection on any axis is no longer a constant of motion. Figure 2.3 presents the energies for the lowest three J states of an asymmetric rotor. Despite this added complexity in the asymmetric top case, the determination of the rotational constants from the experimental spectrum is similar to the linear top case. I assign quantum numbers to as many rotational transitions as possible, which are now linear combinations of the A, B, and C rotational constants, and then perform a least-squares fit to obtain experimentally determined rotational constants. Several software packages are used in my work for the assignment and fitting process, where the choice of the software package is dependent on the molecular system. For the majority of my work

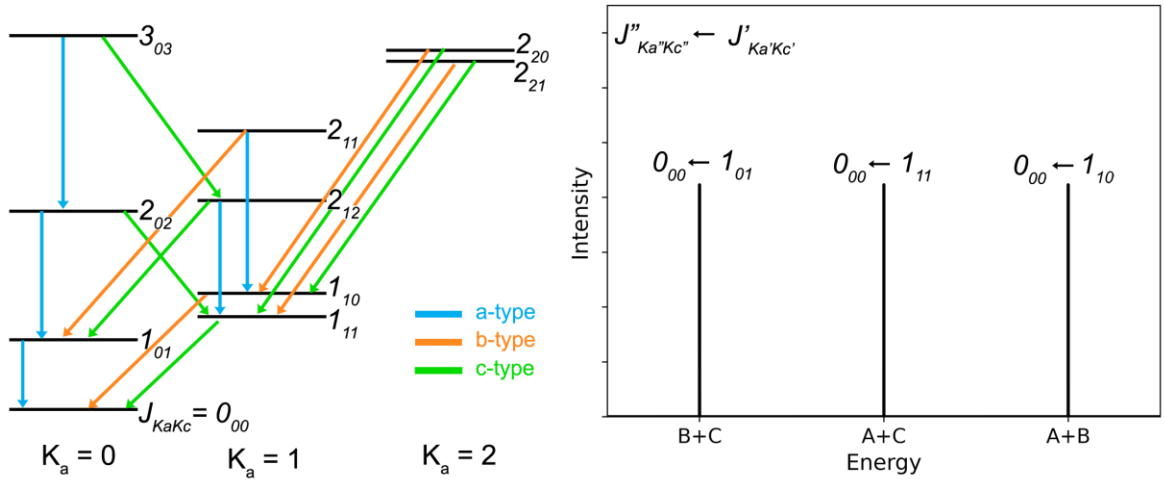

Figure 2.3. An energy level diagram and rotational spectrum of an asymmetric top molecule.

I use the SPCAT/SPFIT program suite[8] for spectral fitting. However, when hindered motions are present, such as methyl internal rotation, I use additional spectral fitting programs such as XIAM.[9]

In addition to the frequency of the transition, the rotational selection rules are also taken into account when assigning quantum numbers to each rotational transition. The rotational selection rules, which are dependent on the electric dipole moment components, provide us information on the allowed or forbidden transitions. For microwave radiation to induce a rotational excitation in a molecule, the molecule must possess a permanent electric dipole moment. An asymmetric molecule, for example, may have a different electric dipole moment component along each axis of the principal inertial axis system (μ_a, μ_b, μ_c). The selection rules for an a-type transition to occur, $\mu_a \neq 0$, are that K_a must change by even increments ($\Delta K_a = 0, \pm 2, ...$) and K_c must change by odd increments ($\Delta K_c = 1, \pm 3, ...$) For example, a typical a-type transition observed for an asymmetric molecule, $J''_{K_a K_c} \leftarrow J'_{K_a K_c}$, would be $1_{01} \leftarrow 0_{00}$. For a b-type transition, $\mu_b \neq 0$, the selection rules are K_a and K_c must change by odd increments ($\Delta K_{a\&c} = 1, \pm 3, ...$). Take the $1_{11} \leftarrow 0_{00}$ transition as an example. Finally, for a c-type transition, $\mu_c \neq 0$, to occur K_a must change by odd increments ($\Delta K_a = 1, \pm 3, ...$) and K_c must change by even increments ($\Delta K_c = 0, \pm 2, ...$). For example, $1_{10} \leftarrow 0_{00}$. As the intensity of a rotational transition is proportional to the square of the transition dipole moment, the electric dipole moment components

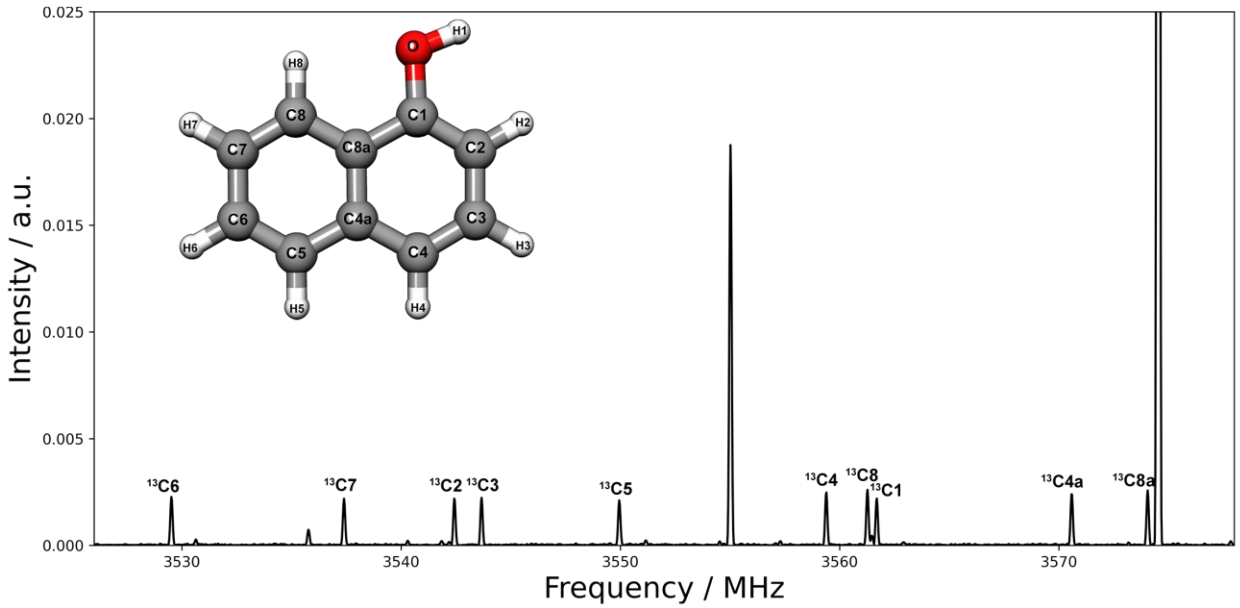

Figure 2.4. A section of the broadband rotational spectrum of *trans*-1-naphthol with all ten singly substituted ^{13}C isotopologues shown.

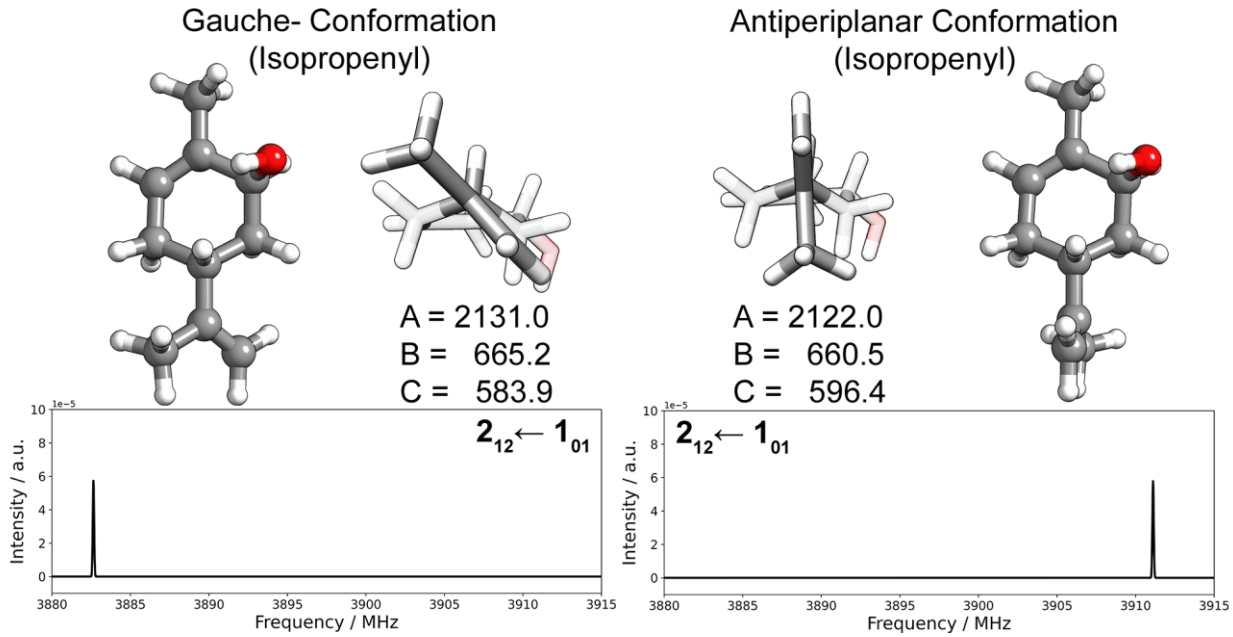

Figure 2.5. Simulated rotational spectra of two different conformers of (-)-carveol. The conformers differ only by their orientation of their isopropenyl group.

also provide information on the relative intensity of each transition, a vital piece of information when assigning a rotational spectrum.

The rotational constants are extremely sensitive to mass and structural changes, making them well suited to distinguish between different conformers of atmospherically relevant molecules and molecular clusters. For example, in Chapter 3, I describe my study of naphthol isomers,[10] where the assignment of all singly substituted ^{13}C isotopologues in natural abundance could be achieved. This single isotope substitution results in a ≈0.7% mass change and, as shown in Figure 2.4, each substituted species can be easily and unambiguously identified in the rotational spectrum. Additionally, structural changes such as rotation about a dihedral angle resulting in gauche and antiperiplanar conformers can also be easily and unambiguously identified. This is discussed in greater detail in Chapter 6, where the complex conformational landscape of (-)-carveol, a photooxidation product of limonene,[11] is described. The sensitivity to changes in dihedral angle position is visualized in Figure 2.5**,** which shows the simulated spectrum of two different conformers of (-)-carveol, one with the isopropenyl group in the gauche – position, and one conformer with the isopropenyl group in the antiperiplanar position. Here, a change in each rotational constant of 0.4-2.1% leads to distinct changes in the rotational spectrum. Note that gauche and antiperiplanar are considered conformers, as they are conformations corresponding to minima on the potential energy curve.

Table 2.1. Effects of centrifugal distortion on bond lengths

Molecule	Equilibrium Bond Length	Change due to distortion, J=10	Change due to distortion, J=30
OH	0.9706 Å	0.0109 Å	0.0922 Å
HCl	1.2746 Å	0.0070 Å	0.0595 Å
CO2	1.1615 Å	0.0000 Å	0.0004 Å

Data taken from Toyama *et al.*[12]

2.2.2. Centrifugal Distortion Effects

As a molecule rotates it experiences a centrifugal force which distorts the bond lengths and bond angles. The effect of this distortion on molecular bond lengths as a function of angular momentum quantum number is shown in Table 2.1 for the cases of OH, HCl, and CO_2. The rotating molecule will now be distorted from the original equilibrium structure. As a consequence, the rotational transitions will be shifted from their hypothetical undistorted values; see Figure 2.2 as an example. The structure will change as a function of rotational level and we can therefore no longer consider the rotational constants as independent of rotational state. However, in most cases the distortion effect accounts for only a small fraction of the rotational energy level and we can consider distortion as a perturbation to the rigid rotor. There are several methods of accounting for the distortion effect, but in Chapters 3-8, I utilize Watson A-reduced quartic centrifugal distortion constants ($\Delta_J, \Delta_{JK}, \Delta_K, \delta_J, and\ \delta_K$).[13]

In my research I obtain the distortion constants using both experimental and theoretical methods. Experimentally, the distortion constants, together with the rotational constants, are obtained using least-squares fit analyses of the measured transition frequencies. The experimental constants are then compared to theoretical constants obtained from electronic structure calculations to validate the spectroscopic assignment. Using theoretical methods, the force constants are directly computed using both harmonic and anharmonic approximations, which are then used to compute the distortion constants.

2.3. Molecular Beam Technique

To introduce the sample into the vacuum chamber, I utilize a technique known as a pulsed molecular beam expansion.[14] In addition to sample introduction, a molecular beam expansion

allows one to move population to low *J* states, generate and stabilize molecular clusters, prevent the decoherence of the molecular signal, and minimize doppler broadening.

In a molecular beam expansion, the molecular species of interest is mixed with a carrier gas, which serves as a collision partner with the sample, at a relatively high pressure. In Chapters 3-8, helium and neon are used as a backing gas, with a backing pressure of 1-4 atm. The gas mixture is then pulsed through a small orifice adiabatically into the vacuum chamber ($\sim 10^{-8}$ atm). In my experiments the orifice diameter is ~1 mm, and is chosen such that the mean-free path of the molecules is significantly smaller than the orifice diameter. When the nozzle is open (400-900 μs) to the vacuum chamber, numerous collisions occur predominately between the sample and the carrier gas near the orifice. During the collision process the carrier gas dissipates the excess kinetic energy of the molecular species of interest, resulting in not only the formation of molecular clusters, but also the cooling of molecular degrees of freedom. A molecular beam expansion is a non-equilibrium process, meaning that each degree of freedom is characterized by its own unique temperature, where the temperature in turn describes the distribution of population across each state. In my experiments, the molecular sample is cooled to a rotational temperature of ~1 K, so that only low *J* states are significantly populated. Additionally, as many of the monomers and molecular clusters studied in my work possess a distribution of different conformers, the ensemble can also be characterised by a conformational temperature. In my experiments the ensemble is cooled to a conformational temperature of 50-100 K.[15–17] However, this temperature is poorly defined as it is not only dependent on the beam conditions, such as the choice of the carrier gas and orifice dimensions, but also the barrier heights of conformer interconversion pathways. For interconversion to occur, Ruoff *et al.*[18] found that the upper barrier that permits relaxation to a lower energy conformer is about 5.0 kJ mol^{-1}. The many barrier heights found within the conformational landscape of a molecular system can be above or below this 5.0 kJ mol^{-1} threshold, resulting in different conformational temperatures in the same system, which contributes to the ambiguity of the conformational temperature.

Once past the nozzle orifice, the molecular ensemble quickly approaches terminal velocity along a single direction and remains unchanged for the duration of the expansion. The molecular systems now exists in a collision-free environment, preventing the breakdown of molecular clusters from additional collisions.

2.4. Chirped Pulse Fourier Transform Microwave Spectroscopy

Generally, the time sequence of a CP-FTMW experiment is as follows. Once the sample is introduced into the vacuum chamber via molecular beam expansion, an arbitrary waveform generator is used to produce a chirped pulse of microwave radiation, which linearly sweeps from an initial frequency to a final frequency. The chirped pulse is amplified, and then broadcasted via a horn antenna into the vacuum chamber. Before the radiation is broadcasted, the molecular sample is first introduced into the chamber via a molecular beam expansion. The chirped pulse then irradiates the molecular beam to produce superposition states between rotational energy levels involved in rotational transitions. The subsequent molecular spontaneous emission signal is then detected in the time domain. The signal is digitized using a fast oscilloscope, where it is averaged and then Fourier transformed to obtain a frequency domain spectrum. An outline of components and the order in which they operate is presented in Figure 2.6.

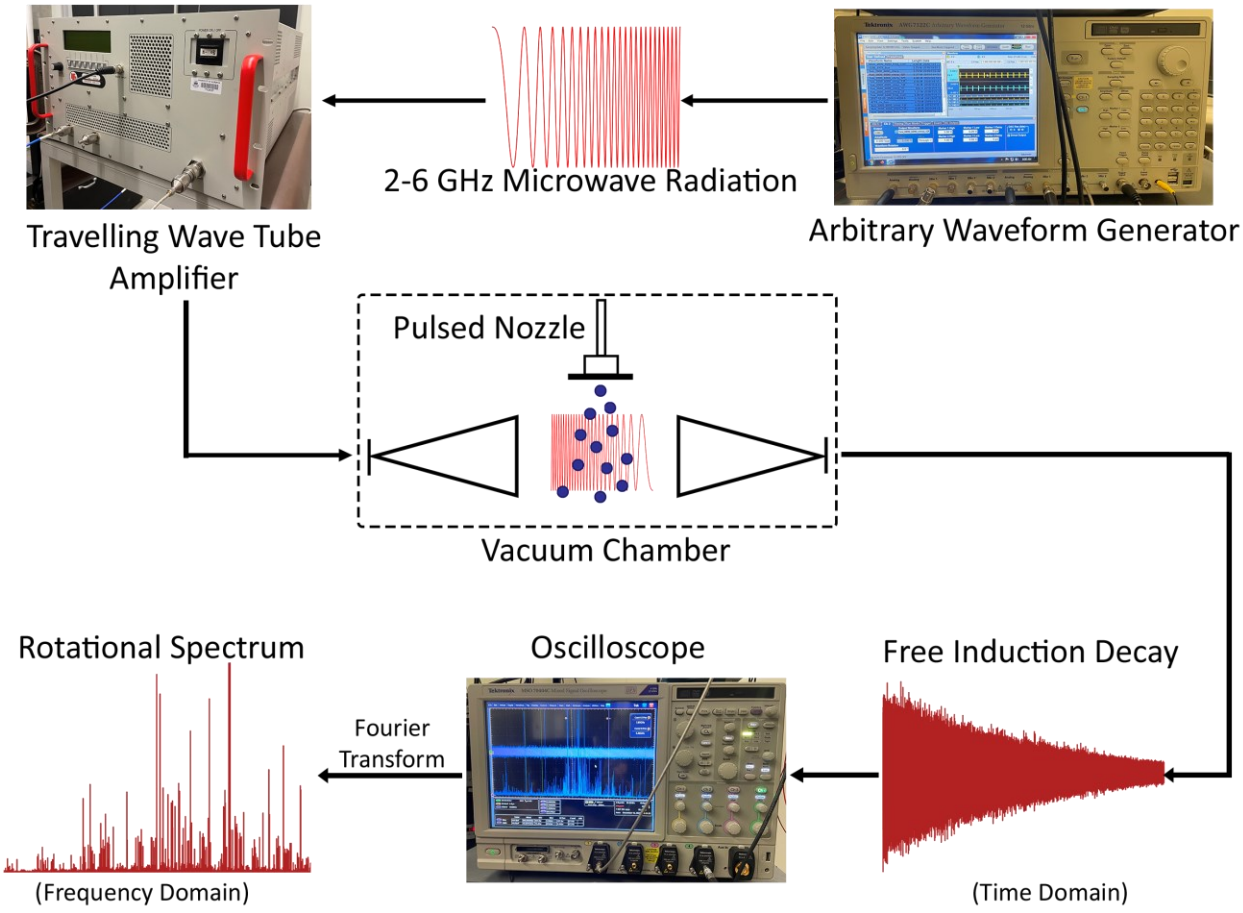

Figure 2.6. An overview of the chirped pulse Fourier transform microwave spectrometer used in my research.

The signal intensity in CP-FTMW spectroscopy is proportional to the macroscopic polarization induced in the sample by the excitation pulse:

$$|P| = \frac{2\mu_{ab}^2 \varepsilon \cdot \Delta N_0}{\hbar} \sqrt{\frac{\pi}{\alpha}} \tag{2.4}$$

where $|P|$ is the magnitude of the polarization response, μ_{ab} is the transition dipole moment, ε is the electric field, ΔN_0 is the initial population difference of a two-level system, $\hbar$ is the reduced Planck's constant, and α is the sweep rate of the chirped pulse. For a more detailed description of the polarization response in CP-FTMW spectroscopy, please see Park and Field.[19]

2.4.1. Excitation and Detection in the 2-6 GHz CP-FTMW Spectrometer

An overview of the general scheme of the CP-FTMW spectrometer is given in Figure 2.6. A Tektronix 7000 series, arbitrary waveform generator (AWG) with a sampling rate of 12 GS/s (Giga-Samples/second) is used to generate a 1μs long, 2-6 GHz chirped pulse. The length of the chirp can be adjusted to increase the signal strength. For example, if a molecular system possesses a relatively small dipole moment, one can increase the duration of the chirp, which allows the microwave radiation to irradiate a particular transition for a longer time, subsequently increasing the intensity of the measured emission signal. As outlined by the Nyquist-Shannon sampling theorem,[20,21] the highest frequency of radiation an AWG with a 12 GS/s sampling rate can produce is 6 GHz. Transmitted through subminiature version A (SMA) cables, the chirped pulse is then amplified with a travelling wave tube amplifier (IFI GT7525-400), rated for radiation between 2.5-7.5 GHz, with a maximum power output of 400 W. The now amplified chirped pulse is then broadcasted into the vacuum chamber using a horn antenna (Steatite Q-Par QWH-SL-2-18-N-HG-R), rated for radiation between 2-18 GHz, where it then irradiates the molecular beam. An analogous horn antenna is used to receive the molecular signal. A power limiter (Aeroflex ACLM-4537) is placed directly after the receiving horn antenna to protect any downstream electronics from the high-powered chirped pulse. A single-pull single-throw (SPST) switch is not only used to also protect downstream electronics from the high-powered chirp, but when in the low insertion loss state, allows for the free induction decay (FID) to pass through. During the irradiation process the SPST switch (Sierra Microwave 1CY63) is in the isolation state, preventing radiation from passing through. When the SPST switch is set to the low insertion loss state, the FID is then amplified after passing through a Narda-MITEQ low noise amplifier, rated for radiation between

2-8 GHz. The now amplified FID is then digitized using a Tektronix DPO70000 series oscilloscope with a sampling rate of 25 GS/s, which permits a 12.5 GHz bandwidth. To maintain phase coherence, a rubidium frequency standard (Stanford research systems FS725) is connected to the AWG and oscilloscope.

2.4.2. Transistor-Transistor Logic (TTL) Pulses and Timing System

To manage the timing sequence within the CP-FTMW spectrometer, transistor-transistor logic (TTL) pulses are used, which allow for easy and precise control of each component. Without precise control of the timing sequence, not only will the phase coherence of the molecular signal be disrupted, but it will also result in damages to the electronic components due to the passage of high powered microwave radiation. Two digital delay generators are used to create and manage the TTL pulses. The first is the Master TTL (Stanford research systems DG645), which sets the overall repetition rate of the experiment and sets the timing for the pulsed nozzle and AWG. The second digital delay generator is the Slave TTL (Quantum Composers 9520), which sets the trigger timing for the travelling wave tube amplifier and SPST switch. A summary of all of the TTL pulses

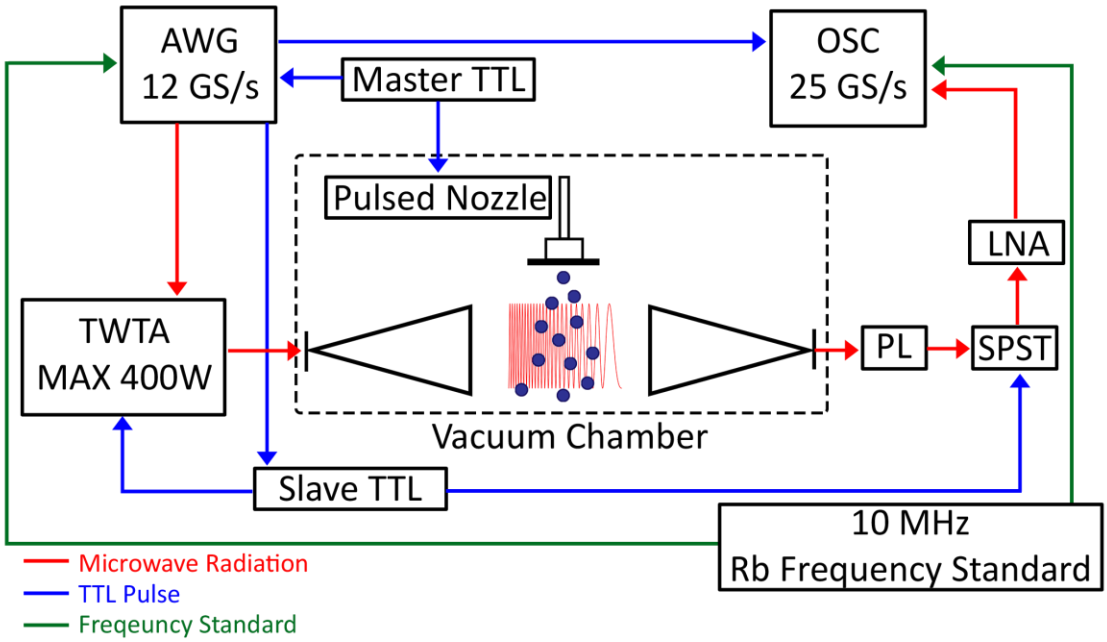

Figure 2.7. A schematic of the chirped pulse Fourier transform microwave spectrometer, with the pathways of the microwave radiation, transistor-transistor logic (TTL) pulses, and 10 MHz rubidium frequency standard, shown in red, blue, and green, respectively. The long form of each abbreviation is as follows: arbitrary waveform generator (AWG), travelling wave tube amplifier (TWTA), power limiter (PL), single pole single throw (SPST) switch, low noise amplifier (LNA), oscilloscope (OSC).

is shown in Figure 2.7. The order in which the two digital delay generators operate is as follows. First, the Master TTL sends a trigger signal to the pulse nozzle driver to lift the poppet covering the orifice, allowing for the molecular beam expansion to occur. After the trigger signal is sent to the pulse driver, the Master TTL will send a trigger signal to the AWG, which in turn will send a trigger signal to the Slave TTL. The Slave TTL will then send a trigger to the SPST switch to go into the isolation state, preventing high power radiation from saturating the low noise amplifier and oscilloscope. Immediately after the SPST switch trigger signal is sent, the Slave TTL will send a trigger signal to the travelling wave tube amplifier to transmit the chirped pulse. Once the irradiation process is complete, the switch is set to low insertion loss and a trigger signal from the AWG to the oscilloscope starts detection of the molecular signal.

2.5. Theoretical Techniques

Some of the molecules I studied have complex conformational landscapes, resulting in several different conformers which may be present simultaneously in the molecular expansion. In addition, the molecular monomers can form complexes and clusters with themselves, with water (which is always present in the sample system), and with carrier gas atoms. With the exception of the carrier gas atoms, these species are typically microwave active, resulting in extremely dense spectra (~15 transition per 10 MHz; see Chapter 6) which are difficult to assign to a specific molecular species without an aid to help with the assignment process. Quantum chemistry calculations not only assist in the assignment process, but also provide information about physical properties of the system, such as the electron density distribution within a molecule, which cannot be obtained from rotational spectroscopy experiments. My typical theoretical workflow is as follows. First, using a conformational searching algorithm an ensemble of different molecular conformers is generated. Next, high-level electronic structure calculations are carried out on the molecular conformers, which provide higher quality structure and energy data. The resulting theoretical conformer structures are then used to help with the experimental assignment process. After the assignment process, additional theoretical calculations are completed to further characterize the system, such as visualizing and quantifying the strength of non-covalent interactions within a system.

2.5.1. Conformational Ensemble Search

As presented in Chapter 6, the conformational landscape of a molecule can be extensive when a molecule possesses flexible dihedral angles and a flexible ring structure. Investigating the conformational landscape of a molecular system can become more difficult when a conformationally flexible molecule non-covalently aggregates with another molecule to form a molecular complex. To ensure that an extensive and thorough conformational search is completed, the conformer-rotamer ensemble sampling tool (CREST)[4] is utilized. CREST is a type of meta-dynamics simulation[22] which allows one to investigate different protomers and tautomers, as well as different conformers of monomers and aggregates. Like other meta-dynamic methods, CREST is able to explore each minimum on a potential energy surface by using a bias sampling method, which adds bias potentials over time to augment the potential energy surface. One can think of bias sampling as "filling" a potential well, allowing for large barrier heights to be overcome. The details of CREST and the bias sampling can be found in the original publication of Pracht *et al*.[4] CREST will run a series of meta-dynamic simulations, generating an ensemble of different rotamers and conformers. CREST will then filter out redundant conformers by doing either an energy comparison between each conformer or a Cartesian coordinate and rotational constant comparison between each conformer. To optimize the geometries and determine energetic data for each generated conformer, CREST utilizes a tight binding,[23] semiempirical method, called Geometry, Frequency, Noncovalent, eXtended Tight binding (GFN2-xTB).[24,25] GFN2-xTB is a relatively inexpensive method, which provides adequate optimized geometries, frequencies, and energetic data.

2.5.2. Electronic structure calculations

To refine the energies and geometries of the CREST conformers, high-level electronic structure calculations are carried out. Coupled cluster (CC) methods provide accurate geometries and energies, and are the gold standard for electronic structure methods, but come at great computational costs ($\sim N^7$ scaling for CCSD(T) method).[26] In my work I utilize density functional theory (DFT).[27] Compared to Post-Hartree-Fock methods, such as CC methods, DFT is an inexpensive method, which provides accurate geometries and reasonable relative energies.[28] In my work, I predominately use the Becke, 3-parameter, Lee-Yang-Parr (B3LYP)[29,30] DFT hybrid functional, which is a mixture of Hartree-Fock exchange and density functional exchange and

correlation terms. B3LYP is not only computationally inexpensive, but also provides improved accuracy over other DFT methods for the prediction of molecular properties such as energies, structures, and vibrational frequencies.[31] Despite its computational potency, B3LYP, and in general DFT, suffers from poor treatment of long range interactions, such as non-covalent interactions.[32] This is problematic as in the majority of my work I study non-covalently bound molecular clusters. Thus, long range interactions are corrected for using a dispersion correction and a damping function (D3BJ).[33,34]

2.6. Assignment and Fitting Process

The rotational transitions of the molecular systems studied throughout my work were measured using a CP-FTMW spectrometer. Once measured, rotational quantum numbers were assigned to as many of the measured transitions as possible. The transition frequencies were then used in a least-squares fitting procedure to obtain spectroscopic parameters, such as rotational constants and centrifugal distortion constants, of the respective molecular system, where the quality of the fit is validated by a low root-mean-square error (< 10 kHz). Here, I briefly describe how I use theory to help assign quantum numbers to the rotational transitions in order to experimentally fit spectroscopic parameters.

Once the rotational spectrum has been measured, the ensemble of theoretical structures, and the corresponding rotational constants, are used as 'guess' structures for the assignment process. The ensemble of theoretical structures can be extensive (>100 structures in some instances) and I must therefore carefully select which structures to use. This selection is based on the relative zero-point corrected energy, where I typically use conformers below 5.0 kJ mol^{-1} as their abundance in the molecular expansion may be sufficiently high for observation. The dipole moment components are also taken into consideration, as species with no electric dipole moment will not be observable in rotational spectroscopy experiments. Once the guess structures are selected, their respective rotational constants are used to simulate a spectrum. Based on the intensity of each simulated transition, the location of the transition with respect to other transitions, or other spectral patterns, rotational quantum numbers are assigned to as many transitions as possible, followed by a least-squares fit to obtain experimental rotational constants.

2.7. Non-Covalent Interactions Analyses

Once an experimental assignment is achieved and the spectra analysis completed, several different theoretical techniques are implemented to further characterize the molecular system and to interpret the experimental results. Non-covalent interactions (NCI) analyses[6] are utilized throughout my work, and are used to identify, visualize, and characterize non-covalent interactions, such as hydrogen bonding and van der Waals interactions, within a molecule or molecular cluster. An NCI plot is obtained by plotting the reduced density gradient, $s(r)$, against the electron density. The reduced density gradient is given by:

$$s(r) = \frac{|\nabla\rho(r)|}{2(3\pi^2)^{\frac{1}{3}}\rho(r)^{\frac{4}{3}}} \tag{2.5}$$

where $\rho(r)$ is the electron density and $\nabla\rho$ is the gradient of the electron density. Areas with high $s(r)$ and low $\rho(r)$ indicate regions far from the nucleus, areas with low $s(r)$ and high $\rho(r)$ correspond to covalent bonds, and areas of low $s(r)$ and low $\rho(r)$ correspond to non-covalent interactions. To distinguish between attractive and repulsive interactions, the sign of the Laplacian of the density at each point on the isosurface, $\nabla^2\rho(r)$, is used. The Laplacian is the trace of the

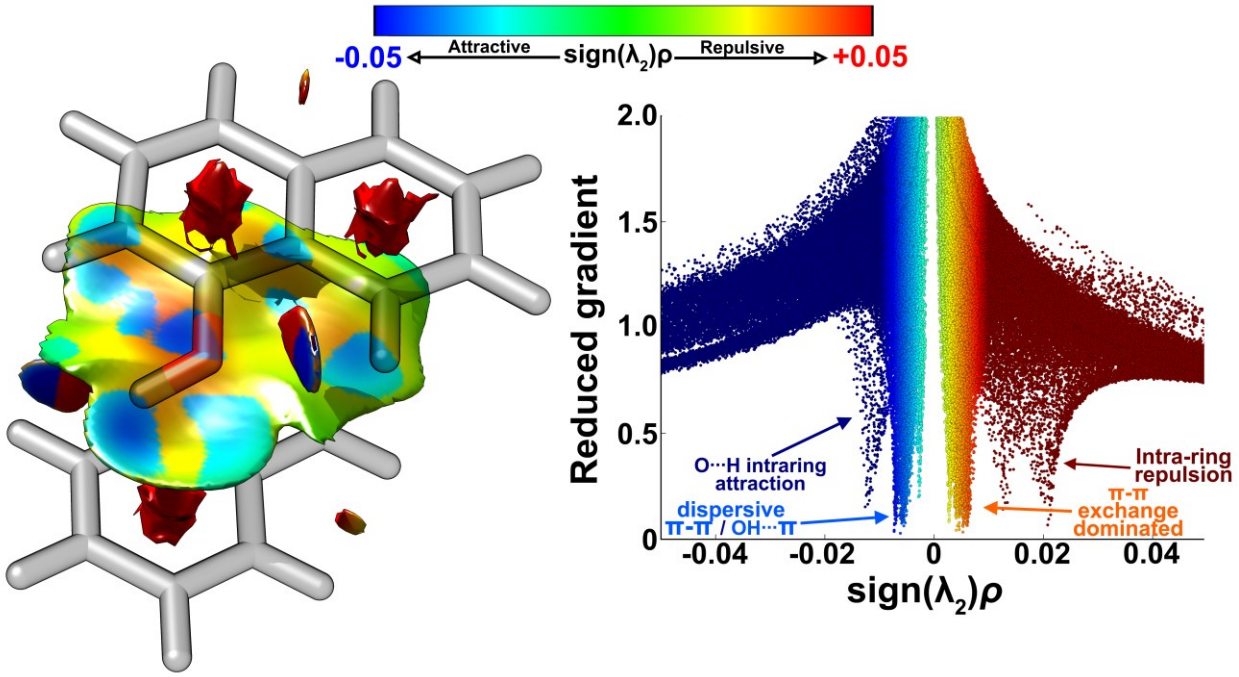

Figure 2.8. Results of a non-covalent interactions analysis of 1-naphthol dimer. An isosurface of the reduced density gradient, coloured with the values of $sign(\lambda_2)\rho(r)$, is shown on the left, and a plot of the reduced density gradient against $sign(\lambda_2)\rho(r)$ is shown on the right. Reduced density gradient values for the isosurface were cut-off at s=0.8 a.u.

Hessian matrix, the second order derivative of the electron density, with eigenvalues λ_i, where $\lambda_1 \leq \lambda_2 \leq \lambda_3$. At the nuclei, the density is at a local maximum and all eigenvalues are negative ($0 \leq \lambda_1, 0 \leq \lambda_2, 0 \leq \lambda_3$). Regions between bound atoms are characterized by one positive and two negative eigenvalues. For bonding or stabilizing interactions, such as covalent bonds, hydrogen bonds, and dispersion interactions, the second eigenvalue is negative ($\lambda_2 < 0$). For nonbonding or destabilizing interactions, such as steric repulsion, the second eigenvalue is positive ($\lambda_2 > 0$). Therefore, the sign of the second eigenvalue, λ_2, provides information on the type of interaction, while the electron density, $\rho(r)$, can provide information on the relative strength of the interaction. This is visualized in Figure 2.8, which plots the reduced density gradient, $s(r)$, against electron density multiplied by the sign of the second eigenvalue of the Hessian, $sign(\lambda_2)\rho(r)$, for the 1-napthol dimer.[35] In Figure 2.8 the isosurface of the reduced density gradient is also plotted. Typically, when plotting the isosurface two parameters are manually set. First, a cut-off value is set for the reduced density gradient. In the case of 1-naphthol dimer, the values are cut-off for $s >$ 0.8 a.u. Second, colours are manually assigned to $sign(\lambda_2)\rho$. For 1-naphthol dimer, the attraction and repulsion limit was set to -0.05 a.u. and 0.05 a.u, respectively.

2.8. References

1 C. H. Townes and A. L. Schawlow, *Microwave spectroscopy*, Courier Corporation, 2013.

2 T. J. Balle and W. H. Flygare, *Rev. Sci. Instrum.*, 1981, **52**, 33–45.

3 G. G. Brown, B. C. Dian, K. O. Douglass, S. M. Geyer, S. T. Shipman and B. H. Pate, *Rev. Sci. Instrum.*, 2008, **79**, 053103.

4 P. Pracht, F. Bohle and S. Grimme, *Phys. Chem. Chem. Phys.*, 2020, **22**, 7169–7192.

5 J. Contreras-García, E. R. Johnson, S. Keinan, R. Chaudret, J.-P. Piquemal, D. N. Beratan and W. Yang, *J. Chem. Theory Comput.*, 2011, **7**, 625–632.

6 E. R. Johnson, S. Keinan, P. Mori-Sánchez, J. Contreras-García, A. J. Cohen and W. Yang, *J. Am. Chem. Soc.*, 2010, **132**, 6498–6506.

7 W. Gordy, R. L. Cook and A. Weissberger, *Microwave molecular spectra*, Wiley New York, 1984, vol. 18.

8 H. M. Pickett, *SPFIT/SPCAT package*, 2009.

9 H. Hartwig and H. Dreizler, *Z. Für Naturforschung A*, 1996, **51**, 923–932.

10 A. S. Hazrah, S. Nanayakkara, N. A. Seifert, E. Kraka and W. Jäger, *Phys. Chem. Chem. Phys.*, 2022, **24**, 3722–3732.

11 A. S. Hazrah, M. Al-Jabiri, R. Speelman and W. Jäger, *Phys. Chem. Chem. Phys.*, 2021, **23**, 15159–15168.

12 M. Toyama, T. Oka and Y. Morino, *J. Mol. Spectrosc.*, 1964, **13**, 193–213.

13 J. K. Watson, *J. Chem. Phys.*, 1967, **46**, 1935–1949.

14 J. P. Valleau and J. M. Deckers, *Can. J. Chem.*, 1965, **43**, 6–17.

15 N. Borho and Y. Xu, *Phys. Chem. Chem. Phys.*, 2007, **9**, 4514–4520.

16 N. A. Seifert, I. A. Finneran, C. Perez, D. P. Zaleski, J. L. Neill, A. L. Steber, R. D. Suenram, A. Lesarri, S. T. Shipman and B. H. Pate, *J. Mol. Spectrosc.*, 2015, **312**, 13–21.

17 F. Xie, N. A. Seifert, M. Heger, J. Thomas, W. Jäger and Y. Xu, *Phys. Chem. Chem. Phys.*, 2019, **21**, 15408–15416.

18 R. S. Ruoff, T. D. Klots, T. Emilsson and H. S. Gutowsky, *J. Chem. Phys.*, 1990, **93**, 3142–3150.

19 G. B. Park and R. W. Field, *J. Chem. Phys.*, 2016, **144**, 200901.

20 H. Nyquist, *Trans. Am. Inst. Electr. Eng.*, 1928, **47**, 617–644.

21 C. E. Shannon, *Proc. IRE*, 1949, **37**, 10–21.

22 A. Barducci, M. Bonomi and M. Parrinello, *Wiley Interdiscip. Rev. Comput. Mol. Sci.*, 2011, **1**, 826–843.

23 S. Grimme, *J. Chem. Theory Comput.*, 2019, **15**, 2847–2862.

24 S. Grimme, C. Bannwarth and P. Shushkov, *J. Chem. Theory Comput.*, 2017, **13**, 1989–2009.

25 C. Bannwarth, S. Ehlert and S. Grimme, *J. Chem. Theory Comput.*, 2019, **15**, 1652–1671.

26 C. Dykstra, G. Frenking, K. Kim and G. Scuseria, *Theory and applications of computational chemistry: the first forty years*, Elsevier, 2011.

27 W. Kohn and L. J. Sham, *Phys. Rev.*, 1965, **140**, A1133.

28 M. Orio, D. A. Pantazis and F. Neese, *Photosynth. Res.*, 2009, **102**, 443–453.

29 C. Lee, W. Yang and R. G. Parr, *Phys. Rev. B*, 1988, **37**, 785.

30 A. D. Becke, *Phys. Rev. A*, 1988, **38**, 3098.

31 J. Tirado-Rives and W. L. Jorgensen, *J. Chem. Theory Comput.*, 2008, **4**, 297–306.

32 J. Toulouse, F. Colonna and A. Savin, *Phys. Rev. A*, 2004, **70**, 062505.

33 S. Grimme, J. Antony, S. Ehrlich and H. Krieg, *J. Chem. Phys.*, 2010, **132**, 154104.

34 S. Grimme, S. Ehrlich and L. Goerigk, *J. Comput. Chem.*, 2011, **32**, 1456–1465.

35 N. A. Seifert, A. S. Hazrah and W. Jäger, *J. Phys. Chem. Lett.*, 2019, **10**, 2836–2841.

3

Structural Study of 1- and 2-Naphthol: New Insights into the Non-covalent H-H Interaction in *cis*-1-Naphthol

Contents

3.1. Introduction · · · · · 29
3.2. Methods · · · · · 31
3.2.1. Theoretical Methods · · · · · 31
3.2.2. Experimental Methods · · · · · 33
3.3. Results and Discussion · · · · · 33
3.3.1. Experimental Results · · · · · 33
3.3.2. Electronic Structure Calculations · · · · · 36
3.3.3. Structures · · · · · 38
3.3.4. Interpretation of the close contact in *cis*-1-naphthol · · · · · 42
3.3.5. Biphenyl: a related system · · · · · 52
3.4. Conclusions · · · · · 54
3.5. References · · · · · 55

3.1. Introduction

1- and 2-naphthol, hydroxy-derivatives of naphthalene, the simplest polycyclic aromatic hydrocarbon, are used as precursors in the dye, perfume, insecticide, and pharmaceutical industries[1] and are metabolites of naphthalene itself,[2] which has uses as pesticide.[3] Naphthols can also be considered as naphthalene homologues of phenol and are, from an intermolecular interactions point of view, of interest because they contain a hydrophobic part, i.e. the bicycle with an extended π-electron system, and a hydrophilic OH group.

Indeed, a number of weakly bound complexes involving the naphthols have been studied using spectroscopic techniques. The Leutwyler group in particular has studied 1-naphthol – $(H_2O)_N$ (N=1 to 50)[4] and 2-naphthol – $(NH_3)_N$ (N=1-10)[5] complexes and clusters with laser spectroscopic techniques in an effort to determine the solvation threshold for excited state proton transfer from naphthol to water, 1-naphthol – alkane complexes,[6–8] 1-naphthol – rare gas and N_2 complexes,[9] hydrogen-bonded complexes of naphthol,[10–12] and most recently complexes of 1-naphthol with

linear molecules.[13] Naphthol – water clusters have also been studied by the Fujii group,[14] by Knochenmuss and Smith,[15] and by Pratt et al.[16] The 1-naphthol dimer has been studied by infrared dip spectroscopy[17] and more recently the microwave spectrum of the 1-naphthol dimer has been measured, assigned, and interpreted, with the help of theoretical calculations, in terms of a structure that is dominated by π-π stacking interactions over canonical hydrogen bonding.[18]

There are a number of earlier spectroscopic studies of the naphthol monomers. Pratt's group has studied the fluorescence spectra of 1- and 2-naphthol[19] and established the existence of *cis*- and *trans*-conformers for both monomers. This was followed by a microwave spectroscopic study of *cis*- and *trans*-1-naphthol by Brown and co-workers,[20] who identified a close contact between the hydroxyl H and the neighbouring ring H-atom. Saeki et al.[17] reported then on infrared dip spectra of *trans*- and *cis*-1-naphthol. Recently, Goubet et al.[21] measured rotational and vibrational spectra of *cis*-2-naphthol and re-examined the spectra of *trans*-1-naphthol.

Close H-H contacts of the type identified by Brown and co-workers in *cis*-1-naphthol have been found also in other systems. Analysis and characterization of these close H-H contacts has attracted considerable attention in the past two decades or so. Bader and co-workers[22–24] examined close-contact H-H interactions in several crystal structures and isolated polycyclic aromatic hydrocarbons. They found, within the framework of the quantum theory of atoms in molecules (QTAIM), a bond critical point between close-contact hydrogen atoms indicative of a *bonding* interaction. The authors ultimately conclude that these close-contact H-H interactions are attractive interactions which help stabilize the overall structure of the crystal or molecule. This conclusion has, however, been contested in several other studies[25–27] which argue that close-contact H-H interactions are indeed repulsive or steric interactions. For example, Grimme et al.[26] showed experimentally that the steric congestion of the close-contact hydrogens results in shorter C-H bond lengths, indicated by a vibrational blue shift, which aligns with the traditional view of steric repulsion. The studies discussed focus on molecules or systems where the close-contact hydrogens are "fixed" in place where the two hydrogens are forced to interact with each other. This is not the case with the naphthol monomers where the hydroxyl hydrogen is not locked into position like the C-H hydrogens considered in previous studies. *Cis*-1-naphthol thus provides an interesting test case to analyze the close-contact H-H interaction in detail, where the other isomers can play the role of internal references. What makes 1-naphthol even more suited is that it affords us the

opportunity to computationally follow electronic properties along the smooth OH internal rotation coordinate from the close H-H contact *cis*-conformer to the *trans*-conformer.

Here, I describe the rotational spectrum of *trans*-2-naphthol measured with a chirped-pulse Fourier transform microwave spectrometer in the 2 to 6 GHz range. Spectra of all singly substituted ^{13}C isotopologues were also recorded, in addition to those of *cis*- and *trans*-1-naphthol and *cis* 2-naphthol. The isotopic data were used to derive heavy atom Kraitchman substitution coordinates[28] and semi-experimental structures for both conformers of both isomers. The close H-H contact in *cis*-1-naphthol is a main focus of this study. A Quantum Theory of Atoms-in-Molecules (QTAIM)[29] analysis revealed a bond critical point between the two hydrogen atoms and a Non-Covalent Interactions (NCI) analysis[30] resulted in a reduced electron density gradient isosurface with positive sign of the second Hessian eigenvalue, which is often an indication for an attractive interaction. Several approaches were applied to provide further insights into the weak intramolecular interactions within each conformer. The electron density topology was also analyzed using the Independent Gradient Model (IGM)[31–33] to extract the Intrinsic Bond Strength Index (IBSI)[34] for relevant individual bonds in 1-naphthol. The local vibrational mode theory[35] originally introduced by Konkoli, Cremer et al.[36–40] was utilized to assess and compare the intrinsic strength of the OH bond in both isomers of 1- and 2-naphthol. Finally, Charge Model 5 (CM5)[41] and Natural Bond Orbitals (NBO)[42,43] approaches were used to gain further insights into the close-contact H-H interaction.

Close-contact H-H interactions of the type observed in *cis*-1-naphthol have been extensively and controversially discussed in the literature. A main purpose of the analyses applied here to the naphthol isomers is to arrive at a consistent and convincing physical-chemical picture of such close-contact H-H interactions.

3.2. Materials and Methods

3.2.1. Theoretical Methods

Utilizing density functional theory (DFT)[44] and the Gaussian 16 program suite,[45] geometry optimizations and harmonic frequency calculations were performed at the B3LYP-D3(BJ)[46–48]level of theory with the def2-TZVP basis set[49] and at the Møller-Plesset second order perturbation theory (MP2)[50] level with the aug-cc-pVTZ basis set.

Analyses of the molecular electron density distribution based on Bader's quantum theory of atoms in molecules (QTAIM),[29] including non-covalent interactions (NCI)[30] and IGM analyses,[31–33] were done using the AIMAll,[51] MultiWfn,[52] and IGMPlot programs, respectively, and then visualized using UCSF Chimera**.**[53] The local mode analyses were carried out with the program LModeA.[54]

Normal vibrational modes are generally delocalized as a result of mass coupling. [42-45] This implies that if one considers a particular normal stretching mode between two atoms of interest, it can be coupled to other normal modes such as bending or torsion, which hampers the direct correlation between stretching frequency and bond strength as well as the comparison between stretching modes of similar nature. As a consequence, the normal stretching force constant cannot be used as a direct bond strength measure, which results in the need to derive a local counterpart that is free from any mode-mode coupling. Konkoli, Cremer et al.[36–40] approached this problem by solving the mass-decoupled analogue of Wilson's equation of vibrational spectroscopy[55] leading to local vibrational modes, associated local mode frequencies, and local mode force constants. Zou and Cremer showed that the local stretching force constant reflects the curvature of the PES in the direction of the bond stretching.[56] This important result qualifies the local stretching force constants k^a as a unique quantitative measure of the intrinsic strength of a chemical bond and/or weak chemical interaction based on vibrational spectroscopy, which has been extensively applied in previous work.[35] (For some recent work see also Refs. [57–60].) Another important feature of the local vibrational mode theory is that any complete set of non-redundant local modes can be transformed into the corresponding set of normal modes via an adiabatic connection scheme.[61] This unique one-to-one correspondence has led to a new comprehensive analysis of infrared/Raman spectra via the characterization of normal modes (CNM) procedure[38,62] which allows for the decomposition of each normal mode into its respective local mode counterparts, thereby facilitating the identification of their individual contributions. The local mode analysis (LMA) was applied in this work to assess the strength of the O-H bonds in *cis*- and *trans*- 1- and 2-naphthol and to evaluate the local character of the corresponding O-H normal modes. For convenience, k^a values were converted into more chemically intuitive bond strength orders (BSO $\boldsymbol{n}$) by utilizing an extended Badger rule.[39,63] The latter relates BSO $\boldsymbol{n}$ to k^a via a power relationship, which is fully determined based on two well-known reference molecules and the requirement that for a zero-force constant, the corresponding BSO $\boldsymbol{n}$ is zero:

$$BSO\ \boldsymbol{n} = a(k^a)^b \quad (3.1)$$

In this work, the constants a and b were evaluated using F-H and $[F{---}H{---}F]^-$ as the references with BSO $\boldsymbol{n}$ values 1 and 0.5, respectively, which resulted in a=0.518 (0.490) and b=0.291 (0.319) (values for MP2/aug-cc-pVTZ calculations are shown first, followed by those of B3LYP-D3(BJ)/def2-TZVP calculations in parentheses). The corresponding k^a values for F-H and $[F{---}H{---}F]^-$ are 9.584 (9.367) mDyn/Å and 0.884 (1.064) mDyn/Å, respectively. The O-H bonds of interest were scaled the BSO $\boldsymbol{n}$ values obtained via equation (1), according to which the O-H bond in H_2O has BSO $\boldsymbol{n}$ values of 0.961 (0.957) by a factor of 1.041 (1.045), so that BSO $\boldsymbol{n}$ OH in H_2O is 1.

3.2.2. Experimental Methods

Rotational spectra of the naphthols were recorded with a pulsed nozzle chirped-pulse Fourier transform spectrometer in the frequency range between 2 and 6 GHz. Our instrument operates analogously to the spectrometer designed by the Pate group,[64] with some variances in component specifications.[65] Per molecular pulse, six free induction decays (FIDs) were recorded. About 3.8 M (850 k) FIDs were averaged and then Fourier transformed to generate the broadband rotational spectrum for 1-naphthol (2-naphthol). 3.8 M averages were necessary to measure ^{13}C transition for the *cis*-1-naphthol conformer with sufficient signal to noise ratio.

The 1- and 2-naphthol (≥ 99 %) samples were purchased from Millipore-Sigma and used without any further modification or purification. Both 1- and 2-naphthol are solids with melting points of about 95 and 120 °C, respectively. To generate the vapour pressure needed to bring a sufficient number of molecules into the gas phase, we utilized a special attachment to a General Valve, Series 9, pulsed valve which contains a sample reservoir and can be heated. For 1-naphthol the attachment was heated to 100 °C and for 2-naphthol to 120 °C. Neon (helium) was used as backing gas at pressures of about 3 atm for 1-naphthol (2-naphthol). Neon backing gas improved the signal to noise ratio for 1-naphthol and was used to measure its ^{13}C transitions.

3.3. Results and Discussion

3.3.1. Experimental Results

Sections of the broadband rotational spectra for 1-naphthol and 2-naphthol are shown in Figure 3.1. Rotational and centrifugal distortion constants from the literature[20,21] and from

Table 3.1. Spectroscopic parameters for the naphthol isomers from theory and from fits of experimental data.

	1-naphthol			
	cis- (theory)	[a]*cis*- (experiment)	*trans*- (theory)	[a,c]*trans*- (experiment)
A / MHz	1959.8594	1947.51340(61)	1955.1739	1942.10135(21)
B / MHz	1130.8399	1124.307930(90)	1139.0560	1133.623460(88)
C / MHz	717.1278	713.096200(63)	719.7438	716.017810(49)
Δ_J / kHz	0.05262	[0.0136][b]	0.05331	0.01810(70)
Δ_{JK} / kHz	-0.08807	[0.0409][b]	-0.09152	0.0240(35)
Δ_K / kHz	0.04032	0.30(12)	0.04306	0.059(20)
δ_J / kHz	0.01201	0.00382(21)	0.01177	0.00630(34)
δ_K / kHz	-0.01278	0.0440(98)	-0.01482	0.0355(19)
N	-	60	-	117
σ / kHz	-	2.1	-	2.2
ΔE_0 / kJ mol^{-1}	3.3	-	0.0	-
Δ / amu Å^2	-0.0443	-0.2925(2)	0.0001	-0.2124(2)
|μ|/ D	μ_a=1.4, μ_b=0.3, μ_c=0.1	$\mu_a > \mu_b$	μ_a=1.2, μ_b=0.1, μ_c=0.0	$\mu_a > \mu_b$
	2-naphthol			
	cis- (theory)	[c]*cis*- (experiment)	*trans*- (theory)	*trans*- (experiment)
A / MHz	2870.7044	2849.15700(28)	2868.6589	2845.35720(37)
B / MHz	828.9859	824.63285(12)	829.6421	825.5363521(13)
C / MHz	643.2358	639.72412(11)	643.5280	640.087128(16)
Δ_J / kHz	0.00797	0.0130(27)	0.00793	0.00706(17)
Δ_{JK} / kHz	0.01426	[0.014844][d]	0.01508	[0.015080][e]
Δ_K / kHz	0.18312	0.170(29)	0.18328	0.2615(17)
δ_J / kHz	0.00200	0.00260(60)	0.00197	0.00180(92)
δ_K / kHz	0.02966	[0.030525][d]	0.02969	[0.02969][e]
N	-	41	-	49
σ / kHz	-	1.4	-	2.7
ΔE_0 / kJ mol^{-1}	0.0	-	2.1	-
Δ / amu Å^2	0.0001	-0.2366(2)	0.0000	-0.251(1)
|μ|/ D	μ_a=0.2, μ_b=1.0, μ_c=0.1	$\mu_b > \mu_a$	μ_a=0.6, μ_b=1.4, μ_c=0.0	$\mu_b > \mu_a$

Theoretical parameters were determined at the B3LYP-D3(BJ)/def2-TZVP level of theory. [a]Assigned rotational transitions from Whitham et al.[20] are included in fit.[b]Fixed at the values from Whitham et al.[20] [c]Note that the spectroscopic constants derived by Goubet et al.[21] for *trans*-1-naphthol and *cis*-2-naphthol have significantly

higher accuracy than the values reported here because of the much larger number of transitions in the fits. Unfortunately, their transition frequencies are not published, so that they were not included in our fits. [c]Fixed at the values from Goubet et al.[21] [d]Fixed at the values from theory.

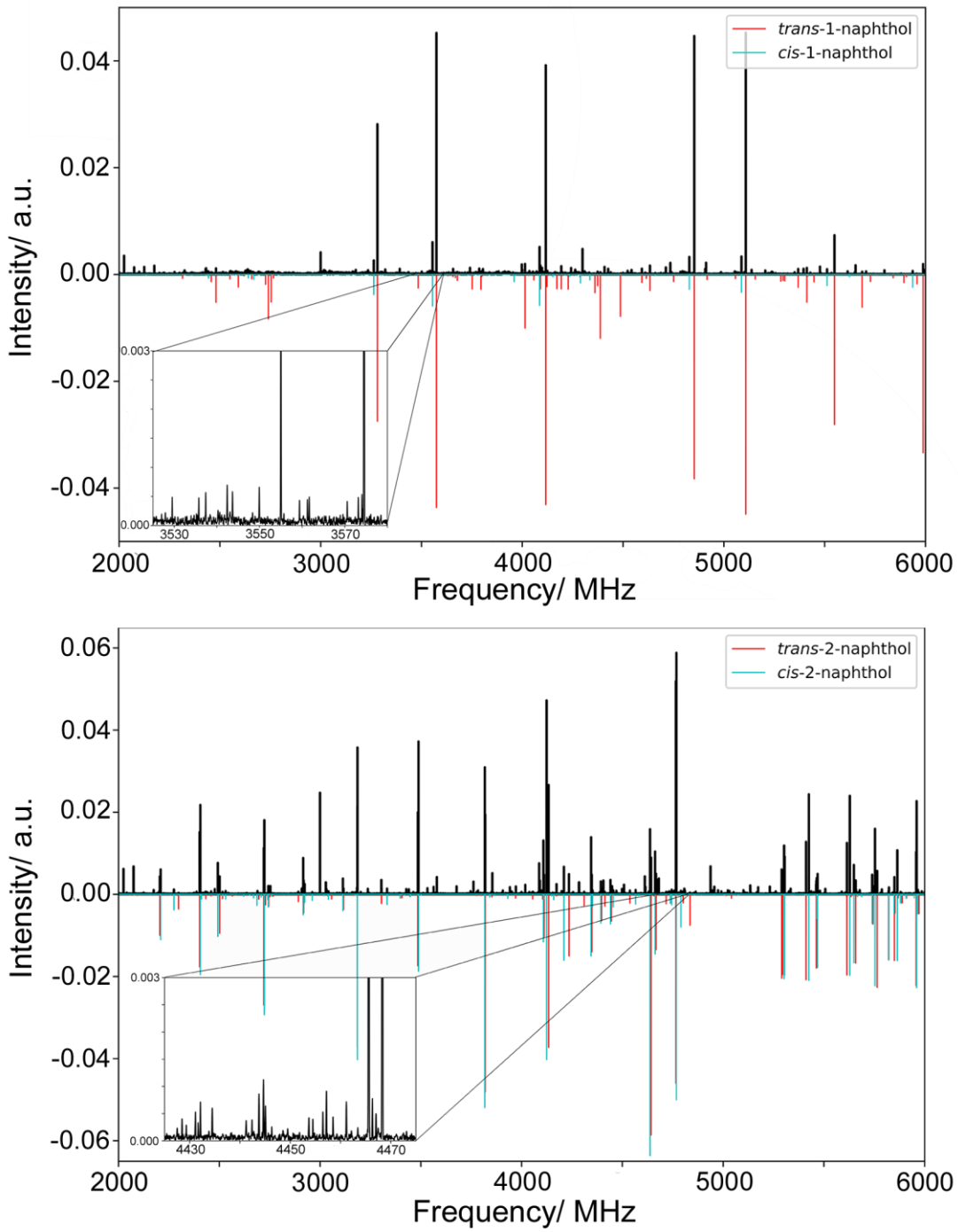

Figure 3.1. Broadband rotational spectra of 1-naphthol (top) and 2-naphthol (bottom). The experimental spectra are in black, while the red and blue spectra represent the simulated spectra for the *trans*- and *cis*-conformer, respectively.

DFT calculations were used to locate the rotational transitions for the normal isotopologues of *cis*- and *trans*-conformers of 1-and 2-naphthol. The transition frequencies are in Tables A.1-A.3, Appendix A, together with the quantum number assignments. The measured frequencies were used, together with those from the literature where available, in fitting procedures using the SPCAT/SPFIT program suite[66] and Watson's A-reduction Hamiltonian in its I^r representation to determine experimental rotational and quartic centrifugal distortion constants. The fit results for *trans*- and *cis*-2-naphthol, *trans*- and *cis*- 1-naphthol, with frequencies from earlier work included, are presented in Table A.1 of Appendix A. The transitions were strong enough that all ten singly substituted ^{13}C isotopologues for both conformers of 1- and 2-naphthol could be detected in their natural abundances. The resulting transition frequencies with quantum number assignments are in Tables A.5 to A.8 of Appendix A and the corresponding spectroscopic constants are given in Tables A.9 to A.12 of Appendix A. For the normal isotopologues of *cis*- and *trans*-1-naphthol and *cis*-2-naphthol, the derived spectroscopic constants agree with the literature values to within the respective uncertainties.

3.3.2. Electronic Structure Calculations

Geometry optimizations and harmonic vibrational frequency calculations were performed at the B3LYP-D3(BJ)/def2-TZVP and MP2/aug-cc-pVTZ level for both *trans*- and *cis*-conformers of 1- and 2-naphthol. The resulting structural parameters are given in Tables A.13 to A.16 of Appendix A and the corresponding rotational constants, centrifugal distortion constants, and dipole moment components are in Table 3.1; the structures are shown in Figure 3.2. The dihedral angles τ(C2-C1-O1-H1) for 1-naphthol and τ(C1-C2-O1-H2) for 2-naphthol were scanned to obtain potential energy curves (Figure 3.3) that connect the *trans*- to the *cis*-isomers via barriers of 13.6 kJ/mol (1-naphthol) and 12.8 kJ/mol (2-naphthol). At the B3LYP-D3(BJ)/def2-TZVP level of theory, the relative zero-point energy differences between the *trans*- and *cis*-isomers are 3.4 kJ/mol (1-naphthol) and 1.9 kJ/mol (2-naphthol). In 1-naphthol, the *trans*-conformer is lower in energy, while in 2-naphthol the *cis*-conformer is the lower energy conformer. This ordering is consistent with previous determinations.[21,67,68]

To gain insights into the intramolecular interactions in the naphthol monomers, a QTAIM (Figure 3.4), NCI (Figure A.1, Appendix A), and IGM analyses of the molecular electron density distributions were performed. Interestingly, apart from the expected bond and ring critical points

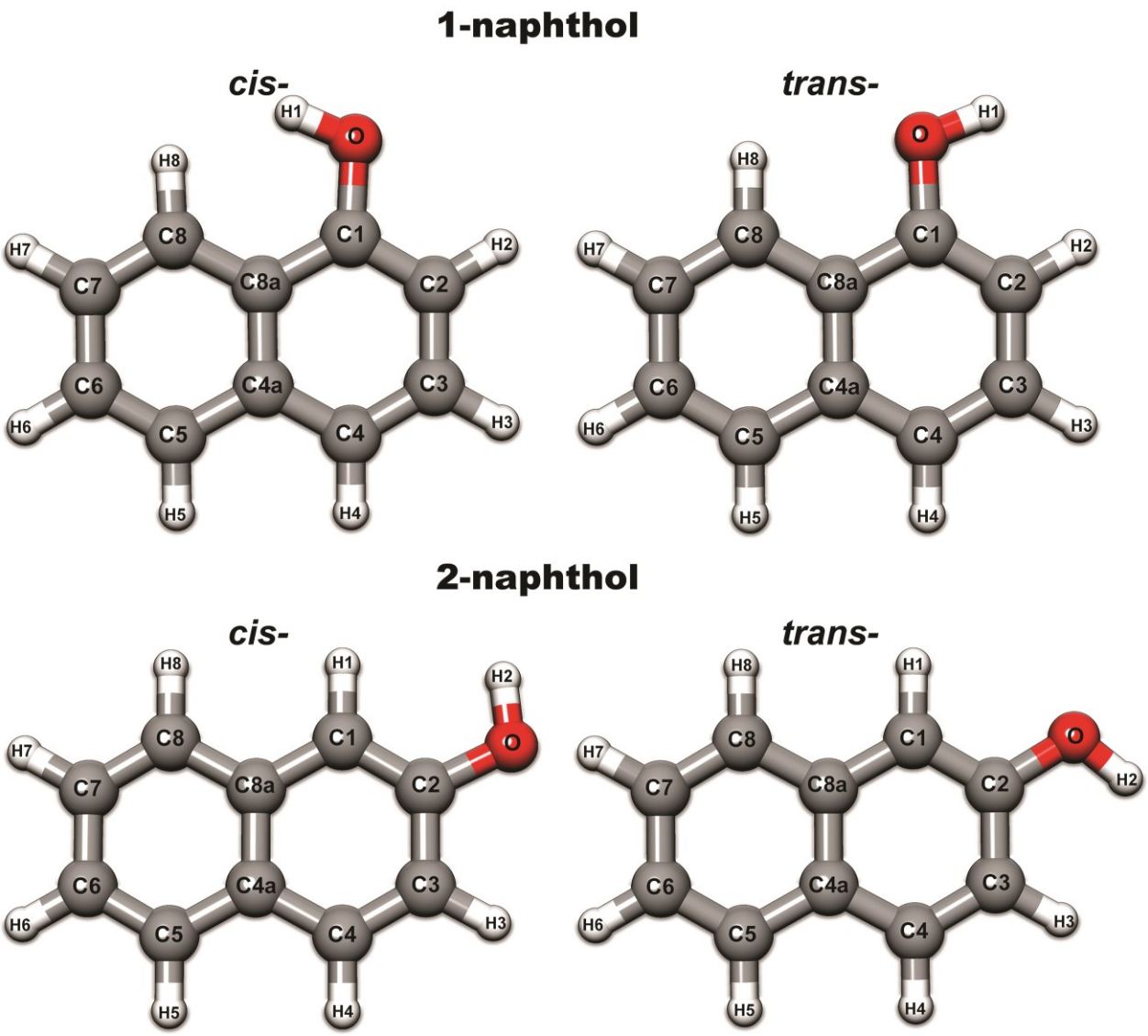

Figure 3.2. Atom number labelling for all four isomers of naphthol.

in the naphthol skeleton, a bond path with a bond critical point between the hydroxyl H-atom and the neighbouring H-atom at the adjacent ring in *cis*-1-naphthol (see Figure 3.4) in the QTAIM analysis. Numerical results from these analyses are given in Table A.17, Appendix A. Additional electronic structure calculations were done at the ωB97XD[69]/Jun-cc-pVTZ[70] and, MP2/aug-cc-pVTZ levels of theory to confirm that the bond critical point and the numerical data from the QTAIM analyses are not unique to the B3LYP-D3(BJ)/def2-TZVP level of theory. The results of this comparison are shown in Table A.18 of Appendix A.

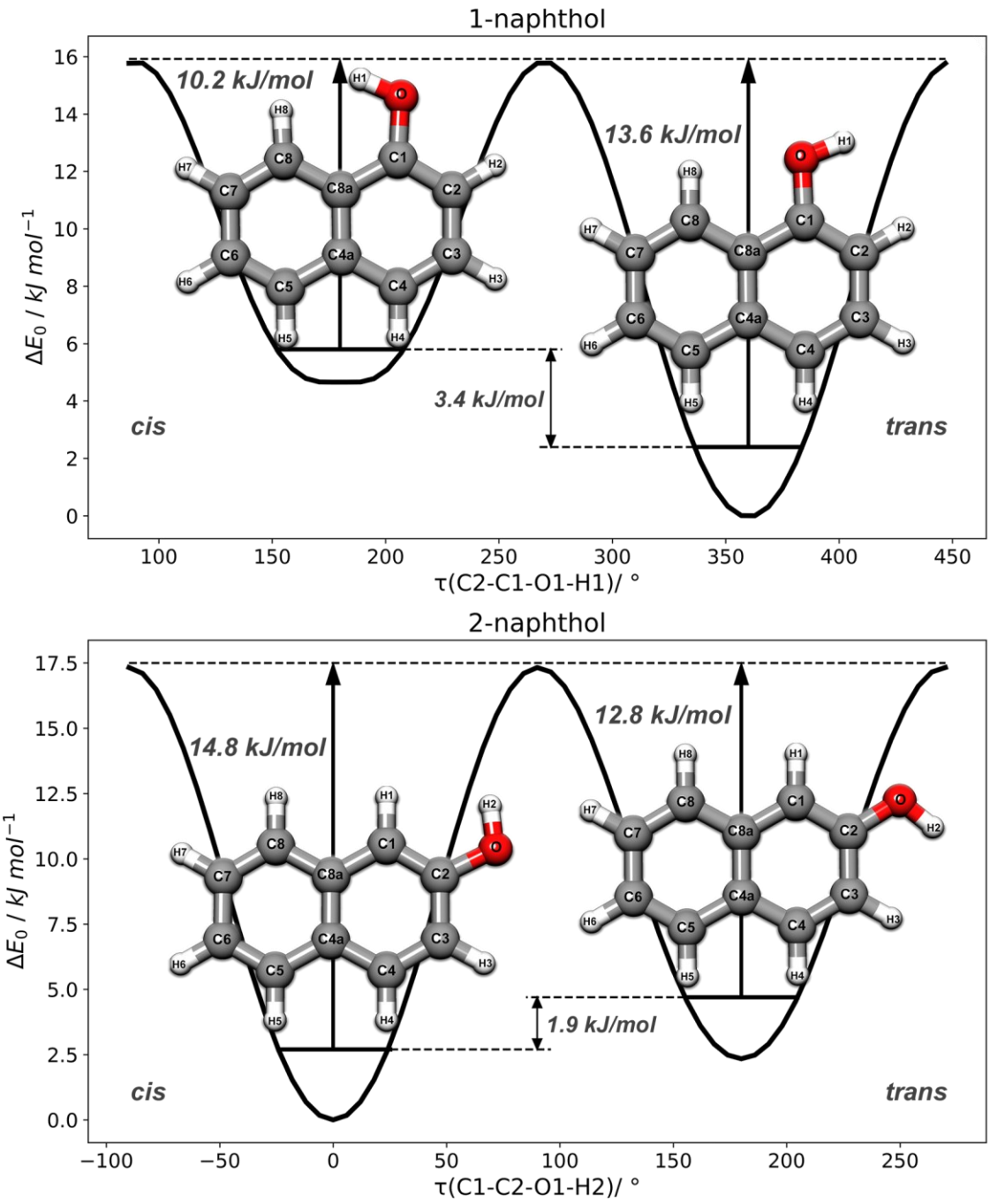

Figure 3.3. Potential energy curves and zero-pointed corrected *cis-trans* barriers for 1-naphthol (top) and 2-naphthol (bottom), calculated at the B3LYP-D3(BJ)/def2-TZVP level of theory.

3.3.3. Structures

The experimental and theoretical (B3LYP-D3(BJ)/def2-TZVP level of theory) rotational constants for *cis*- and *trans*-isomers of both 1- and 2-naphthol in Table 3.1, differ by at most 0.8 %, which is indicative of reasonable agreement between theoretical structural parameters and those

underlying the experimental rotational constants. For a meaningful comparison, however, one needs to take into account the effects of zero-point vibrational motions that cause the difference between equilibrium (r_e) structure and equilibrium (A_e, B_e, C_e) rotational constants on one hand and effective (r_o) structure and ground state (A_0, B_0, C_0) rotational constants on the other. The anharmonic vibrational contributions to the rotational constants were calculated using vibrational perturbation theory (VPT2) at the B3LYP-D3(BJ)/def2-TZVP level and subtracted from the experimental constants to arrive at the so-called semi-experimental rotational constants,[71–73] given in Table 3.2 and Tables A.19 to A.23 in Appendix A. The largest difference to the theoretical equilibrium constants is now less than 0.1 %.

To further assess the quality of the semi-experimental rotational constants, one may look at the inertial defects, defined as $\Delta_I = I_C - (I_A + I_B)$. For a planar rigid molecule Δ_I is zero. The inertial defects for the naphthol isomers (Table 3.1) range from -0.212 to -0.293 amu Å^2 and are consistent with bicyclic heterocycles whose Δ_I values have been discussed in detail by Jahn et al.[74] The negative values are a result of greater contributions by out-of-plane zero-point vibrational motions to the inertial defect compared to the in-plane vibrations. The *cis*-1-naphthol isomer has the largest magnitude Δ_I value. The difference in Δ_I between *cis*- and *trans*-1-naphthol is -0.080 amu Å^2, in reasonable agreement with the theoretical value of Δ_I for *cis*-1-naphthol (-0.047 amu Å^2). The non-zero theoretical value of Δ_I for *cis*-1-naphthol is attributable to the out-of-plane location of the OH H-atom with a dihedral angle τ of 6°. The experimental difference between Δ_I values of 0.080 amu Å^2 corresponds to a dihedral angle τ of 10°. The Δ_I values calculated from the semi-experimental constants (Table A.19, Appendix A) are reduced by about 80% and have magnitudes on the order of 0.05 amu Å^2 or smaller. It is interesting to note that there is an overcorrection for Δ_I in *cis*-1-naphthol compared to the other isomers. This leads to a positive semi-experimental Δ_I value that is not consistent anymore with the out-of-plane OH H-atom in *cis*-1-naphthol. It is likely that the large amplitude motion of the OH H-atom from above to below the heavy atom plane in *cis*-1-naphthol is not captured properly in the anharmonic calculations, thus leading to the inconsistency.

Table 3.2. Experimental, semi-experimental, and theoretical rotational constants of *cis*-1-naphthol.

	Experiment	Semi-Experimental	B3LYP-D3(BJ)
A / MHz	1947.51310	1962.355	1959.859
B / MHz	1124.30739	1130.679	1130.834
C / MHz	713.09734	717.334	717.128

Additionally, the inertial defect values were compared to those discussed by Jahn et al.[74] to examine how naphthol compares to other heterocyclic molecules. The calculated values in Table A.25, Appendix A, for the four isomers of naphthol were computed by summing Oka's equation[75] over the lowest out-of-plane vibrations:

$$\Delta_{0l} = -\sum_{l=1}^{n} \frac{33.175}{\nu_l} \; amu\text{Å}^2 \; cm^{-1} \tag{3.2}$$

Oka noted that Eq. (2) overestimates the magnitude of Δ_0 and introduced an empirical correction to compensate for this overcorrection:

$$\Delta_0 = \Delta_{0l} + \alpha\sqrt{I_{cc}} \tag{3.3}$$

Here, α is a unitless value used to describe the slope of Eq. (3), and $\sqrt{I_{cc}}$ is the square root of the moment of inertia along the *c* principal inertial axis.

As outlined by Jahn et al. the number of out-of-plane modes used in the sum is equal to the number of rings present, or for molecules with an extra low wavenumber out-of-plane vibration (<100 cm^{-1}) is equal to the number of rings +1. The five lowest out-of-plane vibrations for all four isomers of naphthol, with their respective displacement vectors, are presented in Figures A.5-A.8. Based on the results of Jahn et al., for *trans*-1-naphthol and both isomers of 2-naphthol the two lowest out-of-plane vibrations should be used, while the three lowest out-of-plane vibrations should be used for *cis*-1-naphthol to account for the existence of an extra low wavenumber OH out-of-plane vibration. A plot showing the differences between the experimental inertial defect and calculated inertial defect values for different numbers of out-of-plane vibrational modes is shown in Figure A.9. The frequencies of the vibrational modes for each isomer were obtained from the B3LYP-D3(BJ)/def2-TZVP results. The calculated and experimental inertial defect values and the difference between the two are shown in Table A.25 of Appendix A. The calculated inertial defect values from the five lowest out-of-plane modes and the difference between the calculated

and experimental defects values are presented in Tables A.26 and A.27 of Appendix A, respectively. *Cis*-1-naphthol has a difference of ≈0.49 amu Å^2 (three modes), while the differences for *trans* 1-naphthol and both isomers of 2-naphthol range from 0.21-0.23 amu Å^2 (two modes). Comparing these results to the Jahn et al. fit presented in Figure A.9, there is a discrepancy in the $\sqrt{I_{cc}}$ values determined from the plot using the inertial defect difference and the experimental $\sqrt{I_{cc}}$ values. For *trans*-1-naphthol the fit slightly underestimates the experimental $\sqrt{I_{cc}}$ value (≈26.6 amu$^{1/2}$ Å) by several amu$^{1/2}$ Å when the two lowest out-of-plane vibrations are used in the sum. The fit also underestimates the experimental $\sqrt{I_{cc}}$ values for both isomers of 2-naphthol when the two lowest out-of-plane vibrations are used, where the averaged 28.1 amu$^{1/2}$ Å value does not correspond to an average inertial defect difference of 0.22 amu Å^2. The largest discrepancy between the fit data and our results are for *cis*-1-naphthol where the inertial difference of 0.49 amu Å^2 is severely overestimated by the fit of Jahn et al., when the three lowest out-of-plane modes are used to account for the extra low wavenumber out-of-plane vibration. Using the two lowest out-of-plane vibrations instead of the three lowest, the difference (0.32amu Å^2) becomes much closer to the fit of Jahn et al. One potential reason for the discrepancy may be the molecules selected by the authors to construct the fit, which does indeed contain a wider range of sizes of heterocyclic compounds, but do not have any conformational flexibility. Although the skeleton structure of naphthol is not flexible, the hydroxyl group does provide a degree of flexibility which most likely leads to the discrepancy between the result herein and the Jahn et al. fit.

The semi-experimental rotational constants of normal and singly substituted ^{13}C isotopologues of both conformers of 1- and 2-naphthol were used in a fitting procedure to produce the structural parameters in Tables A.13 to A.16, Appendix A. Comparison with the theoretical structure in the same tables shows, in general, good agreement with the average differences on the order of 0.04 Å and 0.9° for bond lengths and angles, respectively.

Another way to minimize the effects of zero-point vibrational motions on structural parameters that is purely based on experimental data is a Kraitchman substitution analysis.[28] Since rotational constants are available for all singly substituted ^{13}C isotopologues, substitution coordinates for all carbon atoms of *cis*- and *trans*- 1- and 2-naphthol were determined. The resulting substitution, r_s, structural parameters are also in Tables A.13 to A.16 of Appendix A and

are in very good agreement with the theoretical and semi-experimental values. The largest differences are on the order of 0.03 Å and 2° for bond lengths and angles, respectively.

3.3.4. Interpretation of the close contact in *cis*-1-naphthol

The naphthol monomers are well suited to shed light on the nature of close-contact H-H interactions. A reason is the availability of the other isomers which can be utilized as internal standards. In this sense, *trans*-1-naphthol is particularly relevant because of the relatively shallow conversion pathway to *cis*-1-naphthol, which allowed us to map relevant properties smoothly from a close-contact H-H interaction to the absence of such interaction (vide infra). Interpretation of the nature of the H-H close contact in *cis*-1-naphthol was done via several approaches: a) atomic energies from QTAIM and NCI plots; b) IGM analysis; c) local mode analysis; d) CM5 atomic charge analysis; e) NBO analysis (electron occupancy, stabilization energies, and steric exchange energies). *Trans*-1-naphthol, *cis*-2-naphthol, and *trans*-2-naphthol were used as control molecules.

a) QTAIM and NCI results

The bond path between the close-contact hydrogen atoms and the corresponding bond critical point found in the QTAIM analysis of *cis*-1-naphthol appears to be indicating a *bonding* interaction between those two H-atoms. This is in stark contrast with the traditional notion of a steric repulsion at a separation of only 1.9 Å, much shorter than the sum of the van der Waals radii of ≈2.4 Å. Accompanying the H-H bond critical point is a ring critical point that is associated with the 6-ring formed by the H-H interaction, in accord with the Poincaré-Hopf relationship. One can follow the evolution of these two critical points along the *cis*-*trans* conversion coordinate and finds that they coalesce and disappear if the dihedral angle τ becomes greater than 21°. Similar effects have been found by the Bader group in pure hydrocarbons, such as phenanthrene,[22] where the two close-contact H-atoms are also connected by a bond path with a bond critical point. This apparent bonding interaction between two equally or similarly charged hydrogen atoms was termed hydrogen-hydrogen, or H-H, bonding, in contrast to dihydrogen bonding, where the two interacting H-atoms have a charge difference of about 1 *e* or more.[22] Bader and co-workers have considered atomic energies within the framework of QTAIM to rationalize the existence of H-H bonding. The atomic energies are obtained by partitioning the molecular kinetic electronic energy among the atomic basins whose extents are defined by the topology of the electron density. Bader

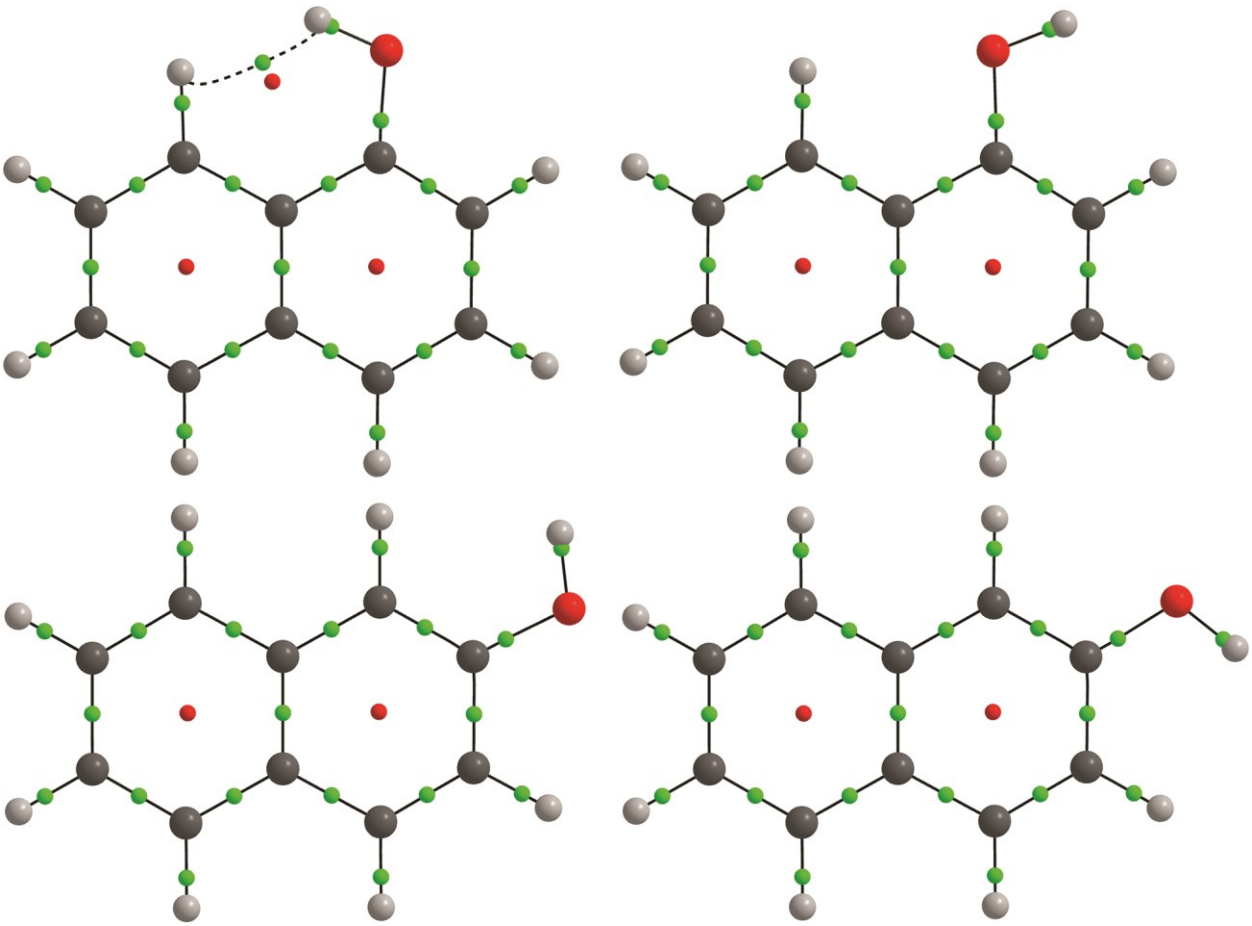

Figure 3.4. Results from QTAIM analyses for the four experimentally observed isomers of naphthol. The green spheres denote bond critical points, while the red spheres denote ring critical points.

and co-workers note that the presence of the H-H bond path is accompanied by a lowering of the collective H-atom energy, in the case of phenanthrene versus its linear isomer anthracene, for example. The concurrent increase in carbon skeleton energy is less in magnitude, such that overall phenanthrene is lower in energy than anthracene.

In some of the hydrocarbons considered by Bader and co-workers, the H-atoms are forced into close contact by the rigid structure of the C-atom skeletons. The case of *cis*-1-naphthol is interesting because of the flexibility in the OH-group orientation; the close H-H contact is adopted 'voluntarily'. We carried out analyses analogous to those by Bader and co-workers for *cis*- and *trans*-1-naphthol using the AIMAll program. A compilation of relevant data from these analyses is given in Table A.17 of Appendix A. It has been asserted before that the electron density distribution is rather insensitive to the level of theory employed,[30,76] so that, for larger systems, even the use of promolecular densities is suggested for electron density analyses. (See, however, also, for example, Joubert et al.[77]) Nevertheless, to make sure that the analyses and conclusions

drawn are not an artifact of the level of theory employed, we did calculations also at the ωB97XD/Jun-cc-pVTZ and MP2/aug-cc-pVTZ levels of theory for *cis*-1-naphthol. The results are in excellent agreement with those from the B3LYP-D3(BJ)/def2-TZVP calculations (see Table A.18), confirming the level of theory has relatively small effect on the molecular electron density distribution.

Properties of the H-H bond critical point and the newly formed ring critical point are in accord with those of other systems with H-H close contacts.[22] For example, the H-H bond critical point is characterized by a low value of 0.015 au for ρ, the electron density, a small positive value of 0.058 au for $\nabla^2\rho$, the Laplacian of the electron density, an energy density H, of 0.0025 au, and a relatively large value of 1.1 for the bond ellipticity, ε. For comparison, the values for the bond critical point of the strong hydrogen bonding interaction in the water dimer are: ρ = 0.026 au, $\nabla^2\rho$ = 0.090 au, H = 0.00098 au, ε = 0.025 at the B3LYP-D3(BJ)/def2-TZVP level of theory. For the acyclic formic acid dimer, the strong hydrogen bond has values of ρ = 0.033 au, $\nabla^2\rho$ = 0.114 au, H = 0.000094 au, ε = 0.033 and the weaker hydrogen bond ρ = 0.011 au, $\nabla^2\rho$ = 0.037 au, H = 0.0011 au, ε = 0.086, also at the B3LYP-D3(BJ)/def2-TZVP level of theory. In *cis*-1-naphthol, the low value of the electron density, the small positive value of the Laplacian, the values for ρ, $\nabla^2\rho$, and H for the H-H close-contact critical point are quite comparable to those of the weaker hydrogen bond in the acyclic formic acid dimer. The ellipticity, ε, though is relatively high in *cis*-1-naphthol, consistent with the close proximity of the ring and bond critical points. Bond and ring critical points move closer to each other as the dihedral angle τ is increased, indicating that the conformer becomes topologically unstable; at τ=21° bond and ring critical points annihilate each other.

I found that the atomic energy, E_A, of the close-contact C-bonded H-atom in *cis*-1-naphthol is *lower* by 48.5 kJ/mol compared to the average energy of all other C-bonded H-atoms. In contrast, the same H-atom is higher in energy by 22.2 kJ/mol in *trans*-1-naphthol. The corresponding stabilization of the close-contact H-atoms in phenanthrene (total of 39.3 kJ/mol) has been interpreted by Bader and co-workers to be a result of a bonded interaction, i.e. H-H bonding.[22] The total H-atom energy is lower by 29.3 kJ/mol in *cis*-1-naphthol and the total heavy atom energy is higher by 33.9 kJ/mol than in *trans*-1-naphthol, consistent with what Bader and coworkers found for the phenanthrene/anthracene case, for example. In total, *trans*-1-naphthol is more stable by 4.6

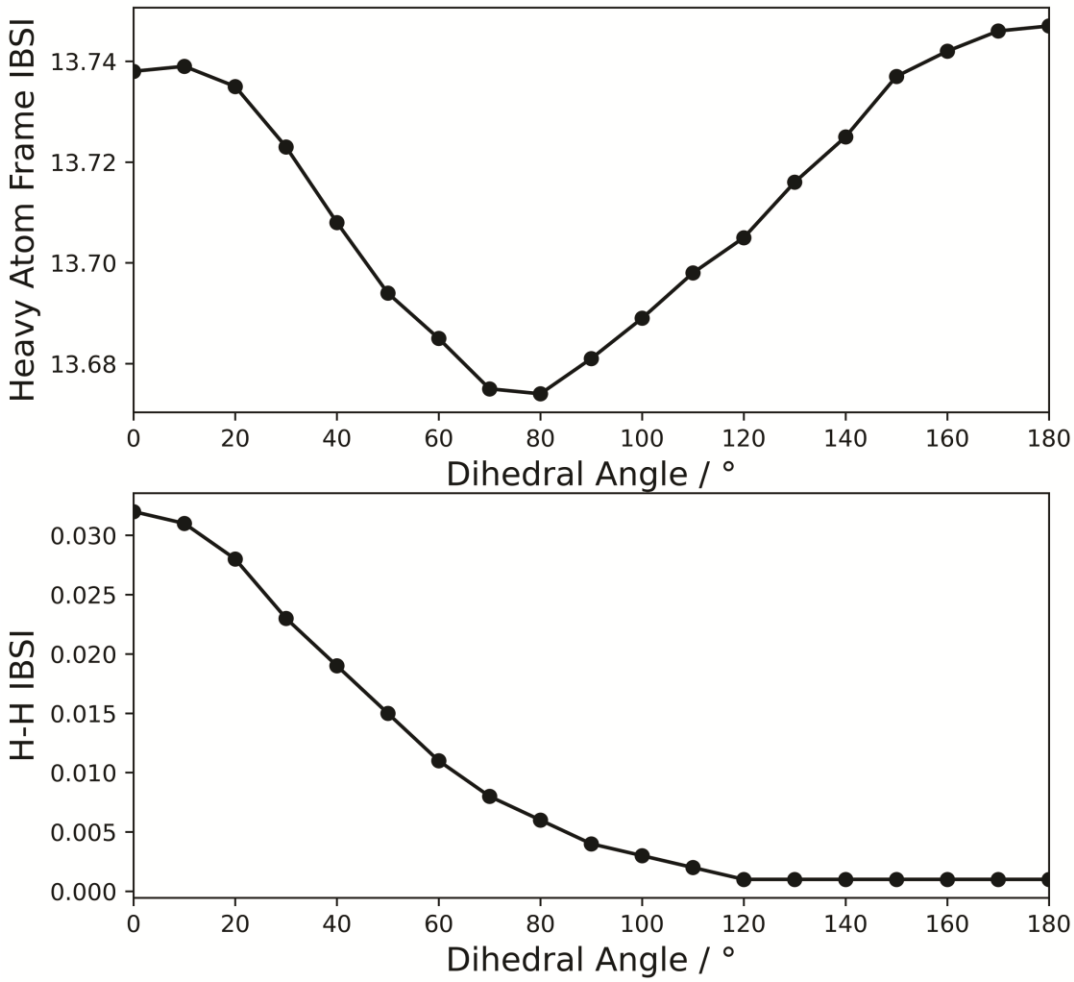

Figure 3.5. Intrinsic bond strength indexes (IBSI), obtained from the independent gradient model (IGM) analysis, for the sum of the bonds in the heavy atom frame (top) and bonds participating in the close-contact H-H interaction (bottom) as a function of dihedral angle. The dihedral angle corresponds to the rotation of the hydroxyl group out of the ring plane.

kJ/mol, consistent with the theoretical calculations. A compilation of relevant data from the AIMAll calculations is in Table A.17 of Appendix A.

The interpretation by Bader and co-workers of the bond path and bond critical point between the close-contact H-atoms in terms of bonding, i.e. H-H bonding, interactions has been criticized, for example by Bickelhaupt and co-workers.[27] In particular, they point out that the physical meaning of the atomic energy, E_A, is not particularly clear. They consider that the reduction of the H-atom E_A when two H-atoms come into close contact may be a result of mainly a reduction in atomic basin volume, for the case of insignificant charge transfer. Grimme et al.[26] have also voiced their doubts about interpreting the bond critical point between the close-contact H-atoms in terms of a bonding interaction. They analysed the experimental splitting between

symmetric and antisymmetric stretching normal modes of vibration involving close-contact D-atoms in dideuteriophenantrene. From this analysis and by comparison with theoretical calculations, they conclude that the observations are inconsistent with a bonding interaction between the close-contact D-atoms. See also the rebuttal by Bader.[24]

Cremer, Kraka et al. introduced a new aromaticity delocalization index assessing π-delocalization in aromatic systems based on vibrational frequencies.[78,79] They could clarify that the larger stability of phenanthrene relative to anthracene predominantly results from its higher resonance energy, a direct consequence of the topology of ring annellation and not from a maximum electron density path between the bay H atoms.[78] Furthermore, they pointed out that the close spatial proximity of ring and bond critical points in the bay region of phenanthrene and their low electron densities, as well as the positive energy density at the bond critical point, are indicative of an electrostatic, destabilizing interaction, confirming the findings of Grimme et al.[26]

b) IGM analyses

To obtain more quantitative insights into the bond strengths within 1-naphthol, independent gradient model (IGM) analyses[31–33] were carried out. The intrinsic bond strength index (IBSI) is based on the δg descriptor of the IGM approach and was recently introduced by Klein et al.[34] A particular strength of the IGM approach is the ability to isolate and characterize interactions between pairs of atoms (or between fragments). The IBSI values are related to the bond strength and was shown that there is a good linear correlation between IBSI values and the corresponding local force constants. Weak interactions have IBSI values $\lesssim 0.15$ and for stronger or covalent interactions IBSI $\gtrsim 0.15$.

The IBSI value for the close-contact H-H interaction in *cis*-1-naphthol is 0.031. Those for the hydrogen bond and for the O-H bond in the hydrogen bond acceptor molecule in the water dimer are 0.059 and 1.394, respectively, and for the strong and weak hydrogen bonds in the acyclic formic acid dimer 0.091 and 0.020, respectively.

To understand how the bonding situation in 1-naphthol evolves with dihedral angle τ, IBSI values for all bonds were determined, except the C-H bonds not involved in the H-H close contact, as function of τ. Figure 3.5 displays the IBSI value corresponding to the close-contact H-H interaction and the sum of all IBSI values of all bonds involving only heavy atom as function of τ. The latter gives us an indication of the aggregate bond strength of the heavy atom skeleton as τ is

varied. As anticipated, the H-H IBSI value decreases as τ increases. The aggregate IBSI value for the heavy atom skeleton decreases initially, indicating a destabilization as τ increases. This can be interpreted as a destabilization of a π-electron resonance structure as the π-electron delocalization into the C-O bond is hindered as the dihedral is increased. Once the OH H-atom begins to move to the *trans*-side, the aggregate heavy atom skeleton IBSI value increases again and reaches a slightly higher value at 180° than at 0°.

c) Local Mode analyses

An in-depth assessment of the O-H bond strengths can provide important indicators about the nature of the C-H - H-O interaction in *cis*-1-naphthol. The power relationship between BSO n and k^a of O-H bonds in naphthol and some reference molecules are shown in Figure 3.6 and their respective local mode force constants and local mode frequencies are reported in Table A.24, Appendix A. In case of 1-naphthol, a bonding interaction between H-atoms would lead to a weakening of the O-H bond for the *cis* conformer compared to the *trans* conformer as electron density is moved from the O-H bond region. Conversely, a stronger O-H bond in *cis*-1-naphthol would be consistent with the traditional notion of a steric repulsion between the H-atoms. In comparison to the reference molecules, it can be seen that the O-H bond strengths in naphthol compounds tend to be weaker than those in water, propen-2-ol, and methanol while they are comparable to those in phenol and 2-propanol. Importantly, it is revealed that the O-H bond strengths in naphthol compounds vary in the order, *cis*-1-naphthol > *trans*-2-naphthol > *trans*-1-naphthol > *cis*-2-naphthol. This supports a mainly *repulsive* H-H interaction in *cis*-1-naphthol and contradicts the possibility of a dominant bonding interaction as one would speculate based on the bond critical point between the H-atoms. This observed trend in the O-H bond strengths for the naphthol compounds can also be visualized as a blue shift in the IR spectrum provided that the OH normal mode is not coupling with the other modes, e.g., bending modes. This was investigated via the characterization of normal modes (CNM) procedure for *cis* and *trans* conformers of 1-naphthol calculated at the B3LYP-D3(BJ) level of theory. In Figures A.2 and A.3 of Appendix A, the decomposition plots for all normal modes (51 modes) into a non-redundant set of 51 local modes, for *cis*- and *trans*- conformers of 1-naphthol, are shown where the OH normal mode is highlighted in yellow. It is observed that the OH normal stretching mode (3817 cm^{-1}) in the *cis* conformer has 99.9% contribution from O-H local stretching mode with up to 0.06% contributions from the two

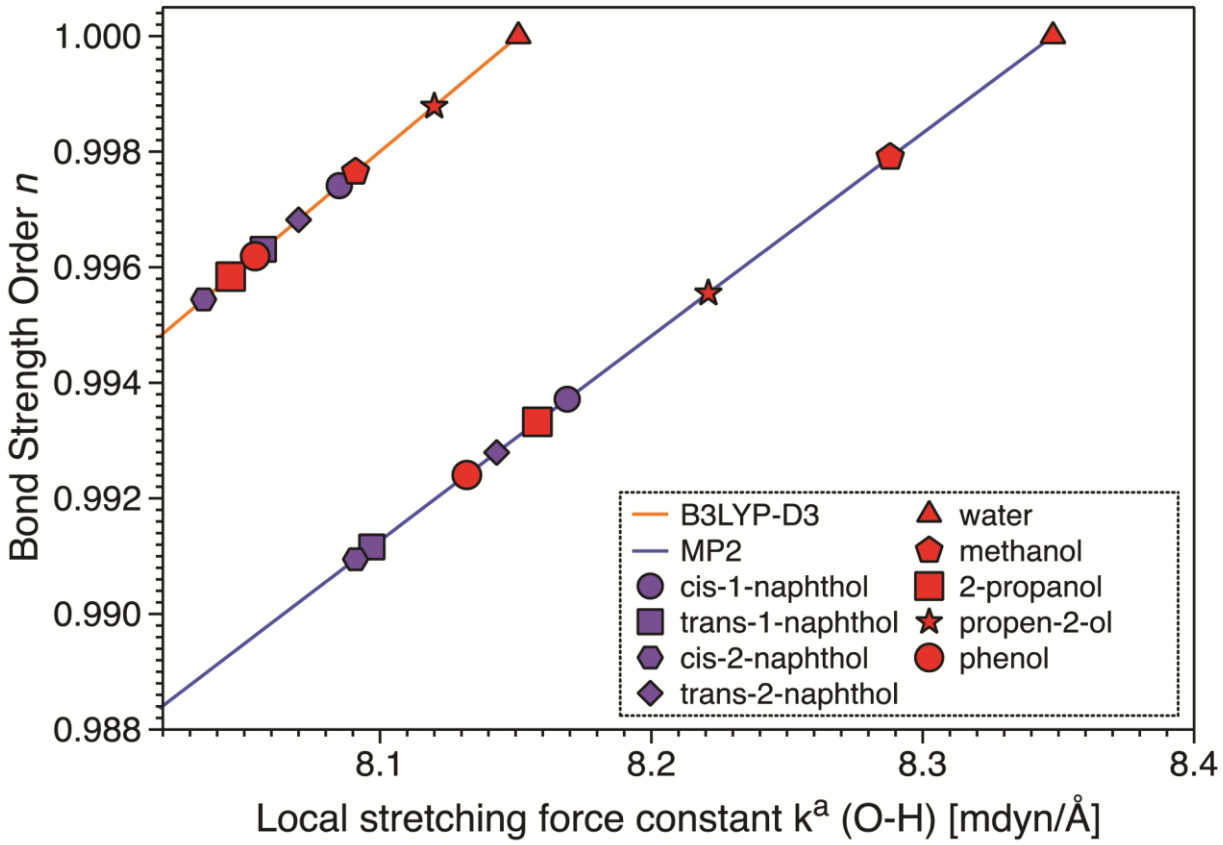

Figure 3.6. Power relationship between bond strength order (BSO) n and k^a of O-H bonds in *cis*- and *trans*-, 1- and 2- naphthol (in purple) and reference molecules (in red) for B3LYP-D3(BJ) (orange line) and MP2 (blue line) calculations. (BSO) n has been scaled by a factor of 1.045 and 1.041 for B3LYP-D3(BJ) and MP2 calculations, respectively.

O-C-C local bending modes. Also, in the *trans* conformer, the O-H local stretching mode dominates with 99.93% contribution to the OH normal mode (3804 cm^{-1}). As the O-H normal modes in both conformers possess the character of an almost pure O-H stretching mode, one can directly compare the corresponding O-H normal modes. Thus, as reflected by the blue shift, which has also been confirmed experimentally,[15] of *cis*-1-naphthol the repulsive aspect of the close-contact H-atoms can be quantified based on vibrational spectroscopy.

d) CM5 atomic charge analysis

In an effort to build on the previous methods discussed herein and further examine the interaction between the two close-contact H-atoms, a Charge Model 5 (CM5)[41] charge analysis was carried out, which derives partial atomic charges from a Hirshfeld population analysis. By measuring the CM5 atomic charges as the dihedral angle τ of *cis*-1-naphthol is varied from 90° to 0°, one can

ultimately infer how the electron density around each atom changes as the two hydrogens approach each other. Because of the absence of a bond critical point (QTAIM and NCI plot in Figure 3.4 and Figure A.1 of Appendix A, respectively) between the two hydrogens, *trans*-1-naphthol, *cis*-2-naphthol, and *trans*-2-naphthol were used as control molecules. The charges of the five atoms which play the most prominent role in this interaction were examined : the hydroxyl hydrogen (H'), oxygen (O'), the carbon bound to the oxygen (C'), the close-contact hydrogen (H"), and the carbon bound to the close-contact hydrogen (C"). The labelling is summarized in Figure 3.7. The charge as a function of dihedral angle for all four isomers of naphthol, and the net charge change for each atom are summarized in Figure 3.8 and Table A.29 of Appendix A, respectively. Based on Figure 3.8 and Table A.29, no anomalies are observed for atoms C" and C' of *cis* 1-naphthol as the charge change generally follows the same pattern as in the other isomers. For the most part the O' atom follows the trends of the other isomers, with the net change (Table A.29) only slightly smaller than in its counterparts. Interestingly, for the two hydrogens the charge pattern for *cis*-1-naphthol deviates significantly from the other isomers. For the H" atom the charge, and thus the electron density at the atom, does not change significantly in *cis*-1-naphthol, while the electron density decreases for the other isomers with increasing dihedral angle. For the H' atom the charge decreases (increasing electron density) as the dihedral angle approaches 0°, while it stays almost

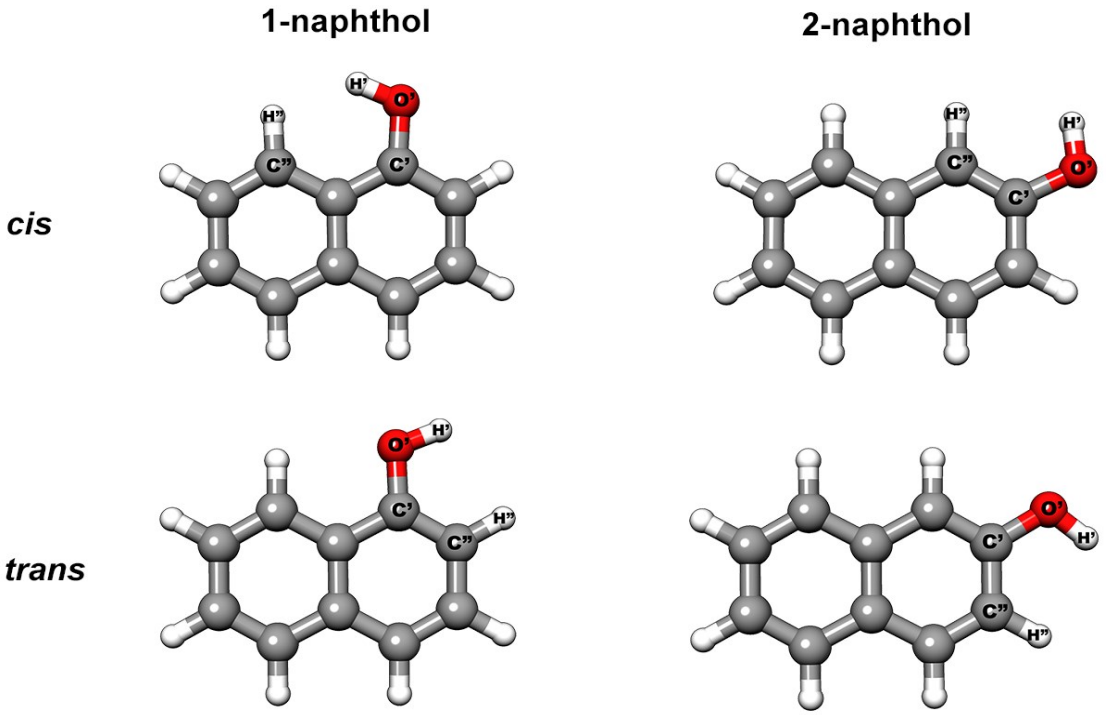

Figure 3.7. Atom labelling used in the descriptions of the H-H interactions

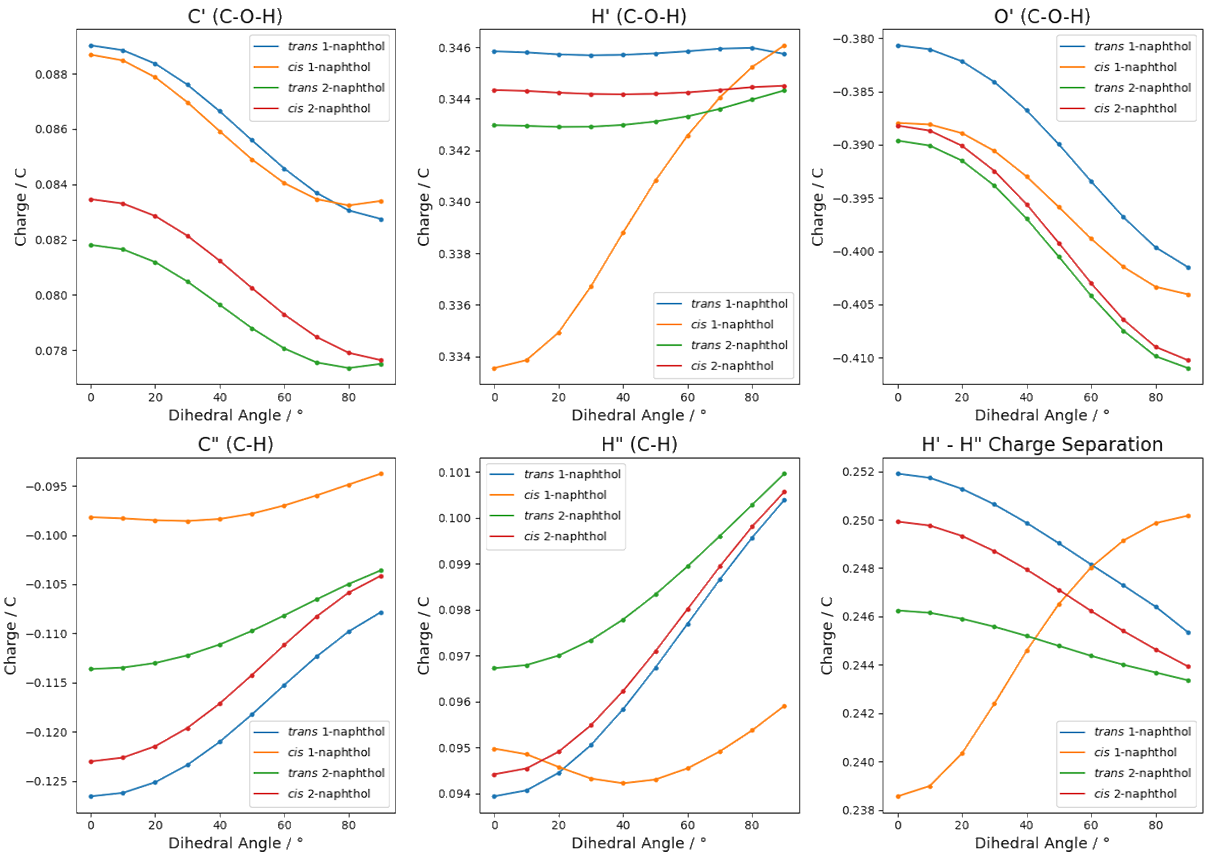

Figure 3.8. Charge Model 5 (CM5) charges for atoms involved in the H-H interaction for all four naphthol isomers. The H'-H" charge separation was calculated by subtracting the H" charge from the H' charge.

constant for the other isomers. Although there is a clear increase in electron density for H', attributing this to a bonding or non-bonding interaction is not so straightforward. On one hand the slightly smaller change in net charge of O', and therefore less electron density being moved away from the O' atom, may indicate a steric repulsive H-H interaction. On the other hand, an increase in electron density for the H' atom may be indicative of a bonding interaction as electron density is being transferred to the H' atom from the H" atom.

e) NBO analysis

To further examine this electron transfer and clarify the CM5 results, a Natural Bond Orbital (NBO) analysis[42,43] was carried out. We extended a previous analysis[21] to provide a more comprehensive breakdown of the close-contact H-H interaction into its respective stabilization and steric exchange energies. An NBO analysis allows for the decomposition of non-covalent and covalent interactions into localized bonding and antibonding orbitals. In the framework of NBO an intermolecular

interaction, or an intramolecular interaction as considered here, can be considered a charge transfer interaction where electron density is transferred from a bonding orbital (BD) at the donor site to an antibonding orbital (BD*) on the acceptor site. For example, if a bonding interaction was to be present in *cis*-1-naphthol one would observe an electron density transfer from the O'-H' BD to the C"-H" BD* and/or from the C"-H" BD to the O'-H' BD*. Table A.30 of Appendix A presents the electron occupancies for the O'-H' BD, C"-H" BD, O'-H' BD*, and the C"-H" BD*. From Table A.30, there is a slightly lower occupancy in both the O'-H' BD and C"-H" BD and a higher occupancy in both the O'-H' BD* and C"-H" BD* in *cis*-1-naphthol compared to the other isomers, supporting the notion of a bonding interaction. Using a second order perturbative treatment of the Fock matrix, the two interactions (C"-H" BD --- O'-H' BD* and O'-H' BD --- C"-H" BD*) can be quantified in terms of stabilization energies as a function of dihedral angle τ (Tables A.31-A.34). The sum of the two BD-BD* interactions for the close-contact H-H interaction is plotted in Figure 3.5 for each isomer. The total summed donor-acceptor interactions for 1-naphthol with the close-contact H-H interaction subtracted from the total energy is shown in Figure A.11 of Appendix A. From Figure 3.9 one can clearly see that the stabilization energies are several kJ mol^{-1} higher for *cis*-1-naphthol than for the other isomers, suggesting an attractive interaction between the two hydrogen atoms. To examine the repulsive components of the close-contact hydrogens we looked at the pairwise steric exchange energies between the C"-H" BD and O'-H' BD. The results are also plotted in Figure 3.9. The total steric exchange energy with the close-contact H-H interaction subtracted from the total steric exchange energy is presented in Figure A.11 of Appendix A. The steric exchange energy for *cis*-1-naphthol increases far more compared to the other isomers as the dihedral angle approaches 0° and outweighs the stabilization energy by a factor of almost three. The ωB97XD/Jun-cc-pVTZ results are also consistent with these findings, see Table A.35 of Appendix A. Therefore, a large steric or repulsive interaction between the two hydrogens is present. Finally, comparing the steric (repulsion) energies to the stabilization (attraction) energies (Figure 3.9) one can clearly see that although the stabilization energy is considerably larger compared to the other isomers, the steric energy is even larger and outweighs the stabilization contribution.

After these analyses, a coherent, albeit qualitative, picture of the close-contact H-H interaction emerges. At the equilibrium structure, there are no net forces acting on the atoms and therefore the repulsive forces between the two close-contact H atoms must be compensated for by

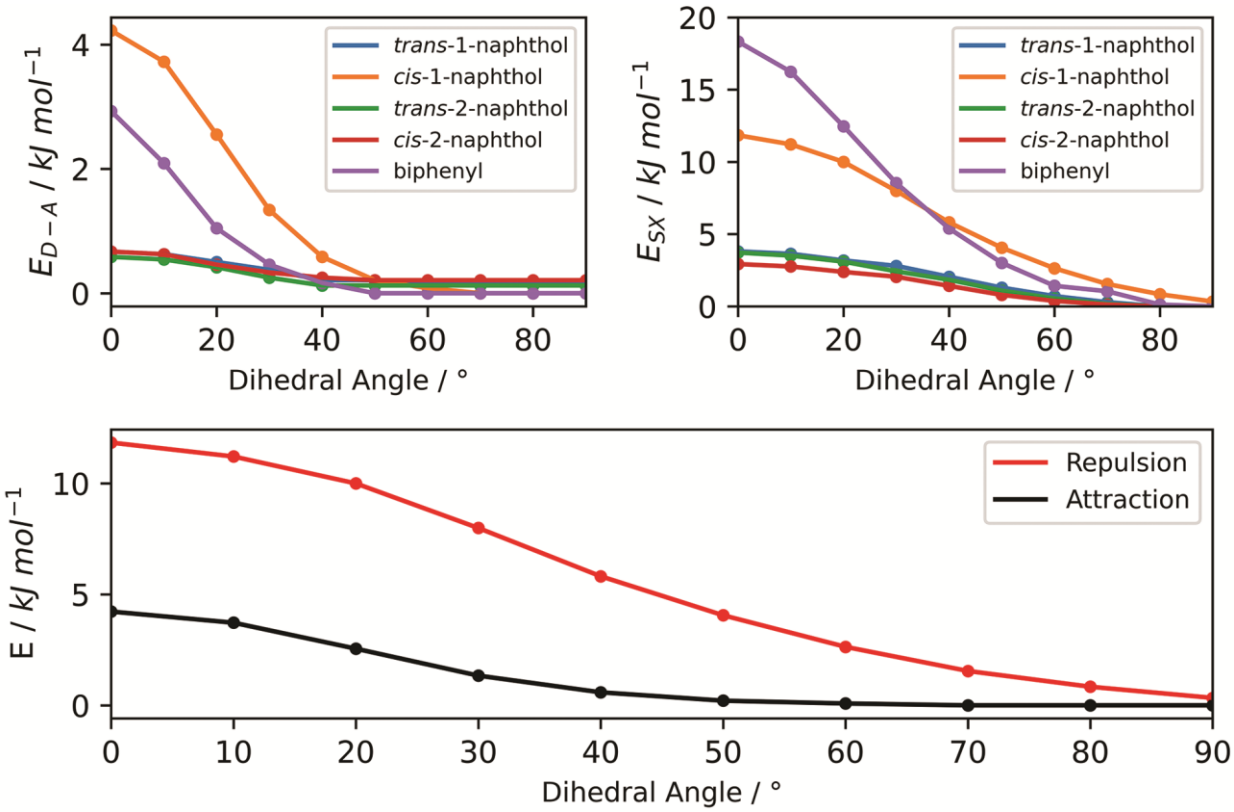

Figure 3.9. Summed donor-acceptor (attraction) energies for the O-H bonding orbital (BD) --- C-H antibonding orbital (BD*) and C-H BD --- O-H BD* interactions (top left). Pairwise steric exchange (repulsion) energies between the C-H BD and O-H BD (top right). Comparison between the repulsive and attractive energies for cis-1-naphthol (bottom).

bonding or some restoring forces. The topology of the electron density between the two close H-atoms, resembles, at least qualitatively, that of a weak hydrogen bond and it is difficult not to ascribe some bonding, i.e. stabilizing, character to it. This, however, appears not to be the dominant stabilizing interaction; that role we attribute to the resistance of the heavy atom skeleton to be forced out of one of its π-electron resonance structures. The role of maximizing the π-electron delocalisation in stabilizing the close H-H contact in *cis*-1-naphthol has already been pointed out by Whitham et al.[20]

3.3.5. Biphenyl: a related system

It is desirable to confirm the findings about the close-contact H-H interaction in *cis*-1-naphthol by comparing with similar systems. It is, however, difficult to find an analogue molecular system and biphenyl is used for comparison. Biphenyl has a soft coordinate, i.e. the phenyl – phenyl rotation, along which the H-H separation can be varied, similar to the OH rotation coordinate in *cis*-1-

naphthol. Upon rotation by 180°, however, biphenyl assumes its original configuration and conversion to a conformer without close H-H contact, as in 1-naphthol, is not possible. Analogous to *cis*-1-naphthol, the single bond connecting the aromatic rings in biphenyl also exhibits a partial π character, thus hindering the rotation about that bond. As found previously,[80,22] biphenyl contains a BCP between two close-contact hydrogens in its planar geometry, which, much like *cis*-1-naphthol, annihilates with the corresponding RCP at τ ≈22°. Its equilibrium geometry is ≈40° out of plane. Figure 3.10 presents the results from an NCI analysis of the planar and equilibrium geometries of biphenyl. Just as with *cis*-1-naphthol, the planar geometry exhibits strong attraction between two pairs of similarly charged hydrogens, indicated by the blue colouration. This attraction is diminished in the equilibrium structure, consistent with the annihilation of the BCP with the RCP at ≈22°. Figure 3.9 and Figure A.10 of Appendix A present the NBO and CM5 results for the close-contact H-H atoms, respectively. The CM5 results for biphenyl differ somewhat from those of *cis*-1-naphthol where the atomic CM5 charge change is not as drastic in biphenyl (see Table A.29 of Appendix A). The biphenyl NBO results are analogous to *cis*-1-naphthol, that is the donor-acceptor energy is relatively large when the two hydrogen atoms are in close contact, indicating an attraction, with the steric exchange energy also large when in close contact. In addition, the biphenyl close-contact case has a weaker attraction component and a stronger steric component than *cis*-1-naphthol, suggesting that the H-H interaction is actually stronger and more favourable in *cis*-1-naphthol than in biphenyl.

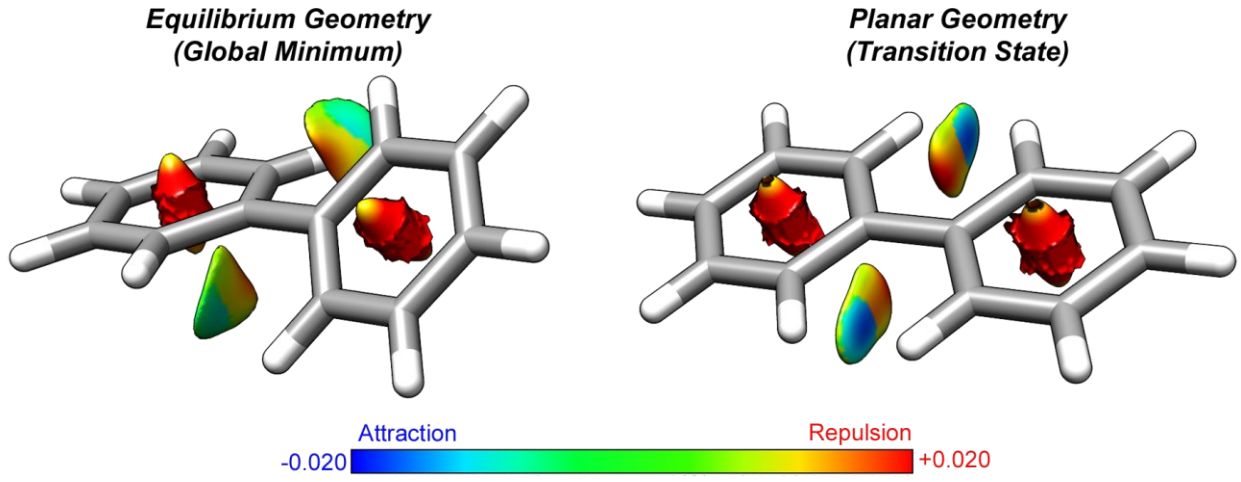

Figure 3.10. Results from non-covalent interactions (NCI) analyses of biphenyl. The 3D isosurfaces presented contain attractive (blue) and repulsive (red) regions (s=0.75).

Despite the similarities between the two systems there is one underlying issue with biphenyl. Unlike *cis*-1-naphthol, where a BCP is present in the equilibrium geometry, the equilibrium geometry in biphenyl does not have a BCP between the close-contact hydrogen atoms; the close-contact H-H interaction is strongest in the planar geometry which is actually a transition state and not an equilibrium structure. Ultimately, the steric repulsion in biphenyl outcompetes the attractive component of the H-H interaction and the restoring force of the heavy atom frame, a result of the rotation about the partial π bond. This is in contrast with *cis*-1-naphthol where the steric repulsion of the two hydrogen atoms cannot overcome the combination of the attraction component and restoring force of the heavy atom skeleton.

3.4. Conclusions

Rotational spectra of the 1-naphthol and 2-naphthol monomers were recorded using a CP-FTMW spectrometer in the 2-6 GHz range. The spectrum of *trans*-2-naphthol was assigned and extended the measurements for the other isomers. In addition to the parent species, spectra of ten ^{13}C isotopologues were assigned for each conformer. The ^{13}C isotopologues were then used to determine carbon-skeleton substitution structures. The corresponding bond lengths and bond angles are in good agreement with the theoretical results.

For *cis*-1-naphthol, QTAIM and NCI analyses of the B3LYP-D3(BJ)/def2-TZVP calculated electron density give a bond path with bond critical point between the close-contact OH and ring H-atom. The IGM analysis reveals that the heavy atom skeleton aids in stabilizing the close-contact hydrogens, where the stabilizing force originates from the steric strain provided by the weakening of the π-electron delocalization. Local mode analyses were carried out for the naphthols and the O-H bond strengths were compared for all four conformers. The results show that *cis*-1-naphthol has the strongest O-H bond among the four isomers. This is consistent with the traditional notion of a steric repulsion between the two close-contact H-atoms, in accord also with the blue-shift of the OH stretching frequency in *cis*-1-naphthol. Charge Model 5 and, in particular, Natural Bond Orbital analyses of *cis*-1-naphthol do support the notion of a weak bonding H-H interaction, which, however, is outweighed by steric repulsion. The major part of the stabilizing force is presumably provided by a maximization of π-electron delocalization, as already pointed out by Whitham et al.[20] In the flexible comparison molecule biphenyl, the steric repulsion of the

two close-contact hydrogens outcompetes the attraction and heavy atom skeleton restoring force, in contrast with *cis*-1-naphthol, and the BCP disappears in the non-planar equilibrium structure.

The idea of a non-bonding or bonding H-H interaction has been previously met with controversy, with both camps presenting arguments for their conclusions. However, much like categorizing non-covalent interactions as either weak or strong, labelling the close-contact H-H interaction in *cis*-1-naphthol as purely non-bonding/repulsive or bonding/attractive does perhaps not give the whole picture. As presented with the several methods completed herein, close-contact H-H interactions involve a mixture of attractive and repulsive forces, with contributions from both the close-contact hydrogens and the heavy atom skeleton. Although there is an attractive component in the close-contact H-H interaction, it is overwhelmed by the repulsive component.

3.5. References

1 H. Shindy, *Chem Int*, 2016, **2**, 2016.

2 C. Sams, *Toxics*, 2017, **5**, 3.

3 D. L. Sudakin, D. L. Stone and L. Power, *Curr. Top. Toxicol.*, 2011, **7**, 13.

4 R. Knochenmuss and S. Leutwyler, *J. Chem. Phys.*, 1989, **91**, 1268–1278.

5 T. Droz, R. Knochenmuss and S. Leutwyler, *J. Chem. Phys.*, 1990, **93**, 4520–4532.

6 S. Maity, R. Knochenmuss, C. Holzer, G. Féraud, J. Frey, W. Klopper and S. Leutwyler, *J. Chem. Phys.*, 2016, **145**, 164304.

7 S. Maity, P. Ottiger, F. A. Balmer, R. Knochenmuss and S. Leutwyler, *J. Chem. Phys.*, 2016, **145**, 244314.

8 R. Knochenmuss, S. Maity, F. Balmer, C. Müller and S. Leutwyler, *J. Chem. Phys.*, 2018, **149**, 034306.

9 R. Knochenmuss, R. K. Sinha and S. Leutwyler, *J. Chem. Phys.*, 2018, **148**, 134302.

10 M. Schütz, T. Bürgi, S. Leutwyler and T. Fischer, *J. Chem. Phys.*, 1993, **99**, 1469–1481.

11 C. Wickleder, D. Henseler and S. Leutwyler, *J. Chem. Phys.*, 2002, **116**, 1850–1857.

12 R. Knochenmuss, R. K. Sinha, A. Poblotzki, T. Den and S. Leutwyler, *J. Chem. Phys.*, 2018, **149**, 204311.

13 R. Knochenmuss, R. K. Sinha and S. Leutwyler, *J. Chem. Phys.*, 2019, **150**, 234303.

14 R. Yoshino, K. Hashimoto, T. Omi, S. Ishiuchi and M. Fujii, *J. Phys. Chem. A*, 1998, **102**, 6227–6233.

15 R. D. Knochenmuss and D. E. Smith, *J. Chem. Phys.*, 1994, **101**, 7327–7336.
16 S. J. Humphrey and D. W. Pratt, *J. Chem. Phys.*, 1996, **104**, 8332–8340.
17 M. Saeki, S. Ishiuchi, M. Sakai and M. Fujii, *J. Phys. Chem. A*, 2007, **111**, 1001–1005.
18 N. A. Seifert, A. S. Hazrah and W. Jäger, *J. Phys. Chem. Lett.*, 2019, **10**, 2836–2841.
19 J. R. Johnson, K. D. Jordan, D. F. Plusquellic and D. W. Pratt, *J. Chem. Phys.*, 1990, **93**, 2258–2273.
20 C. J. Whitham, R. J. Jackson and J. M. Brown, *J. Mol. Spectrosc.*, 1999, **195**, 172–176.
21 M. Goubet, M.-A. Martin-Drumel, F. Réal, V. Vallet and O. Pirali, *J. Phys. Chem. A*, 2020, **124**, 4484–4495.
22 C. F. Matta, J. Hernández-Trujillo, T.-H. Tang and R. F. Bader, *Chem. Eur. J.*, 2003, **9**, 1940–1951.
23 C. F. Matta, in *Hydrogen Bonding—New Insights*, Springer, 2006, pp. 337–375.
24 R. F. Bader, *J. Phys. Chem. A*, 2009, **113**, 10391–10396.
25 N. K. Monteiro and C. L. Firme, *J. Phys. Chem. A*, 2014, **118**, 1730–1740.
26 S. Grimme, C. Mück-Lichtenfeld, G. Erker, G. Kehr, H. Wang, H. Beckers and H. Willner, *Angew. Chem. Int. Ed.*, 2009, **48**, 2592–2595.
27 J. Poater, M. Solà and F. M. Bickelhaupt, *Chem. Eur. J.*, 2006, **12**, 2889–2895.
28 J. Kraitchman, *Am. J. Phys.*, 1953, **21**, 17–24.
29 R. F. W. Bader, *Chem. Rev.*, 1991, **91**, 893–928.
30 E. R. Johnson, S. Keinan, P. Mori-Sánchez, J. Contreras-García, A. J. Cohen and W. Yang, *J. Am. Chem. Soc.*, 2010, **132**, 6498–6506.
31 C. Lefebvre, G. Rubez, H. Khartabil, J.-C. Boisson, J. Contreras-García and E. Hénon, *Phys. Chem. Chem. Phys.*, 2017, **19**, 17928–17936.
32 C. Lefebvre, H. Khartabil, J.-C. Boisson, J. Contreras-García, J.-P. Piquemal and E. Hénon, *ChemPhysChem*, 2018, **19**, 724–735.
33 M. Ponce-Vargas, C. Lefebvre, J.-C. Boisson and E. Hénon, *J. Chem. Inf. Model.*, 2020, **60**, 268–278.
34 J. Klein, H. Khartabil, J.-C. Boisson, J. Contreras-García, J.-P. Piquemal and E. Hénon, *J. Phys. Chem. A*, 2020, **124**, 1850–1860.
35 E. Kraka, W. Zou and Y. Tao, *Wiley Interdiscip. Rev. Comput. Mol. Sci.*, 2020, **10**, e1480.
36 Z. Konkoli and D. Cremer, *Int. J. Quantum Chem.*, 1998, **67**, 1–9.

37 Z. Konkoli and D. Cremer, *Int. J. Quantum Chem.*, 1998, **67**, 29–40.

38 Z. Konkoli, J. A. Larsson and D. Cremer, *Int. J. Quantum Chem.*, 1998, **67**, 11–27.

39 E. Kraka, J. A. Larsson and D. Cremer, *Comput. Spectrosc. Grunenberg J Ed Wiley N. Y. NY USA*, 2010, 105–149.

40 D. Cremer, J. A. Larsson and E. Kraka, in *Theoretical and computational chemistry*, Elsevier, 1998, **5**, 259–327.

41 A. V. Marenich, S. V. Jerome, C. J. Cramer and D. G. Truhlar, *J. Chem. Theory Comput.*, 2012, **8**, 527–541.

42 E. D. Glendening, C. R. Landis and F. Weinhold, *J. Comput. Chem.*, 2013, **34**, 1429–1437.

43 A. E. Reed and F. Weinhold, *J. Chem. Phys.*, 1983, **78**, 4066–4073.

44 W. Kohn and L. J. Sham, *Phys. Rev.*, 1965, **140**, A1133.

45 M. J. Frisch, G. W. Trucks, H. B. Schlegel, G. E. Scuseria, M. A. Robb, J. R. Cheeseman, G. Scalmani, V. Barone, G. A. Petersson, H. Nakatsuji, X. Li, M. Caricato, A. V. Marenich, J. Bloino, B. G. Janesko, R. Gomperts, B. Mennucci, H. P. Hratchian, J. V. Ortiz, A. F. Izmaylov, J. L. Sonnenberg, D. Williams-Young, F. Ding, F. Lipparini, F. Egidi, J. Goings, B. Peng, A. Petrone, T. Henderson, D. Ranasinghe, V. G. Zakrzewski, J. Gao, N. Rega, G. Zheng, W. Liang, M. Hada, M. Ehara, K. Toyota, R. Fukuda, J. Hasegawa, M. Ishida, T. Nakajima, Y. Honda, O. Kitao, H. Nakai, T. Vreven, K. Throssell, J. A. Montgomery Jr., J. E. Peralta, F. Ogliaro, M. J. Bearpark, J. J. Heyd, E. N. Brothers, K. N. Kudin, V. N. Staroverov, T. A. Keith, R. Kobayashi, J. Normand, K. Raghavachari, A. P. Rendell, J. C. Burant, S. S. Iyengar, J. Tomasi, M. Cossi, J. M. Millam, M. Klene, C. Adamo, R. Cammi, J. W. Ochterski, R. L. Martin, K. Morokuma, O. Farkas, J. B. Foresman and D. J. Fox, Gaussian 16, Gaussian Inc., Wallingford, CT, 2016.

46 S. Grimme, S. Ehrlich and L. Goerigk, *J. Comput. Chem.*, 2011, **32**, 1456–1465.

47 A. D. Becke, *J. Chem. Phys.*, 1992, **96**, 2155–2160.

48 A. D. Becke and E. R. Johnson, *J. Chem. Phys.*, 2005, **123**, 154101.

49 F. Weigend and R. Ahlrichs, *Phys. Chem. Chem. Phys.*, 2005, **7**, 3297–3305.

50 Chr. Møller and M. S. Plesset, *Phys. Rev.*, 1934, **46**, 618–622.

51 T. A. Keith, AIMALL, TK Gristmill Software, Overland Park, KS, 2017.

52 T. Lu and F. Chen, *J. Comput. Chem.*, 2012, **33**, 580–592.

53 E. F. Pettersen, T. D. Goddard, C. C. Huang, G. S. Couch, D. M. Greenblatt, E. C. Meng and T. E. Ferrin, *J. Comput. Chem.*, 2004, **25**, 1605–1612.

54 W. Zou, Y. Tao, M. Freindorf, M. Z. Makos´, N. Verma, D. Cremer and E. Kraka, Local Vibrational Mode Analysis (LModeA), Computational and Theoretical Chemistry Group (CATCO), Southern Methodist University, Dallas, TX, USA, 2021.

55 E. B. Wilson, J. C. Decius and P. C. Cross, *Molecular vibrations: the theory of infrared and Raman vibrational spectra*, Courier Corporation, 1980.

56 W. Zou and D. Cremer, *Chem. Eur. J.*, 2016, **22**, 4087–4099.

57 E. Kraka and M. Freindorf, .

58 M. Freindorf and E. Kraka, *J. Mol. Model.*, 2020, **26**, 1–15.

59 S. Yannacone, M. Freindorf, Y. Tao, W. Zou and E. Kraka, *Crystals*, 2020, **10**, 556.

60 A. A. Delgado, D. Sethio, I. Munar, V. Aviyente and E. Kraka, *J. Chem. Phys.*, 2020, **153**, 224303.

61 W. Zou, R. Kalescky, E. Kraka and D. Cremer, *J. Chem. Phys.*, 2012, **137**, 084114.

62 N. Verma, Y. Tao, W. Zou, X. Chen, X. Chen, M. Freindorf and E. Kraka, *Sensors*, 2020, **20**, 2358.

63 R. M. Badger, *J. Chem. Phys.*, 1934, **2**, 128–131.

64 G. G. Brown, B. C. Dian, K. O. Douglass, S. M. Geyer, S. T. Shipman and B. H. Pate, *Rev. Sci. Instrum.*, 2008, **79**, 053103.

65 N. A. Seifert, J. Thomas, W. Jäger and Y. Xu, *Phys. Chem. Chem. Phys.*, 2018, **20**, 27630–27637.

66 H. M. Pickett, *J. Mol. Spectrosc.*, 1991, **148**, 371–377.

67 R. D. Chirico, W. V. Steele and A. F. Kazakov, *J. Chem. Thermodyn.*, 2015, **86**, 106–115.

68 D. Schemmel and M. Schütz, *J. Chem. Phys.*, 2008, **129**, 07B615.

69 J.-D. Chai and M. Head-Gordon, *Phys. Chem. Chem. Phys.*, 2008, **10**, 6615–6620.

70 E. Papajak, J. Zheng, X. Xu, H. R. Leverentz and D. G. Truhlar, *J. Chem. Theory Comput.*, 2011, **7**, 3027–3034.

71 P. Pulay, W. Meyer and J. E. Boggs, *J. Chem. Phys.*, 1978, **68**, 5077–5085.

72 F. Pawłowski, P. Jørgensen, J. Olsen, F. Hegelund, T. Helgaker, J. Gauss, K. L. Bak and J. F. Stanton, *J. Chem. Phys.*, 2002, **116**, 6482–6496.

73 M. Piccardo, E. Penocchio, C. Puzzarini, M. Biczysko and V. Barone, *J. Phys. Chem. A*, 2015, **119**, 2058–2082.

74 M. K. Jahn, J.-U. Grabow, M. J. Travers, D. Wachsmuth, P. D. Godfrey and D. McNaughton, *Phys. Chem. Chem. Phys.*, 2017, **19**, 8970–8976.

75 T. Oka, *J. Mol. Struct.*, 1995, **352**, 225–233.

76 P. L. A. Popelier, F. M. Aicken and S. E. O'Brien, *Atoms in molecules*, Prentice Hall Manchester, 2000.

77 V. Tognetti and L. Joubert, *J. Phys. Chem. A*, 2011, **115**, 5505–5515.

78 R. Kalescky, E. Kraka and D. Cremer, *J. Phys. Chem. A*, 2014, **118**, 223–237.

79 D. Setiawan, E. Kraka and D. Cremer, *J. Org. Chem.*, 2016, **81**, 9669–9686.

80 J. Cioslowski and S. T. Mixon, *J. Am. Chem. Soc.*, 1992, **114**, 4382–4387.

4

The 1-Naphthol Dimer and Its Surprising Preference for π-π Stacking over Hydrogen Bonding

Contents

4.1. Introduction · · · · · 60
4.2. Methods · · · · · 61
4.2.1. Experimental Methods · · · · · 61
4.2.2. Theoretical Methods · · · · · 62
4.3. Results and Discussion · · · · · 63
4.3.1. Spectroscopic Assignment · · · · · 63
4.3.2. Theoretical Discussion · · · · · 65
4.3.3. Non-Covalent Interactions Analyses · · · · · 67
4.4. Conclusions · · · · · 70
4.5. References · · · · · 70

4.1. Introduction

Attractive interactions between aromatic compounds are ubiquitous in nature. Stacked aromatic structural motifs can be found in a countless number of chemical contexts, including DNA, where a balance between electrostatic and dispersive attractive effects stabilize a stacked orientation between nucleobases.[1] Protein structure searches reveal similar motifs, where aromatic residues strongly direct protein tertiary structure.[2,3] Appearances of π-π stacking motifs are not merely limited to biochemical contexts; they play a crucial role in understanding stereoselective organic reactivity,[4] rational *de novo* catalyst design,[5] and the stabilization of supramolecular complexes.[6]

The physical basis for the π-π stacking interaction is defined by a subtle balance of competing energetic contributions. The Hunter-Sanders model suggests that the classic parallel stacked and T-shape orientations of aromatic dimers arise from favorable interactions between each ring's out-of-plane electric quadrupole.[7] However, recent studies show that for small systems it is misleading to assume that the stacked motif arises primarily from effects unique to the electronic environment of a delocalized π system. Modern analyses from Grimme[8] and Iverson[9]

find that the stacked arrangement of model aromatic systems arises only because such an arrangement is merely topologically favored due to additive dispersive forces and a reduction in Pauli exchange repulsion as compared to equivalent stacked complexes of saturated compounds, where exchange plays a greater destabilizing role.

In the case of complexes containing derivatized aromatics, substituent effects can exhibit the strongest influence on structure.[10] A relevant example of functionalization driving structure is the phenol dimer, which has been extensively studied using high resolution spectroscopy.[11–16] The two phenol subunits are oriented to maximize the linearity of the hydrogen bond, far from the traditional "stacked" or "T-shaped" geometry expected of aromatic dimers. Nevertheless, the predicted structure of the phenol dimer is dependent on accurate treatment of the dispersive forces between the rings. From this example, both π-π and substituent effects play critical roles in the intermolecular interactions of aromatic compounds.

Here, the rotational spectroscopy and identification of a gas-phase dimer of 1-naphthol, a naphthalene analogue of phenol, using chirped-pulse Fourier transform microwave (CP-FTMW) spectroscopy[17] is reported. The presence of the additional ring increases the complexity of the interaction potential energy surface compared to the phenol dimer, leading to a variety of energetically low-lying isomers with structures that are more strongly directed by π-π effects than by hydrogen bonding. This leads to energetics that are strongly dependent on proper treatment of electron correlation due to the large contribution from dispersion, increasing the computational challenge of accurately capturing these effects.[18]

The 1-naphthol dimer has been observed experimentally using UV-IR dip double resonance spectroscopy by Saeki *et al.*,[19] who concluded that the structure is largely π-π stacked in nature, unlike the phenol dimer. However, their structure determination was limited in scope since their experimental evidence centers largely on the observation of two distinct O-H stretching bands. They attribute this O-H stretch doublet to a hydrogen bond between the hydroxyl groups. We also find that the structure of the observed 1-naphthol dimer has a π-π stacking motif. However, the structure deduced from our experimental data and improved theoretical analysis is inconsistent with the conclusions of the IR dip study.

4.2. Methods

4.2.1. Experimental Methods

For measuring the rotational spectra of 1-naphthol and its dimer, we used the 2.0-6.0 GHz chirped-pulse Fourier transform microwave spectrometer[17] at the University of Alberta,[39] whose design was inspired by the original 2.0-8.0 GHz CP-FTMW instrument developed at the University of Virginia.[40] A solid sample of 1-naphthol (Aldrich, >99%) was heated *in situ* to 80° C in a standard pulsed valve nozzle modified to include a reservoir for heating low-volatility liquid and solid samples. The naphthol vapor is then mixed with 3 bar Ne, and the resultant mixture is pulsed supersonically at 2 Hz repetition rate into a vacuum chamber held at ca. 10^{-6} Torr. The resulting adiabatic expansion leads to rotational cooling of the sample to approximately 1 K. The sample is then polarized using a 1 μs chirped (2.0 to 6.0 GHz) microwave pulse amplified with a pulsed traveling wave tube (TWT) amplifier. The resultant molecular free induction decay (FID) is then detected for 20 μs at a sampling rate of 25 Gs/s, amplified, and averaged coherently in the time-domain on a high-speed oscilloscope and then Fourier transformed. Six FIDs were recorded per gas pulse. Where the final data set consists of an average of approximately 900 000 FIDs.

After assigning the rotational transitions associated with the *cis*-/*trans*- conformers of the 1-naphthol monomer[20] and the simple monohydrated and neon complexes of the global minimum *cis*- conformer, the AUTOFIT program[21] was used to search the spectrum for the dimer. The predicted B3LYP-D3(BJ)/6-311++g(d,p) rotational constants for the two monomeric conformers are in excellent agreement with theory, with absolute mean percent deviations of 0.12% and 0.13% for the *cis*- and *trans*- conformers, respectively.

4.2.2. Theoretical Methods

To determine candidate structures and approximate rotational constants for the dimers, we re-optimized the five isomers in the previous study by Saeki *et al.* at the B3LYP-D3(BJ)/6-311++g(d,p) level of theory, which are ordered ***a*** through ***e***, identical to Saeki's order of decreasing binding energy. These isomers are all π-π stacked but not all include hydrogen bonds between the hydroxyl groups. In fact, Saeki's lowest energy structure, Saeki-***a***, is a C_2 symmetric stack where the hydroxyl groups point in opposite directions, as shown in Figure 4.1. While the rotational constants of these candidate structures are all quite similar, they can be differentiated by their electric dipole moments.

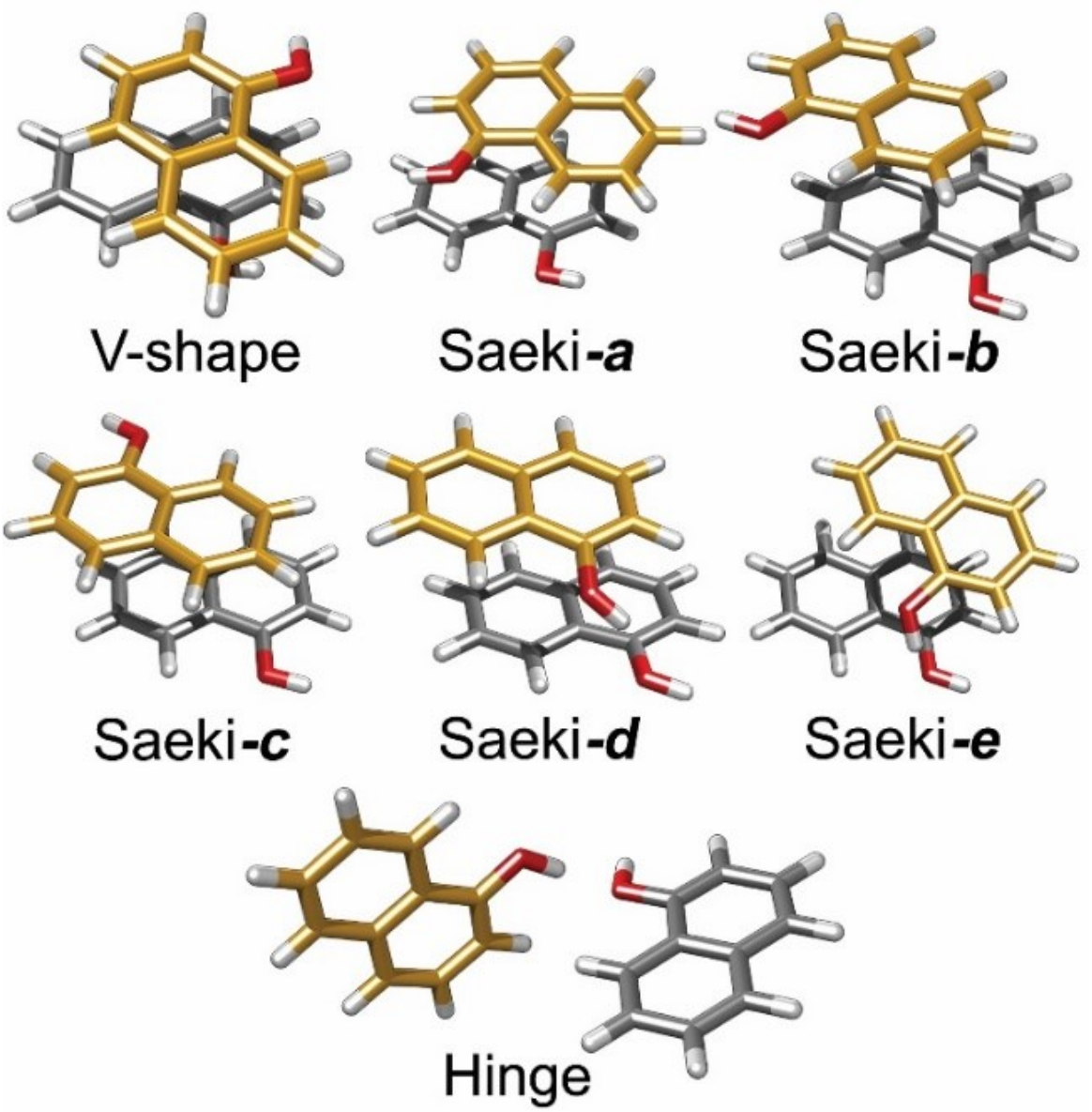

Figure 4.1. Seven predicted 1-naphthol dimer structures, including those from the previous paper by Saeki et al.[19], optimized at the B3LYP-D3(BJ)/6-311++g(d,p) level of theory.

4.3. Results and Discussion

4.3.1. Spectroscopic Assignment

AUTOFIT found a single set of transitions in the experimental spectrum which gives rotational constants that are similar to those of the Saeki structures. The fitted rotational and centrifugal distortion constants for the assigned dimer can be found in Table 4.1. This dimer-like spectrum is quite weak and its intensity seems to be largely invariant to experimental conditions;

Table 4.1. Experimental spectroscopic parameters for the detected 1-naphthol dimer

Parameter	Experimental Dimer Fit
A / MHz	462.44026(65)
B / MHz	275.85770(43)
C / MHz	252.47547(49)
Δ_J / kHz	0.0550(34)
Δ_{JK} / kHz	-0.166(14)
Δ_K / kHz	0.203(16)
δ_J / kHz	0.0054(15)
δ_K / kHz	[0][a]
[b]N	78
[c]σ / kHz	8.2

[a]Fixed to theory in the fit. [b]Number of lines used in the fit. [c]Root mean square error of fit.

similar intensities regardless of nozzle temperature, backing gas, or stagnation pressure. However, the intensity of the dimer was slightly anti-correlated to the intensity of the 1-naphthol monohydrate's spectrum, which suggests that dimer formation is in competitive equilibrium with the residual water in the 1-naphthol sample.

Note that the observed spectrum displays no μ_a-type transitions and has distinct quartets arising from μ_b- and μ_c-type asymmetry doublets, with a relative intensity ratio of about 1.3 : 1 for μ_c : μ_b dipole components. An example of these quartets can be found in Figure 4.2. The lack of μ_a-type transitions eliminates one of the two C_1-symmetric hydrogen bonded dimer structures (Saeki-***d***) proposed in the Saeki paper, and the second (Saeki-***e***) can be eliminated by rotational constants alone.

With an experimental dimer-like spectrum but no theoretical structure fully consistent with our data, a more thorough search of the dimer potential energy surface at the B3LYP-D3(BJ)/6-311++g(d,p) level of theory using GAUSSIAN 09[22,23] was performed. The predicted spectroscopic parameters for the seven lowest energy isomers found in this search are summarized in Table 4.2. The relative energies are corrected for zero-point vibrational energy (ZPE) and basis set superposition error (BSSE).[24] A wide selection of initial ring orientations were chosen with no bias towards specific orientations. In general, the optimized geometries preferred nearly co-parallel

but offset π-π stacks. Most initial guess structures converged to the five isomers already presented in Saeki's study.

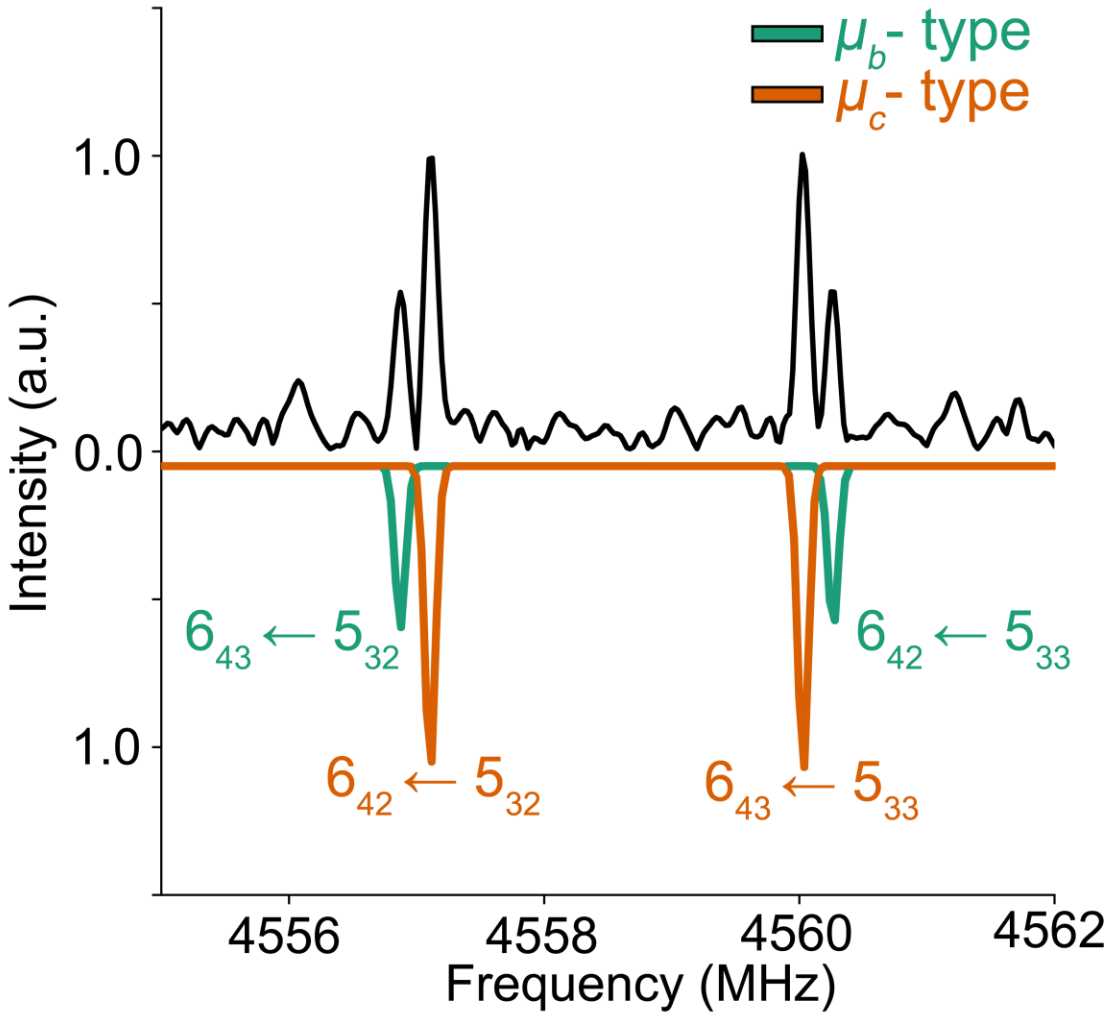

Figure 4.2. Experimental spectrum (top, black trace) and predictions (bottom, colored traces) for the J' = 6, K_a' = 4 μ_b/μ_c-type quartet in the $(1\text{-naphthol})_2$ CP-FTMW spectrum.

4.3.2. Theoretical Discussion

Like Saeki *et al.*, our theoretical search was limited to dimers containing only the *trans* conformer of 1-naphthol. This is justified since the *cis* conformer is 5.3 kJ mol^{-1} higher in energy relative to *trans*, consistent with the observed *cis*/*trans* monomer relative abundance in the CP-FTMW spectrum. Although it is known that intermolecular interactions can affect the relative stability of monomeric subunits,[25] We expect no *cis* conformer-containing dimers are at detectable abundances since the detected dimer spectrum is quite weak.

Table 4.2. Calculated properties of seven isomers of the 1-naphthol dimer, predicted using different levels of theory.

Isomer	B3LYP-D3(BJ)/6-311++g(d,p)					MP2/cc-pVDZ
	A / MHz	B / MHz	C / MHz	$\lvert(\mu_a, \mu_b, \mu_c)\rvert$ / D	[a,b]ΔE_0 / kJ mol^{-1}	ΔE_0 / kJ mol^{-1}
V-shape	468.2	284.6	257.9	(0.2, 0.7, 0.9)	0.0	1.4
Saeki-a	449.6	301.2	286.2	(0.0, 0.0, 0.7)	1.0	0.0
Saeki-b	479.0	273.5	272.2	(0.0, 0.0, 0.6)	0.5	4.9
Saeki-c	454.9	298.6	286.0	(0.0, 0.0, 0.0)	1.0	5.0
Saeki-d	480.4	276.0	270.8	(2.5, 0.3, 0.6)	2.5	1.6
Saeki-e	421.0	326.5	270.7	(0.4, 1.1, 1.8)	2.1	0.1
Hinge	594.1	131.3	125.6	(2.9, 1.0, 0.6)	10	N/A

Isomer	[c]SCS-MP2-F12 ΔE / kJ mol^{-1}	[c]SCS-LMP2-F12 ΔE / kJ mol^{-1}	[c]LCCS(T)-F12 ΔE / kJ mol^{-1}
V-shape	0.7	0.0	0.0
Saeki-a	0.0	0.0	1.6
Saeki-b	1.7	1.6	4.4
Saeki-c	3.3	2.8	5.3
Saeki-d	1.7	2.4	4.9
Saeki-e	2.0	2.9	4.9
Hinge	12.9	8.0	1.8

[a]Relative energy with harmonic zero-point vibrational energy (ZPE) correction and [b]basis set superposition error (BSSE). [c]B3LYP-D3 geometries were used to calculate relative electronic energies

Several structures with reasonable rotational constant agreement were found, albeit with significant differences in their dipole moment directions and magnitudes. One of these structures is the C_2-symmetric structure Saeki-***a***, which is within 1 kJ mol^{-1} of our global minimum structure, dubbed "**V-shape**" due to the V-like skewed orientation of the two rings. The V-shape isomer was not presented in Saeki's study; however, its predicted rotational constants and μ_c/μ_b dipole component ratio of 1.3 are in excellent agreement with experiment, as shown in Figure 4.2. Although the V-shape optimized geometry suggests a small, but non-zero μ_a dipole component, the predicted magnitude of 0.2 D implies a 12-fold reduction in μ_a-type intensity with respect to the μ_b-type transitions, below the detection limits achieved in our experiment.

To corroborate our B3LYP-D3 results, the relative energies at a much higher level of theory were calculated, specifically density fitted (DF)[26], explicitly correlated (F12b)[27] CCSD(T) with

local correlation approximations[28] [DF-LCCSD(T*)-F12b/cc-pVDZ-F12] using MOLPRO[29]; the resulting energies are also tabulated in Table 4.2. These energies are left uncorrected for harmonic ZPE and BSSE. However, application of the DFT ZPE corrections do not affect the LCCSD(T) energy ordering and benchmarking studies show that the F12 explicit correlation compensates for BSSE, especially with double-ζ basis sets.[30] Table 4.2 also presents the relative electronic energies of the seven isomers optimized at the MP2/cc-pVDZ level of theory, identical to that employed by Saeki *et al.*'s study. However, the hinge isomer is not a real minimum at this level of theory; in fact, hinge-like initial structural guesses optimize to the Saeki-**d** isomer.

The V-shape isomer is the LCCSD(T) global minimum. Otherwise, the LCCSD(T) ordering is quite different from the DFT results. Initially, the disagreement between DFT and LCCSD(T) was assumed to be an artifact of a poorly configured localization scheme. However, full MP2-F12 shows similar results as LMP2-F12 using the same local cut-offs as LCCSD(T). Therefore, the LCCSD(T) energies are likely reliable, and the discrepancies across methods illustrate the difficulty of evaluating energetics for large, dispersively bound systems to accuracies within a few kJ mol^{-1}.

Saeki *et al.* assign their IR data to either Saeki-**d** and Saeki-**e** despite these structures not being global minimum structures at their level of theory (MP2/cc-pVDZ). They rationalize their energetic discrepancy as a symptom of MP2 being "apt to overestimate the binding energy of the π-π interaction," which is empirically true.[31,32] However, their assumption that such overestimation is larger in Saeki-***a*** than -***d*** or -***e*** because -***a*** exhibits no hydrogen bonding may not be valid, since by this logic the V-shape isomer would be competitive in energy with Saeki-***a*** as neither exhibit formal hydrogen bonds. Yet, the V-shape isomer falls energetically nearer Saeki-***d*** and -***e*** at their level of theory. An alternate conclusion is that MP2 is so poor at capturing the energetics of the dispersion-dominated potential energy surface that it has essentially no predictive power for conclusive spectroscopic assignments.

4.3.3. Non-Covalent Interactions Analyses

Interestingly, there is an absence of canonical hydrogen bonding in the V-shape isomer. To interpret the preference for π-π stacking over hydrogen bonding, we applied a non-covalent interactions (NCI) analyses.[33] NCI methods can visualize attractive and repulsive behavior in regions of small electron density [$\rho(\boldsymbol{r})$]. Since the density gradient, $\nabla\rho(\boldsymbol{r})$, approaches zero in

regions of the electronic structure where bonding occurs, specific non-covalent interactions can be identified in regions where $\rho(\boldsymbol{r})$ and $\nabla\rho(\boldsymbol{r})$ are both small. In this case, NCI methodology uses the dimensionless *reduced* density gradient [s] as the appropriate metric. In order to distinguish between attractive and repulsive non-covalent interactions, $\rho(\boldsymbol{r})$ is multiplied by sign(λ_2), where λ_2 is the so-called second eigenvalue of the electron density Hessian $\nabla^2\rho(\boldsymbol{r})$. In regions associated with non-covalent interactions, e.g. in the limit of $\rho(\boldsymbol{r}) \rightarrow 0$, the sign of λ_2 changes depending on the bonding characteristics. $\lambda_2 < 0$ implies bonding character whereas a positive λ_2 implies non-bonding or repulsive character. Therefore, indexing specific regions of the s vs. sign(λ_2)ρ graph allows us to identify specific qualitative non-covalent characteristics in a molecular system.

In all the π-π stacked isomers, there is a delocalized interaction surface characterized by pockets of weakly attractive and repulsive regions. These regions have small values of electron density (sign(λ_2)$\rho \approx \pm 0.015$ a.u.) at low values ($s < 0.8$ a.u.) of the reduced density gradient, which can be interpreted as a competition between dispersion and exchange (Pauli) repulsion of the two naphthalene rings. The NCI data with comparisons to hydrogen bonded systems can be found in Figure 4.3, and a full diagram of the NCI results for the V-shape isomer is available in Appendix B, Figure B.1.

The V-shape isomer shows an attractive region where the OH group of one subunit is slightly tilted towards the ring of the other subunit, indicative of a weak OH···π interaction. As shown by Figure 4.3**,** this interaction is completely different from what is observed in the NCI analyses of $(\text{phenol})_2$ and $(H_2O)_2$, which show a distinctive tail in their NCI diagrams at $-0.02 <$ sign(λ_2)$\rho < -0.04$, associated with strong hydrogen bonds. It is instructive to compare this to Saeki-***d****,* which features a more traditional OH···O hydrogen bond between the two subunits. NCI analysis of Saeki-***d*** (see Appendix B, Figure B.3) reveals that this hydrogen bond is similar to the interaction in the V-shape isomer. Therefore, it is fair to consider the OH···O interaction in Saeki-***d*** more as a van der Waals-like interaction rather than a canonical hydrogen bond.

We focus briefly on Saeki *et al.*'s strategy to assign a plausible 1-naphthol dimer. They observe two O-H stretch bands, split by $\Delta\nu = 42$ cm^{-1}, and conclude that these are associated with free/bound hydrogen bonded hydroxyl groups. They conclude that the Saeki-***d***/***e*** structures must be close to the correct one, since they both exhibit hydrogen bonding and have MP2/cc-pVDZ O-H stretch splittings of 59 and 57 cm^{-1} respectively, in reasonable agreement with the experimental value. However, DFT also predicts a splitting of similar magnitude for the V-shape isomer, as

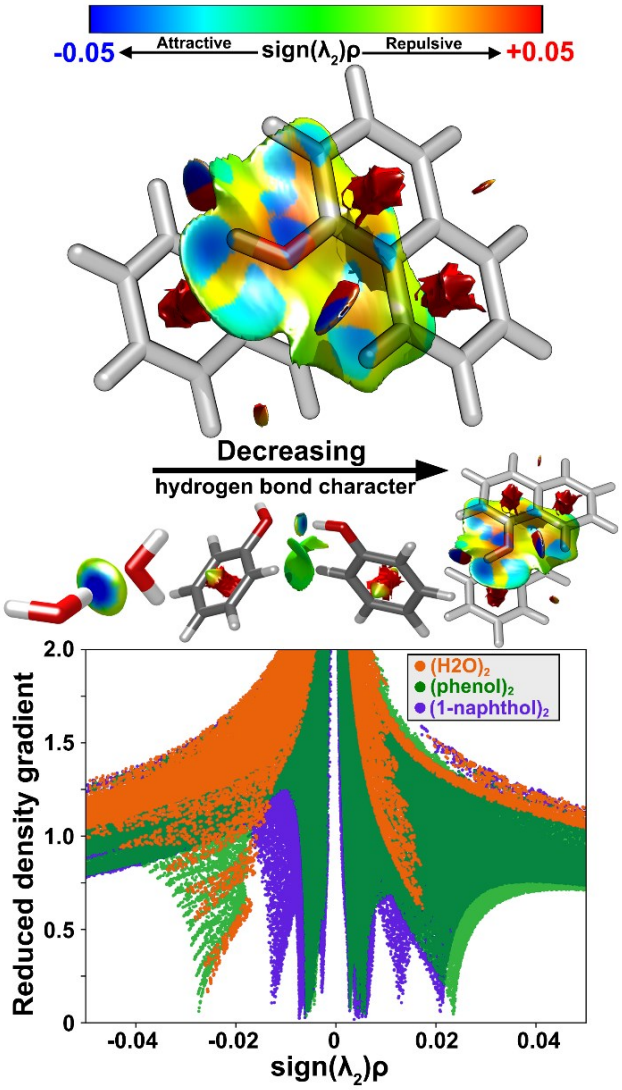

Figure 4.3. Non-covalent interactions (NCI) analysis of the observed V-shape 1-naphthol dimer (top). The 3D surface (top) shows attractive (blue) and repulsive (red) regions of the reduced density gradient (s) isosurface, with a cutoff of s = 0.8. The full (s, sign(λ_2)ρ) diagram is shown (bottom), with comparisons to the water dimer and phenol dimer.

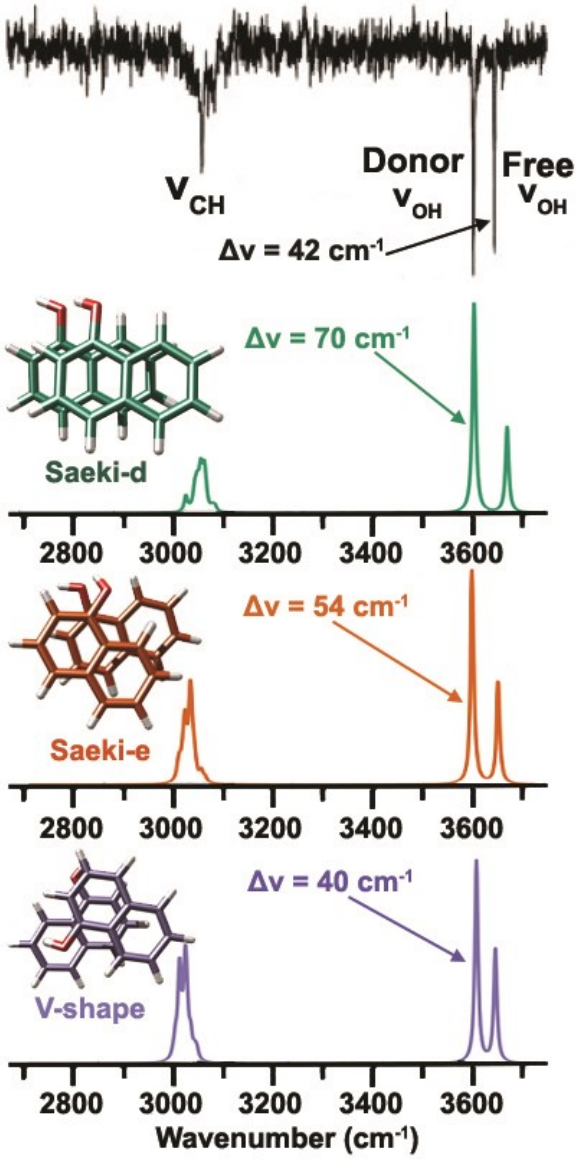

Figure 4.4. Experimental IR dip spectrum of the naphthol dimer from Saeki et al., in comparison to the B3LYP-D3(BJ)/6-311++g(d,p) harmonic vibrational spectra for the observed V-shape isomer and the originally proposed hydrogen-bonded isomers, Saeki-**d**/**e**. The original IR dip spectrum was reproduced with permission from Ref. 19. Copyright 2007 American Chemical Society.

shown in the Figure 4.4. In fact, the V-shape isomer has a predicted splitting of 54 cm^{-1} at Saeki's chosen MP2/cc-pVDZ level of theory. The similarity of the O-H stretch splittings predicted for the V-shape and Saeki-***d***/***e*** isomers is also rationalized by the NCI analyses, which suggest that the hydrogen bond in Saeki-***d***/***e*** is not particularly different nor stronger than the weak O-H···π interaction in the V-shape isomer.

The V-shape isomer may not be dissimilar to structures of other polyaromatic dimers. Although neither Saeki *et al.*'s earlier study on the naphthalene dimer,[34] nor an earlier search by Lee *et al.,*[35] identified a similar structure using MP2, a recent dispersion-corrected DFT study found a V-like, parallel-stacked, global minimum structure.[36] Our predicted $(1\text{-naphthol})_2$ V-shape structure has the two subunits rotated relative to each other by 114°, which is close to the 123° angle between the two subunits in the aforementioned parallel-stacked $(\text{naphthalene})_2$ structure. However, the authors note that many of their low-lying structures were within 1.3 kJ mol^{-1} of the global minimum and do not provide BSSE or ZPE corrections, so they make no claims regarding a firm energy ordering. There are no high resolution spectroscopic measurements of the neutral naphthalene dimer; however, the photodissociation spectrum of the naphthalene dimer cation was assigned to a partially overlapped and stacked structure.[37] Our observation of this structural motif in 1-naphthol dimer may provide some additional evidence for a V-like neutral naphthalene dimer. Additionally, a recent CP-FTMW study of aromatic dimers also shows that dibenzofuran and fluorene exhibit similar V-like stacked structures.[38]

4.4. Conclusions

The dimers of water, phenol, 1-naphthol are a simple, yet compelling example of how intermolecular interactions evolve dramatically as a function of molecular complexity. The interactions in these prototypical systems run from directional, pure hydrogen bonding to delocalized, dispersive stabilization found in π-π systems. However, these two regimes are not mutually exclusive. At increasing chemical complexity, the canonical non-covalent interactions form a blurry continuum, and it is important not to assume that our intuition on the favorable thermodynamics of hydrogen bonding will always point us towards the correct answer.

4.5. References

1 E. T. Kool, *Annu. Rev. Biophys. Biomol. Struct.*, 2001, **30**, 1–22.

2 S. Marsili, R. Chelli, V. Schettino and P. Procacci, *Phys. Chem. Chem. Phys.*, 2008, **10**, 2673–2685.

3 Chelli Riccardo, Gervasio Francesco Luigi, Procacci Piero, and Schettino Vincenzo, *Proteins Struct. Funct. Bioinforma.*, 2004, **55**, 139–151.

4 E. H. Krenske and K. N. Houk, *Acc. Chem. Res.*, 2013, **46**, 979–989.

5 A. J. Neel, M. J. Hilton, M. S. Sigman and F. D. Toste, *Nature*, 2017, **543**, 637–646.

6 J. Hermann, D. Alfè and A. Tkatchenko, *Nat. Commun.*, 2017, **8**, 14052.

7 C. A. Hunter and J. K. M. Sanders, *J. Am. Chem. Soc.*, 1990, **112**, 5525–5534.

8 Grimme Stefan, *Angew. Chem. Int. Ed.*, 2008, **47**, 3430–3434.

9 C. R. Martinez and B. L. Iverson, *Chem. Sci.*, 2012, **3**, 2191–2201.

10 S. E. Wheeler and K. N. Houk, *J. Am. Chem. Soc.*, 2008, **130**, 10854–10855.

11 T. Ebata, T. Watanabe and N. Mikami, *J. Phys. Chem.*, 1995, **99**, 5761–5764.

12 M. Schmitt, M. Böhm, C. Ratzer, D. Krügler, K. Kleinermanns, I. Kalkman, G. Berden and W. L. Meerts, *Chemphyschem Eur. J. Chem. Phys. Phys. Chem.*, 2006, **7**, 1241–1249.

13 A. Weichert, C. Riehn and B. Brutschy, *J. Phys. Chem. A*, 2001, **105**, 5679–5691.

14 K. Fuke and K. Kaya, *Chem. Phys. Lett.*, 1983, **94**, 97–101.

15 K. Fuke and K. Kaya, *Chem. Phys. Lett.*, 1982, **91**, 311–314.

16 N. A. Seifert, A. L. Steber, J. L. Neill, C. Pérez, D. P. Zaleski, B. H. Pate and A. Lesarri, *Phys. Chem. Chem. Phys.*, 2013, **15**, 11468–11477.

17 G. G. Brown, B. C. Dian, K. O. Douglass, S. M. Geyer, S. T. Shipman and B. H. Pate, *Rev. Sci. Instrum.*, 2008, **79**, 053103.

18 C. D. Sherrill, *Acc. Chem. Res.*, 2013, **46**, 1020–1028.

19 M. Saeki, S. Ishiuchi, M. Sakai and M. Fujii, *J. Phys. Chem. A*, 2007, **111**, 1001–1005.

20 J. R. Johnson, K. D. Jordan, D. F. Plusquellic and D. W. Pratt, *J. Chem. Phys.*, 1990, **93**, 2258–2273.

21 N. A. Seifert, I. A. Finneran, C. Perez, D. P. Zaleski, J. L. Neill, A. L. Steber, R. D. Suenram, A. Lesarri, S. T. Shipman and B. H. Pate, *J. Mol. Spectrosc.*, 2015, **312**, 13–21.

22 S. Grimme, S. Ehrlich and L. Goerigk, *J. Comput. Chem.*, 2011, **32**, 1456–1465.

23 Gaussian 09, Revision E.01, M. J. Frisch, G. W. Trucks, H. B. Schlegel, G. E. Scuseria, M. A. Robb, J. R. Cheeseman, G. Scalmani, V. Barone, G. A. Petersson, H. Nakatsuji, X. Li, M. Caricato, A. Marenich, J. Bloino, B. G. Janesko, R. Gomperts, B. Mennucci, H. P.

Hratchian, J. V. Ortiz, A. F. Izmaylov, J. L. Sonnenberg, D. Williams-Young, F. Ding, F. Lipparini, F. Egidi, J. Goings, B. Peng, A. Petrone, T. Henderson, D. Ranasinghe, V. G. Zakrzewski, J. Gao, N. Rega, G. Zheng, W. Liang, M. Hada, M. Ehara, K. Toyota, R. Fukuda, J. Hasegawa, M. Ishida, T. Nakajima, Y. Honda, O. Kitao, H. Nakai, T. Vreven, K. Throssell, J. A. Montgomery, Jr., J. E. Peralta, F. Ogliaro, M. Bearpark, J. J. Heyd, E. Brothers, K. N. Kudin, V. N. Staroverov, T. Keith, R. Kobayashi, J. Normand, K. Raghavachari, A. Rendell, J. C. Burant, S. S. Iyengar, J. Tomasi, M. Cossi, J. M. Millam, M. Klene, C. Adamo, R. Cammi, J. W. Ochterski, R. L. Martin, K. Morokuma, O. Farkas, J. B. Foresman, and D. J. Fox, Gaussian, Inc., Wallingford CT, 2016.

24 S. F. Boys and F. Bernardi, *Mol. Phys.*, 1970, **19**, 553–566.

25 J. Thomas, N. A. Seifert, W. Jäger and Y. Xu, *Angew. Chem. Int. Ed.*, 2017, **56**, 6289–6293.

26 A. E. DePrince and C. D. Sherrill, *J. Chem. Theory Comput.*, 2013, **9**, 2687–2696.

27 T. B. Adler, G. Knizia and H.-J. Werner, *J. Chem. Phys.*, 2007, **127**, 221106.

28 T. B. Adler and H.-J. Werner, *J. Chem. Phys.*, 2011, **135**, 144117.

29 MOLPRO, version 2015.1, a package of ab initio programs, H.-J. Werner, P. J. Knowles, G. Knizia, F. R. Manby, M. Schütz, P. Celani, W. Györffy, D. Kats, T. Korona, R. Lindh, A. Mitrushenkov, G. Rauhut, K. R. Shamasundar, T. B. Adler, R. D. Amos, A. Bernhardsson, A. Berning, D. L. Cooper, M. J. O. Deegan, A. J. Dobbyn, F. Eckert, E. Goll, C. Hampel, A. Hesselmann, G. Hetzer, T. Hrenar, G. Jansen, C. Köppl, Y. Liu, A. W. Lloyd, R. A. Mata, A. J. May, S. J. McNicholas, W. Meyer, M. E. Mura, A. Nicklass, D. P. O'Neill, P. Palmieri, D. Peng, K. Pflüger, R. Pitzer, M. Reiher, T. Shiozaki, H. Stoll, A. J. Stone, R. Tarroni, T. Thorsteinsson, and M. Wang, , see http://www.molpro.net.

30 B. Brauer, M. K. Kesharwani and J. M. L. Martin, *J. Chem. Theory Comput.*, 2014, **10**, 3791–3799.

31 J. Řezáč and P. Hobza, *Chem. Rev.*, 2016, **116**, 5038–5071.

32 K. E. Riley, J. A. Platts, J. Řezáč, P. Hobza and J. G. Hill, *J. Phys. Chem. A*, 2012, **116**, 4159–4169.

33 E. R. Johnson, S. Keinan, P. Mori-Sánchez, J. Contreras-García, A. J. Cohen and W. Yang, *J. Am. Chem. Soc.*, 2010, **132**, 6498–6506.

34 M. Saeki, H. Akagi and M. Fujii, *J. Chem. Theory Comput.*, 2006, **2**, 1176–1183.

35 N. K. Lee, S. Park and S. K. Kim, *J. Chem. Phys.*, 2002, **116**, 7910–7917.

36 N. O. Dubinets, A. A. Safonov and A. A. Bagaturyants, *J. Phys. Chem. A*, 2016, **120**, 2779–2782.

37 Y. Inokuchi, K. Ohashi, M. Matsumoto and N. Nishi, *J. Phys. Chem.*, 1995, **99**, 3416–3418.

38 M. Schnell, M. Fatima, C. Perez, A. Steber, S. Zinn and A. Poblotzki, *Angew. Chem. Int. Ed.*, 2019, **131**, 3140-3145.

39 C. D. Carlson, N. A. Seifert, M. Heger, F. Xie, J. Thomas and Y. Xu, *J. Mol. Spectrosc.*, 2018, **351**, 62–67.

40 C. Pérez, S. Lobsiger, N. A. Seifert, D. P. Zaleski, B. Temelso, G. C. Shields, Z. Kisiel and B. H. Pate, *Chem. Phys. Lett.*, 2013, **571**, 1–15.

5

Examining Intermolecular Interactions Between Hydrocarbon and Water: A Broadband Rotational Spectroscopic and Theoretical Study of the α-pinene – Water Complex

Contents

5.1. Introduction · · · · · 74
5.2. Methods · · · · · 76
5.2.1. Experimental Methods · · · · · 76
5.2.2. Theoretical Methods · · · · · 76
5.3. Results and Discussion · · · · · 78
5.3.1. Theoretical Results · · · · · 78
5.3.2. Experimental Results · · · · · 83
5.3.3. Conformer Assignment · · · · · 85
5.3.4. Water Tunneling · · · · · 87
5.3.5. NCI/QTAIM/IGM Analyses · · · · · 88
5.3.6. NBO Analyses · · · · · 92
5.3.7. Theoretical Discussion · · · · · 94
5.3.8. Atmospheric Implications – Thermodynamics · · · · · 96
5.3.9. Atmospheric Implications – Kinetics · · · · · 98
5.4. Conclusions · · · · · 102
5.5. References · · · · · 102

5.1. Introduction

Released into the atmosphere by vegetation, biogenic volatile organic compounds (VOCs) contribute substantially to yearly carbon emission, amounting to approximately 1150 Tg of carbon per year.[1] These biogenic VOCs include isoprenoids, alkanes, alkenes, carbonyls, alcohols, esters, ethers, and acids, for example. α-pinene, a bicyclic monoterpene, is not only one of the most abundant biogenic VOCs released, but also plays a critical role in generation of secondary organic aerosol. Once released, α-pinene can be photo-oxidized by atmospheric species such as ozone or various radical species.[2] The resulting products have considerably lower volatility than α-pinene, and can be further oxidized, combine with existing aerosol particles increasing their size, or

nucleate to form new aerosol particles.[3,4] Variations in the atmospheric concentrations of α-pinene or its reactivity may therefore have a direct effect on nucleation or growth of secondary organic aerosol particles. For example, a molecule clustered with α-pinene may potentially block the π-system and prevent an ozonolysis reaction from occurring, which will have subsequent effects on the concentration of the photo-oxidized products. Water is relatively abundant in the atmosphere and has therefore a high probability of a close encounter with α-pinene. Complexation with water may affect the reactivity with species such as ozone, thus altering product yield, and ultimately rate of aerosol formation. It is difficult to predict a preferred structure for the α-pinene-water cluster using chemical intuition alone, and a study of its structure and energetics can provide insights into intermolecular interactions between weakly-polar hydrocarbons and hydrogen bonding capable species, as well as data relevant to atmospheric processes. Although a study of water complexation with ionized α-pinene has been done previously using electron impact and mass spectrometry methods,[5] the complexation of neutral α-pinene with water has not been examined to date. In addition to the relevant atmospheric data, a detailed study of the α-pinene-water complex would also provide valuable benchmark data for theory. For example, many systems with strong canonical hydrogen bonds have been used in various benchmark studies and their structures and energetics are well predicted by current electronic structure methods.[6–8] However, predicting the structures and energetics of pure hydrocarbon-water complexes poses more stringent challenges for electronic structure calculations and these systems are therefore important benchmarks for the modelling of weak interactions.

Here I present findings from an experimental, rotational spectroscopic study of the α-pinene-water complex using a broadband chirped pulse Fourier transform microwave (CP-FTMW) spectroscopy, supplemented with theoretical calculations. In total, 21 structural conformers were identified from the theoretical results. Experimentally, two conformers of α-pinene-water were assigned. Transitions were resolved enough to observe a splitting pattern into doublet components with a 3:1 intensity ratio. The splittings are associated with the *ortho* and *para* spin states of water, and are a result of a water tunnelling motion. The assigned spectrum is consistent with the two lowest-energy conformers from the theoretical results. Non-covalent interactions (NCI)[9] and quantum theory of atoms-in-molecules (QTAIM) analyses[10,11] revealed two bonding interactions, indicated by bond critical points (BCPs), between the water molecule and α-pinene for both experimentally found conformers. Using the experimental rotational constants, calculations were

done to see how the seasonal abundance of hydrated α-pinene compares to that of other atmospheric species. Rate constants were then determined for the reaction of α-pinene and the α-pinene-water complexes with ozone, which indicates that complexation with water can catalyze ozonolysis.

5.2. Methods

5.2.1. Experimental Methods

The rotational spectrum of the α-pinene-water complex was recorded using a pulsed nozzle, CP-FTMW spectrometer operating in the 2-6 GHz range. With some variations in design, our instrument operates analogously to the spectrometer designed by the Pate group.[12] The details of our instrument have been described previously.[13] The frequency range of the instrument is well suited to study the relatively large α-pinene-water complex, as many low rotational states fall within its frequency range. 40 μs long free induction decays (FID) were recorded, rather than the usual 20 μs FID, to better resolve some narrow splittings. Six FIDs were recorded per molecular beam pulse.

α-pinene was purchased from Millipore Sigma and was used without any further modifications or purifications. Its volatility allowed for a sufficient number of molecules to be introduced into the gas phase without heating of the sample. The sample was injected by utilizing a home-made attachment to a General Valve, Series 9, nozzle, containing a reservoir for the α-pinene sample. Water was introduced using a sample cylinder containing 3 Torr of water mixed with neon at a backing pressure of about 60 psi. Approximately 2.1 million FIDs were averaged and then Fourier transformed to obtain the broadband rotational spectrum. The relatively deep average was necessary to ensure that the weak α-pinene-water signals could be identified among the noise and other molecular signals.

5.2.2. Theoretical Methods

The Gaussian 16 program suite[14] was used for density functional theory (DFT)[15] geometry optimizations and harmonic frequency calculations of the α-pinene monomer at the B3LYP-D3(BJ)[16–18] level of theory with the def2-TZVP[19] basis set. Using Multiwfn[20] and VMD[21], an electrostatic potential was plotted to visualize possible candidate sites for the interaction with water. Once interaction sites were identified, preliminary calculations of the α-pinene-water complex,

which included geometry optimizations and harmonic frequency calculations, were completed also at the B3LYP-D3(BJ)/def2-TZVP level of theory. The optimized structures were then used as input structures for Grimme's semi-empirical Conformer-Rotamer Ensemble Sampling Tool (CREST)[22], which was utilized at the GFN2-xTB[23] level of theory. The molecular structures obtained from CREST were then further refined using density functional theory calculations at the B3LYP-D3(BJ) level with the larger Jun-cc-pVTZ basis set (roughly 200 more basis functions than def2-TZVP basis set).

Discrepancies between the experimental results and theoretical results led us to a more extensive theoretical study of the complex, where several methods were utilized in an attempt to better match theory to experiment. To ensure that the global minimum structure was correctly identified at each level of theory, one dimensional potential energy scans, corresponding to internal motions of the water molecule, were completed at 6 different levels of theory: B3LYP-D3(BJ)/6-311++g(d,p)[24–26], B3LYP-D3(BJ)/def2-TZVP, B3LYP-D3(BJ)/def2-TZVPPD[19,27] (obtained from Basis Set Exchange[28]), B3LYP-D3(BJ)/Jun-cc-pVTZ[29], ωB97XD[30]/Jun-cc-pVTZ, and B2PLYPD3[16,31]/Jun-cc-pVTZ. Different basis sets for the B3LYP-D3(BJ) calculations were initially used in the hope to provide results closer to experiment and to see if the position of the water molecule is dependent on the level of theory. The implementation of the ωB97XD long range corrected hybrid functional was based on previous studies[30,32,33] where the excellent ability of this approach to accurately capture dispersion interactions within weakly bound systems was demonstrated. The B2PLYPD3 double hybrid functional was also chosen based on previous work[34] where it was shown that B2PLYPD3 outperforms other approaches rooted in DFT such as B3LYP, and provides accurate harmonic frequencies comparable to those from CCSD(T) approaches. Once global minima were confirmed from the potential energy scans, final geometry optimizations and harmonic frequency calculations were carried out at each level of theory.

Anharmonic corrections were obtained using a general hybrid approach, i.e. B2PLYPD3/B3LYP-D3(BJ) (Harmonic/Anharmonic forces) with the Jun-cc-pVTZ basis set. Several studies[35–37] have shown that this hybrid approach yields an excellent compromise between accuracy and computation time for both covalent and non-covalent interactions. Structures were first optimized at the B3LYP-D3(BJ)/Jun-cc-pVTZ level, followed by computation of harmonic and anharmonic forces. The structure was then optimized at the B2PLYPD3/Jun-cc-pVTZ level.

The anharmonic corrections to the rotational constant from the B3LYP-D3(BJ) results were then applied to the B2PLYPD3 rotational constants for comparison with the experimental values.

To investigate the pathway of possible internal motions and determine the respective barriers, the nudged-elastic band (NEB) method[38] was utilized. Using the ORCA 5.0.3 program suite[39], the NEB-TS[40] procedure with 32 images between each minimum was used at the B3LYP-D3(BJ)/Jun-cc-pVTZ level of theory. The transition state structure obtained from the NEB-TS procedure was then re-optimized in Gaussian 16, followed by a harmonic frequency calculation, at the same level of theory.

To visualize the intermolecular interactions within the α-pinene - water complex, QTAIM[10,11] and NCI[9] analyses were performed. The QTAIM analyses were done and visualized using Keith's AIMALL[41] program suite, and are based on the electron density from the B3LYP-D3(BJ)/Jun-cc-pVTZ calculations. To further characterize the complexes, NCI analyses were performed, also based on the electron density from the B3LYP-D3(BJ)/Jun-cc-pVTZ calculations. The NCI calculations were done using Multiwfn[20], followed by visualization in USCF Chimera.[42] To better quantify the intermolecular interactions, natural bond orbital (NBO)[43] analyses were carried out. NBO version 6.0[44] as implemented in the Gaussian 16 program suite was used at the B3LYP-D3(BJ)/Jun-cc-pVTZ level. Finally, the natural resonance theory (NRT)[45–47] feature of NBO version 6.0 was used, which provides bond orders for covalent and non-covalent interactions. The bond orders were utilized to make inferences about the strength of each interaction. In addition to the bond order, NRT was used to determine the degree of covalent and ionic character for each intermolecular bond.

5.3. Results and Discussion

5.3.1. Theoretical Results

From the electrostatic potential surface (Figure C.1, Appendix C), two minima were found as candidate water interaction sites, above and below the π bond of the α-pinene molecule, respectively. The complex with the water molecule positioned adjacent to the methyl groups of the four-membered ring is denoted as the syn-conformer and the other one, with water opposite to the methyl groups, as the anti-conformer (Figure 5.1). From the density functional theory refined CREST results, 21 unique conformers of the α-pinene - water complex were identified within 10 kJ mol^{-1}, where the lowest energy conformer and second lowest energy conformer correspond to

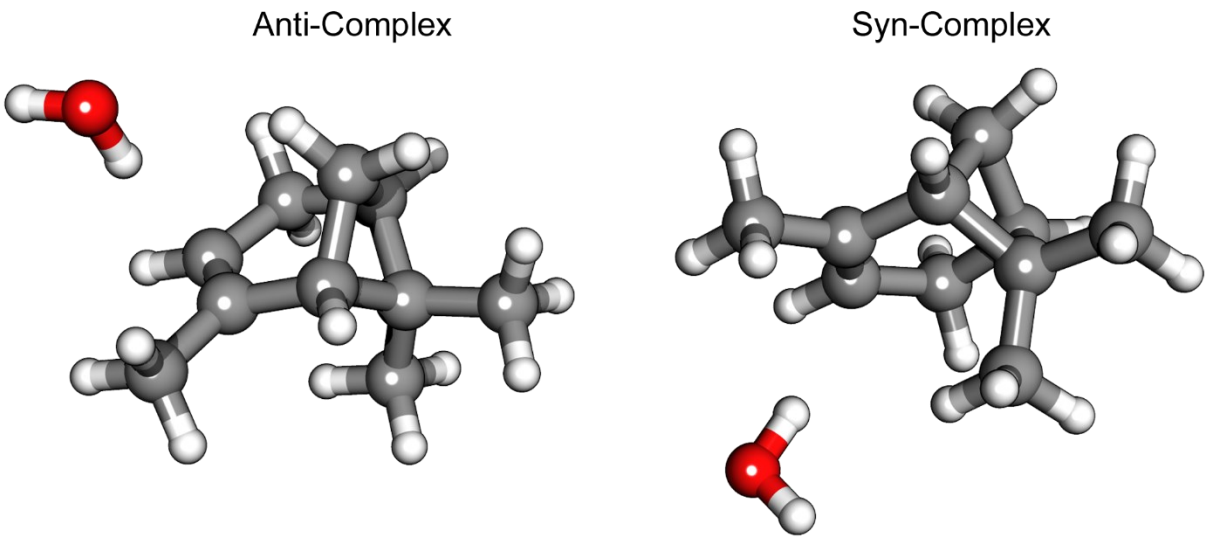

Figure 5.1. Optimized structures for the anti-conformer and syn-conformer at the B3LYP-D3(BJ)/Jun-cc-pVTZ level of theory.

the anti-conformer and syn-conformer, respectively. The zero-point corrected energy, rotational constants, and dipole moment components for each identified conformer are presented in Table C.1 of Appendix C.

As a consequence of the discrepancies between the theoretical and experimental rotational constants (see below), global minimum structures were determined at various levels of theory for both anti- and syn-conformer at the B3LYP-D3(BJ)/Jun-cc-pVTZ, B3LYP-D3(BJ)/6-311++g(d,p), B3LYP-D3(BJ)/def2-TZVPPD, B3LYP-D3(BJ)/def2-TZVP, ωB97XD/Jun-cc-pVTZ, and B2PLYPD3/Jun-cc-pVTZ levels of theory. The rotational constants and dipole moment components for the two minimum energy structures at each level of theory are presented in Table 5.1. The structures of the anti- and syn-conformers at the B3LYP-D3(BJ)/Jun-cc-pVTZ level of theory are presented in Figure 5.2. In Table 5.2 vibrationally uncorrected, vibrationally anharmonic corrected, and experimental rotational constants are given. Table C.2 of Appendix C contains a comparison of relative zero-point corrected energies between the anti- and syn-conformers at each level of theory. The anti-conformer is on average ~3.1 kJ mol^{-1} (zero-point corrected) lower in energy than the syn-conformer across all levels of theory. We anticipated a relatively low barrier for a rotation of the free O-H about (approximately) the O-H---π bond and performed one-dimensional relaxed potential energy scans along the C4-C3-O1-H17 dihedral angle (see Figure C.2. Appendix C, for atom numbering). The B3LYP-D3(BJ)/Jun-cc-pVTZ scans are shown in Figure 5.2 and the scans obtained at the other levels of theory in Figures C.3 and C.4, Appendix C; the barrier heights are given in Table 5.3.

Table 5.1. Rotational constants and dipole moment components at six different levels of theory for the anti- and syn-complexes.

	anti-conformer					
Level of Theory	**A / MHz**	**B / MHz**	**C / MHz**	**μ_a / D**	**μ_b / D**	**μ_c / D**
B3LYP-D3(BJ) /6-311++G(d,p)	1594.1324	785.1615	720.0765	0.69	1.83	0.76
B3LYP-D3(BJ) /def2-TZVP	1620.6405	771.7793	716.4670	2.28	0.84	-0.90
B3LYP-D3(BJ) /def2-TZVPPD	1612.8346	778.2742	719.5653	0.75	0.94	1.35
B3LYP-D3(BJ) /Jun-cc-pVTZ	1612.9913	778.9000	719.9694	0.74	0.98	1.34
ωB97XD /Jun-cc-pVTZ	1631.5242	772.7888	717.4473	1.12	0.26	1.48
B2PLYP-D3 /Jun-cc-pVTZ	1609.5429	780.9930	721.9800	0.61	1.19	1.20
	syn-conformer					
Level of Theory	**A / MHz**	**B / MHz**	**C / MHz**	**μ_a / D**	**μ_b / D**	**μ_c / D**
B3LYP-D3(BJ) /6-311++G(d,p)	1411.3933	815.5643	738.8522	2.39	-0.2	-1.12
B3LYP-D3(BJ) /def2-TZVP	1408.8739	833.9299	747.9587	2.44	-0.01	-0.65
B3LYP-D3(BJ) /def2-TZVPPD	1426.2411	815.5141	738.4884	2.31	0.23	-0.42
B3LYP-D3(BJ) /Jun-cc-pVTZ	1425.6400	816.4853	739.0993	2.33	0.27	-0.42
ωB97XD /Jun-cc-pVTZ	1419.5093	830.7307	745.7407	2.34	0.12	-0.44
B2PLYP-D3 /Jun-cc-pVTZ	1435.1192	811.8316	736.8779	2.27	0.35	-0.24

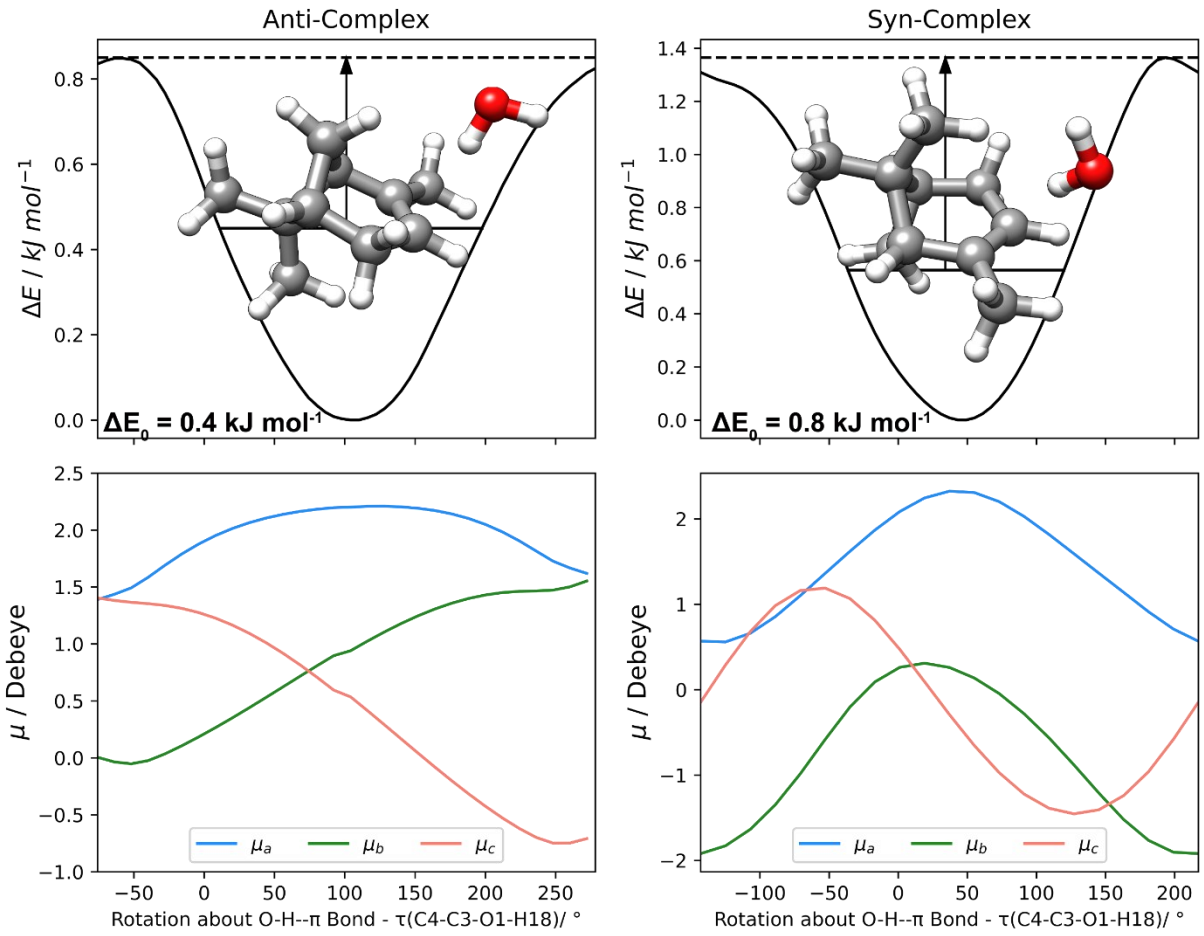

Figure 5.2. One-dimensional relaxed potential energy scans along the C4-C3-O1-H17 (see Figure C.X. for atom labelling) dihedral angle, corresponding to rotation about the O-H---π intermolecular bond, at the B3LYP-D3(BJ)/Jun-cc-pVTZ level of theory. The plots below each dihedral energy scan are the calculated dipole moment components at each point along the potential energy curve.

Figure 5.3 presents a potential energy curve for the anti-conformer water tunneling motion, obtained from the NEB-TS calculation at the B3LYP-D3(BJ)/Jun-cc-pVTZ level of theory**.** From the potential energy curve, it was found that two different identifiable motions were responsible for the overall proton exchange pathway. The two motions for the anti-conformer are summarized in Figure 5.3. The zero-point corrected barrier height of this pathway was found to be 6.0 kJ mol^{-1}. Two different water tunneling potential energy curves were obtained from the NEB-TS calculations for the syn-conformer (Figure 5.4). The relative zero-point corrected barrier heights for the first and second pathway are 2.7 kJ mol^{-1} and 3.6 kJ mol^{-1}, respectively.

Figure 5.6 and Figure C.5 show visualizations of the results from the NCI and QTAIM analyses, respectively, for both conformers. Two intermolecular bonds, indicated by BCPs, are

Table 5.2. Rotational constants and dipole moment components for the experimental, uncorrected, and corrected anharmonic results.

	anti-conformer			
	Experiment		**B2PLYP-D3(BJ)/Jun-cc-pVTZ**	
	Ortho	***Para***	**[a]Equilibrium**	**[b]Vib. Corrected**
A / MHz	1621.25361(55)	1621.30010(81)	1609.543	1576.986
B / MHz	756.19082(32)	756.17321(59)	780.993	780.802
C / MHz	704.67817(32)	704.66487(56)	721.980	708.826
Δ_J / kHz	0.2509(40)	0.253(13)	0.185	0.359
Δ_{JK} / kHz	-0.377(19)	-0.333(32)	-0.292	-0.791
Δ_K / kHz	1.388(50)	1.470(92)	0.879	0.536
δ_J / kHz	0.0415(37)	0.0480(78)	0.0341	0.0877
δ_k / kHz	0.71(12)	0.62(22)	0.416	2.790
N	64	50	-	-
σ /kHz	4.2	5.2	-	-
Observed [c]μ	$\mu_a > \mu_c > \mu_b$			
	syn-conformer			
	Experiment		**B2PLYP-D3(BJ)/Jun-cc-pVTZ**	
	Ortho	***Para***	**[a]Equilibrium**	**[b]Vib. Corrected**
A / MHz	1433.243(32)	1433.319(44)	1435.119	1434.639
B / MHz	788.68980(49)	788.67080(68)	811.832	783.379
C / MHz	718.99750(59)	718.98020(68)	736.878	717.362
Δ_J / kHz	0.299(11)	0.317(19)	0.186	0.300
Δ_{JK} / kHz	-0.510(50)	-0.380(59)	0.0450	-0.496
Δ_K / kHz	[0.283]	[0.283]	0.283	0.283
δ_J / kHz	[0.0568]	[0.0568]	0.0408	0.0568
δ_k / kHz	[2.58]	[2.58]	-0.413	2.58
N	17	15	-	-
σ /kHz	2.8	3.0	-	-
[c]μ	μ_a			

[a]The theoretical uncorrected or theoretical equilibrium rotational constants obtained from the B2PLYPD3/Jun-cc-pVTZ results. [b]The theoretically corrected or theoretical effective rotational constants were obtained by adding the anharmonic vibrational corrections obtained at the B3LYP-D3(BJ)/Jun-cc-pVTZ level to the equilibrium rotational constants. [c]Relative magnitude of experimental dipole moment components.

Table 5.3. Relative zero-point corrected energies between the anti- and syn-conformer at different levels of theory. The energies are relative to the lower energy conformer.

Level of Theory	Syn-Conformer / kJ mol^{-1}	Anti-Conformer / kJ mol^{-1}
B3LYP-D3(BJ)		
6-311++G(d,p)	3.3	0.0
def2-TZVP	2.7	0.0
def2-TZVPPD	3.3	0.0
Jun-cc-pVTZ	3.3	0.0
ωB97XD/Jun-cc-pVTZ	2.8	0.0
B2PLYP-D3/Jun-cc-pVTZ	3.2	0.0

present between the α-pinene and water molecule in both conformers. A summary of the relevant electron topology parameters for the intermolecular bonds obtained from the QTAIM analyses are presented in Table 5.4. For both conformers, the decomposition of these two interactions in terms of donor and acceptor NBOs is presented in Table 5.5, with the bond orders and the ionic and covalent percentages of each bond, presented in Table C.4 (Appendix C). The full decomposition into donor and acceptor NBOs between the water and α-pinene molecule is presented in Table C.3**,** Appendix C. A comparison of the stabilization energies and bond orders of this study contrasted to a monomer of carveol[48], an analogous system containing an O-H---π bond, is presented in Table 5.6.

5.3.2 Experimental Results

The broadband rotational spectrum is presented in Figure 5.5 Both the anti- and syn-conformers were experimentally identified and assigned. Strong a-type and c-type transitions, with weaker b-type transitions, were observed for the anti-conformer, while exclusively a-type transitions were observed for the syn-conformer. The relatively high-resolution capability of the CP-FTMW spectrometer allowed for observation of line splittings, for both the anti- and syn-conformers (see Figure 5.5), into doublet components with an intensity ratio of about 3:1. The intensity ratio corresponds to the nuclear spin statistical weights of *ortho* and *para* water, and the splittings originate from a tunneling motion that interchanges the hydrogen-bonded and non-bonded H-atoms of water. Transitions associated with the *para* and *ortho* states were fitted separately using

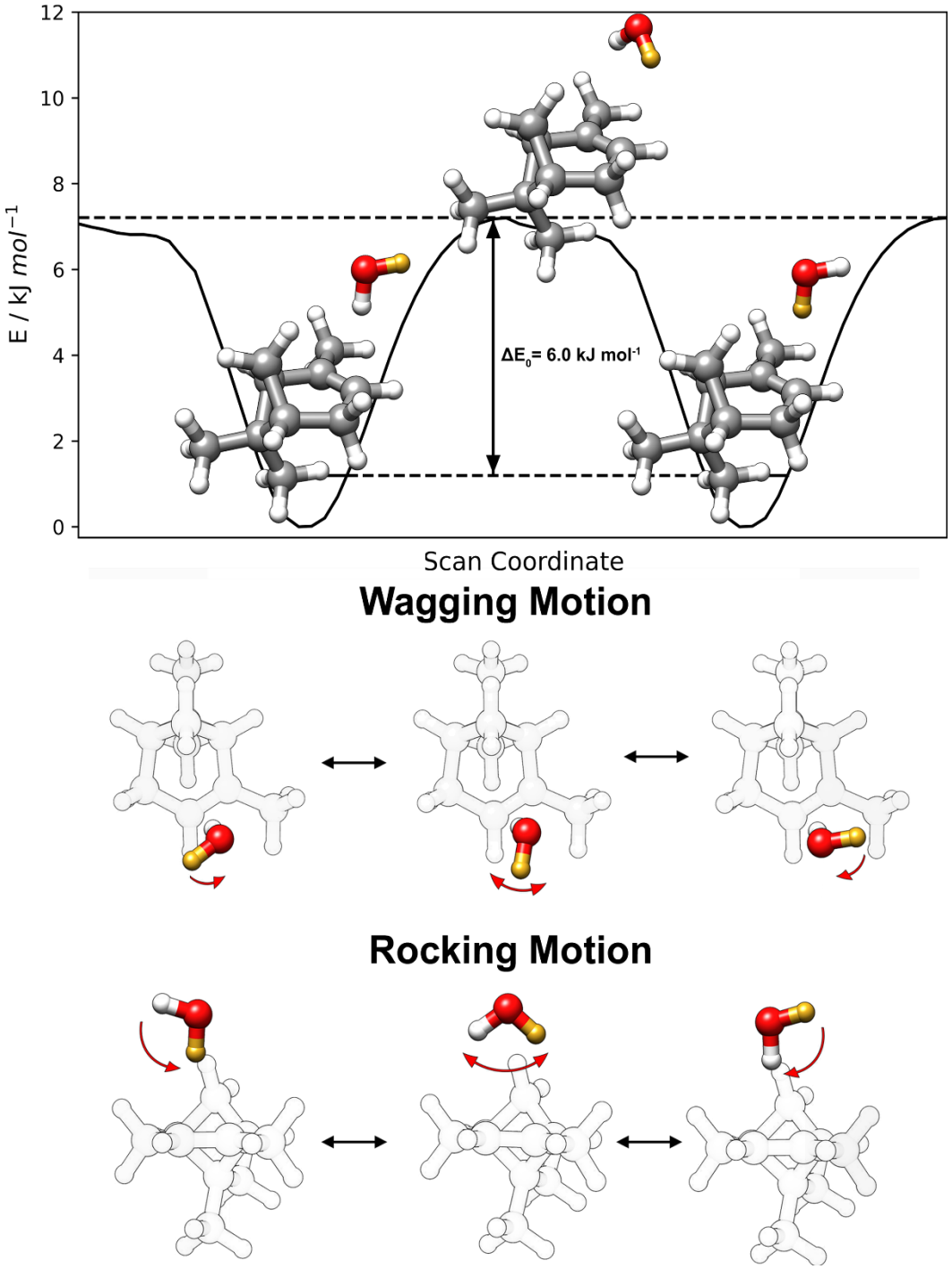

Figure 5.3. A potential energy curve for the anti-conformer water tunneling motion, obtained from the NEB-TS calculation at the B3LYP-D3(BJ)/Jun-cc-pVTZ level of theory.

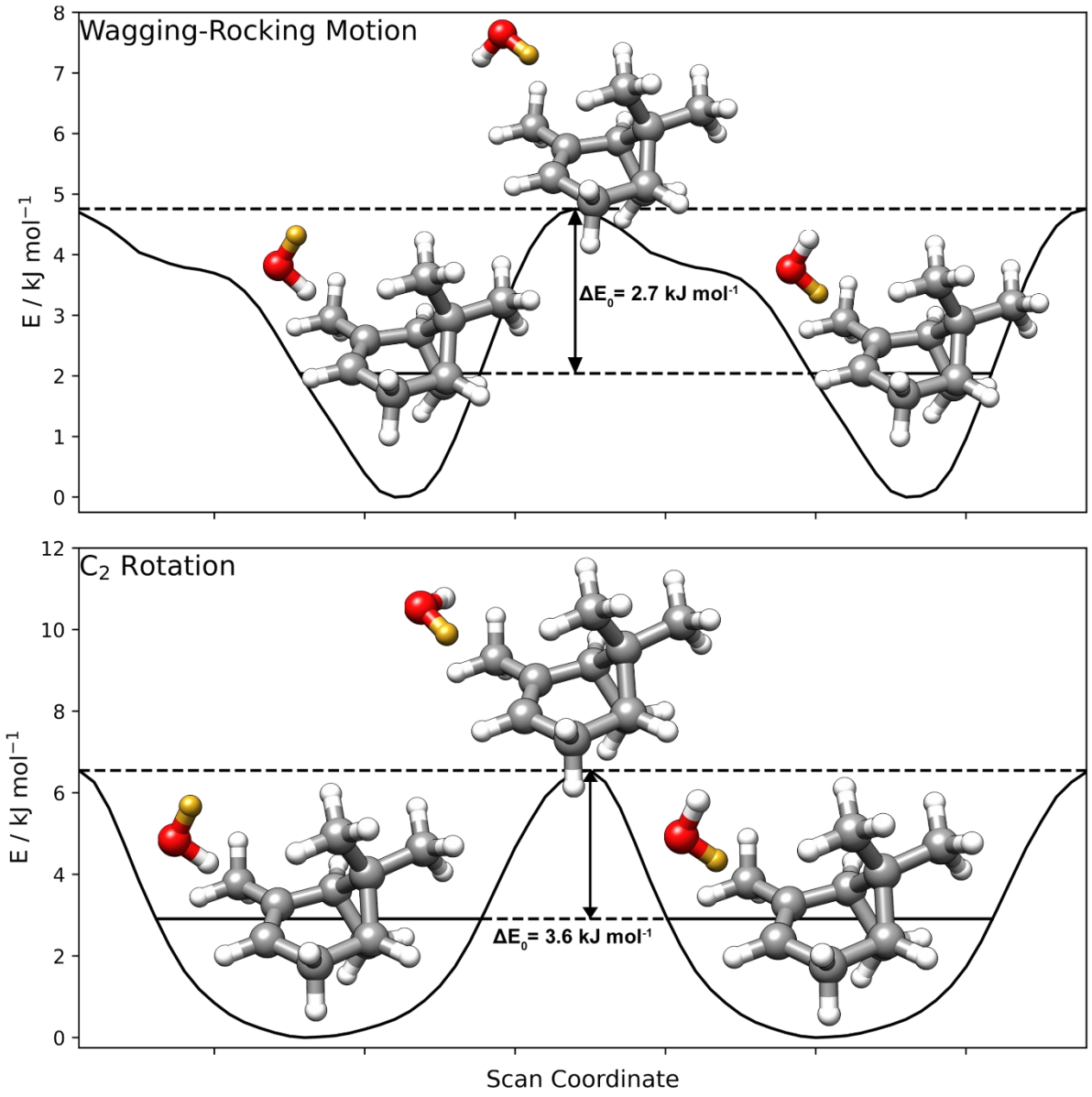

Figure 5.4. Two different potential energy curves for the syn-conformer water tunneling motion, obtained from the NEB-TS calculation at the B3LYP-D3(BJ)/Jun-cc-pVTZ level of theory.

Pickett's SPCAT/SPFIT[49] program suite. The resulting spectroscopic parameters for the *ortho* and *para* states of the two hydrates are presented in Table 5.2. The assigned transition frequencies, with their respective quantum number assignment, are presented in Tables C.5-C.8, Appendix C.

5.3.3. Conformer Assignment

Two new spectral assignments could be achieved in the experimental spectrum and the identification of the anti- and syn-conformers of α-pinene-water as the associated assignments was

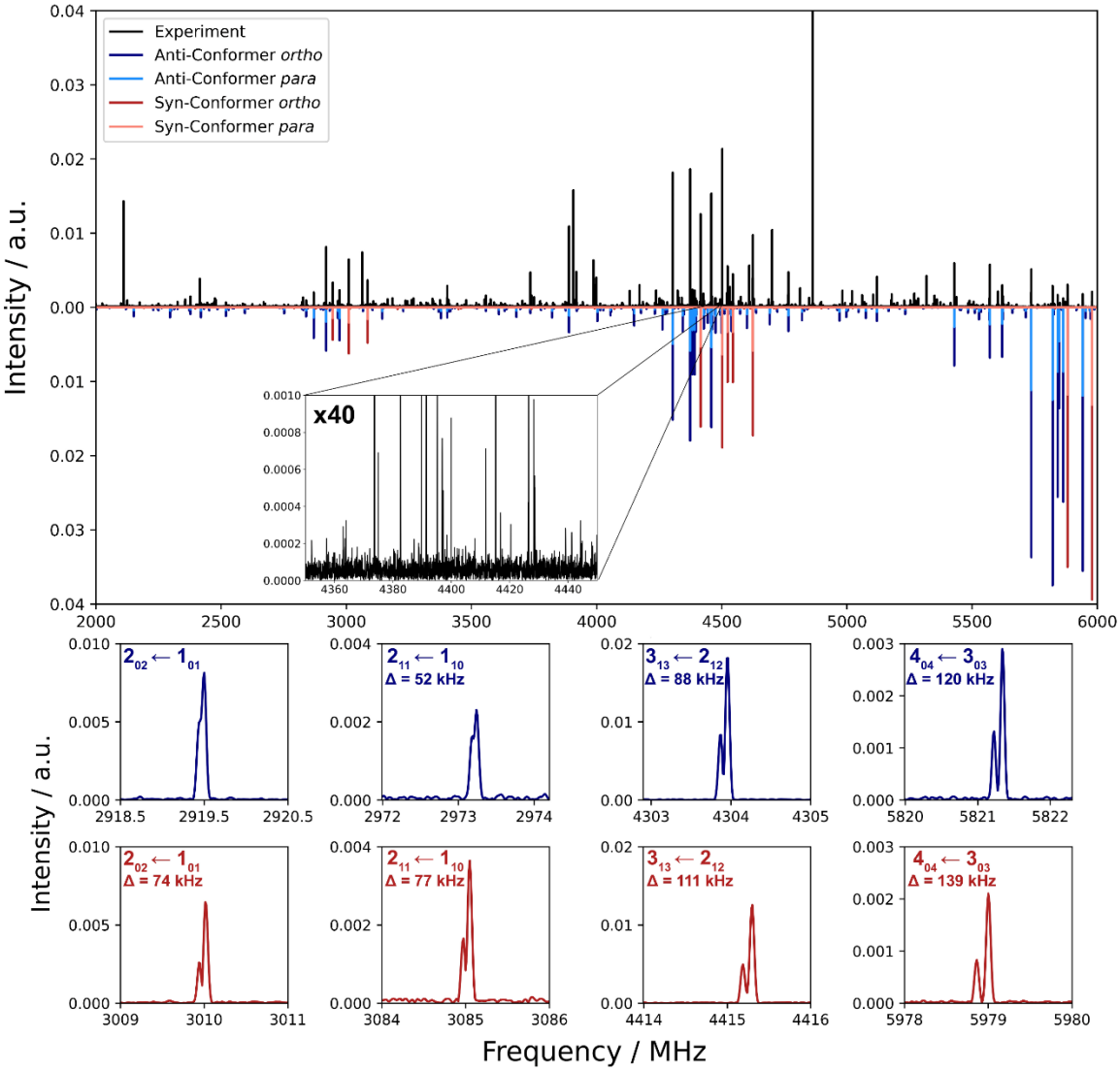

Figure 5.5. The broadband rotational spectrum of the α-pinene water complex. The experimental spectrum is shown in black, while the simulated spectra of the ortho and para states of the syn- and anti-conformers of are shown in reds and blues, respectively.

relatively straightforward. Comparing the experimental (Table 5.2) and calculated (Table 5.1) rotational constants for the anti-conformer, the average difference between the A, B, and C rotational constant across each level of theory is on average 11.1, 21.8, and 14.5 MHz, respectively. The anharmonic corrections reduce the average differences for B and C rotational constants to 21.6 and 2.0 MHz, respectively, but increase the average difference for the A rotational constant significantly (11.1 to 40.2 MHz). Consideration of the experimental and theoretical dipole moment components for the anti-conformer reveals further issues. The theoretical results (Table 5.1) give μ_a, μ_b, and μ_c dipole moment components of varying magnitude for each level of theory. In the

experiment, strong *a*-type and *c*-type transitions, with weaker *b*-type transitions, were observed for the anti-conformer. The variations in dipole moment components with level of theory are mainly the result of slightly different orientations of the water subunit within the complex. This sensitivity of the dipole moment components on the water orientation is visualized in Figure 5.2. The discrepancies between the theoretical results and experimental results will be discussed below.

For the syn-conformer, the difference of the A, B, and C rotational constant between experiment and each level of theory (Table 5.1) is on average 12.7, 32.0, and 22.2 MHz, respectively. After applying the anharmonic contributions the average difference for the A, B, and C constant now becomes 13.1, 6.6, and 3.2 MHz. The assignment to the syn-conformer is further confirmed by dipole moment considerations. In the theoretical calculations (Table 5.1), the μ_a dipole moment component is consistently the largest (~2 D), with much smaller values for the μ_b and μ_c components. This is consistent with the experimental spectrum, where only *a*-type transitions could be observed.

5.3.4. Water tunneling

The observed line splittings with an intensity ratio of about 3:1 (see Figure 5.5) can be attributed to a water tunneling motion. There are several different motions the tunneling pathway can be credited to. For example, in a trifluoroacetic acid-water complex study,[50] Ouyang and coworkers propose three unique water tunneling motions that could be associated with their experimental splitting pattern: a rotation about the C_2 axis of the water molecule, a rotation about the intermolecular bond, and a wagging motion of the non-bonded hydrogen atom of the water molecule. Unlike the trifluoroacetic acid-water complex, the possible motions in the anti- and syn-conformer are not so apparent and do not clearly fit under any one of these three motions. Based on the NEB-TS results, the water tunneling motion for the anti-conformer (Figure 5.3) consists of two different concatenated motions. The first part is a wagging motion about the O-H---π intermolecular bond and the second is a rocking motion about an axis perpendicular to the H_2O molecular plane. The wagging motion is also coincidently captured by the one-dimensional potential energy scan of the C4-C3-O1-H17 dihedral angle, see above for details. The relative zero-point corrected water tunneling barrier height for the anti-conformer was found to be 6.0 kJ mol^{-1}. The NEB-TS results for the syn-conformer yield two possible water tunnelling pathways (Figure 5.4). The first pathway is analogous to the anti-conformer, where the pathway consist of

two concatenated motions: a wagging and rocking motion. The relative zero-point corrected barrier height of the wagging-rocking motion pathway is 2.7 kJ mol^{-1} at the B3LYP-D3(BJ)/Jun-cc-pVTZ level of theory. The second pathway is analogous to one of the motions described in the trifluoroacetic acid-water complex study,[50] where the two protons are exchanged by a rotation about the C_2 axis of the water molecule. The relative zero-point corrected barrier height for this pathway is 3.6 kJ mol^{-1} at the B3LYP-D3(BJ)/Jun-cc-pVTZ level of theory. Based on the relatively small energetic difference between each pathway (<1.0 kJ mol^{-1}), it is difficult to draw a definitive conclusion as to which pathway the proton exchange travels along, however, based on the shorter barrier height and the similarity with the anti-conformer pathway, one can reasonably conclude that the wagging-rocking motion pathway is more favorable. The energetic ordering of the barrier heights for each conformer ($^{Anti}\Delta E_0 > {}^{Syn}\Delta E_0$) is also consistent with the experimental spectrum (Figure 5.5), where a larger separation between ortho and para-transitions for the syn-conformer compared to the anti-conformer is observed. A reason for the higher barrier height in the anti-conformer may be the strength of the intermolecular interactions within the complex, as will be discussed below.

5.3.5. NCI/QTAIM/IGM Analyses

a) anti-Conformer

The results from the QTAIM analysis of the anti-conformer are presented in Figure C.5, Appendix C. Two bonding interactions, as indicated by bond critical points (BCPs) and their respective bond paths, are observed between water and α-pinene. The first interaction is between a lone pair of the oxygen and the hydrogen bound to one of the methyl groups in the bicyclic ring (O---H-C). The second interaction occurs between the hydrogen atom of the water molecule and one of the carbons in the π system (O-H--- π). The ring critical point (RCP) between the two BCPs is located quite close to the BCP of the O---H-C interaction, an indication that the O-H---π interaction is the stronger of the two. This is supported by the results of the NCI analysis (Figure 5.6) which show a strong hydrogen bond interaction between the water molecule and the π-system, and a weaker O---H-C interaction. To quantify these interactions electron density derived parameters were utilized at the BCP, which include the electron density (ρ), the Laplacian of the electron density ($\nabla^2\rho$), and the bond ellipticity (ε) which is a measure of the anisotropy of the electron density curvature[51] (see Table 5.4). The values at the BCP of the O---H-C (O-H---π) interaction are

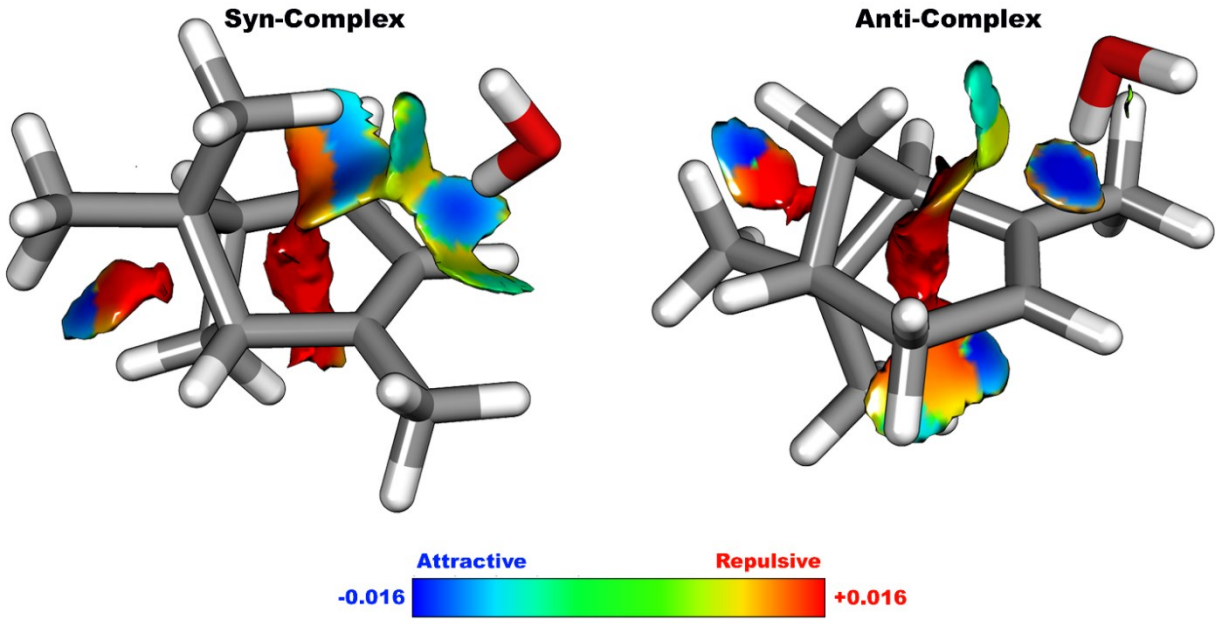

Figure 5.6. Results from non-covalent interactions (NCI) analyses of the syn- and anti-conformers.

ρ=0.0060 (0.0168) a.u., $\nabla^2\rho$=0.0221 (0.0389) a.u., and ε=0.00609 (0.02019) a.u. at the B3LYP-D3(BJ)/Jun-cc-pVTZ level of theory. For comparison, the parameters for the strong H-bond in the water dimer and the strong and weak hydrogen bonds in the acyclic formic acid dimer are presented in Table 5.4, calculated at the B3LYP-D3(BJ)/Jun-cc-pVTZ level of theory. The values for electron density and Laplacian at the O-H---π BCP are somewhat smaller than those for the strong $(H_2O)_2$ and acyclic formic acid dimer H-bonds, indicating that the O-H---π interaction is of intermediate strength. The O---H-C bond can be classified as a weak H-bond, by comparison of the ρ and $\nabla^2\rho$ values with those of the weak H-bond in the acyclic formic acid dimer.

To further assess and quantify the strengths of these interactions the intrinsic bond strength index (IBSI)[52] were utilized, which is derived using the independent gradient model (IGM).[53,54] IBSI values have been utilized in a recent study where its ability to measure non-covalent bond strengths was used to evaluate close-contact H-H interactions in naphthol.[55] Weak interactions have IBSI values $\lesssim$ 0.15 and for stronger or covalent interactions IBSI $\gtrsim$ 0.15. IBSI values can only be calculated for atom-atom interactions and for the case of the O-H---π interaction the atoms connected by the QTAIM bond path, i.e., the water hydrogen and carbon C3 (see Figure C.2 of Appendix C for atom numbering) were taken to be consistent with the QTAIM results The IBSI values for the O---H-C and O-H---π interactions, as well as the O---H-O water dimer interaction, are 0.00609, 0.02019, and 0.04103, respectively. Consistent with the picture from the

Table 5.4. Electron density topology parameters obtained from QTAIM analyses at the B3LYP-D3(BJ)/Jun-cc-pVTZ level of theory.

	Anti-Complex	
	C-H --- O	**O-H --- π**
BCP ρ (e/bohr^3)	0.0060	0.0168
BCP $\nabla^2\rho$ (e/bohr^5)	0.0221	0.0389
BCP ε	1.9167	0.4303
IBSI	0.00609	0.02019
	Syn-Complex	
	O-H --- H-C	**O-H --- π**
BCP ρ (e/bohr^3)	0.0073	0.0128
BCP $\nabla^2\rho$ (e/bohr^5)	0.0219	0.0346
BCP ε	1.0933	0.5411
IBSI	0.01281	0.01570
	Acyclic Formic Acid Dimer	
	O-H --- O	**C-H --- O**
BCP ρ (e/bohr^3)	0.0410	0.0128
BCP $\nabla^2\rho$ (e/bohr^5)	0.0938	0.0486
BCP ε	0.0086	0.0891
IBSI	0.06913	0.01747
	Water dimer	**cis-1-naphthol**
	O-H --- O^g	**O-H --- H-C^f**
BCP ρ (e/bohr^3)	0.0255	0.0153
BCP $\nabla^2\rho$ (e/bohr^5)	0.0801	0.0550
BCP ε	0.0302	0.8986
IBSI	0.04103	0.02224

electron density derived parameters, the IBSI data reveal that the O-H---π interaction is stronger than the O---H-C interaction, with values comparable to other strongly hydrogen-bonded systems. The quantitative data of the IBSI and electron density derived values correlate well with the picture painted by the NCI and QTAIM analyses.

b) syn-Conformer

The QTAIM analysis for the syn-complex also reveals two bonding intermolecular interactions. Similar to the anti-conformer, one of the interactions occurs between the hydrogen atom of the water molecule and the π-system (O-H---π). The second, somewhat surprising, interaction is a hydrogen-hydrogen interaction between the water hydrogen and the hydrogen of α-pinene (O-H---H-C). This interaction is discussed in greater detail below. RCP and BCP are closest for the O-H---H-C interaction, indicating that the O-H---π interaction is the stronger

interaction of the two. This is corroborated by the NCI analysis which shows a darker blue colouration for the O-H---π interaction than the O-H---H-C interaction. The electron density derived parameters and IBSI value for the O-H---π interaction of the syn-complex are as follows: ρ=0.0128, $\nabla^2\rho$=0.0346, ε=0.5411, and IBSI=0.01570. Comparing these values to the water dimer and the O-H---π interaction in the anti-conformer (Table 5.4) comparable values were observed indicating this can also be labeled as a relatively strong interaction.

The O-H---H-C interaction could be characterized as either an H-H interaction or a dihydrogen interaction. The term H-H interaction derives from the work of Bader and coworkers[56] and Matta,[57] who interpret a BCP between two close-contact, similarly charged H-atoms as a bonding interaction, where this close-contact is defined as a distance smaller than two times the van Der Waals radius of the hydrogen atom. Conversely, a dihydrogen interaction is primarily an electrostatic interaction between two hydrogens of opposite charge. For example, in a BH_3---NH_3 study[58] where a dihydrogen bond was found, the hydridic hydrogen bound to boron and acidic hydrogen bound to nitrogen, bear QTAIM charges of -0.7e and +0.5e, respectively. The QTAIM charges of the hydrogen bound to α-pinene and the water hydrogen are -0.02e and +0.58e, respectively. The distance between the two hydrogen atoms is ~2.2 Å, which is less than two times the van der Waals radius of hydrogen (2.36 Å)[59]. With an QTAIM atomic charge separation of 0.6e, as well as the distance of the close contact, this interaction is classified as an H-H rather than a dihydrogen interaction. Moreover, comparing the O-H---H-C interaction to the O-H---π interaction, comparable electron density derived parameters and IBSI values are observed, suggesting the two interactions are surprisingly similar in their interaction strengths.

As discussed in a recent *cis*-1-naphthol study,[55] the H-H interaction and its subsequent classification are not only difficult to decipher but has also been met with controversy. Herein, the electron density derived parameters and IBSI values are used from *cis*-1-naphthol as a comparison to the O-H---H-C interaction in the syn-complex. For a more detailed discussion please see Ref. 55. The electron density derived parameters and IBSI value for the O-H---H-C interaction in the syn-complex are ρ=0.0073, $\nabla^2\rho$=0.0219, ε=1.0933, and IBSI=0.01281. The electron density derived parameters and IBSI value for the O-H---H-C interaction in *cis*-1-naphthol are ρ=0.0153, $\nabla^2\rho$=0.0550, ε=0.8986, and IBSI=0.02224. As one can see, the interactions are quite similar to each other, implying that the electron topology in the syn-complex is quite similar to the H-H interaction in *cis*-1-naphthol.

5.3.6. NBO Analyses

To further analyze and quantify the non-covalent interactions within each complex, Natural Bond Orbital (NBO) analyses were carried out at the B3LYP-D3(BJ)/Jun-cc-pVTZ level of theory. In an NBO analysis a bonding interaction is identified by the transfer of electron density from a donor or bonding orbital (BD) to an adjacent acceptor or antibonding orbital (BD*). For example, in the water dimer system the lone pair (LP) orbital on the O-atom is donating electron density to the O-H BD* or acceptor orbital. Table 5.5 presents the NBO results for the syn- and anti-conformers. The syn-conformer NBO stabilization energy of the two intermolecular interactions is 9.5 kJ mol^{-1}, where the O-H---π stabilization energy (8.3 kJ mol^{-1}) contributes more significantly than the O-H---H-C interaction (1.2 kJ mol^{-1}). The O-H---π interaction is dominated by the interaction between the C2-C3 BD(π) and the O1-H17 BD*(σ) orbitals, with minor contributions from an interaction between the O1-H17 BD(σ) and excited or Rydberg (RY) orbitals of the C2 and C3 carbons. The anti-conformer NBO stabilization energy of the two intermolecular interactions is 18.1 kJ mol^{-1}, and much like the syn-conformer is dominated by the O-H---π interaction (16.3 kJ mol^{-1}), with a smaller contribution from the O---H-C interaction (1.8 kJ mol^{-1}). Also in the anti-conformer, the O-H---π interaction is dominated by the C2-C3 BD(π)---O1-H17 BD*(σ) interaction, with now a larger contribution from the O1-H17 BD(σ)---C2 RY(4) interaction. Overall, the NBO interaction energy of the two intermolecular interactions is larger by ~8.6 kJ mol^{-1} in the anti-conformer (18.1 kJ mol^{-1}) than the syn-conformer (9.5 kJ mol^{-1}).

The total interaction energy, which in addition to the two predominant intermolecular interactions discussed above, includes minor contributions from other weak intermolecular interactions between water and α-pinene. The total interaction energy is presented in Table C.3 of the ESI. The total interaction energy in the syn-(anti-) conformers is 12.0 kJ mol^{-1} (19.9 kJ mol^{-1}). This is in reasonable agreement with the complexation energies obtained from counterpoise calculations: 15.3 kJ mol^{-1} for the syn-complex and 18.5 kJ mol^{-1} for the anti-complex, at the B3LYP-D3(BJ)/Jun-cc-pVTZ level of theory.

Table 5.6 presents the stabilization energies and bond orders of the two intermolecular interactions of the anti- and syn-conformer, compared with previous results from NBO analyses

Table 5.5. Decomposition of the two intermolecular interactions into donor and acceptor Natural Bond Orbitals (NBO) at the B3LYP-D3(BJ)/Jun-cc-pVTZ level of theory.

Anti-Complex		
Donor	Acceptor	E /kJ mol^{-1}
O-H --- π		
BD(σ) C2-C3	RY(2) H17	0.3
BD(π) C2-C3	BD*(σ) O1-H17	12.5
BD(π) C2-C3	RY(3) O1	0.3
BD(π) C2-C3	RY(4) H28	0.3
LP(1)[f] O1	BD(π) C2-C3	0.3
BD(σ) O1-H17	RY(1) C2	0.5
BD(σ) O1-H17	RY(4) C2	1.5
O --- H-C		
LP(1) O1	BD*(σ) C7-H7	0.8
LP(2) O1	BD*(σ) C7-H7	0.6
BD(1) O1-H17	BD*(σ) C7-H7	0.4
O-H---π[g]	O---H-C[g]	Total[f]
16.3 kJ mol^{-1}	1.8 kJ mol^{-1}	18.1 kJ mol^{-1}
Syn-Complex		
Donor	Acceptor	E /kJ mol^{-1}
O-H --- π		
BD(π)[a] C2-C3	BD*(σ)[b] O1-H17	6.8
BD(σ)[c] O1-H17	BD*(π)[d] C2-C3	0.3
BD(σ) O1-H17	RY(4)[e] C2	0.4
BD(σ) O1-H17	RY(5) C2	0.3
BD(σ) O1-H17	RY(4) C3	0.5
O-H --- H-C		
BD(σ) C9-H12	BD*(σ) O1-H17	0.5
BD(σ) O1-H17	BD*(σ) C9-H12	0.7
O-H---π [g]	O-H---H-C[g]	Total[f]
8.3 kJ mol^{-1}	1.2 kJ mol^{-1}	9.5 kJ mol^{-1}

[a]π bonding orbital, [b]σ antibonding orbital, [c]σ bonding orbital and [d]π antibonding orbital [e]Excited or Rydberg orbital, with the number in brackets indicating the Rydberg orbital the interaction is occurring with. [f]Lone pair orbital, with the number in brackets indicating the lone pair the interaction is occurring with. [g]Sum of the donor-acceptor pairs for each respective intermolecular interaction. [h]Total stabilization energy, obtained from summing both intermolecular interactions.

Table 5.6. Stabilization energies and bond orders obtained from NBO analyses.

System	Interaction Type	E / kJ mol^{-1}	Bond Order
Syn-Complex	O-H---π	8.3	0.0043
Anti-Complex	O-H---π	16.3	0.0058
[a]Carveol	O-H---π	8.4	0.0014
Syn-Complex	O-H---H-C	1.2	0
Anti-Complex	O---H-C	1.8	0
H_2O-H_2O	O---H-O	49.0	0.0059
Carveol-H_2O	O---H-O	43.1	0.0075

[a]Results from a previous study.[48]

of water dimer (O---H-O), carveol (O-H---π), and a carveol water complex (O---H-O).[48] The energy of the O-H---π interaction in the anti-conformer is greater by 7.9 kJ mol^{-1} than in carveol. The O-H---π interaction in the syn-conformer is more comparable to carveol. The higher stabilization energy in the anti-conformer compared to the carveol monomer and syn-conformer O-H---π interaction may be simply due to less steric repulsion between water and α-pinene. For example, in the syn-conformer, the proximity of the methyl group to the water molecule may introduce some steric repulsion to the system. The methyl group, and consequently the steric repulsion, is absent in the anti-conformer allowing for the water molecule to interact with the π system relatively unimpeded. This is reflected in the O-H---π distances of 2.29 Å in the anti-conformer and 2.41 Å in the syn-conformer.

5.3.7. Theoretical Discussion

Across each level of theory, the theoretical results for the anti-conformer vary considerably. Generally, the global minimum structure for each level of theory has the non-bonded H-atom of water pointing away from the α-pinene unit. However, the specific orientation of the non-bonded hydrogen varies greatly resulting in inconsistent dipole moments across the levels of theory. Additionally, the shapes of the dihedral energy curves change with level of theory. At lower levels multiple minima are observed, and at higher levels only a single minimum. For example, adding a second polarization and diffuse function to the def2-TZVP basis set changes the shape of the potential energy scan completely and results in a different global minimum (see Figure C.3). Although the variation in uncorrected barrier height is only about 0.7 kJ/mol, the zero-point

corrected energy barriers vary more significantly. In several cases the zero-point energy lies above the barrier. The very low barrier or barrierless potential energy curves for the water rotation about the O-H---π axis suggest a greater delocalization of the non-bonded hydrogen in the anti-conformer. This highly delocalized H-atom will have a direct effect on the direction and magnitude of the dipole moment, and is likely the reason for the variation across the different levels of theory. Another reason for the fluctuating dipole moment components may also be due to the position of the water molecule in the principal inertial axis system. α-pinene has a relatively low dipole moment of approximately 0.2 Debye, hence the major contributor to the overall dipole moment of the α-pinene-water complex is the water molecule. For the anti-conformer, the water molecule sits almost directly along the principal inertial *a*-axis, therefore the slightest change in its position can drastically change the dipole moment of the whole complex. The anti- and syn-conformer, with their three principal axes, are presented in Figure C.2 of Appendix C. The sensitivity to position, combined with the delocalization of the water molecule will result in a large fluctuation in dipole moment and subsequently the inability of theoretical calculations to accurately predict the structure and respective dipole moment components. This fluctuation can be visualized in Figure 5.2, where in the dihedral energy scan the dipole moment components change drastically along the coordinate.

Not only are the dipole moment components inconsistent between the levels of theory, they are also inconsistent with the observed experimental dipole moment components. In the experiment, strong *a*-type and *c*-type transitions, with weaker *b*-type transitions, are observed. The best agreement between theory and experiment in terms of dipole moment components seems to be with the ωB97XD/Jun-cc-pVTZ level of theory, which also has large μ_a and μ_c components, with a weaker μ_b component. Now comparing the experimental rotational constants to the uncorrected theoretical rotational constants, in the order of which they are presented in Table 5.1, the RMS error is 43, 20, 28, 29, 23, and 32 MHz, respectively. The RMS errors after including the vibrational corrections are 66, 37, 46, 47, 28, and 51 MHz, respectively. Taking into account the uncorrected and corrected rotational constants, as well as the dipole moment components, it seems the ωB97XD/Jun-cc-pVTZ results predict the experimental structure the best out of all the levels of theory. Interestingly, it appears that the vibrational corrections worsen the RMS errors for each level of theory, despite the excellent agreement observed with the syn-conformer. The reason for this is unclear, but may be another example of the difficulties encountered by theory in accurately predicting the structure of the anti-conformer.

For the syn-conformer there is an overall consistency in the global minimum structures and potential energy scans of the water rotation about the O-H---π axis for the various levels of theory. In each case, the global minimum structure has the water oxygen pointing away from α-pinene, with the rotational constants and dipole moment components in reasonable agreement with each other, as well as with the experimental results. `

5.3.8. Atmospheric Implications – Thermodynamics

To investigate the atmospheric implications of the α-pinene-water complex, the thermodynamic abundances are evaluated of the syn- and anti-conformers using equilibrium constants. Equilibrium constants can be computed directly from partition functions and dissociation energies:

$$K_p = \frac{Q_{AB}(T)}{Q_A(T)Q_B(T)} \exp\left(\frac{D_0}{RT}\right) \quad (5.1)$$

where R is the gas constant in J mol^{-1} K^{-1}, T is temperature in K, and D_0 is the dissociation energy in J mol^{-1}. Dissociation energies were calculated according to Ref. 57, where the zero-point energies of the fragments and complex were subtracted from the counterpoise-corrected interaction energy. For this study daily average ambient temperature measurements taken in Edmonton, Alberta, Canada, from January 1st, 2018, to January 1st, 2021 were used . The measurements were obtained from the Earth and Atmospheric Sciences (EAS) weather station,[60] located at the University of Alberta. $Q_A(T)$ and $Q_B(T)$ are the total partition functions for water and α-pinene, and $Q_{AB}(T)$ is the total partition function for the α-pinene-water complex. Here, equilibrium constants were computed for the syn- and anti-conformers, with and without anharmonic corrections.

For the vibrational partition function, the vibrational temperature for each normal mode was calculated using the harmonic and anharmonic results obtained from Gaussian 16, at the B3LYP-D3(BJ)/Jun-cc-pVTZ level of theory. All 81 vibrational modes were except for the anharmonic case of the anti-conformer. In this instance, the frequencies of the two lowest lying modes became imaginary upon applying the anharmonic correction and only 79 modes were used. For the rotational partition function, the symmetry number for all species is one, with the exception of water having a symmetry number of two. The rotational temperatures for the syn- and anti-conformers were calculated using the experimental rotational constants. The rotational temperatures for water and α-pinene were computed using rotational constants from previous

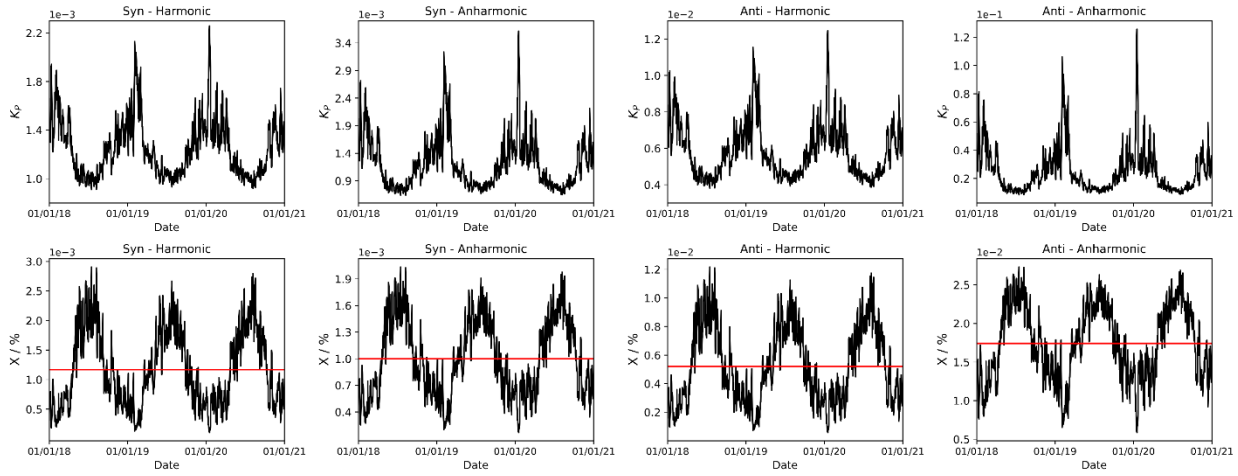

Figure 5.7. Equilibrium constants and relative abundance plots for the syn- and anti-conformers, with and without the anharmonic approximation. The red line indicates the average over the three-year period.

studies.[61,62] The daily equilibrium constant values over the three year period mentioned above are plotted in Figure 5.7 for the harmonic and anharmonic results.

The abundance of hydrated α-pinene is dependent on atmospheric water concentrations and the relative hydrate abundance can be calculated according to

$$\chi = K_p \left[\frac{p(H_2O)}{p_a}\right] 100\% \qquad (5.2)$$

where K_p is the equilibrium constant calculated above, $p(H_2O)$ is the partial pressure of water, and p_a is the ambient atmospheric pressure. The ambient air pressure was obtained from the EAS weather station, while the partial pressure of water was calculated using the vapour pressure parameterization of the World Meteorological Organization.[63] The resulting hydrate abundances for the syn- and anti-conformers are presented in Figure 5.7. The seasonal variation of the equilibrium constants and relative abundances are relatively small. The equilibrium constants are the highest in the winter months and the lowest in the summer months, while the percentage of hydrated α-pinene is highest in the summer months and lowest in the winter months. The abundance trends correlate with the trends in the vapour pressure of water, implying that water vapor pressure plays a larger role than the equilibrium constants in α-pinene hydrate formation.

The average abundances for the syn- and anti-conformers using the equilibrium constants calculated with harmonically (anharmonically) derived partition functions are 0.0012% (0.0010%) and 0.0052% (0.017%), respectively. The derived abundances of the α-pinene monohydrate are

much lower than those of the benzoic acid monohydrate[64] and the toluic acid monohydrate[65], for example, owing to the weaker hydrogen bonding interactions.

At first sight, the low abundances of α-pinene monohydrate compared to other atmospheric species suggests that it is atmospherically irrelevant. However, in a recent modelling study[66] the yearly emission rate of α-pinene in the northern hemisphere alone was estimated to be around 33 Tg $year^{-1}$. Therefore, taking the anharmonic yearly relative abundance for the syn- and anti-conformer, with their respective mol fractions of 0.05 and 0.23, one can estimate the yearly flux of the anti-conformer(syn-conformer) to be 1290.3 Mg $year^{-1}$(16.5 Mg $year^{-1}$), ignoring any additional thermodynamic or kinetic effects. In contrast, a previous study found that the atmospheric concentration of benzoic acid in the Indo-Gangetic-Plain outflow is approximately 0.3 ng m^{-3}.[67] These measurements were recorded over a 20 hour collection window. Therefore, assuming a uniform column density in the troposphere, the northern hemispheric yearly flux of benzoic acid is approximately 0.3 g $year^{-1}$ and 0.003 g $year^{-1}$ for the benzoic acid – water complex.

5.3.9. Atmospheric Implications – Kinetics

The primary pathway of atmospheric degradation of α-pinene often involves a reaction with either atmospheric radicals or ozone. Ozone reacts with α-pinene via the Criegee mechanism of alkene ozonolysis,[68] where the initial step consists of cycloaddition of ozone to the double bond forming a primary ozonide. The primary ozonide undergoes unimolecular isomerization forming activated carbonyl oxides, also known as Criegee intermediates. Depending on the atmospheric conditions, such as temperature and relative humidity, the Criegee intermediates will then undergo collisional stabilization or unimolecular reactions to form a variety of products which may cluster forming secondary organic aerosol. Interestingly, it was shown in a recent study[69] examining α-pinene ozonolysis pathways, that the two structurally different Criegee intermediates predominately and unexpectedly form constituents with identical structures. A summary of the reaction mechanism is shown in Figure C.7 of Appendix C. The first critical step is the cycloaddition of ozone at the double bond and any changes which promote or inhibit this first step will ultimately alter the concentration of downstream products and subsequently involvement in secondary organic aerosol formation. These changes may be an interaction with a molecule, such as water, bound via intermolecular interactions to the π system. For example, the water-π interaction may alter electron density around the double bond or physically block the reaction site, promoting or preventing

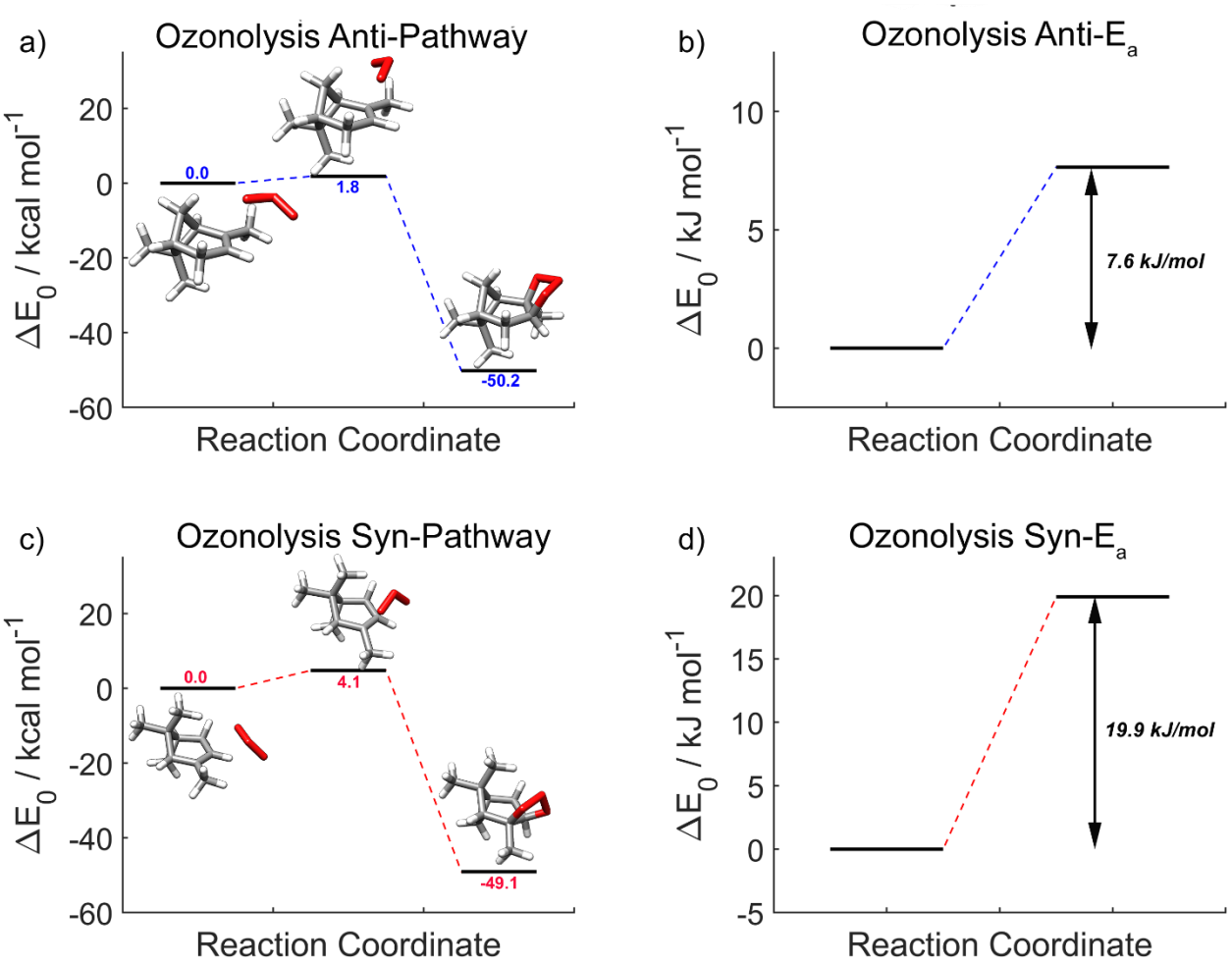

Figure 5.8. Reaction pathway for ozonolysis of α-pinene, for ozone attacking from the anti- and syn-positions. Subfigure a(c) presents the reactants, transition state, and products for ozone attacking from the anti-(syn-) in kcal mol^{-1}. Subfigure b(d) presents the activation energy going from reactants to transition state for the anti-(syn-) reaction in kJ mol^{-1}. Energies were calculated at the B3LYP-D3(BJ)/def-TZVP level of theory.

ozone cycloaddition. To quantify this effect rate constants and activation energies for the reaction were determined. Expanding on previous studies,[70] rate constants and activation energies for ozone reacting in a syn- and anti-approach to the double bond for the α-pinene monomer and its monohydrate were determined. For reactions with water present, the ozone molecule was positioned on the opposite side of the double bond to water. In this study only the first step in the ozonolysis mechanism and not the following formation of the Criegee intermediates were examined.

To determine the activation energy, the structures of α-pinene clustered with ozone in the syn- and anti-positions were optimized near the double bond, followed by a harmonic frequency calculation and determination of the zero-point corrected energies at the B3LYP-D3(BJ)/def2-

TZVP level of theory. The structure with ozone attacking from the syn-position is 4.2 kJ mol^{-1} higher in energy than ozone attacking from the anti-position. The same method was used for the primary ozonide (PO) in the ground vibrational state, where the anti-PO is 11.4 kJ mol^{-1} lower in energy than the syn-PO. To locate the transition state, and subsequently determine the activation energy, the Synchronous Transit Quasi-Newton (STQN) method of Schlegel and coworkers was used.[71,72] From these results, the activation barrier for ozone attacking from the syn-position was determined to be 19.9 kJ mol^{-1}, and 7.6 kJ mol^{-1} for the anti-position. The structures, reaction pathways, and relative zero-point energies are shown in Figure 5.8. The bimolecular rate constant of α-pinene ozonolysis was then determined using classic transition state theory.[73–75]

$$k = \frac{k_b T}{h} \frac{Q_{AB}^{\ddagger}}{Q_A Q_B} \exp\left(-\frac{\Delta E_0}{RT}\right) \tag{5.3}$$

Here, R is the gas constant, h is Planck's constant, T is the temperature in K, $Q_{AB}^{\ddagger}$ is the partition function of the transition state, Q_x is the vibrational partition function for the reactants, and ΔE_0 is the zero-point corrected activation energy in J mol^{-1}. The rate constants are presented in Table 5.7. Ozone attacking from the anti- (syn-) position has a rate constant of 1.27 x 10^{-17} cm^3 molecules^{-1} s^{-1} (2.61 x 10^{-21} cm^3 molecules^{-1} s^{-1}) at 298.15 K. The rate constant for the anti-position is in good agreement with previous theoretical and experimental studies,[70,76–80] which all report a rate constant on the 10^{-17} cm^3 molecules^{-1} s^{-1} scale. Interestingly, when ozone attacks from the syn-position the reaction proceeds four orders of magnitude slower compared to the anti-position. The larger activation energy, and resultant lower rate constant, for the syn-position are a result of the steric repulsion from the neighboring methyl group which may prevent a closer contact between the ozone molecule and double bond compared to the anti-position, where the ozone molecule can approach the double bond unimpeded.

The same procedure was carried out for the monohydrates, where the water molecule interacts with the double bond on the opposite side of ozone. The complex with ozone positioned in the syn-position is 3.0 kJ mol^{-1} higher in energy than the one with ozone in the anti-position.

Table 5.7. Theoretical rate constants for the anti- and syn- conformers at 298.15 K, calculated at the B3LYP-D3(BJ)/def2-TZVP level of theory.

	Rate Constant (cm^3 molecules^{-1} s^{-1})	**Rate Constant with H_2O (cm^3 molecules^{-1} s^{-1})**
Anti-Complex	1.27e-17	1.29e-16
Syn-Complex	2.61e-21	8.54e-20

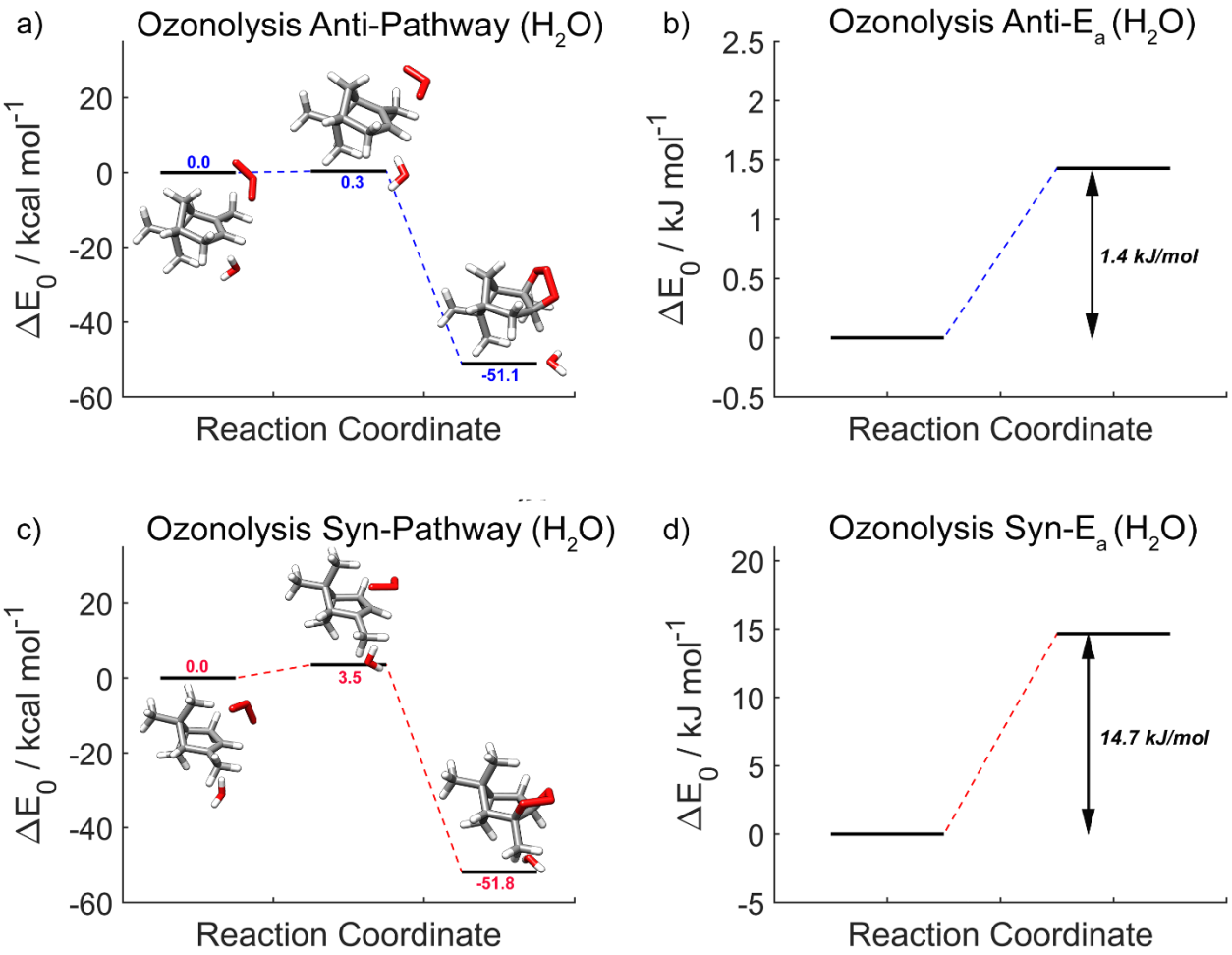

Figure 5.9. Reaction pathway for ozonolysis of α-pinene, with a water molecule non-covalently bound, for ozone attacking from the anti- and syn-. Subfigure a(c) presents the reactants, transition state, and products for ozone attacking from the anti-(syn-), with a water molecule non-covalently bound, in kcal mol^{-1}. Subfigure b(d) presents the activation energy going from reactants to transition state for the Anti-(Syn-) reaction in kJ mol^{-1}. Energies were calculated at the B3LYP-D3(BJ)/def-TZVP level of theory.

The primary ozonide in the anti-position is <0.4 kJ mol^{-1} lower in energy than the syn-position. The activation barrier for the syn-approach is now 14.6 kJ mol^{-1} and 1.4 kJ mol^{-1} for the anti-approach. The structures, reactions pathway, and relative zero-point energies are shown in Figure 5.9. For the rate constant determination, I made the assumption that the water molecule does not directly participate in the reaction. The reaction is thus a bimolecular reaction, where Q_A is the partition function for the α-pinene-water complex and Q_B is the partition function for ozone. The rate constants are presented in Table 5.7. Ozone attacking from the anti- (syn-) position now has a rate constant of 1.29 x 10^{-16} cm^3 molecules^{-1} s^{-1} (8.54 x 10^{-20} cm^3 molecules^{-1} s^{-1}). Analogous to the case without water, when ozone attacks from the syn-position the reaction proceeds four orders of magnitude slower than the attack from the anti-position.

There is a significant reduction in ozonolysis activation energy when going from the α-pinene monomer to the monohydrate. The activation energy for the anti- (syn-) attack is lowered from 7.6 kJ mol^{-1} (19.9 kJ mol^{-1}) to only 1.4 kJ mol^{-1} (14.6 kJ mol^{-1}). In both cases water lowers the activation energy, acting as a catalyst for generation of the primary ozonide. Although there is some uncertainty behind the exact mechanism, a reasonable conclusion may be that the water molecule draws electron density away from the double bond making the backside more electron deficient and subsequently a stronger electrophile for the nucleophilic ozone. This is supported by the NBO results which show that electron density from the π system is indeed being transferred to the water molecule.

5.4 Conclusions

The rotational spectrum of α-pinene-water was recorded using a 2-6 GHz CP-FTMW spectrometer. From the theoretical results two possible structures were identified based on the position of the water molecule relative to the π-bond. Two hydrates were experimentally assigned. Dihedral energy scans show shallow minima with low barriers implying that the water molecule can rotate fairly freely about the O-H---π bond. The water tunneling pathway was associated to a wagging and rocking motion of the water molecule. NCI and QTAIM analyses were carried out for both complexes and it was shown two hydrogen bonds are observed between water and α-pinene, indicated by BCPs. Using classic transition state theory it was also shown that water lowers the activation energy, and subsequently increases the bimolecular rate constant, for α-pinene ozonolysis. This study not only provides a more detailed structural study of the α-pinene-water, but also insights into the unique intermolecular interactions present.

5.5 References

1 A. Guenther, C. N. Hewitt, D. Erickson, R. Fall, C. Geron, T. Graedel, P. Harley, L. Klinger, M. Lerdau and W. A. McKay, *J. Geophys. Res. Atmospheres*, 1995, **100**, 8873–8892.

2 J. H. Seinfeld and J. F. Pankow, *Annu. Rev. Phys. Chem.*, 2003, **54**, 121–140.

3 S. Koch, R. Winterhalter, E. Uherek, A. Kolloff, P. Neeb and G. K. Moortgat, *Atmos. Environ.*, 2000, **34**, 4031–4042.

4 B. Bonn and G. K. Moortgat, *Atmospheric Chem. Phys. Discuss.*, 2002, **2**, 469–506.

5 J. Poštulka, P. Slavíček, A. Domaracka, A. Pysanenko, M. Fárník and J. Kočišek, *Phys. Chem. Chem. Phys.*, 2019, **21**, 13925–13933.

6 S. J. Grabowski, *Annu. Rep. Sect. CPhysical Chem.*, 2006, **102**, 131–165.

7 J. Rezac, *J. Chem. Theory Comput.*, 2017, **13**, 4804–4817.

8 Y. Zhao and D. G. Truhlar, *J. Phys. Chem. C*, 2008, **112**, 6860–6868.

9 J. Contreras-García, E. R. Johnson, S. Keinan, R. Chaudret, J.-P. Piquemal, D. N. Beratan and W. Yang, *J. Chem. Theory Comput.*, 2011, **7**, 625–632.

10 R. F. W. Bader, *Chem. Rev.*, 1991, **91**, 893–928.

11 K. E. Laidig and R. F. Bader, *J. Chem. Phys.*, 1990, **93**, 7213–7224.

12 G. G. Brown, B. C. Dian, K. O. Douglass, S. M. Geyer, S. T. Shipman and B. H. Pate, *Rev. Sci. Instrum.*, 2008, **79**, 053103.

13 N. A. Seifert, J. Thomas, W. Jäger and Y. Xu, *Phys. Chem. Chem. Phys.*, 2018, **20**, 27630–27637.

14 M. J. Frisch, G. W. Trucks, H. B. Schlegel, G. E. Scuseria, M. A. Robb, J. R. Cheeseman, G. Scalmani, V. Barone, G. A. Petersson, H. Nakatsuji, X. Li, M. Caricato, A. V. Marenich, J. Bloino, B. G. Janesko, R. Gomperts, B. Mennucci, H. P. Hratchian, J. V. Ortiz, A. F. Izmaylov, J. L. Sonnenberg, D. Williams-Young, F. Ding, F. Lipparini, F. Egidi, J. Goings, B. Peng, A. Petrone, T. Henderson, D. Ranasinghe, V. G. Zakrzewski, J. Gao, N. Rega, G. Zheng, W. Liang, M. Hada, M. Ehara, K. Toyota, R. Fukuda, J. Hasegawa, M. Ishida, T. Nakajima, Y. Honda, O. Kitao, H. Nakai, T. Vreven, K. Throssell, J. A. Montgomery Jr., J. E. Peralta, F. Ogliaro, M. J. Bearpark, J. J. Heyd, E. N. Brothers, K. N. Kudin, V. N. Staroverov, T. A. Keith, R. Kobayashi, J. Normand, K. Raghavachari, A. P. Rendell, J. C. Burant, S. S. Iyengar, J. Tomasi, M. Cossi, J. M. Millam, M. Klene, C. Adamo, R. Cammi, J. W. Ochterski, R. L. Martin, K. Morokuma, O. Farkas, J. B. Foresman and D. J. Fox, Gaussian 16, Gaussian Inc., Wallingford, CT, 2016.

15 W. Kohn and L. J. Sham, *Phys. Rev.*, 1965, **140**, A1133.

16 S. Grimme, S. Ehrlich and L. Goerigk, *J. Comput. Chem.*, 2011, **32**, 1456–1465.

17 A. D. Becke, *J. Chem. Phys.*, 1992, **96**, 2155–2160.

18 A. D. Becke and E. R. Johnson, *J. Chem. Phys.*, 2005, **123**, 154101.

19 F. Weigend and R. Ahlrichs, *Phys. Chem. Chem. Phys.*, 2005, **7**, 3297–3305.

20 T. Lu and F. Chen, *J. Comput. Chem.*, 2012, **33**, 580–592.

21 W. Humphrey, A. Dalke and K. Schulten, *J. Mol. Graph.*, 1996, **14**, 33–38.

22 S. Grimme, C. Bannwarth and P. Shushkov, *J. Chem. Theory Comput.*, 2017, **13**, 1989–2009.

23 C. Bannwarth, S. Ehlert and S. Grimme, *J. Chem. Theory Comput.*, 2019, **15**, 1652–1671.

24 T. Clark, J. Chandrasekhar, G. W. Spitznagel and P. V. R. Schleyer, *J. Comput. Chem.*, 1983, **4**, 294–301.

25 D. Feller, *J. Comput. Chem.*, 1996, **17**, 1571–1586.

26 R. Krishnan, J. S. Binkley, R. Seeger and J. A. Pople, *J. Chem. Phys.*, 1980, **72**, 650–654.

27 D. Rappoport and F. Furche, *J. Chem. Phys.*, 2010, **133**, 134105.

28 B. P. Pritchard, D. Altarawy, B. Didier, T. D. Gibson and T. L. Windus, *J. Chem. Inf. Model.*, 2019, **59**, 4814–4820.

29 E. Papajak, J. Zheng, X. Xu, H. R. Leverentz and D. G. Truhlar, *J. Chem. Theory Comput.*, 2011, **7**, 3027–3034.

30 J.-D. Chai and M. Head-Gordon, *Phys. Chem. Chem. Phys.*, 2008, **10**, 6615–6620.

31 L. Goerigk and S. Grimme, *J. Chem. Theory Comput.*, 2011, **7**, 291–309.

32 T. Tsuneda and K. Hirao, *Wiley Interdiscip. Rev. Comput. Mol. Sci.*, 2014, **4**, 375–390.

33 T. Sato, T. Tsuneda and K. Hirao, *J. Chem. Phys.*, 2007, **126**, 234114.

34 M. Biczysko, P. Panek, G. Scalmani, J. Bloino and V. Barone, *J. Chem. Theory Comput.*, 2010, **6**, 2115–2125.

35 W. Li, L. Spada, N. Tasinato, S. Rampino, L. Evangelisti, A. Gualandi, P. G. Cozzi, S. Melandri, V. Barone and C. Puzzarini, *Angew. Chem. Int. Ed.*, 2018, **57**, 13853–13857.

36 E. Penocchio, M. Piccardo and V. Barone, *J. Chem. Theory Comput.*, 2015, **11**, 4689–4707.

37 C. Puzzarini, J. Bloino, N. Tasinato and V. Barone, *Chem. Rev.*, 2019, **119**, 8131–8191.

38 V. Ásgeirsson and H. Jónsson, *Handb. Mater. Model. Methods Theory Model.*, 2020, 689–714.

39 F. Neese, *Wiley Interdiscip. Rev. Comput. Mol. Sci.*, 2012, **2**, 73–78.

40 V. Ásgeirsson, B. O. Birgisson, R. Bjornsson, U. Becker, F. Neese, C. Riplinger and H. Jónsson, *J. Chem. Theory Comput.*, 2021, **17**, 4929–4945.

41 T. A. Keith, AIMALL, TK Gristmill Software, Overland Park, KS, 2017.

42 E. F. Pettersen, T. D. Goddard, C. C. Huang, G. S. Couch, D. M. Greenblatt, E. C. Meng and T. E. Ferrin, *J. Comput. Chem.*, 2004, **25**, 1605–1612.

43 A. E. Reed and F. Weinhold, *J. Chem. Phys.*, 1983, **78**, 4066–4073.

44 E. D. Glendening, C. R. Landis and F. Weinhold, *J. Comput. Chem.*, 2013, **34**, 1429–1437.

45 E. D. Glendening and F. Weinhold, *J. Comput. Chem.*, 1998, **19**, 593–609.

46 E. D. Glendening and F. Weinhold, *J. Comput. Chem.*, 1998, **19**, 610–627.

47 E. D. Glendening, J. K. Badenhoop and F. Weinhold, *J. Comput. Chem.*, 1998, **19**, 628–646.

48 A. S. Hazrah, M. Al-Jabiri, R. Speelman and W. Jäger, *Phys. Chem. Chem. Phys.*, 2021, **23**, 15159–15168.

49 H. M. Pickett, *SPFIT/SPCAT package*, 2009.

50 B. Ouyang, T. G. Starkey and B. J. Howard, *J. Phys. Chem. A*, 2007, **111**, 6165–6175.

51 C. S. López, O. N. Faza, F. P. Cossío, D. M. York and A. R. De Lera, *Chem. Eur. J.*, 2005, **11**, 1734–1738.

52 J. Klein, H. Khartabil, J.-C. Boisson, J. Contreras-García, J.-P. Piquemal and E. Hénon, *J. Phys. Chem. A*, 2020, **124**, 1850–1860.

53 C. Lefebvre, G. Rubez, H. Khartabil, J.-C. Boisson, J. Contreras-García and E. Hénon, *Phys. Chem. Chem. Phys.*, 2017, **19**, 17928–17936.

54 C. Lefebvre, H. Khartabil, J.-C. Boisson, J. Contreras-García, J.-P. Piquemal and E. Hénon, *ChemPhysChem*, 2018, **19**, 724–735.

55 A. S. Hazrah, S. Nanayakkara, N. A. Seifert, E. Kraka and W. Jäger, *Phys. Chem. Chem. Phys.*, 2022, **24**, 3722–3732.

56 C. F. Matta, J. Hernández-Trujillo, T.-H. Tang and R. F. Bader, *Chem. Eur. J.*, 2003, **9**, 1940–1951.

57 C. F. Matta, in *Hydrogen Bonding—New Insights*, Springer, 2006, pp. 337–375.

58 P. L. A. Popelier, *J. Phys. Chem. A*, 1998, **102**, 1873–1878.

59 M. Mantina, A. C. Chamberlin, R. Valero, C. J. Cramer and D. G. Truhlar, *J. Phys. Chem. A*, 2009, **113**, 5806–5812.

60 EAS Weather Station | Earth and Atmospheric Sciences, https://www.ualberta.ca/earth-sciences/facilities/weather.html, (accessed 8 March 2022).

61 J. K. Messer, F. C. De Lucia and P. Helminger, *Int. J. Infrared Millim. Waves*, 1983, **4**, 505–539.

62 E. M. Neeman, J. R. Avilés Moreno and T. R. Huet, *J. Chem. Phys.*, 2017, **147**, 214305.

63 W. M. Organization, *Guide to Instruments and Methods of Observation*, WMO Geneva, 2018, vol. 1.

64 E. G. Schnitzler and W. Jäger, *Phys. Chem. Chem. Phys.*, 2014, **16**, 2305–2314.

65 E. G. Schnitzler, B. L. Zenchyzen and W. Jäger, *Phys. Chem. Chem. Phys.*, 2016, **18**, 448–457.

66 A. Zare, J. H. Christensen, A. Gross, P. Irannejad, M. Glasius and J. Brandt, *Atmospheric Chem. Phys.*, 2014, **14**, 2735–2756.

67 S. K. Boreddy, T. Mochizuki, K. Kawamura, S. Bikkina and M. M. Sarin, *Atmos. Environ.*, 2017, **167**, 170–180.

68 S. Hatakeyama, K. Izumi, T. Fukuyama and H. Akimoto, *J. Geophys. Res. Atmospheres*, 1989, **94**, 13013–13024.

69 Z. Zhao, W. Zhang, T. Alexander, X. Zhang, D. B. Martin and H. Zhang, *Environ. Sci. Technol.*, 2021, **55**, 6700–6709.

70 D. Zhang and R. Zhang, *J. Chem. Phys.*, 2005, **122**, 114308.

71 C. Peng and H. Bernhard Schlegel, *Isr. J. Chem.*, 1993, **33**, 449–454.

72 C. Peng, P. Y. Ayala, H. B. Schlegel and M. J. Frisch, *J. Comput. Chem.*, 1996, **17**, 49–56.

73 M. G. Evans and M. Polanyi, *Trans. Faraday Soc.*, 1935, **31**, 875–894.

74 H. Eyring, *J. Chem. Phys.*, 1935, **3**, 107–115.

75 K. J. Laidler and M. C. King, *J. Phys. Chem.*, 1983, **87**, 2657–2664.

76 R. Atkinson, A. M. Winer and J. N. Pitts Jr, *Atmospheric Environ. 1967*, 1982, **16**, 1017–1020.

77 J. Arey, R. Atkinson and S. M. Aschmann, *J. Geophys. Res. Atmospheres*, 1990, **95**, 18539–18546.

78 M. Witter, T. Berndt, O. Böge, F. Stratmann and J. Heintzenberg, *Int. J. Chem. Kinet.*, 2002, **34**, 394–403.

79 F. Nolting, W. Behnke and C. Zetzsch, *J. Atmospheric Chem.*, 1988, **6**, 47–59.

80 V. G. Khamaganov and R. A. Hites, *J. Phys. Chem. A*, 2001, **105**, 815–822.

6

A Rotational Spectroscopic and *Ab Initio* Study of *Cis*- and *Trans*-(-)-Carveol: Further Insights into Conformational Dynamics in Monoterpenes and Monoterpenoids

Contents

6.1. Introduction · · · · · 107
6.2. Methods · · · · · 110
6.2.1. Configuration and Conformer Nomenclature · · · · · 110
6.2.2. Theoretical Methods · · · · · 111
6.2.3. Experimental Methods · · · · · 114
6.3. Results and Discussion · · · · · 114
6.3.1. Theoretical Results · · · · · 114
6.3.2. Experimental Results and Conformational Cooling · · · · · 117
6.3.3. Spectroscopic Assignments · · · · · 120
6.3.4. Experimental Intensities and Relative Energy Ordering · · · · · 122
6.3.5. Axial Isopropenyl Conformation · · · · · 124
6.4. Conclusions · · · · · 126
6.5. References · · · · · 127

6.1. Introduction

Carveol, a primary constituent of spearmint and peppermint oil, is a monocyclic monoterpenoid alcohol that is produced in the atmosphere by the photooxidation of limonene, one of the most abundant biogenic volatile organic compounds.[1] In the atmosphere, limonene reacts with O_3, OH radical, and NO_X species, to produce lower volatility compounds such as carveol.[2,3] Carveol can in turn either further oxidize to form additional low volatility compounds,[4] or become involved in nucleation processes that lead to the formation of secondary organic aerosol,[5,6] which is known to have detrimental effects on both climate[7] and human health.[8] In addition, carveol is commonly used in the biological field as a chemoprevention agent[9] against breast cancer, and recently as a potential antidiabetic agent.[10] Carveol, a molecule containing two chiral centers, has three substituents (methyl, hydroxyl, and isopropenyl groups) attached to its cyclohexene ring, all of

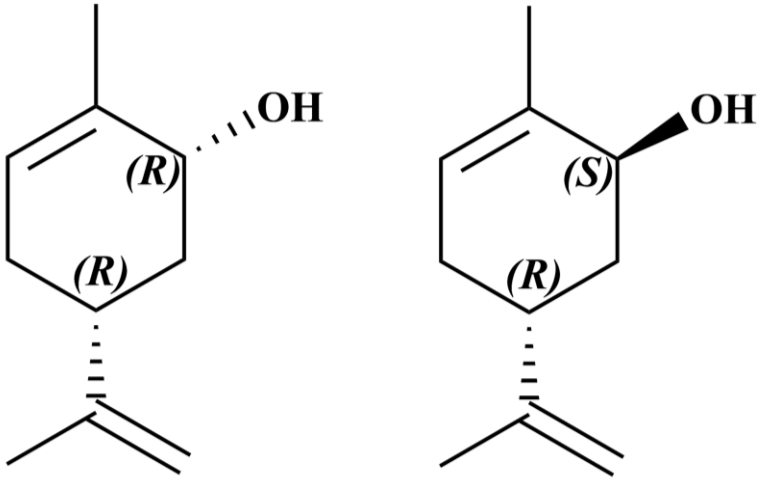

Figure 6.1. Left: *cis* conformer of (-)-carveol where both stereocenters are in the R configuration. Right: *trans* diastereomer of (-)-carveol where the hydroxyl stereocenter is in the S and the isopropenyl center in the R configuration.

which can rotate about the respective single bonds. The two chiral centers of carveol result in four unique stereoisomers. If the carbon bound to the isopropenyl group is in the R configuration it is known as (-)-carveol and can have two stereoisomers, *cis* (R) or *trans* (S), depending on the chirality of the carbon linked to the hydroxyl group. The two conformers are shown in Figure 1. If the carbon bound to the isopropenyl group is in the S configuration it is known as (+)-carveol, which can also have two stereoisomers, *cis* (R) and *trans* (S). In this work I focus on the *cis* and *trans* configurations of (-)-carveol. Compared to cyclohexane where both chair and boat conformations exist, the presence of the double bond makes the cyclohexene ring in (-)-carveol more rigid. This rigidity results in a half-chair form and a boat form with the latter 22.9 kJ/mol higher in energy for the cyclohexene monomer at the B3LYP-D3(BJ)/def2-TZVP level of theory. The hydroxyl and isopropenyl groups can adopt axial or equatorial positions. Additionally, the hydroxyl and isopropenyl groups can also rotate about their respective bonds to the ring carbon atoms resulting in three unique conformers: antiperiplanar, gauche -, and gauche + (see Figure 6.2). The combination of the two chiral centers, ring conformers, and rotatable substituents introduces a complex conformational landscape that is quite difficult to elucidate experimentally.

Conformational landscapes of limonene and limonene derivatives have been explored extensively using Fourier transform microwave (FTMW) spectroscopic techniques. In a 2009 FTMW perillaldehyde study,[11] a ketone substituted analogue to limonene with a rotatable isopropenyl group, three stable low-energy conformers were predicted, all of them with an

equatorial position of the isopropenyl group and separated by roughly 1.0-1.5 kJ mol^{-1}. Of the three, the two lowest energy structures were experimentally assigned while the third structure was suspected of conformationally cooling out to the second one. Similarly, a 2013 study[12] of both limonene and carvone (limonene with a keto group directly on the cyclohexene ring) resulted in two conformers observed experimentally for each molecule, all with the isopropenyl group in the equatorial position. In a limonene oxide broadband FTMW study[13] several conformers with the isopropenyl group in the equatorial position were experimentally assigned, but in addition a conformer with the isopropenyl in the axial position was identified theoretically and assigned experimentally. In a 2019 study[14] examining the conformational landscape of perillyl alcohol, Grimme's new conformational searching algorithm CREST[15] was utilized to explore the conformational space more thoroughly. In their study, Xu and coworkers identified 54 theoretical conformers and assigned eight experimental conformers (six with isopropenyl in the equatorial position, and two with isopropenyl in the axial position). Similar to the previous studies, the axial isopropenyl conformer is several kJ mol^{-1} higher in energy than its equatorial position counterpart, which is also reflected in the experimental spectrum. In a 2019 rotational spectroscopic and theoretical study[16] of limonene, carvone, and perillaldehyde, additional conformers with the isopropenyl in the equatorial and axial positions were identified. There, it was shown that intramolecular dispersion interactions aid in the stabilization of the isopropenyl in the axial position. In the long line of exploring conformational landscapes of limonene/limonene derivatives using FTMW spectroscopy, carveol presents added conformational complexity and provides thus further challenges in understanding intramolecular conformational dynamics. It not only contains two chiral centers, but also the close proximity of the hydroxyl and the isopropenyl groups may lead to interesting conformational preferences. Chirped-pulse (CP) Fourier transform microwave spectroscopy is an excellent tool for this investigation, as the resulting rotational spectra are highly sensitive to the slightest structural differences between conformers.

In this report, several *cis* and *trans* (-)-carveol conformers were identified using a conformational searching algorithm as well as a two-dimensional potential energy scan over two dihedral angles. The theoretical results for *cis* (-)-carveol show a unique preference for the isopropenyl unit in the axial position, to the extent that it becomes the global minimum, something that has not been observed before in related systems. Interconversion barriers were calculated to determine cooling pathways for each conformer. The cooling pathways and theoretical results were

then used as an aid to assign the dense CP-FTMW spectrum. A total of five conformers was assigned, four of them with the isopropenyl group in the equatorial position and one with isopropenyl in the axial position. From the theoretical and experimental results, it was determined that most of the *cis* conformers cool out to three conformers, while the majority of *trans* conformers cools to only two. In addition, the non-covalent interactions present within each conformer were investigated using Quantum Theory of Atoms-in-Molecules (QTAIM)[17] and Non-Covalent Interactions (NCI)[18] analyses. With this study we hope to provide valuable benchmarking data for the further development of theory, and provide new insights into the growing field of conformational dynamics.

6.2. Methods

6.2.1. Configuration and Conformer Nomenclature

The structural variability found in (-)-carveol results in a range of different configurations and conformers. However, explicitly describing each one with their long form is tedious and here a nomenclature that allows for quick and unambiguous identification of each configuration and conformer is identified. There are two stereoisomers of (-)-carveol, one with the hydroxyl group in the R configuration (*cis*) and the other with the hydroxyl group in the S configuration (*trans*). The cyclohexene ring exists in two conformers, a boat conformer and half-chair conformer, which will be referred to as (B) and (C), respectively. We define the substituent positions in the boat form analogous to the case of cyclohexane: the upwards pointing "flagpole" hydrogens, at the bow and

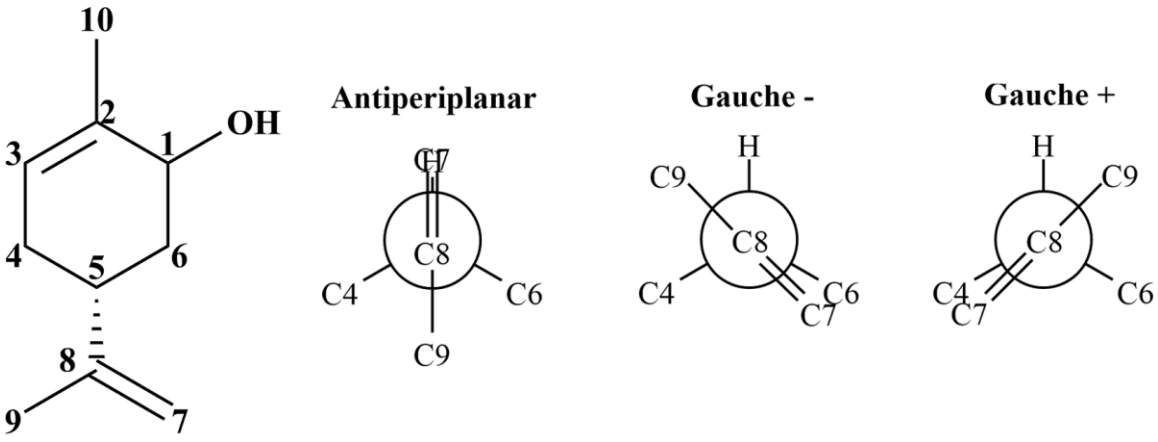

Figure 6.2. Carbon atom numbering of (-)-carveol. The Newman projections of the antiperiplanar, gauche -, and gauche + conformations of the isopropenyl group are also displayed. The same naming scheme applies to the hydroxyl conformations.

stern of the boat, are axial, as are hydrogens on the other two singly bound carbons (C-C eclipsed bond), which point downwards. In the half-chair conformer the axial hydrogens point alternately upwards and downwards. See Figure D.1 for the axial substituent definitions for the boat and half-chair conformers. Next on the structural hierarchy are the positions of the hydroxyl and isopropenyl group, which can be either axial (Ax) or equatorial (E). Finally, free rotation of the hydroxyl group and isopropenyl group about their respective bonds to cyclohexene results in three unique conformers, antiperiplanar (A), gauche – (G-), and gauche + (G+). Each configuration/conformer will be referred to using a (V)WXYZ nomenclature, where (V) can either be (B) or (C), W can be Ax_I or E_I for the isopropenyl group, X can be Ax_H or E_H for the hydroxyl group, Y can be A, G-, or G+ for the isopropenyl group, and Z can be A, G-, or G+ for the hydroxyl group. For example, an isomer with a *cis*-(C)Ax_IE_HAG+ specification will have both the hydroxyl and isopropenyl chiral centres in the R configuration, the cyclohexene in the half-chair conformer, the isopropenyl in the axial position, the hydroxyl in the equatorial position, the isopropenyl in the antiperiplanar conformer, and the hydroxyl group in the gauche + conformer. If not required, the Y and Z labels will be omitted.

6.2.2. Theoretical Methods

In order to assist with spectroscopic assignments Grimme's semi-empirical Conformer–Rotamer Ensemble Sampling Tool (CREST)[15] was utilized at the GFN2-xTB[19–21] level of theory to identify potential conformers of *trans* and *cis* (-)-carveol. The conformational searching algorithm within the CREST program makes it an excellent tool to study flexible molecules, such as carveol. To further refine our conformational search, geometry optimizations and harmonic frequency calculations were performed on the structures obtained from CREST using both the Gaussian 16 program[22] suite and MOLPRO (version 2015.1)[23] at the B3LYP-D3(BJ)[24,25]/def2-TZVP[26,27] and density fitted (df)[28] MP2[29]/aug-cc-pVTZ[30] levels of theory, respectively. The df-MP2 results were used to supplement and confirm the relative energies from the DFT calculations as it has been shown to predict relative conformer energies well.[31] For a comparison to the CREST results and identification of transition states/barrier heights, relaxed two-dimensional dihedral potential energy scans were carried out for *trans* and *cis* (-)-carveol by rotating the isopropenyl and hydroxyl groups in 12˚ increments. Analyses of the molecular electron density distribution based on QTAIM,[17] including NCI analyses,[18] were done using the AIMA11[32] and MultiWfn[33] programs.

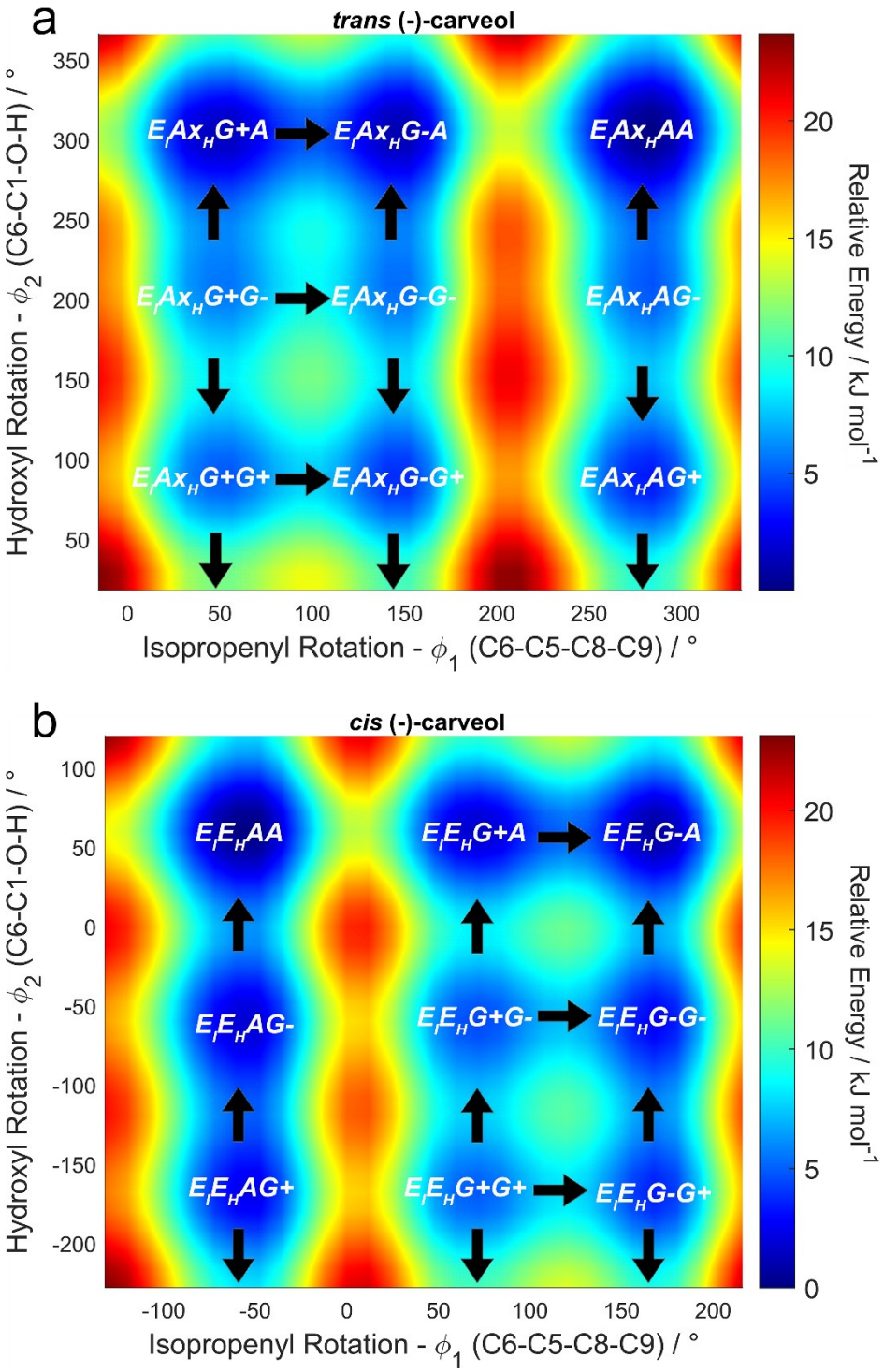

Figure 6.3. Graphical representation of a two-dimensional potential energy scan of the half-chair conformation of *trans* (a) and *cis* (b) (-)-carveol along the isopropenyl dihedral angle, φ_1, and the hydroxyl dihedral angle, φ_2. The white labels in the potential energy wells correspond to the theoretical conformers in Table 6.1. For atom numbering refer to Figure 6.2. The dihedral angles shown represent one full rotation (360°) about the respective single bonds. The black arrows are the directions of conformational cooling based on an empirical ~5 kJ mol^{-1} threshold.[38]

Table 6.1. Theoretical results for *trans* and *cis* (-)-carveol conformers obtained from the 2D PES scan and CREST searches

***trans* (-)-carveol**								
(V)W_IX_HYZ[a]	**ΔE_0 / kJ mol^{-1} df-MP2**	**ΔE_0 / kJ mol^{-1} B3LYP**	**A / MHz[d]**	**B / MHz[d]**	**C / MHz[d]**	**μ_a / D[d]**	**μ_b / D[d]**	**μ_c / D[d]**
(C)E_IAx_HAA[b]	**0.0**	**0.0**	**2134.81**	**663.21**	**597.58**	**0.5**	**1.6**	**0.1**
(C)E_IAx_HG-A[c]	**0.8**	**1.0**	**2145.20**	**665.47**	**584.85**	**-0.5**	**-1.7**	**0.0**
(C)E_IAx_HG+A	1.0	1.3	2122.44	697.78	570.25	0.3	1.1	0.4
(C)E_IAx_HAG+	1.6	2.9	2136.89	666.86	598.25	0.3	0.1	1.6
(C)E_IAx_HG-G+	1.9	3.3	2143.46	668.36	587.64	0.2	0.4	0.7
(C)E_IAx_HAG-	2.8	3.9	2129.35	668.19	600.10	1.3	1.2	0.7
(C)E_IAx_HG+G+[c]	3.2	4.3	2120.71	701.17	571.90	-0.2	0.7	1.1
(C)E_IAx_HG-G-	3.2	4.5	2137.99	669.85	588.75	1.3	1.2	0.3
(C)E_IAx_HG+G-	3.7	4.6	2116.63	703.47	572.92	1.4	0.6	0.2
(C)Ax_IE_HG+A	2.9	6.1	1627.21	843.77	725.21	0.6	0.7	1.3
(C)Ax_IE_HG+G+	4.1	8.1	1657.93	834.27	717.12	1.5	0.8	0.1
(C)Ax_IE_HG+G-	4.6	8.2	1638.70	841.88	720.61	0.2	0.5	0.8
***cis* (-)-carveol**								
(V)W_IX_HYZ[a]	**ΔE_0 / kJ mol^{-1} df-MP2**	**ΔE_0 / kJ mol^{-1} B3LYP**	**A / MHz[d]**	**B / MHz[d]**	**C / MHz[d]**	**μ_a / D[d]**	**μ_b / D[d]**	**μ_c / D[d]**
(C)Ax_IAx_HG+A[b]	**0.0**	**0.0**	**1689.73**	**902.97**	**802.91**	**0.7**	**1.5**	**0.6**
(C)E_IE_HAA[b]	**6.8**	**4.3**	**2130.68**	**647.17**	**568.57**	**0.7**	**0.9**	**1.1**
(C)E_IE_HG-A[b]	**7.5**	**5.1**	**2161.15**	**662.04**	**541.75**	**0.8**	**1.3**	**0.6**
(C)E_IE_HAG-	7.1	5.8	2148.98	646.6	568.35	0.9	0.5	0.5
(C)E_IE_HG+A[c]	8.7	6.0	2103.62	661.45	552.70	0.6	-0.9	-0.2
(C)E_IE_HAG+	8.4	6.4	2134.10	650.22	569.49	0.8	0.9	0.6
(C)E_IE_HG-G-	8.0	6.7	2182.58	660.73	541.74	1.1	0.0	1.1
(C)E_IE_HG-G+	9.5	7.6	2165.73	664.22	542.67	0.5	1.4	1.2
(C)E_IE_HG+G-[c]	10.0	8.4	2123.10	661.23	551.51	1.0	0.8	1.0
(C)E_IE_HG+G+	11.1	9.0	2108.52	665.09	551.98	0.7	0.4	1.5

[a]Nomenclature describing the conformer of each conformer. The letter in parentheses describes whether the conformer is in the half-chair (C) or boat (B) conformer. The following *WXYZ* letters describe the axial or equatorial position of the isopropenyl group, the axial or equatorial position of the hydroxyl group, the conformer of the isopropenyl group (A or G- or G+), and the conformer of the hydroxyl group (A or G- or G+), respectively. A, G-, and G+ are antiperiplanar, gauche -, and gauche + conformers, respectively. [b]Conformers highlighted in bold were experimentally identified. [c]Conformers identified from the 2D PES scan. [d]The rotational constants and dipole moment components reported were calculated at the B3LYP-D3(BJ)/def2-TZVP level of theory.

To investigate the conformational interconversion barriers the Synchronous Transit Quasi-Newton (STQN) method of Schlegel and coworkers[34,35] was used to locate transition state structures and to determine their zero-point energies, at the B3LYP-D3(BJ)/def2-TZVP level of theory. The STQN method was requested by the QST3 keyword in Gaussian, which requires three molecular specifications: reactants, products, and a candidate transition state. The geometries of all three of these molecular specifications were obtained from the 2D potential energy scan. Once located, additional harmonic frequency calculations were performed to determine the zero-point corrected transition state energies. The zero-point energy of each transition state was then compared to the zero-point energies of reactant (conformer x) and product (conformer y) to determine the interconversion barrier height (conformer x → conformer y).

6.2.3. Experimental Methods

A sample of (-)-carveol, containing a mixture of *cis* and *trans* stereoisomers, was purchased from Millipore-Sigma. The carveol sample was placed in a heatable sample reservoir, within a special attachment to a General Valve, Series 9, nozzle, which was used to produce a molecular expansion. To generate the necessary vapour pressure to introduce a sufficient amount of carveol sample into the gas phase, the attachment was heated to 80˚C. Helium was used as a carrier gas at approximately 40 psi. The rotational spectrum of carveol was recorded using a CP-FTMW spectrometer, in the frequency range between the 2 and 6 GHz. Our instrument operates analogously to the spectrometer designed by the Pate group,[36] with some variances in component specifications.[37] Per molecular pulse, 12 free induction decays (FIDs) were recorded and 2.4 million FIDs were averaged and then Fourier transformed to the get the broadband rotational spectrum of (-)-carveol. The large number of acquisitions was necessary for the potential detection of higher energy conformers.

6.3. Results and Discussion

6.3.1. Theoretical Results

From the CREST results 21 unique conformers for *trans* (-)-carveol were identified, of which 15 are in the half-chair and the remaining six in the boat conformer. Among the 15 half-chair conformers, seven have isopropenyl in the equatorial position and hydroxyl in the axial position, i.e. *trans*-(C)E_IAx_H, and eight have isopropenyl in the axial position with the hydroxyl in the

equatorial position, i.e. *trans*-(C)Ax_IE_H. Of the six boat conformers, four have both isopropenyl and hydroxyl in the equatorial position, i.e. *trans*-(B)E_IE_H, and two have both substituents in the axial position, i.e. *trans*-(B)Ax_IAx_H. The 2D potential energy scan (Figure 6.3a) reveals two additional *trans*-(C)E_IAx_H conformers, one of which corresponds to an experimentally assigned conformer. Unsurprisingly, the lower energy conformers all have a *trans*-(C)E_IAx_H conformer. A summary of the relative zero-point energies, conformers, rotational constants, and dipole moment components for the theoretically identified conformers of *trans* (-)-carveol with relative energies below 10 kJ mol^{-1} is shown in Table 6.1**.** See Table D.1 of Appendix D for a listing of all 23 conformers**.**

17 unique conformers for *cis* (-)-carveol were identified with CREST, 12 in the half-chair and five in the boat conformer. Of the half-chair conformers seven have the isopropenyl and hydroxyl group in the *cis*-(C)E_IE_H, and five in the *cis*-(C)Ax_IAx_H conformer. For the boat conformers, four are in the *cis*-(B)Ax_IE_H, and one in the *cis*-(B)E_IAx_H conformer. Similar to the *trans* case, two additional conformers were found in the 2D potential energy scan for *cis* (-)-carveol (Figure 6.3b). Somewhat surprisingly, the global minimum structure for *cis* (-)-carveol occupies the *cis*-(C)Ax_IAx_H conformer, which has not been observed before in analogous limonene derivatives.[11,12,14,16] Excluding the global minimum structure, the lowest nine conformers follow the same pattern as in *trans* (-)-carveol: (C) with isopropenyl in the E position. A summary of the relative zero-point energies, conformers, rotational constants, and dipole moment components for conformers below 10 kJ mol^{-1} for *cis* (-)-carveol is given in Table 6.1. The data for all 19 conformers are shown in Table D.2 of the ESI.

Comparing the results of the *cis* and *trans* conformers a pattern emerges. For *trans*, when cyclohexene is in the (C) conformer the hydroxyl group and isopropenyl group can only occupy positions opposite to each other, *trans*-(C)Ax_IE_H or *trans*-(C)E_IAx_H, while for the (B) conformer the two groups can only occupy the same position, *trans*-(B)Ax_IAx_H or *trans*-(B)E_IE_H. In the *cis* case the opposite is observed. This asymmetry is a direct consequence of the two different chiral configurations of (-)-carveol. For the nine *cis*-(C)E_IE_H and nine *trans*-(C)E_IAx_H conformers found for both *cis* and *trans* (-)-carveol, respectively, transitions states were identified using the STQN method to calculate barrier heights to neighbouring conformers, and ultimately assess whether the conformer would be conformationally cooled out or relax to a lower

Table 6.2. Relative zero-point corrected barrier heights for converting from conformer X to conformer Y of *trans* and *cis* (-)-carveol, calculated at the B3LYP-D3(BJ)/def2-TZVP level of theory.

***Trans* Half-chair – Equatorial – Isopropenyl**					
G+[a] (X)	**A[b] (Y)**	**ΔE_0[d] / kJ mol^{-1} (X→Y)**	**G-[c] (X)**	**A (Y)**	**ΔE_0 / kJ mol^{-1} (X→Y)**
E_IAx_HG+A	E_IAx_HAA	11.7	E_IAx_HG-A	E_IAx_HAA	12.8
E_IAx_HG+G+	E_IAx_HAG-	12.1	E_IAx_HG-G+	E_IAx_HAG-	13.5
E_IAx_HG+G-	E_IAx_HAG+	12.1	E_IAx_HG-G-	E_IAx_HAG+	13.2
G+ (X)	**G- (Y)**	**ΔE_0 / kJ mol^{-1} (X→Y)**			
E_IAx_HG+A	E_IAx_HG-A	3.0			
E_IAx_HG+G+	E_IAx_HG-G+	2.4			
E_IAx_HG+G-	E_IAx_HG-G-	2.1			
***Trans* Half-chair – Axial – Hydroxyl**					
G+[a] (X)	**A[b] (Y)**	**ΔE_0[d] / kJ mol^{-1} (X→Y)**	**G-[c] (X)**	**A (Y)**	**ΔE_0 / kJ mol^{-1} (X→Y)**
E_IAx_HAG+	E_IAx_HAA	2.9	E_IAx_HAG-	E_IAx_HAA	1.9
E_IAx_HG-G+	E_IAx_HG-A	2.9	E_IAx_HG-G-	E_IAx_HG-A	4.3
E_IAx_HG+G+	E_IAx_HG+A	-0.1	E_IAx_HG+G-	E_IAx_HG+A	6.3
G+ (X)	**G- (Y)**	**ΔE_0 / kJ mol^{-1} (X→Y)**			
E_IAx_HAG+	E_IAx_HAG-	4.0			
E_IAx_HG-G+	E_IAx_HG-G-	4.4			
E_IAx_HG+G+	E_IAx_HG+G-	5.3			
***Cis* Half-chair – Equatorial – Isopropenyl**					
G+[a] (X)	**A[b] (Y)**	**ΔE_0[d] / kJ mol^{-1} (X→Y)**	**G-[c] (X)**	**A (Y)**	**ΔE_0 / kJ mol^{-1} (X→Y)**
E_IE_HG+A	E_IE_HAA	11.6	E_IE_HG-A	E_IE_HAA	13.6
E_IE_HG+G-	E_IE_HAG+	11.1	E_IE_HG-G-	E_IE_HAG+	13.8
E_IE_HG+G+	E_IE_HAG-	10.8	E_IE_HG-G+	E_IE_HAG-	13.9
G+ (X)	**G- (Y)**	**ΔE_0 / kJ mol^{-1} (X→Y)**			
E_IE_HG+A	E_IE_HG-A	3.0			

E_IE_HG+G-	E_IE_HG-G-	4.7
E_IE_HG+G+	E_IE_HG-G+	2.7

***Cis* Half-chair – Equatorial – Hydroxyl**					
G+[a] (X)	**A[b] (Y)**	**ΔE_0[d] / kJ mol^{-1} (X→Y)**	**G-[c] (X)**	**A (Y)**	**ΔE_0 / kJ mol^{-1} (X→Y)**
E_IE_HAG+	E_IE_HAA	2.1	E_IE_HAG-	E_IE_HAA	5.1
E_IE_HG-G+	E_IE_HG-A	1.2	E_IE_HG-G-	E_IE_HG-A	5.4
E_IE_HG+G+	E_IE_HG+A	2.1	E_IE_HG+G-	E_IE_HG+A	4.5

G+ (X)	**G- (Y)**	**ΔE_0 / kJ mol^{-1} (X→Y)**
E_IE_HAG+	E_IE_HAG-	4.3
E_IE_HG-G+	E_IE_HG-G-	1.2
E_IE_HG+G+	E_IE_HG+G-	4.1

[a]Gauche +, [b]antiperiplanar, and [c]gauche - conformers. [d]The barrier height was calculated by subtracting the zero-point corrected energy for conformer X from the transition state energy.

energy one in the molecular beam expansion. The calculated barrier heights for *cis* (-)-carveol and *trans* (-)-carveol are presented in Table 6.2.

Note that the barrier to methyl internal rotation is too high (~ 7.6 kJ mol^{-1} for the C10 methyl group and ~ 7.3 kJ mol^{-1} for the C9 methyl group, at the B3LYP-D3(BJ)/def2-TZVP level) to produce an observable splitting of rotational transitions.

NCI and QTAIM analyses were completed to examine the non-covalent interactions present within each conformer, and to find a justification for the unique preference for the *cis*-(C)Ax_IAx_H conformer of *cis* (-)-carveol. NCI and QTAIM results for the five experimentally assigned conformers are presented in Figure 6.5 and Figure D.2 of the ESI, respectively.

6.3.2. Experimental Results and Conformational Cooling

The recorded broadband rotational spectrum of (-)-carveol is shown in Figure 6.4. A total of 32 conformers were identified from the theoretical results. However, attempting to assign this many conformers in a dense broadband spectrum is a daunting task. The heights of the conformational conversion barriers in Table 6.2 were used to aid in the experimental assignments. Ruoff *et al.*[38] found that the upper barrier that permits relaxation to a lower energy conformer in a molecular expansion is about 5 kJ mol^{-1}. Higher energy conformers with a lower barrier would therefore relax to more stable forms and be absent from the experimental spectrum if the energy difference is

sufficiently high. Based on this assumption, relative zero-point energies, and the energetic uncertainties in DFT calculations,[39] We filtered out conformers that should be observable for *cis* (-)-carveol. It was found that only the lowest energy *cis*-(C)Ax_IAx_H conformer should be present in the experiment as the other *cis*-(C)Ax_IAx_H conformers are too high in energy. The barrier height converting the *cis*-(C)E_IE_H form to *cis*-(C)Ax_IAx_H is 31.3 kJ mol^{-1} (B3LYP-D3(BJ)/def2-TZVP level), and therefore *cis*-(C)E_IE_H conformers are expected to be observable in experiment. The conformers with the isopropenyl in the equatorial position relax to conformers *cis*-(C)E_IE_HAA and *cis*-(C)E_IE_HG-A. The proposed cooling pathways are presented in Figure 6.3a where the black arrows indicate the direction of the cooling paths and the lack of an arrow between conformers indicates that the barrier is sufficiently high so that no relaxation occurs. In contrast to *cis* (-)-carveol, no conformers with the isopropenyl in the axial position should be experimentally present

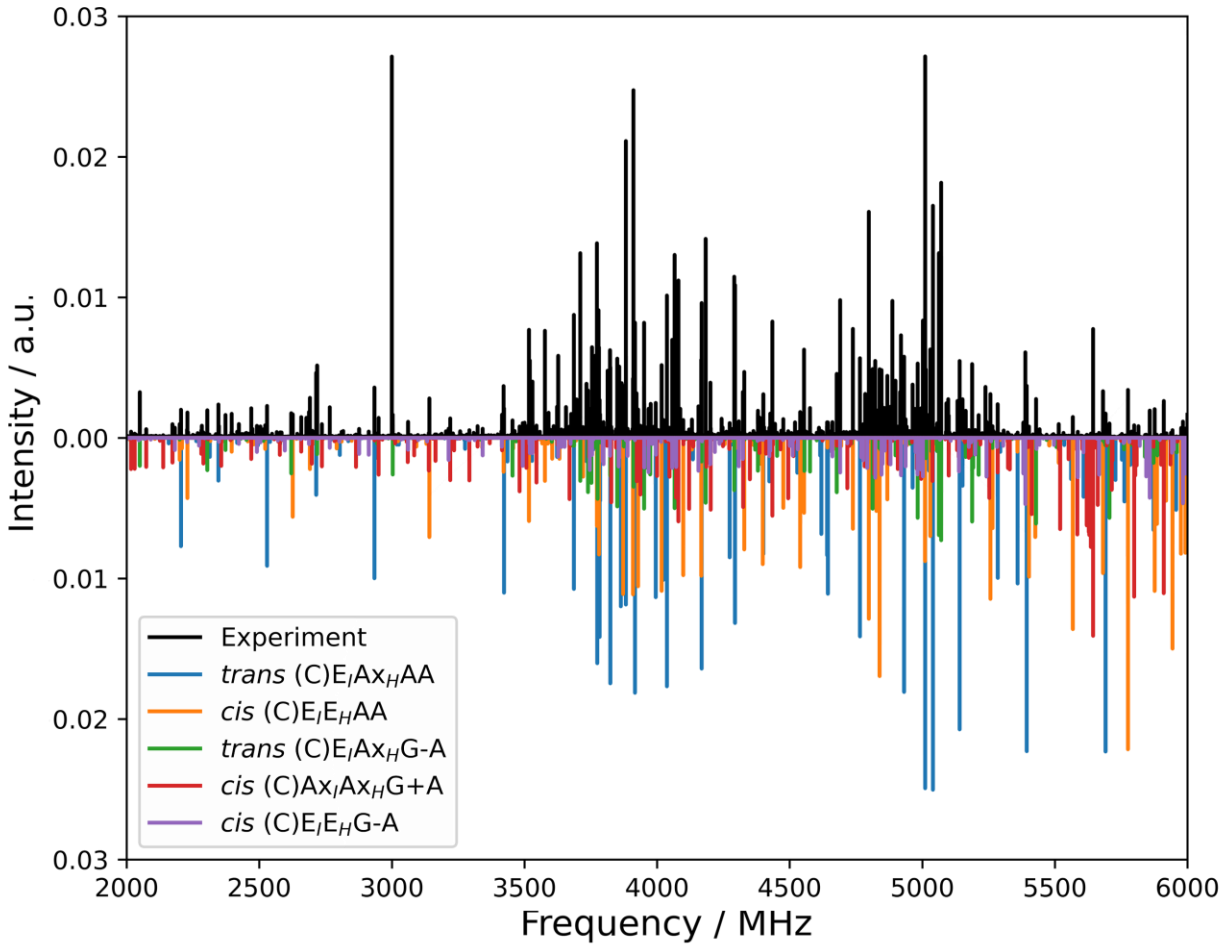

Figure 6.4. Broadband rotational spectrum of *cis* and *trans* (-)-carveol. The experimental spectrum is shown in black, while the simulated spectra of the five experimentally assigned conformers are coloured.

Table 6.3. Spectroscopic parameters for the five experimentally assigned conformers of (-)-carveol

	Conformer E1	**Conformer E2**	**Conformer E3**
A / MHz	2130.99910(81)	2150.22733(47)	2122.02820(73)
B / MHz	665.16017(26)	660.47853(13)	662.63495(17)
C / MHz	583.88177(25)	541.08651(15)	596.35973(18)
Δ_J / kHz	0.0166(26)	---[d]	0.0115(15)
Δ_{JK} / kHz	0.106(17)	---[d]	0.091(14)
Δ_K / kHz	---[d]	---[d]	0.365(12)
δ_J / kHz	---[d]	0.00282(22)	0.00155(35)
δ_K / kHz	0.165(28)	0.109(29)	-0.255(24)
[a]N	50	67	66
[b]σ / kHz	4.2	5.8	5.2
[c]|μ|	b>a	b>a>c	b>a>>c
	Conformer E4	**Conformer E5**	
A / MHz	1664.60349(57)	2120.28916(69)	
B / MHz	907.27707(25)	645.66680(28)	
C / MHz	805.36654(24)	567.21505(28)	
Δ_J / kHz	0.1019(31)	0.0101(41)	
Δ_{JK} / kHz	-0.3131(87)	0.119(41)	
Δ_K / kHz	0.8093(40)	---[d]	
δ_J / kHz	0.00669(18)	---[d]	
δ_K / kHz	---[d]	-0.357(38)	
[a]N	73	81	
[b]σ / kHz	7.0	6.6	
[c]|μ|	b>a>c	c ≃b≃a	

[a]Number of lines used in the fit. [b]Root mean square error of the fit. [c]Relative dipole moment components, estimated from signal strengths. [d]Values fixed to zero in fit.

for *trans* (-)-carveol because of their relatively high energies. This contrast will be discussed in greater detail later. Analogous to *cis* (-)-carveol, two equatorial isopropenyl candidate structures for *trans* (-)-carveol were identified, *trans*-(C)$E_I Ax_H$AA and *trans*-(C)$E_I Ax_H$G-A, as most of the conversion barriers are easily surmountable in the molecular beam expansion. The proposed cooling pathways are presented in Figure 6.3b. We note here that we also recorded a spectrum using neon as carrier gas in our search for hydrates of carveol. Neon is a more effective relaxant than helium, but I could identify in the spectrum the same five conformers as with the helium expansion. Our analysis matches the experimental results well as a total of five conformers could

be experimentally assigned. Their rotational constants, dipole moment components, and other spectroscopic parameters are summarized in Table 6.3. The transition frequencies with their associated quantum number assignments are given in Tables S5 to S9 of the ESI. With the arguments discussed above in mind, it was determined that of the five conformers, three are *cis* (-)-carveol (two *cis*-(C)E_IE_H and one *cis*-(C)Ax_IAx_H), and two are *trans* (-)-carveol (both *trans*-(C)E_IAx_H). In addition to the five carveol assignments, two conformers of carvone were also detected, which have been reported in a previous study.[11] We assume that carvone was used in the synthesis process as a precursor to carveol. The detection of two carvone conformers in a sample with >95% carveol purity demonstrates the power of CP-FTMW, where in a complex mixture, chemical species can be easily and unambiguously identified.

For both *cis*- and *trans*- (-)-carveol a clear preference is observed for the conformers of the isopropenyl and hydroxyl groups. In all five conformers the hydroxyl group is in the antiperiplanar conformer, pointing toward the centre of the ring, thereby minimizing repulsion from any of the neighbouring hydrogens. Two conformers are preferred for the isopropenyl group, the antiperiplanar conformer and the gauche - conformer, where the antiperiplanar conformer is energetically favoured over the gauche - conformer. The carbon atom numbering and a Newman projection for each conformer is presented in Figure 6.2. For *cis*(*trans*) (-)-carveol, the isopropenyl and hydroxyl groups both assume the antiperiplanar conformer in conformers *cis*-(C)E_IE_HAA and *trans*-(C)E_IAx_HAA, and the gauche - conformer (isopropenyl) and antiperiplanar (hydroxyl) conformer in conformers *cis*-(C)E_IE_HG-A and *trans*-(C)E_IAx_HG-A.

6.3.3. Spectroscopic Assignments

The spectroscopic parameters for the five experimentally assigned conformers (labelled E1 through E5) are presented in Table 6.3. The relatively small differences in theoretical rotational constants of different conformers made attributing experimental assignments to theory quite difficult. For example, the RMS error in rotational constants between experimentally observed conformer E1 and the five lowest energy conformers for both *cis* (14.4, 14.2, 36.4, 15.6, 13.4 MHz) and *trans* (23.6, 51.9, 30.1, 41.7, 21.0 MHz) range from 13-50 MHz, with the *trans* form having a better agreement than *cis* (-)-carveol. These ambiguities led us to a comparison of relative experimental dipole moment components with theoretical ones. Strong b-type transitions, weaker (~3×) a-type transitions, and no c-type transitions were observed for experimentally assigned

conformer E1. Comparing with theory reduces the number of potential candidates as no *cis* conformer and only two *trans* conformers (*trans*-(C)E_IAx_HAA and *trans*-(C)E_IAx_HG-A) match the experimental dipole moment components observations. These two conformers are also predicted to be experimentally present based on the conformational cooling considerations above. Comparing the theoretical and experimental rotational constants for *trans*-(C)E_IAx_HAA and *trans*-(C)E_IAx_HG-A, we found RMS errors of 14.4 MHz and 14.2 MHz, respectively. A process-of-elimination approach was then taken, where the five experimental assignments were first ascribed to the *cis* or *trans* configuration based on dipole moment components and RMS error and then further compared within each subgroup. The hope was that by matching the more definitive

Table 6.4. Abundances of *cis* and t*rans* (-)-carveol conformers at 298K and 353K (source temperature).

***cis* (C)E_IE_H**	***298 K*** [a](%)	***353 K*** [a](%)	***353 K*** [c](%)	***cis* (C)Ax_IAx_H**[b]	***298 K*** [b](%)	***353 K*** [b](%)	***353 K*** [c](%)
(C)E_IE_HAA	24.1	21.8	11.1	***(C)Ax_IAx_HG+A***	98.9	97.4	47.7
(C)E_IE_HG-A	17.3	16.5	8.4	***(C)Ax_IAx_HG-A***	0.6	1.4	0.7
(C)E_IE_HAG-	13.1	13.0	6.6	***(C)Ax_IAx_HG+G-***	0.2	0.5	0.2
(C)E_IE_HG+A	11.9	12.0	6.1	***(C)Ax_IAx_HAG-***	0.2	0.4	0.2
(C)E_IE_HAG+	10.0	10.4	5.3	***(C)Ax_IAx_HAG+***	0.1	0.2	0.1
(C)E_IE_HG-G-	9.0	9.5	4.8				
(C)E_IE_HG-G+	6.3	7.0	3.6				
(C)E_IE_HG+G-	4.6	5.4	2.8				
(C)E_IE_HG+G+	3.6	4.4	2.2				
***trans* (C)E_IAx_H**	***298 K*** [a](%)	***353 K*** [a](%)	***353 K*** [c](%)	***trans* (C)Ax_IE_H**	***298 K*** [b](%)	***353 K*** [b](%)	***353 K*** [c](%)
(C)E_IAx_HAA	28.3	25.2	30.7	***(C)Ax_IE_HG+A***	47.1	41.9	3.8
(C)E_IAx_HG-A	18.6	17.7	21.5	***(C)Ax_IE_HG+G+***	21.0	21.2	1.9
(C)E_IAx_HG+A	17.0	16.4	19.9	***(C)Ax_IE_HG+G-***	20.5	20.7	1.9
(C)E_IAx_HAG+	8.8	9.4	11.4	***(C)Ax_IE_HAA***	4.3	5.6	0.5
(C)E_IAx_HG-G+	7.4	8.1	9.9	***(C)Ax_IE_HG-A***	2.6	3.6	0.3
(C)E_IAx_HAG-	5.9	6.7	8.2	***(C)Ax_IE_HAG+***	2.2	3.2	0.3
(C)E_IAx_HG+G+	4.9	5.8	7.0	***(C)Ax_IE_HAG-***	1.5	2.3	0.2
(C)E_IAx_HG-G-	4.7	5.5	6.7	***(C)Ax_IE_HG-G-***	0.9	1.6	0.1
(C)E_IAx_HG+G-	4.4	5.2	6.4				

[a]Equatorial isopropenyl conformer and [b]axial isopropenyl conformer partition functions. [c]The abundances when the two partitions are combined.

conformers the assignment for the more ambiguous ones would become clear. Conformers E1 and E3 were assigned to the *trans-,* E2, E4, and E5 to the *cis*- subgroups. Much like the case for E1, RMS error and dipole moment components comparisons narrowed the possible candidate structures for E3 to either *trans*-(C)E_IAx_HAA or *trans*-(C)E_IAx_HG-A. However, unlike E1, weak c-type transitions could be detected in the experiment for E3. We therefore assign E3 to be *trans*-(C)E_IAx_HAA and the remaining *trans*-(C)E_IAx_HG-A conformer must be E1. In the *cis* conformer subgroup the assignment was more straightforward; E2=*cis*-(C)E_IE_HG-A, E4=*cis*-(C)Ax_IAx_HG+A, and E5= *cis*-(C)E_IE_HAA. A comparison of experimental and theoretical dipole moment components and rotational constants is presented in Tables S3 and S4 of the ESI. Theoretical geometries for the five experimentally assigned conformers, optimized at the B3LYP-D3(BJ)/def2-TZVP level, are presented in Tables S10 to S14 of the ESI. Generally, the B3LYP-D3(BJ) results agree well with the experimental rotational constants, where for conformers E1, E2, E3, E4, and E5 the RMS errors are 14.2, 11.1, 21.8, 25.6, and 10.6 MHz, respectively.

6.3.4. Experimental Intensities and Relative Energy Ordering

In the lowest energy equatorial isopropenyl structure for both *cis* and *trans* (-)-carveol the isopropenyl group assumes an antiperiplanar conformer, *cis*-(C)E_IE_HAA and *trans*-(C)E_IAx_HAA, while the isopropenyl has a gauche - conformer in the second lowest equatorial isopropenyl structure, *cis*-(C)E_IE_HG-A and *trans*-(C)E_IAx_HG-A. Based on this ordering one would assume the lower energy, *cis*-(C)E_IE_HAA and *trans*-(C)E_IAx_HAA form to have higher line intensities than the *cis*-(C)E_IE_HG-A and *trans*-(C)E_IAx_HG-A form. In fact, quite the opposite is observed in our spectrum, and the higher energy *cis*-(C)E_IE_HG-A and *trans*-(C)E_IAx_HG-A forms are approximately three times more intense. This could be a result of the larger dipole moment components for the *cis*-(C)E_IE_HG-A and *trans*-(C)E_IAx_HG-A form or a population enhancement through conformational relaxation processes. For the *trans* diastereomer, conformers E1 (*trans*-(C)E_IAx_HG-A) and E3 (*trans*-(C)E_IAx_HAA) have similar dipole moment components, therefore the higher intensity of E1 lines is likely a result of greater population.

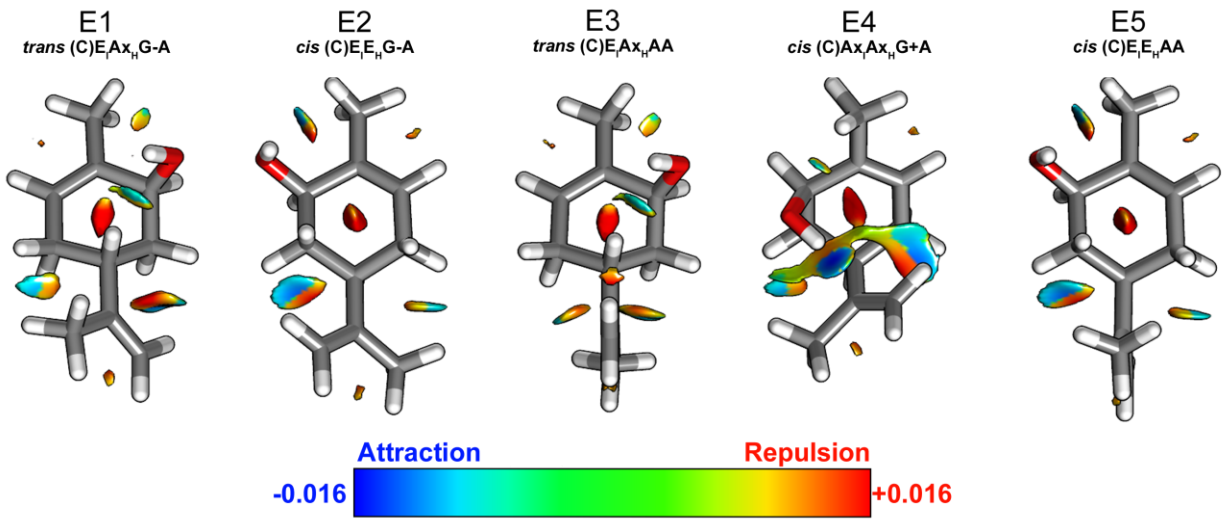

Figure 6.5. Isosurfaces of the reduced electron density gradient from NCI analyses of the five experimentally assigned conformers. Blue colored surfaces represent attractive, and red ones repulsive regions.

The abundances of different conformers presented in Table 6.4 were determined by calculating the partition function for an ensemble composed exclusively of half-chair equatorial isopropenyl or half-chair axial isopropenyl conformers at both 298 K and 353 K (source temperature), without considering any effects of conformational cooling. The decision to calculate each partition function exclusively for the (C)EqX and (C)AxX (X can be Ax or E) forms is based on several reasons. First, the axial and equatorial isopropenyl positions cannot interconvert without breaking covalent bonds. Second, the global minimum structure of the *cis* configuration is half-chair and has the isopropenyl in the axial position, thus we wanted to see how the abundances change with and without the (C)Ax_IAx_HG+A conformer incorporated into the partition function. Finally, as the boat conformers for both *cis* and *trans* are significantly higher in energy when compared to the global minimum structure the abundance contributions are negligible. If no conformational cooling is considered *trans*(C)E_IAx_HAA is approximately 7.5% (9.7%) more abundant than *trans*-(C)E_IAx_HG-A at 353K (298K). Looking at possible relaxation pathways (see Figure 6.3), one can see that two conformers (*trans*-(C)E_IAx_HAG+ and *trans*-(C)E_IAx_HAG-) can convert to *trans*-(C)E_IAx_HAA, while five conformers (*trans*-(C)E_IAx_HG+A, *trans*-(C)E_IAx_HG-G+, *trans*-(C)E_IAx_HG+G+, *trans-(C)*E_IAx_HG-G-, and *trans*-(C)E_IAx_HG+G-) relax to the *trans*-(C)E_IAx_HG-A form. The larger number of conformers cooling to the gauche - isopropenyl

conformer form translates into a greater abundance after the molecular beam expansion, which is likely the reason for the more intense *trans*-(C)E_IAx_HG-A transitions in the experiment.

A similar argument can be made to rationalize the signal intensities of the *cis*-(C)E_IE_HG-A conformer. As can be seen in Figure 6.3, *cis*-(C)E_IE_HG+A, *cis*-(C)E_IE_HG-G-, *cis*-(C)E_IE_HG-G+, *cis*-(C)E_IE_HG+G-, and *cis*-(C)E_IE_HG+G+ will all relax to *cis*-(C)E_IE_HG-A, with the remaining conformers (*cis*-(C)E_IE_HAG- and *cis*-(C)E_IE_HAG+) converting to *cis*-(C)E_IE_HAA. The population enhancement results in not only greater signal intensity as compared to the conformers with isopropenyl in the antiperiplanar conformer, but also roughly equal intensity to *cis*-(C)Ax_IAx_HG+A, despite the ~4 kJ/mol energy difference.

6.3.5. Axial Isopropenyl Conformer

The presence of *cis*-(C)Ax_IAx_H conformers in the theoretical and experimental results is not all that surprising, as analogous ones have been observed before in the cases of limonene and limonene derivatives. For example, in a recent broadband rotational spectroscopy study of perillyl alcohol,[13] which contains only a single chiral centre and a hydroxyl group positioned on the methyl group rather than on the ring, two axial isopropenyl conformers were experimentally observed, whose lines are much weaker than those of their equatorial position counterparts. This also is reflected in the corresponding CREST results where the isopropenyl axial position is predicted to be several kJ mol^{-1} higher in energy than the global minimum conformer, which has the isopropenyl in the equatorial position.

Table 6.5. Results from NBO analyses for H_2O-H_2O, carveol and carveol- H_2O

	[a]Donor	[a]Acceptor	E / kJ mol^{-1}
H_2O-H_2O	LP O	BD* O-H	49.0
Carveol	BD C-C	BD* O-H	8.4
Carveol-H_2O	LP O	BD* O-H	43.1
	Bond Order	**%Covalent**	**%Ionic**
H_2O-H_2O	0.0059	1.7	98.3
Carveol	0.0014	0.0	100
Carveol-H_2O	0.0075	1.3	98.7

[a]**LP:** lone pair, **BD:** bonding orbital, and **BD*:** antibonding orbital.

In contrast to not only the perillyl alcohol study, but to all limonene derivative studies, we have identified and assigned a global minimum structure in which the isopropenyl group assumes an axial position. To rationalize this preference, we analyse the results from NCI and QTAIM calculations shown in in Figure 6.5 and Figure D.2 of the ESI, respectively. The NCI plots of the *cis*-(C)E_IE_H and *trans*-(C)E_IAx_H conformers show relatively weak repulsive and attractive forces, primarily between neighbouring hydrogens, while the *cis*-(C)Ax_IAx_HG+A conformer show various regions of strong attractive forces. The attraction between the π-system of the isopropenyl group and the hydroxyl group is particularly strong, indicating a *bonding* interaction. This is corroborated by the QTAIM analysis, which shows a bond critical point between the two groups and the interaction can be classified as a hydrogen bond. The hydrogen bond within the *cis*-(C)Ax_IAx_HG+A conformer, and the lack thereof in the equatorial isopropenyl conformers, provides an explanation as to why the *cis*-(C)Ax_IAx_HG+A form is preferred over the isopropenyl in the equatorial position.

To further investigate the hydrogen bond between the hydroxyl group and the isopropenyl π system a Natural Bond Orbital (NBO)[40,41] analysis was performed. An NBO nalysis allows for the decomposition of non-covalent and covalent interactions into localized bonding and antibonding orbitals. As opposed to Canonical Molecular Orbitals (CMOs), NBO utilizes Localized Molecular Orbitals (LMOs) and provides a more intuitive way of describing the electron density in bonds.[42] To assess the strength of the hydrogen bond, WE contrast the *cis*-(C)Ax_IAx_HG+A conformer with two other systems, which each contain a strong H---O-H hydrogen bond, the first being the water dimer, and the second a carveol-water complex. Both systems are shown in Figure D.3 of Appendix D. Table 6.5 contains the donor and acceptor orbitals for the hydrogen bonds in each respective species, with the corresponding stabilization energy obtained from second order perturbative treatment of the Fock matrix. For the water dimer the oxygen lone pair of the first water molecule is donating electron density to the acceptor species, which is the O-H antibonding orbital of the second water molecule. For the carveol-water system, the donor species is the oxygen lone pair of the carveol molecule, and the acceptor species is the O-H antibonding orbital of the water molecule. Their stabilization energies are 49.0 kJ mol^{-1} and 43.1 kJ mol^{-1}, respectively. Similarly, for the *cis*-(C)Ax_IAx_HG+A conformer the acceptor species is also the O-H antibonding orbital. However, the donor species in this case is a C-C bonding orbital, i.e. the π-system of isopropenyl. As compared to the oxygen lone pair, the lower electron

density found in the isopropenyl π system leads to a weaker hydrogen bond, which is reflected in the lower stabilization energy of 8.4 kJ mol^{-1}.

To further break down the interaction the Natural Resonance Theory (NRT)[43–45] feature in the NBO program suite was used, which provides a bond order. The bond orders may be correlated to the strengths of hydrogen bond interactions. In addition to the total bond order, an NRT analysis also provides the fraction of covalent and ionic character of a bond. For example, a C-C covalent bond will have a bond character of one with predominately covalent character. An O-H covalent bond will also have a bond order of one, but will have roughly equal ionic and covalent character. Table 6.5 contains the bond orders with the percentages of covalent and ionic character for each system. As expected, for all three systems the hydrogen bond possesses primarily ionic character. Analogously to the trend in stabilization energies, the bond order for the π---O-H interaction in *cis*-(C)Ax_IAx_HG+A conformer is much smaller indicating a relatively weaker hydrogen bond. The π---O-H hydrogen bond is, despite its relative weakness, a major driving force for the stabilization of the axial positions of isopropenyl and hydroxyl groups in the *cis*-(C)Ax_IAx_HG+A conformer of *cis* (-)-carveol.

6.4. Conclusions

Using a CP-FTMW spectrometer broadband rotational spectra of *cis* and *trans* (-)-carveol were measured in the 2-6 GHz range. The high conformational flexibility (hydroxyl rotation, isopropenyl rotation, and ring conformers) of (-)-carveol and the diastereomeric pair of molecules present made the experimental assignments non-trivial. A two-dimensional potential energy scan and the CREST sampling tool were utilized to probe the conformational landscape of *cis* and *trans* (-)-carveol. From the theoretical results a total of 19 *cis* conformers and 23 *trans* conformers were identified. Using the theoretical results as an aid for experimental assignments, five conformers were successfully identified, three for *cis* and two for *trans* (-)-carveol. Both experimental *trans* conformers assume a *trans*-(C)E_IAx_H conformer. From a comparison to theory, we determined that the isopropenyl group for the first assigned conformer is in the gauche - conformer, and the second in the antiperiplanar conformer, with the hydroxyl for both conformers in the antiperiplanar conformer. Analogous to *trans*-(-)-carveol, the two *cis* conformers take the gauche - and antiperiplanar conformers of the isopropenyl, and both the antiperiplanar conformer for the hydroxyl group. However, for *cis*-(-)-carveol, an additional *cis*-(C)Ax_IAx_H conformer was

assigned, which is also the global minimum structure. Although in previous studies the isopropenyl axial position was experimentally identified, this is the first study to show a preference for the axial isopropenyl position. To investigate, and provide a cause for, this preference NCI and QTAIM analyses were carried out. From this a hydrogen bonding interaction was identified between the hydroxyl group and the isopropenyl π system. Using an NBO analysis we found that, when compared to other systems, the hydrogen bond is relatively weak, but strong enough to affect the preference for the axial over the equatorial position of the isopropenyl group.

6.5 References

1 J. Laothawornkitkul, J. E. Taylor, N. D. Paul and C. N. Hewitt, *New Phytol.*, 2009, **183**, 27–51.

2 F. M. N. Nunes, M. C. C. Veloso, P. A. de P. Pereira and J. B. de Andrade, *Atmos. Environ.*, 2005, **39**, 7715–7730.

3 T. E. Graedel, *Rev. Geophys.*, 1979, **17**, 937–947.

4 I. G. Kavouras, N. Mihalopoulos and E. G. Stephanou, *Environ. Sci. Technol.*, 1999, **33**, 1028–1037.

5 J. Zhu and J. E. Penner, *J. Geophys. Res. Atmospheres*, 2019, **124**, 8260–8286.

6 E. G. Schnitzler and W. Jäger, *Phys. Chem. Chem. Phys.*, 2014, **16**, 2305–2314.

7 J. Hendricks, M. Righi and V. Aquila, in *Atmospheric Physics: Background – Methods – Trends*, ed. U. Schumann, Springer, Berlin, Heidelberg, 2012, 561–576.

8 U. Pöschl, *Angew. Chem. Int. Ed.*, 2005, **44**, 7520–7540.

9 P. L. Crowell, W. S. Kennan, J. D. Haag, S. Ahmad, E. Vedejs and M. N. Gould, *Carcinogenesis*, 1992, **13**, 1261–1264.

10 M. S. Ahmed, A. Khan, L. T. A. Kury and F. A. Shah, *Front. Pharmacol.*, 2020, **11**, 919.

11 J. R. A. Moreno, F. P. Ureña, J. J. L. González and T. R. Huet, *Chem. Phys. Lett.*, 2009, **473**, 17–20.

12 J. R. A. Moreno, T. R. Huet and J. J. L. González, *Struct. Chem.*, 2013, **24**, 1163–1170.

13 D. Loru, M. M. Quesada-Moreno, J. R. Avilés-Moreno, N. Jarman, T. R. Huet, J. J. López-González and M. E. Sanz, *ChemPhysChem*, 2017, **18**, 274–280.

14 F. Xie, N. A. Seifert, M. Heger, J. Thomas, W. Jäger and Y. Xu, *Phys. Chem. Chem. Phys.*, 2019, **21**, 15408–15416.

15 P. Pracht, F. Bohle and S. Grimme, *Phys. Chem. Chem. Phys.*, 2020, **22**, 7169–7192.

16 D. Loru, A. Vigorito, A. F. Santos, J. Tang and M. E. Sanz, *Phys. Chem. Chem. Phys.*, 2019, **21**, 26111–26116.

17 R. F. W. Bader, *Chem. Rev.*, 1991, **91**, 893–928.

18 E. R. Johnson, S. Keinan, P. Mori-Sánchez, J. Contreras-García, A. J. Cohen and W. Yang, *J. Am. Chem. Soc.*, 2010, **132**, 6498–6506.

19 P. Pracht, E. Caldeweyher, S. Ehlert and S. Grimme, *A Robust Non-Self-Consistent Tight-Binding Quantum Chemistry Method for large Molecules*, 2019.

20 C. Bannwarth, S. Ehlert and S. Grimme, *J. Chem. Theory Comput.*, 2019, **15**, 1652–1671.

21 S. Grimme, C. Bannwarth and P. Shushkov, *J. Chem. Theory Comput.*, 2017, **13**, 1989–2009.

22 M. J. Frisch, G. W. Trucks, H. B. Schlegel, G. E. Scuseria, M. A. Robb, J. R. Cheeseman, G. Scalmani, V. Barone, G. A. Petersson, H. Nakatsuji, X. Li, M. Caricato, A. V. Marenich, J. Bloino, B. G. Janesko, R. Gomperts, B. Mennucci, H. P. Hratchian, J. V. Ortiz, A. F. Izmaylov, J. L. Sonnenberg, D. Williams-Young, F. Ding, F. Lipparini, F. Egidi, J. Goings, B. Peng, A. Petrone, T. Henderson, D. Ranasinghe, V. G. Zakrzewski, J. Gao, N. Rega, G. Zheng, W. Liang, M. Hada, M. Ehara, K. Toyota, R. Fukuda, J. Hasegawa, M. Ishida, T. Nakajima, Y. Honda, O. Kitao, H. Nakai, T. Vreven, K. Throssell, J. A. Montgomery Jr., J. E. Peralta, F. Ogliaro, M. J. Bearpark, J. J. Heyd, E. N. Brothers, K. N. Kudin, V. N. Staroverov, T. A. Keith, R. Kobayashi, J. Normand, K. Raghavachari, A. P. Rendell, J. C. Burant, S. S. Iyengar, J. Tomasi, M. Cossi, J. M. Millam, M. Klene, C. Adamo, R. Cammi, J. W. Ochterski, R. L. Martin, K. Morokuma, O. Farkas, J. B. Foresman and D. J. Fox, Gaussian 16, Gaussian Inc., Wallingford, CT, 2016.

23 H.-J. Werner, P. J. Knowles, G. Knizia, F. R. Manby, M. Schu¨tz, P. Celani, W. Gyo¨rffy, D. Kats, T. Korona, R. Lindh, A. Mitrushenkov, G. Rauhut, K. R. Shamasundar, T. B. Adler, R. D. Amos, A. Bernhardsson, A. Berning, D. L. Cooper, M. J. O. Deegan, A. J. Dobbyn, F. Eckert, E. Goll, C. Hampel, A. Hesselmann, G. Hetzer, T. Hrenar, G. Jansen, C. Ko¨ppl, Y. Liu, A. W. Lloyd, R. A. Mata, A. J. May, S. J. McNicholas, W. Meyer, M. E. Mura, A. Nicklass, D. P. O'Neill, P. Palmieri, D. Peng, K. Pflu¨ger, R. Pitzer, M. Reiher, T. Shiozaki, H. Stoll, A. J. Stone, R. Tarroni, T. Thorsteinsson and M. Wang, MOLPRO, version 2015. 1, a package of ab initio programs, see http://www.molpro.net

24 S. Grimme, J. Antony, S. Ehrlich and H. Krieg, *J. Chem. Phys.*, 2010, **132**, 154104.
25 A. D. Becke and E. R. Johnson, *J. Chem. Phys.*, 2005, **123**, 154101.
26 F. Weigend and R. Ahlrichs, *Phys. Chem. Chem. Phys.*, 2005, **7**, 3297–3305.
27 A. Schäfer, H. Horn and R. Ahlrichs, *J. Chem. Phys.*, 1992, **97**, 2571–2577.
28 A. E. DePrince and C. D. Sherrill, *J. Chem. Theory Comput.*, 2013, **9**, 2687–2696.
29 Chr. Møller and M. S. Plesset, *Phys. Rev.*, 1934, **46**, 618–622.
30 L. Goerigk and S. Grimme, *J. Chem. Theory Comput.*, 2011, **7**, 291–309.
31 J. Kaminsky, R. A. Mata, H.-J. Werner and F. Jensen, *Mol. Phys.*, 2008, **106**, 1899–1906.
32 T. A. Keith, AIMALL, TK Gristmill Software, Overland Park, KS, 2017.
33 T. Lu and F. Chen, *J. Comput. Chem.*, 2012, **33**, 580–592.
34 C. Peng and H. Bernhard Schlegel, *Isr. J. Chem.*, 1993, **33**, 449–454.
35 C. Peng, P. Y. Ayala, H. B. Schlegel and M. J. Frisch, *J. Comput. Chem.*, 1996, **17**, 49–56.
36 G. G. Brown, B. C. Dian, K. O. Douglass, S. M. Geyer, S. T. Shipman and B. H. Pate, *Rev. Sci. Instrum.*, 2008, **79**, 053103.
37 N. A. Seifert, J. Thomas, W. Jäger and Y. Xu, *Phys. Chem. Chem. Phys.*, 2018, **20**, 27630–27637.
38 R. S. Ruoff, T. D. Klots, T. Emilsson and H. S. Gutowsky, *J. Chem. Phys.*, 1990, **93**, 3142–3150.
39 M. D. Wodrich, C. Corminboeuf and P. von R. Schleyer, *Org. Lett.*, 2006, **8**, 3631–3634.
40 E. D. Glendening, C. R. Landis and F. Weinhold, *J. Comput. Chem.*, 2013, **34**, 1429–1437.
41 A. E. Reed and F. Weinhold, *J. Chem. Phys.*, 1983, **78**, 4066–4073.
42 F. Weinhold, *J. Comput. Chem.*, 2012, **33**, 2363–2379.
43 E. D. Glendening and F. Weinhold, *J. Comput. Chem.*, 1998, **19**, 593–609.
44 E. D. Glendening and F. Weinhold, *J. Comput. Chem.*, 1998, **19**, 610–627.
45 E. D. Glendening, J. K. Badenhoop and F. Weinhold, *J. Comput. Chem.*, 1998, **19**, 628–646.

7

Structure and Conformers of 3-Methylcatechol: A Rotational Spectroscopic and Theoretical study

Contents

7.1. Introduction · · · · · 130
7.2. Methods · · · · · 131
7.2.1. Experimental Methods · · · · · 131
7.2.2. Theoretical Methods · · · · · 132
7.3. Results and Discussion · · · · · 134
7.3.1. Theoretical Results · · · · · 134
7.3.2. Experimental Results · · · · · 135
7.3.3. Interconversion Pathways · · · · · 137
7.3.4. Spectroscopic Parameters · · · · · 139
7.3.5. Structures · · · · · 139
7.4. Conclusions · · · · · 141
7.5. References · · · · · 141

7.1. Introduction

The damaging environmental effects of climate change which have been predicted or demonstrated in numerous modelling and field studies,[1–4] include, among other things, a dramatic increase in average temperature across the globe. As a consequence of the elevated global temperature, there has already been a substantial increase in the frequency and size of biomass burning.[5] During biomass burning, large amounts of vegetation are combusted, releasing complex mixtures of organic molecules into the atmosphere. For example, the microfibrils in plant cells, which make up the majority of the mass of the cell wall, consist of three general molecular components, i.e., hemicellulose, cellulose, and lignin.[6] When undergoing pyrolysis, lignin emits various substituted catechols into the atmosphere, one such species being 3-methylcatechol.[7] In the atmosphere, 3-methylcatechol can be photo-oxidized by species such as ozone[8] resulting ultimately in the generation of secondary organic aerosol particles. This has been shown in previous photo-reaction

chamber experiments, where aerosol yields of 32%-67% were reported.[9] Conversely, 3-methylcatechol may also nucleate with other atmospheric species to form secondary organic aerosol particles.[10] Ammonia, water, and sulfuric acid, for example, may aggregate with 3-methylcatechol non-covalently to form nucleation precursors, which are complexes containing several molecules. These precursors are an important first step in the formation of atmospheric aerosol; however, despite their significance, energetic and structural properties of the early phases of nucleation are poorly understood. To effectively study and understand the aggregation of 3-methylcatechol with other atmospheric species, and their subsequent atmospheric significance, it is beneficial to first perform an in-depth study of the monomer structure. Studying, for instance, the conformational landscape of 3-methylcatechol, can provide data into the structure and energetic ordering of different conformers, as has been done in previous studies[11,12] containing atmospherically relevant molecules. This data can in turn be used to better predict and deduce the structural conformers of higher order 3-methylcatechol clusters.

Using a molecular beam expansion, 3-methylcatechol was introduced into a vacuum chamber and its rotational spectrum then measured using a chirped pulse Fourier transform microwave spectrometer. Two conformers, with their hydroxyl groups positioned in different orientations, were assigned to the experimental spectrum. The transitions were strong enough to detect and then assign seven singly substituted ^{13}C isotopologues for each conformer. The ^{13}C isotopologue rotational constants were used in fitting procedures to determine substitution and semi-experimental structural parameters

7.2. Methods

7.2.1. Experimental Methods

A sample of 3-methylcatechol was purchased from Santa Cruz Biotechnology and used without further modifications or purifications. To generate the necessary vapour pressure to introduce a sufficient number of 3-methylcatechol into the gas phase, the sample was placed into a sample reservoir within a special attachment to a General Valve, Series 9, nozzle, and then heated to 70 °C. Helium was used as a backing gas at approximately 40 psi.

The rotational spectrum of 3-methylcatechol was measured using a broad-band, chirped pulse Fourier transform microwave spectrometer, operating in the 2-6 GHz frequency range. Our instrument operates analogously to the spectrometer designed by the Pate group,[13] with some

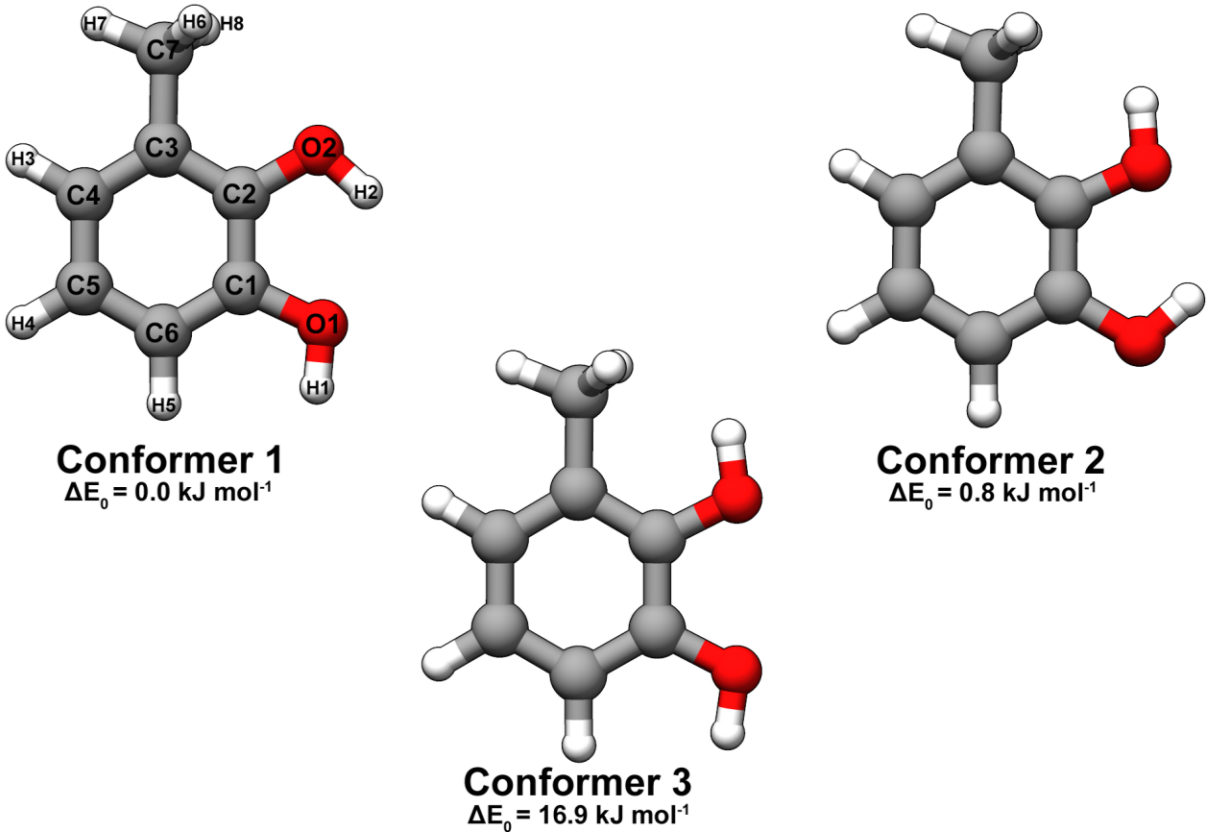

Figure 7.1. The three possible conformers of 3-methylcatechol. The labelling is based on the relative zero-point energies (ωB97XD/Jun-cc-pVTZ) which are shown below each conformer.

variances in component specifications.[14] Twelve 20 µs free induction decays (FIDs) were recorded per molecular pulse. A total of 1.9 million FIDs were recorded, averaged, and then Fourier transformed to obtain the broadband rotational spectrum of 3-methylcatechol. The large number of averages was necessary to measure transitions of singly ^{13}C substituted species with sufficient signal to noise ratio.

7.2.2 Theoretical Methods

To determine the structures of possible conformers of 3-methylcatechol, a relaxed two-dimensional dihedral angle energy scan was carried out at the ωB97XD[15]/Jun-cc-pVTZ[16] level of theory by varying the C3-C2-O2-H2 and C6-C1-O1-H1 dihedral angles (see Figure 7.1 for atom labelling). The two dihedral angles are associated with a rotation of the two hydroxyl groups. Each dihedral angle was varied by increments of 15° until the total angular displacement was 180°. Geometry optimizations and harmonic frequency calculations were performed at the ωB97XD/Jun-cc-pVTZ level of theory for the minima identified from the two-dimensional

potential energy scan. The two-dimensional scan, geometry optimizations, and frequency calculations were completed using the Gaussian 16 program suite.[17]

For the semi-experimental structure fit the anharmonic vibrational corrections to the rotational constants were obtained from generalized second order vibrational perturbation theory (GVPT2)[18,19] at the B3LYP-D3(BJ)[20–22]/def2-TZVP[23] level of theory. To examine the interconversion barriers between the three conformers, the Synchronous Transit Quasi-Newton (STQN) method of Schlegel and coworkers[24,25] was used to locate transition state structures at the ωB97XD/Jun-cc-pVTZ level of theory. Once located, the zero-point energies of the transition states were compared to the zero-point energies of the minima to yield zero-point corrected barrier heights. The methyl internal rotation barriers for all three conformers were determined in a similar fashion. The transition state was first located using the STQN method, which was followed by a

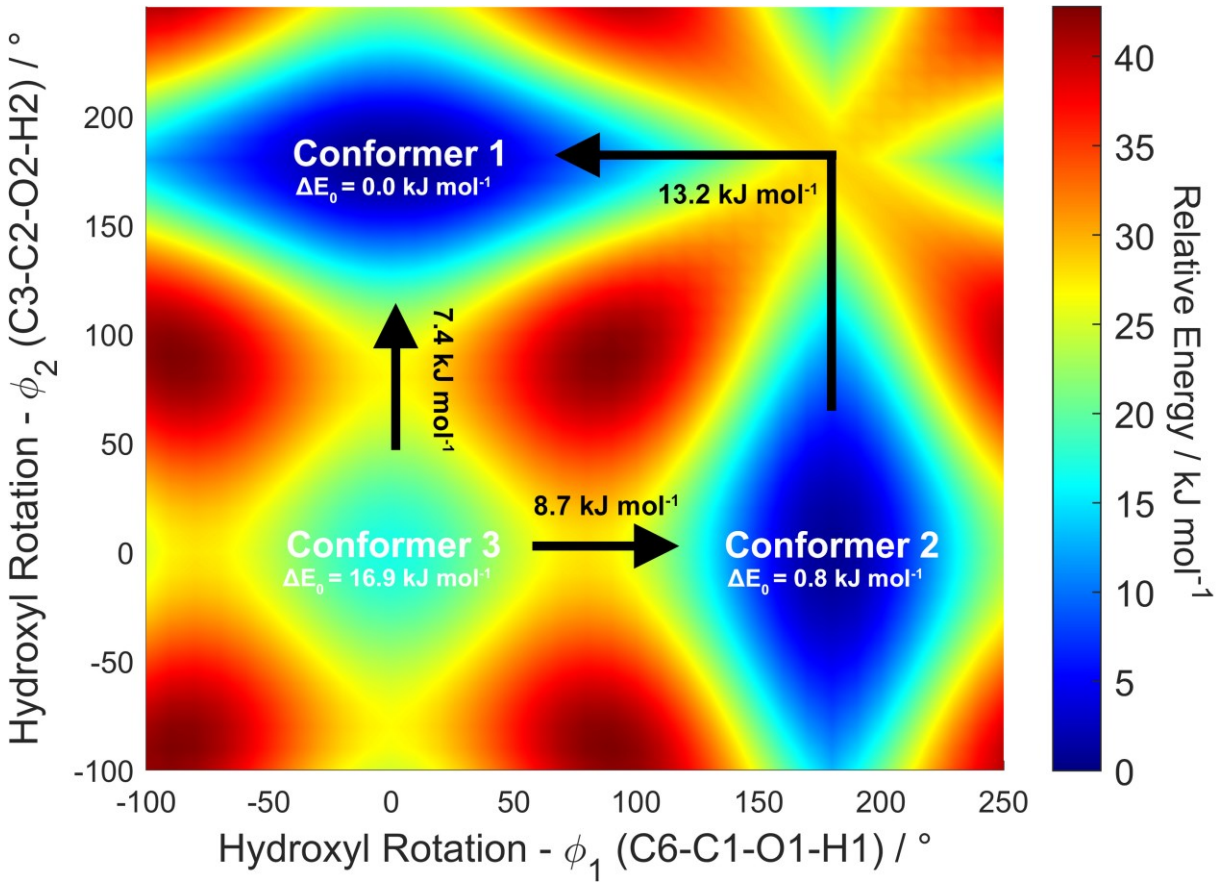

Figure 7.2. A two-dimensional relaxed potential energy scan of the rotation of the two hydroxyl groups. The black arrows represent interconversion pathways between conformers and the black numbers are the barriers going from the higher to the lower energy conformer.

Table 7.1. Theoretical results for the three conformers of 3-methylcatechol

	Conformer 1	Conformer 2	Conformer 3
A / MHz	2335.365	2332.671	2340.694
B / MHz	1823.709	1821.213	1808.151
C / MHz	1030.484	1029.292	1026.652
μ_a / D	-1.7	2.5	1.0
μ_b /D	0.9	1.2	-1.0
μ_c /D	0.0	0.0	0.0
ΔE_0 /kJ mol^{-1}	0.0	0.8	16.9
ΔG /kJ mol^{-1}	0.0	1.3	17.7
[a]298 K (%)	63.0	37.0	0.1
[a,b]368 K (%)	60.5	39.3	0.2

[a]Relative conformer abundances, calculated using the relative free energies. [b]Sample temperature.

comparison of zero-point energies between the transition state and minimum to obtain zero-point corrected barrier heights. To probe the intramolecular interactions present in each conformer, non-covalent interactions (NCI) analyses[26] were completed at the ωB97XD/Jun-cc-pVTZ level of theory using Multiwfn.[27]

7.3. Results and Discussion

7.3.1. Theoretical Results

The results of the two-dimensional potential energy scan, with interconversion barrier heights, are presented in Figure 7.2**.** From the scan, three different conformers were identified, i.e., Conformer 1, Conformer 2, and Conformer 3, in order of their relative zero-point corrected energies**.** The optimized structures, with their relative zero-point corrected energies at the ωB97XD/Jun-cc-pVTZ level of theory, are shown in Figure 7.1. The respective Cartesian coordinates for each conformer are given in Table E.1 of Appendix E. The relative zero-point corrected energy, theoretical rotational constants, and dipole moment components for all three conformers are presented in Table 7.1. The results obtained from the NCI analyses are plotted in Figure 7.3.

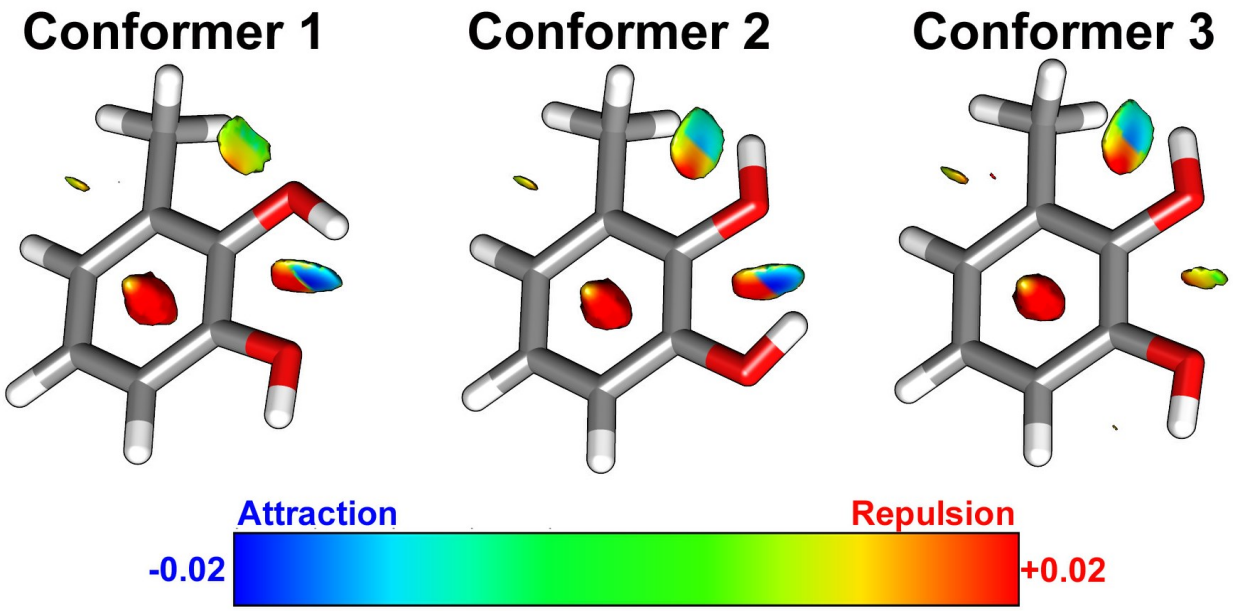

Figure 7.3. Isosurfaces of the reduced electron density gradient (s=0.7) from NCI analyses of the three conformers 3-methylcatechol.

7.3.2. Experimental Results

The recorded broadband rotational spectrum of 3-methylcatechol is shown in Figure 7.4. Of the three theoretical conformers, two could be experimentally assigned, Conformer 1 and Conformer 2. Strong *a*-type transitions, with weaker *b*-type transitions were observed for both conformers. The transition frequencies, together with the quantum number assignments, for Conformer 1 and Conformer 2 are presented in Tables E.2 and E.3 of Appendix E, respectively. Using Colin Western's PGOPHER program suite[28] and Pickett's SPCAT/SPFIT program suite,[29] the measured transition frequencies were used in fitting procedures with Watson's A-Reduction Hamiltonian[30] in its I^r representation to obtain experimental rotational constants and quartic centrifugal distortion constants (see Table 7.2). The relatively high-resolution capability of the chirped pulse Fourier transform microwave spectrometer allowed for observation of line splittings for conformer 1 into doublet components with an intensity ratio of about 1:1, which is consistent with the splitting pattern of a methyl internal rotor. The XIAM[31,32] internal rotor program and the initial A-species fit obtained from PGOPHER, were used to predict, and then subsequently fit, the measured transition frequencies of the observed doublets, to obtain rotational constants, quartic centrifugal distortion constants, and internal rotation parameters, i.e., V_3, the height of the three-fold barrier, and δ, the angle between the internal rotor axis and the a-axis. The angle between the *b*-principal

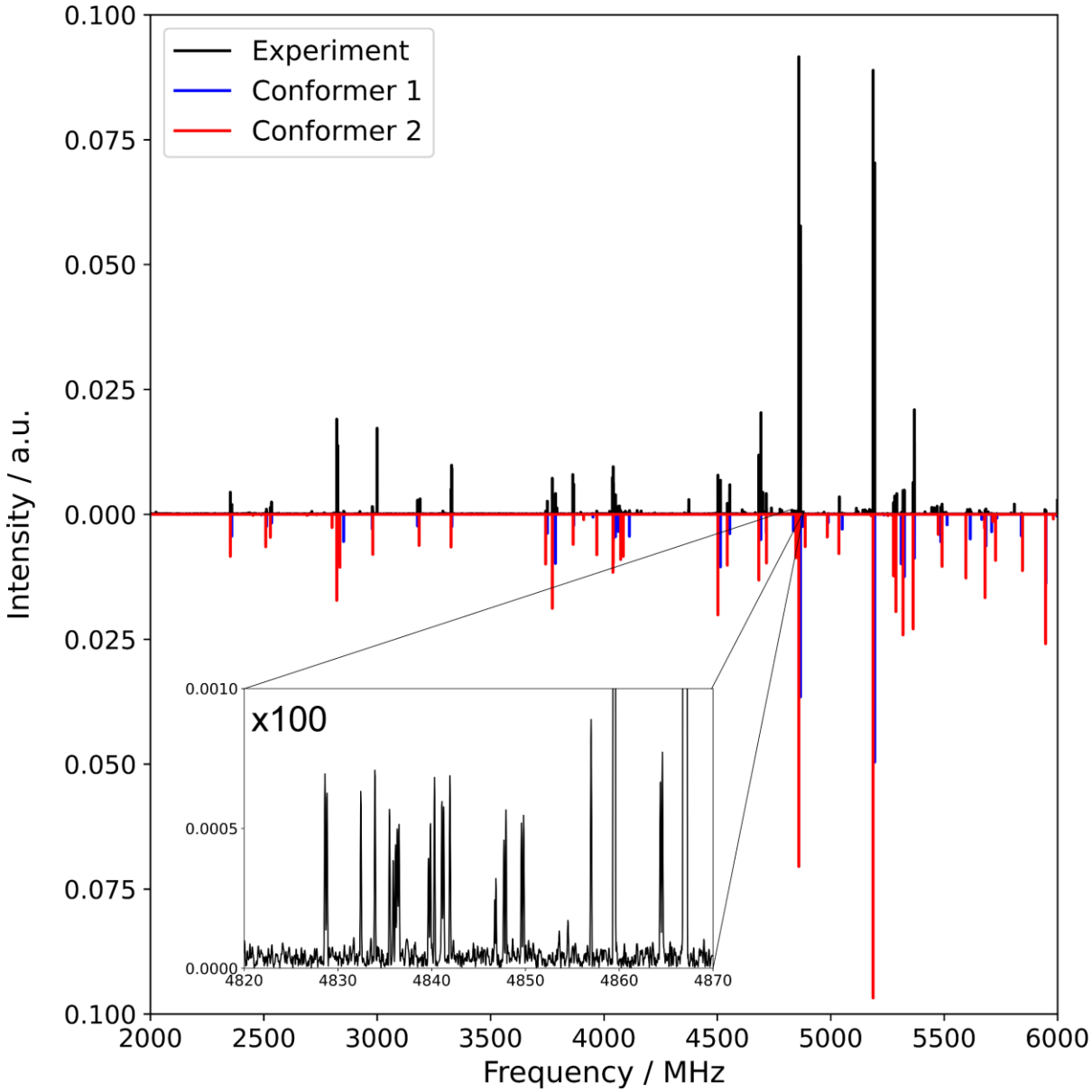

Figure 7.4. Broad-band rotational spectrum of 3-methylcatechol. The experimental spectrum is shown in black, while the simulated spectra of the two experimentally assigned conformers are coloured.

inertial axis and the projection of the internal rotor axis onto the *bc*-inertial plane, ε, was set to zero as the methyl group lies in the *ab*-plane. The resulting spectroscopic parameters for both conformers are presented in Table 7.2.

The signal-to-noise ratio was large enough such that all seven singly substituted ^{13}C isotopologues could be detected for both conformers in their natural abundances. The resulting spectroscopic parameters, obtained from PGOPHER and SPCAT/SPFIT, are presented in Tables E.4 and E.5 of Appendix E, with the transition frequencies and their respective quantum number

Table 7.2. Spectroscopic parameters for the two experimentally assigned conformers of 3-methylcatechol

	Conformer 1	**Conformer 2**
A /MHz	2308.71002(56)	2306.98680(93)
B /MHz	1806.48865(39)	1803.01660(66)
C /MHz	1020.11829(34)	1018.81503(61)
Δ_J /kHz	0.068(36)[e]	0.046(25)
Δ_{JK} /kHz	-	-
Δ_K /kHz	0.085(26)[e]	-0.276(52)
δ_J /kHz	0.0307(40)[e]	0.0115(45)
δ_K /kHz	0.028(14)[e]	0.111(37)
V_3 /kJ mol^{-1}	3.5970(5)	-
ε /rad	[0][a]	-
[a]δ /rad	0.4870(11)	-
[b]N	46	37
[c]σ /kHz	6.6	4.8
[d]|μ|/ D	$\mu_a > \mu_b$	$\mu_a > \mu_b$

[a]Fixed to zero in the fit. [b]Number of lines used in the fit. [c]Root mean square error of the fit. [d]Relative magnitudes of dipole moment components, estimated from signal strengths. [e]Fixed to values from the A-species fit.

assignments presented in Tables E.6 and E.7 of Appendix E. Using the ^{13}C isotopic data for both conformers we derived substitution structures from Kraitchman's[33] equations. We utilized the STRFIT[34] program to obtain effective and semi-experimental structures.[35–37] The fitted bond lengths and bond angles from each analysis, for both conformers, are shown in Tables 7.3 and 7.4. The coordinates obtained from the Kraitchman analyses are presented in Table E.8 of Appendix E.

7.3.3. Interconversion Pathways

From the two-dimensional potential energy scan (Figure 7.2), three possible conformers of 3-methylcatechol were identified. The global minimum structure, Conformer 1, has both of the hydroxyl groups pointing away from the methyl group, while the second lowest energy structure, Conformer 2, has the hydroxyl groups pointing towards the methyl group. The highest energy structure, Conformer 3, has the hydroxyl groups pointing away from each other. The zero-point corrected energies for Conformer 2 and Conformer 3, relative to Conformer 1, are 0.8 kJ mol^{-1} and

16.9 kJ mol^{-1}, respectively. Taking into account these energy differences, only Conformer 1 and Conformer 2 were expected to be sufficiently abundant in the molecular expansion to be experimentally observable. For example, using the free energies at the source temperature of 368 K for Conformer 1, Conformer 2, and Conformer 3, their relative abundances are 60.5%, 39.3%, and 0.2%, respectively. To rationalize these energy differences we performed NCI analyses, which were utilized to examine the intramolecular interactions present within each conformer. The results of the NCI analyses are presented in Figure 7.3. Comparing the NCI plot of Conformer 3 to the other conformers, it becomes clear why Conformer 3 is significantly higher in energy. As indicated by the blue colouration, both Conformer 1 and Conformer 2 possess a hydrogen bond interaction between the two hydroxyl groups. In Conformer 3 this hydrogen bond is absent, a consequence of the orientations of the two hydroxyl groups.

To properly account for the conformers present in the experimental spectrum one must not only consider the relative abundances of the species, but also take into account the kinetics of the cooling process during the molecular beam expansion. More specifically, one must closely examine the barrier heights of interconversion paths between each of the conformers. During the cooling process, higher energy conformers will collisionally cool down to lower energy conformers, provided the interconversion barrier height is sufficiently low. Ruoff et al.[38] found that the upper barrier height that permits collisional cooling is approximately 5.0 kJ mol^{-1}. The interconversion pathways and the respective barrier heights can be obtained from the two-dimensional potential energy scan presented in Figure 7.2. Three possible interconversion pathways exist, Conformer 3 to Conformer 1, Conformer 3 to Conformer 2, and Conformer 2 to Conformer 1, with interconversion barrier heights of 7.4 kJ mol^{-1}, 8.7 kJ mol^{-1}, and 13.2 kJ mol^{-1}, respectively. Based on these barrier heights, as well as the 5.0 kJ mol^{-1} energetic limit, we expect no conformational cooling to occur, and therefore the presence of each conformer in the experimental spectrum is solely based on the initial abundances in the heated nozzle reservoir. These thermodynamic and kinetic considerations rationalize the absence of Conformer 3 in our experimental spectrum.

Table 7.3. Effective (r_0), substitution (r_s), semi-experimental (r_{se}), and theoretical structure parameters for Conformer 1

	Bond Lengths			
	r_0	**r_s**	**r_{se}**	**ωB97XD**
r(C1-C2)	1.40(3)	1.353(3)	1.40(1)	1.392
r(C2-C3)	1.40(7)	1.380(2)	1.39(2)	1.390
r(C3-C4)	1.4(2)	1.424(1)	1.39(6)	1.391
r(C4-C5)	1.4(2)	1.375(1)	1.38(7)	1.385
r(C5-C6)	1.4(2)	1.399(2)	1.40(6)	1.387
r(C3-C7)	1.51(9)	1.516(2)	1.50(2)	1.500
	Bond Angles			
	r_0	**r_s**	**r_{se}**	**ωB97XD**
∠(C1-C2-C3)	121(5)	121.6(2)	120(1)	120.5
∠(C2-C3-C4)	118(7)	118.1(1)	118(2)	118.2
∠(C3-C4-C5)	122(5)	121.0(1)	122(2)	121.4
∠(C4-C5-C6)	120(1)	119.6(1)	120.0(5)	120.0
∠(C7-C3-C2)	119(11)	119.0(1)	119(3)	119.5

7.3.4. Spectroscopic Parameters

The theoretical rotational constants are in good agreement with the experimentally determined rotational constants, with RMS errors of 33.4 MHz and 33.2 MHz for Conformer 1 and Conformer 2, respectively. The theoretical, zero-point corrected barrier height of the methyl internal rotor for Conformer 1 was found to be 3.2 kJ mol^{-1}, which agrees well with the experimental barrier height, 3.5970(5) kJ mol^{-1}. No line splittings were observed for Conformer 2. The theoretical zero-point corrected methyl internal rotor barrier for Conformer 2 was found to be 5.1 kJ mol^{-1} and the line splittings predicted with the XIAM code are on the order of 6 kHz, too small to be resolved with the chirped pulse spectrometer. The larger barrier height for Conformer 2 relative to Conformer 1 is a result of the close proximity of the methyl group to the hydrogen atom of the adjacent hydroxyl group.

7.3.5. Structures

The effective structures (r_0) for both conformers were fit in terms of bond lengths and bond angles using the ground state rotational constants of the parent species and the ^{13}C isotopologues; the results for Conformer 1 and Conformer 2 are shown in Tables 7.3 and 7.4, respectively. In the fits

Table 7.4. Effective (r_0), substitution (r_s), semi-experimental (r_{se}), and theoretical structure parameters for Conformer 2

	Bond Lengths			
	r_0	**r_s**	**r_{se}**	**ωB97XD**
r(C1-C2)	1.40(3)	1.355(2)	1.41(1)	1.394
r(C2-C3)	1.40(6)	1.402(2)	1.39(2)	1.388
r(C3-C4)	1.4(2)	1.439(2)	1.39(8)	1.392
r(C4-C5)	1.4(2)	1.367(1)	1.36(9)	1.384
r(C5-C6)	1.4(2)	1.417(4)	1.41(7)	1.386
r(C3-C7)	1.51(8)	1.491(2)	1.50(3)	1.503
	Bond Angles			
	r_0	**r_s**	**r_{se}**	**ωB97XD**
∠(C1-C2-C3)	121(4)	123.2(2)	120(2)	121.4
∠(C2-C3-C4)	118(6)	116.0(1)	119(3)	118.1
∠(C3-C4-C5)	121(5)	121.3(1)	121(2)	120.9
∠(C4-C5-C6)	120(1)	120.3(2)	120.6(6)	120.4
∠(C7-C3-C2)	120(11)	120.2(1)	119(5)	120.1

it was only possible to determine structural parameters related to the C-atom skeleton, despite significant efforts, and it was necessary to fix the remaining bond lengths and angles to the theoretical values. The relatively large uncertainties in the structural parameters may be a result of this approach, as the theoretical values do not take zero-point vibrational effects into account, for example. Using the experimental rotational constants of the ^{13}C isotopologues, we performed Kraitchman substitution analyses[33] to obtain C-atom coordinates and from those, bond lengths and bond angles (see Tables 7.3 and 7.4). The *b*-coordinate of the C3 atom was set to zero, as it drastically improved the results of the fit, leading to much better consistency between Conformer 1 and Conformer 2 and the theoretical data. There is reasonable agreement between the substitution structural parameters (r_s) and those from the ωB97XD/Jun-cc-pVTZ calculations. For Conformer 1 (Conformer 2) the average percent differences for the bond lengths and bond angles are 1.4% (1.9%) and 0.4% (0.8%), respectively. In the Kraitchman analyses, zero-point vibrational effects are partially taken into account, but in an attempt to replicate the equilibrium structure as closely as possible, semi-experimental equilibrium structures[35–37] (r_{se}) were evaluated. This was done by first subtracting the calculated anharmonic vibrational corrections from the experimental rotational constants of the ^{13}C isotopologues and then using the results in the STRFIT program to fit the semi-experimental structure in terms of bond lengths and bond angles (see Tables 7.3 and 7.4). As

with the effective, r_o, structure fits, only the C-atom skeleton related bond lengths and angles were able to be determined. The semi-experimental parameters are closer to the ωB97XD/Jun-cc-pVTZ results than the Kraitchman bond lengths and angles. The average percent difference of Conformer 1 (Conformer 2) for the bond angles and bond lengths improves to 0.3% (0.9%) and 0.3% (0.6%), respectively. This improvement validates the semi-experimental structure approach and is, at the same time, an indicator of the high quality of the theoretical structures. This improvement with the semi-experimental structure fit has also been observed in analogous aromatic systems, for example 1- and 2-naphthol monomer.[39]

7.4. Conclusions

Microwave spectra of 3-methylcatechol were recorded using a chirped pulse Fourier transform microwave spectrometer, operating in the 2-6 GHz region. To search for possible conformers, and examine interconversion pathways, a two-dimensional relaxed potential energy scan along the two hydroxyl group rotation coordinates was completed. Three possible conformers, which differ by the orientation of their hydroxyl groups, were identified. However, due to thermodynamic and kinetic considerations only Conformer 1 and Conformer 2 are present in the experimental spectrum. Strong *a*-type and *b*-type transitions were observed for both conformers, which agrees well with the theoretical predictions. Line splittings were observed exclusively for Conformer 1, consistent with an internal rotation of the methyl group. The experimental barrier height of the methyl internal rotor was determined to be 3.5970(5) kJ mol^{-1}, which is in good agreement with the theoretical prediction (3.2 kJ mol^{-1}). All seven singly substituted ^{13}C isotopologues, in natural abundance, were detected for both conformers and were used in structure fitting procedures to obtain effective, substitution, and semi-experimental structural parameters.

7.5. References

1 E. Kalnay, M. Kanamitsu, R. Kistler, W. Collins, D. Deaven, L. Gandin, M. Iredell, S. Saha, G. White and J. Woollen, *Bull. Am. Meteorol. Soc.*, 1996, **77**, 437–472.

2 J. W. Hurrell, *Science*, 1995, **269**, 676–679.

3 C. Parmesan and G. Yohe, *nature*, 2003, **421**, 37–42.

4 C. D. Thomas, A. Cameron, R. E. Green, M. Bakkenes, L. J. Beaumont, Y. C. Collingham, B. F. Erasmus, M. F. De Siqueira, A. Grainger and L. Hannah, *Nature*, 2004, **427**, 145–148.

5 T. Schoennagel, J. K. Balch, H. Brenkert-Smith, P. E. Dennison, B. J. Harvey, M. A. Krawchuk, N. Mietkiewicz, P. Morgan, M. A. Moritz and R. Rasker, *Proc. Natl. Acad. Sci.*, 2017, **114**, 4582–4590.

6 F. H. Isikgor and C. R. Becer, *Polym. Chem.*, 2015, **6**, 4497–4559.

7 M. Asmadi, H. Kawamoto and S. Saka, *J. Anal. Appl. Pyrolysis*, 2011, **92**, 88–98.

8 J. Sun, B. Wei, Q. Mei, Z. An, X. Wang and M. He, *Chem. Eng. J.*, 2019, **358**, 456–466.

9 C. Coeur-Tourneur, V. Foulon and M. Laréal, *Atmos. Environ.*, 2010, **44**, 852–857.

10 C. Coeur-Tourneur, A. Tomas, A. Guilloteau, F. Henry, F. Ledoux, N. Visez, V. Riffault, J. C. Wenger and Y. Bedjanian, *Atmos. Environ.*, 2009, **43**, 2360–2365.

11 A. S. Hazrah, M. Al-Jabiri, R. Speelman and W. Jäger, *Phys. Chem. Chem. Phys.*, 2021, **23**, 15159–15168.

12 F. Xie, N. A. Seifert, M. Heger, J. Thomas, W. Jäger and Y. Xu, *Phys. Chem. Chem. Phys.*, 2019, **21**, 15408–15416.

13 G. G. Brown, B. C. Dian, K. O. Douglass, S. M. Geyer, S. T. Shipman and B. H. Pate, *Rev. Sci. Instrum.*, 2008, **79**, 053103.

14 N. A. Seifert, J. Thomas, W. Jäger and Y. Xu, *Phys. Chem. Chem. Phys.*, 2018, **20**, 27630–27637.

15 J.-D. Chai and M. Head-Gordon, *Phys. Chem. Chem. Phys.*, 2008, **10**, 6615–6620.

16 E. Papajak, J. Zheng, X. Xu, H. R. Leverentz and D. G. Truhlar, *J. Chem. Theory Comput.*, 2011, **7**, 3027–3034.

17 M. J. Frisch, G. W. Trucks, H. B. Schlegel, G. E. Scuseria, M. A. Robb, J. R. Cheeseman, G. Scalmani, V. Barone, G. A. Petersson, H. Nakatsuji, X. Li, M. Caricato, A. V. Marenich, J. Bloino, B. G. Janesko, R. Gomperts, B. Mennucci, H. P. Hratchian, J. V. Ortiz, A. F. Izmaylov, J. L. Sonnenberg, D. Williams-Young, F. Ding, F. Lipparini, F. Egidi, J. Goings, B. Peng, A. Petrone, T. Henderson, D. Ranasinghe, V. G. Zakrzewski, J. Gao, N. Rega, G. Zheng, W. Liang, M. Hada, M. Ehara, K. Toyota, R. Fukuda, J. Hasegawa, M. Ishida, T. Nakajima, Y. Honda, O. Kitao, H. Nakai, T. Vreven, K. Throssell, J. A. Montgomery Jr., J. E. Peralta, F. Ogliaro, M. J. Bearpark, J. J. Heyd, E. N. Brothers, K. N. Kudin, V. N.

Staroverov, T. A. Keith, R. Kobayashi, J. Normand, K. Raghavachari, A. P. Rendell, J. C. Burant, S. S. Iyengar, J. Tomasi, M. Cossi, J. M. Millam, M. Klene, C. Adamo, R. Cammi, J. W. Ochterski, R. L. Martin, K. Morokuma, O. Farkas, J. B. Foresman and D. J. Fox, Gaussian 16, Gaussian Inc., Wallingford, CT, 2016.

18 H. H. Nielsen, *Rev. Mod. Phys.*, 1951, **23**, 90.

19 I. M. Mills, *J. Mol. Spectrosc.*, 1961, **5**, 334–340.

20 S. Grimme, S. Ehrlich and L. Goerigk, *J. Comput. Chem.*, 2011, **32**, 1456–1465.

21 A. D. Becke, *J. Chem. Phys.*, 1992, **96**, 2155–2160.

22 A. D. Becke and E. R. Johnson, *J. Chem. Phys.*, 2005, **123**, 154101.

23 F. Weigend and R. Ahlrichs, *Phys. Chem. Chem. Phys.*, 2005, **7**, 3297–3305.

24 C. Peng and H. Bernhard Schlegel, *Isr. J. Chem.*, 1993, **33**, 449–454.

25 C. Peng, P. Y. Ayala, H. B. Schlegel and M. J. Frisch, *J. Comput. Chem.*, 1996, **17**, 49–56.

26 J. Contreras-García, E. R. Johnson, S. Keinan, R. Chaudret, J.-P. Piquemal, D. N. Beratan and W. Yang, *J. Chem. Theory Comput.*, 2011, **7**, 625–632.

27 T. Lu and F. Chen, *J. Comput. Chem.*, 2012, **33**, 580–592.

28 C. M. Western, *J. Quant. Spectrosc. Radiat. Transf.*, 2017, **186**, 221–242.

29 H. M. Pickett, *J. Mol. Spectrosc.*, 1991, **148**, 371–377.

30 J. K. Watson, *J. Chem. Phys.*, 1967, **46**, 1935–1949.

31 N. Hansen, H. Mäder and T. Bruhn, *Mol. Phys.*, 1999, **97**, 587–595.

32 H. Hartwig and H. Dreizler, *Z. Für Naturforschung A*, 1996, **51**, 923–932.

33 J. Kraitchman, *Am. J. Phys.*, 1953, **21**, 17–24.

34 Z. Kisiel, *J. Mol. Spectrosc.*, 2003, **218**, 58–67.

35 J. Demaison, *Mol. Phys.*, 2007, **105**, 3109–3138.

36 E. Penocchio, M. Piccardo and V. Barone, *J. Chem. Theory Comput.*, 2015, **11**, 4689–4707.

37 M. Piccardo, E. Penocchio, C. Puzzarini, M. Biczysko and V. Barone, *J. Phys. Chem. A*, 2015, **119**, 2058–2082.

38 R. S. Ruoff, T. D. Klots, T. Emilsson and H. S. Gutowsky, *J. Chem. Phys.*, 1990, **93**, 3142–3150.

39 A. S. Hazrah, S. Nanayakkara, N. A. Seifert, E. Kraka and W. Jäger, *Phys. Chem. Chem. Phys.*, 2022, **24**, 3722–3732.

8

Wetting vs. Droplet Aggregation: A Broadband Rotational Spectroscopic Study of 3-Methylcatechol··· (Water)$_N$ Clusters

Contents

8.1. Introduction · · · · · 144
8.2. Methods · · · · · 146
8.2.1. Experimental Methods · · · · · 146
8.2.2. Theoretical Methods · · · · · 146
8.3. Results and Discussion · · · · · 147
8.3.1. Experimental Results · · · · · 147
8.3.2. Theoretical Results · · · · · 148
8.3.3. Spectroscopic Assignment · · · · · 150
8.3.4. Wetting vs. Droplet Aggregation · · · · · 153
8.3.5. Splittings of Rotational Transitions · · · · · 157
8.4. Conclusions · · · · · 158
8.5. References · · · · · 159

8.1. Introduction

Produced during forest fires,[1] 3-methylcatechol is of atmospheric significance as it can non-covalently bind with relevant molecules, such as water, organic acids, and sulfuric acid, to form secondary atmospheric aerosol particles.[2] The impact of atmospheric aerosols on climate, climate change, and human health is well documented and there are several reports on aerosol particles containing 3-methylcatechol and its many oxidation products.[3–7] The ready incorporation of 3-metyhylcatechol into aerosol particles is a consequence of its multiple hydrogen bonding acceptor and donor sites. As such, it also provides an interesting template for aggregation of water molecules to study fundamental aspects of solvation on a microscopic scale. It is a long-standing goal of chemists to better understand the early phases of solvation, and more specifically, the link between molecular-level aggregation and properties of solutions on the macroscopic scale.[8–12] One method of elucidating the process of solvation is to study molecules, i.e., solutes, with only few

water molecules aggregated with them, preferably in a step-wise fashion, as has been done in previous work.[13–16] In those studies, it has been shown that water molecules aggregate predominately with themselves and only the respective hydrogen bond donor or acceptor groups of the solute molecule are involved in the early steps of the solvation process. In this aggregation process, other parts of the solute molecule interact only minimally with the water molecules, and the solute molecule serves essentially as a base for the formation of a droplet-like $(water)_N$ structure. In terms of intermolecular interactions, this pathway can be described as molecular cluster formation driven essentially by hydrogen bonding, where water-solute dispersion interactions play only a minor structure-determining role. For example, in a previous UV double resonance experiment,[17] hydrated phenol with up to five water molecules was investigated. The study revealed a complex hydrogen bond network among the water molecules, with only a single interaction between the solvent (water) and solute molecule (phenol). More recently, a broadband Fourier transform microwave (FTMW) spectroscopic study of 3-methyl-3-oxetanemethanol-$(H_2O)_{N=1-6}$ clusters revealed an analogous aggregation process where the water molecules are forming a sub-cluster predominately with themselves.[18] This pattern is also observed in another recent FTMW study, examining the fenchone-$(H_2O)_{N=1-7}$ complexes.[19,20] Indeed, these studies, as well as those of several other systems,[13–16,21,22] show a preference for this style of hydrogen bond dominated solvent aggregation. It is interesting that a solvation process whose initial stages involve a "wetting" of a molecular aromatic "surface" has not been extensively documented in literature. Such solvation pathway would involve dispersion interactions, apart from hydrogen bonding, as structure-defining interactions, similar to what is now established for the process of protein folding,[23–25] for example. Glimpses of such wetting style of aggregation have recently been seen in the study of 1,4-naphthoquinone-$(H_2O)_{N=1-3}$ complexes,[26] where in-plane and above-plane water configurations were found; a complete wetting of an aromatic ring surface could, however, not be observed, likely because an insufficient number of solvating water molecules. Although pure water clusters containing up to seven H_2O units have been studied with rotational spectroscopy, there are relatively few reports of organic molecules hydrated with three H_2O units,[19,27–31] and only three reports on higher organic hydrates.[18,32,33]

With its two neighbouring hydroxyl groups and its aromatic π-system, 3-methylcatechol provides multiple and flexible hydrogen bonding opportunities and one can anticipate a complex conformational manifold of low order hydrates. Here we describe an electronic structure and

rotational spectroscopic study of the micro-solvation of 3-methylcatechol with one to four water molecules in a stepwise fashion to explore this conformational complexity with high structural resolution.

8.2. Methods

8.2.1. Experimental methods

A sample of 3-methylcatechol was purchased from Santa Cruz Biotechnology. To generate the necessary vapour pressure to introduce a sufficient number of 3-methylcatechol into the gas phase, the sample was placed into a sample reservoir within a special attachment to a General Valve, Series 9, nozzle, and then heated to 70 °C. The sample consisted of neons mixed with ~0.2% water at a backing pressure of approximately 20 psi. To measure $H_2{}^{18}O$ substituted species, a 4:1 mixture of $H_2{}^{18}O$: $H_2{}^{16}O$ was used. The rotational spectra of 3-methylcatechol and its respective hydrates were measured using a chirped pulse Fourier transform microwave spectrometer, operating in the 2-6 GHz frequency range. Our instrument operates analogously to the spectrometer designed by the Pate group,[34] with some variances in component specifications.[35]

Six, 40 μs free induction decays (FIDs) were recorded per molecular pulse. A total of 1.1 and 2.6 million FIDs were recorded, averaged, and then Fourier transformed to obtain the broadband rotational spectrum of 3-methylcatechol with $H_2{}^{16}O$ and $H_2{}^{18}O$, respectively. The relatively long detection time of 40 μs was needed for the hydrate spectra to better resolve transitions that were split by various internal motions.

8.2.2. Theoretical Methods

To assist in the spectroscopic and quantum number assignments, the conformer-rotamer ensemble sampling tool CREST[36] was utilized at the GFN2-xTB[37] level of theory to generate ensembles of mono-, di-, tri-, tetra-, and penta-hydrate conformers of 3-methylcatechol. The structures from the CREST calculations were further refined by geometry optimizations and harmonic frequency calculations at the ωB97XD[38]/Jun-cc-pVTZ[39] level of theory using the Gaussian 16 program suite.[40] The ωB97XD functional, and long range corrected functionals in general, have been shown to accurately capture non-covalent interactions[41–43] in molecular clusters, for example, dispersion interactions between aromatic systems.[44] This theoretical procedure was repeated three times, with the exception of the pentahydrate which was only completed once due to computational cost. To

validate the ωB97XD results, geometry optimizations and harmonic frequency calculations of the CREST candidates were also carried out at the B3LYP-D3BJ/def2-TZVP level of theory.

To determine barrier heights for the water tunneling motions, the nudged-elastic band (NEB) method[45] was utilized. Using the ORCA 5.0.3 program suite[46], the NEB-TS[47] procedure with 24 images between each minimum was computed at the ωB97XD/Jun-cc-pVTZ level of theory. To examine conformational interconversion barriers for the hydrates, as well as methyl internal rotation barriers, the Synchronous Transit Quasi-Newton (STQN) method[48] of Schlegel and coworkers was used to locate transition state structures at the ωB97XD/Jun-cc-pVTZ level of theory. Once located, the zero-point energies of the transition states were compared to the zero-point energies of the minima to yield zero-point corrected barrier heights. To probe the intermolecular interactions present in each hydrate, quantum theory of atoms-in-molecules (QTAIM)[49] and non-covalent interactions (NCI)[50] analyses were completed at the ωB97XD/Jun-cc-pVTZ level of theory, using AIMA11[51] and Multiwfn[52], respectively. QTAIM and NCI analyses were carried out exclusively for the experimentally assigned hydrate species.

8.3. Results and Discussion

8.3.1. Theoretical Results

Following the theoretical procedure discussed above, 16, 30, 100, 130, and 246 conformers containing one, two, three, four, and five water complexes, respectively, were generated at the ωB97XD/Jun-cc-pVTZ level of theory. When considering conformers below 5.0 kJ mol^{-1} - conformers with a high enough population density to be experimentally observed - the number of conformers for one, two, three, four, and five water molecules is reduced to 2, 3, 15, 21, and 5, respectively. The energetic and spectroscopic properties of all conformers are summarized in Table F.1, Appendix F. Each hydrate conformer, for example MC1-1W II, will be named by the conformer of the 3-methylcatechol subunit (MC1), number of water molecules (1W), and energy ordering (II) for the hydrates with more than one water molecule assigned, with I being the most stable one for each hydrate. For one, two, three, four, and five water complexes, the ratios of conformers below 5.0 kJ mol^{-1} containing MC1 or MC2 as their monomer subunit are 1:1, 3:0, 9:6, 20:1, and 5:0, respectively. The B3LYP results are not only consistent with the ωB97XD results in terms of the number of conformers produced (16, 24, 107, 174, and 253 for one, two, three, four, and five waters respectively), but also produce analogous structures for the low energy (<5.0 kJ

mol^{-1}) conformers. The energetic and spectroscopic properties for all conformers at the B3LYP-D3BJ/def2-TZVP are summarized in Table F.2, Appendix F.

8.3.2. Experimental Results

The broadband rotational spectrum of 3-methylcatechol with water is presented in Figure 8.1. With help from the theoretical results, as well as a previous monomer study of 3-methylcatechol,[53] two monohydrates (monohydrate 1 and monohydrate 2), one dihydrate, one trihydrate, one tetrahydrate, and one pentahydrate of 3-methylcatechol, labelled MC1-1W I, MC2-1W II, MC1-2W, MC1-3W, MC1-4W, and MC1-5W, respectively, could be assigned to the experimental spectrum. The fitted spectroscopic parameters for these species are presented in Table 8.1, with the assigned transition frequencies and their respective quantum number assignments presented in Tables F.13-F.18, Appendix F. For some of the hydrates, rotational lines are split into several components. We ascribe these splittings to intra-cluster motions (*vide infra*) and the corresponding barrier heights

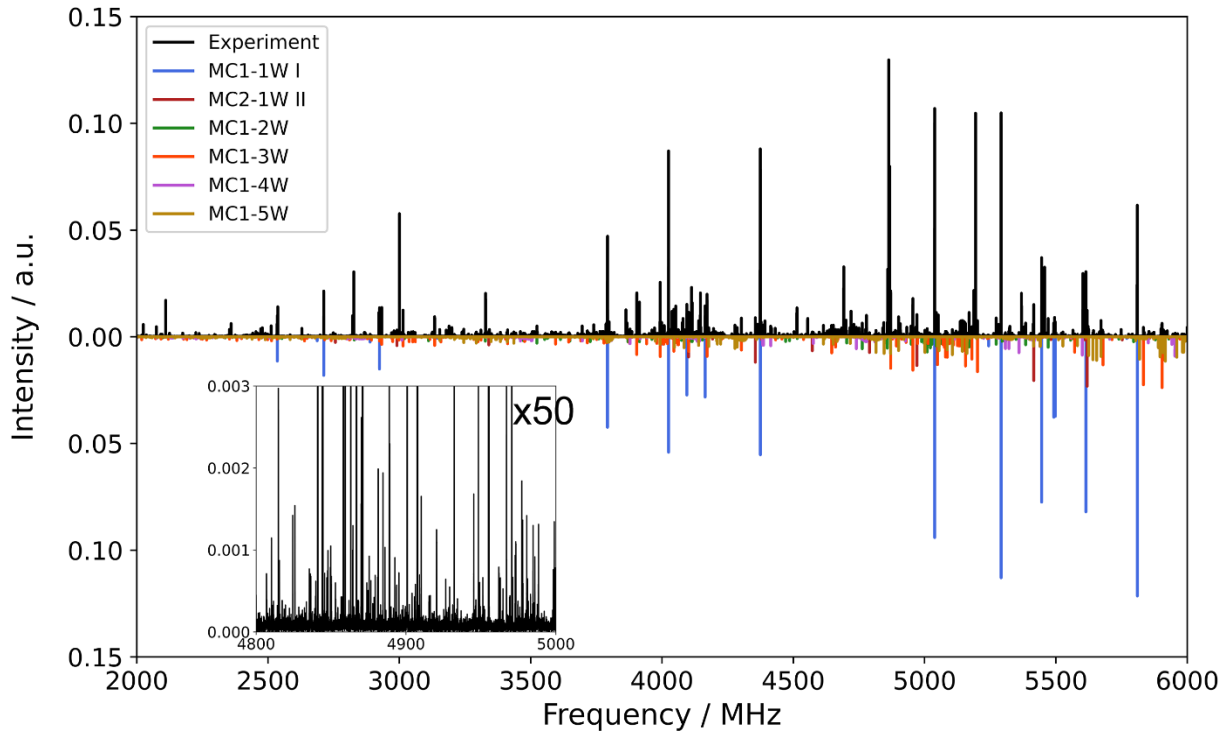

Figure 8.1. A 2-6 GHz broadband rotational spectrum of 3-methylcatechol and water.

Table 8.1. Spectroscopic parameters for the six experimentally assigned hydrates.

	MC1-1W I		**MC2-1W II**
	ortho	***para***	***ortho/para***
A / MHz	2284.111(15)	2287.3802(82)	1857.4623(85)
B / MHz	779.65840(82)	779.59914(45)	908.21870(86)
C / MHz	585.24242(57)	585.17256(32)	616.02400(91)
Δ_J / kHz	0.085(12)[a]	0.099(14)[a]	0.086(20)
Δ_{JK} / kHz	0.400(68)[a]	0.430(76)[a]	0.52(20)
Δ_K / kHz	-	-	[1.06][b]
δ_J / kHz	0.0200(61)[a]	0.0330(71)[a]	[0.0287][b]
δ_K / kHz	0.53(34)[a]	0.68(44)[a]	[0.261][b]
V_3 / kJ mol^{-1}	3.496(7)	3.498(4)	-
ε / rad	[0][c]	[0][c]	-
δ / rad	0.373(19)	0.368(11)	-
N	54	48	14
[d]σ / kHz	16.5	8.6	2.5
[e]|μ| / D	μ_a, no μ_b or μ_c	μ_a, no μ_b or μ_c	μ_a, no μ_b or μ_c
	MC1-2W		**MC1-3W**
	ortho	***para***	***ortho/para***
A / MHz	1381.2415(12)	1381.44270(60)	1081.1073(13)
B / MHz	714.13657(72)	714.14090(63)	539.95111(62)
C / MHz	606.38818(80)	606.42010(40)	472.49592(47)
Δ_J / kHz	0.988(15)	0.927(12)	0.1217(69)
Δ_{JK} / kHz	-2.786(66)	-2.516(31)	0.108(47)
Δ_K / kHz	4.161(91)	3.820(90)	0.27(11)[a]
δ_J / kHz	-0.0312(85)	-0.0510(92)	0.0101(48)
δ_K / kHz	0.79(18)	-	-0.20091(91)[a]
V_3 / kJ mol^{-1}	3.563(1)	-	3.307(4)
ε / rad	[1.9843][b]	-	1.226(55)
δ / rad	-2.6688(21)	-	2.6443(81)
N	108	25	79
[d]σ / kHz	10.2	2.2	9.2
[e]|μ| / D	$\mu_a \approx \mu_b > \mu_c$	$\mu_a \approx \mu_b > \mu_c$	$\mu_a \approx \mu_b$, no μ_c
	MC1-4W	**MC1-5W**	
	ortho/para	***ortho/para***	
A / MHz	783.99055(84)	674.82282(95)	
B / MHz	481.04619(39)	443.58208(26)	

C / MHz	448.19688(38)	395.04652(32)
Δ_J / kHz	0.0387(49)	0.0544(34)
Δ_{JK} / kHz	0.193(26)	[-0.0036][b]
Δ_K / kHz	-0.053(37)	0.102(42)
δ_J / kHz	-0.0181(40)	[0.0013][b]
δ_K / kHz	0.0033(25)	[0.0780][b]
V_3 / kJ mol^{-1}	3.490(3)	3.530(5)
ε / rad	0.274(32)	0.0212(47)
δ / rad	2.783(11)	0.6572(78)
N	54	73
[d]σ / kHz	4.4	6.3
[e]|μ| / D	$\mu_b > \mu_a > \mu_c$	$\mu_a \approx \mu_b > \mu_c$

[a]Fixed to value from the A species fit. [b]Fixed to the theoretical value. [c]Fixed to zero in the fit. [d]Root mean square error of the fit. [e]Relative magnitudes of dipole moment components, estimated from signal strengths.

were determined using the nudged elastic band procedure[45,47] or the synchronous transit quasi-newton method[48] in ORCA 5.0.3[46] and Gaussian 16.

The transitions for MC1-1W I were strong enough such that we were able to assign all seven singly substituted ^{13}C isotopologues in natural abundance. The transition frequencies, with the quantum number assignments, and the corresponding spectroscopic parameters are presented in Tables F.19 and Table F.3 of Appendix F, respectively. Tables F.3-F.6, Appendix F, present the relevant spectroscopic parameters for the singly substituted $H_2{}^{18}O$ hydrates of MC1-1W I, MC2-1W II, MC1-2W, and MC1-3W, with their corresponding transition frequencies and quantum number assignments listed in Tables F.19-F.22, Appendix F. For the dihydrate, the doubly substituted $H_2{}^{18}O$ species was also fit to the experimental spectrum. For the trihydrate, the doubly and triply substituted $H_2{}^{18}O$ species were fit to the experimental spectrum. Using the ^{13}C and $H_2{}^{18}O$ isotopic data, we derived substitution structures using Kraitchman's[54] equations. The resulting structural parameters are presented in Table F.7 of Appendix F.

8.3.3. Spectroscopic Assignment

In the description of the analyses it is necessary to keep track of the different water molecules within the hydrates and we label them successively with Greek letters α (α′), β, γ, δ, and ε. α′ will be used to exclusively label the water in the second monohydrate species, MC2-1W II.

Monohydrate species

Two different conformers of the monohydrate were assigned to the rotational spectrum. The spectroscopic parameters for each monohydrate assignment are presented in Table 8.1. Monohydrate 1 corresponds to the global minimum structure, where the hydroxyl group in the first position is serving as the hydrogen bond donor species to the lone pair of the water molecule. The conformer of the monomer within MC1-1W I most closely resembles that that of the lowest energy monomer,[53] that is, the hydroxyl groups are pointing away from the methyl group. The experimental rotational constants and the theoretical rotational constants are in good agreement with each other (see Table F.1, Appendix F). MC2-1W II corresponds to the second lowest energy DFT refined CREST monomer structure at the ωB97XD/Jun-cc-pVTZ level. In monohydrate 2 the hydroxyl group in the second position is acting as the hydrogen bond donor to the lone pair of the water molecule. The monomer conformer within monohydrate 2 more closely resembles monomer 2, where the hydroxyl groups are both pointing towards the methyl group. The experimental rotational constants and the theoretical rotational constants for monohydrate 2 are also in good agreement with each other.

Dihydrate, Trihydrate, and Pentahydrate Species

Using the CREST results as an aid for experimental assignment we assigned one dihydrate, one trihydrate, and one pentahydrate to the experimental spectrum. Comparing the experimental dipole moment observations to the theoretical values for the conformers within a 5.0 kJ mol^{-1} energy window, we see that the global minimum structure for each respective hydrate best fits the experimental assignment at both levels of theory. The assignment is further supported by the percent differences between the theoretical and experimental rotational constants (Table F.1, Appendix F). The monomer subunit within the dihydrate, trihydrate, and pentahydrate species are similar to monohydrate 1, where the hydroxyl groups are pointing away from the methyl group.

Tetrahydrate species

One tetrahydrate was assigned to the experimental spectrum with the aid of the CREST results. The assignment of the experimental tetrahydrate to the theoretical conformer was quite challenging. Based on the percent differences of the rotational constants and the dipole moment components, four candidate structures stand out for each level of theory. Conformers 1-4 for the ωB97XD/Jun-

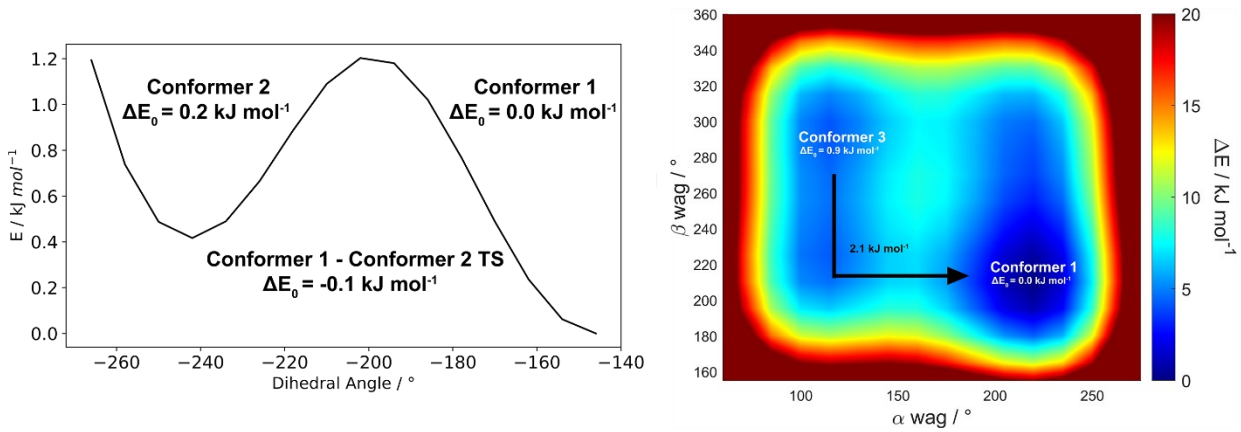

Figure 8.2. Potential energy scans of the water wagging motion for the water molecules in the tetrahydrate. In the left figure is a one-dimensional relaxed potential energy scan of the wagging motion of the δ water molecule. The trace was obtained by scanning over the C2-O2-O6-H9 dihedral angle. The negative energy of the transition state indicates that a large amplitude motion is present. The figure on the right shows a two-dimensional rigid potential energy scan of the wagging motion of the α and β water molecules, and was obtained by scanning over the H5-O4-O5-H8 and H3-O3-O4-H6 dihedral angles, respectively.

cc-pVTZ level of theory. Looking further at the structures of these conformers (Figure 8.4) we see that they differ slightly by the orientations of their α-, β-, and δ-water molecules, where each conformer can be connected by a wag of the non-bonded hydrogen atom in each water molecule. To capture this motion we scanned over the H5-O4-O5-H8, H3-O3-O4-H6, and C2-O2-O6-H9 dihedral angles for the α-, β-, and δ-water molecule, respectively, at the ωB97XD/Jun-cc-pVTZ level of theory; see Figure 8.3 for atom labelling. As the δ-water molecule is relatively isolated from the α- and β-water molecule we performed a one-dimensional relaxed potential energy scan for the δ-water molecule, with the α- and β-water molecules fixed in the position of the global minimum. The results yielded two unique minima, i.e., the global minimum structure and the second lowest energy tetrahydrate conformer at the ωB97XD/Jun-cc-pVTZ level of theory. The relative uncorrected energies for conformer 1, conformer 2, and the transition state which connects them are 0.0 kJ mol^{-1}, 0.4 kJ mol^{-1}, 1.2 kJ mol^{-1}, respectively, and 0.0 kJ mol^{-1}, 0.2 kJ mol^{-1}, -0.1 kJ mol^{-1}, respectively, after zero-point energy correction. The negative energy of the transition state indicates that the two minima are above the barrier, resulting in a large amplitude motion, and subsequently a weighted average of the two conformers in the experimental structure. For the α- and β-water molecules, a two-dimensional rigid potential energy scan was carried out, but now with the δ-water molecule fixed to the position of the molecule in the global minimum structure. Two minima were identified from this scan; the global minimum and conformer 3. The interconversion barrier height between the global minimum and conformer 3 is estimated to be 2.1

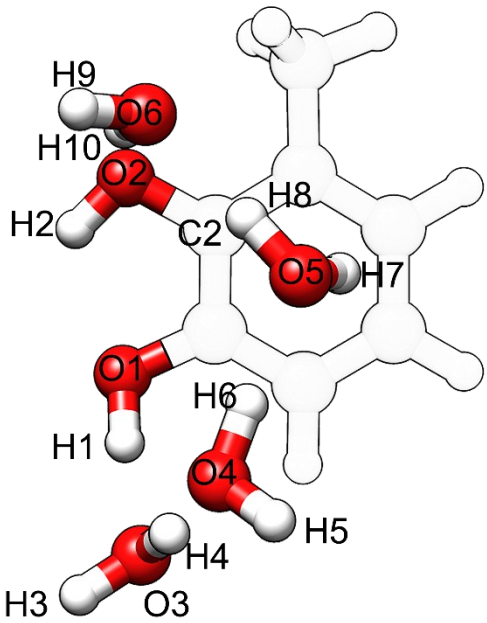

Figure 8.3. Atom numbering of the tetrahydrate species for the atoms involved the dihedral energy scans .

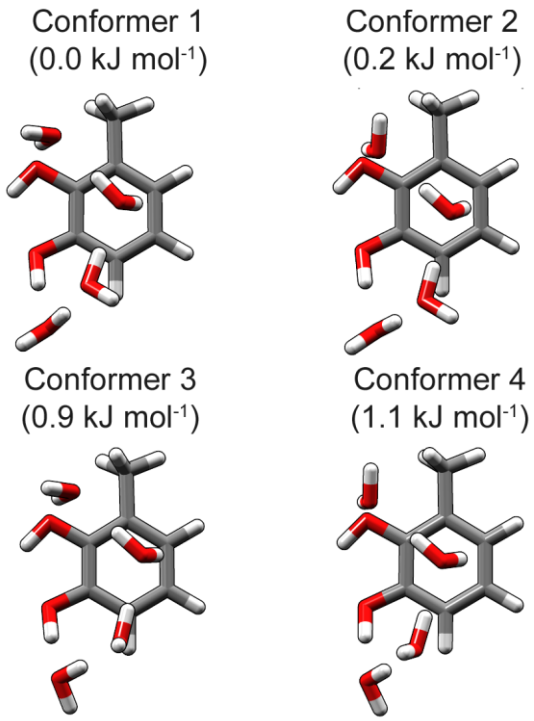

Figure 8.4. Four different conformations of the tetrahydrate species at the ωB97XD/Jun-cc-pVTZ level of theory.

kJ mol^{-1} at the ωB97XD/Jun-cc-pVTZ level of theory. Ruoff et al.[55] found that the upper barrier that permits relaxation to a lower energy conformer in a molecular expansion is about 5 kJ mol^{-1}. We expect therefore that conformer 3 will relax to the global minimum structure. As the δ-water molecule is far enough away from the α- and β-water molecules, such that the orientation of the δ-water will not have an effect on the orientation α- and β-water molecules we therefore assume conformer 4 will relax to conformer 2.

8.3.4. Wetting vs Droplet Aggregation

A qualitative evaluation of the hydrate conformers produced by the DFT refined CREST search reveals two principally different pathways of hydration for 3-methylcatechol. The first pathway, and the pathway observed in so many previous studies,[13–17,19,21,22,26–29,31–33,56] reveals preferential binding among the water molecules, where the solute molecule is acting as an anchor point for the formation of a droplet-like water cluster. We denote this pathway of aggregation as *droplet aggregation* (see Figure 8.5). In the second hydration pathway identified, the water molecules interact favourably with the solute molecule in addition to forming water – water hydrogen bonds.

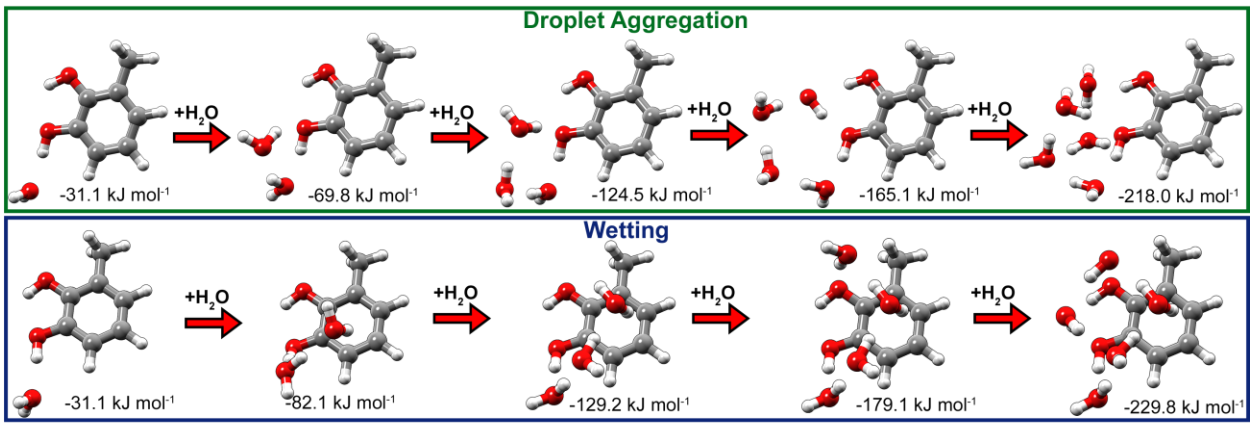

Figure 8.5. Two possible solvation pathways for 3-methylcatechol based on the conformer searches and electronic structure calculations. The wetting pathway was observed experimentally. The counterpoise-corrected complexation energies are listed for each hydrate.

In this instance, the hydration process does not result in the formation of a droplet-like structure, and instead leads to a wetting of the aromatic surface of the molecule; we denote this process as *wetting* (see Figure 8.5). The wetting pathway involves the water molecules hydrogen bonding to the hydroxyl groups as well as the aromatic ring and the methyl group of 3-methylcatechol.

To determine if the *droplet aggregation* or the *wetting* pathway is preferred in 3-methylcatechol, quantum theory of atoms-in-molecules (QTAIM)[49] and non-covalent interaction (NCI) analyses[50] were performed on the experimentally assigned hydrate conformers. These analyses allow for a visualization of the intermolecular interactions present within each complex, and assist in the determination of the favoured solvation pathway. The results from the NCI analyses are shown in Figure 8.6. For both monohydrates we see that the complexes are dominated by a strong hydrogen bond interaction between a hydroxyl group and the water oxygen lone pair, with additional dispersion interactions present with the neighbouring C-H and CH_3 group in monohydrate 1 and monohydrate 2, respectively. For the dihydrate, in addition to the strong hydrogen bond interactions between the hydroxyl group and water molecule, both water molecules are, very interestingly, now interacting with the aromatic system of 3-methylcatechol. Surprisingly, the water molecules are forming a π-interaction facilitated chain-like structure, which wets the aromatic ring of 3-methylcatechol rather than forming a self-aggregated cyclic structure, driven purely by water – water hydrogen-bond interactions. An NCI plot of the droplet aggregation conformers is given in Figure F.2 of Appendix F. Examining the intermolecular interactions further,

we observe a preference for an HO-H---π interaction, which can be seen between the β-water molecule and 3-methylcatechol, over a canonical hydrogen bond. This preference is especially remarkable when considering the close proximity of two hydrogen bonding capable species (hydroxyl groups) to the β-water molecule. The O-H---π interaction is also confirmed by the QTAIM analysis **(**Figure F.3, Appendix F) which shows a bonding interaction between the two moieties. It is also interesting to note that this interaction is so strongly favoured that the hydroxyl group is displaced by ~38° out-of-plane to better accommodate the interaction of the two water molecules with the aromatic ring. For the trihydrate, the π-facilitated hydration continues, as indicated by the blanket of dispersion interaction covering the face of 3-methylcatechol (Figure 8.6**)**. Analogous to the dihydrate, the water molecules are not arranged in a purely hydrogen bond driven cyclic structure, but instead adopt a π-interaction facilitated chain-like structure, which solvates the face of 3-methylcatechol. A preference for an HO-H---π interaction over a canonical hydrogen bond is also observed in the trihydrate, but instead for the β-water, the preference is now present for the γ-water. The HO-H---π interaction is also confirmed by the QTAIM analysis (Figure F.3, Appendix F). Since the aromatic surface of 3-methylcatechol is spatially limited in terms of the number of water molecules it can accommodate, one might hypothesize that in the δ water molecule in the tetrahydrate might finally begin to self-aggregate with the other three water molecules. To our surprise, this is not the case. The δ water molecule further extends the chain-like water structure to also include the solvation of the methyl group of 3-methylcatechol, rather than induce a water self-aggregated structure. For the pentahydrate, the ring is now fully saturated with water molecules, forcing the ε water molecule to insert itself into the only available position, i.e., directly above the hydroxyl group furthest away from the methyl group. Based on the NCI and QTAIM plots, the ε water molecule is forming three canonical hydrogen bonds, two with the solvent, and one with the solute, and is no longer forming a dispersion interaction with 3-methylcatechol. With the addition of the ε water molecule it appears that not only is the chain-like structure extended, but is now looping back to interact with the other part of the water chain.

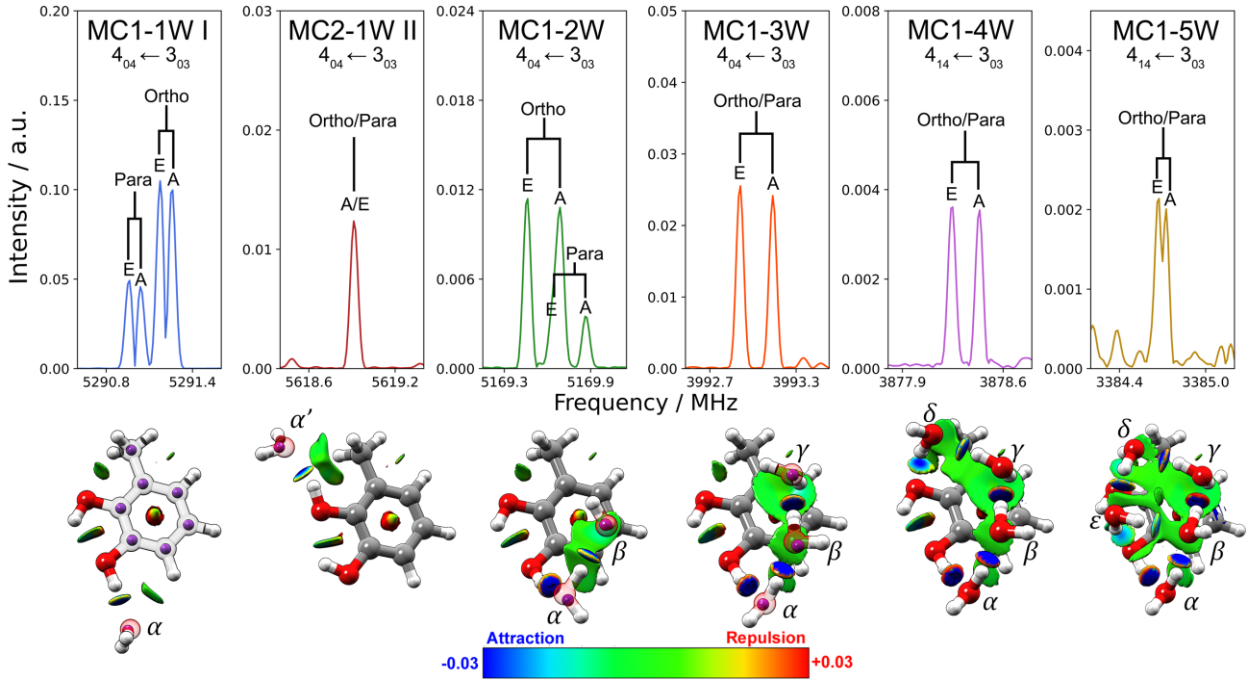

Figure 8.6. Top: Example transitions with characteristic tunneling splittings of the six hydrates assigned experimentally. The frequency span used is 1 MHz for all of them. Bottom: Optimized geometries of the five hydrates observed with the isosurfaces of the reduced electron density gradient from their NCI analyses. Blue (red) coloured surfaces represent attractive (repulsive) regions. The reduced electron density gradient was cut off at s = 0.7 a.u. The successively solvating water molecules within the hydrates are labelled with Greek letters. The purple inner spheres represent the Kraitchman derived atom coordinates obtained using the rotational constants of respective singly substituted isotopologues.

After a closer examination of each experimentally observed hydrate a pattern emerges and the preferred solvation pathway in 3-methylcatechol becomes clear. Based on the experimental assignments, supplemented with NCI and QTAIM analyses, the π-interaction facilitated chain-like structures of water in the hydrates are a clear indication that the *wetting* pathway is favoured over the more conventional *droplet aggregation* pathway. Indeed, not only is the preference for the *wetting* pathway confirmed by the aforementioned methods, but is also validated by the counterpoise corrected complexation energies presented in Figure 8.5, which contrasts the energies for each hydrate along the respective solvation pathways.

To further emphasize the uniqueness of the chain-like structures and the divergence from purely hydrogen bond dominated interactions, we make a comparison to pure water clusters, systems where the lowest energy conformers show a preference for cyclic structures.[57–60] Comparisons of the trihydrate and tetrahydrate, where this difference is most prominent, to the respective pure water clusters are shown in Figure 8.7. It is remarkable that the water molecules

appear to arrange themselves as if they have prior knowledge of the position of the next water molecule, almost as if they were following a preconceived blueprint of hydration. This is especially apparent when comparing the positions of the α, β, and γ water molecules in the trihydrate with their nearly identical relative positions in the tetrahydrate. Indeed, it appears as if the first three water molecules are arranging themselves to better accommodate the insertion of the fourth water molecule.

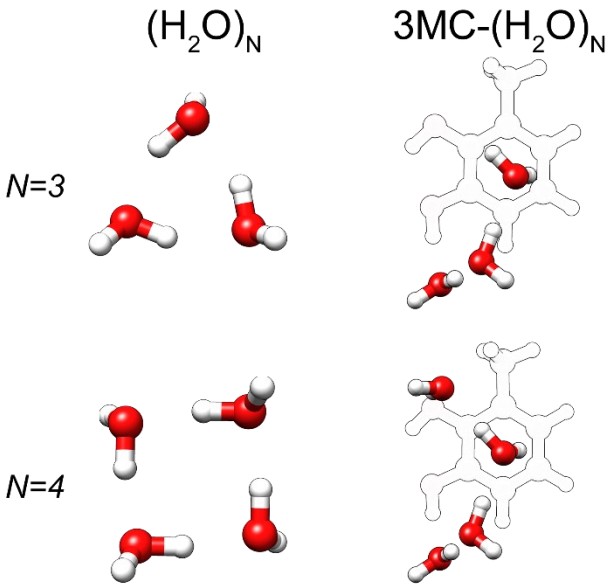

Figure 8.7. A comparison of the 3-methylcatecchol trihydrate and tetrahydrate to the corresponding pure water clusters.[26]

8.3.5. Splittings of Rotational Transitions

In addition to providing insights into the solvation process, the NCI plots can also help justify the observed splitting patterns, or lack thereof, in the experimental spectrum. These splitting patterns do not only provide information about the internal dynamics of the water complexes, but also validate the assignments of the hydrate structures to the experimental spectrum. For MC1-1W I and the MC1-2W species, the lines in the experimental spectrum are sufficiently resolved to observe splittings into quartet patterns. Splitting patterns are also observed for the trihydrate, tetrahydrate, and pentahydrate species, but here the rotational transitions are split into doublets with 1:1 intensity ratio. No splitting patterns are present in the spectrum of MC2-1W II. The development of the splitting patterns across the hydrates is shown in Figure 8.6. The observed

splitting patterns can be attributed to two types of tunnelling motions: the internal rotation of the methyl group (doublet with a 1:1 intensity ratio), and an interchange of the hydrogen atoms of a water molecule (doublet with a 3:1 intensity ratio). The specific intensity ratios are outcomes of nuclear spin statistics associated with the three (two) equivalent H-atoms in the methyl group (water molecule).

Doublets with a 3:1 intensity ratio are present for MC1-1W I and MC1-2W, where the theoretical proton exchange barrier heights were determined to be 3.5 kJ mol^{-1} and 3.7 kJ mol^{-1}, respectively. For MC1-3W, no such splitting was observed; the dispersion interaction between the γ-water molecule and π-system increases the tunnelling barrier sufficiently to make the doublet pattern unresolvable. The theoretical barrier height of the proton exchange was determined to be 7.2 kJ mol^{-1}. For the trihydrate we also assume that the proton exchange barriers for the α- and β-water molecules are too large for the splittings to be resolvable as they are locked into place by intermolecular interactions. The same situation applies to the MC1-4W, and MC1-5W, where now all four and five water molecules, respectively, are locked into place by intermolecular interactions. A 1:1 doublet splitting is observed for MC1-1W I, MC1-2W, MC1-3W, MC1-4W, and MC1-5W, with theoretical methyl internal rotation barrier heights of 3.5 kJ mol^{-1}, 3.5 kJ mol^{-1}, 3.3 kJ mol^{-1}, 3.6 kJ mol^{-1}, and 3.6 kJ mol^{-1}, respectively. These are in excellent agreement with the experimental barrier heights of 3.496(7) kJ mol^{-1}, 3.563(1) kJ mol^{-1}, 3.307(4) kJ mol^{-1}, 3.490(3) kJ mol^{-1}, and 3.530(5) kJ mol^{-1}, respectively.

8.4. Conclusions

We investigated the hydration pathway of 3-methylcatechol in a step-by-step fashion, using CP-FTMW spectroscopy and several theoretical techniques, including the CREST conformational searching algorithm, electronic structure calculations, and NCI and QTAIM analyses. From both the experimental assignments and theoretical analyses, the hydration of 3-methylcatechol proceeds via a dispersion-assisted *wetting* pathway, rather than the more common *droplet aggregation* pathway. The high-resolution capability of the CP-FTMW spectrometer allowed us to resolve spectral line splittings associated with methyl internal rotation and proton exchange tunnelling motions, whose analyses corroborate the picture of a solvent-wetted aromatic ring surface. Our investigation of the 3-methylcatechol-$(water)_N$ complexes does not only provide valuable insights into molecular solvation but also validates the ωB97XD/Jun-cc-pVTZ level of theory for

calculating structures, barriers to internal nuclear motions, and electronic charge distributions for this type of system, i.e., hydrates of organic aromatic molecules and is a nice example of the power of the CREST conformational search tool.

8.5. References

1 T. Schoennagel, J. K. Balch, H. Brenkert-Smith, P. E. Dennison, B. J. Harvey, M. A. Krawchuk, N. Mietkiewicz, P. Morgan, M. A. Moritz and R. Rasker, *Proc. Natl. Acad. Sci.*, 2017, **114**, 4582–4590.

2 C. Coeur-Tourneur, A. Tomas, A. Guilloteau, F. Henry, F. Ledoux, N. Visez, V. Riffault, J. C. Wenger and Y. Bedjanian, *Atmos. Environ.*, 2009, **43**, 2360–2365.

3 M. S. Rana and M. I. Guzman, *Environ. Sci. Technol.*, 2022, **56**, 15437–15448.

4 S. Frka, M. Sala, A. Kroflic, M. Hus, A. Cusak and I. Grgic, *Environ. Sci. Technol.*, 2016, **50**, 5526–5535.

5 R. J. Mayorga, Z. Zhao and H. Zhang, *Atmos. Environ.*, 2021, **244**, 117910.

6 D. Srivastava, T. V. Vu, S. Tong, Z. Shi and R. M. Harrison, *Npj Clim. Atmospheric Sci.*, 2022, **5**, 1–30.

7 C. Coeur-Tourneur, V. Foulon and M. Laréal, *Atmos. Environ.*, 2010, **44**, 852–857.

8 F. Hirata, *Molecular theory of solvation*, Springer Science & Business Media, 2003, vol. 24.

9 R. Zhang, *Science*, 2010, **328**, 1366–1367.

10 R. M. Stratt and M. Maroncelli, *J. Phys. Chem.*, 1996, **100**, 12981–12996.

11 R. J. Davey, S. L. Schroeder and J. H. Ter Horst, *Angew. Chem. Int. Ed.*, 2013, **52**, 2166–2179.

12 A. Rognoni, R. Conte and M. Ceotto, *Chem. Sci.*, 2021, **12**, 2060–2064.

13 T. B. C. Vu, I. Kalkman, W. Leo Meerts, Y. N. Svartsov, C. Jacoby and M. Schmitt, *J. Chem. Phys.*, 2008, **128**, 214311.

14 A. K. Huff, N. Love and K. R. Leopold, *J. Phys. Chem. A*, 2021, **125**, 8033–8046.

15 B. Ouyang, T. G. Starkey and B. J. Howard, *J. Phys. Chem. A*, 2007, **111**, 6165–6175.

16 L. C. Snoek, R. T. Kroemer and J. P. Simons, *Phys. Chem. Chem. Phys.*, 2002, **4**, 2130–2139.

17 C. Jacoby, W. Roth, M. Schmitt, C. Janzen, D. Spangenberg and K. Kleinermanns, *J. Phys. Chem. A*, 1998, **102**, 4471–4480.

18 W. Sun and M. Schnell, *Angew. Chem. Int. Ed.*, 2022, **61**, e202210819.

19 M. Chrayteh, E. Burevschi, D. Loru, T. R. Huet, P. Dréan and M. E. Sanz, *Phys. Chem. Chem. Phys.*, 2021, **23**, 20686–20694.

20 E. Burevschi, M. Chrayteh and D. Loru, 1.

21 J. V. Kildgaard, K. V. Mikkelsen, M. Bilde and J. Elm, *J. Phys. Chem. A*, 2018, **122**, 8549–8556.

22 R. Yoshino, K. Hashimoto, T. Omi, S. Ishiuchi and M. Fujii, *J. Phys. Chem. A*, 1998, **102**, 6227–6233.

23 R. L. Baldwin, *J. Mol. Biol.*, 2007, **371**, 283–301.

24 X. He, L. Fusti-Molnar, G. Cui and K. M. Merz Jr, *J. Phys. Chem. B*, 2009, **113**, 5290–5300.

25 J. Vondrášek, T. Kubař, F. E. Jenney Jr, M. W. Adams, M. Kožíšek, J. Černý, V. Sklenář and P. Hobza, *Chem. Eur. J.*, 2007, **13**, 9022–9027.

26 S. Baweja, S. Panchagnula, M. E. Sanz, L. Evangelisti, C. Pérez, C. West and B. H. Pate, *J. Phys. Chem. Lett.*, 2022, **13**, 9510–9516.

27 S. Blanco, P. Pinacho and J. C. López, *J. Phys. Chem. Lett.*, 2017, **8**, 6060–6066.

28 D. Loru, A. L. Steber, P. Pinacho, S. Gruet, B. Temelso, A. M. Rijs, C. Pérez and M. Schnell, *Phys. Chem. Chem. Phys.*, 2021, **23**, 9721–9732.

29 C. Perez, A. Krin, A. L. Steber, J. C. Lopez, Z. Kisiel and M. Schnell, *J. Phys. Chem. Lett.*, 2016, **7**, 154–160.

30 W. Li, M. M. Quesada-Moreno, P. Pinacho and M. Schnell, *Angew. Chem.*, 2021, **133**, 5383–5390.

31 C. Pérez, A. L. Steber, B. Temelso, Z. Kisiel and M. Schnell, *Angew. Chem.*, 2020, **132**, 8479–8483.

32 A. L. Steber, C. Pérez, B. Temelso, G. C. Shields, A. M. Rijs, B. H. Pate, Z. Kisiel and M. Schnell, *J. Phys. Chem. Lett.*, 2017, **8**, 5744–5750.

33 C. Pérez, J. L. Neill, M. T. Muckle, D. P. Zaleski, I. Peña, J. C. Lopez, J. L. Alonso and B. H. Pate, *Angew. Chem.*, 2015, **127**, 993–996.

34 G. G. Brown, B. C. Dian, K. O. Douglass, S. M. Geyer, S. T. Shipman and B. H. Pate, *Rev. Sci. Instrum.*, 2008, **79**, 053103.

35 N. A. Seifert, J. Thomas, W. Jäger and Y. Xu, *Phys. Chem. Chem. Phys.*, 2018, **20**, 27630–27637.

36 S. Grimme, C. Bannwarth and P. Shushkov, *J. Chem. Theory Comput.*, 2017, **13**, 1989–2009.

37 C. Bannwarth, S. Ehlert and S. Grimme, *J. Chem. Theory Comput.*, 2019, **15**, 1652–1671.

38 J.-D. Chai and M. Head-Gordon, *Phys. Chem. Chem. Phys.*, 2008, **10**, 6615–6620.

39 E. Papajak, J. Zheng, X. Xu, H. R. Leverentz and D. G. Truhlar, *J. Chem. Theory Comput.*, 2011, **7**, 3027–3034.

40 M. J. Frisch, G. W. Trucks, H. B. Schlegel, G. E. Scuseria, M. A. Robb, J. R. Cheeseman, G. Scalmani, V. Barone, G. A. Petersson, H. Nakatsuji, X. Li, M. Caricato, A. V. Marenich, J. Bloino, B. G. Janesko, R. Gomperts, B. Mennucci, H. P. Hratchian, J. V. Ortiz, A. F. Izmaylov, J. L. Sonnenberg, D. Williams-Young, F. Ding, F. Lipparini, F. Egidi, J. Goings, B. Peng, A. Petrone, T. Henderson, D. Ranasinghe, V. G. Zakrzewski, J. Gao, N. Rega, G. Zheng, W. Liang, M. Hada, M. Ehara, K. Toyota, R. Fukuda, J. Hasegawa, M. Ishida, T. Nakajima, Y. Honda, O. Kitao, H. Nakai, T. Vreven, K. Throssell, J. A. Montgomery Jr., J. E. Peralta, F. Ogliaro, M. J. Bearpark, J. J. Heyd, E. N. Brothers, K. N. Kudin, V. N. Staroverov, T. A. Keith, R. Kobayashi, J. Normand, K. Raghavachari, A. P. Rendell, J. C. Burant, S. S. Iyengar, J. Tomasi, M. Cossi, J. M. Millam, M. Klene, C. Adamo, R. Cammi, J. W. Ochterski, R. L. Martin, K. Morokuma, O. Farkas, J. B. Foresman and D. J. Fox, Gaussian 16, Gaussian Inc., Wallingford, CT, 2016.

41 T. Tsuneda and K. Hirao, *Wiley Interdiscip. Rev. Comput. Mol. Sci.*, 2014, **4**, 375–390.

42 T. Sato, T. Tsuneda and K. Hirao, *J. Chem. Phys.*, 2007, **126**, 234114.

43 Z. Chen, Y. Li, Z. He, Y. Xu and W. Yu, *J. Chem. Res.*, 2019, **43**, 293–303.

44 T. Sato, T. Tsuneda and K. Hirao, *J. Chem. Phys.*, 2005, **123**, 104307.

45 V. Ásgeirsson and H. Jónsson, *Handb. Mater. Model. Methods Theory Model.*, 2020, 689–714.

46 F. Neese, *Wiley Interdiscip. Rev. Comput. Mol. Sci.*, 2012, **2**, 73–78.

47 V. Ásgeirsson, B. O. Birgisson, R. Bjornsson, U. Becker, F. Neese, C. Riplinger and H. Jónsson, *J. Chem. Theory Comput.*, 2021, **17**, 4929–4945.
48 C. Peng and H. Bernhard Schlegel, *Isr. J. Chem.*, 1993, **33**, 449–454.
49 R. F. W. Bader, *Chem. Rev.*, 1991, **91**, 893–928.
50 E. R. Johnson, S. Keinan, P. Mori-Sánchez, J. Contreras-García, A. J. Cohen and W. Yang, *J. Am. Chem. Soc.*, 2010, **132**, 6498–6506.
51 T. A. Keith, AIMALL, TK Gristmill Software, Overland Park, KS, 2017.
52 T. Lu and F. Chen, *J. Comput. Chem.*, 2012, **33**, 580–592.
53 A. S. Hazrah, M. H. Al-Jabiri and W. Jäger, *J. Mol. Spectrosc.*, 2022, 111715.
54 J. Kraitchman, *Am. J. Phys.*, 1953, **21**, 17–24.
55 R. S. Ruoff, T. D. Klots, T. Emilsson and H. S. Gutowsky, *J. Chem. Phys.*, 1990, **93**, 3142–3150.
56 W. Sun and M. Schnell, *Angew. Chem.*
57 N. Pugliano and R. J. Saykally, *Science*, 1992, **257**, 1937–1940.
58 J. D. Cruzan, L. B. Braly, K. Liu, M. G. Brown, J. G. Loeser and R. J. Saykally, *Science*, 1996, **271**, 59–62.
59 K. Liu, M. G. Brown, J. D. Cruzan and R. J. Saykally, *Science*, 1996, **271**, 62–64.
60 F. N. Keutsch and R. J. Saykally, *Proc. Natl. Acad. Sci.*, 2001, **98**, 10533–10540.

9

Conclusions

Contents

9.1. Conclusions and Future Work · 163
9.2. References · 168

9.1 Conclusions and Future Work

In this thesis, I describe my work studying the conformational landscapes of nucleation precursors and the non-covalent interactions within them using a hybrid of experimental and computational techniques. To record the broadband rotational spectra of each molecular system studied in this thesis, I used a chirped pulse Fourier transform microwave (CP-FTMW) spectrometer, operating in the 2-6 GHz range. To assist in the assignment of the rotational quantum numbers for each molecular species to the experimentally measured transition frequencies, I utilized several computational techniques, such as the conformer-rotamer ensemble sampling tool (CREST)[1] and electronic structure calculations. Once I completed the assignment process, additional computational analyses are carried out to further characterize the molecular system of interest, providing insights into the physical properties of the respective molecules and molecular clusters such as binding energies. These additional computational analyses include, but are not limited to, the non-covalent interactions (NCI) analysis,[2,3] the quantum theory of atoms-in-molecules (QTAIM) analysis,[4] charge model 5 (CM5),[5] and the natural bond orbital (NBO) analysis.[6] Here I summarize some of my findings from each chapter, describe their impact on the field of aerosol science and our knowledge of non-covalent interactions, and how future work can be aimed to extend these studies.

In Chapter 3 I describe my CP-FTMW spectroscopic and computational study of two different isomers of naphthol monomer. In addition to the measurement of the parent species, all ^{13}C mono-substituted isotopologues of the *cis*- and trans-conformers of 1-naphthol and 2-naphthol

in their natural abundances were measured. The resulting data was then utilized to determine substitution and semi-experimental effective structures. The results from electronic structure calculations show that the OH group of *cis*-1-naphthol points ≈ 6 out of plane, which is consistent with the inertial defect data of *cis*- and *trans*-1-naphthol. The non-planarity of *cis*-1-naphthol is a result of a close-contact H-atom–H-atom interaction. This type of H–H interaction has been the subject of much controversy in the past and I provide an in-depth theoretical analysis of it in Chapter 3. The naphthol system is particularly well-suited for such analysis as it provides internal standards with its four different isomers. The theoretical methods used investigate this interaction include QTAIM, NCI, NBO, CM5, independent gradient model (IGM), and local vibrational mode analysis. I demonstrate that the close-contact H–H interaction is neither a purely attractive nor repulsive interaction, but rather a mixture of the two. In addition to advancing our understanding of non-covalent interactions, investigating the structure and thermodynamic stability of different conformations of naphthol monomer can facilitate the study naphthol containing aggregates. As polycyclic aromatic hydrocarbons (PAH) are known secondary organic aerosol (SOA) particle precursors,[7] the conformational and non-covalent data obtained from this study can be applied to other types of PAH systems. Future studies regarding naphthol monomers should focus on gaining a deeper understanding of H-H interactions. For example, substituting in electron-withdrawing atoms, such as halogens, at different positions around the ring can reveal whether such substitutions affect the balance between attractive and repulsive interactions in the H-H interaction.

In Chapter 4 I describe my experimental and theoretical studies of the most abundant dimer of 1-naphthol. This work was based on the findings from a previous study of phenol dimer which revealed that the dimer structure was held together by a mixture of dispersion and canonical hydrogen bonding between the monomer subunits. The objective of the 1-naphthol dimer study was to investigate how this intermolecular interplay is affected by the addition of a second aromatic ring. Interestingly, the 1-naphthol dimer features a V-shaped, partially overlapping π−π stacked structure with no canonical hydrogen bonds between the subunits. This structural assignment is in contradiction to an earlier study of the 1-naphthol dimer using UV-IR dip double resonance spectroscopy in the O−H stretch region, which assigns a π-stacked but also canonically hydrogen-bonded structure. An improved theoretical analysis was used to resolve this discrepancy and show that the new, V-shaped structure is also consistent with the previously measured UV-IR data. These new computational and spectroscopic results shed light on the complicated nature of

evaluating energetics and structures for larger, dispersion bound systems. This study not only provides insights into the aggregation process of PAH compounds, but also demonstrates the complications and nuances of π–π stacked systems. Future studies should investigate the 1-naphthol trimer to see if the π–π stacking trend persists, or if the bulkiness of three naphthalene rings trigger a rearrangement into a phenol trimer[8]-like arrangement, where once again canonical hydrogen bonding is favoured over π–π stacking.

In Chapter 5 I present findings from an experimental, rotational spectroscopic study of the α-pinene-water complex using CP-FTMW spectroscopy and computational chemistry. Experimentally, I assigned two conformers of α-pinene-water to the rotational spectrum; the anti- and syn-conformer. The water molecule in the anti-conformer is positioned above the π bond, while the water molecule in the syn-conformer is positioned below the π bond. Transitions were resolved enough to observe a splitting pattern into doublet components with a 3:1 intensity ratio. The splittings are associated with the ortho and para spin states of water, and is a result of a water tunnelling motion. Using the nudged elastic band method, it was revealed the tunneling path is composed of a rocking and wagging motion. NCI[2] and QTAIM[4,9] analyses revealed two bonding interactions, indicated by bond critical points (BCPs), between the water molecule and α-pinene for both experimental conformers. Using the experimental rotational constants, calculations were completed to see how the seasonal abundance of hydrated α-pinene compares to that of other atmospheric species. Despite the low relative abundance of the water complexes, it was found that due to the vast quantity of α-pinene released into the atmosphere a significant amount of water α-pinene water complexes are generated per year. With this knowledge, rate constants were then determined for the reaction of α-pinene and the α-pinene-water complexes with ozone, which shows that complexation with water can catalyze ozonolysis. As α-pinene is one of the most abundant biogenic volatile organic compounds (VOCs) released into the atmosphere, any changes to the initial reactivity could impact the formation of downstream products and subsequently SOA particle generation. In addition to the relevant atmospheric data, predicting the structures and energetics of pure hydrocarbon-water complexes poses more stringent challenges for electronic structure calculations and these systems are therefore important benchmarks for the modelling of weak interactions. Future studies should focus on studying these types of interactions with other hydrocarbons, such as β-pinene, to see if these interactions and reactivity trends can be extrapolated to other atmospherically relevant terpene systems.

In Chapter 6, I report my results of the experimental and theoretical study of (-)-carveol. The broadband rotational spectra of *cis*- and *trans*-(-)-carveol were recorded using a chirped pulse Fourier transform microwave spectrometer in the 2–6 GHz region. To aid in spectroscopic assignments a theoretical conformational search was carried out using a combination of a two dimensional potential energy scan, scanning over the isopropenyl and hydroxyl groups torsional angles, and the Conformer– Rotamer Ensemble Sampling Tool. Utilizing these results, a total of five conformers could be assigned in the spectra, two for *trans*- and three for *cis*-(-)-carveol. In both conformers of *trans*-carveol, the isopropenyl group is in an equatorial position and adopts the gauche conformation in one and the antiperiplanar conformation in the other, with the hydroxyl group in the axial position and adopting the antiperiplanar conformation in both. For *cis*-carveol the analogous conformers were found but with the hydroxyl in a equatorial position, in addition to an axial isopropenyl conformer. To interpret the experimental intensity patterns and examine conformational cooling effects, transition states were identified using the Synchronous Transit Quasi-Newton method. I found that most of the higher energy conformers cool out to the five experimentally observed ones and the others are too high in energy to be sufficiently populated in the molecular expansion for an experimental observation. To investigate the interesting preference for the axial position of the isopropenyl group in *cis*-(-)-carveol, which has not been seen before in monoterpenoids, non-covalent interactions and quantum theory of atoms-in-molecules analyses were carried out. These analyses reveal a hydrogen bonding interaction between the hydroxyl group and the isopropenyl π-system. A natural bond orbital analysis of the hydrogen bond allowed us to decompose the interaction into its constituent natural bond orbitals, and to quantify its strength. Although relatively weak, the hydrogen bond tips the balance towards the axial position of the isopropenyl group. This study not only provides insights the complexity of the conformational dynamics within carveol, a photooxidation product of limonene[10,11] but can also be extended to other monoterpene and monoterpenoid systems. This also lays a foundation for future studies examining nucleation precursors containing carveol, for example, molecular aggregates of carveol with water molecules.

In Chapter 7 and 8 I describe my experimental and theoretical studies of 3-methylcatechol monomer and 3-methylcatechol hydrated with up to five water molecules, respectively. The rotational spectrum of 3-methylcatechol monomer was measured using a chirped pulse Fourier transform microwave spectrometer, operating in the 2-6 GHz range. From the theoretical

calculations, three possible monomer conformers were identified which differ by the orientations of the hydroxyl groups. The measured rotational transitions could be assigned to two out of the three theoretical monomer conformers. A splitting pattern, consistent with methyl internal rotation, was observed exclusively for the lower energy monomer conformer. The transitions for the two assigned monomer conformers were strong enough such that all seven singly substituted ^{13}C isotopologues could be detected in natural abundance. Following the assignment, the rotational constants of the ^{13}C isotopologues were used in structure fitting procedures to obtain effective, substitution, and semi-experimental structures for the two assigned monomers. The resulting semi-experimental bond lengths and bond angles agree with those from electronic structure calculations to within ~1.0 %.[12] In Chapter 8 I describe the step-wise solvation of 3-methylcatechol with up to five water molecules using rotational spectroscopy, supplemented with various theoretical techniques, which were used to examine internal motions and the conformational space of each hydrate system. From the theoretical results, two different pathways of solvation emerge. The droplet pathway, which is extensively documented in literature, involves preferential binding among the water molecules, where the solute molecule serves as an anchor point for the formation of the cluster. The second pathway, very surprisingly involves a more favourable, dispersion assisted interaction between the water molecules and solute molecule, wetting the surface of 3-methylcatechol. The experimentally assigned conformers do indeed follow this wetting pathway, and is interestingly one of the first reports of this preference. By examining the experimental splitting pattern, the assignments of each hydrate conformation are further validated. Climate change and its damaging environmental effects has been shown in numerous modelling and field studies,[13–16] which includes a dramatic increase in average temperature readings across the globe. As a consequence of the elevated global temperature, there has been a substantial increase in the frequency and size of biomass burning.[17] which releases complex mixtures of organic molecules into the atmosphere, including 3-methylcatechol.[18] When released into the atmosphere, 3-methylcatechol can be photo-oxidized by species such as ozone[19], or nucleate with other atmospheric species to form secondary organic aerosol particles.[20] Water being one such species, and also one of the most abundant species in the atmosphere, may aggregate with 3-methylcatchol non-covalently to form nucleation precursors. The studies in Chapters 7 and 8 provide valuable insights into the early phases of nucleation, which can be used as benchmark data for existing nucleation theories, such as classical nucleation theory.[21] Future research should focus on

investigating higher-order 3-methylcatechol hydrates to determine whether this solvation pathway is unique to 3-methylcatechol or is also observed with other substituted catechol species.

Aerosol science is an increasingly interdisciplinary field that encompasses various scientific disciplines, including toxicology, physics, and chemistry. In general, scientists have long sought to better understand the transition of molecules into macroscopic phases of matter, which includes the transition of molecules to aerosol particles. To further our understanding of this transition from the molecular to macroscopic regime, it is beneficial to understand the early phases of nucleation. However, the conformational flexibility of the molecular clusters in the early phases of nucleation makes elucidating their structure challenging. Fortunately, advances in experimental and computational technologies have made it more feasible to study these early phases of nucleation and deduce the structure of the aggregates using techniques such as CP-FTMW spectroscopy and computational chemistry. In this report, I present my findings on atmospherically relevant molecules and their respective molecular-scale complexities. The data reported herein not only provides valuable benchmark data for the development of computational chemistry and nucleation theories but also offers insights into the nucleation process at the molecular scale.

9.2. References

1 P. Pracht, F. Bohle and S. Grimme, *Phys. Chem. Chem. Phys.*, 2020, **22**, 7169–7192.

2 J. Contreras-García, E. R. Johnson, S. Keinan, R. Chaudret, J.-P. Piquemal, D. N. Beratan and W. Yang, *J. Chem. Theory Comput.*, 2011, **7**, 625–632.

3 E. R. Johnson, S. Keinan, P. Mori-Sánchez, J. Contreras-García, A. J. Cohen and W. Yang, *J. Am. Chem. Soc.*, 2010, **132**, 6498–6506.

4 R. F. W. Bader, *Chem. Rev.*, 1991, **91**, 893–928.

5 A. V. Marenich, S. V. Jerome, C. J. Cramer and D. G. Truhlar, *J. Chem. Theory Comput.*, 2012, **8**, 527–541.

6 E. D. Glendening, C. R. Landis and F. Weinhold, *J. Comput. Chem.*, 2013, **34**, 1429–1437.

7 A. W. H. Chan, K. E. Kautzman, P. S. Chhabra, J. D. Surratt, M. N. Chan, J. D. Crounse, A. Kürten, P. O. Wennberg, R. C. Flagan and J. H. Seinfeld, *Atmospheric Chem. Phys.*, 2009, **9**, 3049–3060.

8 N. A. Seifert, A. L. Steber, J. L. Neill, C. Pérez, D. P. Zaleski, B. H. Pate and A. Lesarri, *Phys. Chem. Chem. Phys.*, 2013, **15**, 11468–11477.

9 K. E. Laidig and R. F. Bader, *J. Chem. Phys.*, 1990, **93**, 7213–7224.

10 F. M. N. Nunes, M. C. C. Veloso, P. A. de P. Pereira and J. B. de Andrade, *Atmos. Environ.*, 2005, **39**, 7715–7730.

11 T. E. Graedel, *Rev. Geophys.*, 1979, **17**, 937–947.

12 A. S. Hazrah, M. H. Al-Jabiri and W. Jäger, *J. Mol. Spectrosc.*, 2022, **390**, 111715.

13 E. Kalnay, M. Kanamitsu, R. Kistler, W. Collins, D. Deaven, L. Gandin, M. Iredell, S. Saha, G. White and J. Woollen, *Bull. Am. Meteorol. Soc.*, 1996, **77**, 437–472.

14 J. W. Hurrell, *Science*, 1995, **269**, 676–679.

15 C. Parmesan and G. Yohe, *nature*, 2003, **421**, 37–42.

16 C. D. Thomas, A. Cameron, R. E. Green, M. Bakkenes, L. J. Beaumont, Y. C. Collingham, B. F. Erasmus, M. F. De Siqueira, A. Grainger and L. Hannah, *Nature*, 2004, **427**, 145–148.

17 T. Schoennagel, J. K. Balch, H. Brenkert-Smith, P. E. Dennison, B. J. Harvey, M. A. Krawchuk, N. Mietkiewicz, P. Morgan, M. A. Moritz and R. Rasker, *Proc. Natl. Acad. Sci.*, 2017, **114**, 4582–4590.

18 M. Asmadi, H. Kawamoto and S. Saka, *J. Anal. Appl. Pyrolysis*, 2011, **92**, 88–98.

19 J. Sun, B. Wei, Q. Mei, Z. An, X. Wang and M. He, *Chem. Eng. J.*, 2019, **358**, 456–466.

20 C. Coeur-Tourneur, A. Tomas, A. Guilloteau, F. Henry, F. Ledoux, N. Visez, V. Riffault, J. C. Wenger and Y. Bedjanian, *Atmos. Environ.*, 2009, **43**, 2360–2365.

21 V. I. Kalikmanov, in *Nucleation theory*, Springer, 2012, pp. 17–41.

Bibliography

1 U. Pöschl, *Angew. Chem. Int. Ed.*, 2005, **44**, 7520–7540.

2 D. Rosenfeld, S. Sherwood, R. Wood and L. Donner, *Science*, 2014, **343**, 379–380.

3 J. Sun and P. A. Ariya, *Atmos. Environ.*, 2006, **40**, 795–820.

4 R. J. Charlson, J. E. Lovelock, M. O. Andreae and S. G. Warren, *Nature*, 1987, **326**, 655–661.

5 C. Tomasi and A. Lupi, *Atmospheric Aerosols Life Cycles Eff. Air Qual. Clim.*, 2017, 1–86.

6 V. A. Isidorov, I. G. Zenkevich and B. V. Ioffe, *Atmospheric Environ. 1967*, 1985, **19**, 1–8.

7 K. Nikolaou, P. Masclet and G. Mouvier, *Sci. Total Environ.*, 1984, **32**, 103–132.

8 V. A. Lanz, A. S. H. Prévôt, M. R. Alfarra, S. Weimer, C. Mohr, P. F. DeCarlo, M. F. D. Gianini, C. Hueglin, J. Schneider and O. Favez, *Atmospheric Chem. Phys.*, 2010, **10**, 10453–10471.

9 R. Zhang, A. F. Khalizov, J. Pagels, D. Zhang, H. Xue and P. H. McMurry, *Proc. Natl. Acad. Sci.*, 2008, **105**, 10291–10296.

10 W. Li, L. Shao, D. Zhang, C.-U. Ro, M. Hu, X. Bi, H. Geng, A. Matsuki, H. Niu and J. Chen, *J. Clean. Prod.*, 2016, **112**, 1330–1349.

11 E. Andrews, P. J. Sheridan, J. A. Ogren, D. Hageman, A. Jefferson, J. Wendell, A. Alástuey, L. Alados-Arboledas, M. Bergin and M. Ealo, *Bull. Am. Meteorol. Soc.*, 2019, **100**, 123–135.

12 K. Adachi, S. H. Chung and P. R. Buseck, *J. Geophys. Res. Atmospheres*.

13 Y. F. Cheng, M. Berghof, R. M. Garland, A. Wiedensohler, B. Wehner, T. Müller, H. Su, Y. H. Zhang, P. Achtert and A. Nowak, *J. Geophys. Res. Atmospheres*.

14 E. G. Schnitzler, A. Dutt, A. M. Charbonneau, J. S. Olfert and W. Jäger, *Environ. Sci. Technol.*, 2014, **48**, 14309–14316.

15 G. Saliba, R. Subramanian, R. Saleh, A. T. Ahern, E. M. Lipsky, A. Tasoglou, R. C. Sullivan, J. Bhandari, C. Mazzoleni and A. L. Robinson, *Aerosol Sci. Technol.*, 2016, **50**, 1264–1276.

16 J. H. Kroll, N. L. Ng, S. M. Murphy, R. C. Flagan and J. H. Seinfeld, *Environ. Sci. Technol.*, 2006, **40**, 1869–1877.

17 J. H. Kroll and J. H. Seinfeld, *Atmos. Environ.*, 2008, **42**, 3593–3624.

18 S. N. Pandis, R. A. Harley, G. R. Cass and J. H. Seinfeld, *Atmospheric Environ. Part Gen. Top.*, 1992, **26**, 2269–2282.

19 R. Zhang, *Science*, 2010, **328**, 1366–1367.

20 J. Zhao, A. Khalizov, R. Zhang and R. McGraw, *J. Phys. Chem. A*, 2009, **113**, 680–689.

21 C. Li and R. Signorell, *J. Aerosol Sci.*, 2021, **153**, 105676.

22 V. I. Kalikmanov, in *Nucleation theory*, Springer, 2012, pp. 17–41.

23 A. B. Nadykto, A. Al Natsheh, F. Yu, K. V. Mikkelsen and J. Herb, *Adv. Quantum Chem.*, 2008, **55**, 449–478.

24 A. Afzalifar, G. C. Shields, V. R. Fowler and R. H. Ras, *J. Phys. Chem. Lett.*, 2022, **13**, 8038–8046.

25 N. A. Seifert, A. S. Hazrah and W. Jäger, *J. Phys. Chem. Lett.*, 2019, **10**, 2836–2841.

26 G. B. Park and R. W. Field, *J. Chem. Phys.*, 2016, **144**, 200901.

27 T. Shou-Yuan, X. Zhi-Ning, F. Yu-Jie and G. Qian, *Chin. J. Anal. Chem.*, 2008, **36**, 1145–1151.

28 M. Saeki, S. Ishiuchi, M. Sakai and M. Fujii, *J. Phys. Chem. A*, 2007, **111**, 1001–1005.

29 N. Dam, C. Liedenbaum, S. Stolte and J. Reuss, *Chem. Phys. Lett.*, 1987, **136**, 73–80.

30 W. Kohn, A. D. Becke and R. G. Parr, *J. Phys. Chem.*, 1996, **100**, 12974–12980.

31 Chr. Møller and M. S. Plesset, *Phys. Rev.*, 1934, **46**, 618–622.

32 R. J. Bartlett and M. Musiał, *Rev. Mod. Phys.*, 2007, **79**, 291.

33 E. G. Schnitzler and W. Jäger, *Phys. Chem. Chem. Phys.*, 2014, **16**, 2305–2314.

34 M. E. Erupe, D. R. Benson, J. Li, L.-H. Young, B. Verheggen, M. Al-Refai, O. Tahboub, V. Cunningham, F. Frimpong and A. A. Viggiano, *J. Geophys. Res. Atmospheres*.

35 E. G. Moody and L. R. Collins, *Aerosol Sci. Technol.*, 2003, **37**, 403–424.

36 S. Zhang, S. Li, A. Ning, L. Liu and X. Zhang, *Phys. Chem. Chem. Phys.*, 2022, **24**, 13651–13660.

37 A. S. Hazrah, S. Nanayakkara, N. A. Seifert, E. Kraka and W. Jäger, *Phys. Chem. Chem. Phys.*, 2022, **24**, 3722–3732.

38 A. W. H. Chan, K. E. Kautzman, P. S. Chhabra, J. D. Surratt, M. N. Chan, J. D. Crounse, A. Kürten, P. O. Wennberg, R. C. Flagan and J. H. Seinfeld, *Atmospheric Chem. Phys.*, 2009, **9**, 3049–3060.

39 N. E. Stewart, R. E. Millemann and W. P. Breese, *Trans. Am. Fish. Soc.*, 1967, **96**, 25–30.

40 A. Zare, J. H. Christensen, A. Gross, P. Irannejad, M. Glasius and J. Brandt, *Atmospheric Chem. Phys.*, 2014, **14**, 2735–2756.

41 A. S. Hazrah, M. Al-Jabiri, R. Speelman and W. Jäger, *Phys. Chem. Chem. Phys.*, 2021, **23**, 15159–15168.

42 F. M. N. Nunes, M. C. C. Veloso, P. A. de P. Pereira and J. B. de Andrade, *Atmos. Environ.*, 2005, **39**, 7715–7730.

43 T. E. Graedel, *Rev. Geophys.*, 1979, **17**, 937–947.

44 A. S. Hazrah, M. H. Al-Jabiri and W. Jäger, *J. Mol. Spectrosc.*, 2022, **390**, 111715.

45 M. S. Ganewatta, H. N. Lokupitiya and C. Tang, *Polymers*, 2019, **11**, 1176.

46 M. Asmadi, H. Kawamoto and S. Saka, *J. Anal. Appl. Pyrolysis*, 2011, **92**, 88–98.

47 A. N. Glazer and H. Nikaido, *Microbial biotechnology: fundamentals of applied microbiology*, Cambridge University Press, 2007.

48 C. H. Townes and A. L. Schawlow, *Microwave spectroscopy*, Courier Corporation, 2013.

49 T. J. Balle and W. H. Flygare, *Rev. Sci. Instrum.*, 1981, **52**, 33–45.

50 G. G. Brown, B. C. Dian, K. O. Douglass, S. M. Geyer, S. T. Shipman and B. H. Pate, *Rev. Sci. Instrum.*, 2008, **79**, 053103.

51 P. Pracht, F. Bohle and S. Grimme, *Phys. Chem. Chem. Phys.*, 2020, **22**, 7169–7192.

52 J. Contreras-García, E. R. Johnson, S. Keinan, R. Chaudret, J.-P. Piquemal, D. N. Beratan and W. Yang, *J. Chem. Theory Comput.*, 2011, **7**, 625–632.

53 E. R. Johnson, S. Keinan, P. Mori-Sánchez, J. Contreras-García, A. J. Cohen and W. Yang, *J. Am. Chem. Soc.*, 2010, **132**, 6498–6506.

54 W. Gordy, R. L. Cook and A. Weissberger, *Microwave molecular spectra*, Wiley New York, 1984, vol. 18.

55 H. M. Pickett, *SPFIT/SPCAT package*, 2009.

56 H. Hartwig and H. Dreizler, *Z. Für Naturforschung A*, 1996, **51**, 923–932.

57 M. Toyama, T. Oka and Y. Morino, *J. Mol. Spectrosc.*, 1964, **13**, 193–213.

58 J. K. Watson, *J. Chem. Phys.*, 1967, **46**, 1935–1949.
59 J. P. Valleau and J. M. Deckers, *Can. J. Chem.*, 1965, **43**, 6–17.
60 N. Borho and Y. Xu, *Phys. Chem. Chem. Phys.*, 2007, **9**, 4514–4520.
61 N. A. Seifert, I. A. Finneran, C. Perez, D. P. Zaleski, J. L. Neill, A. L. Steber, R. D. Suenram, A. Lesarri, S. T. Shipman and B. H. Pate, *J. Mol. Spectrosc.*, 2015, **312**, 13–21.
62 F. Xie, N. A. Seifert, M. Heger, J. Thomas, W. Jäger and Y. Xu, *Phys. Chem. Chem. Phys.*, 2019, **21**, 15408–15416.
63 R. S. Ruoff, T. D. Klots, T. Emilsson and H. S. Gutowsky, *J. Chem. Phys.*, 1990, **93**, 3142–3150.
64 H. Nyquist, *Trans. Am. Inst. Electr. Eng.*, 1928, **47**, 617–644.
65 C. E. Shannon, *Proc. IRE*, 1949, **37**, 10–21.
66 A. Barducci, M. Bonomi and M. Parrinello, *Wiley Interdiscip. Rev. Comput. Mol. Sci.*, 2011, **1**, 826–843.
67 S. Grimme, *J. Chem. Theory Comput.*, 2019, **15**, 2847–2862.
68 S. Grimme, C. Bannwarth and P. Shushkov, *J. Chem. Theory Comput.*, 2017, **13**, 1989–2009.
69 C. Bannwarth, S. Ehlert and S. Grimme, *J. Chem. Theory Comput.*, 2019, **15**, 1652–1671.
70 C. Dykstra, G. Frenking, K. Kim and G. Scuseria, *Theory and applications of computational chemistry: the first forty years*, Elsevier, 2011.
71 W. Kohn and L. J. Sham, *Phys. Rev.*, 1965, **140**, A1133.
72 M. Orio, D. A. Pantazis and F. Neese, *Photosynth. Res.*, 2009, **102**, 443–453.
73 C. Lee, W. Yang and R. G. Parr, *Phys. Rev. B*, 1988, **37**, 785.
74 A. D. Becke, *Phys. Rev. A*, 1988, **38**, 3098.
75 J. Tirado-Rives and W. L. Jorgensen, *J. Chem. Theory Comput.*, 2008, **4**, 297–306.
76 J. Toulouse, F. Colonna and A. Savin, *Phys. Rev. A*, 2004, **70**, 062505.
77 S. Grimme, J. Antony, S. Ehrlich and H. Krieg, *J. Chem. Phys.*, 2010, **132**, 154104.
78 S. Grimme, S. Ehrlich and L. Goerigk, *J. Comput. Chem.*, 2011, **32**, 1456–1465.
79 H. Shindy, *Chem Int*, 2016, **2**, 2016.
80 C. Sams, *Toxics*, 2017, **5**, 3.
81 D. L. Sudakin, D. L. Stone and L. Power, *Curr. Top. Toxicol.*, 2011, **7**, 13.
82 R. Knochenmuss and S. Leutwyler, *J. Chem. Phys.*, 1989, **91**, 1268–1278.

83 T. Droz, R. Knochenmuss and S. Leutwyler, *J. Chem. Phys.*, 1990, **93**, 4520–4532.

84 S. Maity, R. Knochenmuss, C. Holzer, G. Féraud, J. Frey, W. Klopper and S. Leutwyler, *J. Chem. Phys.*, 2016, **145**, 164304.

85 S. Maity, P. Ottiger, F. A. Balmer, R. Knochenmuss and S. Leutwyler, *J. Chem. Phys.*, 2016, **145**, 244314.

86 R. Knochenmuss, S. Maity, F. Balmer, C. Müller and S. Leutwyler, *J. Chem. Phys.*, 2018, **149**, 034306.

87 R. Knochenmuss, R. K. Sinha and S. Leutwyler, *J. Chem. Phys.*, 2018, **148**, 134302.

88 M. Schütz, T. Bürgi, S. Leutwyler and T. Fischer, *J. Chem. Phys.*, 1993, **99**, 1469–1481.

89 C. Wickleder, D. Henseler and S. Leutwyler, *J. Chem. Phys.*, 2002, **116**, 1850–1857.

90 R. Knochenmuss, R. K. Sinha, A. Poblotzki, T. Den and S. Leutwyler, *J. Chem. Phys.*, 2018, **149**, 204311.

91 R. Knochenmuss, R. K. Sinha and S. Leutwyler, *J. Chem. Phys.*, 2019, **150**, 234303.

92 R. Yoshino, K. Hashimoto, T. Omi, S. Ishiuchi and M. Fujii, *J. Phys. Chem. A*, 1998, **102**, 6227–6233.

93 R. D. Knochenmuss and D. E. Smith, *J. Chem. Phys.*, 1994, **101**, 7327–7336.

94 S. J. Humphrey and D. W. Pratt, *J. Chem. Phys.*, 1996, **104**, 8332–8340.

95 J. R. Johnson, K. D. Jordan, D. F. Plusquellic and D. W. Pratt, *J. Chem. Phys.*, 1990, **93**, 2258–2273.

96 C. J. Whitham, R. J. Jackson and J. M. Brown, *J. Mol. Spectrosc.*, 1999, **195**, 172–176.

97 M. Goubet, M.-A. Martin-Drumel, F. Réal, V. Vallet and O. Pirali, *J. Phys. Chem. A*, 2020, **124**, 4484–4495.

98 C. F. Matta, J. Hernández-Trujillo, T.-H. Tang and R. F. Bader, *Chem. Eur. J.*, 2003, **9**, 1940–1951.

99 C. F. Matta, in *Hydrogen Bonding—New Insights*, Springer, 2006, pp. 337–375.

100 R. F. Bader, *J. Phys. Chem. A*, 2009, **113**, 10391–10396.

101 N. K. Monteiro and C. L. Firme, *J. Phys. Chem. A*, 2014, **118**, 1730–1740.

102 S. Grimme, C. Mück-Lichtenfeld, G. Erker, G. Kehr, H. Wang, H. Beckers and H. Willner, *Angew. Chem. Int. Ed.*, 2009, **48**, 2592–2595.

103 J. Poater, M. Solà and F. M. Bickelhaupt, *Chem. Eur. J.*, 2006, **12**, 2889–2895.

104 J. Kraitchman, *Am. J. Phys.*, 1953, **21**, 17–24.

105 R. F. W. Bader, *Chem. Rev.*, 1991, **91**, 893–928.

106 C. Lefebvre, G. Rubez, H. Khartabil, J.-C. Boisson, J. Contreras-García and E. Hénon, *Phys. Chem. Chem. Phys.*, 2017, **19**, 17928–17936.

107 C. Lefebvre, H. Khartabil, J.-C. Boisson, J. Contreras-García, J.-P. Piquemal and E. Hénon, *ChemPhysChem*, 2018, **19**, 724–735.

108 M. Ponce-Vargas, C. Lefebvre, J.-C. Boisson and E. Hénon, *J. Chem. Inf. Model.*, 2020, **60**, 268–278.

109 J. Klein, H. Khartabil, J.-C. Boisson, J. Contreras-García, J.-P. Piquemal and E. Hénon, *J. Phys. Chem. A*, 2020, **124**, 1850–1860.

110 E. Kraka, W. Zou and Y. Tao, *Wiley Interdiscip. Rev. Comput. Mol. Sci.*, 2020, **10**, e1480.

111 Z. Konkoli and D. Cremer, *Int. J. Quantum Chem.*, 1998, **67**, 1–9.

112 Z. Konkoli and D. Cremer, *Int. J. Quantum Chem.*, 1998, **67**, 29–40.

113 Z. Konkoli, J. A. Larsson and D. Cremer, *Int. J. Quantum Chem.*, 1998, **67**, 11–27.

114 E. Kraka, J. A. Larsson and D. Cremer, *Comput. Spectrosc. Grunenberg J Ed Wiley N. Y. NY USA*, 2010, 105–149.

115 D. Cremer, J. A. Larsson and E. Kraka, in *Theoretical and computational chemistry*, Elsevier, 1998, vol. 5, pp. 259–327.

116 A. V. Marenich, S. V. Jerome, C. J. Cramer and D. G. Truhlar, *J. Chem. Theory Comput.*, 2012, **8**, 527–541.

117 E. D. Glendening, C. R. Landis and F. Weinhold, *J. Comput. Chem.*, 2013, **34**, 1429–1437.

118 A. E. Reed and F. Weinhold, *J. Chem. Phys.*, 1983, **78**, 4066–4073.

119 M. J. Frisch, G. W. Trucks, H. B. Schlegel, G. E. Scuseria, M. A. Robb, J. R. Cheeseman, G. Scalmani, V. Barone, G. A. Petersson, H. Nakatsuji, X. Li, M. Caricato, A. V. Marenich, J. Bloino, B. G. Janesko, R. Gomperts, B. Mennucci, H. P. Hratchian, J. V. Ortiz, A. F. Izmaylov, J. L. Sonnenberg, D. Williams-Young, F. Ding, F. Lipparini, F. Egidi, J. Goings, B. Peng, A. Petrone, T. Henderson, D. Ranasinghe, V. G. Zakrzewski, J. Gao, N. Rega, G. Zheng, W. Liang, M. Hada, M. Ehara, K. Toyota, R. Fukuda, J. Hasegawa, M. Ishida, T. Nakajima, Y. Honda, O. Kitao, H. Nakai, T. Vreven, K. Throssell, J. A. Montgomery Jr., J. E. Peralta, F. Ogliaro, M. J. Bearpark, J. J. Heyd, E. N. Brothers, K. N. Kudin, V. N.

Staroverov, T. A. Keith, R. Kobayashi, J. Normand, K. Raghavachari, A. P. Rendell, J. C. Burant, S. S. Iyengar, J. Tomasi, M. Cossi, J. M. Millam, M. Klene, C. Adamo, R. Cammi, J. W. Ochterski, R. L. Martin, K. Morokuma, O. Farkas, J. B. Foresman and D. J. Fox, Gaussian 16, Gaussian Inc., Wallingford, CT, 2016.

120 A. D. Becke, *J. Chem. Phys.*, 1992, **96**, 2155–2160.

121 A. D. Becke and E. R. Johnson, *J. Chem. Phys.*, 2005, **123**, 154101.

122 F. Weigend and R. Ahlrichs, *Phys. Chem. Chem. Phys.*, 2005, **7**, 3297–3305.

123 T. A. Keith, AIMALL, TK Gristmill Software, Overland Park, KS, 2017.

124 T. Lu and F. Chen, *J. Comput. Chem.*, 2012, **33**, 580–592.

125 E. F. Pettersen, T. D. Goddard, C. C. Huang, G. S. Couch, D. M. Greenblatt, E. C. Meng and T. E. Ferrin, *J. Comput. Chem.*, 2004, **25**, 1605–1612.

126 W. Zou, Y. Tao, M. Freindorf, M. Makos, N. Verma and E. Kraka, *South. Methodist Univ.*

127 E. B. Wilson, J. C. Decius and P. C. Cross, *Molecular vibrations: the theory of infrared and Raman vibrational spectra*, Courier Corporation, 1980.

128 W. Zou and D. Cremer, *Chem. Eur. J.*, 2016, **22**, 4087–4099.

129 E. Kraka and M. Freindorf, .

130 M. Freindorf and E. Kraka, *J. Mol. Model.*, 2020, **26**, 1–15.

131 S. Yannacone, M. Freindorf, Y. Tao, W. Zou and E. Kraka, *Crystals*, 2020, **10**, 556.

132 A. A. Delgado, D. Sethio, I. Munar, V. Aviyente and E. Kraka, *J. Chem. Phys.*, 2020, **153**, 224303.

133 W. Zou, R. Kalescky, E. Kraka and D. Cremer, *J. Chem. Phys.*, 2012, **137**, 084114.

134 N. Verma, Y. Tao, W. Zou, X. Chen, X. Chen, M. Freindorf and E. Kraka, *Sensors*, 2020, **20**, 2358.

135 R. M. Badger, *J. Chem. Phys.*, 1934, **2**, 128–131.

136 N. A. Seifert, J. Thomas, W. Jäger and Y. Xu, *Phys. Chem. Chem. Phys.*, 2018, **20**, 27630–27637.

137 H. M. Pickett, *J. Mol. Spectrosc.*, 1991, **148**, 371–377.

138 R. D. Chirico, W. V. Steele and A. F. Kazakov, *J. Chem. Thermodyn.*, 2015, **86**, 106–115.

139 D. Schemmel and M. Schütz, *J. Chem. Phys.*, 2008, **129**, 07B615.

140 J.-D. Chai and M. Head-Gordon, *Phys. Chem. Chem. Phys.*, 2008, **10**, 6615–6620.

141 E. Papajak, J. Zheng, X. Xu, H. R. Leverentz and D. G. Truhlar, *J. Chem. Theory Comput.*, 2011, **7**, 3027–3034.

142 P. Pulay, W. Meyer and J. E. Boggs, *J. Chem. Phys.*, 1978, **68**, 5077–5085.

143 F. Pawłowski, P. Jørgensen, J. Olsen, F. Hegelund, T. Helgaker, J. Gauss, K. L. Bak and J. F. Stanton, *J. Chem. Phys.*, 2002, **116**, 6482–6496.

144 M. Piccardo, E. Penocchio, C. Puzzarini, M. Biczysko and V. Barone, *J. Phys. Chem. A*, 2015, **119**, 2058–2082.

145 M. K. Jahn, J.-U. Grabow, M. J. Travers, D. Wachsmuth, P. D. Godfrey and D. McNaughton, *Phys. Chem. Chem. Phys.*, 2017, **19**, 8970–8976.

146 T. Oka, *J. Mol. Struct.*, 1995, **352**, 225–233.

147 P. L. A. Popelier, F. M. Aicken and S. E. O'Brien, *Atoms in molecules*, Prentice Hall Manchester, 2000.

148 V. Tognetti and L. Joubert, *J. Phys. Chem. A*, 2011, **115**, 5505–5515.

149 R. Kalescky, E. Kraka and D. Cremer, *J. Phys. Chem. A*, 2014, **118**, 223–237.

150 D. Setiawan, E. Kraka and D. Cremer, *J. Org. Chem.*, 2016, **81**, 9669–9686.

151 J. Cioslowski and S. T. Mixon, *J. Am. Chem. Soc.*, 1992, **114**, 4382–4387.

152 E. T. Kool, *Annu. Rev. Biophys. Biomol. Struct.*, 2001, **30**, 1–22.

153 S. Marsili, R. Chelli, V. Schettino and P. Procacci, *Phys. Chem. Chem. Phys.*, 2008, **10**, 2673–2685.

154 Chelli Riccardo, Gervasio Francesco Luigi, Procacci Piero, and Schettino Vincenzo, *Proteins Struct. Funct. Bioinforma.*, 2004, **55**, 139–151.

155 E. H. Krenske and K. N. Houk, *Acc. Chem. Res.*, 2013, **46**, 979–989.

156 A. J. Neel, M. J. Hilton, M. S. Sigman and F. D. Toste, *Nature*, 2017, **543**, 637–646.

157 J. Hermann, D. Alfè and A. Tkatchenko, *Nat. Commun.*, 2017, **8**, 14052.

158 C. A. Hunter and J. K. M. Sanders, *J. Am. Chem. Soc.*, 1990, **112**, 5525–5534.

159 Grimme Stefan, *Angew. Chem. Int. Ed.*, 2008, **47**, 3430–3434.

160 C. R. Martinez and B. L. Iverson, *Chem. Sci.*, 2012, **3**, 2191–2201.

161 S. E. Wheeler and K. N. Houk, *J. Am. Chem. Soc.*, 2008, **130**, 10854–10855.

162 T. Ebata, T. Watanabe and N. Mikami, *J. Phys. Chem.*, 1995, **99**, 5761–5764.

163 M. Schmitt, M. Böhm, C. Ratzer, D. Krügler, K. Kleinermanns, I. Kalkman, G. Berden and W. L. Meerts, *Chemphyschem Eur. J. Chem. Phys. Phys. Chem.*, 2006, **7**, 1241–1249.

164 A. Weichert, C. Riehn and B. Brutschy, *J. Phys. Chem. A*, 2001, **105**, 5679–5691.

165 K. Fuke and K. Kaya, *Chem. Phys. Lett.*, 1983, **94**, 97–101.

166 K. Fuke and K. Kaya, *Chem. Phys. Lett.*, 1982, **91**, 311–314.

167 N. A. Seifert, A. L. Steber, J. L. Neill, C. Pérez, D. P. Zaleski, B. H. Pate and A. Lesarri, *Phys. Chem. Chem. Phys.*, 2013, **15**, 11468–11477.

168 G. G. Brown, B. C. Dian, K. O. Douglass, S. M. Geyer, S. T. Shipman and B. H. Pate, *Rev. Sci. Instrum.*, 2008, **79**, 053103.

169 C. D. Sherrill, *Acc. Chem. Res.*, 2013, **46**, 1020–1028.

170 M. Saeki, S. Ishiuchi, M. Sakai and M. Fujii, *J. Phys. Chem. A*, 2007, **111**, 1001–1005.

171 C. D. Carlson, N. A. Seifert, M. Heger, F. Xie, J. Thomas and Y. Xu, *J. Mol. Spectrosc.*, 2018, **351**, 62–67.

172 C. Pérez, S. Lobsiger, N. A. Seifert, D. P. Zaleski, B. Temelso, G. C. Shields, Z. Kisiel and B. H. Pate, *Chem. Phys. Lett.*, 2013, **571**, 1–15.

173 J. R. Johnson, K. D. Jordan, D. F. Plusquellic and D. W. Pratt, *J. Chem. Phys.*, 1990, **93**, 2258–2273.

174 N. A. Seifert, I. A. Finneran, C. Perez, D. P. Zaleski, J. L. Neill, A. L. Steber, R. D. Suenram, A. Lesarri, S. T. Shipman and B. H. Pate, *J. Mol. Spectrosc.*, 2015, **312**, 13–21.

175 S. Grimme, S. Ehrlich and L. Goerigk, *J. Comput. Chem.*, 2011, **32**, 1456–1465.

176 *GAUSSIAN 09*, Gaussian, Inc., Wallingford, CT.

177 S. F. Boys and F. Bernardi, *Mol. Phys.*, 1970, **19**, 553–566.

178 J. Thomas, N. A. Seifert, W. Jäger and Y. Xu, *Angew. Chem. Int. Ed.*, 2017, **56**, 6289–6293.

179 A. E. DePrince and C. D. Sherrill, *J. Chem. Theory Comput.*, 2013, **9**, 2687–2696.

180 T. B. Adler, G. Knizia and H.-J. Werner, *J. Chem. Phys.*, 2007, **127**, 221106.

181 T. B. Adler and H.-J. Werner, *J. Chem. Phys.*, 2011, **135**, 144117.

182 H.-J. Werner, P. J. Knowles, G. Knizia, F. R. Manby, M. Schu¨tz, P. Celani, W. Gyo¨rffy, D. Kats, T. Korona, R. Lindh, A. Mitrushenkov, G. Rauhut, K. R. Shamasundar, T. B. Adler, R. D. Amos, A. Bernhardsson, A. Berning, D. L. Cooper, M. J. O. Deegan, A. J.

Dobbyn, F. Eckert, E. Goll, C. Hampel, A. Hesselmann, G. Hetzer, T. Hrenar, G. Jansen, C. Ko¨ppl, Y. Liu, A. W. Lloyd, R. A. Mata, A. J. May, S. J. McNicholas, W. Meyer, M. E. Mura, A. Nicklass, D. P. O'Neill, P. Palmieri, D. Peng, K. Pflu¨ger, R. Pitzer, M. Reiher, T. Shiozaki, H. Stoll, A. J. Stone, R. Tarroni, T. Thorsteinsson and M. Wang, MOLPRO, version 2015. 1, a package of ab initio programs, see http://www.molpro.net

183 B. Brauer, M. K. Kesharwani and J. M. L. Martin, *J. Chem. Theory Comput.*, 2014, **10**, 3791–3799.

184 J. Řezáč and P. Hobza, *Chem. Rev.*, 2016, **116**, 5038–5071.

185 K. E. Riley, J. A. Platts, J. Řezáč, P. Hobza and J. G. Hill, *J. Phys. Chem. A*, 2012, **116**, 4159–4169.

186 E. R. Johnson, S. Keinan, P. Mori-Sánchez, J. Contreras-García, A. J. Cohen and W. Yang, *J. Am. Chem. Soc.*, 2010, **132**, 6498–6506.

187 M. Saeki, H. Akagi and M. Fujii, *J. Chem. Theory Comput.*, 2006, **2**, 1176–1183.

188 N. K. Lee, S. Park and S. K. Kim, *J. Chem. Phys.*, 2002, **116**, 7910–7917.

189 N. O. Dubinets, A. A. Safonov and A. A. Bagaturyants, *J. Phys. Chem. A*, 2016, **120**, 2779–2782.

190 Y. Inokuchi, K. Ohashi, M. Matsumoto and N. Nishi, *J. Phys. Chem.*, 1995, **99**, 3416–3418.

191 M. Schnell, M. Fatima, C. Perez, A. Steber, S. Zinn and A. Poblotzki, *Angew. Chem. Int. Ed.*, , DOI:10.1002/anie.201812556.

192 A. Guenther, C. N. Hewitt, D. Erickson, R. Fall, C. Geron, T. Graedel, P. Harley, L. Klinger, M. Lerdau and W. A. McKay, *J. Geophys. Res. Atmospheres*, 1995, **100**, 8873–8892.

193 J. H. Seinfeld and J. F. Pankow, *Annu. Rev. Phys. Chem.*, 2003, **54**, 121–140.

194 S. Koch, R. Winterhalter, E. Uherek, A. Kolloff, P. Neeb and G. K. Moortgat, *Atmos. Environ.*, 2000, **34**, 4031–4042.

195 B. Bonn and G. K. Moortgat, *Atmospheric Chem. Phys. Discuss.*, 2002, **2**, 469–506.

196 J. Poštulka, P. Slavíček, A. Domaracka, A. Pysanenko, M. Fárník and J. Kočišek, *Phys. Chem. Chem. Phys.*, 2019, **21**, 13925–13933.

197 S. J. Grabowski, *Annu. Rep. Sect. CPhysical Chem.*, 2006, **102**, 131–165.

198 J. Rezac, *J. Chem. Theory Comput.*, 2017, **13**, 4804–4817.

199 Y. Zhao and D. G. Truhlar, *J. Phys. Chem. C*, 2008, **112**, 6860–6868.
200 K. E. Laidig and R. F. Bader, *J. Chem. Phys.*, 1990, **93**, 7213–7224.
201 N. A. Seifert, J. Thomas, W. Jäger and Y. Xu, *Phys. Chem. Chem. Phys.*, 2018, **20**, 27630–27637.
202 W. Humphrey, A. Dalke and K. Schulten, *J. Mol. Graph.*, 1996, **14**, 33–38.
203 T. Clark, J. Chandrasekhar, G. W. Spitznagel and P. V. R. Schleyer, *J. Comput. Chem.*, 1983, **4**, 294–301.
204 D. Feller, *J. Comput. Chem.*, 1996, **17**, 1571–1586.
205 R. Krishnan, J. S. Binkley, R. Seeger and J. A. Pople, *J. Chem. Phys.*, 1980, **72**, 650–654.
206 D. Rappoport and F. Furche, *J. Chem. Phys.*, 2010, **133**, 134105.
207 B. P. Pritchard, D. Altarawy, B. Didier, T. D. Gibson and T. L. Windus, *J. Chem. Inf. Model.*, 2019, **59**, 4814–4820.
208 L. Goerigk and S. Grimme, *J. Chem. Theory Comput.*, 2011, **7**, 291–309.
209 T. Tsuneda and K. Hirao, *Wiley Interdiscip. Rev. Comput. Mol. Sci.*, 2014, **4**, 375–390.
210 T. Sato, T. Tsuneda and K. Hirao, *J. Chem. Phys.*, 2007, **126**, 234114.
211 M. Biczysko, P. Panek, G. Scalmani, J. Bloino and V. Barone, *J. Chem. Theory Comput.*, 2010, **6**, 2115–2125.
212 W. Li, L. Spada, N. Tasinato, S. Rampino, L. Evangelisti, A. Gualandi, P. G. Cozzi, S. Melandri, V. Barone and C. Puzzarini, *Angew. Chem. Int. Ed.*, 2018, **57**, 13853–13857.
213 E. Penocchio, M. Piccardo and V. Barone, *J. Chem. Theory Comput.*, 2015, **11**, 4689–4707.
214 C. Puzzarini, J. Bloino, N. Tasinato and V. Barone, *Chem. Rev.*, 2019, **119**, 8131–8191.
215 V. Ásgeirsson and H. Jónsson, *Handb. Mater. Model. Methods Theory Model.*, 2020, 689–714.
216 F. Neese, *Wiley Interdiscip. Rev. Comput. Mol. Sci.*, 2012, **2**, 73–78.
217 V. Ásgeirsson, B. O. Birgisson, R. Bjornsson, U. Becker, F. Neese, C. Riplinger and H. Jónsson, *J. Chem. Theory Comput.*, 2021, **17**, 4929–4945.
218 E. D. Glendening and F. Weinhold, *J. Comput. Chem.*, 1998, **19**, 593–609.
219 E. D. Glendening and F. Weinhold, *J. Comput. Chem.*, 1998, **19**, 610–627.
220 E. D. Glendening, J. K. Badenhoop and F. Weinhold, *J. Comput. Chem.*, 1998, **19**, 628–646.

221 B. Ouyang, T. G. Starkey and B. J. Howard, *J. Phys. Chem. A*, 2007, **111**, 6165–6175.

222 C. S. López, O. N. Faza, F. P. Cossío, D. M. York and A. R. De Lera, *Chem. Eur. J.*, 2005, **11**, 1734–1738.

223 J. Klein, H. Khartabil, J.-C. Boisson, J. Contreras-García, J.-P. Piquemal and E. Hénon, *J. Phys. Chem. A*, 2020, **124**, 1850–1860.

224 C. Lefebvre, G. Rubez, H. Khartabil, J.-C. Boisson, J. Contreras-García and E. Hénon, *Phys. Chem. Chem. Phys.*, 2017, **19**, 17928–17936.

225 C. Lefebvre, H. Khartabil, J.-C. Boisson, J. Contreras-García, J.-P. Piquemal and E. Hénon, *ChemPhysChem*, 2018, **19**, 724–735.

226 C. F. Matta, in *Hydrogen Bonding—New Insights*, Springer, 2006, pp. 337–375.

227 P. L. A. Popelier, *J. Phys. Chem. A*, 1998, **102**, 1873–1878.

228 M. Mantina, A. C. Chamberlin, R. Valero, C. J. Cramer and D. G. Truhlar, *J. Phys. Chem. A*, 2009, **113**, 5806–5812.

229 EAS Weather Station | Earth and Atmospheric Sciences, https://www.ualberta.ca/earth-sciences/facilities/weather.html, (accessed 8 March 2022).

230 J. K. Messer, F. C. De Lucia and P. Helminger, *Int. J. Infrared Millim. Waves*, 1983, **4**, 505–539.

231 E. M. Neeman, J. R. Avilés Moreno and T. R. Huet, *J. Chem. Phys.*, 2017, **147**, 214305.

232 W. M. Organization, *Guide to Instruments and Methods of Observation*, WMO Geneva, 2018, vol. 1.

233 E. G. Schnitzler, B. L. Zenchyzen and W. Jäger, *Phys. Chem. Chem. Phys.*, 2016, **18**, 448–457.

234 S. K. Boreddy, T. Mochizuki, K. Kawamura, S. Bikkina and M. M. Sarin, *Atmos. Environ.*, 2017, **167**, 170–180.

235 S. Hatakeyama, K. Izumi, T. Fukuyama and H. Akimoto, *J. Geophys. Res. Atmospheres*, 1989, **94**, 13013–13024.

236 Z. Zhao, W. Zhang, T. Alexander, X. Zhang, D. B. Martin and H. Zhang, *Environ. Sci. Technol.*, 2021, **55**, 6700–6709.

237 D. Zhang and R. Zhang, *J. Chem. Phys.*, 2005, **122**, 114308.

238 C. Peng and H. Bernhard Schlegel, *Isr. J. Chem.*, 1993, **33**, 449–454.

239 C. Peng, P. Y. Ayala, H. B. Schlegel and M. J. Frisch, *J. Comput. Chem.*, 1996, **17**, 49–56.

240 M. G. Evans and M. Polanyi, *Trans. Faraday Soc.*, 1935, **31**, 875–894.

241 H. Eyring, *J. Chem. Phys.*, 1935, **3**, 107–115.

242 K. J. Laidler and M. C. King, *J. Phys. Chem.*, 1983, **87**, 2657–2664.

243 R. Atkinson, A. M. Winer and J. N. Pitts Jr, *Atmospheric Environ. 1967*, 1982, **16**, 1017–1020.

244 J. Arey, R. Atkinson and S. M. Aschmann, *J. Geophys. Res. Atmospheres*, 1990, **95**, 18539–18546.

245 M. Witter, T. Berndt, O. Böge, F. Stratmann and J. Heintzenberg, *Int. J. Chem. Kinet.*, 2002, **34**, 394–403.

246 F. Nolting, W. Behnke and C. Zetzsch, *J. Atmospheric Chem.*, 1988, **6**, 47–59.

247 V. G. Khamaganov and R. A. Hites, *J. Phys. Chem. A*, 2001, **105**, 815–822.

248 J. Laothawornkitkul, J. E. Taylor, N. D. Paul and C. N. Hewitt, *New Phytol.*, 2009, **183**, 27–51.

249 I. G. Kavouras, N. Mihalopoulos and E. G. Stephanou, *Environ. Sci. Technol.*, 1999, **33**, 1028–1037.

250 J. Zhu and J. E. Penner, *J. Geophys. Res. Atmospheres*, 2019, **124**, 8260–8286.

251 E. G. Schnitzler and W. Jäger, *Phys. Chem. Chem. Phys.*, 2014, **16**, 2305–2314.

252 J. Hendricks, M. Righi and V. Aquila, in *Atmospheric Physics: Background – Methods – Trends*, ed. U. Schumann, Springer, Berlin, Heidelberg, 2012, pp. 561–576.

253 P. L. Crowell, W. S. Kennan, J. D. Haag, S. Ahmad, E. Vedejs and M. N. Gould, *Carcinogenesis*, 1992, **13**, 1261–1264.

254 M. S. Ahmed, A. Khan, L. T. A. Kury and F. A. Shah, *Front. Pharmacol.*, 2020, **11**, 919.

255 J. R. A. Moreno, F. P. Ureña, J. J. L. González and T. R. Huet, *Chem. Phys. Lett.*, 2009, **473**, 17–20.

256 J. R. A. Moreno, T. R. Huet and J. J. L. González, *Struct. Chem.*, 2013, **24**, 1163–1170.

257 D. Loru, M. M. Quesada-Moreno, J. R. Avilés-Moreno, N. Jarman, T. R. Huet, J. J. López-González and M. E. Sanz, *ChemPhysChem*, 2017, **18**, 274–280.

258 D. Loru, A. Vigorito, A. F. Santos, J. Tang and M. E. Sanz, *Phys. Chem. Chem. Phys.*, 2019, **21**, 26111–26116.

259 P. Pracht, E. Caldeweyher, S. Ehlert and S. Grimme, *A Robust Non-Self-Consistent Tight-Binding Quantum Chemistry Method for large Molecules*, 2019.

260 H.-J. Werner, P. J. Knowles, G. Knizia, F. R. Manby, M. Schütz, and others, *MOLPRO, version 2019.2, a package of ab initio programs*, Cardiff, UK, 2019.

261 A. Schäfer, H. Horn and R. Ahlrichs, *J. Chem. Phys.*, 1992, **97**, 2571–2577.

262 A. E. DePrince and C. D. Sherrill, *J. Chem. Theory Comput.*, 2013, **9**, 2687–2696.

263 J. Kaminsky, R. A. Mata, H.-J. Werner and F. Jensen, *Mol. Phys.*, 2008, **106**, 1899–1906.

264 M. D. Wodrich, C. Corminboeuf and P. von R. Schleyer, *Org. Lett.*, 2006, **8**, 3631–3634.

265 F. Weinhold, *J. Comput. Chem.*, 2012, **33**, 2363–2379.

266 E. Kalnay, M. Kanamitsu, R. Kistler, W. Collins, D. Deaven, L. Gandin, M. Iredell, S. Saha, G. White and J. Woollen, *Bull. Am. Meteorol. Soc.*, 1996, **77**, 437–472.

267 J. W. Hurrell, *Science*, 1995, **269**, 676–679.

268 C. Parmesan and G. Yohe, *Nature*, 2003, **421**, 37–42.

269 C. D. Thomas, A. Cameron, R. E. Green, M. Bakkenes, L. J. Beaumont, Y. C. Collingham, B. F. Erasmus, M. F. De Siqueira, A. Grainger and L. Hannah, *Nature*, 2004, **427**, 145–148.

270 T. Schoennagel, J. K. Balch, H. Brenkert-Smith, P. E. Dennison, B. J. Harvey, M. A. Krawchuk, N. Mietkiewicz, P. Morgan, M. A. Moritz and R. Rasker, *Proc. Natl. Acad. Sci.*, 2017, **114**, 4582–4590.

271 F. H. Isikgor and C. R. Becer, *Polym. Chem.*, 2015, **6**, 4497–4559.

272 J. Sun, B. Wei, Q. Mei, Z. An, X. Wang and M. He, *Chem. Eng. J.*, 2019, **358**, 456–466.

273 C. Coeur-Tourneur, V. Foulon and M. Laréal, *Atmos. Environ.*, 2010, **44**, 852–857.

274 C. Coeur-Tourneur, A. Tomas, A. Guilloteau, F. Henry, F. Ledoux, N. Visez, V. Riffault, J. C. Wenger and Y. Bedjanian, *Atmos. Environ.*, 2009, **43**, 2360–2365.

275 H. H. Nielsen, *Rev. Mod. Phys.*, 1951, **23**, 90.

276 I. M. Mills, *J. Mol. Spectrosc.*, 1961, **5**, 334–340.

277 C. M. Western, *J. Quant. Spectrosc. Radiat. Transf.*, 2017, **186**, 221–242.

278 N. Hansen, H. Mäder and T. Bruhn, *Mol. Phys.*, 1999, **97**, 587–595.

279 Z. Kisiel, *J. Mol. Spectrosc.*, 2003, **218**, 58–67.

280 J. Demaison, *Mol. Phys.*, 2007, **105**, 3109–3138.

281 M. Piccardo, E. Penocchio, C. Puzzarini, M. Biczysko and V. Barone, *J. Phys. Chem. A*, 2015, **119**, 2058–2082.

282 M. S. Rana and M. I. Guzman, *Environ. Sci. Technol.*, 2022, **56**, 15437–15448.

283 S. Frka, M. Sala, A. Kroflic, M. Hus, A. Cusak and I. Grgic, *Environ. Sci. Technol.*, 2016, **50**, 5526–5535.

284 R. J. Mayorga, Z. Zhao and H. Zhang, *Atmos. Environ.*, 2021, **244**, 117910.

285 D. Srivastava, T. V. Vu, S. Tong, Z. Shi and R. M. Harrison, *Npj Clim. Atmospheric Sci.*, 2022, **5**, 1–30.

286 F. Hirata, *Molecular theory of solvation*, Springer Science & Business Media, 2003, vol. 24.

287 R. M. Stratt and M. Maroncelli, *J. Phys. Chem.*, 1996, **100**, 12981–12996.

288 R. J. Davey, S. L. Schroeder and J. H. Ter Horst, *Angew. Chem. Int. Ed.*, 2013, **52**, 2166–2179.

289 A. Rognoni, R. Conte and M. Ceotto, *Chem. Sci.*, 2021, **12**, 2060–2064.

290 T. B. C. Vu, I. Kalkman, W. Leo Meerts, Y. N. Svartsov, C. Jacoby and M. Schmitt, *J. Chem. Phys.*, 2008, **128**, 214311.

291 A. K. Huff, N. Love and K. R. Leopold, *J. Phys. Chem. A*, 2021, **125**, 8033–8046.

292 L. C. Snoek, R. T. Kroemer and J. P. Simons, *Phys. Chem. Chem. Phys.*, 2002, **4**, 2130–2139.

293 C. Jacoby, W. Roth, M. Schmitt, C. Janzen, D. Spangenberg and K. Kleinermanns, *J. Phys. Chem. A*, 1998, **102**, 4471–4480.

294 W. Sun and M. Schnell, *Angew. Chem. Int. Ed.*, 2022, **61**, e202210819.

295 M. Chrayteh, E. Burevschi, D. Loru, T. R. Huet, P. Dréan and M. E. Sanz, *Phys. Chem. Chem. Phys.*, 2021, **23**, 20686–20694.

296 E. Burevschi, M. Chrayteh and D. Loru, 1.

297 J. V. Kildgaard, K. V. Mikkelsen, M. Bilde and J. Elm, *J. Phys. Chem. A*, 2018, **122**, 8549–8556.

298 R. L. Baldwin, *J. Mol. Biol.*, 2007, **371**, 283–301.

299 X. He, L. Fusti-Molnar, G. Cui and K. M. Merz Jr, *J. Phys. Chem. B*, 2009, **113**, 5290–5300.

300 J. Vondrášek, T. Kubař, F. E. Jenney Jr, M. W. Adams, M. Kožíšek, J. Černý, V. Sklenář and P. Hobza, *Chem. Eur. J.*, 2007, **13**, 9022–9027.

301 S. Baweja, S. Panchagnula, M. E. Sanz, L. Evangelisti, C. Pérez, C. West and B. H. Pate, *J. Phys. Chem. Lett.*, 2022, **13**, 9510–9516.

302 S. Blanco, P. Pinacho and J. C. López, *J. Phys. Chem. Lett.*, 2017, **8**, 6060–6066.

303 D. Loru, A. L. Steber, P. Pinacho, S. Gruet, B. Temelso, A. M. Rijs, C. Pérez and M. Schnell, *Phys. Chem. Chem. Phys.*, 2021, **23**, 9721–9732.

304 C. Perez, A. Krin, A. L. Steber, J. C. Lopez, Z. Kisiel and M. Schnell, *J. Phys. Chem. Lett.*, 2016, **7**, 154–160.

305 W. Li, M. M. Quesada-Moreno, P. Pinacho and M. Schnell, *Angew. Chem.*, 2021, **133**, 5383–5390.

306 C. Pérez, A. L. Steber, B. Temelso, Z. Kisiel and M. Schnell, *Angew. Chem.*, 2020, **132**, 8479–8483.

307 A. L. Steber, C. Pérez, B. Temelso, G. C. Shields, A. M. Rijs, B. H. Pate, Z. Kisiel and M. Schnell, *J. Phys. Chem. Lett.*, 2017, **8**, 5744–5750.

308 C. Pérez, J. L. Neill, M. T. Muckle, D. P. Zaleski, I. Peña, J. C. Lopez, J. L. Alonso and B. H. Pate, *Angew. Chem.*, 2015, **127**, 993–996.

309 Z. Chen, Y. Li, Z. He, Y. Xu and W. Yu, *J. Chem. Res.*, 2019, **43**, 293–303.

310 T. Sato, T. Tsuneda and K. Hirao, *J. Chem. Phys.*, 2005, **123**, 104307.

311 A. S. Hazrah, M. H. Al-Jabiri and W. Jäger, *J. Mol. Spectrosc.*, 2022, 111715.

312 W. Sun and M. Schnell, *Angew. Chem.*

313 N. Pugliano and R. J. Saykally, *Science*, 1992, **257**, 1937–1940.

314 J. D. Cruzan, L. B. Braly, K. Liu, M. G. Brown, J. G. Loeser and R. J. Saykally, *Science*, 1996, **271**, 59–62.

315 K. Liu, M. G. Brown, J. D. Cruzan and R. J. Saykally, *Science*, 1996, **271**, 62–64.

316 F. N. Keutsch and R. J. Saykally, *Proc. Natl. Acad. Sci.*, 2001, **98**, 10533–10540.

317 E. D. Glendening, C. R. Landis and F. Weinhold, *J. Comput. Chem.*, 2013, **34**, 1429–1437.

318 N. A. Seifert, A. L. Steber, J. L. Neill, C. Pérez, D. P. Zaleski, B. H. Pate and A. Lesarri, *Phys. Chem. Chem. Phys.*, 2013, **15**, 11468–11477.

Appendix A

Supplementary Information for Chapter 3

Structural Study of 1- and 2-Naphthol: New Insights into the Non-covalent H-H Interaction in *cis*-1-Naphthol

Contents:

1. **Rotational Transition Frequencies for Parent Species**
    a. **Table A.1.** Assigned rotational transitions for *cis*-1-naphthol
    b. **Table A.2.** Assigned rotational transitions for *trans*-1-naphthol
    c. **Table A.3.** Assigned rotational transitions for *cis*-2-naphthol
    d. **Table A.4.** Assigned rotational transitions for *trans*-2-naphthol
2. **Rotational Transition Frequencies for ^{13}C Isotopologues**
    a. **Table A.5.** Assigned rotational transitions for *cis*-1-naphthol ^{13}C isotopologues
    b. **Table A.6.** Assigned rotational transitions for *trans*-1-naphthol ^{13}C isotopologues
    c. **Table A.7.** Assigned rotational transitions for *cis*-2-naphthol ^{13}C isotopologues
    d. **Table A.8.** Assigned rotational transitions for *trans*-2-naphthol ^{13}C isotopologues
3. **Rotational and Centrifugal Distortion Constants for ^{13}C Isotopologues**
    a. **Table A.9.** Rotational transitions for ^{13}C isotopologues of *cis*-1-naphthol
    b. **Table A.10.** Rotational transitions for ^{13}C isotopologues of *trans*-1-naphthol
    c. **Table A.11.** Rotational transitions for ^{13}C isotopologues of *cis*-2-naphthol
    d. **Table A.12.** Rotational transitions for ^{13}C isotopologues of *trans*-2-naphthol
4. **Structural Parameters**
    a. **Table A.13.** Structural parameters for *cis*-1-naphthol
    b. **Table A.14.** Structural parameters for *trans*-1-naphthol
    c. **Table A.15.** Structural parameters for *cis*-2-naphthol
    d. **Table A.16.** Structural parameters for *trans*-2-naphthol
5. **AIMA11**
    a. **Table A.17.** Data from AIMA11 QTAIM calculations
    b. **Table A.18.** *Cis*-1-naphthol theoretical method comparison
6. **Semi-experimental Rotational Frequencies for ^{12}C and ^{13}C Isotopologues**
    a. **Table A.19.** Semi-experimental rotational constants for parent species
    b. **Table A.20.** Semi-experimental rotational constants for *cis*-1-naphthol ^{13}C isotopologues
    c. **Table A.21.** Semi-experimental rotational constants for *trans*-1-naphthol ^{13}C isotopologues
    d. **Table A.22.** Semi-experimental rotational constants for *cis*-2-naphthol ^{13}C isotopologues
    e. **Table A.23.** Semi-experimental rotational constants for *trans*-2-naphthol ^{13}C isotopologues
7. **Non-Covalent Interactions**
    a. **Figure A.1.** Non-covalent interactions plot of naphthol conformers
8. **Local Mode Analysis**
    a. **Figure A.2.** Decomposition plot for all normal modes of *cis*-1-naphthol
    b. **Figure A.3.** Decomposition plot for all normal modes of *trans*-1-naphthol
    c. **Figure A.4.** Vibrational displacement vectors for the O-H stretching motion
    d. **Table A.24.** Local Mode Force Constants and Local Mode Frequencies
9. **Inertial Defect Differences**
    a. **Table A.25.** Moment of inertia and Inertial defect values for calculated and experimental results
    b. **Table A.26.** Calculated inertial defect values obtained from Oka's equation

c. **Table A.27.** Inertial defect differences between calculated and experimental defect values
d. **Table A.28.** Lowest out-of-plane modes for naphthol isomers and previous work
e. **Figure A.5.** Lowest out-of-plane vibrational modes for *cis*-1-naphthol
f. **Figure A.6.** Lowest out-of-plane vibrational modes for *trans*-1-naphthol
g. **Figure A.7.** Lowest out-of-plane vibrational modes for *cis*-2-naphthol
h. **Figure A.8.** Lowest out-of-plane vibrational modes for *trans*-2-naphthol
i. **Figure A.9.** Inertial defect differences for the four isomers of naphthol compared to the results of Jahn et al.

10. Charge Model 5

a. **Figure A.10.** CM5 charges for atoms involved in the biphenyl H-H interaction
b. **Table A.29.** Net CM5 charge change for naphthol and biphenyl

11. NBO Analysis

a. **Table A.30.** Bonding and antibonding orbital occupancy
b. **Table A.31.** Interaction Energies between bonding and antibonding orbitals for *trans*-1-naphthol
c. **Table A.32.** Interaction Energies between bonding and antibonding orbitals for *cis*-1-naphthol
d. **Table A.33.** Interaction Energies between bonding and antibonding orbitals for *trans*-2-naphthol
e. **Table A.34.** Interaction Energies between bonding and antibonding orbitals for *cis*-2-naphthol
f. **Figure A.11.** Heavy atom steric exchange and donor-acceptor interaction energies
g. **Table A.35.** *Cis*-1-naphthol theoretical method comparison

Rotational Transition Frequencies

Table A.1. Measured frequencies of assigned rotational transitions of *cis*-1-naphthol. $\Delta\nu^a$ is the difference between observed and calculated frequencies.

J'	K_a'	K_c'	J''	K_a''	K_c''	ν_{Exp}/ MHz	$\Delta\nu^a$/ MHz
1	0	1	0	0	0	1837.398	-0.007
5	2	3	5	2	4	2668.247	-0.001
2	1	2	1	1	1	3263.597	-0.002
2	0	2	1	0	1	3555.025	-0.002
4	1	3	4	1	4	3960.015	0.007
2	1	1	1	1	0	4086.020	0.001
2	1	2	1	0	1	4086.800	-0.004
2	2	1	2	0	2	4235.020	-0.005
6	2	4	6	2	5	4289.167	-0.007
3	2	2	3	0	3	4659.584	0.001
3	1	3	2	1	2	4828.862	-0.002
3	0	3	2	0	2	5087.650	-0.003
4	2	3	4	0	4	5417.279	0.002
3	2	2	2	2	1	5512.212	-0.000
5	1	4	5	1	5	5623.450	0.005
3	2	1	2	2	0	5936.774	0.001
3	1	2	2	1	1	6039.545	-0.001
4	1	4	3	1	3	6341.026	-0.003
4	0	4	3	0	3	6496.777	-0.001
4	2	3	3	2	2	7254.472	0.001
5	1	5	4	1	4	7812.217	0.005
4	1	3	3	1	2	7856.723	-0.001
5	0	5	4	0	4	7884.514	0.006
6	1	6	5	1	5	9258.636	0.004
5	1	4	4	1	3	9475.640	-0.008
5	3	2	4	3	1	9809.353	0.001

Table A.2. Measured frequencies of assigned rotational transitions of *trans*-1-naphthol. $\Delta\nu^a$ is the difference between observed and calculated frequencies.

J'	K_a'	K_c'	J''	K_a''	K_c''	ν_{Exp}/ MHz	$\Delta\nu^a$/ MHz
1	0	1	0	0	0	1849.640	-0.001
3	2	1	3	1	2	2457.272	-0.002
3	1	2	3	1	3	2481.055	-0.000
2	2	0	2	1	1	2550.181	-0.001
1	1	1	0	0	0	2658.118	-0.001
4	2	2	4	1	3	2726.881	0.003
5	2	3	5	2	4	2740.972	0.002
7	3	4	7	3	5	2754.832	-0.001
2	0	2	1	1	1	2766.057	0.002
2	1	2	1	1	1	3281.677	-0.000
5	2	3	5	1	4	3484.039	-0.003
2	0	2	1	0	1	3574.533	-0.001
3	1	2	2	2	1	3656.192	-0.000
2	2	1	2	1	2	3678.248	-0.001
4	1	3	4	1	4	4013.698	-0.001
2	1	2	1	0	1	4090.154	-0.001
2	1	1	1	1	0	4116.887	-0.001
4	1	3	4	0	4	4123.074	0.000
4	3	1	4	2	2	4171.805	-0.002
2	2	1	2	0	2	4193.869	-0.001
3	2	2	3	1	3	4373.798	0.013
6	2	4	6	2	5	4387.622	-0.001
8	3	5	8	3	6	4487.575	-0.004
3	0	3	2	1	2	4593.506	-0.000
3	3	0	3	2	1	4615.560	0.001
3	2	2	3	0	3	4633.665	-0.001
6	2	4	6	1	5	4751.213	-0.000
3	1	3	2	1	2	4853.387	0.001
3	0	3	2	0	2	5109.127	-0.001

3	3	1	3	2	2	5155.527	-0.001
4	2	3	4	1	4	5302.553	-0.003
3	1	3	2	0	2	5369.008	0.000
4	2	3	4	0	4	5411.929	-0.002
4	3	2	4	2	3	5447.473	-0.006
3	2	2	2	2	1	5548.922	-0.000
5	1	4	5	1	5	5686.213	-0.002
5	1	4	5	0	5	5727.304	-0.003
5	3	3	5	2	4	5958.694	0.001
3	2	1	2	2	0	5988.718	0.001
4	1	3	3	2	2	6010.509	-0.001
3	1	2	2	1	1	6081.625	-0.001
7	2	5	7	2	6	6223.969	0.002
4	0	4	3	1	3	6261.220	-0.001
4	1	4	3	1	3	6370.596	-0.000
7	2	5	7	1	6	6380.619	0.009
5	2	4	5	1	5	6429.283	-0.003
5	2	4	5	0	5	6470.377	-0.001
4	0	4	3	0	3	6521.101	-0.001
2	2	1	1	1	0	6542.319	-0.002
4	1	4	3	0	3	6630.474	-0.002
5	3	3	5	1	4	6701.765	-0.001
4	3	2	4	1	3	6736.338	0.002
2	2	0	1	1	1	7084.677	0.002
4	2	3	3	2	2	7299.366	-0.000
6	1	5	6	1	6	7336.284	-0.001
4	3	2	3	3	1	7591.315	-0.002
6	2	5	6	0	6	7714.264	-0.001
4	3	1	3	3	0	7729.093	0.001
5	1	5	4	1	4	7846.416	-0.001
2	2	0	1	0	1	7893.159	0.006
4	1	3	3	1	2	7903.243	0.004
5	0	5	4	0	4	7914.702	0.002
5	1	5	4	0	4	7955.792	0.000

Table A.3. Measured frequencies of assigned rotational transitions of *cis*-2-naphthol. $\Delta\nu^a$ is the difference between observed and calculated frequencies.

J'	K_a'	K_c'	J''	K_a''	K_c''	ν_{Exp}/ MHz	$\Delta\nu^a$/ MHz
1	1	0	1	0	1	2209.433	0.001
2	1	1	2	0	2	2406.436	-0.001
3	0	3	2	1	2	2493.315	-0.001
3	1	2	3	0	3	2724.020	0.001
2	1	2	1	1	1	2743.806	0.002
2	0	2	1	0	1	2916.615	-0.002
2	1	1	1	1	0	3113.621	-0.001
4	1	3	4	0	4	3186.057	-0.001
4	3	1	5	2	4	3332.956	0.003
1	1	1	0	0	0	3488.881	0.001
5	1	4	5	0	5	3817.735	-0.002
3	1	3	2	1	2	4108.378	-0.001
4	0	4	3	1	3	4124.399	-0.001
6	1	5	5	2	4	4210.154	0.000
3	0	3	2	0	2	4345.026	-0.000
3	2	2	2	2	1	4393.069	-0.000
3	2	1	2	2	0	4441.112	-0.000
3	3	1	4	2	2	4566.116	-0.003
6	1	5	6	0	6	4637.525	0.002
3	1	2	2	1	1	4662.609	0.000
3	3	0	4	2	3	4744.698	0.001
2	1	2	1	0	1	4768.330	0.002
6	2	4	6	1	5	5302.829	-0.002
7	2	5	7	1	6	5305.223	-0.004
5	2	3	5	1	4	5425.342	-0.000

4	1	4	3	1	3	5464.836	0.001
8	2	6	8	1	7	5468.910	-0.003
4	2	2	4	1	3	5628.617	-0.000
7	1	6	7	0	7	5648.833	0.000
4	0	4	3	0	3	5739.464	0.001
5	0	5	4	1	4	5753.640	0.001
9	2	7	9	1	8	5822.737	-0.001
4	2	3	3	2	2	5848.006	-0.000
3	2	1	3	1	2	5864.169	0.001
4	3	2	3	3	1	5880.199	0.002
4	3	1	3	3	0	5883.163	-0.001
3	1	3	2	0	2	5960.089	-0.001
4	2	2	3	2	1	5965.948	-0.003
2	2	0	2	1	1	6085.668	0.004
4	1	3	3	1	2	6201.504	0.003
2	2	1	2	1	2	6628.296	0.001

Table A.4. Measured frequencies of assigned rotational transitions of *trans*-2-naphthol. $\Delta\nu^a$ is the difference between observed and calculated frequencies.

J'	K_a'	K_c'	J"	K_a"	K_c"	ν_{Exp}/ MHz	$\Delta\nu^a$/ MHz
1	1	0	1	0	1	2205.270	0.000
5	1	4	4	2	3	2298.211	-0.010
2	1	1	2	0	2	2402.909	-0.002
3	0	3	2	1	2	2501.886	0.001
2	2	0	3	1	3	2516.691	0.004
3	1	2	3	0	3	2721.618	-0.002
8	2	6	7	3	5	2728.994	0.005
2	1	2	1	1	1	2745.798	0.001
4	3	2	5	2	3	2892.790	0.004
2	0	2	1	0	1	2919.051	-0.003
7	4	3	8	3	6	2919.739	-0.003
2	1	1	1	1	0	3116.697	0.002
4	1	3	4	0	4	3185.433	-0.004
4	3	1	5	2	4	3305.007	-0.005
1	1	1	0	0	0	3485.444	0.001
5	1	4	5	0	5	3819.652	-0.009
3	1	3	2	1	2	4111.311	0.001
4	0	4	3	1	3	4134.196	0.000
6	1	5	5	2	4	4235.301	-0.008
6	4	3	7	3	4	4310.392	-0.002
3	0	3	2	0	2	4348.448	0.001
3	2	2	2	2	1	4396.869	0.000
6	4	2	7	3	5	4413.621	0.006
3	2	1	2	2	0	4445.291	0.000
3	3	1	4	2	2	4537.629	0.001
6	1	5	6	0	6	4642.702	-0.010
3	1	2	2	1	1	4667.156	0.000
3	3	0	4	2	3	4717.604	0.007
2	1	2	1	0	1	4765.619	0.003
9	2	7	8	3	6	4836.036	-0.031
6	2	4	6	1	5	5290.499	-0.006
7	2	5	7	1	6	5295.399	-0.010
5	2	3	5	1	4	5411.525	-0.003
8	2	6	8	1	7	5462.669	-0.016
4	1	4	3	1	3	5468.650	0.004
4	2	2	4	1	3	5614.197	-0.001
7	1	6	7	0	7	5657.738	-0.021
4	0	4	3	0	3	5743.622	0.001
5	0	5	4	1	4	5764.281	0.002
9	2	7	9	1	8	5821.179	-0.021
3	2	1	3	1	2	5849.785	0.001
4	2	3	3	2	2	5852.999	0.000
4	3	2	3	3	1	5885.443	0.003
4	3	1	3	3	0	5888.447	0.002
5	4	1	6	3	4	5909.708	-0.006
3	1	3	2	0	2	5957.873	0.001
4	2	2	3	2	1	5971.849	-0.004
2	2	0	2	1	1	6071.652	0.003
4	1	3	3	1	2	6207.438	0.000
7	1	6	6	2	5	6212.612	-0.008

Rotational Transition Frequencies for ^{13}C Isotopologues

Table A.5. Frequencies of rotational transitions of ^{13}C isotopologues of *cis*-1-naphthol. $\Delta\nu^a$ is the difference between observed and calculated frequencies.

J'	K_a'	K_c'	J"	K_a"	K_c"	ν_{Exp}/ MHz	$\Delta\nu^a$/ MHz
C1							
2	1	1	1	1	0	4069.750	0.000
3	0	3	2	0	2	5070.468	0.007
3	1	2	2	1	1	6016.128	-0.020
4	1	4	3	1	3	6318.845	-0.003
C2							
2	0	2	1	0	1	3523.205	-0.010
2	1	1	1	1	0	4041.101	-0.010
2	1	2	1	1	1	3234.272	0.001
3	1	3	2	1	2	4787.668	0.001
3	0	3	2	0	2	5048.596	-0.002
3	2	1	2	2	0	5864.477	0.000
3	1	2	2	1	1	5976.626	0.080
C3							
2	1	2	1	1	1	3235.800	-0.001
2	0	2	1	0	1	3524.722	0.000
2	1	1	1	1	0	4052.38	-0.002
3	1	3	2	1	2	4787.421	0.002
3	0	3	2	0	2	5043.366	0.000
3	2	1	2	2	0	5888.905	-0.002
3	1	2	2	1	1	5989.328	-0.000
4	0	4	3	0	3	6439.765	-0.007
C4							
2	1	2	1	1	1	3250.353	-0.010
2	0	2	1	0	1	3540.305	0.005
2	1	1	1	1	0	4079.394	-0.004
3	1	3	2	1	2	4806.556	0.009
3	0	3	2	0	2	5058.696	-0.003
3	2	2	2	2	1	5497.317	-0.002
3	1	2	2	1	1	6025.395	0.003
4	0	4	3	0	3	6456.079	-0.002
C4a							
2	1	2	1	1	1	3260.108	-0.001
2	0	2	1	0	1	3551.162	-0.002
2	1	1	1	1	0	4083.796	-0.002
3	1	3	2	1	2	4823.105	-0.007
3	2	2	2	2	1	5507.934	0.005
3	1	2	2	1	1	6035.329	-0.000
4	1	4	3	1	3	6332.783	0.005
C5							
2	1	2	1	1	1	3241.183	-0.007
2	0	2	1	0	1	3530.640	0.002
2	1	1	1	1	0	4057.083	-0.002
3	1	3	2	1	2	4795.947	0.000
3	0	3	2	0	2	5053.449	0.003
3	2	2	2	2	1	5473.714	0.008
3	1	2	2	1	1	5997.152	-0.004
4	0	4	3	0	3	6453.439	-0.002
C6							
2	0	2	1	0	1	3510.074	-0.000
2	1	1	1	1	0	4022.589	-0.001
3	1	3	2	1	2	4770.681	0.000
3	0	3	2	0	2	5032.463	-0.000
3	1	2	2	1	1	5950.630	0.001
C7							
2	1	2	1	1	1	3229.464	-0.005
2	0	2	1	0	1	3517.951	-0.003
2	1	1	1	1	0	4037.621	0.005
3	1	3	2	1	2	4779.894	0.002
3	0	3	2	0	2	5039.086	0.002
3	1	2	2	1	1	5970.399	-0.005
3	2	2	2	2	1	5450.315	0.006
C8							
2	1	2	1	1	1	3251.607	0.001

2	0	2	1	0	1	3541.851	0.003
2	1	1	1	1	0	4074.887	0.001
3	1	3	2	1	2	4810.055	0.002
3	0	3	2	0	2	5065.703	-0.001
3	2	2	2	2	1	5494.866	-0.002
3	1	2	2	1	1	6021.397	-0.000
C8a							
2	1	2	1	1	1	3263.166	0.011
2	0	2	1	0	1	3554.530	0.005
3	1	3	2	1	2	4828.066	0.006
3	0	3	2	0	2	5086.512	0.004
3	1	2	2	1	1	6039.271	-0.004
4	1	4	3	1	3	6339.789	-0.012

Table A.6. Frequencies of rotational transitions of ^{13}C isotopologues of *trans*-1-naphthol. $\Delta\nu^a$ is the difference between observed and calculated frequencies.

J'	K_a'	K_c'	J"	K_a"	K_c"	ν_{Exp}/ MHz	$\Delta\nu^a$/ MHz
C1							
2	1	2	1	1	1	3269.839	0.001
2	0	2	1	0	1	3561.694	0.001
2	1	1	1	1	0	4100.547	0.001
3	1	3	2	1	2	4836.292	0.001
3	0	3	2	0	2	5091.958	0.000
3	2	2	2	2	1	5527.785	-0.002
3	1	2	2	1	1	6058.148	0.000
4	1	4	3	1	3	6348.641	0.000
4	0	4	3	0	3	6499.734	0.000
C2							
2	1	2	1	1	1	3251.972	0.000
2	0	2	1	0	1	3542.433	0.000
2	1	1	1	1	0	4071.202	-0.001
3	1	3	2	1	2	4811.766	0.001
3	0	3	2	0	2	5069.925	-0.001
3	2	2	2	2	1	5492.377	-0.002
3	1	2	2	1	1	6017.818	0.002
4	1	4	3	1	3	6318.697	0.000
4	0	4	3	0	3	6474.256	0.000
C3							
2	1	2	1	1	1	3253.375	0.000
2	0	2	1	0	1	3543.672	0.001
2	1	1	1	1	0	4082.334	-0.002
3	1	3	2	1	2	4811.267	0.001
3	0	3	2	0	2	5064.260	0.000
3	2	2	2	2	1	5501.783	0.001
3	2	1	2	2	0	5939.306	0.001
3	1	2	2	1	1	6030.160	0.000
4	1	4	3	1	3	6314.995	-0.002
4	0	4	3	0	3	6463.488	0.001
C4							
2	1	2	1	1	1	3268.209	0.001
2	0	2	1	0	1	3559.391	0.000
2	1	1	1	1	0	4110.011	0.000
3	1	3	2	1	2	4830.640	0.001
3	0	3	2	0	2	5079.509	0.000
3	2	2	2	2	1	5533.661	-0.002
3	2	1	2	2	0	5987.817	0.001
3	1	2	2	1	1	6066.888	0.000
4	1	4	3	1	3	6337.451	-0.001
4	0	4	3	0	3	6479.799	0.001
C4a							
2	1	2	1	1	1	3278.135	-0.002
2	0	2	1	0	1	3570.586	-0.001
2	1	1	1	1	0	4114.671	-0.001
3	1	3	2	1	2	4847.529	0.001
3	0	3	2	0	2	5101.715	-0.001
3	2	2	2	2	1	5544.604	-0.001
3	2	1	2	2	0	5987.496	0.002
3	1	2	2	1	1	6077.354	0.000

4	1	4	3	1	3	6362.178	-0.001
4	0	4	3	0	3	6510.838	0.002
C5							
2	1	2	1	1	1	3259.082	0.001
2	0	2	1	0	1	3549.952	-0.001
2	1	1	1	1	0	4087.707	-0.001
3	1	3	2	1	2	4820.199	0.000
3	0	3	2	0	2	5074.657	0.000
3	2	2	2	2	1	5510.088	-0.002
3	2	1	2	2	0	5945.525	0.001
3	1	2	2	1	1	6038.892	0.000
4	1	4	3	1	3	6327.305	-0.001
4	0	4	3	0	3	6477.411	0.002
C6							
2	1	2	1	1	1	3240.063	0.000
2	0	2	1	0	1	3529.528	0.000
2	1	1	1	1	0	4052.926	-0.001
3	1	3	2	1	2	4795.052	0.000
3	0	3	2	0	2	5054.120	-0.001
3	2	2	2	2	1	5469.741	-0.001
3	2	1	2	2	0	5885.364	0.001
3	1	2	2	1	1	5992.234	0.000
4	1	4	3	1	3	6297.835	-0.001
4	0	4	3	0	3	6455.410	0.002
C7							
2	1	2	1	1	1	3247.407	-0.002
2	0	2	1	0	1	3537.398	0.000
2	1	1	1	1	0	4068.086	0.000
3	1	3	2	1	2	4804.307	0.000
3	0	3	2	0	2	5060.666	0.000
3	2	2	2	2	1	5486.620	0.000
3	2	1	2	2	0	5912.574	0.000
3	1	2	2	1	1	6012.090	0.000
4	1	4	3	1	3	6308.065	0.001
4	0	4	3	0	3	6461.422	-0.001
C8							
2	1	2	1	1	1	3269.650	0.000
2	0	2	1	0	1	3561.270	0.000
2	1	1	1	1	0	4105.737	0.000
3	1	3	2	1	2	4834.498	0.000
3	0	3	2	0	2	5087.039	-0.001
3	2	2	2	2	1	5531.539	0.000
3	2	1	2	2	0	5976.037	-0.001
3	1	2	2	1	1	6063.382	0.001
4	1	4	3	1	3	6344.518	0.001
4	0	4	3	0	3	6491.496	0.000
C8a							
2	1	2	1	1	1	3281.250	-0.002
2	0	2	1	0	1	3574.049	-0.001
3	1	3	2	1	2	4852.614	0.000
3	0	3	2	0	2	5108.030	0.000
3	2	2	2	2	1	5548.588	0.001
3	2	1	2	2	0	5989.143	-0.001
3	1	2	2	1	1	6081.364	0.000
4	1	4	3	1	3	6369.417	0.002
4	0	4	3	0	3	6519.511	-0.001

Table A.7. Frequencies of rotational transitions of ^{13}C isotopologues of *cis*-2-naphthol. $\Delta\nu^a$ is the difference between observed and calculated frequencies.

J'	K_a'	K_c'	J"	K_a"	K_c"	ν_{Exp}/ MHz	$\Delta\nu^a$/ MHz

C1							
2	1	1	2	0	2	2389.725	0.017
4	1	3	4	0	4	3172.361	-0.006
1	1	1	0	0	0	3467.968	-0.005
4	0	4	3	1	3	4128.181	0.016
2	1	2	1	0	1	4743.803	0.000
5	0	5	4	1	4	5752.625	-0.012
3	1	3	2	0	2	5931.802	0.000
C2							
4	1	3	4	0	4	3175.116	-0.010
1	1	1	0	0	0	3484.749	-0.001
5	1	4	5	0	5	3797.195	0.007
4	0	4	3	1	3	4080.998	-0.009
2	1	2	1	0	1	4757.210	0.006
5	0	5	4	1	4	5701.479	0.007
3	1	3	2	0	2	5942.966	-0.003
C3							
4	1	3	4	0	4	3164.651	0.010
1	1	1	0	0	0	3462.809	0.000
5	1	4	5	0	5	3794.545	-0.006
4	0	4	3	1	3	4106.272	0.000
3	0	3	2	0	2	4319.604	0.001
2	1	2	1	0	1	4734.495	-0.007
3	1	3	2	0	2	5918.868	0.003
C4							
2	1	1	2	0	2	2367.779	0.012
4	1	3	4	0	4	3160.057	0.012
1	1	1	0	0	0	3442.654	-0.011
5	1	4	5	0	5	3803.144	-0.009
4	0	4	3	1	3	4154.077	-0.003
3	0	3	2	0	2	4334.256	-0.008
2	1	2	1	0	1	4717.144	-0.004
5	0	5	4	1	4	5776.494	0.008
3	1	3	2	0	2	5903.128	0.005
C4a							
2	1	1	2	0	2	2397.935	0.013
3	1	2	3	0	3	2716.329	0.007
4	1	3	4	0	4	3179.710	-0.010
1	1	1	0	0	0	3478.498	-0.001
4	0	4	3	1	3	4128.773	-0.006
2	1	2	1	0	1	4756.507	-0.002
5	0	5	4	1	4	5756.096	0.009
3	1	3	2	0	2	5946.697	-0.005
C5							
3	0	3	2	1	2	2486.093	-0.009
3	1	2	3	0	3	2701.819	-0.005
4	1	3	4	0	4	3162.801	-0.012
1	1	1	0	0	0	3459.924	0.007
5	1	4	5	0	5	3793.203	0.009
4	0	4	3	1	3	4107.109	0.006
2	1	2	1	0	1	4731.159	0.006
5	0	5	4	1	4	5725.785	0.000
4	0	4	3	0	3	5703.776	0.001
3	1	3	2	0	2	5915.025	-0.007
C6							
1	1	0	1	0	1	2214.260	0.008
2	1	1	2	0	2	2406.207	-0.009
3	1	2	3	0	3	2715.161	0.011
4	1	3	4	0	4	3163.862	-0.006
1	1	1	0	0	0	3479.655	-0.007
5	1	4	5	0	5	3776.733	0.000
4	0	4	3	1	3	4038.624	-0.014
3	0	3	2	0	2	4292.009	-0.011
2	1	2	1	0	1	4745.078	0.010
5	0	5	4	1	4	5650.256	0.018
3	1	3	2	0	2	5924.750	-0.005
C7							
3	1	2	3	0	3	2705.361	-0.008
4	1	3	4	0	4	3158.752	0.010
1	1	1	0	0	0	3466.034	0.006

5	1	4	5	0	5	3778.291	-0.004
4	0	4	3	1	3	4062.688	0.001
2	1	2	1	0	1	4732.159	0.001
3	1	3	2	0	2	5911.975	-0.004
C8							
3	1	2	3	0	3	2694.877	0.016
4	1	3	4	0	4	3160.402	-0.014
1	1	1	0	0	0	3449.820	0.001
5	1	4	5	0	5	3797.328	0.000
4	0	4	3	1	3	4130.874	0.008
6	1	5	6	0	6	4623.745	0.002
2	1	2	1	0	1	4722.426	0.001
5	0	5	4	1	4	5751.089	-0.005
3	1	3	2	0	2	5907.089	-0.003
C8a							
2	1	1	2	0	2	2401.077	-0.002
3	1	2	3	0	3	2719.289	0.008
4	1	3	4	0	4	3182.335	-0.004
1	1	1	0	0	0	3482.455	0.000
4	0	4	3	1	3	4128.181	0.003
2	1	2	1	0	1	4761.165	-0.001
3	1	3	2	0	2	5952.084	0.000

Table A.8. Frequencies of rotational transitions of ^{13}C isotopologues of *trans*-2-naphthol. $\Delta\nu^a$ is the difference between observed and calculated frequencies.

J'	K_a'	K_c'	J"	$K_a"$	$K_c"$	ν_{Exp}/ MHz	$\Delta\nu^a$/ MHz
C1							
4	1	3	4	0	4	3171.826	-0.001
1	1	1	0	0	0	3464.708	0.005
2	1	2	1	0	1	4741.258	0.002
5	2	3	5	1	4	5362.168	-0.001
3	1	3	2	0	2	5929.754	-0.003
C2							
4	1	3	4	0	4	3174.484	0.002
4	0	4	3	1	3	4090.654	-0.001
2	1	2	1	0	1	4754.524	-0.011
3	1	3	2	0	2	5940.797	0.008
C3							
2	1	1	2	0	2	2383.807	-0.012
4	1	3	4	0	4	3163.991	0.003
1	1	1	0	0	0	3459.285	0.000
2	1	2	1	0	1	4731.714	0.010
5	2	3	5	1	4	5362.957	0.002
3	1	3	2	0	2	5916.555	-0.007
C4							
3	1	2	3	0	3	2687.666	0.003
1	1	1	0	0	0	3439.034	-0.010
4	0	4	3	1	3	4164.006	0.011
2	1	2	1	0	1	4714.223	-0.008
5	2	3	5	1	4	5287.898	0.003
5	0	5	4	1	4	5787.189	-0.008
3	1	3	2	0	2	5900.683	0.008
C4a							
1	1	1	0	0	0	3475.018	-0.002
5	1	4	5	0	5	3814.894	0.000
2	1	2	1	0	1	4753.735	0.004
3	1	3	2	0	2	5944.413	-0.002
C5							
3	1	2	3	0	3	2699.485	0.002
1	1	1	0	0	0	3456.552	-0.012
4	0	4	3	1	3	4116.584	-0.001
2	1	2	1	0	1	4728.508	0.009
C6							
4	1	3	4	0	4	3163.142	-0.010
1	1	1	0	0	0	3476.291	0.004
5	1	4	5	0	5	3778.448	0.007
4	0	4	3	1	3	4048.277	-0.003
2	1	2	1	0	1	4742.411	-0.003

4	2	2	4	1	3	5647.609	-0.002
3	1	3	2	0	2	5922.605	0.004
C7							
3	1	2	3	0	3	2702.907	0.006
1	1	1	0	0	0	3462.492	-0.015
5	1	4	5	0	5	3780.186	0.001
2	1	2	1	0	1	4729.345	-0.022
3	2	1	3	1	2	5832.618	0.004
3	1	3	2	0	2	5909.708	0.020
C8							
4	1	3	4	0	4	3160.054	0.000
1	1	1	0	0	0	3446.433	-0.002
2	1	2	1	0	1	4719.799	0.004
3	1	3	2	0	2	5904.970	-0.002
C8a							
3	1	2	3	0	3	2716.954	0.004
4	1	3	4	0	4	3181.767	-0.002
1	1	1	0	0	0	3479.101	-0.001
2	1	2	1	0	1	4758.540	-0.004
3	1	3	2	0	2	5949.967	0.003

Rotational and Centrifugal Distortion Constants for ^{13}C Isotopologues

Table A.9. Experimental rotational constants and centrifugal distortion constants for ^{13}C Isotopologues of *cis*-1-naphthol.

	^{13}C-1	**^{13}C-2**	**^{13}C-3**	**^{13}C-4**	**^{13}C-4a**
A / MHz	1944.27(16)	1947.050(26)	1928.5610(90)	1919.490(25)	1940.959(41)
B / MHz	1119.6924(67)	1111.1331(17)	1115.16790(63)	1123.4788(15)	1123.9108(10)
C / MHz	710.6501(69)	707.7129(17)	706.87770(60)	708.9618(15)	712.06640(92)
Δ_J / kHz	[0.0136]	[0.0136]	[0.0136]	[0.0136]	[0.0135]
Δ_{JK} / kHz	[0.0409]	[0.0409]	[0.0409]	[0.0409]	[0.0408]
δ_J	[-0.006]	[-0.006]	[-0.006]	[-0.006]	[-0.006]
δ_K	[-0.0018]	[-0.0018]	[-0.0018]	[-0.0018]	[-0.0018]
N	4	7	8	8	7
σ / kHz	14.4	6.5	2.4	5.7	3.9
Δ / amu Å^2	-0.14(2)	-0.2920(9)	-0.2908(9)	-0.2784(9)	-0.299(7)
	^{13}C-5	**^{13}C-6**	**^{13}C-7**	**^{13}C-8**	**^{13}C-8a**
A / MHz	1935.954(21)	1947.0190(65)	1938.910(22)	1932.3160(78)	1946.112(49)
B / MHz	1116.2582(12)	1105.69790(27)	1110.4222(11)	1121.63140(41)	1124.3530(31)
C / MHz	708.3112(12)	705.49660(32)	706.3493(10)	709.99190(39)	712.9342(18)
Δ_J / kHz	[0.0135]	[0.0136]	[0.0134]	[0.0134]	[0.0136]
Δ_{JK} / kHz	[0.0408]	[0.0409]	[0.0406]	[0.0404]	[0.0409]
δ_J	[-0.006]	[-0.006]	[-0.006]	[-0.006]	[-0.006]
δ_K	[-0.0019]	[-0.0018]	[-0.0019]	[-0.0018]	[-0.0018]
N	8	5	7	7	6
σ / kHz	4.1	0.7	3.8	1.4	7.8
Δ / amu Å^2	-0.294(3)	-0.1369(9)	-0.294(3)	-0.306(1)	-0.299(7)

Table A.10. Experimental rotational constants and centrifugal distortion constants for ^{13}C isotopologues of *trans*-1-naphthol.

	^{13}C-1	**^{13}C-2**	**^{13}C-3**	**^{13}C-4**	**^{13}C-4a**
A / MHz	1938.1110(43)	1941.7080(49)	1923.4450(36)	1914.1280(21)	1935.5150(38)
B / MHz	1128.97530(26)	1120.20480(30)	1124.20450(25)	1132.72820(15)	1133.23540(27)
C / MHz	713.62120(21)	710.58920(24)	709.72380(21)	711.82680(13)	714.967100(22)
Δ_J / kHz	[0.0170]	[0.0170]	[0.0170]	[0.0170]	[0.0170]
Δ_{JK} / kHz	[0.021]	[0.021]	[0.021]	[0.021]	[0.021]
Δ_K / kHz	[0.070]	[0.070]	[0.070]	[0.070]	[0.070]
δ_J / kHz	[0.0059]	[0.0059]	[0.0059]	[0.0059]	[0.0059]
δ_K / kHz	[0.023]	[0.023]	[0.023]	[0.023]	[0.023]
N	9	9	10	10	10
σ / kHz	1.1	1.2	1.2	0.7	1.3
Δ / amu Å^2	-0.2131(6)	-0.2130(7)	-0.2118(5)	-0.2119(3)	-0.2134(6)
	^{13}C-5	**^{13}C-6**	**^{13}C-7**	**^{13}C-8**	**^{13}C-8a**
A / MHz	1930.4220(34)	1941.5720(27)	1933.6590(21)	1927.0710(20)	1940.8140(36)
B / MHz	1125.50560(24)	1114.84010(18)	1119.60650(15)	1130.94520(14)	1133.66830(27)
C / MHz	711.19190(19)	708.40780(15)	709.26740(12)	712.90180(12)	715.86120(21)
Δ_J / kHz	[0.0170]	[0.0170]	[0.0170]	[0.0170]	[0.0170]
Δ_{JK} / kHz	[0.021]	[0.021]	[0.021]	[0.021]	[0.021]
Δ_K / kHz	[0.070]	[0.070]	[0.070]	[0.070]	[0.070]
δ_J / kHz	[0.0059]	[0.0059]	[0.0059]	[0.0059]	[0.0059]
δ_K / kHz	[0.023]	[0.023]	[0.023]	[0.023]	[0.023]
N	10	10	10	10	9
σ / kHz	1.1	0.9	0.7	0.7	1.1
Δ / amu Å^2	-0.2127(5)	-0.2122(4)	-0.2121(3)	-0.2126(3)	-0.2128(5)

Table A.11. Experimental rotational constants and centrifugal distortion constants for ^{13}C isotopologues of *cis*-2-naphthol.

	^{13}C-1	**^{13}C-2**	**^{13}C-3**	**^{13}C-4**	**^{13}C-4a**
A / MHz	2830.202(11)	2848.666(11)	2827.105(11)	2805.5672(74)	2839.6381(61)
B	823.2344(26)	818.8827(19)	820.0495(24)	824.2133(13)	824.2505(14)
C	637.9165(25)	636.2285(19)	635.8482(21)	637.2430(13)	639.0066(13)
Δ_J / kHz	[0.0130]	[0.0130]	[0.0130]	[0.0130]	[0.0130]
Δ_K	[0.140]	[0.140]	[0.140]	[0.140]	[0.140]
δ_J	[0.00410]	[0.00410]	[0.00410]	[0.00410]	[0.00410]
N	7	7	7	9	8
σ / kHz	10.3	6.8	5.4	8.5	7.7
Δ / amu Å^2	-0.229(3)	-0.230(3)	-0.230(3)	-0.229(2)	-0.228(2)
	^{13}C-5	**^{13}C-6**	**^{13}C-7**	**^{13}C-8**	**^{13}C-8a**
A / MHz	2824.4429(43)	2847.1016(55)	2833.107(10)	2813.658(10)	2843.242(11)
B	819.89499(74)	813.1838(10)	814.9305(27)	821.9521(18)	824.5297(53)
C	635.61953(76)	632.7051(11)	633.0662(24)	636.3053(18)	639.3568(14)
Δ_J / kHz	[0.0130]	[0.0130]	[0.0130]	[0.0130]	[0.0130]
Δ_{JK}	[0.140]	[0.140]	[0.140]	[0.140]	[0.140]
δ_J	[0.00410]	[0.00410]	[0.00410]	[0.00410]	[0.00410]
N	10	11	7	9	7
σ / kHz	7.1	9.9	5.6	7.7	3.6
Δ / amu Å^2	-0.129(1)	-0.220(1)	-0.230(4)	-0.229(2)	-0.228(4)

Table A.12. Experimental rotational constants and centrifugal distortion constants for ^{13}C isotopologues of *trans*-2-naphthol.

	^{13}C-1	**^{13}C-2**	**^{13}C-3**	**^{13}C-4**	**^{13}C-4a**
A / MHz	2826.4266(13)	2844.7845(71)	2823.0746(29)	2801.4505(33)	2835.6648(58)
B	824.12060(87)	819.7675(17)	820.9595(20)	825.1224(12)	825.0998(23)
C	638.27650(66)	636.5836(14)	636.2098(14)	637.5932(11)	639.3556(17)
Δ_J / kHz	[0.0130]	[0.0130]	[0.0130]	[0.0130]	[0.0130]
Δ_K	[0.140]	[0.140]	[0.140]	[0.140]	[0.140]
δ_K	[0.00410]	[0.00410]	[0.00410]	[0.00410]	[0.00410]
N	5	4	6	7	4
σ / kHz	2.7	6.8	7.2	7.6	2.4
Δ / amu Å^2	-0.252(1)	-0.249(2)	-0.254(2)	-0.253(2)	-0.278(3)
	^{13}C-5	**^{13}C-6**	**^{13}C-7**	**^{13}C-8**	**^{13}C-8a**
A / MHz	2824.4429(63)	2843.2229(20)	2829.0763(53)	2809.7545(59)	2839.3825(11)
B	819.89499(21)	814.06279(75)	815.8434(34)	822.9028(30)	825.4301(27)
C	635.61953(16)	633.06372(69)	633.4304(28)	636.6802(17)	639.7204(15)
Δ_J / kHz	[0.0130]	[0.0130]	[0.0130]	[0.0130]	[0.0130]
Δ_{JK}	[0.140]	[0.140]	[0.140]	[0.140]	[0.140]
δ_K	[0.00410]	[0.00410]	[0.00410]	[0.00410]	[0.00410]
N	5	7	6	4	5
σ / kHz	8.4	5.5	13.8	2.4	3.0
Δ / amu Å^2	-0.2286(4)	-0.253(1)	-0.249(4)	-0.236(3)	-0.251(3)

Structural Parameters

Table A.13. Substitution (r_s), semi-experimental (r_{se}), and theoretical structural parameters for *cis*-1-naphthol

Bond length	r_s	r_{se}	MP2	B3LYP-D3	*Bond angle*	r_s	r_{se}	MP2	B3LYP-D3
r(1-2)	1.340(8)	1.40(3)	1.379	1.373	**∠(2-1-8a)**	121.7(6)	121.0(24)	120.83	120.41
r(1-8a)	1.421(5)	1.38(3)	1.421	1.424	**∠(1-2-3)**	120.1(3)	119.2(22)	120.27	120.44
r(2-3)	1.421(7)	1.38(4)	1.406	1.406	**∠(2-3-4)**	120.7(1)	121.4(22)	120.62	120.15
r(4a-8a)	1.426(7)	1.41(2)	1.433	1.429	**∠(3-4-4a)**	119.3(2)	120.9(21)	120.15	121.11
r(3-4)	1.375(3)	1.35(5)	1.377	1.370	**∠(4-4a-8a)**	119.9(5)	118.2(22)	119.75	118.44
r(4-4a)	1.407(5)	1.43(6)	1.413	1.414	**∠(5-4a-8a)**	118.7(5)	120.0(19)	118.40	119.22
r(4a-5)	1.440(5)	1.53(3)	1.415	1.415	**∠(7-8-8a)**	121.3(2)	120.5(23)	120.13	120.87
r(5-6)	1.380(4)	1.21(4)	1.377	1.370	**∠(1-8a-8)**	123.9(5)	122.4(22)	121.87	122.08
r(6-7)	1.411(6)	1.50(40	1.409	1.409	**∠(4a-5-6)**	121.2(2)	120.1(21)	120.99	120.86
r(7-8)	1.383(3)	1.40(4)	1.379	1.371	**∠(5-6-7)**	120.0(1)	120.1(22)	120.18	120.01
r(8-8a)	1.437(4)	1.39(3)	1.415	1.415	**∠(6-7-8)**	120.4(1)	120.9(22)	120.55	120.58

Table A.14. Substitution (r_s), semi-experimental (r_{se}), and theoretical structural parameters for *trans*-1-naphthol

Bond length	r_s	r_{se}	MP2	B3LYP-D3	*Bond angle*	r_s	r_{se}	MP2	B3LYP-D3
r(1-2)	1.364(5)	1.39(2)	1.378	1.371	**∠(2-1-8a)**	121.4(3)	120.6(6)	120.83	120.41
r(1-8a)	1.392(1)	1.46(4)	1.419	1.412	**∠(1-2-3)**	119.4(2)	120.5(5)	120.27	120.44
r(2-3)	1.423(6)	1.39(2)	1.410	1.413	**∠(2-3-4)**	120.5(1)	120.9(4)	120.62	120.15
r(4a-8a)	1.414(4)	1.39(2)	1.429	1.428	**∠(3-4-4a)**	119.4(1)	120.9(4)	120.15	121.11
r(3-4)	1.379(3)	1.36(1)	1.376	1.369	**∠(4-4a-8a)**	119.9(3)	120.7(6)	119.75	118.44
r(4-4a)	1.408(4)	1.42(2)	1.415	1.414	**∠(5-4a-8a)**	119.1(2)	117.3(6)	118.40	119.22
r(4a-5)	1.436(4)	1.41(2)	1.415	1.414	**∠(7-8-8a)**	120.7(1)	118.8(6)	120.13	120.45
r(5-6)	1.381(4)	1.37(2)	1.378	1.370	**∠(1-8a-8)**	121.9(3)	120.6(6)	121.87	122.08
r(6-7)	1.410(6)	1.42(2)	1.410	1.412	**∠(4a-5-6)**	120.8(2)	120.8(9)	120.99	120.86
r(7-8)	1.380(2)	1.37(1)	1.379	1.370	**∠(5-6-7)**	120.3(1)	120.3(4)	120.18	120.01
r(8-8a)	1.392(1)	1.38(2)	1.414	1.417	**∠(6-7-8)**	120.5(1)	120.3(5)	120.55	120.58

Table A.15. Substitution (r_s), semi-experimental (r_{se}), and theoretical structural parameters for *cis*-2-naphthol

Bond length	r_s	r_{se}	MP2	B3LYP-D3	*Bond angle*	r_s	r_{se}	MP2	B3LYP-D3
r(1-2)	1.398(6)	1.368(4)	1.377	1.371	**∠(2-1-8a)**	118.8(3)	120.3(4)	120.353	120.52
r(1-8a)	1.403(9)	1.45(1)	1.414	1.415	**∠(1-2-3)**	121.6(1)	121.2(4)	120.623	120.59
r(2-3)	1.378(9)	1.409(6)	1.411	1.413	**∠(2-3-4)**	119.9(1)	119.7(3)	120.031	119.88
r(3-4)	1.375(3)	1.356(7)	1.374	1.366	**∠(3-4-4a)**	120.7(1)	121.8(5)	121.034	121.36
r(4-4a)	1.420(4)	1.421(7)	1.416	1.416	**∠(4-4a-8a)**	118.6(4)	118.5(4)	118.646	118.49
r(4a-5)	1.426(3)	1.414(7)	1.414	1.413	**∠(5-4a-8a)**	119.9(4)	118.8(4)	119.230	119.14
r(4a-8a)	1.404(4)	1.422(4)	1.429	1.426	**∠(1-8a-8)**	121.3(2)	121.9(4)	121.912	122.25
r(5-6)	1.384(3)	1.370(4)	1.378	1.371	**∠(4a-5-6)**	120.2(2)	120.9(6)	120.670	120.91
r(6-7)	1.378(4)	1.411(5)	1.411	1.410	**∠(5-6-7)**	120.2(1)	119.9(3)	120.19	119.98
r(7-8)	1.378(2)	1.366(5)	1.379	1.371	**∠(6-7-8)**	120.7(1)	120.3(3)	120.366	120.53
r(8-8a)	1.436(7)	1.398(5)	1.415	1.415	**∠(7-8-8a)**	120.5(3)	120.4(4)	120.775	120.85

Table A.16. Substitution (r_s), semi-experimental (r_{se}), and theoretical structural parameters for *trans*-2-naphthol

Bond length	r_s	r_{se}	MP2	B3LYP-D3	*Bond angle*	r_s	r_{se}	MP2	B3LYP-D3
r(1-2)	1.386(5)	1.40(4)	1.376	1.371	**∠(2-1-8a)**	119.2(3)	117(3)	120.269	119.267
r(1-8a)	1.393(6)	1.22(7)	1.412	1.415	**∠(1-2-3)**	120.0(2)	121(2)	120.471	120.999
r(2-3)	1.402(8)	1.42(2)	1.411	1.413	**∠(2-3-4)**	119.9(1)	120(2)	120.286	119.919
r(3-4)	1.382(3)	1.32(3)	1.377	1.366	**∠(3-4-4a)**	120.5(1)	122(2)	120.817	120.574
r(4-4a)	1.429(4)	1.50(3)	1.414	1.416	**∠(4-4a-8a)**	118.4(4)	112(7)	118.578	117.748
r(4a-5)	1.414(3)	1.49(3)	1.414	1.413	**∠(5-4a-8a)**	120.2(3)	124(8)	119.323	121.297
r(4a-8a)	1.411(3)	1.48(4)	1.430	1.426	**∠(1-8a-8)**	121.3(2)	119(3)	121.763	121.125
r(5-6)	1.380(3)	1.20(2)	1.378	1.371	**∠(4a-5-6)**	119.5(2)	123(3)	120.611	119.930
r(6-7)	1.411(4)	1.50(1)	1.411	1.410	**∠(5-6-7)**	120.1(1)	120(2)	120.204	120.128
r(7-8)	1.386(2)	1.37(2)	1.378	1.371	**∠(6-7-8)**	120.4(1)	121(2)	120.406	120.504
r(8-8a)	1.435(5)	1.47(4)	1.416	1.415	**∠(7-8-8a)**	120.9(2)	121(3)	120.796	120.757

Data from AIMA11 QTAIM Calculations

Table A.17. Compilation of results from QTAIM calculations with the AIMA11 program for *cis*- and *trans*-1-naphthol. All energies are in kcal/mol.

	***trans*-1-naphthol**	***cis*-1-naphthol**	**Δ (*trans* – *cis*)**
***ab initio* energy**	-2.8948295089E+05	-2.8948181925E+05	-1.1316397750
C-skeleton[a]	-2.3893145383E+05	-2.3892238752E+05	-9.0663095050
C-skeleton + O-atom	-2.8655709929E+05	-2.8654901952E+05	-8.0797621625
Ring H-atoms	-2.6895304201E+03	-2.6952714802E+03	5.7410600680
All H-atoms	-2.9258579782E+03	-2.9328113415E+03	6.9533632738
Total AIM energy	-2.8948295726E+05	-2.8948183087E+05	-1.1263938750
av H-atoms (not OH, H-H contact)	-3.8498116888E+02	-3.8338342209E+02	-1.5977467875
(av H-atoms) – (H-H contact)	-5.3377620175	11.587525563	
H12 (C-H … H)	-3.7964340686E+02	-3.9497094765E+02	15.327540793
H19 (O-H … H)	-2.3632755809E+02	-2.3753986129E+02	1.2123032057
O18	-4.7625645456E+04	-4.7626632003E+04	0.98654734250
q(H12)[b] / e	0.05672089246O	-0.0046104091000	
q(H19) / e	0.57607206328	0.57506762675	
C4-C11-O18 angle / °	116.469	121.826	
H … H distance / Å	2.27396	1.87624	
Bond Path Length / Å		2.098360697	
C4-C11-O18-H19 / °	-180	6.462	

[a]The energies are the scaled electronic kinetic energies of the atoms ("K_scaled" in AIMAll), an approximation to the virial-based total energies. [b]Net charge of the atom in units of the electron charge.

Table A.18. Electron density derived properties related to the H12-H19 close contact in *cis*-1-naphthol at different levels of theory.

	B3LYP-D3	**wB97XD**	**MP2**
BCP ρ [e/bohr^3][a]	0.01496	0.01534	0.01581
BCP $\Delta^2\rho$ [e/bohr^5][b]	0.05825	0.05530	0.05783
BCP H [hartree/bohr^3][c]	-0.002514	-0.001843	-0.001549
BCP ε [d]	1.0898	0.9651	1.0868
RCP ρ [e/bohr^3]	0.01456	0.01581	0.01539
RCP $\Delta^2\rho$ [e/bohr^5]	0.06948	0.07003	0.07061
q(H12) [e][e]	-0.004610	-0.014655	0.006553
q(H19) [e]	0.5751	0.5996	0.6135
IBSI[f]	0.031	0.036	0.045

[a] Electron density; [b] Laplacian of electron density; [c] Total energy density; [d] Bond ellipticity $\varepsilon=(\lambda_1/\lambda_2)-1$; [e] Net charge of atom; Intrinsic Bond Strength Index.

Semi-Experimental Rotational Constants for ^{12}C and ^{13}C Isotopologues

Table A.19. Experimental, semi-experimental, and ab initio rotational constants and inertial defects for all four conformers of naphthol

***cis*-1-naphthol**	**Experiment**	**Semi-Experiment**	**B3LYP-D3**
A / MHz	1947.51310	1962.355	1959.859
B / MHz	1124.30739	1130.679	1130.8340
C / MHz	713.09734	717.334	717.128
Δ_I / amu Å^2	-0.2925	0.0175	-0.0468
***trans*-1-naphthol**			
A / MHz	1942.10150	1955.784	1955.174
B / MHz	1133.62357	1141.283	1139.056
C / MHz	716.01804	720.758	719.744
Δ_I / amu Å^2	-0.2124	-0.0417	-0.0003
***cis*-2-naphthol**			
A / MHz	2849.15630	2870.909	2870.704
B / MHz	824.63286	829.670	828.986
C / MHz	639.7240	643.692	643.236
Δ_I / amu Å^2	-0.2364	-0.0415	-0.0001
***trans*-2-naphthol**			
A / MHz	2845.35700	2867.769	2868.659
B / MHz	825.53621	830.467	829.642
C / MHz	640.08728	644.012	643.528
Δ_I / amu Å^2	-0.2510	-0.0398	-0.0000

Table A.20. Semi-experimental rotational constants and inertial defects for ^{13}C isotopologues of *cis*-1-naphthol

	^{13}C-1	**^{13}C-2**	**^{13}C-3**	**^{13}C-4**	**^{13}C-4a**
A / MHz	1959.089	1961.892	1943.403	1934.332	1955.801
B	1126.065	1117.505	1121.539	1129.851	1130.283
C	714.889	711.951	711.116	713.200	716.304
Δ / amu Å^2	0.167	0.014	0.024	0.042	0.010
	^{13}C-5	**^{13}C-6**	**^{13}C-7**	**^{13}C-8**	**^{13}C-8a**
A / MHz	1950.796	1961.861	1953.752	1947.158	1960.954
B	1122.630	1112.070	1116.794	128.003	1130.725
C	712.549	709.734	710.587	714.230	717.172
Δ / amu Å^2	0.018	0.017	0.016	0.009	0.011

Table A.21. Semi-experimental rotational constants and inertial defects for ^{13}C isotopologues of *trans*-1-naphthol

	^{13}C-1	**^{13}C-2**	**^{13}C-3**	**^{13}C-4**	**^{13}C-4a**
A / MHz	1951.794	1955.391	1937.120	1927.810	1949.200
B	1120.205	1127.864	1131.860	1140.390	1140.890
C	710.5892	715.392	714.464	716.567	719.707
Δ / amu Å^2	-0.042	-0.041	-0.038	-0.038	-0.042
	^{13}C-5	**^{13}C-6**	**^{13}C-7**	**^{13}C-8**	**^{13}C-8a**
A / MHz	1944.105	1955.260	1947.340	1940.750	1954.500
B	1133.165	1122.500	1127.270	1138.600	1141.330
C	715.932	713.148	714.007	717.642	720.601
Δ / amu Å^2	-0.040	-0.039	-0.039	-0.040	-0.042

Table A.22. Semi-experimental rotational constants and inertial defects for ^{13}C isotopologues of *cis*-2-naphthol

	^{13}C-1	**^{13}C-2**	**^{13}C-3**	**^{13}C-4**	**^{13}C-4a**
A / MHz	2851.955	2870.419	2848.858	2827.320	2861.391
B	828.271	823.919	825.086	829.250	829.287
C	641.884	640.196	639.816	641.211	642.974
Δ / amu Å^2	-0.029	-0.036	-0.032	-0.025	-0.032
	^{13}C-5	**^{13}C-6**	**^{13}C-7**	**^{13}C-8**	**^{13}C-8a**
A / MHz	2846.196	2868.854	2854.860	2835.411	2864.995
B	824.931	818.221	819.967	826.989	829.566
C	639.587	636.672	637.034	640.273	643.324
Δ / amu Å^2	-0.030	-0.035	-0.033	-0.028	-0.032

Table A.23. Semi-experimental rotational constants and inertial defects for ^{13}C isotopologues of *trans*-2-naphthol

	^{13}C-1	**^{13}C-2**	**^{13}C-3**	**^{13}C-4**	**^{13}C-4a**
A / MHz	2848.8383	2867.1962	2845.486	2823.8622	2858.0765
B	829.05174	824.69864	825.8906	830.05354	830.03094
C	642.20149	640.50859	640.1348	641.51819	643.28059
Δ / amu Å^2	-0.037	-0.040	-0.034	-0.032	-0.065
	^{13}C-5	**^{13}C-6**	**^{13}C-7**	**^{13}C-8**	**^{13}C-8a**
A / MHz	2846.8546	2865.6346	2851.488	2832.166	2861.7942
B	824.82613	818.99393	820.77454	827.8339	830.36124
C	639.54452	636.98871	637.35539	640.6052	643.64539
Δ / amu Å^2	-0.014	-0.043	-0.036	-0.017	-0.038

Non-Covalent Interaction (NCI) Plots

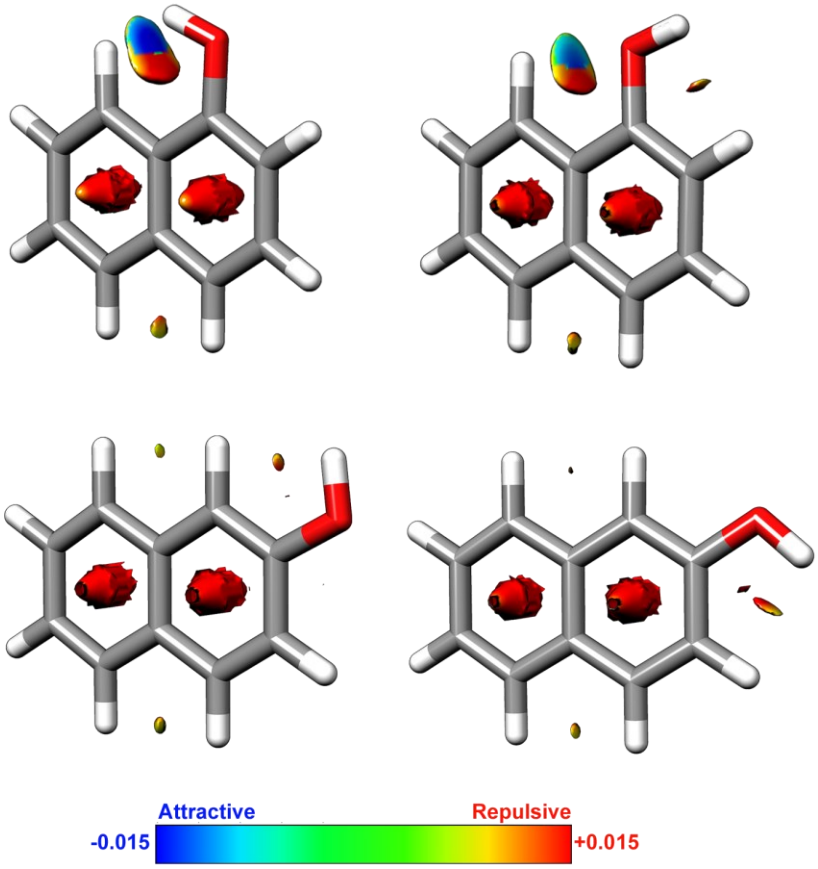

Figure A.1. Results from non-covalent interactions (NCI) analyses of the four experimentally assigned naphthol conformers (s=0.75). The 3D isosurfaces presented contain attractive (blue) and repulsive (red) regions. See, however, the text for the close-contact H-atoms in *cis*-1-naphthol.

Local Mode Analyses

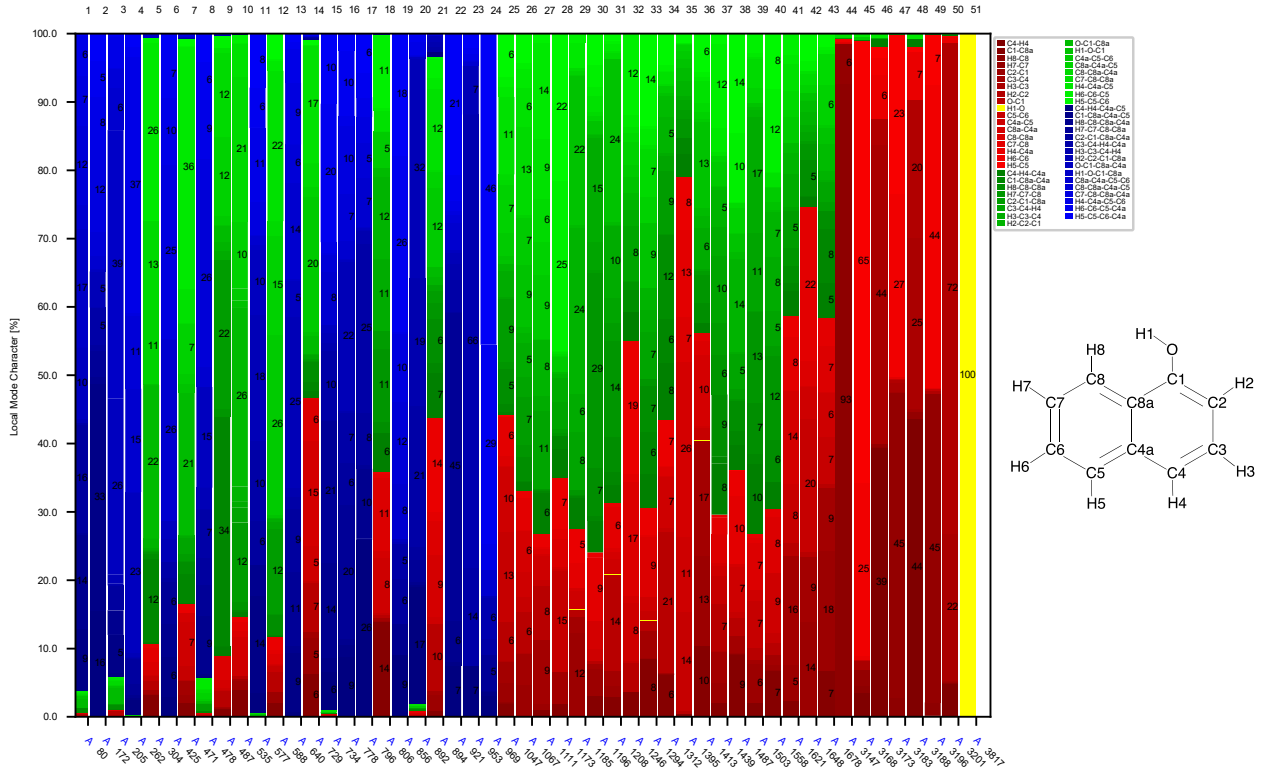

Figure A.2. Decomposition of normal vibrational modes into %LVM contributions for *cis*-1-naphthol (B3LYP-D3(BJ)). % Contribution from O-H local stretching mode to O-H normal mode (3817 cm^{-1}) is shown in yellow. Numbering of local modes are as in the scheme.

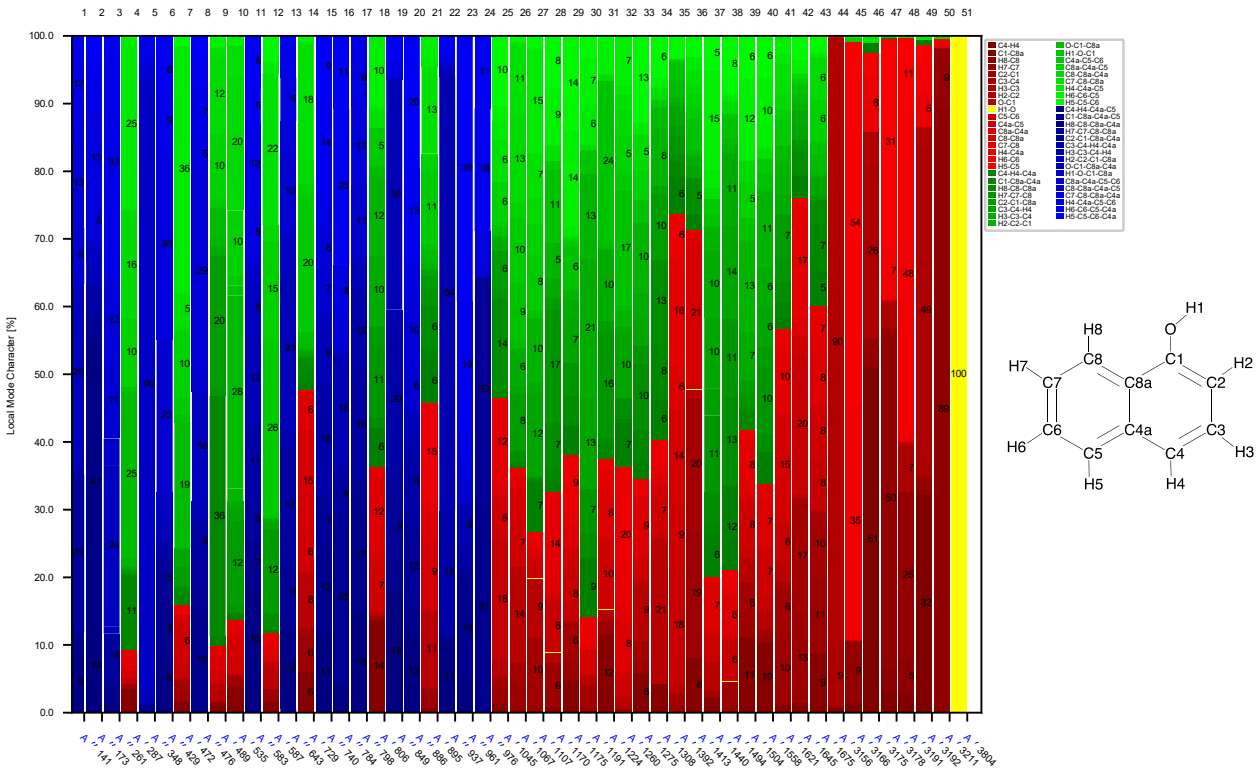

Figure A.3. Decomposition of normal vibrational modes into %LVM contributions for *trans*-1-naphthol (B3LYP-D3(BJ)). % Contribution from O-H local stretching mode to O-H normal mode (3804 cm^{-1}) is shown in yellow. Numbering of local modes are as in the scheme.

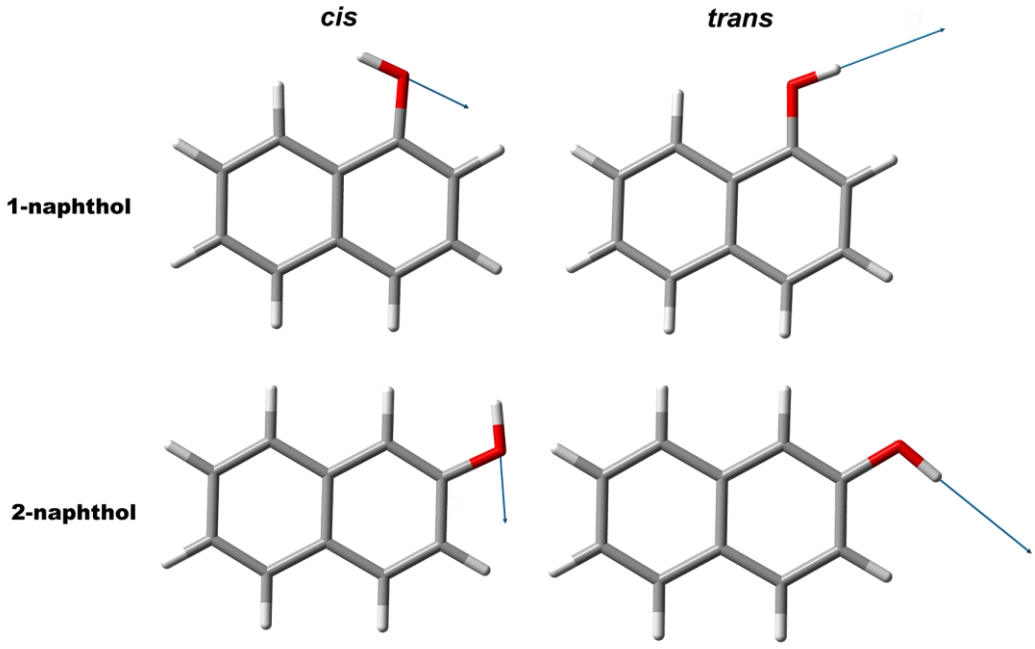

Figure A.4. Vibrational displacement vectors for the O-H stretching vibration

Table A.24. [b] For each local mode, the local mode force constant k^a (mDyn/Å for stretching and mDyn.Å/Rad^2 for bending vibrations) and local mode frequency ω^a (cm^{-1}) are given. Reported values are for MP2/aug-cc-pVTZ calculations followed by values for B3LYP-D3(BJ)/def2-TZVP calculations in parentheses.

	***cis*-1-naphthol**		***trans*-1-naphthol**	
Parameter[b]	**k^a**	**ω^a**	**k^a**	**ω^a**
O1-H1	8.169 (8.085)	3824.2 (3804.5)	8.097 (8.057)	3807.2 (3797.8)
C1-O1	5.825 (5.609)	1200.8 (1178.3)	5.790 (5.673)	1197.3 (1185.0)
H1-O1-C1	0.743 (0.735)	1254.1 (1248.9)	0.745 (0.749)	1253.1 (1258.6)
O1-C1-C2	1.716 (1.694)	774.6 (772.9)	1.756 (1.804)	798.1 (810.7)
O1-C1-C3	1.771 (1.728)	787.2 (777.0)	1.727 (1.777)	762.8 (774.6)
	***cis*-2-naphthol**		***trans*-2-naphthol**	
	k^a	**ω^a**	**k^a**	**ω^a**
O1-H1	8.091 (8.035)	3805.8 (3792.6)	8.143 (8.070)	3818.0 (3800.9)
C1-O1	5.851 (5.735)	1203.6 (1191.5)	5.824 (5.709)	1200.7(1188.8)
H1-O1-C1	0.749 (0.754)	1256.4 (1262.6)	0.754 (0.759)	1261.4 (1267.0)
O1-C1-C2	1.599 (1.647)	763.1(776.3)	1.540 (1.593)	735.9 (751.6)
O1-C1-C3	1.548 (1.600)	723.3 (736.4)	1.597 (1.646)	748.1 (759.2)
	References					
	water		**methanol**		**2-propanol**	
	k^a	**ω^a**	**k^a**	**ω^a**	**k^a**	**ω^a**
O1-H1	8.348 (8.151)	3865.9 (3819.9)	8.288 (8.091)	3851.9 (3805.9)	8.158 (8.045)	3821.5 (3795.0)
C1-O1			4.775 (4.628)	1087.3 (1070.4)	4.417 (4.220)	1045.6 (1022.1)
H1-O1-C1	-	-	0.731 (0.736)	1241.6 (1245.2)	0.718 (0.723)	1227.0 (1232.1)
O1-C1-C2	-	-	-	-	1.280 (1.301)	609.3 (613.6)
O1-C1-C3	-	-	-	-	1.323 (1.340)	608.8 (613.0)
	propen-2-ol				**phenol**	
	k^a	**ω^a**	**k^a**	**ω^a**		
O1-H1	8.221 (8.120)	3836.4 (3812.7)	8.132 (8.054)	3815.5 (3797.1)		
C1-O1	5.572 (5.426)	1174.5 (1159.0)	5.838 (5.729)	1202.2 (1190.9)		
H1-O1-C1	0.762 (0.768)	1269.9 (1275.3)	0.751 (0.755)	1258.4 (1264.0)		
O1-C1-C2	1.408 (1.461)	668.6 (680.3)	1.599 (1.642)	756.0 (767.0)		
O1-C1-C3	1.375 (1.428)	708.4 (724.7)	1.543 (1.590)	729.8 (743.0)		

Inertial Defect Differences

Table A.25. Inertial defects and defect differences between calculated and experimental defect values for all four naphthol conformers. [a]The experimental inertial defect values. [b]The calculated inertial defect values obtained from summing Oka's equation over the lowest out-of-plane vibrational modes. [c]Moment of inertia values from the fit of Jahn et al..

	[a]Δ_e / amu Å^2	[b]$\Delta_{l=2}$/ amu Å^2	$\Delta_e - \Delta_{l=2}$ / amu Å^2	[c]$(I_{cc})^{1/2}$ / amu$^{0.5}$ Å	$(I_{cc})^{1/2}$ / amu$^{0.5}$ Å
***cis*-1-naphthol**	-0.2925	-0.62	0.33	30.8	26.6
***trans*-1-naphthol**	-0.2124	-0.43	0.22	20.6	26.6
***cis*-2-naphthol**	-0.2365	-0.46	0.23	21.5	28.1
***trans*-2-naphthol**	-0.251	-0.46	0.21	19.6	28.1

Table A.26. The calculated inertial defect values obtained from summing Oka's equation over the lowest out-of-plane vibrational modes.

	[a]$\Delta_{l=1}$/ amu Å^2	[b]$\Delta_{l=2}$/ amu Å^2	[c]$\Delta_{l=3}$/ amu Å^2	[d]$\Delta_{l=4}$/ amu Å^2	[e]$\Delta_{l=5}$/ amu Å^2
***cis*-1-naphthol**	-0.42	-0.62	-0.78	-0.91	-0.99
***trans*-1-naphthol**	-0.24	-0.43	-0.56	-0.68	-0.78
***cis*-2-naphthol**	-0.28	-0.46	-0.57	-0.67	-0.74
***trans*-2-naphthol**	-0.28	-0.46	-0.57	-0.68	-0.76

[a]Summed over the lowest out-of-plane modes, [b]two lowest out-of-plane modes, [c]three lowest out-of-plane modes, [d]four lowest out-of-plane modes, [e]five lowest out-of-plane modes.

Table A.27. Inertial defect differences between the experiment and calculated inertial defect values summed over Oka's equation.

	$\Delta_e - \Delta_{l=1}$ / amu Å^2	$\Delta_e - \Delta_{l=2}$ / amu Å^2	$\Delta_e - \Delta_{l=3}$ / amu Å^2	$\Delta_e - \Delta_{l=4}$ / amu Å^2	$\Delta_e - \Delta_{l=5}$ / amu Å^2
***cis*-1-naphthol**	0.13	0.33	0.49	0.62	0.70
***trans*-1-naphthol**	0.03	0.22	0.35	0.47	0.57
***cis*-2-naphthol**	0.04	0.23	0.34	0.43	0.51
***trans*-2-naphthol**	0.03	0.21	0.32	0.43	0.52

Table A.28. Lowest out-of-plane modes and the theoretical and experimental inertial defects from previous work and for the four isomers of naphthol.

	Δ_{exp} / amu Å^2	Lowest out-of-plane (l=1) / cm^{-1}	(l=2)	(l=3)	(l=4)	(l=5)	$(I_{cc})^{1/2}$	Rings
Quinoline[a]	-0.13405	173[g]	182[g]	-	-	-	23.6	2
Isoquinoline[a]	-0.13485	171[g]	185[g]	-	-	-	23.8	2
Phthalazine[b]	-0.154	170[g]	177[g]	-	-	-	23.7	2
Quinazoline[b]	-0.136	172[g]	180[g]	-	-	-	23.5	2
Quinoxaline[b]	-0.119	173[g]	184[g]	-	-	-	23.3	2
Acridine[c]	-0.4363	93[g]	114[g]	238[g]	-	-	36.3	3
Phenanthroline[c]	-0.4423	98[g]	104[g]	238[g]	-	-	34.4	3
Phenanthridine[c]	-0.4576	99[g]	104[g]	233[g]	-	-	34.9	3
5,6-Benzoquinoline[d]	-0.471	93[g]	100[g]	222[g]	-	-	34.9	3
7,8-Benzoquinoline[d]	-0.413	98[g]	115[g]	228[g]	-	-	34.6	3
Benzanthrone[e]	-1.054	45[g]	94[g]	135[g]	165[g]	-	43.9	4
Naphthalene[f]	-0.137	172	186	395	480	487	23.9	2
cis-1-naphthol	-0.2925	80	172	205	262	425	26.6	2
trans-1-naphthol	-0.2124	141	173	261	287	348	26.6	2
cis-2-naphthol	-0.2365	122	182	300	366	411	28.1	2
trans-2-naphthol	-0.251	122	181	299	307	411	28.1	2

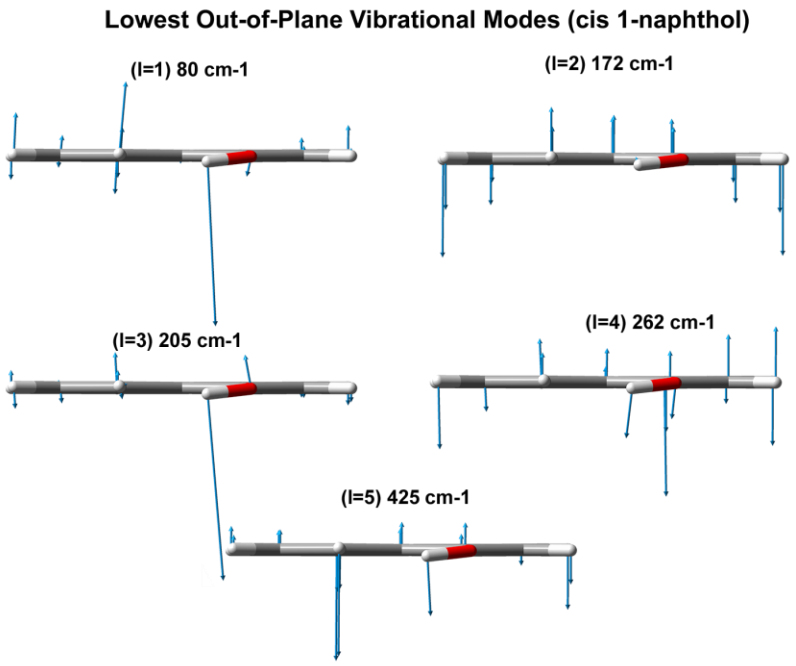

Figure A5. Lowest out-of-plane vibrational modes, with their respective displacement vectors, for *cis*-1-naphthol calculated at the B3LYP-D3(BJ)/def2-TZVP level of theory.

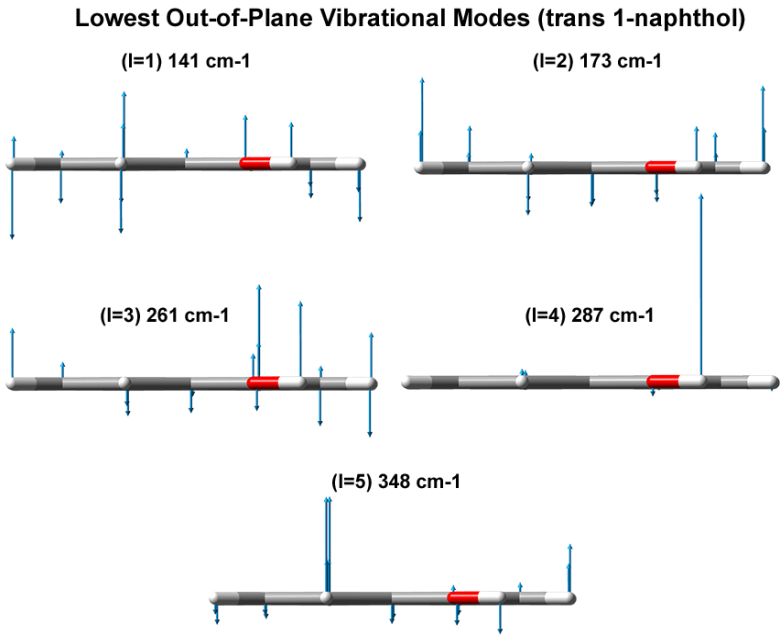

Figures A6. Lowest out-of-plane vibrational modes, with their respective displacement vectors, for *trans*-1-naphthol calculated at the B3LYP-D3(BJ)/def2-TZVP level of theory.

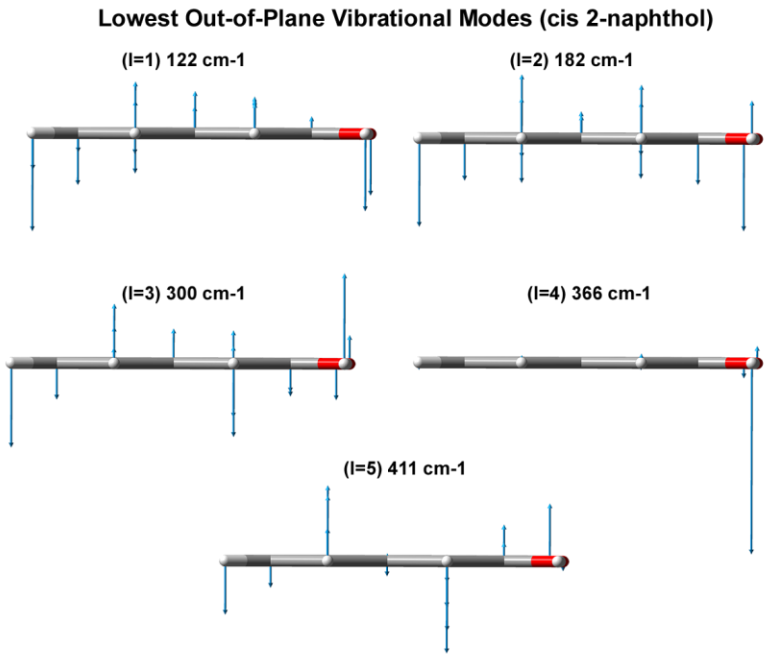

Figures A.7. Lowest out-of-plane vibrational modes, with their respective displacement vectors, for *cis*-2-naphthol calculated at the B3LYP-D3(BJ)/def2-TZVP level of theory.

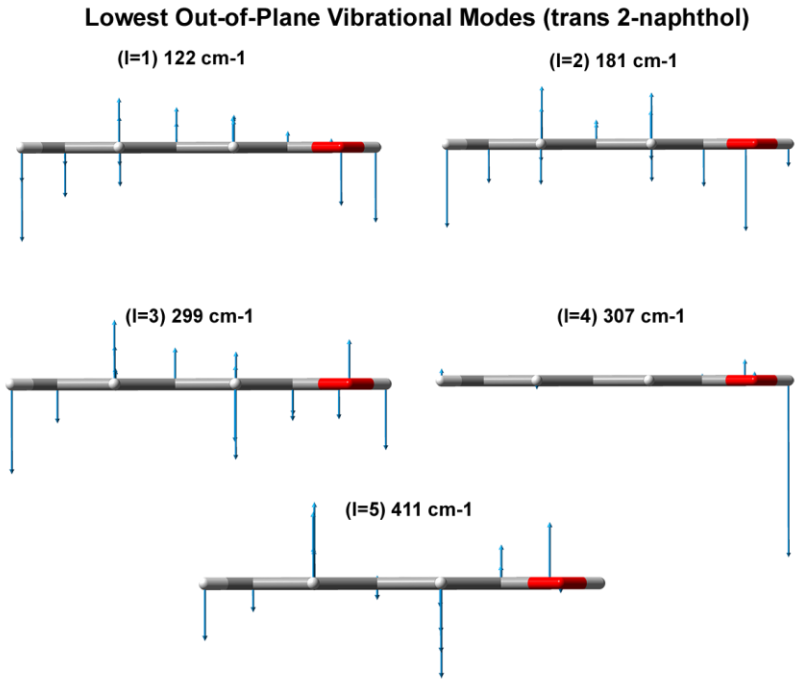

Figures A.8. Lowest out-of-plane vibrational modes, with their respective displacement vectors, for *trans*-2-naphthol calculated at the B3LYP-D3(BJ)/def2-TZVP level of theory.

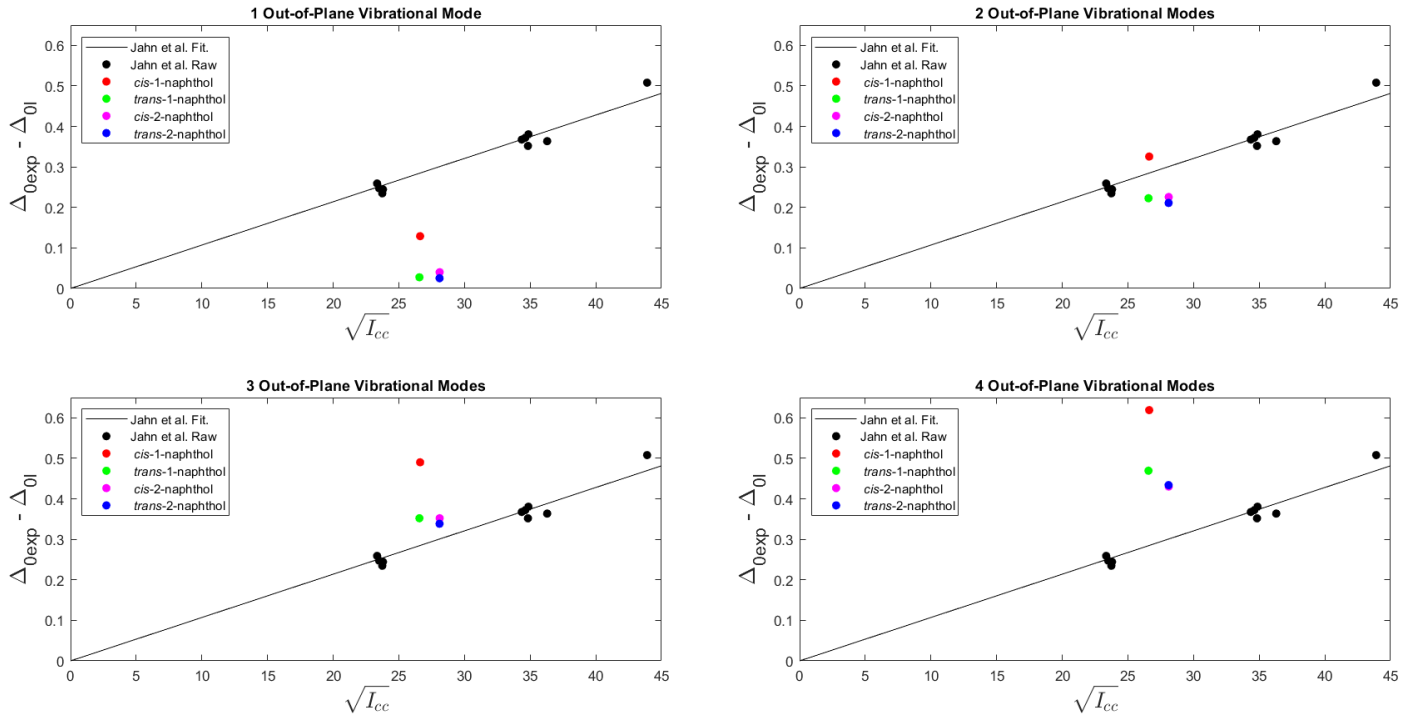

Figure A.9. Inertial defect differences for the four isomers of naphthol compared to the results of Jahn et al. The four plots contain different numbers of out-of-plane vibrations used to sum over Oka's equation.

Charge Model 5 Analysis

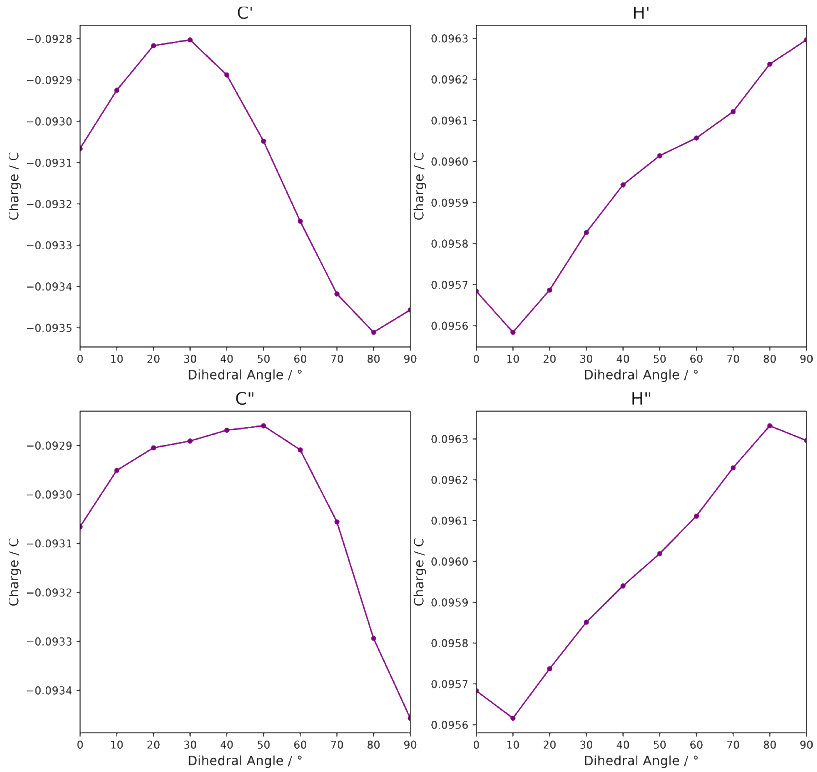

Figure A.10. Charge Model 5 (CM5) charges for atoms involved in the H-H interaction for biphenyl. The H'-H" charge separation was calculated by subtracting the H" charge from the H' charge.

Table A.29. Net CM5 charge change from 90° to 0° for five atom types. Positive charge difference indicates electron density decreases as the dihedral angle approaches zero. Negative charge difference indicates electron density increases as the dihedral angle approaches zero.

	C'	O'	H'	H"	C"
***trans*-1-naphthol**	0.006276	0.020825	0.000103	-0.006450	-0.018738
***cis*-1-naphthol**	0.005287	0.016097	-0.012526	-0.000930	-0.004424
***trans*-2-naphthol**	0.004300	0.021359	-0.001350	-0.004230	-0.010043
***cis*-2-naphthol**	0.005819	0.022029	-0.000165	-0.006150	-0.018889
Biphenyl	0.000391	-	-0.000610	-0.000613	-0.093294

Table A.30. Occupancy for each bonding[b] and anti-bonding[c] orbital for all four isomers of naphthol. [a]Average occupancy for *trans* 1-naphthol, *cis* 2-naphthol, and *trans* 2-naphthol.

	***trans*-1-naphthol**	***Cis*-2-naphthol**	***trans*-2-naphthol**	**Average[a]**	***cis*-1-naphthol**
O'-H' BD[b]	1.98737	1.98764	1.98781	1.98761	1.98690
O'-H' BD*[c]	0.00690	0.00681	0.00648	0.00673	0.00911
C"-H" BD	1.97857	1.97741	1.97873	1.97824	1.97677
C"-H" BD*	0.01287	0.01422	0.01334	0.01348	0.01561

NBO Analysis

Table A.31. Interaction energies between bonding and antibonding orbitals obtained from second order perturbative treatment of the Fock matrix for *trans*-1-naphthol

***trans*-1-naphthol**	**C-H BD --- O-H BD* / kJ mol^{-1}**	**O-H BD --- C-H BD* / kJ mol^{-1}**	**Sum of Interactions / kJ mol^{-1}**
0	0.46	0.21	0.67
10	0.42	0.21	0.63
20	0.29	0.21	0.50
30	0.17	0.21	0.38
40	0.00	0.21	0.21
50	0.00	0.17	0.17
60	0.00	0.17	0.17
70	0.00	0.17	0.17
80	0.00	0.21	0.21
90	0.00	0.00	0.00

Table A.32. Interaction energies between bonding and antibonding orbitals obtained from second order perturbative treatment of the Fock matrix for c*is*-1-naphthol

***cis*-1-naphthol**	**C-H BD --- O-H BD* / kJ mol^{-1}**	**O-H BD --- C-H BD* / kJ mol^{-1}**	**Sum of Interactions / kJ mol^{-1}**
0	3.85	0.38	4.23
10	3.35	0.38	3.72
20	2.26	0.29	2.55
30	1.13	0.21	1.34
40	0.42	0.17	0.59
50	0.13	0.08	0.21
60	0.08	0.00	0.08
70	0.00	0.00	0.00
80	0.00	0.00	0.00
90	0.00	0.00	0.00

Table A.33. Interaction energies between bonding and antibonding orbitals obtained from second order perturbative treatment of the Fock matrix for *trans*-2-naphthol

***trans*-2-naphthol**	**C-H BD --- O-H BD* / kJ mol^{-1}**	**O-H BD --- C-H BD* / kJ mol^{-1}**	**Sum of Interactions / kJ mol^{-1}**
0	0.42	0.17	0.59
10	0.38	0.17	0.54
20	0.25	0.17	0.42
30	0.13	0.13	0.25
40	0.00	0.13	0.13
50	0.00	0.13	0.13
60	0.00	0.13	0.13
70	0.00	0.13	0.13
80	0.00	0.13	0.13
90	0.00	0.13	0.13

Table A.34. Interaction energies between bonding and antibonding orbitals obtained from second order perturbative treatment of the Fock matrix for c*is*-2-naphthol

***cis*-2-naphthol**	**C-H BD --- O-H BD* / kJ mol^{-1}**	**O-H BD --- C-H BD* / kJ mol^{-1}**	**Sum of Interactions / kJ mol^{-1}**
0	0.42	0.25	0.67
10	0.38	0.25	0.63
20	0.25	0.21	0.46
30	0.13	0.21	0.33
40	0.04	0.21	0.25
50	0.00	0.21	0.21
60	0.00	0.21	0.21
70	0.00	0.21	0.21
80	0.00	0.21	0.21
90	0.00	0.21	0.21

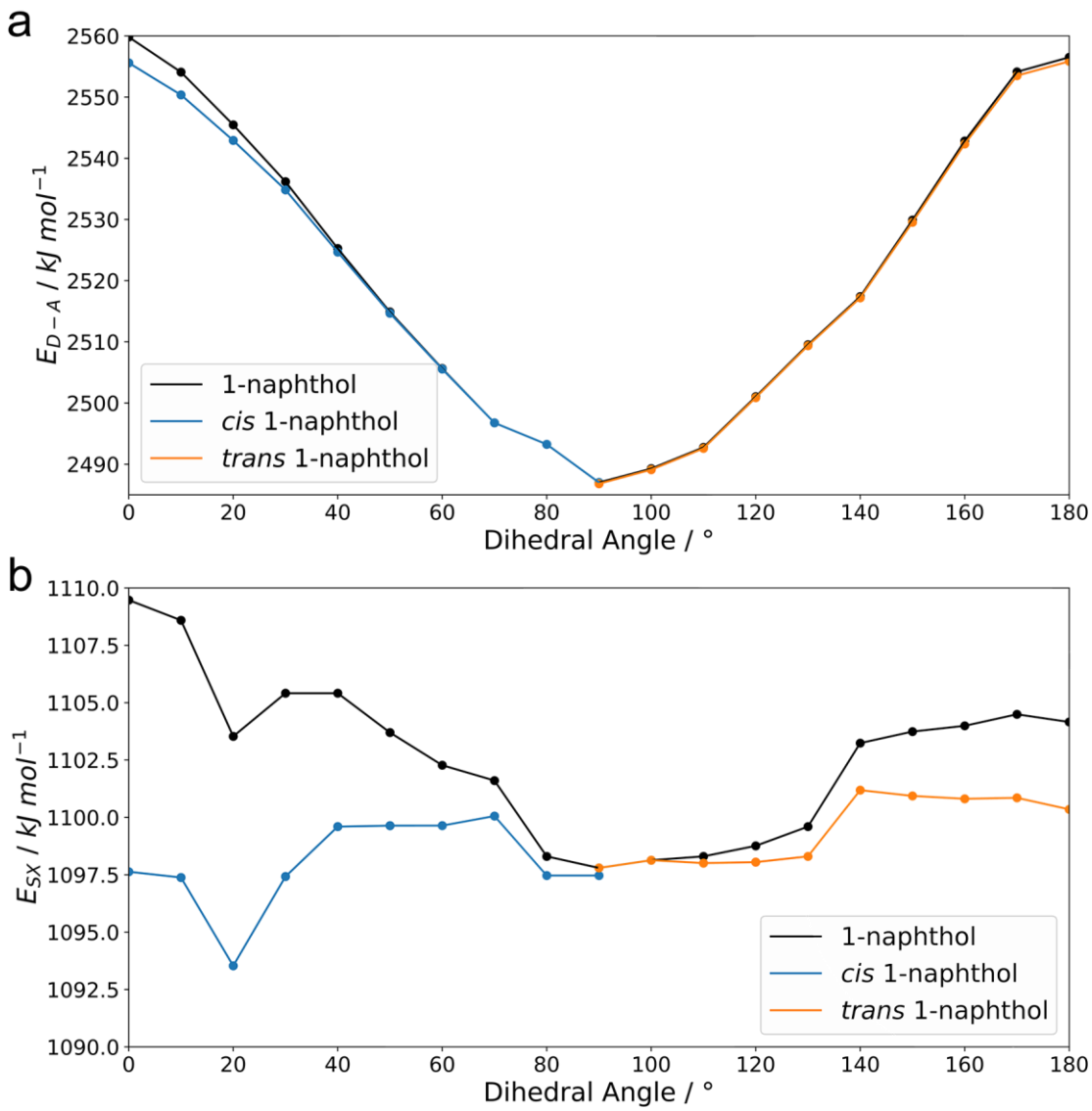

Figure A.11. [a]Summed donor-acceptor (attraction) energies for 1-naphthol with the close contact H-H interactions subtracted. [b]Pairwise steric exchange (repulsion) energies for 1-naphhtol with close contact H-H interactions subtracted.

Table A.35. Attraction and repulsion energy comparison for *cis*-1-naphthol at the B3LYP-D3(BJ)/def-TZVP and ωB97XD/Jun-cc-pVTZ level of theory

	Attraction /kJ mol^{-1}		Repulsion /kJ mol^{-1}	
Dihedral Angle	**B3LYP-D3(BJ)**	**ωB97XD**	**B3LYP-D3(BJ)**	**ωB97XD**
0	4.2	4.8	11.8	13.5
30	1.3	1.7	8.0	8.7
60	0.1	0.1	2.6	2.7
90	0.0	0.0	0.3	0.3

Appendix B

Supplementary Information for Chapter 4

The 1-Naphthol Dimer and Its Surprising Preference for π-π Stacking over Hydrogen Bonding

Contents:

1. **Rotational Transition Frequencies**
   a. **Table B.1.** Assigned rotational transitions for the 1-naphthol dimer
2. **Non-Covalent Interactions Analyses**
   a. **Figure B.1.** NCI plots and diagram for the V-shape isomer
   b. **Figure B.2.** NCI plots and diagram for the Saeki-a isomer
   c. **Figure B.3.** NCI plots and diagram for the Saeki-d isomer
   d. **Figure B.4.** NCI plots and diagram for the phenol dimer
3. **Cartesian Coordinates for B3LYP-D3(BJ) Optimized Structures**
   a. **Table B.2.** Cartesian coordinates for the B3LYP-D3(BJ) optimized structure of the V-shape isomer
   b. **Table B.3.** Cartesian coordinates for the B3LYP-D3(BJ) optimized structure of the Saeki-a isomer
   c. **Table B.4.** Cartesian coordinates for the B3LYP-D3(BJ) optimized structure of the Saeki-b isomer
   d. **Table B.5.** Cartesian coordinates for the B3LYP-D3(BJ) optimized structure of the Saeki-c isomer
   e. **Table B.6.** Cartesian coordinates for the B3LYP-D3(BJ) optimized structure of the Saeki-d isomer
   f. **Table B.7.** Cartesian coordinates for the B3LYP-D3(BJ) optimized structure of the Saeki-e isomer
   g. **Table B.8.** Cartesian coordinates for the B3LYP-D3(BJ) optimized structure of the Hinge isomer

Rotational Transition Frequencies

Table B.1. Assigned rotational transitions for the 1-naphthol dimer. $\Delta\nu^a$ is the difference between observed and calculated frequencies.

J'	K_a'	K_c'	J"	K_a"	K_c"	ν_{Exp}/ MHz	$\Delta\nu^a$/ MHz
4	1	3	3	0	3	2432.8786	0.0027
5	0	5	4	1	4	2498.2015	-0.0220
3	3	1	2	2	1	2577.6049	0.0053
3	3	0	2	2	0	2575.6370	-0.0140
3	3	0	2	2	1	2577.6987	-0.0150
4	2	3	3	1	2	2637.7296	-0.0160
4	2	2	3	1	2	2667.6748	-0.0005
5	1	5	4	0	4	2681.5601	0.0188
4	2	3	3	1	3	2777.9178	-0.0054
5	1	4	4	0	4	3029.1014	-0.0059
6	0	6	5	1	5	3033.5921	0.0003
4	3	2	3	2	1	3099.5294	0.0015
4	3	1	3	2	1	3100.3255	0.0013
4	3	2	3	2	2	3109.7350	-0.0015
4	3	1	3	2	2	3110.5289	-0.0040
5	2	4	4	1	3	3119.2093	-0.0040
6	1	6	5	0	5	3163.2781	0.0033
5	2	3	4	1	3	3186.2574	0.0031
5	2	4	4	1	4	3352.2412	0.0061
5	2	3	4	1	4	3419.2660	-0.0099
4	4	0	3	3	0	3501.4992	0.0036
4	4	1	3	3	1	3501.6082	0.0036
7	0	7	6	1	6	3561.4664	-0.0033
6	2	5	5	1	4	3590.1044	-0.0137
5	3	3	4	2	2	3615.7223	0.0114

5	3	2	4	2	2	3618.8676	-0.0007
6	1	5	5	0	5	3644.9460	-0.0069
5	3	3	4	2	3	3645.6393	-0.0012
7	1	7	6	0	6	3648.2985	0.0017
5	3	2	4	2	3	3648.7967	-0.0013
6	2	4	5	1	4	3716.2791	0.0034
8	1	7	7	2	5	3749.4471	0.0030
6	2	5	5	1	5	3937.6834	-0.0008
5	4	1	4	3	1	4029.9852	0.0191
5	4	2	4	3	2	4030.7001	-0.0151
5	4	1	4	3	2	4030.7735	0.0111
7	2	6	6	1	5	4052.2294	0.0047
8	0	8	7	1	7	4082.4679	0.0077
6	3	4	5	2	3	4119.9265	0.0035
6	3	3	5	2	3	4129.2568	0.0065
8	1	8	7	0	7	4138.0449	0.0088
6	3	4	5	2	4	4186.9663	0.0024
6	3	3	5	2	4	4196.2902	-0.0009
7	2	5	6	1	5	4261.9270	0.0027
7	1	6	6	0	6	4280.2144	-0.0013
5	5	1	4	4	1	4426.4264	-0.0021
5	5	0	4	4	0	4426.4264	-0.0021
8	2	7	7	1	6	4508.2916	-0.0066
7	2	6	6	1	6	4533.8941	-0.0086
6	4	3	5	3	2	4556.8764	0.0018
6	4	2	5	3	2	4557.1147	0.0059
6	4	3	5	3	3	4560.0311	-0.0009
6	4	2	5	3	3	4560.2609	-0.0053
9	0	9	8	1	8	4598.0028	-0.0021
7	3	5	6	2	4	4609.1580	0.0029
7	3	4	6	2	4	4631.8967	0.0062
9	1	9	8	0	8	4632.3443	-0.0045
7	3	5	6	2	5	4735.3149	0.0023
7	3	4	6	2	5	4758.0576	0.0097
8	2	6	7	1	6	4826.2236	0.0058
8	1	7	7	0	7	4931.6004	0.0236
7	4	4	6	3	3	5080.6411	-0.0027
7	4	3	6	3	3	5081.4961	0.0006
8	3	6	7	2	5	5082.3923	-0.0109
7	4	4	6	3	4	5089.9676	-0.0035
7	4	3	6	3	4	5090.8372	0.0144
8	3	5	7	2	5	5130.5068	0.0013
8	2	7	7	1	7	5140.2194	0.0022
8	3	6	7	2	6	5292.1006	-0.0024
6	6	0	5	5	0	5351.2841	-0.0045
9	2	7	8	1	7	5411.5250	-0.0222
7	5	2	6	4	2	5483.8581	-0.0038
7	5	3	6	4	3	5484.0869	0.0051
8	4	5	7	3	4	5598.5679	-0.0003
8	4	4	7	3	4	5601.0905	-0.0014
8	4	5	7	3	5	5621.2989	-0.0047
8	4	4	7	3	5	5623.8163	-0.0109
9	3	6	8	2	6	5631.4283	0.0076
7	6	1	6	5	1	5880.2483	0.0013
7	6	2	6	5	2	5880.2483	0.0013

Non-Covalent Interactions Analyses

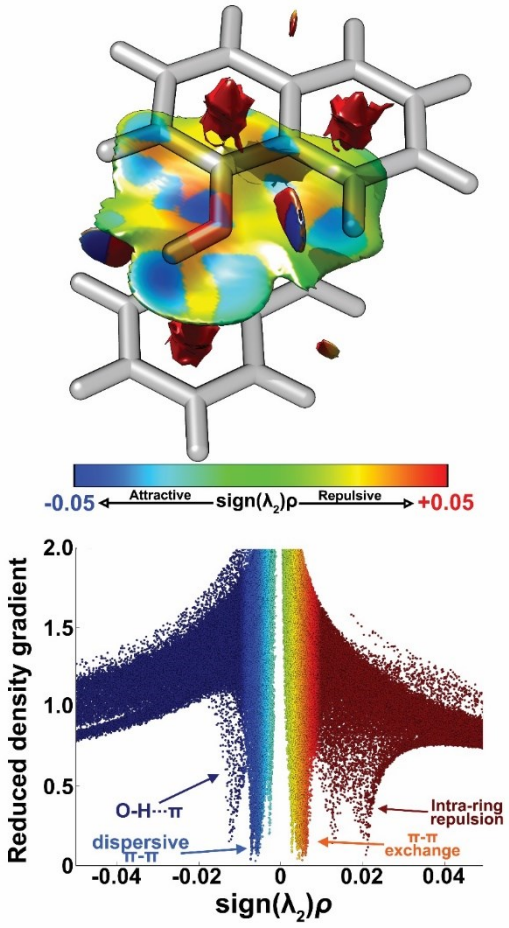

Figure B.1. NCI isosurface and (s, sign(λ_2)ρ) for V-shape, calculated at the B3LYP-D3(BJ)/6-311++g(d,p) level of theory.

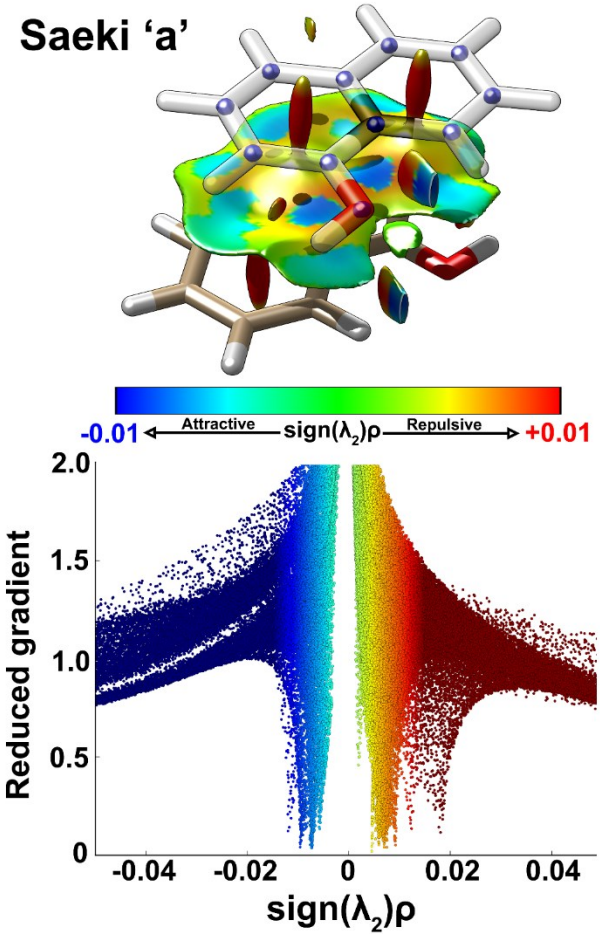

Figure B.2. NCI isosurface and (s, sign(λ_2)ρ) for Saeki-**a**, calculated at the B3LYP-D3(BJ)/6-311++g(d,p) level of theory.

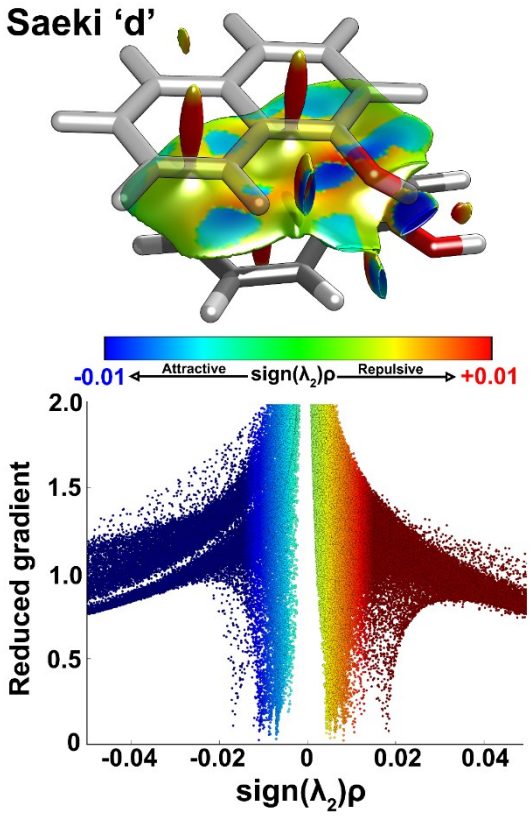

Figure B.3. NCI isosurface and (s, sign(λ_2)ρ) for Saeki-**d**, calculated at the B3LYP-D3(BJ)/6-311++g(d,p) level of theory.

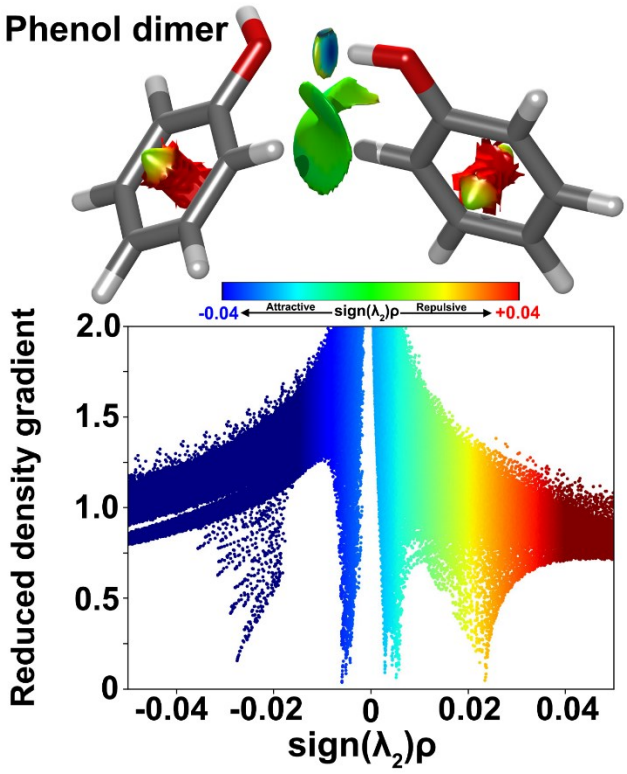

Figure B.4. Full NCI isosurface and (s, sign(λ_2)ρ) for $(phenol)_2$, calculated at the B3LYP-D3(BJ)/6-311++g(d,p) level of theory.

Cartesian Coordinates for B3LYP-D3(BJ) Optimized Structures

Table B.2. Cartesian coordinates for the B3LYP-D3(BJ)/6-311++g(d,p) optimized structure of the V-shape isomer of the 1-naphthol dimer. Coordinates have been rotated into the principal inertial axis system.

Atom	*a* (Å)	*b* (Å)	*c* (Å)
C	-3.5972	-1.5051	0.4681
C	-3.4941	-0.1344	0.4862
C	-2.4561	0.5288	-0.2156
C	-1.5142	-0.2629	-0.9395
C	-1.6422	-1.6726	-0.9436
C	-2.6654	-2.2812	-0.2568
H	-3.0420	2.5358	0.3449
H	-4.3978	-1.9957	1.0101
H	-4.2101	0.4624	1.0413
C	-2.3176	1.9415	-0.2007
C	-0.4460	0.3972	-1.6116
H	-0.9124	-2.2558	-1.4885
H	-2.7558	-3.3613	-0.2623
C	-0.3395	1.7687	-1.5876
C	-1.2835	2.5402	-0.8776
H	-1.1805	3.6195	-0.8741
H	0.4848	2.2541	-2.0976
O	0.4467	-0.4024	-2.2654
H	1.2976	0.0473	-2.3341
C	3.4883	-1.4912	-0.7930
C	2.5071	-1.9805	0.0340
C	1.6702	-1.1082	0.7763
C	1.8831	0.2992	0.6585
C	2.9012	0.7820	-0.2009
C	3.6842	-0.0953	-0.9166
H	0.4508	-2.6588	1.6624
H	4.1127	-2.1728	-1.3588
H	2.3470	-3.0495	0.1211
C	0.6185	-1.5908	1.5951
C	1.0266	1.1760	1.3806
H	3.0493	1.8509	-0.2823
H	4.4636	0.2818	-1.5691
C	0.0084	0.6807	2.1606
C	-0.1942	-0.7113	2.2641
H	-1.0166	-1.0784	2.8655
H	-0.6526	1.3636	2.6834
O	1.2661	2.5150	1.2379
H	0.5251	3.0076	1.6055

Table B.3. Cartesian coordinates for the B3LYP-D3(BJ)/6-311++g(d,p) optimized structure of the Saeki-**a** isomer of the 1-naphthol dimer. Coordinates have been rotated into the principal inertial axis system.

Atom	*a* (Å)	*b* (Å)	*c* (Å)
C	3.6332	-0.5412	-0.3554
C	2.8633	0.0726	-1.3131
C	1.7441	0.8660	-0.9551
C	1.4350	1.0153	0.4312
C	2.2478	0.3794	1.4012
C	3.3241	-0.3847	1.0157
H	1.1589	1.3623	-2.9769
H	4.4841	-1.1459	-0.6481
H	3.0978	-0.0474	-2.3652
C	0.9220	1.4901	-1.9272
C	0.2931	1.7853	0.7900
H	2.0006	0.5050	2.4468
H	3.9465	-0.8629	1.7639
C	-0.4889	2.3776	-0.1731
C	-0.1687	2.2256	-1.5382
H	-0.8073	2.6897	-2.2804
H	-1.3683	2.9420	0.1166

O	0.0237	1.8882	2.1268
H	-0.8627	2.2463	2.2411
C	-3.6324	0.5454	-0.3533
C	-2.8606	-0.0576	-1.3163
C	-1.7421	-0.8551	-0.9650
C	-1.4359	-1.0201	0.4201
C	-2.2505	-0.3950	1.3955
C	-3.3261	0.3733	1.0165
H	-1.1529	-1.3282	-2.9911
H	-4.4828	1.1534	-0.6409
H	-3.0930	0.0743	-2.3675
C	-0.9182	-1.4681	-1.9425
C	-0.2947	-1.7943	0.7724
H	-2.0055	-0.5324	2.4402
H	-3.9499	0.8432	1.7689
C	0.4890	-2.3759	-0.1958
C	0.1717	-2.2081	-1.5597
H	0.8117	-2.6637	-2.3058
H	1.3675	-2.9440	0.0893
O	-0.0277	-1.9124	2.1084
H	0.8586	-2.2717	2.2201

Table B.4. Cartesian coordinates for the B3LYP-D3(BJ)/6-311++g(d,p) optimized structure of the Saeki-**b** isomer of the 1-naphthol dimer. Coordinates have been rotated into the principal inertial axis system.

Atom	*a* (Å)	*b* (Å)	*c* (Å)
C	0.6533	-2.4932	0.1341
C	-0.0147	-1.9265	1.1917
C	-1.1698	-1.1326	0.9824
C	-1.6232	-0.9339	-0.3567
C	-0.9166	-1.5289	-1.4296
C	0.1976	-2.2954	-1.1878
H	-1.5122	-0.6779	3.0688
H	1.5427	-3.0859	0.3122
H	0.3434	-2.0653	2.2049
C	-1.8704	-0.5268	2.0571
C	-2.7757	-0.1265	-0.5651
H	-1.2648	-1.3605	-2.4395
H	0.7413	-2.7356	-2.0151
C	-3.4442	0.4417	0.4950
C	-2.9830	0.2387	1.8138
H	-3.5192	0.7001	2.6350
H	-4.3220	1.0554	0.3164
O	-3.1694	0.0484	-1.8648
H	-3.9539	0.6057	-1.8870
C	-0.6534	2.4849	-0.2424
C	0.0173	2.0862	0.8876
C	1.1721	1.2695	0.7990
C	1.6216	0.8679	-0.4950
C	0.9117	1.2914	-1.6444
C	-0.2015	2.0867	-1.5196
H	1.5212	1.1402	2.9294
H	-1.5421	3.0986	-0.1548
H	-0.3381	2.3784	1.8687
C	1.8763	0.8357	1.9517
C	2.7740	0.0382	-0.5808
H	1.2570	0.9700	-2.6176
H	-0.7477	2.3953	-2.4030
C	3.4461	-0.3607	0.5518
C	2.9887	0.0421	1.8252
H	3.5278	-0.2876	2.7058
H	4.3240	-0.9940	0.4667
O	3.1644	-0.3332	-1.8396
H	3.9493	-0.8869	-1.7786

Table B.5. Cartesian coordinates for the B3LYP-D3(BJ)/6-311++g(d,p) optimized structure of the Saeki-**c** isomer of the 1-naphthol dimer. Coordinates have been rotated into the principal inertial axis system.

Atom	*a* (Å)	*b* (Å)	*c* (Å)

C	0.4879	-2.4780	-0.9003
C	-0.4769	-2.4798	0.0768
C	-1.4936	-1.4922	0.0994
C	-1.4847	-0.4871	-0.9150
C	-0.4755	-0.5047	-1.9075
C	0.4891	-1.4825	-1.9015
H	-2.4962	-2.2362	1.8660
H	1.2621	-3.2365	-0.8970
H	-0.4705	-3.2362	0.8536
C	-2.5016	-1.4720	1.0974
C	-2.4973	0.5120	-0.8832
H	-0.4703	0.2719	-2.6598
H	1.2680	-1.4778	-2.6539
C	-3.4674	0.5063	0.0918
C	-3.4644	-0.4948	1.0881
H	-4.2351	-0.4795	1.8501
H	-4.2308	1.2783	0.1016
O	-2.4411	1.4659	-1.8643
H	-3.1719	2.0820	-1.7503
C	-0.6131	2.0782	1.4767
C	0.1595	2.3516	0.3745
C	1.2745	1.5412	0.0471
C	1.5802	0.4338	0.8954
C	0.7693	0.1744	2.0255
C	-0.3060	0.9810	2.3102
H	1.8340	2.6335	-1.7348
H	-1.4722	2.6981	1.7046
H	-0.0842	3.1847	-0.2752
C	2.0785	1.7936	-1.0951
C	2.6940	-0.3851	0.5593
H	1.0039	-0.6762	2.6510
H	-0.9338	0.7660	3.1661
C	3.4586	-0.1187	-0.5527
C	3.1445	0.9800	-1.3834
H	3.7582	1.1712	-2.2559
H	4.3031	-0.7571	-0.7948
O	2.9510	-1.4378	1.3963
H	3.7167	-1.9219	1.0711

Table B.6. Cartesian coordinates for the B3LYP-D3(BJ)/6-311++g(d,p) optimized structure of the Saeki-**d** isomer of the 1-naphthol dimer. Coordinates have been rotated into the principal inertial axis system.

Atom	*a* (Å)	*b* (Å)	*c* (Å)
C	0.5568	-2.5291	0.6933
C	-0.2594	-2.4157	-0.4052
C	-1.3468	-1.5074	-0.4150
C	-1.5606	-0.6917	0.7385
C	-0.7203	-0.8449	1.8675
C	0.3154	-1.7467	1.8431
H	-2.0414	-2.0066	-2.4002
H	1.3961	-3.2139	0.6782
H	-0.0779	-3.0162	-1.2895
C	-2.2120	-1.3805	-1.5322
C	-2.6009	0.2751	0.6850
H	-0.8927	-0.2268	2.7376
H	0.9660	-1.8452	2.7033
C	-3.4378	0.3695	-0.3990
C	-3.2449	-0.4786	-1.5132
H	-3.9093	-0.3885	-2.3644
H	-4.2241	1.1179	-0.4178
O	-2.6746	1.1549	1.7495
H	-3.5104	1.6322	1.7101
C	3.9031	-0.6561	-0.1715
C	3.1046	-0.4457	-1.2691
C	1.9483	0.3723	-1.1866
C	1.6293	0.9711	0.0708
C	2.4704	0.7398	1.1867
C	3.5849	-0.0543	1.0680
H	1.3426	0.1237	-3.2481

H	4.7827	-1.2847	-0.2525
H	3.3466	-0.9068	-2.2206
C	1.0984	0.5897	-2.3003
C	0.4464	1.7559	0.1679
H	2.2069	1.1925	2.1331
H	4.2219	-0.2277	1.9279
C	-0.3479	1.9682	-0.9354
C	-0.0216	1.3729	-2.1716
H	-0.6756	1.5337	-3.0203
H	-1.2432	2.5715	-0.8440
O	0.1401	2.2656	1.4024
H	-0.8206	2.2883	1.5103

Table B.7. Cartesian coordinates for the B3LYP-D3(BJ)/6-311++g(d,p) optimized structure of the Saeki-**e** isomer of the 1-naphthol dimer. Coordinates have been rotated into the principal inertial axis system.

Atom	*a* (Å)	*b* (Å)	*c* (Å)
C	3.4656	-1.1645	-0.4402
C	2.6577	-1.3658	0.6516
C	1.7332	-0.3755	1.0694
C	1.6636	0.8451	0.3291
C	2.5105	1.0299	-0.7911
C	3.3911	0.0448	-1.1684
H	0.9196	-1.5122	2.7174
H	4.1634	-1.9343	-0.7494
H	2.7062	-2.2952	1.2079
C	0.8725	-0.5742	2.1774
C	0.7148	1.8194	0.7378
H	2.4530	1.9569	-1.3452
H	4.0332	0.1939	-2.0287
C	-0.1018	1.6092	1.8218
C	-0.0197	0.4010	2.5447
H	-0.6887	0.2443	3.3819
H	-0.8429	2.3525	2.0956
O	0.6269	2.9608	-0.0354
H	0.0241	3.5774	0.3935
C	-0.9831	-3.1726	-0.0578
C	-1.9694	-2.3895	0.4916
C	-2.1448	-1.0437	0.0805
C	-1.2696	-0.5203	-0.9202
C	-0.2582	-1.3466	-1.4668
C	-0.1203	-2.6463	-1.0456
H	-3.7962	-0.6090	1.4078
H	-0.8610	-4.1991	0.2694
H	-2.6288	-2.7903	1.2540
C	-3.1393	-0.2056	0.6456
C	-1.4200	0.8404	-1.3078
H	0.4137	-0.9247	-2.2012
H	0.6648	-3.2676	-1.4596
C	-2.4093	1.6253	-0.7594
C	-3.2676	1.0970	0.2284
H	-4.0362	1.7318	0.6546
H	-2.5219	2.6519	-1.0909
O	-0.5401	1.3246	-2.2408
H	-0.2589	2.2066	-1.9649

Table B.8. Cartesian coordinates for the B3LYP-D3(BJ)/6-311++g(d,p) optimized structure of the Hinge isomer of the 1-naphthol dimer. Coordinates have been rotated into the principal inertial axis system.

Atom	*a* (Å)	*b* (Å)	*c* (Å)
C	2.9261	-2.9280	-0.2386
C	4.0310	-2.2122	0.1535
C	3.9983	-0.7960	0.2189
C	2.7842	-0.1256	-0.1318
C	1.6615	-0.8879	-0.5409
C	1.7323	-2.2593	-0.5904
H	6.0445	-0.5596	0.8777
H	2.9670	-4.0102	-0.2807

H	4.9499	-2.7220	0.4211
C	5.1305	-0.0388	0.6173
C	2.7659	1.2932	-0.0503
H	0.7441	-0.3898	-0.8189
H	0.8659	-2.8306	-0.9014
C	3.8726	2.0069	0.3376
C	5.0673	1.3304	0.6707
H	5.9319	1.9081	0.9745
H	3.8298	3.0902	0.3939
O	1.5763	1.9206	-0.3771
H	1.7077	2.8754	-0.3707
C	-5.4515	-0.8046	1.2367
C	-5.2021	-0.6884	-0.1097
C	-3.9779	-0.1500	-0.5829
C	-3.0067	0.2715	0.3764
C	-3.2869	0.1391	1.7584
C	-4.4849	-0.3881	2.1798
H	-4.4371	-0.3479	-2.6894
H	-6.3928	-1.2185	1.5802
H	-5.9425	-1.0088	-0.8348
C	-3.6957	-0.0236	-1.9683
C	-1.7740	0.8157	-0.0918
H	-2.5389	0.4596	2.4712
H	-4.6916	-0.4860	3.2393
C	-1.5293	0.9307	-1.4447
C	-2.4975	0.5037	-2.3807
H	-2.2811	0.6016	-3.4384
H	-0.5925	1.3535	-1.7884
O	-0.8814	1.2041	0.8583
H	-0.0396	1.4561	0.4438

Appendix C

Supplementary Information for Chapter 5

Examining Intermolecular Interactions Between Hydrocarbon and Water: A Broadband Rotational Spectroscopic and Theoretical Study of the α-pinene – Water Complex

Contents:

1. **Electrostatic plot**
    a. **Figure C.1.** An electrostatic plot of the α-pinene monomer
2. **CREST results**
    a. **Table C.1.** Conformers obtained from the CREST searches at the B3LYP-D3(BJ)/Jun-cc-pVTZ level of theory
3. **Atom Labeling**
    a. **Figure C.2.** Inertial axis system for anti- and syn-conformer and the atom labelling for α-pinene and water
4. **Barrier Height and Potential Energy Curves**
    a. **Table C.2.** Raw and zero-point energy corrected barrier heights for the rotation of the water unit about the O-H---π bond.
    b. **Figure C.3.** Potential energy scans for rotation about the O-H---π intermolecular bond of the anti-conformer at various levels of theory
    c. **Figure C.4.** Potential energy scans for rotation about the O-H---π intermolecular bond of the syn-conformer at various levels of theory
5. **Non-Covalent Interactions (NCI) and Quantum Theory of Atoms-in-Molecules (QTAIM) Analyses**
    a. **Figure C.5.** QTAIM analyses of syn- and anti- complexes
    b. **Figure C.6.** NCI analysis of the transition state for the C_2 motion
6. **Natural Bond Orbital Analysis**
    a. **Table C.3.** A full NBO analysis of the anti- and syn-complex
    b. **Table C.4.** Intermolecular bond characterization obtained from an NBO analysis
7. **Atmospheric Implications**
    a. **Figure C.7.** Scheme of an ozonolysis reaction with α-pinene
8. **Rotational Transition Frequencies**
    a. **Table C.5.** Measured frequencies of assigned rotational transitions with their quantum number assignments of the ortho spin isomer of the anti-water complex
    b. **Table C.6.** Measured frequencies of assigned rotational transitions with their quantum number assignments of the para spin isomer of the anti-water complex
    c. **Table C.7.** Measured frequencies of assigned rotational transitions with their quantum number assignments of the ortho spin isomer of the syn-water complex
    d. **Table C.8.** Measured frequencies of assigned rotational transitions with their quantum number assignments of the para spin isomer of the anti-water complex

Electrostatic Plot

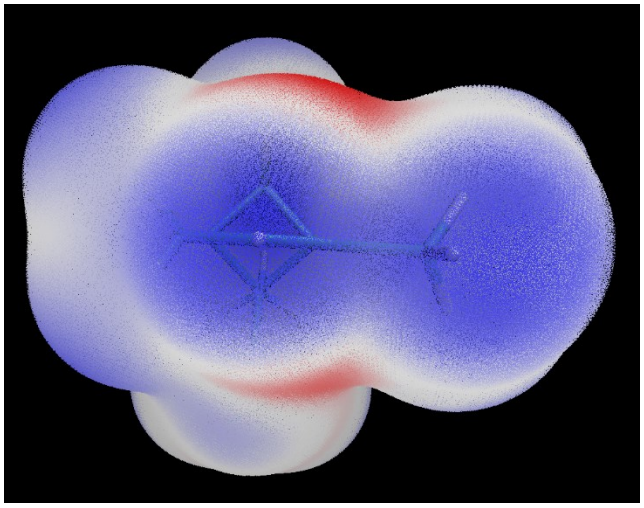

Figure C.1. An electrostatic plot of the α-pinene monomer, at the B3LYP-D3(BJ)/def2-TZVP level of theory.

CREST Results

Table C.1. Conformers obtained from the CREST searches at the B3LYP-D3(BJ)/Jun-cc-pVTZ level of theory.

	ΔE_0 / kJ mol^{-1}	A / MHz[d]	B / MHz	C / MHz	μ_a / D[d]	μ_b / D[d]	μ_c / D[d]	Conformer	[a]298 K / %
1	0.0	1612.94	778.97	720.02	0.7	1.0	1.3	anti-	51.0
2	3.3	1424.12	816.76	739.21	2.3	0.2	0.5	syn-	13.6
3	6.1	1307.23	839.47	725.17	0.6	0.1	1.5	anti-	4.3
4	7.0	1235.29	844.07	706.23	1.7	1.2	0.8	anti-	3.0
5	7.2	1229.18	972.00	714.38	0.5	1.7	0.5	syn-	2.8
6	7.6	1245.44	827.45	651.83	1.0	0.3	1.5	anti-	2.4
7	7.6	1220.25	990.86	726.21	0.0	0.8	1.3	syn-	2.4
8	7.7	1228.72	981.05	720.69	0.4	0.1	1.6	syn-	2.3
9	8.0	1237.49	822.11	647.17	2.3	0.7	0.3	anti-	2.1
10	8.1	1618.92	735.17	679.20	0.4	0.7	1.3	syn-	2.0
11	8.5	1155.19	842.76	674.66	0.7	0.5	1.5	syn-	1.7
12	8.7	1279.40	832.78	673.69	1.1	1.4	0.1	syn-	1.5
13	8.8	1279.84	829.56	673.62	1.0	1.3	0.5	anti-	1.4
14	8.9	1426.08	665.14	619.06	2.5	0.7	0.0	syn-	1.4
15	8.9	1471.30	659.68	621.79	2.3	0.4	0.5	anti-	1.4
16	9.2	1578.23	616.50	569.00	2.2	0.1	0.3	syn-	1.3
17	9.2	1563.11	620.26	571.88	1.9	1.0	0.9	syn-	1.3
18	9.3	1740.35	663.94	623.20	0.5	1.7	0.1	anti-	1.2
19	9.6	1355.68	705.16	597.67	0.7	1.1	1.1	anti-	1.0
20	9.7	1146.67	746.39	605.85	1.6	1.6	0.0	syn-	1.0
21	9.8	1257.09	839.45	654.32	1.2	1.1	0.1	syn-	1.0

[a]Percent abundance at 298.15 K.

Atom Labelling

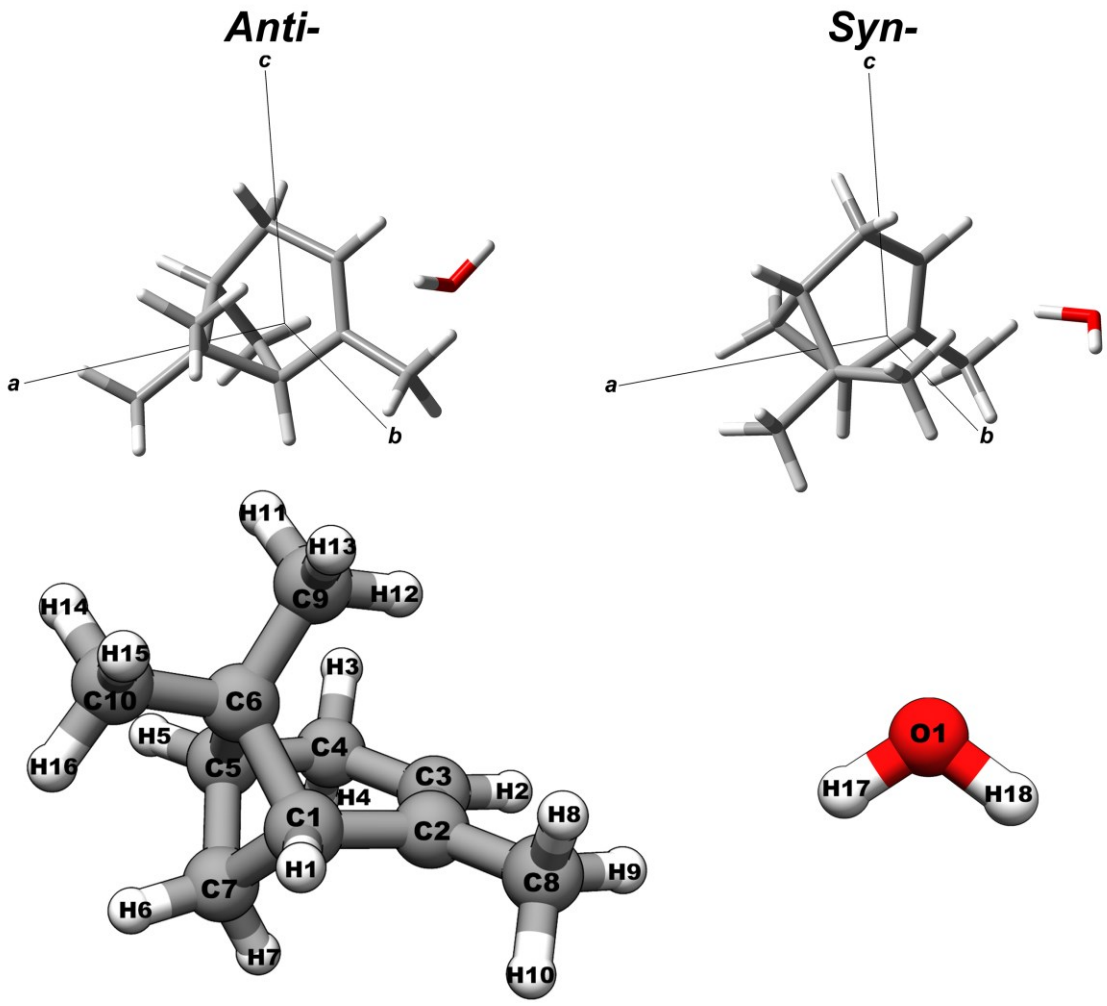

Figure C.2. Inertial axis system for anti- and syn-conformer and the atom labelling for α-pinene and water.

Barrier Heights and Potential Energy Curves

Table C.2. Raw and zero-point energy corrected barrier heights for the rotation of the water unit about the O-H---π bond.

	Syn-Conformer /kJ mol^{-1}		Anti-Conformer /kJ mol^{-1}	
Level of Theory	E[a]	E+ZPE[b]	E[a]	E+ZPE[b]
B3LYP-D3(BJ)				
6-311++G(d,p)	1.7	1.1	0.8	-0.1
def2-TZVP	2.1	1.2	0.7	-0.2
def2-TZVPPD	1.3	0.8	0.9	0.3
Jun-cc-pVTZ	1.4	0.8	0.8	0.4
ωB97XD/Jun-cc-pVTZ	1.7	0.1	0.6	-0.3
B2PLYP-D3/Jun-cc-pVTZ	1.3	0.8	0.6	0.4

[a]Raw Energy barrier heights
[b]Zero-point corrected barrier heights

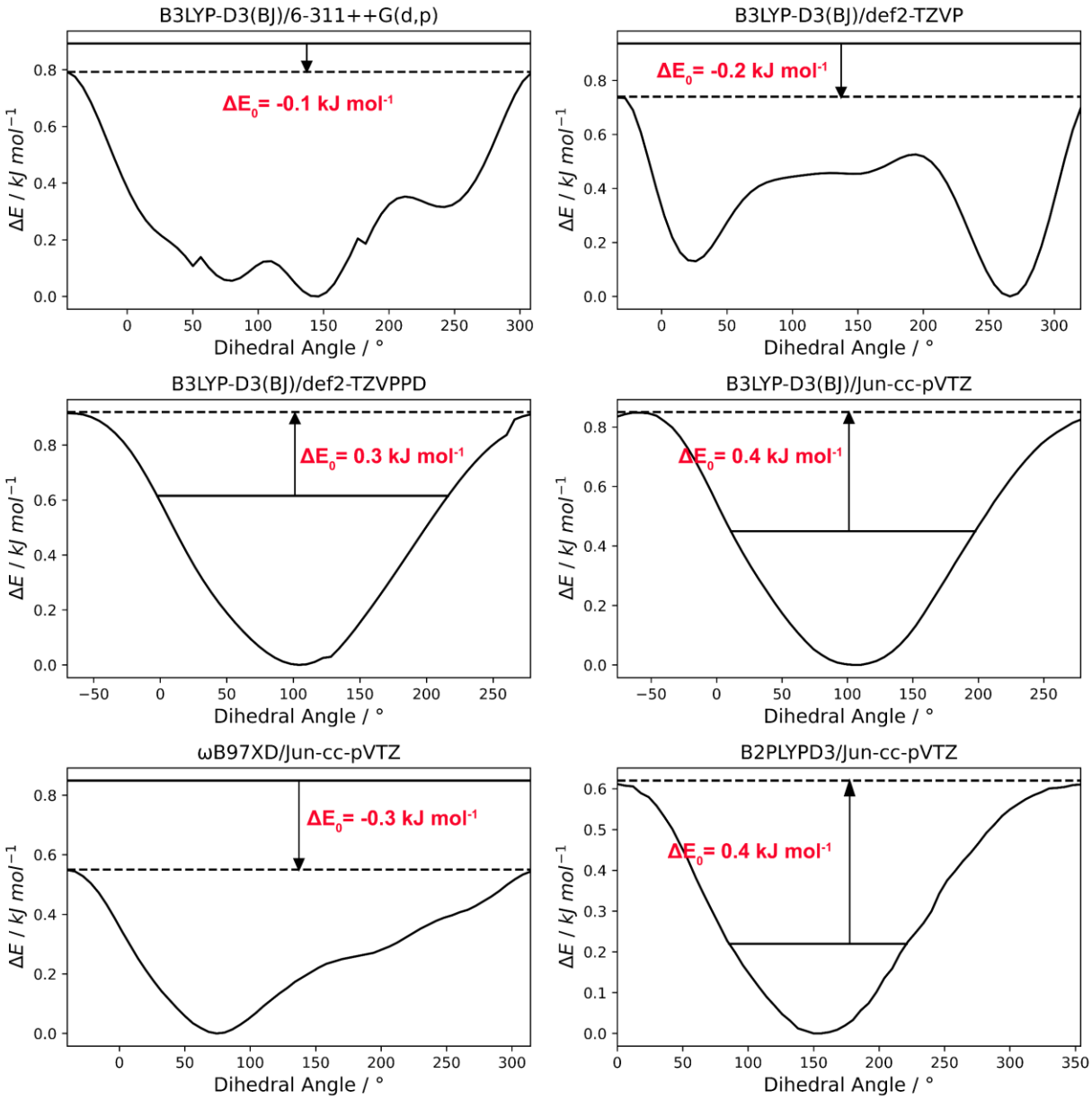

Figure C.3. One-dimensional relaxed potential energy scans along the C4-C3-O1-H17 (see Figure C.X. for atom labelling) dihedral angle for the anti-conformer, corresponding to rotation about the O-H---π intermolecular bond, at various levels of theory.

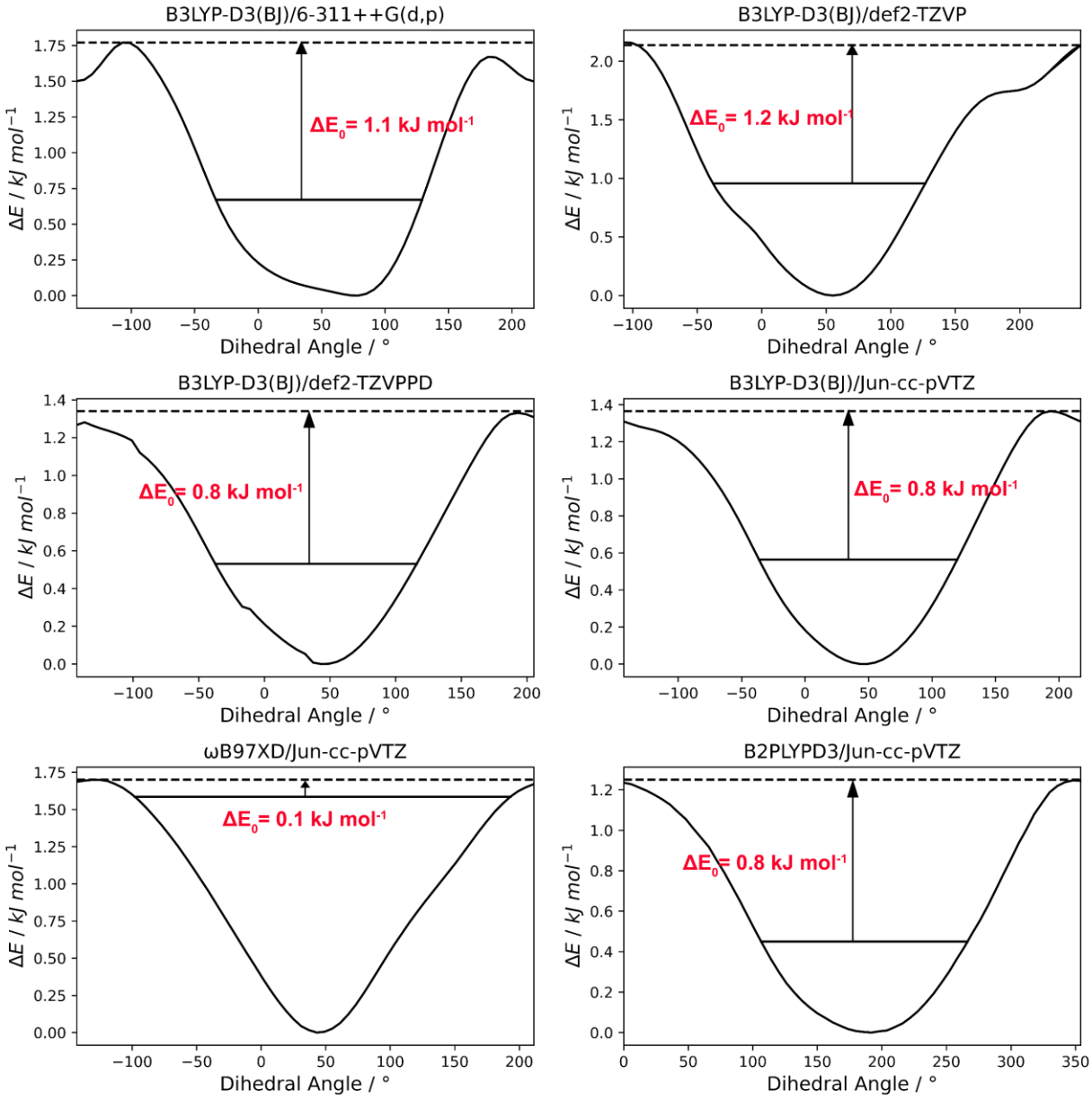

Figure C.4. One-dimensional relaxed potential energy scans along the C4-C3-O1-H17 (see Figure C.X. for atom labelling) dihedral angle for the syn-conformer, corresponding to rotation about the O-H---π intermolecular bond, at various levels of theory.

Non-Covalent Interactions (NCI) and Quantum Theory of Atoms-in-Molecules (QTAIM) Analyses

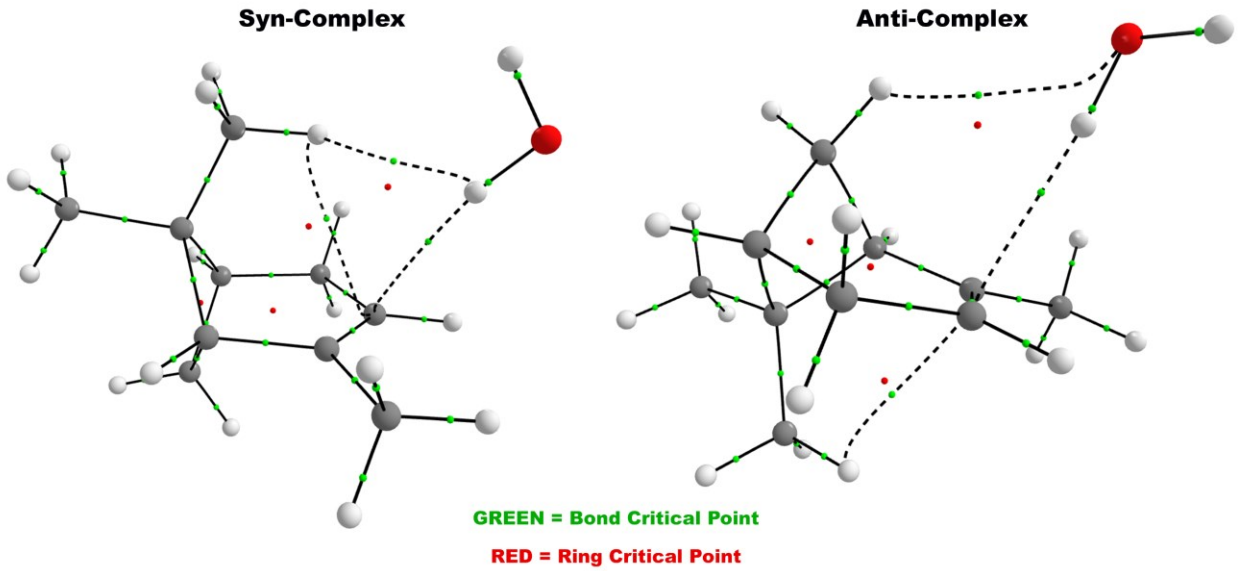

Figure C.5. QTAIM analyses of syn- and anti- complexes at the B3LYP-D3(BJ)/Jun-cc-pVTZ level.

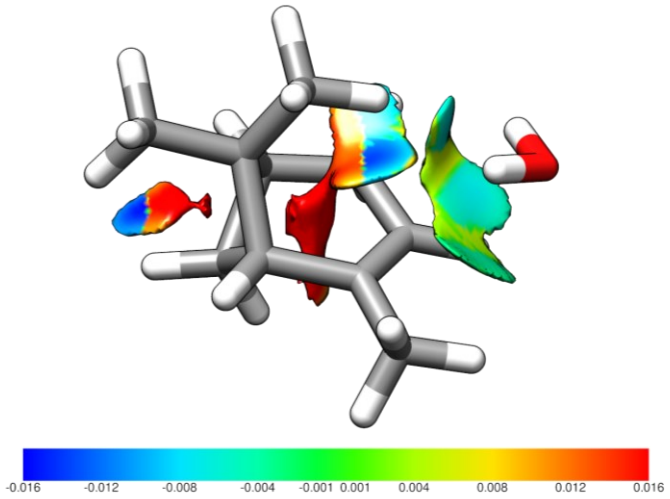

Figure C.6. NCI analysis of the transition state for the C_2 motion.

Natural Bond Orbital Analysis

Table C.3. A full NBO analysis of the anti- and syn-complex

Syn-Complex			Anti-Complex		
Donor	Acceptor	E /kJ mol^{-1}	Donor	Acceptor	E /kJ mol^{-1}
α-pinene to H_2O			α-pinene to H_2O		
BD(π) C2-C3	BD*(σ) O1-H17	6.8	BD(σ) C2-C3	RY(2) H17	0.3
BD(σ) C3 H2	BD*(σ) O1-H17	0.3	BD(π) C2-C3	BD*(σ) O1-H17	12.5
BD(σ) C9-H12	BD*(σ) O1-H17	0.5	BD(π) C2-C3	RY(3) O1	0.3
H_2O to α-pinene			BD(π) C2-C3	RY(4) H17	0.3
LP(1) O1	BD*(σ) C9-H12	0.3	BD(σ) C7-H7	BD*(σ) O1-H17	0.3
LP(2) O1	BD*(π) C2-C3	0.4	H_2O to α-pinene		
LP(2) O1	BD*(σ) C9-H12	0.3	LP(1) O1	BD(π) C2-C3	0.3
LP(2) O1	BD*(σ) C8-H10	0.5	LP(1) O1	BD*(σ) C7-H7	0.8
BD(σ) O1-H17	BD(σ) C1-C2	0.2	LP(1) O1	RY(2) C3	0.3
BD(σ) O1-H17	BD*(π) C2-C3	0.3	LP(2) O1	BD*(π) C2-C3	0.5
BD(σ) O1-H17	BD*(σ) C9-H12	0.7	LP(2) O1	BD*(σ) C8-H8	0.3
BD(σ) O1-H17	BD*(σ) C8-H10	0.5	LP(2) O1	BD*(σ) C7-H7	0.6
BD(σ) O1-H17	RY(4) C2	0.4	BD(σ) O1-H17	BD*(σ) C7-H7	0.4
BD(σ) O1-H17	RY(5) C2	0.3	BD(σ) O1-H17	RY(1) C2	0.5
BD(σ) O1-H17	RY(4) C3	0.5	BD(σ) O1-H17	RY(4) C2	1.5
			BD(σ) O1-H18	RY(4) C2	0.2
			BD(σ) O1-H18	RY(1) H7	0.5
α-pinene to H_2O	H_2O to α-pinene	Total	α-pinene to H_2O	H_2O to α-pinene	Total
7.6 kJ mol^{-1}	4.4 kJ mol^{-1}	12.0 kJ mol^{-1}	13.7 kJ mol^{-1}	6.2 kJ mol^{-1}	19.9 kJ mol^{-1}

Table C.4. Intermolecular bond characterization obtained from an NBO analysis

	Bond Order	%Covalent	%Ionic
Syn-Complex			
C2 --- H17	0	0	0
C3 --- H17	0.0043	0	100
H12 --- H17	0	0	0
Anti-Complex			
C2 --- H12	0	0	0
C3 --- H12	0.0058	0	100
O1 --- H7	0	0	0

Atmospheric Implications

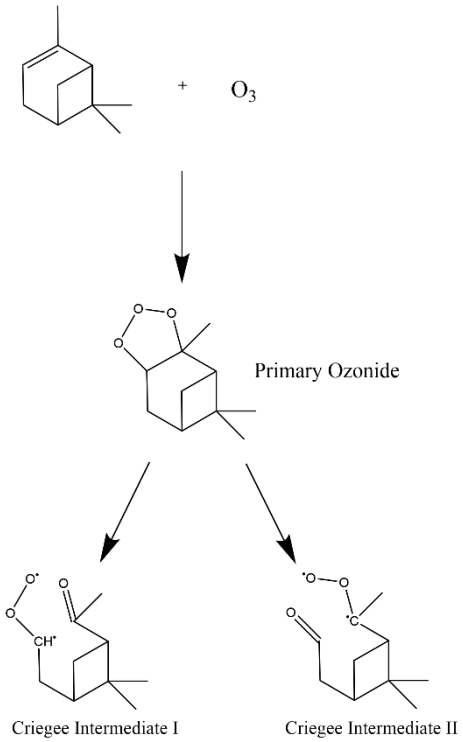

Figure C.7. The ozonolysis pathway of α-pinene

Measured Transition Frequencies

Table C.5. Measured frequencies of assigned rotational transitions with their quantum number assignments of the ortho spin isomer of the anti-water complex. $\Delta\nu^a$ is the difference between observed and calculated frequencies.

J'	K_a'	K_c'	J''	K_a''	K_c''	ν_{Exp}/ MHz	$\Delta\nu^a$/ MHz
5	2	4	5	1	4	2295.980	-0.001
1	1	1	0	0	0	2325.922	-0.010
1	1	0	0	0	0	2377.431	-0.011
4	2	3	4	1	3	2419.265	-0.001
3	2	2	3	1	2	2519.352	-0.001
2	2	0	2	1	2	2751.930	-0.009
3	2	1	3	1	3	2839.475	0.003
2	1	2	1	1	1	2870.214	-0.009
2	0	2	1	0	1	2919.494	-0.004
4	2	3	4	1	4	2933.906	-0.002
4	2	2	4	1	4	2967.111	0.002
2	1	1	1	1	0	2973.237	-0.003
5	2	4	5	1	5	3066.860	-0.004
5	2	3	5	1	5	3143.469	-0.003
3	0	3	2	1	1	3403.361	-0.003
4	1	3	3	2	1	3411.299	0.009
4	1	3	3	2	2	3422.427	0.005
3	0	3	2	1	2	3557.889	-0.001
2	1	2	1	0	1	3735.289	0.002
2	1	1	1	0	1	3889.811	-0.002
5	1	5	4	2	2	4199.217	0.002
5	1	5	4	2	3	4232.414	-0.002
7	3	5	7	2	5	4262.941	-0.001
3	1	3	2	1	2	4303.956	0.000
6	3	4	6	2	4	4343.729	0.000
3	0	3	2	0	2	4373.679	-0.001
3	2	2	2	2	1	4382.595	0.006
3	2	1	2	2	0	4391.494	0.004
5	3	3	5	2	3	4396.849	-0.001
5	3	2	5	2	3	4398.542	0.003
4	3	2	4	2	2	4428.226	-0.003
3	3	1	3	2	1	4444.263	0.002
3	1	2	2	1	1	4458.417	0.000
4	3	2	4	2	3	4461.429	-0.001
4	3	1	4	2	3	4461.860	0.007
5	3	3	5	2	4	4473.454	-0.004
5	3	2	5	2	4	4475.150	0.003
6	3	3	6	2	5	4499.189	-0.004
7	3	4	7	2	6	4538.937	0.002
4	0	4	3	1	2	4766.288	-0.002
5	1	4	4	2	2	4970.094	-0.005
4	0	4	3	1	3	5075.277	0.000
3	1	3	2	0	2	5119.749	0.004
3	1	2	2	0	2	5428.726	-0.005
8	3	6	7	4	4	5483.531	0.001
6	1	6	5	2	4	5527.420	-0.004
2	2	1	1	1	0	5568.423	0.003
2	2	0	1	1	0	5570.657	0.005
2	2	1	1	1	1	5619.932	0.002
2	2	0	1	1	1	5622.165	0.003
4	1	4	3	1	3	5736.119	-0.001
4	0	4	3	0	3	5821.341	-0.001
4	2	3	3	2	2	5841.688	-0.001
4	2	2	3	2	1	5863.756	-0.001
4	1	3	3	1	2	5941.774	-0.001
5	0	5	4	1	3	6085.318	0.001
4	1	4	3	0	3	6482.178	-0.007
5	0	5	4	1	4	6599.950	-0.008
3	2	2	2	1	1	6977.773	0.004
3	2	1	2	1	1	6988.904	0.002
4	1	3	3	0	3	6996.829	0.002

3	2	2	2	1	2	7132.300	0.004
5	1	5	4	1	4	7166.335	0.010
5	0	5	4	0	4	7260.801	0.000

Table C.6. Measured frequencies of assigned rotational transitions with their quantum number assignments of the para spin isomer of the anti-water complex. $\Delta\nu^a$ is the difference between observed and calculated frequencies.

J'	K_a'	K_c'	J''	K_a''	K_c''	ν_{Exp}/ MHz	$\Delta\nu^a$/ MHz
1	1	1	0	0	0	2325.986	0.021
1	1	0	0	0	0	2377.489	0.019
3	2	2	3	1	2	2519.551	0.003
2	2	1	2	1	1	2595.365	-0.005
2	2	0	2	1	2	2752.119	0.003
3	2	1	3	1	3	2839.640	0.001
4	2	3	4	1	4	2934.066	-0.001
4	2	2	4	1	4	2967.259	-0.001
2	1	1	1	1	0	2973.184	0.011
5	2	3	5	1	5	3143.600	0.003
3	0	3	2	1	1	3403.218	-0.001
4	1	3	3	2	1	3410.964	0.001
3	0	3	2	1	2	3557.732	0.000
2	1	2	1	0	1	3735.289	-0.003
2	1	1	1	0	1	3889.811	0.004
5	1	5	4	2	3	4232.117	0.000
7	3	5	7	2	5	4263.280	-0.002
3	1	3	2	1	2	4303.868	-0.002
6	3	4	6	2	4	4344.058	0.006
3	0	3	2	0	2	4373.587	-0.002
3	2	2	2	2	1	4382.494	-0.001
3	2	1	2	2	0	4391.392	-0.001
5	3	3	5	2	3	4397.162	0.000
4	3	2	4	2	2	4428.530	-0.005
4	3	1	4	2	2	4428.962	0.004
3	3	1	3	2	1	4444.569	0.004
3	3	0	3	2	2	4455.752	-0.004
3	1	2	2	1	1	4458.316	0.000
4	3	2	4	2	3	4461.729	0.000
4	3	1	4	2	3	4462.156	0.004
5	3	3	5	2	4	4473.746	-0.007
5	3	2	5	2	4	4475.444	0.004
6	3	3	6	2	5	4499.479	0.001
7	3	4	7	2	6	4539.207	0.000
4	0	4	3	1	2	4766.126	0.001
5	1	4	4	2	2	4969.737	0.001
4	0	4	3	1	3	5075.085	0.000
2	2	1	1	1	0	5568.542	-0.001
2	2	0	1	1	0	5570.774	-0.001
2	2	1	1	1	1	5620.046	-0.003
2	2	0	1	1	1	5622.280	-0.001
4	1	4	3	1	3	5736.004	-0.001
4	0	4	3	0	3	5821.221	-0.002
4	2	3	3	2	2	5841.563	0.000
4	2	2	3	2	1	5863.625	-0.002
4	1	3	3	1	2	5941.641	-0.001
3	2	1	2	1	1	6988.993	-0.002
4	1	3	3	0	3	6996.737	-0.003
3	2	2	2	1	2	7132.370	-0.009
5	0	5	4	0	4	7260.662	0.005

Table C.7. Measured frequencies of assigned rotational transitions with their quantum number assignments of the ortho spin isomer of the syn-water complex. $\Delta\nu^a$ is the difference between observed and calculated frequencies.

J'	K_a'	K_c'	J"	K_a"	K_c"	ν_{Exp}/ MHz	$\Delta\nu^a$/ MHz
2	1	2	1	1	1	2945.687	0.000
2	0	2	1	0	1	3010.017	-0.003
2	1	1	1	1	0	3085.049	0.001
3	1	3	2	1	2	4415.296	-0.003
3	0	3	2	0	2	4501.847	-0.010
3	2	2	2	2	1	4523.039	0.000
3	2	1	2	2	0	4544.226	0.009
3	1	2	2	1	1	4624.072	-0.005
4	1	4	3	1	3	5881.371	-0.012
4	0	4	3	0	3	5979.001	-0.023
4	2	3	3	2	2	6026.524	-0.013
4	3	2	3	3	1	6040.668	0.016
4	3	1	3	3	0	6042.201	0.012
4	2	2	3	2	1	6078.200	0.014
4	1	3	3	1	2	6158.532	-0.015
5	1	5	4	1	4	7343.284	-0.023
5	0	5	4	0	4	7439.714	-0.045

Table C.7. Measured frequencies of assigned rotational transitions with their quantum number assignments of the para spin isomer of the syn-water complex. $\Delta\nu^a$ is the difference between observed and calculated frequencies.

J'	K_a'	K_c'	J"	K_a"	K_c"	ν_{Exp}/ MHz	$\Delta\nu^a$/ MHz
2	1	2	1	1	1	2945.621	0.004
2	0	2	1	0	1	3009.943	-0.003
2	1	1	1	1	0	3084.972	0.002
3	1	3	2	1	2	4415.185	-0.005
3	0	3	2	0	2	4501.739	-0.001
3	2	2	2	2	1	4522.926	-0.002
3	2	1	2	2	0	4544.109	0.002
3	1	2	2	1	1	4623.957	0.001
4	1	4	3	1	3	5881.225	-0.006
4	0	4	3	0	3	5978.862	0.001
4	2	3	3	2	2	6026.375	-0.006
4	3	2	3	3	1	6040.508	0.005
4	3	1	3	3	0	6042.038	-0.002
4	2	2	3	2	1	6078.038	0.005
4	1	3	3	1	2	6158.382	0.004

Appendix D

Supplementary Information for Chapter 6

A rotational spectroscopic and *ab initio* study of *cis* and *trans* (-)-carveol: Further insights into conformational dynamics in monoterpenes and monoterpenoids

Contents:

1. **Conformations of Cyclohexene**
    a. **Figure D.1.** Boat and half-chair conformations of cyclohexane
2. **Quantum theory of atoms-in-molecules (QTAIM) results**
    a. **Figure D.2.** QTAIM analyses of the five experimentally assigned conformers
3. **Theoretical Conformers**
    a. **Table D.1.** Theoretical conformers for *trans* (-)-carveol
    b. **Table D.2.** Theoretical conformers for *cis* (-)-carveol
4. **Experimental Assignment to Theoretical Results Comparison**
    a. **Table D.3.** *cis* (-)-carveol, Experiment vs. Theory
    b. **Table D.4.** *trans* (-)-carveol, Experiment vs. Theory
5. **Rotational Transition Frequencies for Experimental Conformers**
    a. **Table D.5.** Assigned rotational transitions for E1
    b. **Table D.6.** Assigned rotational transitions for E2
    c. **Table D.7.** Assigned rotational transitions for E3
    d. **Table D.8.** Assigned rotational transitions for E4
    e. **Table D.9.** Assigned rotational transitions for E5
6. **Theoretical Geometries for the Experimental Conformers**
    a. **Table D.10**. Geometry for E1
    b. **Table D.11.** Geometry for E2
    c. **Table D.12.** Geometry for E3
    d. **Table D.13.** Geometry for E4
    e. **Table D.14.** Geometry for E5
7. **Molecular Systems for Hydrogen Bond NBO Analyses**
    a. **Figure D.3**. Three hydrogen bond containing systems used for the NBO analyses

Conformations of Cyclohexene

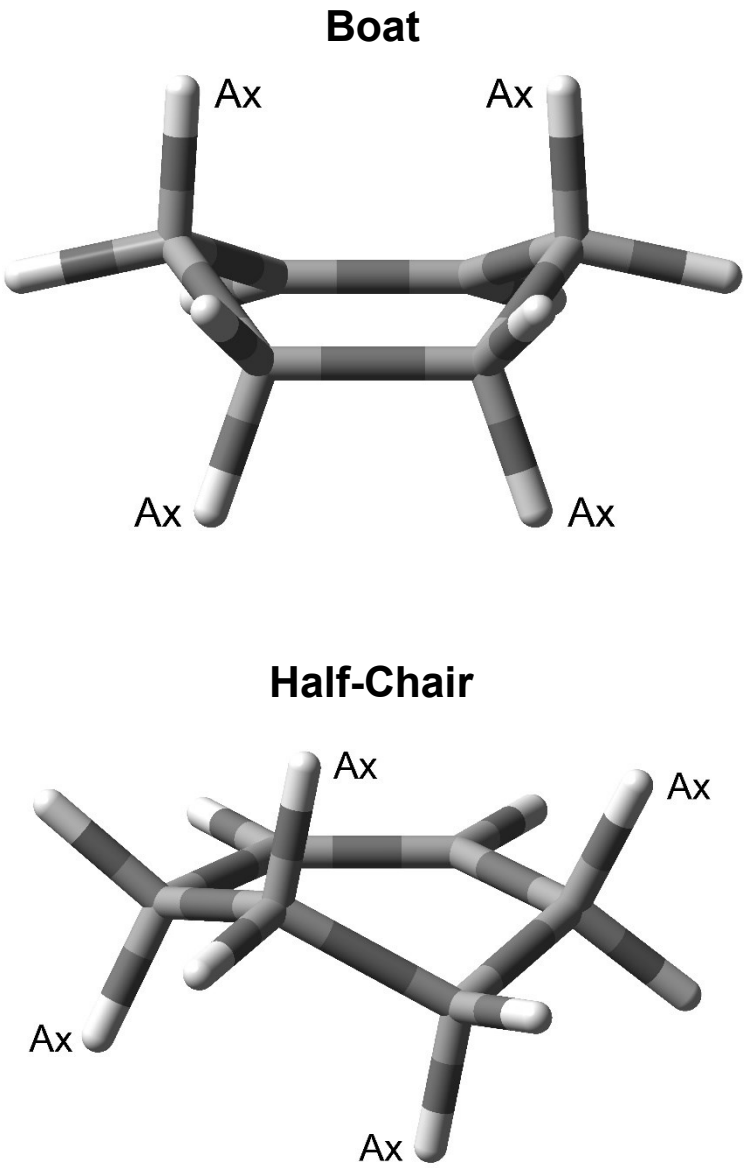

Figure D.1. Boat and half-chair conformations of cyclohexene. Hydrogens in the axial position are labelled Ax.

Quantum theory of atoms-in-molecules (QTAIM) results

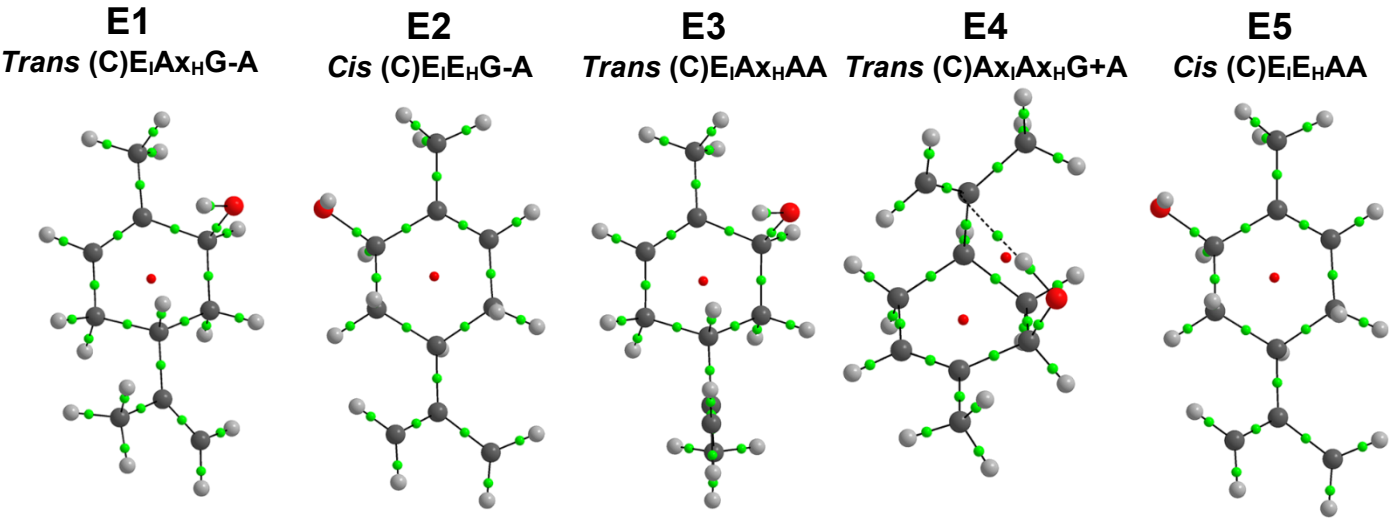

Figure D.2. Graphical representations of QTAIM results of the five experimentally assigned conformers.

Theoretical Conformers

Table D.1. Theoretical results for *trans* (-)-carveol conformers obtained from the 2D PES scan and CREST searches

(V)W_IX_HYZ[a]	ΔE_0 / kJ mol^{-1} df-MP2	ΔE_0 / kJ mol^{-1} B3LYP-D3(BJ)	A / MHz[d]	B / MHz[d]	C / MHz[d]	μ_a / D[d]	μ_b / D[d]	μ_c / D[d]
(C)E_IAx_HAA[b]	**0.0**	**0.0**	**2134.81**	**663.21**	**597.58**	**0.5**	**1.6**	**0.1**
(C)E_IAx_HG-A[c]	**0.8**	**1.0**	**2145.20**	**665.47**	**584.85**	**-0.5**	**-1.7**	**0.0**
(C)E_IAx_HG+A	1.0	1.3	2122.44	697.78	570.25	0.3	1.1	0.4
(C)E_IAx_HAG+	1.6	2.9	2136.89	666.86	598.25	0.3	0.1	1.6
(C)E_IAx_HG-G+	1.9	3.3	2143.46	668.36	587.64	0.2	0.4	0.7
(C)E_IAx_HAG-	2.8	3.9	2129.35	668.19	600.10	1.3	1.2	0.7
(C)E_IAx_HG+G+[c]	3.2	4.3	2120.71	701.17	571.90	-0.2	0.7	1.1
(C)E_IAx_HG-G-	3.2	4.5	2137.99	669.85	588.75	1.3	1.2	0.3
(C)E_IAx_HG+G-	3.7	4.6	2116.63	703.47	572.92	1.4	0.6	0.2
(C)Ax_IE_HG+A	2.9	6.1	1627.21	843.77	725.21	0.6	0.7	1.3
(C)Ax_IE_HG+G+	4.1	8.1	1657.93	834.27	717.12	1.5	0.8	0.1
(C)Ax_IE_HG+G-	4.6	8.2	1638.70	841.88	720.61	0.2	0.5	0.8
(C)Ax_IE_HAA	10.5	12.1	1728.38	798.12	721.15	0.3	1.0	1.2
(C)Ax_IE_HG-A	10.7	13.4	1668.29	819.18	721.91	1.0	1.4	1.2
(C)Ax_IE_HAG+	10.8	13.7	1741.26	797.49	717.59	0.9	0.3	0.3
(C)Ax_IE_HAG-	12.5	14.7	1735.08	798.15	717.65	0.3	1.2	0.9
(C)Ax_IE_HG-G-	12.9	15.9	1678.18	817.35	714.82	0.4	1.0	0.9
(B)Ax_IAx_HAG-	21.8	24.0	1901.97	753.84	659.03	1.3	1.4	0.1
(B)E_IE_HAG+	22.9	24.9	2120.28	667.19	583.32	1.0	0.5	0.7
(B)E_IE_HAA	24.3	25.0	2099.87	667.65	582.76	0.3	0.7	0.7
(B)E_IE_HAG-	24.2	25.6	2105.32	665.24	582.16	0.7	0.8	1.3
(B)E_IE_HG+A	26.3	26.9	2076.87	668.65	558.24	0.5	0.3	1.4
(B)Ax_IAx_HG-G-	27.0	30.2	1863.48	756.31	684.64	0.6	1.0	0.4

[a]Nomenclature describing the conformation of each conformer. The letter in parentheses describes whether the conformer is in the half-chair (C) or boat (B) conformation. The following *WXYZ* letters describe the axial or equatorial position of the isopropenyl group, the axial or equatorial position of the hydroxyl group, the conformation of the isopropenyl group (A or G- or G+), and the conformation of the hydroxyl group(A or G- or G+), respectively. A, G-, and G+ are antiperiplanar, gauche -, and gauche + conformations, respectively. [b]Conformers highlighted in bold were experimentally identified. [c]Conformers identified from the 2D PES scan. [d]The rotational constants and dipole moment components reported were calculated at the B3LYP-D3(BJ)/def2-TZVP level of theory.

Table D.2. Theoretical results for *cis* (-)-carveol conformers obtained from the 2D PES scan and CREST searches

(V)W_IX_HYZ[a]	ΔE_0 / kJ mol^{-1} df-MP2	ΔE_0 / kJ mol^{-1} B3LYP-D3(BJ)	A / MHz[d]	B / MHz[d]	C / MHz[d]	μ_a / D[d]	μ_b / D[d]	μ_c / D[d]
(C)Ax_IAx_HG+A[b]	**0.0**	**0.0**	**1689.73**	**902.97**	**802.91**	**0.7**	**1.5**	**0.6**
(C)E_IE_HAA[b]	**6.8**	**4.3**	**2130.68**	**647.17**	**568.57**	**0.7**	**0.9**	**1.1**
(C)E_IE_HG-A[b]	**7.5**	**5.1**	**2161.15**	**662.04**	**541.75**	**0.8**	**1.3**	**0.6**
(C)E_IE_HAG-	7.1	5.8	2148.98	646.6	568.35	0.9	0.5	0.5
(C)E_IE_HG+A[c]	8.7	6.0	2103.62	661.45	552.70	0.6	-0.9	-0.2
(C)E_IE_HAG+	8.4	6.4	2134.10	650.22	569.49	0.8	0.9	0.6
(C)E_IE_HG-G-	8.0	6.7	2182.58	660.73	541.74	1.1	0.0	1.1
(C)E_IE_HG-G+	9.5	7.6	2165.73	664.22	542.67	0.5	1.4	1.2
(C)E_IE_HG+G-[c]	10.0	8.4	2123.10	661.23	551.51	1.0	0.8	1.0
(C)E_IE_HG+G+	11.1	9.0	2108.52	665.09	551.98	0.7	0.4	1.5
(C)Ax_IAx_HG-A	12.7	12.5	1534.19	948.05	804.45	1.1	1.8	0.5
(C)Ax_IAx_HG+G-	15.3	15.6	1609.81	923.35	805.76	0.1	0.6	1.8
(C)Ax_IAx_HAG-	17.0	15.8	1716.23	863.42	791.20	0.4	0.1	1.5
(C)Ax_IAx_HAG+	20.6	18.3	1719.58	855.58	781.92	2.0	0.8	0.2
(B)E_IAx_HAG+	25.2	24.3	2165.58	700.65	641.62	1.7	0.6	0.2
(B)Ax_IE_HAG-	24.8	25.0	1931.74	721.83	641.64	0.4	0.6	0.7
(B)Ax_IE_HAA	26.9	25.8	1916.68	721.32	639.50	0.6	0.9	0.7
(B)Ax_IE_HAG+	26.7	26.3	1912.30	726.96	645.28	1.0	1.1	0.9
(B)Ax_IE_HG+A	30.1	29.5	1813.47	749.67	629.05	0.9	0.2	0.4

[a]Nomenclature describing the conformation of each conformer (see footnote, Table D.13). [b]Conformers in bold were experimentally identified. [c]Conformers identified from the 2D PES scan. [d]The rotational constants and dipole moment components reported were calculated at the B3LYP-D3(BJ)/def2-TZVP level of theory.

Experimental Assignment to Theoretical Results Comparison

Table D.3. *cis* (-)-carveol experiment vs. theory comparison. [a]RMS difference between experiment and theory (B3LYP-D3(BJ)/def2-TZVP level).

	E2	**(C)E_IE_HG-A**	**E4**	**(C)Ax_IAx_HG+A**
A / MHz	2150.22733(47)	2161.15	1664.60349(57)	1689.73
B	660.47853(13)	662.04	907.27707(25)	902.97
C	541.08651(15)	541.75	805.36654(24)	802.91
$\|\mu\|$	$\mu_b > \mu_a > \mu_c$	μ_a=0.8, μ_b=1.3, μ_c=0.6	$\mu_b > \mu_a > \mu_c$	μ_a=0.7, μ_b=1.5, μ_c=0.6
$^a\sigma$ / MHz	-	11.1	-	25.6
	E5	**(C)E_IE_H AA**		
A / MHz	2120.28916(69)	2130.68		
B	645.66680(28)	647.17		
C	567.21505(28)	568.57		
$\|\mu\|$	$\mu_c > \mu_a \simeq \mu_b$	μ_a=0.7, μ_b=0.9, μ_c=1.1		
$^a\sigma$ / MHz	-	10.6		

Table D.4. *trans* (-)-carveol experiment vs. theory comparison. [a]RMS difference between experiment and theory (B3LYP-D3(BJ)/def2-TZVP level).

	E1	**(C)E_IAx_HG-A**	**E3**	**(C)E_IAx_HAA**
A / MHz	2130.99910(81)	2145.20	2122.02820(73)	2143.81
B	665.16017(26)	665.47	662.63495(17)	663.21
C	583.88177(25)	584.85	596.35973(18)	597.58
$\|\mu\|$	$\mu_b > \mu_a$	μ_a=0.5, μ_b=1.7, μ_c=0.0	$\mu_b > \mu_a >> \mu_c$	μ_a=0.5, μ_b=1.6, μ_c=0.1
$^a\sigma$ / MHz	-	14.2	-	21.8

Rotational Transition Frequencies for Experimental Conformers

Table D.5. Measured frequencies of assigned rotational transitions of E1 (*trans*-(C)E_IAx_HG-A). $\Delta\nu^a$ is the difference between observed and calculated frequencies.

J'	K_a'	K_c'	J"	K_a"	K_c"	ν_{Exp}/ MHz	$\Delta\nu^a$/ MHz
2	1	1	2	0	2	1631.675	-0.006
3	1	2	3	0	3	1764.614	0.002
4	1	3	4	0	4	1952.887	0.000
5	1	4	5	0	5	2204.981	0.001
3	0	3	2	1	2	2346.164	0.000
2	1	2	1	1	1	2416.811	0.006
2	0	2	1	0	1	2494.804	0.008
6	1	5	6	0	6	2529.681	0.001
2	1	1	1	1	0	2579.352	-0.009
1	1	1	0	0	0	2714.878	-0.003
7	1	6	7	0	7	2934.370	0.000
8	1	7	8	0	8	3423.118	0.001
3	1	3	2	1	2	3623.192	-0.001
4	0	4	3	1	3	3686.583	-0.002
3	0	3	2	0	2	3734.010	-0.002
8	2	6	8	1	7	3774.661	-0.001
9	2	7	9	1	8	3783.763	0.000
6	1	5	5	2	4	3785.213	0.001
7	2	5	7	1	6	3823.863	0.000
10	2	8	10	1	9	3863.485	-0.003
3	1	2	2	1	1	3866.940	-0.003
2	1	2	1	0	1	3882.640	-0.005
6	2	4	6	1	5	3916.833	-0.001
9	1	8	9	0	9	3995.163	0.003
11	2	9	11	1	10	4024.091	0.002
5	2	3	5	1	4	4037.288	0.000
4	2	2	4	1	3	4168.361	0.004
3	2	1	3	1	2	4294.100	0.006
4	1	4	3	1	3	4827.292	0.016
4	2	3	4	1	4	4931.601	-0.004
4	0	4	3	0	3	4963.610	-0.003
4	2	3	3	2	2	4993.604	0.001
3	1	3	2	0	2	5011.037	-0.004
4	2	2	3	2	1	5026.150	-0.001
5	0	5	4	1	4	5040.334	-0.003
5	2	4	5	1	5	5141.022	-0.004
4	1	3	3	1	2	5151.885	-0.003
7	1	6	6	2	5	5285.000	-0.002
6	2	5	6	1	6	5394.134	-0.002
7	2	6	7	1	7	5691.275	0.004
5	1	5	4	1	4	6028.473	-0.001
8	2	7	8	1	8	6032.377	0.005
4	1	4	3	0	3	6104.303	-0.002
5	0	5	4	0	4	6181.028	-0.001
5	2	4	4	2	3	6237.902	0.008
5	2	3	4	2	2	6302.048	-0.005
6	0	6	5	1	5	6396.557	-0.001
9	2	8	9	1	9	6416.839	-0.006
5	1	4	4	1	3	6433.123	0.002
5	1	5	4	0	4	7169.170	0.004

Table D.6. Measured frequencies of assigned rotational transitions of E2 (*cis*-(C)E_IE_HG-A). $\Delta\nu^a$ is the difference between observed and calculated frequencies.

J'	K_a'	K_c'	J"	K_a"	K_c"	ν_{Exp}/ MHz	$\Delta\nu^a$/ MHz
3	1	2	3	0	3	1937.482	-0.007
3	0	3	2	1	2	2200.031	0.002
4	1	3	4	0	4	2229.290	-0.001
2	1	2	1	1	1	2283.738	-0.001
2	0	2	1	0	1	2396.243	0.004
2	1	1	1	1	0	2522.515	-0.006
5	1	4	5	0	5	2626.324	0.002
1	1	1	0	0	0	2691.315	0.000
4	0	4	3	1	2	2801.182	-0.012
1	1	0	0	0	0	2810.703	-0.003
6	1	5	6	0	6	3141.613	0.003
3	1	3	2	1	2	3421.421	0.002
6	2	5	6	1	5	3457.246	-0.002
4	0	4	3	1	3	3517.296	0.002
3	0	3	2	0	2	3577.281	0.002
5	0	5	4	1	3	3647.137	0.002
6	1	5	5	2	4	3721.199	-0.004
2	1	2	1	0	1	3773.489	0.001
3	1	2	2	1	1	3779.345	0.001
7	1	6	7	0	7	3781.031	0.005
5	2	4	5	1	4	3784.068	0.000
7	2	5	7	1	6	3871.972	-0.002
6	2	4	6	1	5	3909.605	-0.001
8	2	6	8	1	7	3928.528	-0.002
5	2	3	5	1	4	4017.288	0.001
4	2	3	4	1	3	4065.000	-0.010
9	2	7	9	1	8	4098.867	-0.002
2	1	1	1	0	1	4131.663	0.000
4	2	2	4	1	3	4166.894	0.005
13	3	11	14	1	14	4263.195	0.000
3	2	2	3	1	2	4294.591	-0.008
3	2	1	3	1	2	4328.925	0.018
10	2	8	10	1	9	4398.601	0.002
8	1	7	8	0	8	4539.926	0.004
4	1	4	3	1	3	4554.412	0.001
4	0	4	3	0	3	4738.686	0.003
3	1	3	2	0	2	4798.671	0.003
4	2	3	3	2	2	4800.901	0.006
4	3	2	3	3	1	4819.325	-0.002
5	0	5	4	1	4	4839.305	-0.003
4	2	2	3	2	1	4868.463	-0.003
3	2	2	3	1	3	5010.693	-0.005
4	1	3	3	1	2	5030.486	0.001
3	2	1	3	1	3	5045.021	0.014
4	2	3	4	1	4	5257.164	-0.019
7	1	6	6	2	5	5265.129	-0.012
4	2	2	4	1	4	5359.070	0.009
9	1	8	9	0	9	5402.710	0.003
3	1	2	2	0	2	5514.771	0.003
5	2	4	5	1	5	5567.999	0.000
5	1	5	4	1	4	5681.699	0.001
4	1	4	3	0	3	5775.804	0.004
5	0	5	4	0	4	5876.425	-0.001
6	2	5	6	1	6	5943.780	0.002
5	2	4	4	2	3	5992.520	0.005
5	3	3	4	3	2	6029.002	-0.002
5	3	2	4	3	1	6034.201	-0.001
5	2	3	4	2	2	6123.855	0.000
6	0	6	5	1	5	6147.589	-0.003
5	1	4	4	1	3	6273.458	0.002
7	2	6	7	1	7	6384.278	-0.009
5	1	5	4	0	4	6718.821	0.005
6	1	6	5	1	5	6802.672	0.001
6	0	6	5	0	5	6989.986	0.003
6	2	4	5	2	3	7397.591	0.000
3	2	2	2	1	1	8073.927	-0.015
7	0	7	6	0	6	8082.981	0.009

Table D.7. Measured frequencies of assigned rotational transitions of E3 (*trans*-(C)$E_I Ax_H AA$). $\Delta\nu^a$ is the difference between observed and calculated frequencies.

J'	K_a'	K_c'	J''	K_a''	K_c''	ν_{Exp}/ MHz	$\Delta\nu^a$/ MHz
3	1	2	3	0	3	1700.973	0.002
4	1	3	4	0	4	1850.887	0.000
5	1	4	5	0	5	2049.833	-0.005
6	1	5	6	0	6	2304.358	-0.003
3	0	3	2	1	2	2372.853	0.002
2	1	2	1	1	1	2451.700	-0.013
2	0	2	1	0	1	2515.790	0.007
2	1	1	1	1	0	2584.262	-0.003
7	1	6	7	0	7	2620.680	0.002
1	1	1	0	0	0	2718.384	-0.003
8	1	7	8	0	8	3003.552	0.000
7	1	7	6	2	4	3215.682	0.005
9	1	8	9	0	9	3455.148	0.003
3	1	3	2	1	2	3676.212	0.001
4	0	4	3	1	3	3710.697	0.001
9	2	7	9	1	8	3739.774	-0.002
6	1	5	5	2	4	3743.832	0.004
10	2	8	10	1	9	3752.670	-0.001
3	0	3	2	0	2	3768.172	-0.001
8	2	6	8	1	7	3775.767	-0.002
3	2	2	2	2	1	3776.976	-0.004
9	6	4	10	5	5	3795.814	0.000
11	2	9	11	1	10	3823.440	-0.001
7	2	5	7	1	6	3850.160	-0.002
3	1	2	2	1	1	3874.992	-0.001
2	1	2	1	0	1	3911.101	-0.003
6	2	4	6	1	5	3951.169	-0.002
12	2	10	12	1	11	3959.686	0.000
10	1	9	10	0	10	3974.222	0.000
5	2	3	5	1	4	4066.327	0.000
13	2	11	13	1	12	4167.774	0.004
4	2	2	4	1	3	4183.382	0.007
3	2	1	3	1	2	4291.183	0.008
2	2	0	2	1	1	4380.366	-0.012
14	2	12	14	1	13	4452.758	-0.001
11	1	10	11	0	11	4555.928	-0.001
3	2	2	3	1	3	4677.773	0.004
12	3	10	11	4	7	4733.513	-0.001
4	2	3	4	1	4	4812.879	-0.002
4	1	4	3	1	3	4899.146	0.002
5	2	4	5	1	5	4982.843	-0.005
4	0	4	3	0	3	5014.058	0.001
4	2	3	3	2	2	5034.255	-0.001
4	2	2	3	2	1	5056.174	0.000
5	2	3	5	1	5	5059.196	0.012
5	0	5	4	1	4	5063.114	0.002
3	1	3	2	0	2	5071.531	-0.002
4	1	3	3	1	2	5163.972	-0.001
6	2	5	6	1	6	5188.147	-0.005
7	1	6	6	2	5	5212.787	-0.005
7	2	6	7	1	7	5429.159	-0.004
3	1	2	2	0	2	5469.161	0.017
8	2	7	8	1	8	5706.025	-0.006
9	2	8	9	1	9	6018.614	0.001
5	1	5	4	1	4	6120.096	0.003
4	1	4	3	0	3	6202.504	-0.001
7	2	6	7	0	7	6203.713	0.018
5	0	5	4	0	4	6251.558	-0.001
5	2	4	4	2	3	6290.065	0.005
5	4	1	4	4	0	6299.855	-0.009
5	2	3	4	2	2	6333.462	0.000
6	0	6	5	1	5	6422.315	0.001
5	1	4	4	1	3	6450.508	-0.002
2	2	0	1	1	1	7030.909	-0.010

5	1	5	4	0	4	7308.541	0.000
7	0	7	6	1	6	7780.267	0.001

Table D.8. Measured frequencies of assigned rotational transitions of E4 (*cis*-(C)Ax$_I$Ax$_H$G+A). $\Delta\nu^a$ is the difference between observed and calculated frequencies.

J'	K_a'	K_c'	J"	K_a"	K_c"	ν_{Exp}/ MHz	$\Delta\nu^a$/ MHz
5	2	3	5	1	4	2016.688	-0.009
6	2	4	6	1	5	2030.329	0.012
4	2	2	4	1	3	2073.946	-0.002
7	2	5	7	1	6	2137.889	-0.005
3	2	1	3	1	2	2172.911	-0.005
2	2	0	2	1	1	2281.592	0.011
6	1	5	6	0	6	2289.559	0.012
8	2	6	8	1	7	2356.802	0.000
1	1	1	0	0	0	2469.961	-0.008
1	1	0	0	0	0	2571.881	0.001
2	2	1	2	1	2	2577.707	0.002
2	0	2	1	1	1	2658.354	0.004
3	2	2	3	1	3	2736.311	-0.010
7	1	6	7	0	7	2864.999	0.003
4	2	3	4	1	4	2950.278	-0.005
10	3	7	10	2	8	3060.033	-0.002
11	3	8	11	2	9	3084.392	0.007
9	3	6	9	2	7	3139.571	0.004
10	2	8	10	1	9	3164.716	-0.008
5	2	4	5	1	5	3220.237	-0.001
8	3	5	8	2	6	3292.438	0.005
2	1	2	1	1	1	3323.375	0.000
2	0	2	1	0	1	3415.672	-0.003
7	3	4	7	2	5	3481.753	0.012
8	1	7	8	0	8	3507.554	0.007
2	1	1	1	1	0	3527.194	-0.001
6	2	5	6	1	6	3545.503	-0.001
6	3	3	6	2	4	3670.095	0.009
5	3	2	5	2	3	3827.359	-0.001
4	1	4	3	2	1	3845.298	-0.002
14	12	2	13	13	1	3872.386	0.000
7	2	6	7	1	7	3923.606	-0.005
4	3	1	4	2	2	3937.414	0.003
3	3	0	3	2	1	4000.217	0.013
3	3	1	3	2	2	4047.127	0.007
2	1	2	1	0	1	4080.692	-0.009
3	0	3	2	1	1	4129.293	0.008
9	1	8	9	0	9	4186.411	-0.002
6	3	4	6	2	5	4202.431	-0.001
7	3	5	7	2	6	4324.653	-0.007
8	2	7	8	1	8	4350.167	-0.014
2	1	1	1	0	1	4386.431	-0.002
3	0	3	2	1	2	4435.019	0.003
8	3	6	8	2	7	4494.709	-0.004
6	1	5	5	3	2	4644.371	0.009
9	3	7	9	2	8	4717.608	-0.002
4	1	3	3	2	1	4860.441	0.006
4	1	3	3	2	2	4907.940	0.018
3	1	3	2	1	2	4979.308	-0.002
10	3	8	10	2	9	4996.010	-0.005
3	0	3	2	0	2	5100.036	-0.005
3	2	2	2	2	1	5137.932	0.005
3	2	1	2	2	0	5175.806	0.000
5	1	5	4	2	2	5182.793	-0.013
3	1	2	2	1	1	5284.469	-0.002
4	0	4	3	1	2	5604.021	0.001
3	1	3	2	0	2	5644.327	-0.009
17	3	14	17	3	15	5699.508	0.002
2	2	1	1	1	0	5799.159	-0.010
2	2	0	1	1	0	5808.782	0.005
2	2	1	1	1	1	5901.094	0.015
2	2	0	1	1	1	5910.694	0.007

10	1	9	9	4	6	6045.148	-0.002
4	0	4	3	1	3	6214.916	0.004
3	1	2	2	0	2	6255.231	0.003
4	1	4	3	1	3	6629.104	-0.003
4	0	4	3	0	3	6759.207	0.001
4	2	3	3	2	2	6843.070	0.001
4	1	3	3	1	2	7033.336	-0.015
4	1	4	3	0	3	7173.398	-0.004
3	2	2	2	1	1	7409.886	-0.014
5	0	5	4	1	4	7978.150	0.003
3	2	1	2	1	2	7763.123	0.004

Table D.9. Measured frequencies of assigned rotational transitions of E5 (*cis*-(C)E_IE_HAA). $\Delta\nu^a$ is the difference between observed and calculated frequencies.

J'	K_a'	K_c'	J"	K_a"	K_c"	ν_{Exp}/ MHz	$\Delta\nu^a$/ MHz
2	1	1	2	0	2	1633.941	-0.011
5	1	4	5	0	5	2181.871	0.006
3	0	3	2	1	2	2227.987	0.005
2	1	2	1	1	1	2348.208	-0.002
2	0	2	1	0	1	2423.333	-0.005
6	1	5	6	0	6	2491.230	0.000
2	1	1	1	1	0	2504.512	-0.004
1	1	1	0	0	0	2687.796	-0.007
1	1	0	0	0	0	2765.953	-0.004
7	1	6	7	0	7	2876.654	0.001
9	2	8	9	1	8	2912.952	-0.003
4	0	4	3	1	2	3061.422	-0.002
8	2	7	8	1	7	3214.211	0.002
8	1	7	8	0	8	3342.539	0.003
6	1	5	5	2	3	3414.923	-0.002
7	2	6	7	1	6	3493.714	-0.008
6	1	5	5	2	4	3519.172	0.013
3	1	3	2	1	2	3520.459	0.000
4	0	4	3	1	3	3530.271	0.002
3	0	3	2	0	2	3627.473	-0.002
6	2	5	6	1	5	3746.311	-0.005
3	1	2	2	1	1	3754.842	-0.002
9	2	7	9	1	8	3795.267	0.006
8	2	6	8	1	7	3798.423	0.000
2	1	2	1	0	1	3822.826	-0.006
7	2	5	7	1	6	3855.238	-0.002
10	2	8	10	1	9	3857.756	0.005
9	1	8	9	0	9	3889.008	-0.010
6	2	4	6	1	5	3951.698	-0.004
5	2	4	5	1	4	3968.074	-0.010
11	2	9	11	1	10	3995.925	-0.007
2	1	1	1	0	1	4057.286	-0.004
5	0	5	4	1	3	4065.397	-0.003
5	2	3	5	1	4	4072.328	0.010
4	2	3	4	1	3	4156.162	-0.010
4	2	2	4	1	3	4201.243	-0.001
3	2	1	3	1	2	4323.661	0.007
2	2	1	2	1	1	4423.871	0.008
2	2	1	2	1	2	4658.326	0.004
4	1	4	3	1	3	4690.578	-0.003
7	1	6	6	2	4	4769.672	0.001
3	2	1	3	1	3	4792.507	0.007
4	0	4	3	0	3	4822.745	-0.001
5	0	5	4	1	4	4846.417	-0.002
4	2	3	3	2	2	4850.372	0.006
4	3	2	3	3	1	4858.549	-0.004
4	3	1	3	3	0	4859.008	0.016
4	2	2	3	2	1	4880.338	-0.007
3	1	3	2	0	2	4919.947	-0.004
4	2	3	4	1	4	4937.185	-0.007
7	1	6	6	2	5	4975.046	-0.012
4	2	2	4	1	4	4982.265	0.001
4	1	3	3	1	2	5002.753	-0.002

5	2	4	5	1	5	5138.328	-0.008
5	2	3	5	1	5	5242.566	-0.003
6	2	5	6	1	6	5381.407	-0.005
3	1	2	2	0	2	5388.793	-0.004
6	2	4	6	1	6	5586.798	-0.001
7	2	6	7	1	7	5666.768	-0.010
7	0	7	6	1	5	5844.710	-0.011
5	1	5	4	1	4	5858.031	-0.002
4	1	4	3	0	3	5983.052	-0.005
5	0	5	4	0	4	6006.728	-0.003
5	2	4	4	2	3	6059.179	0.003
5	4	2	4	4	1	6072.620	0.012
5	2	3	4	2	2	6118.335	-0.003
6	0	6	5	1	5	6166.264	0.000
5	1	4	4	1	3	6247.261	-0.004
9	2	8	9	1	9	6363.936	0.009
4	1	3	3	0	3	6764.074	-0.003
2	2	1	1	1	0	6928.396	0.017
2	2	1	1	1	1	7006.545	0.013
5	1	5	4	0	4	7018.342	-0.002
6	1	6	5	1	5	7022.397	-0.001
6	0	6	5	0	5	7177.882	0.004
6	2	5	5	2	4	7265.477	0.002
7	0	7	6	1	6	7479.826	0.009
6	1	5	5	1	4	7487.235	-0.008
6	1	6	5	0	5	8034.003	-0.008
3	2	1	2	1	1	8078.508	0.009
7	1	7	6	0	6	9039.560	0.013

Theoretical Geometries for the Experimental Conformers

Table D.10. Atom positions for conformer E1 (*trans*-(C)E_IAx_HG-A), optimized at the B3LYP-D3(BJ)/def2-TZVP level of theory.

Atom	X	Y	Z
O	1.69981	1.57166	-1.11818
C	1.43380	0.97094	0.16237
C	1.96711	-0.44068	0.20308
C	1.13711	-1.48320	0.22806
C	-0.36026	-1.39097	0.22097
C	-0.87342	0.00211	-0.18452
C	-0.04310	1.05835	0.53753
C	-2.93847	0.98917	0.83378
C	-2.36993	0.11794	0.00439
C	-3.20307	-0.83457	-0.80980
C	3.46008	-0.58386	0.19216
H	1.38580	0.96490	-1.79819
H	2.00817	1.58748	0.85869
H	1.55579	-2.48512	0.26274
H	-0.74794	-1.63668	1.21824
H	-0.76157	-2.15498	-0.44881
H	-0.68971	0.10883	-1.26335
H	-0.39572	2.06295	0.30189
H	-0.13895	0.91886	1.61890
H	-2.36499	1.68167	1.43331
H	-4.01534	1.03676	0.93823
H	-3.04071	-1.87083	-0.50273
H	-2.94049	-0.77523	-1.87033
H	-4.26571	-0.61784	-0.70716
H	3.76340	-1.62966	0.14115
H	3.89791	-0.14339	1.09335
H	3.89254	-0.05245	-0.65863

Table D.11. Atom positions for conformer E2 (*cis*-(C)$E_I$$E_H$G-A), optimized at the B3LYP-D3(BJ)/def2-TZVP level of theory.

Atom	X	Y	Z
O	-2.30029	1.81432	0.01854
C	-1.40879	0.77951	0.44972
C	-1.87757	-0.58954	0.00394
C	-1.01288	-1.49979	-0.44347
C	0.47336	-1.30841	-0.52465
C	0.95303	-0.09292	0.29081
C	0.02015	1.08077	0.01228
C	2.87421	1.27709	-0.55035
C	2.42182	0.18410	0.05858
C	3.36609	-0.87416	0.56009
C	-3.34621	-0.86760	0.13493
H	-2.26167	1.85548	-0.94458
H	-1.47285	0.82806	1.54246
H	-1.39088	-2.46907	-0.75600
H	0.96845	-2.21820	-0.17681
H	0.78205	-1.18242	-1.57008
H	0.84256	-0.36023	1.35066
H	0.36180	1.98671	0.51396
H	0.01314	1.28965	-1.06381
H	2.21689	2.05316	-0.91663
H	3.93519	1.43176	-0.70241
H	4.40497	-0.57694	0.42164
H	3.21571	-1.82392	0.04050
H	3.20190	-1.06833	1.62420
H	-3.94038	-0.17778	-0.46645
H	-3.67303	-0.72839	1.17004
H	-3.58082	-1.88847	-0.16615

Table D.12. Atom positions for conformer E3 (*trans*-(C)E_IAx_HAA), optimized at the B3LYP-D3(BJ)/def2-TZVP level of theory.

Atom	X	Y	Z
O	1.66799	-1.90467	0.40956
C	1.37532	-0.85144	-0.52548
C	1.96219	0.45654	-0.04886
C	1.17775	1.45028	0.36966
C	-0.32151	1.40152	0.41397
C	-0.86691	-0.02878	0.29771
C	-0.11818	-0.75371	-0.82517
C	-3.14626	-0.51181	1.12395
C	-2.36953	-0.06526	0.14019
C	-2.95072	0.41510	-1.16060
C	3.45950	0.54785	-0.05910
H	1.40793	-1.60028	1.28645
H	1.89606	-1.16347	-1.43467
H	1.63939	2.37610	0.70138
H	-0.68072	1.85571	1.34148
H	-0.72323	2.02432	-0.39420
H	-0.63579	-0.54128	1.23757
H	-0.51274	-1.76111	-0.96827
H	-0.24911	-0.20942	-1.76519
H	-2.72746	-0.87125	2.05621
H	-4.22508	-0.53642	1.03102
H	-2.62540	1.43102	-1.39787
H	-2.63176	-0.21886	-1.99180
H	-4.03954	0.40738	-1.12882
H	3.80788	1.48524	0.37478
H	3.84504	0.47904	-1.08114
H	3.90074	-0.28105	0.49897

Table D.13. Atom positions for conformer E4 (*cis*-(C)Ax_IAx_HG+A), optimized at the B3LYP-D3(BJ)/def2-TZVP level of theory.

Atom	X	Y	Z
O	-0.46503	-1.91295	0.33530
C	-0.93961	-0.96054	-0.62865
C	-1.74692	0.12772	0.04341
C	-1.29786	1.38031	0.10502
C	0.01086	1.85123	-0.46318
C	0.98158	0.71043	-0.78300
C	0.18952	-0.40409	-1.49422
C	1.53097	0.51237	1.66785
C	1.78038	0.18900	0.39939
C	2.91409	-0.73488	0.04659
C	-3.05006	-0.30339	0.64598
H	0.07708	-1.42652	0.97107
H	-1.60855	-1.54522	-1.26644
H	-1.91184	2.13377	0.59046
H	-0.18465	2.41140	-1.38577
H	0.47678	2.56698	0.21803
H	1.72249	1.08621	-1.49720
H	-0.24439	0.01755	-2.40565
H	0.83634	-1.22687	-1.79836
H	0.71530	1.16230	1.95152
H	2.14605	0.12606	2.47128
H	2.54389	-1.66172	-0.39710
H	3.50244	-0.99426	0.92590
H	3.57761	-0.27140	-0.68896
H	-3.54200	0.51697	1.16899
H	-2.89285	-1.12378	1.34996
H	-3.73118	-0.67677	-0.12530

Table D.14. Atom positions for conformer E5 (*cis*-(C)E_IE_HAA), optimized at the B3LYP-D3(BJ)/def2-TZVP level of theory.

Atom	X	Y	Z
O	2.17369	-1.88703	-0.05963
C	1.35471	-0.82016	0.43252
C	1.89044	0.53705	0.02465
C	1.07239	1.51374	-0.36899
C	-0.42421	1.41208	-0.42459
C	-0.94927	0.20652	0.37045
C	-0.09997	-1.01983	0.02354
C	-3.29201	0.22730	1.15841
C	-2.43073	-0.01757	0.17413
C	-2.89225	-0.52352	-1.16438
C	3.37543	0.72495	0.13169
H	2.12138	-1.88032	-1.02295
H	1.44226	-0.91320	1.52068
H	1.50213	2.47048	-0.65182
H	-0.87135	2.32971	-0.03241
H	-0.75003	1.34781	-1.46933
H	-0.79182	0.42819	1.43082
H	-0.49046	-1.91866	0.50388
H	-0.13119	-1.19097	-1.05828
H	-2.95818	0.58032	2.12667
H	-4.35795	0.08325	1.03094
H	-2.49695	-1.52266	-1.36505
H	-2.54958	0.11948	-1.97894
H	-3.97936	-0.57609	-1.20937
H	3.66226	1.74208	-0.13485
H	3.91631	0.02758	-0.51005
H	3.71586	0.52579	1.15253

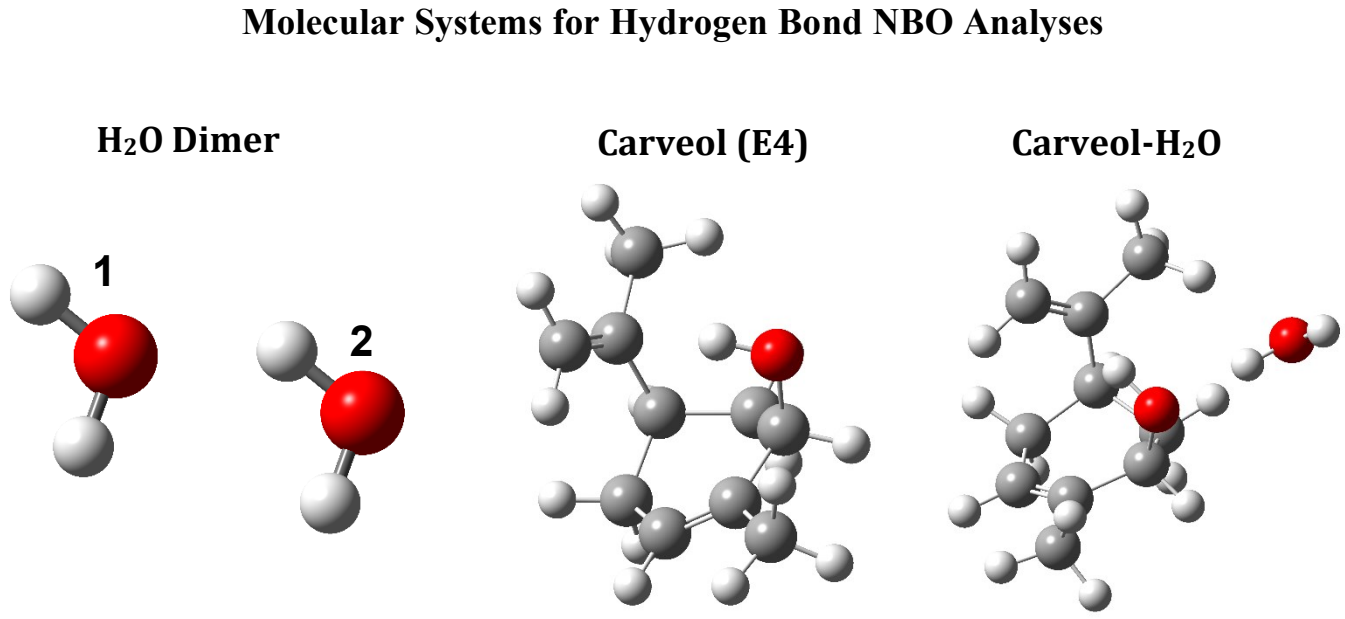

Figure D.3. Three hydrogen bond containing systems used for the NBO analyses

Appendix E

Supplementary Information for Chapter 7

Structure and conformations of 3-methylcatechol: A rotational spectroscopic and theoretical study

Contents:

1. Theoretical Cartesian coordinates for 3-methylcatechol conformers
    a. **Table E.1.** Cartesian coordinates for all three conformers
2. Assigned rotational transitions
    a. **Table E.2.** Assigned rotational transitions of Conformer 1
    b. **Table E.3.** Assigned rotational transitions of Conformer 2
3. Experimental spectroscopic parameters for ^{13}C isotopologues
    a. **Table E.4.** Spectroscopic parameters for the ^{13}C isotopologues of Conformer 1
    b. **Table E.5.** Spectroscopic parameters for the ^{13}C isotopologues of Conformer 2
4. Assigned rotational transitions of ^{13}C isotopologues
    a. **Table E.6.** Assigned rotational constants of the ^{13}C isotopologues of Conformer 1
    b. **Table E.7.** Assigned rotational constants of the ^{13}C isotopologues of Conformer 2
5. Kraitchman Analyses
    a. **Table E.8.** C-atom coordinates for Conformer 1 and Conformer 2

Theoretical Cartesian coordinates for 3-methylcatechol conformers

Table E.1. Cartesian coordinates for the three monomer conformers optimized at the ωB97XD/Jun-cc-pVTZ level of theory

Conformer 1				Conformer 2			
Atom	X	Y	Z	Atom	X	Y	Z
C1	-1.212	-0.070	0.000	C1	1.238	-0.097	0.000
C2	0.044	-0.678	0.000	C2	-0.037	-0.659	0.000
C3	1.203	0.095	0.000	C3	-1.176	0.134	0.000
C4	1.071	1.483	0.000	C4	-1.012	1.516	0.000
C5	-0.177	2.090	0.000	C5	0.251	2.082	0.000
C6	-1.329	1.310	0.000	C6	1.380	1.278	0.000
C7	2.543	-0.582	0.000	C7	-2.538	-0.503	0.000
H1	-3.108	-0.438	0.000	H1	2.047	-1.808	0.000
H2	-0.743	-2.409	0.000	H2	-0.972	-2.344	0.000
H3	1.966	2.092	-0.001	H3	-1.890	2.149	0.000
H4	-0.259	3.169	-0.001	H4	0.360	3.158	0.000
H5	-2.311	1.770	0.000	H5	2.375	1.700	0.000
H6	2.662	-1.220	0.878	H6	-3.317	0.256	0.000
H7	3.347	0.154	-0.005	H7	-2.694	-1.127	0.884
H8	2.658	-1.228	-0.873	H8	-2.694	-1.128	-0.884
O1	0.149	-2.038	0.000	O1	2.336	-0.891	0.000
O2	-2.284	-0.935	0.000	O2	-0.068	-2.029	0.000

Conformer 3			
Atom	X	Y	Z
C1	-1.225	-0.168	0.000
C2	0.072	-0.685	0.000
C3	1.170	0.171	0.000
C4	0.954	1.545	0.000
C5	-0.328	2.062	0.000
C6	-1.417	1.203	0.000
C7	2.561	-0.402	0.000
H1	-3.081	-0.584	0.000
H2	1.121	-2.278	0.000
H3	1.807	2.212	0.000
H4	-0.486	3.131	0.000
H5	-2.426	1.598	0.000
H6	2.746	-1.018	-0.884
H7	2.746	-1.018	0.884
H8	3.303	0.394	0.000
O1	-2.250	-1.060	0.000
O2	0.194	-2.039	0.000

Assigned rotational transitions

Table E.2. Assigned rotational transitions of Conformer 1

J'	K_a'	K_c'	J"	K_a"	K_c"	ν_{Exp} / MHz	$\Delta\nu^a$ / MHz	Type
1	0	1	0	0	0	2826.6569	0.003	A
1	0	1	0	0	0	2826.5254	-0.006	E
4	3	1	4	2	2	2978.7078	0.003	A
4	3	1	4	2	2	2979.4907	0.006	E
3	3	0	3	2	1	3178.1393	0.007	A
3	3	0	3	2	1	3189.2961	-0.006	E
1	1	1	0	0	0	3329.1261	0.002	A
1	1	1	0	0	0	3328.2313	0.000	E
4	2	2	4	2	3	3786.4989	0.003	A
4	2	2	4	2	3	3786.9146	-0.001	E
2	2	1	2	1	2	3866.6255	0.004	A
2	2	1	2	1	2	3862.7259	-0.010	E
2	2	1	2	0	2	4041.7280	0.006	A
2	2	1	2	0	2	4037.5369	-0.009	E
4	2	2	4	1	3	4050.9240	0.007	A
4	2	2	4	1	3	4050.7778	-0.010	E
5	4	1	5	3	2	4063.7636	0.008	A
5	4	1	5	3	2	4068.9074	-0.009	E
3	1	2	3	1	3	4514.0918	0.008	A
3	1	2	3	1	3	4513.6013	-0.004	E
3	1	2	3	0	3	4555.1108	0.007	A
3	1	2	3	0	3	4554.5327	-0.009	E
2	0	2	1	1	1	4691.8009	-0.002	A
2	0	2	1	1	1	4692.3110	0.002	E
2	1	2	1	1	1	4866.9032	-0.001	A
2	1	2	1	1	1	4867.1228	0.003	E
2	0	2	1	0	1	5194.2710	-0.002	A
2	0	2	1	0	1	5194.0109	0.002	E
3	2	2	3	1	3	5283.7950	0.009	A
3	2	2	3	1	3	5281.9519	-0.006	E
2	1	2	1	0	1	5369.3727	-0.002	A
2	1	2	1	0	1	5368.8216	0.002	E
4	3	2	4	2	3	5684.5605	0.009	A
4	3	2	4	2	3	5680.8012	-0.009	E
5	2	3	5	2	4	6235.1947	0.008	A
5	2	3	5	2	4	6234.8120	-0.008	E
2	1	1	1	1	0	6439.7141	0.002	A
2	1	1	1	1	0	6439.1033	-0.003	E
3	0	3	2	0	2	7196.8758	-0.003	A
3	0	3	2	0	2	7196.5849	0.007	E
3	1	3	2	0	2	7237.8950	-0.004	A
3	1	3	2	0	2	7237.5156	0.001	E
3	2	2	2	2	1	8479.9651	0.003	A
3	2	2	2	2	1	8481.9344	0.008	E
3	1	2	2	1	1	9217.6620	-0.007	A
3	1	2	2	1	1	9217.0241	-0.005	E

[a] $\Delta\nu$ is the difference between measured and calculated frequencies.

Table E.3. Assigned rotational transitions of Conformer 2

J'	K_a'	K_c'	J"	K_a"	K_c"	ν_{Exp} / MHz	$\Delta\nu^a$ / MHz
3	2	1	3	2	2	1734.3821	0.008
2	1	1	2	1	2	2352.6044	0.002
2	1	1	2	0	2	2528.9390	0.002
1	0	1	0	0	0	2821.8330	0.002
4	3	1	4	2	2	2980.9726	-0.006
3	3	0	3	2	1	3184.8581	0.001
1	1	1	0	0	0	3325.8020	0.000
5	3	2	5	2	3	3742.9004	0.007
4	2	2	4	2	3	3772.3785	0.000
2	2	1	2	1	2	3864.5097	-0.009
4	2	2	4	1	3	4039.6930	0.004
7	4	3	7	4	4	4085.5454	0.009
3	1	2	3	1	3	4502.6892	0.000
3	1	2	3	0	3	4544.1893	0.000
2	0	2	1	1	1	4683.1263	0.000
4	4	0	4	3	1	4846.7306	0.005
2	1	2	1	1	1	4859.4627	0.002
2	0	2	1	0	1	5187.0950	-0.002
3	2	2	3	1	3	5277.1595	-0.003
6	3	3	6	3	4	5287.4070	-0.011
3	2	2	3	0	3	5318.6671	0.005
2	1	2	1	0	1	5363.4297	-0.002
6	3	3	6	2	4	5596.5049	-0.004
5	2	3	5	2	4	6216.7357	-0.007
2	1	1	1	1	0	6427.8630	0.000
3	0	3	2	1	2	7011.3458	0.000
4	2	3	4	0	4	7044.5042	0.007
3	1	3	2	1	2	7052.8480	0.002
3	0	3	2	0	2	7187.6834	0.003
3	1	3	2	0	2	7229.1830	0.002
2	2	1	1	1	0	7939.7687	-0.010
3	2	2	2	2	1	8465.4976	0.008
4	1	4	3	1	3	9141.5521	-0.005
4	0	4	3	0	3	9175.0357	0.000
3	1	2	2	1	1	9202.9352	0.002
3	2	1	2	2	0	9743.2948	-0.004
4	2	3	3	2	2	10900.8708	0.001

[a] $\Delta\nu$ is the difference between measured and calculated frequencies.

Experimental spectroscopic parameters for ^{13}C isotopologues

Table E.4. Spectroscopic parameters for the ^{13}C isotopologues of Conformer 1

	^{13}C-1	**^{13}C-2**	**^{13}C-3**	**^{13}C-4[c]**
A / MHz	2308.7797(60)	2304.050(21)	2308.418(11)	2288.134(13)
B	1797.6147(95)	1806.345(19)	1796.5094(87)	1797.1555(33)
C	1017.3013(33)	1019.3221(52)	1017.0776(26)	1013.1188(30)
[a]Δ_J / kHz	[0.068]	[0.068]	[0.068]	[0.068]
[a]Δ_K	[0.085]	[0.085]	[0.085]	[0.085]
[a]δ_J	[0.0307]	[0.0307]	[0.0307]	[0.0307]
[a]δ_K	[0.028]	[0.028]	[0.028]	[0.028]
V_3 /kJ mol^{-1}	3.63(2)	3.56(6)	3.53(4)	-
[b]ε /rad	[0]	[0]	[0]	-
δ /rad	0.443(25)	0.502(67)	1.061(17)	-
N	10	7	7	4
σ /kHz	7.5	16.6	10.5	4.2

	^{13}C-5	**^{13}C-6**	**^{13}C-7**
A / MHz	2262.662(21)	2288.506(16)	2303.8903(94)
B	1806.5014(53)	1796.5867(43)	1765.5257(78)
C	1011.0320(49)	1013.0868(37)	1006.0008(20)
Δ_J / kHz	[0.068]	[0.068]	[0.068]
Δ_K	[0.085]	[0.085]	[0.085]
δ_J	[0.0307]	[0.0307]	[0.0307]
δ_K	[0.028]	[0.028]	[0.028]
V_3 /kJ mol^{-1}	3.59(1)	3.58(1)	3.62(3)
[b]ε /rad	[0]	[0]	[0]
δ /rad	0.492(16)	0.452(15)	0.418(37)
N	10	8	9
σ /kHz	15.8	11.7	8.3

[a] Constants were fixed to the values of the parent species in fit.
[b] Constants were fixed to zero in fit.
[c] A-species fit only.

Table E.5. Spectroscopic parameters for the ^{13}C isotopologues of Conformer 2

	^{13}C-1	**^{13}C-2**	**^{13}C-3**	**^{13}C-4**
A / MHz	2307.064(39)	2302.4918(46)	2307.022(12)	2286.0280(60)
B / MHz	1794.0571(29)	1803.1003(18)	1793.2270(32)	1793.6426(15)
C / MHz	1015.9635(27)	1017.9651(11)	1015.6936(30)	1011.7323(14)
Δ_J / kHz	[0.046][a]	[0.046]	[0.046]	[0.046]
Δ_K / kHz	[-0.276]	[-0.276]	[-0.276]	[-0.276]
δ_J / kHz	[0.0115]	[0.0115]	[0.0115]	[0.0115]
δ_K / kHz	[0.111]	[0.111]	[0.111]	[0.111]
N	4	6	5	5
σ / kHz	3.8	3.3	5.4	2.5

	^{13}C-5	**^{13}C-6**	**^{13}C-7**
A / MHz	2261.2832(59)	2287.325(85)	2302.2910(65)
B / MHz	1803.0296(22)	1793.1351(99)	1761.9557(17)
C / MHz	1009.8106(15)	1011.8321(99)	1004.6780(12)
Δ_J / kHz	[0.046]	[0.046]	[0.046]
Δ_K / kHz	[-0.276]	[-0.276]	[-0.276]
δ_J / kHz	[0.0115]	[0.0115]	[0.0115]
δ_K / kHz	[0.111]	[0.111]	[0.111]
N	6	4	5
σ / kHz	4.2	12.7	2.9

[a] Square brackets indicate the constants were fixed to the values of the parent species in fit.

Assigned rotational transitions of ^{13}C isotopologues

Table E.6. Assigned rotational transitions of the ^{13}C isotopologues of Conformer 1

Atom	J'	K_a'	K_c'	J"	K_a"	K_c"	ν_{Exp}/ MHz	Δν/ MHz	Type
C1	2	0	2	1	1	1	4668.163	-0.008	A
	2	0	2	1	1	1	4668.714	0.003	E
	2	0	2	1	0	1	5179.601	0.005	A
	2	0	2	1	0	1	5179.341	-0.004	E
	1	0	1	0	0	0	2814.960	0.004	A
	2	1	2	1	1	1	4849.576	0.004	A
	2	1	2	1	1	1	4849.801	0.001	E
	2	1	2	1	0	1	5360.991	-0.006	A
	2	1	2	1	0	1	5360.439	0.006	E
	1	1	1	0	0	0	3326.378	-0.003	A
C2	2	0	2	1	0	1	5189.986	-0.014	A
	2	0	2	1	0	1	5189.725	0.000	E
	2	1	2	1	1	1	4864.388	0.008	A
	2	1	2	1	1	1	4864.602	0.000	E
	2	1	2	1	0	1	5362.336	0.004	A
	1	1	1	0	0	0	3323.676	0.002	A
	2	1	1	1	1	0	6438.504	0.001	A
C3	2	0	2	1	1	1	4666.180	0.006	A
	2	1	2	1	1	1	4847.927	-0.008	A
	2	1	2	1	1	1	4847.706	0.000	E
	2	0	2	1	0	1	5177.999	-0.002	A
	2	0	2	1	0	1	5177.742	0.000	E
	2	1	2	1	0	1	5359.765	0.004	A
	2	1	1	1	1	0	6407.138	0.000	A
C4	2	0	2	1	0	1	5158.783	-0.007	A
	2	1	2	1	1	1	4836.514	0.004	A
	2	1	2	1	0	1	5327.492	0.003	A
	2	1	1	1	1	0	6404.582	0.001	A
	1	0	1	0	0	0	2817.575	-0.009	A
C5	1	0	1	0	0	0	2817.575	-0.009	A
	1	0	1	0	0	0	2817.429	-0.028	E
	2	0	2	1	0	1	5148.758	0.007	A
	2	0	2	1	0	1	5148.483	0.001	E
	2	1	2	1	0	1	5296.057	-0.001	A
	2	1	2	1	0	1	5295.524	-0.003	E
	2	1	1	1	1	0	6430.671	0.000	A
	2	1	1	1	1	0	6430.070	0.009	E
	2	1	2	1	1	1	4839.662	0.000	A
	2	1	2	1	1	1	4839.866	0.005	E
C6	2	0	2	1	0	1	5158.591	-0.015	A
	2	0	2	1	0	1	5158.340	0.003	E
	2	1	2	1	1	1	4835.909	0.005	A
	2	1	2	1	1	1	4836.149	0.001	E
	2	1	2	1	0	1	5328.093	0.005	A
	1	0	1	0	0	0	2809.719	0.002	A
	2	1	1	1	1	0	6402.961	0.001	A
	2	1	1	1	1	0	6402.369	-0.001	E
C7	2	0	2	1	0	1	5120.607	0.009	A
	2	0	2	1	0	1	5120.355	0.000	E
	2	1	2	1	0	1	5322.208	-0.008	A
	2	1	2	1	0	1	5321.624	0.000	E
	2	0	2	1	1	1	4581.953	-0.006	A
	1	0	1	0	0	0	2771.566	0.005	A
	2	1	2	1	1	1	4783.580	0.004	A
	2	1	2	1	1	1	4783.836	0.000	E
	2	1	1	1	1	0	6302.664	-0.001	A

Table E.7. Assigned rotational transitions of the ^{13}C isotopologues of Conformer 2

Atom	J'	K_a'	K_c'	J''	K_a''	K_c''	ν_{Exp}/ MHz	$\Delta\nu$/ MHz
C1	2	0	2	1	0	1	5172.234	-0.006
	2	1	2	1	1	1	4841.950	0.003
	2	1	2	1	0	1	5354.957	0.003
	2	1	1	1	1	0	6398.133	0.001
C2	2	1	2	1	1	1	4856.999	0.004
	2	0	2	1	1	1	4683.513	-0.004
	2	1	2	1	0	1	5356.383	-0.004
	2	0	2	1	0	1	5182.913	0.004
	1	0	1	0	0	0	2821.065	0.000
	2	1	1	1	1	0	6427.264	0.000
C3	1	0	1	0	0	0	2808.931	0.011
	2	1	2	1	1	1	4840.303	-0.004
	2	1	1	1	1	0	6395.369	-0.003
	2	0	2	1	0	1	5170.825	0.003
	2	1	2	1	0	1	5354.102	-0.001
C4	1	0	1	0	0	0	2805.380	0.005
	2	0	2	1	0	1	5151.375	-0.002
	2	1	1	1	1	0	6392.657	-0.001
	2	1	2	1	0	1	5321.225	0.001
	2	1	2	1	1	1	4828.839	0.000
C5	2	1	2	1	1	1	4832.453	-0.008
	1	0	1	0	0	0	2812.845	0.005
	2	0	2	1	1	1	4683.813	0.004
	2	0	2	1	0	1	5142.066	0.002
	2	1	1	1	1	0	6418.895	-0.002
	2	1	2	1	0	1	5290.716	0.001
C6	1	0	1	0	0	0	2804.991	0.024
	2	1	1	1	1	0	6391.229	-0.006
	2	1	2	1	1	1	4828.625	-0.006
	2	0	2	1	0	1	5151.820	0.000
C7	1	0	1	0	0	0	2766.640	0.006
	2	1	1	1	1	0	6290.541	-0.001
	2	1	2	1	1	1	4775.988	-0.001
	2	0	2	1	0	1	5113.238	-0.001
	2	0	2	1	1	1	4572.902	0.000

Kraitchman Analyses

Table E.8. C-atom coordinates for Conformer 1 and Conformer 2

Conformer 1				Conformer 2			
Atom	*a*	*b*	*c*	Atom	*a*	*b*	*c*
C1	-1.177(1)	0[a]	0	C1	-1.186(1)	0[a]	0
C2	0[a]	-0.667(2)	0	C2	0[a]	-0.655(2)	0
C3	1.208(1)	0[b]	0	C3	1.239(1)	0[a]	0
C4	1.185(2)	1.426(1)	0	C4	1.192(1)	1.438(1)	0
C5	0[a]	2.1156(9)	0	C5	0[a]	2.1091(7)	0
C6	-1.209(2)	1.412(1)	0	C6	-1.224(4)	1.394(3)	0
C7	2.5442(6)	-0.716(2)	0	C7	2.5521(6)	-0.707(2)	0

[a] Values are imaginary and were set to zero.
[b] Set to zero to improve structure fit (see the text for details).

Appendix F

Supplementary Information for Chapter 8

Wetting vs Droplet Aggregation: A Broadband Rotational Spectroscopic Study of 3-Methylcatechol ⋯ Water Clusters

Contents:

1. **Theoretical Conformers**
   a. **Table F.1.** ωB97XD/Jun-cc-pVTZ level of theory refined CREST results of each hydrate within 5.0 kJ mol^{-1}
   b. **Table F.2.** B3LYP-D3BJ/def2-TZVP level of theory refined CREST results of each hydrate within 5.0 kJ mol^{-1}
   c. **Figure F.1.** Examples of different types of aggregation
2. **Non-covalent interactions analyses of droplet conformers**
   a. **Figure F.2.** NCI analyses of the droplet aggregation conformers
3. **Quantum theory of atoms-in-molecules (QTAIM) results**
   a. **Figure F.3.** QTAIM analyses of the five experimentally assigned hydrates
4. **Isotopologues Spectroscopic Parameters**
   a. **Table F.3.** Spectroscopic Parameters of the ^{13}C and ^{18}O isotopologues of MC1-1W I
   b. **Figure F.4.** Carbon atom numbering
   c. **Table F.4.** Spectroscopic Parameters of the ^{18}O isotopologues of the MC2-1W II
   d. **Table F.5.** Spectroscopic Parameters of the ^{18}O isotopologues of the dihydrate
   e. **Table F.6.** Spectroscopic Parameters of the ^{18}O isotopologues of the trihydrate
5. **Structural Parameters**
   a. **Table F.7.** Structural parameters for the mono-, di-, and trihydrate species
6. **Theoretical Geometries for the Experimental Conformers**
   a. **Table F.8**. Geometries for monohydrates
   b. **Table F.9.** Geometry for Dihydrate species
   c. **Table F.10.** Geometry for Trihydrate species
   d. **Table F.11.** Geometry for Tetrahydrate species
   e. **Table F.12.** Geometry for Pentahydrate species
7. **Rotational Transition Frequencies for Experimental Conformers**
   a. **Table F.13.** Assigned rotational transitions for Monohydrate 1
   b. **Table F.14.** Assigned rotational transitions for Monohydrate 2
   c. **Table F.15.** Assigned rotational transitions for Dihydrate
   d. **Table F.16.** Assigned rotational transitions for Trihydrate
   e. **Table F.17.** Assigned rotational transitions for Tetrahydrate
   f. **Table F.18.** Assigned rotational transitions for Pentahydrate
8. **Rotational Transition Frequencies for Experimental Isotopologue Species**
   a. **Table F.19.** Assigned rotational transitions for MC1-1W I ^{18}O and ^{13}C isotopologues
   b. **Table F.20.** Assigned rotational transitions for MC2-1W II ^{18}O isotopologues
   c. **Table F.21.** Assigned rotational transitions for dihydrate ^{18}O isotopologues
   d. **Table F.22.** Assigned rotational transitions for trihydrate ^{18}O isotopologues
9. **Complete DFT refined CREST results**
   a. **Table F.23.** ωB97XD/Jun-cc-pVTZ level of theory refined CREST results of monohydrate
   b. **Table F.24.** ωB97XD/Jun-cc-pVTZ level of theory refined CREST results of dihydrate
   c. **Table F.25.** ωB97XD/Jun-cc-pVTZ level of theory refined CREST results of trihydrate

d. **Table F.26.** ωB97XD/Jun-cc-pVTZ level of theory refined CREST results tetrahydrate
e. **Table F.27.** ωB97XD/Jun-cc-pVTZ level of theory refined CREST results of pentahydrate
f. **Table F.28.** B3LYP-D3BJ/def2-TZVP level of theory refined CREST results of monohydrate
g. **Table F.29.** B3LYP-D3BJ/def2-TZVP level of theory refined CREST results of dihydrate
h. **Table F.30.** B3LYP-D3BJ/def2-TZVP level of theory refined CREST results of trihydrate
i. **Table F.31.** B3LYP-D3BJ/def2-TZVP level of theory refined CREST results of tetrahydrate
j. **Table F.32.** B3LYP-D3BJ/def2-TZVP level of theory refined CREST results of pentahydrate

Theoretical Conformers

Table F.1. ωB97XD/Jun-cc-pVTZ refined CREST results for hydrate conformers within a 5.0 kJ mol^{-1} energetic window.

	ΔE_0 /kJ mol^{-1}	A /MHz	B /MHz	C /MHz	μ_a /D	μ_b /D	μ_c /D	[a]ΔA /%	[a]ΔB /%	[a]ΔC /%	Monomer Subunit	Aggregation Type ([b]D/[c]W/[d]M)
[e]Monohydrate												
1	0.0	2314.29	790.45	592.97	5.0	0.1	0.0	1.3 (24.6)	1.4 (-13.0)	1.3 (-3.7)	MC1	D
2	4.6	1882.93	935.74	633.09	5.1	0.7	0.5	-17.6 (1.4)	20.0 (3.0)	8.2 (2.8)	MC2	D
Dihydrate												
1	0.0	1376.27	734.18	620.09	0.8	1.9	0.7	-0.4	2.8	2.3	MC1	W
2	0.2	1412.22	726.32	619.39	1.0	0.4	1.7	2.2	1.7	2.1	MC1	W
3	1.1	1448.79	693.19	577.20	2.0	2.0	1.2	4.9	-2.9	-4.8	MC1	W
Trihydrate												
1	0.0	1093.47	555.13	485.62	1.4	1.3	0.4	1.1	2.8	2.8	MC1	W
2	1.3	1101.71	560.72	483.25	1.3	1.5	0.1	1.9	3.8	2.3	MC1	W
3	1.4	863.20	763.06	599.22	1.2	0.7	0.5	-20.2	41.3	26.8	MC2	M
4	1.8	928.78	621.97	563.29	1.7	1.6	0.3	-14.1	15.2	19.2	MC2	W
5	2.1	913.91	717.43	594.66	0.1	0.3	0.4	-15.5	32.9	25.9	MC1	M
6	2.2	875.44	751.50	602.66	1.2	1.3	0.2	-19.0	39.2	27.5	MC2	M
7	2.3	937.24	695.02	581.92	1.3	1.4	0.6	-13.3	28.7	23.2	MC1	M
8	2.9	935.84	698.45	588.67	0.1	2.0	0.2	-13.4	29.4	24.6	MC1	M
9	2.9	875.28	751.90	605.98	0.3	0.9	0.4	-19.0	39.3	28.3	MC2	M
10	3.3	1085.76	526.67	468.96	1.7	1.5	0.5	0.4	-2.5	-0.7	MC1	W
11	3.3	1088.37	525.06	467.47	1.7	1.5	0.5	0.7	-2.8	-1.1	MC1	W
12	3.4	938.87	631.55	567.65	2.0	1.9	0.3	-13.2	17.0	20.1	MC2	W
13	3.7	1063.15	574.76	524.27	0.2	0.1	0.6	-1.7	6.4	11.0	MC1	W
14	3.9	892.38	749.45	662.81	0.4	1.8	0.4	-17.5	38.8	40.3	MC1	M
15	4.7	1124.93	579.28	496.31	0.2	0.0	0.2	4.1	7.3	5.0	MC2	W
Tetrahydrate												
1	0.0	791.67	495.15	461.48	0.7	0.6	0.4	1.0	2.9	3.0	MC1	W
2	0.2	797.34	495.64	458.65	1.1	1.0	0.6	1.7	3.0	2.3	MC1	W
3	0.9	790.80	493.29	466.52	0.8	0.3	0.6	0.9	2.5	4.1	MC1	W
4	1.1	797.02	490.71	467.91	0.8	0.6	0.2	1.7	2.0	4.4	MC1	W
5	1.5	858.91	525.35	453.42	1.1	2.0	0.6	9.6	9.2	1.2	MC1	M1
6	1.6	702.14	620.95	541.60	0.7	0.1	1.1	-10.4	29.1	20.8	MC1	M1
7	1.7	825.63	537.01	491.44	2.0	0.2	0.8	5.3	11.6	9.6	MC1	M1
8	2.0	795.94	550.30	514.56	0.3	0.4	2.3	1.5	14.4	14.8	MC1	M1
9	2.0	829.69	558.82	469.92	0.2	3.3	0.5	5.8	16.2	4.8	MC2	M1
10	2.7	854.45	525.96	452.97	0.5	1.9	1.1	9.0	9.3	1.1	MC1	M1
11	2.8	884.23	471.41	437.86	0.4	0.8	1.3	12.8	-2.0	-2.3	MC1	M1
12	3.0	854.23	535.82	458.48	1.2	2.3	0.6	9.0	11.4	2.3	MC1	M1
13	3.0	954.29	411.35	397.23	0.5	0.1	1.6	21.7	-14.5	-11.4	MC1	M2
14	3.2	945.01	428.66	396.55	0.2	0.0	1.5	20.5	-10.9	-11.5	MC1	M1
15	3.4	881.36	467.58	437.77	0.3	0.7	1.2	12.4	-2.8	-2.3	MC1	M2
16	3.7	875.40	479.77	444.65	0.9	0.5	0.3	11.7	-0.3	-0.8	MC1	M2
17	3.8	739.60	574.57	560.33	0.7	0.4	1.7	-5.7	19.4	25.0	MC1	M1
18	4.2	809.80	543.93	499.82	1.9	0.3	0.5	3.3	13.1	11.5	MC1	M1
19	4.6	804.67	523.20	483.09	2.2	0.6	0.1	2.6	8.8	7.8	MC1	M2
20	4.6	801.31	523.10	495.43	1.2	0.4	2.3	2.2	8.7	10.5	MC1	M2
21	4.7	855.14	530.95	454.01	0.2	2.4	1.1	9.1	10.4	1.3	MC1	M1
Pentahydrate												

1	0.0	691.99	458.59	408.54	1.5	2.5	0.1	2.5	3.4	3.4	MC1	W
2	3.6	655.46	444.84	381.00	3.2	0.8	1.1	-2.9	0.3	-3.6	MC1	W
3	3.7	586.51	499.62	415.70	1.5	2.0	0.3	-13.1	12.6	5.2	MC1	W
4	4.0	581.53	502.27	415.57	0.6	1.4	2.2	-13.8	13.2	5.2	MC1	W
5	4.4	667.73	457.18	421.08	2.8	0.4	1.0	-1.1	3.1	6.6	MC1	W

[a]Percent differences between the theoretical rotational constants and the experimentally assigned rotational constants. [b]Droplet aggregation. [c]Wetting. [d]Mixed aggregation, involving a structure with primarily hydrogen bonds, with minimal dispersion interactions with the π system. [e]Percentages in brackets are the precent differences between MC2 2W and theoretical conformers. Conformers in red indicate that they were experimentally identified

Table F.2. B3LYP-D3(BJ)/def2-TZVP refined CREST results for hydrate conformers within a 5.0 kJ mol^{-1} energetic window.

	ΔE_0 /kJ mol^{-1}	A /MHz	B /MHz	C /MHz	μ_a /D	μ_b /D	μ_c /D	[a]ΔA /%	[a]ΔB /%	[a]ΔC /%	Monomer Subunit	Aggregation Type ([b]D/[c]W/[d]M)
[e]Monohydrate												
1	0.0	2298.63	792.57	593.16	5.4	0.2	0.0	0.6 (23.8)	1.7 (-12.7)	1.4 (-3.7)	MC1	D
2	4.6	1885.03	1004.80	667.27	0.6	2.7	1.5	-17.5 (1.5)	28.9 (10.6)	14.0 (8.3)	MC1	D
3	5.1	1803.45	955.70	649.05	5.5	0.3	0.3	-21.0 (-2.9)	22.6 (5.2)	10.9 (5.4)	MC2	D
Dihydrate												
1	0.0	1423.72	716.28	603.88	1.2	0.3	1.9	3.1	0.3	-0.4	MC1	W
2	0.8	1451.37	690.72	571.41	2.1	2.0	1.3	5.1	-3.3	-5.8	MC1	W
3	3.0	1217.05	831.02	606.25	0.5	1.8	1.4	-11.9	16.4	0.0	MC1	D
4	3.5	1230.13	841.72	636.23	0.6	0.2	2.5	-10.9	17.9	4.9	MC1	D
Trihydrate												
1	0.0	1089.05	553.95	484.83	1.6	1.4	0.5	0.7	2.6	2.6	MC1	W
2	0.4	854.20	770.64	597.12	1.4	0.6	0.6	-21.0	42.7	26.4	MC2	M
3	1.0	1097.58	558.22	483.32	1.4	1.5	0.0	1.5	3.4	2.3	MC1	W
4	1.2	949.82	683.43	574.94	1.2	1.6	0.7	-12.1	26.6	21.7	MC1	M
5	1.3	868.32	757.59	606.03	0.1	1.0	0.4	-19.7	40.3	28.3	MC2	M
6	1.7	865.16	758.15	600.45	1.5	1.4	0.2	-20.0	40.4	27.1	MC2	M
7	1.7	948.43	685.77	582.38	0.2	2.3	0.1	-12.3	27.0	23.3	MC1	M
8	2.3	913.21	620.16	566.98	1.8	1.6	0.3	-15.5	14.9	20.0	MC2	W
9	3.2	929.50	631.05	568.37	2.1	1.9	0.2	-14.0	16.9	20.3	MC2	W
10	3.3	1354.15	428.07	398.11	1.6	1.5	0.1	25.3	-20.7	-15.7	MC1	D
11	3.4	895.82	748.79	660.85	0.4	1.9	0.4	-17.1	38.7	39.9	MC2	M
12	3.5	1224.24	465.08	372.80	2.9	0.0	0.4	13.2	-13.9	-21.1	[f]TS	D
13	3.5	1234.16	464.40	408.04	1.2	0.8	1.0	14.2	-14.0	-13.6	MC1	D
14	3.5	1230.96	466.00	409.31	1.1	0.8	1.0	13.9	-13.7	-13.4	MC1	D
15	3.7	1118.64	522.03	389.14	3.0	1.2	0.6	3.5	-3.3	-17.6	TS	D
16	3.8	1107.23	513.57	458.29	1.9	1.4	0.6	2.4	-4.9	-3.0	MC1	W
17	3.9	1325.74	429.46	383.69	2.6	0.2	0.4	22.6	-20.5	-18.8	TS	D
18	4.2	1191.55	486.71	398.16	2.7	0.3	0.2	10.2	-9.9	-15.7	TS	D
19	4.2	1121.20	516.73	412.75	1.5	0.8	1.6	3.7	-4.3	-12.6	TS	D
20	4.3	1329.59	482.60	423.55	1.8	0.3	2.3	23.0	-10.6	-10.4	TS	D
21	4.4	953.83	699.39	641.53	0.3	1.0	0.2	-11.8	29.5	35.8	MC1	M
22	4.4	1338.80	416.76	363.40	2.5	0.4	0.3	23.8	-22.8	-23.1	MC1	D
23	4.5	1324.40	484.22	424.42	1.6	1.5	2.3	22.5	-10.3	-10.2	TS	D
24	4.7	865.76	673.20	495.47	1.5	0.8	1.6	-19.9	24.7	4.9	MC2	D
25	4.8	970.76	607.74	571.04	2.0	0.7	1.6	-10.2	12.6	20.9	TS	W
26	4.8	1001.33	585.27	478.27	0.4	0.4	1.8	-7.4	8.4	1.2	MC1	D
27	4.9	1120.46	531.09	421.36	2.0	0.1	0.8	3.6	-1.6	-10.8	TS	D
Tetrahydrate												
1	0.0	702.85	620.00	542.97	0.8	0.0	1.2	10.3	28.9	21.1	MC1	M1
2	0.2	865.30	521.45	450.46	1.3	2.0	0.6	10.4	8.4	0.5	MC1	M1
3	0.3	698.65	622.22	542.76	0.8	0.2	1.3	10.9	29.3	21.1	MC1	M1
4	0.7	790.88	495.70	462.36	0.6	0.8	0.3	0.9	3.0	3.2	MC1	W
5	1.0	797.35	495.94	459.69	1.2	1.2	0.7	1.7	3.1	2.6	MC1	W
6	1.0	816.24	538.86	497.80	2.1	0.2	0.7	4.1	12.0	11.1	MC1	M1
7	1.4	778.91	556.09	528.59	0.2	0.5	2.3	0.6	15.6	17.9	MC1	M1
8	1.5	790.34	493.64	466.63	0.8	0.6	0.5	0.8	2.6	4.1	MC1	W
9	1.7	860.91	521.60	449.81	0.7	1.9	1.3	9.8	8.4	0.4	MC1	M1
10	1.9	796.78	491.00	468.91	1.0	0.9	0.3	1.6	2.1	4.6	MC1	W
11	2.0	830.67	557.61	468.36	0.4	3.4	0.5	6.0	15.9	4.5	MC1	M1
12	2.3	857.25	533.42	456.36	1.5	2.3	0.5	9.3	10.9	1.8	MC1	M1
13	2.8	723.10	582.96	568.16	0.7	1.3	1.2	7.8	21.2	26.8	MC1	D

14	3.2	958.16	437.89	386.02	0.5	2.2	1.3	22.2	9.0	13.9	TS	D
15	3.2	900.37	456.62	426.06	0.3	0.7	1.3	14.8	5.1	4.9	MC1	M1
16	3.5	808.06	545.03	500.87	2.1	0.3	0.5	3.1	13.3	11.8	MC1	M1
17	3.7	898.79	453.88	425.01	0.5	0.8	1.3	14.6	5.6	5.2	MC1	M1
18	3.7	857.77	529.04	452.03	0.4	2.4	1.3	9.4	10.0	0.9	MC1	M1
19	3.7	953.18	413.47	399.59	0.4	0.1	1.6	21.6	14.0	10.8	MC1	M2
20	3.9	889.37	466.19	434.41	1.1	0.7	0.5	13.4	3.1	3.1	MC1	M1
21	4.5	952.73	420.34	392.83	0.2	0.0	1.4	21.5	12.6	12.4	MC1	M1
22	4.6	960.21	411.88	396.41	0.8	1.1	0.0	22.5	14.4	11.6	MC1	M2
23	4.9	800.67	521.61	495.57	1.1	0.3	2.4	2.1	8.4	10.6	MC1	M1
24	4.9	805.16	522.75	483.66	2.5	0.6	0.1	2.7	8.7	7.9	MC1	M1
Pentahydrate												
1	0.0	694.72	455.99	406.17	1.7	2.6	0.1	2.9	2.8	2.8	MC1	W
2	2.7	581.00	503.40	416.75	0.7	1.5	2.3	-13.9	13.5	5.5	MC1	W
3	3.1	586.81	500.89	417.42	1.7	2.2	0.4	-13.0	12.9	5.7	MC1	W
4	3.8	660.94	441.48	381.64	3.5	0.7	1.2	-2.1	-0.5	-3.4	MC1	W
5	3.9	706.85	447.98	410.19	2.0	4.0	0.5	4.7	1.0	3.8	MC1	M
6	4.5	586.95	496.84	418.77	1.4	0.6	0.2	-13.0	12.0	6.0	MC1	W
7	4.6	680.27	439.64	391.39	3.5	1.8	0.7	0.8	-0.9	-0.9	MC1	W
8	4.8	671.75	453.88	422.06	3.0	0.6	0.9	-0.5	2.3	6.8	MC1	W

[a]Percent differences between the theoretical rotational constants and the experimentally assigned rotational constants. [b]Droplet aggregation. [c]Wetting. [d]Mixed aggregation, involving a structure with primarily hydrogen bonds, with minimal dispersion interactions with the π system. [e]Percentages in brackets are the precent differences between MC2 2W and theoretical conformers. Conformers in red indicate that they were experimentally identified

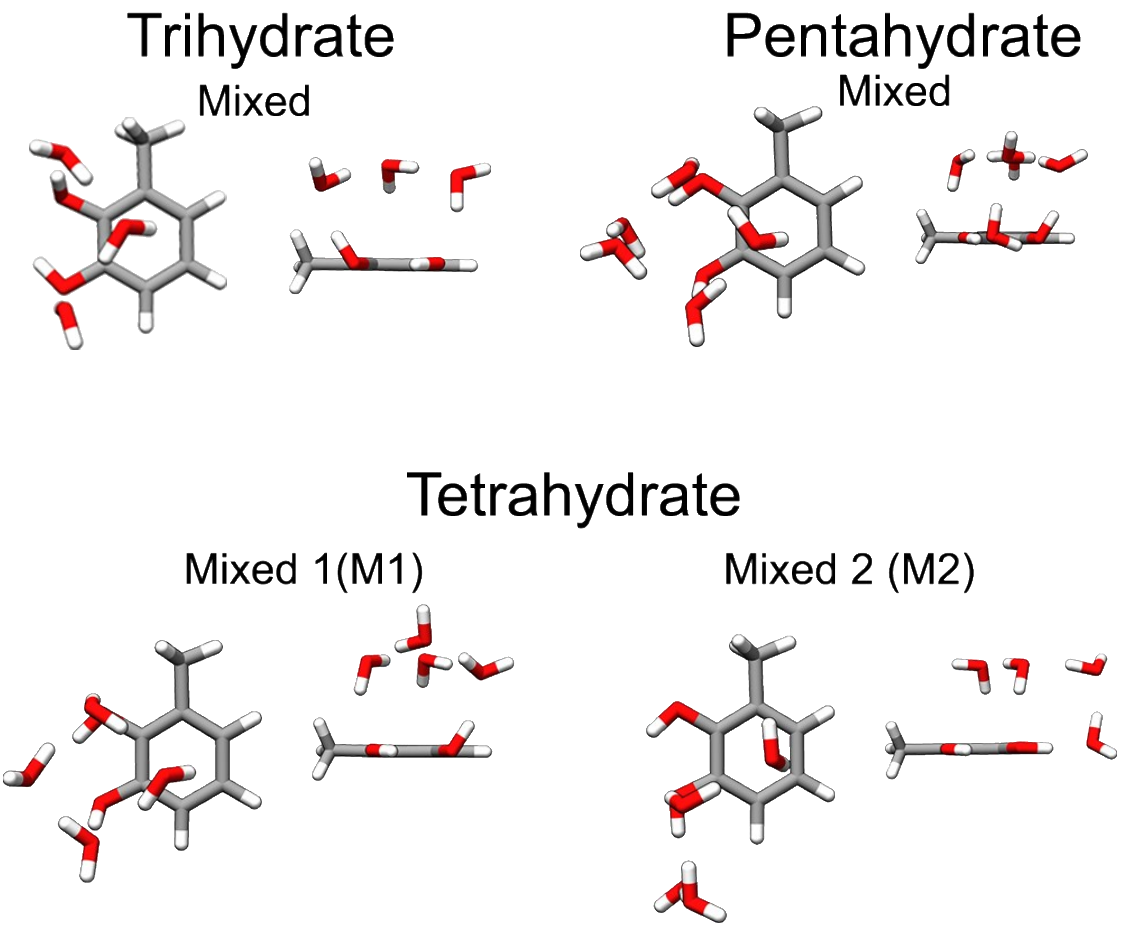

Figure F.1. Example structures for the different mixed aggregation type.

Non-Covalent Interactions (NCI) Analyses

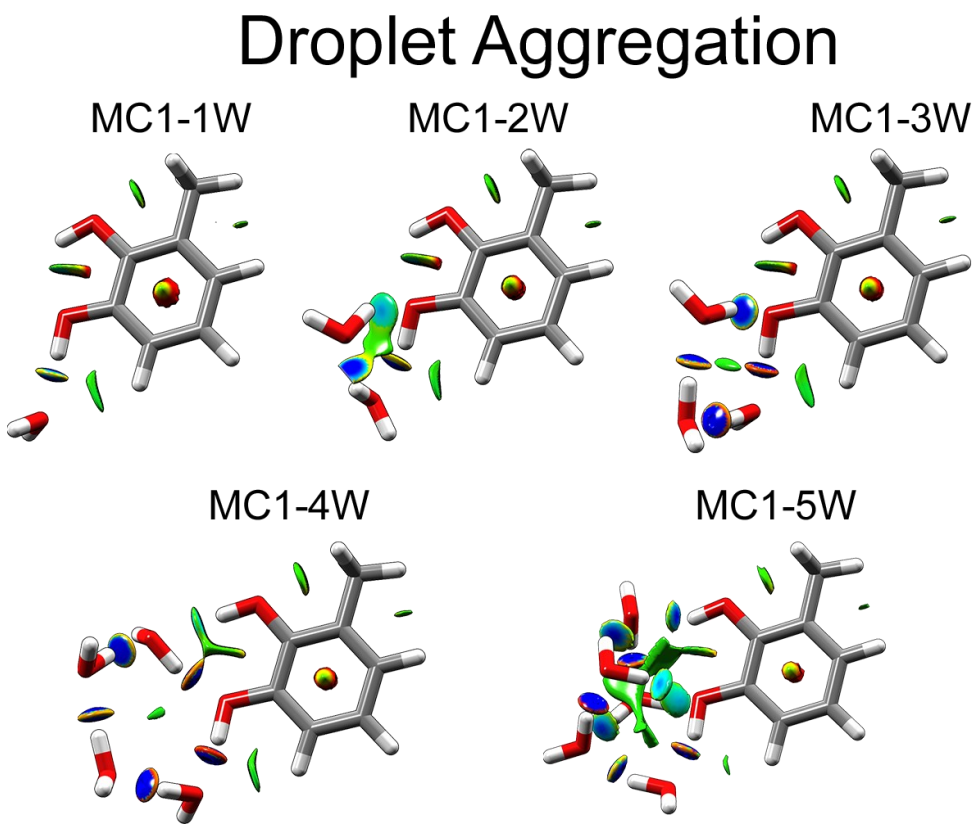

Figure F.2. NCI analysis of the droplet conformers.

Quantum theory of atoms-in-molecules (QTAIM) results

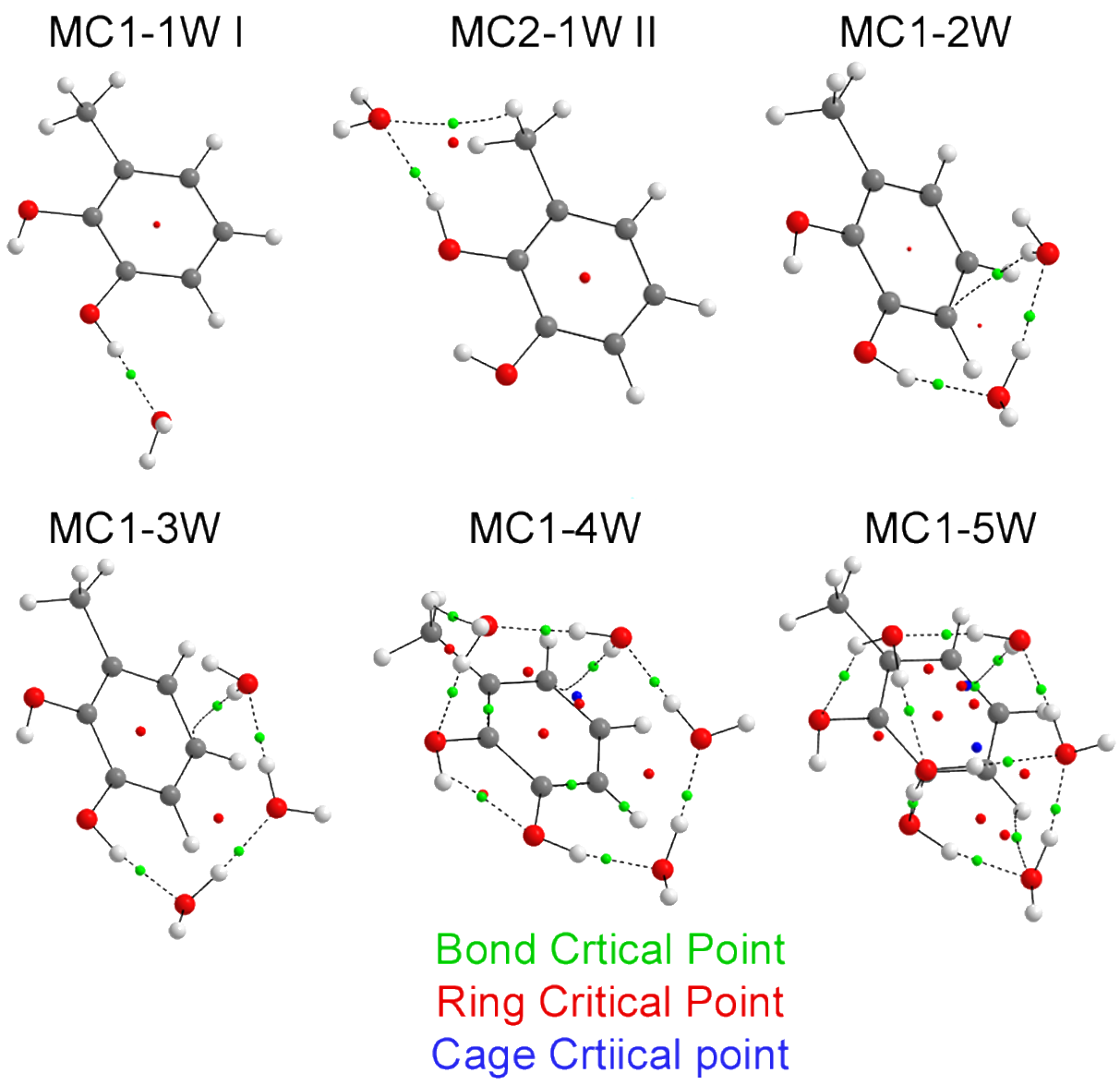

Figure F.3. QTAIM analysis of five experimentally assigned hydrate conformers.

Isotopologue Spectroscopic Parameters

Table F.3. Spectroscopic parameters for the ^{13}C isotopologues of Monohydrate 1

	^{13}C-1		^{13}C-2		^{13}C-3	
	Ortho	*Para*	*Ortho*	*Para*	*Ortho*	*Para*
A /MHz	2283.987(20)	2287.189(80)	2279.644(22)	2282.837(45)	2283.896(26)	2287.135(43)
B /MHz	779.28660(40)	779.2255(37)	779.04410(45)	778.9815(12)	775.61430(53)	775.55291(93)
C /MHz	585.03097(34)	584.9631(17)	584.60571(38)	584.53918(74)	582.95114(44)	582.88403(68)
[a]Δ_J /kHz	[0.085]	[0.099]	[0.085]	[0.099]	[0.085]	[0.099]
[a]Δ_{JK} /kHz	[0.400]	[0.520]	[0.400]	[0.520]	[0.400]	[0.520]
V_3 /kJ mol^{-1}	3.501(4)	3.499(37)	3.507(4)	3.51(1)	3.509(5)	3.505(9)
[b]ε /rad	[0]	[0]	[0]	[0]	[0]	[0]
δ /rad	0.3750(97)	0.416(72)	0.363(11)	0.368(28)	0.359(14)	0.368(23)
N	22	9	23	14	22	15
σ /kHz	4.0	10.6	4.6	7.0	5.3	6.7

	^{13}C-4		^{13}C-5		^{13}C-6	
	Ortho	*Para*	*Ortho*	*Para*	*Ortho*	*Para*
A /MHz	2259.706(15)	2262.817(74)	2240.327(19)	2243.324(42)	2268.556(17)	2271.688(41)
B /MHz	776.46555(32)	776.4044(20)	779.52669(41)	779.4657(13)	778.95353(34)	778.8928(11)
C /MHz	581.84266(27)	581.7751(12)	582.25083(40)	582.18432(75)	583.82650(29)	583.75908(70)
[a]Δ_J /kHz	[0.085]	[0.099]	[0.085]	[0.099]	[0.085]	[0.099]
[a]Δ_{JK} /kHz	[0.400]	[0.520]	[0.400]	[0.520]	[0.400]	[0.520]
V_3 /kJ mol^{-1}	3.507(3)	3.51(1)	3.502(3)	3.51(1)	3.503(3)	3.504(8)
[b]ε /rad	[0]	[0]	[0]	[0]	[0]	[0]
δ /rad	0.3652(81)	0.351(55)	0.3737(92)	0.350(30)	0.3659(83)	0.346(27)
N	22	13	21	14	22	13
σ /kHz	3.2	11.1	3.8	6.8	3.5	6.3

	^{13}C-7	
	Ortho	*Para*
A /MHz	2282.275(26)	2285.397(58)
B /MHz	767.39299(45)	767.33407(86)
C /MHz	578.19255(39)	578.12652(57)
[a]Δ_J /kHz	[0.085]	[0.099]
[a]Δ_{JK} /kHz	[0.400]	[0.520]
V_3 /kJ mol^{-1}	3.510(4)	3.506(5)
[b]ε /rad	[0]	[0]
δ /rad	0.350(12)	0.368(20)
N	21	12
σ /kHz	4.7	5.1

[a]Fixed to parent species value. [b]Fixed to zero

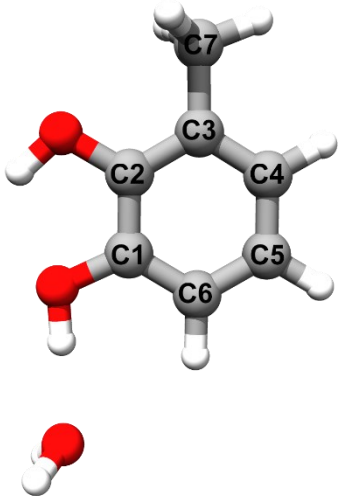

Figure F.4. Carbon atom numbering for Monohydrate 1.

Table F.4. Spectroscopic parameters for the ^{18}O isotopologues of the monohydrates

	MC1-1W I		MC1-1W II
	$^{18}O_{\alpha}$ - *Ortho*	$^{18}O_{\alpha}$ - *Para*	$^{18}O_{\alpha'}$ - *Ortho/Para*
A /MHz	2283.9417(74)	2287.1890(95)	1856.174(11)
B /MHz	740.61633(14)	740.55007(18)	861.99190(45)
C /MHz	562.95548(13)	562.88604(17)	594.29110(45)
$^{a}\Delta_J$ /kHz	[0.085]	[0.085]	[0.086]
$^{a}\Delta_{JK}$ /kHz	[0.400]	[0.400]	[0.52]
$^{a}\Delta_K$ /kHz	-	-	[1.06]
$^{a}\delta_J$ /kHz	[0.0200]	[0.0200]	[0.0287]
$^{a}\delta_K$ /kHz	[0.53]	[0.53]	[0.261]
V_3 /kJ mol^{-1}	3.497(1)	3.498(1)	-
$^{b}\varepsilon$ /rad	[0]	[0]	-
δ /rad	0.3683(32)	0.3662(41)	-
N	46	45	12
σ /kHz	2.1	2.6	2.9

[a]Fixed to parent species value. [b]Fixed to zero.

Table F.5. Spectroscopic parameters for the ^{18}O isotopologues of MC1-2W

	Singly Substituted		**Doubly Substituted**
	$^{18}O_{\alpha}{}^{16}O_{\beta}$	$^{16}O_{\alpha}{}^{18}O_{\beta}$	$^{18}O_{\alpha}{}^{18}O_{\beta}$
A /MHz	1380.72920(88)	1346.90255(79)	1346.15881(42)
B /MHz	690.74305(37)	702.19111(43)	679.91593(30)
C /MHz	589.21994(34)	598.83051(37)	582.26953(32)
$^{a}\Delta_J$ /kHz	[0.956]	[0.956]	[0.956]
$^{a}\Delta_{JK}$ /kHz	[-2.534]	[-2.534]	[-2.534]
$^{a}\Delta_K$ /kHz	[3.901]	[3.901]	[3.901]
$^{a}\delta_J$ /kHz	[-0.0196]	[-0.0196]	[-0.0196]
$^{a}\delta_K$ /kHz	[0]	[0]	[0]
V_3 /kJ mol^{-1}	3.563(1)	[3.562]	[3.562]
$^{b}\varepsilon$ /rad	[1.914]	[1.984]	[1.928]
δ /rad	0.47673(33)	2.65984(31)	2.65768(23)
N	62	56	96
σ /kHz	8.8	8.9	10.1

[a]Fixed to parent species value. [b]Fix to theory.

Table F.6. Spectroscopic parameters for the ^{18}O isotopologues of MC1-3W

	Triply Substituted		**Doubly Substituted**	
	$^{18}O_\alpha{}^{18}O_\beta{}^{18}O_\gamma$	$^{18}O_\alpha{}^{18}O_\beta{}^{16}O_\gamma$	$^{18}O_\alpha{}^{16}O_\beta{}^{18}O_\gamma$	$^{16}O_\alpha{}^{18}O_\beta{}^{18}O_\gamma$
A /MHz	1037.97272(91)	1063.61182(91)	1047.95420(89)	1045.25726(80)
B /MHz	513.89687(34)	515.59872(29)	525.24973(25)	525.54067(22)
C /MHz	448.15755(24)	451.88880(19)	457.87064(19)	458.09721(16)
$^a\Delta_J$ /kHz	[0.1217]	[0.1217]	[0.1217]	[0.1217]
$^a\Delta_{JK}$ /kHz	[0.108]	[0.108]	[0.108]	[0.108]
$^a\Delta_K$ /kHz	[0.27]	[0.27]	[0.27]	[0.27]
$^a\delta_J$ /kHz	[0.0101]	[0.0101]	[0.0101]	[0.0101]
$^a\delta_K$ /kHz	[-0.20091]	[-0.20091]	[-0.20091]	[-0.20091]
V_3 /kJ mol^{-1}	[3.307]	[3.307]	[3.307]	[3.307]
ε /rad	1.2231(28)	1.2207(55)	1.2322(57)	1.2129(31)
δ /rad	2.64166(19)	2.64226(76)	2.65104(77)	2.63433(20)
N	54	45	51	48
σ /kHz	8.9	6.3	6.4	5.7

	Singly Substituted		
	$^{18}O_\alpha{}^{16}O_\beta{}^{16}O_\gamma$	$^{16}O_\alpha{}^{18}O_\beta{}^{16}O_\gamma$	$^{16}O_\alpha{}^{16}O_\beta{}^{18}O_\gamma$
A /MHz	1074.6913(13)[a]	1070.75143(92)	1054.4847(40)
B /MHz	527.13138(57)	527.43813(38)	537.85568(41)
C /MHz	461.78601(46)	461.95943(28)	468.43339(27)
$^a\Delta_J$ /kHz	[0.1217][b]	[0.1217]	[0.1217]
$^a\Delta_{JK}$ /kHz	[0.108]	[0.108]	[0.108]
$^a\Delta_K$ /kHz	[0.27]	[0.27]	[0.27]
$^a\delta_J$ /kHz	[0.0101]	[0.0101]	[0.0101]
$^a\delta_K$ /kHz	[-0.20091]	[-0.20091]	[-0.20091]
$^aV_3$ /kJ mol^{-1}	[3.307]	[3.307]	[3.307]
ε /rad	1.243(10)	1.2235(83)	1.2320(77)
δ /rad	2.6522(14)	2.63462(74)	2.64256(69)
N	29	29	30
σ /kHz	8.8	6.1	5.7

[a]Fixed to parent species value.

Structural Parameters

Table F.7. Substitution (r_s) and theoretical structure parameters.

	r_s	**B3LYP**	**ωB97XD**		**r_s**	**B3LYP**	**ωB97XD**
MC1-1W I							
r(C1-C2)	1.376(8)	1.398	1.394	**∠(C1-C2-C3)**	120.9(9)	120.9	120.8
r(C2-C3)	1.385(9)	1.392	1.388	**∠(C2-C3-C4)**	117.0(4)	118.1	118.1
r(C3-C4)	1.42(1)	1.40	1.39	**∠(C3-C4-C5)**	120.8(2)	121.2	121.2
r(C4-C5)	1.398(6)	1.389	1.384	**∠(C4-C5-C6)**	119.9(1)	120.2	120.2
r(C5-C6)	1.385(5)	1.392	1.388	**∠(C5-C6-C1)**	118.9(3)	119.3	119.3
r(C3-C7)	1.497(6)	1.501	1.500	**∠(C6-C1-C2)**	122.5(8)	120.2	120.3
r(C1-C6)	1.36(2)	1.39	1.38	**∠(C7-C3-C2)**	122(1)	119.6	120
				∠(C7-C3-C4)	121.1(6)	122.2	122.3
MC1-2W							
r(O_α-O_β)	2.599(5)	2.784	2.788				
MC1-3W							
r(O_α-O_β)	2.749(2)	2.706	2.716	**∠(O_α-O_β-O_γ)**	110.44(4)	111.99	113.29
r(O_α-O_γ)	4.610(3)	4.527	4.576	**∠(O_γ-O_α-O_β)**	35.59(3)	34.35	33.67
r(O_β-O_γ)	2.863(3)	2.755	2.762	**∠(O_β-O_γ-O_α)**	33.97(3)	33.66	33.04

Theoretical Geometries

Table F.8. Cartesian coordinates for the two monohydrate conformers optimized at the ωB97XD/Jun-cc-pVTZ level of theory

Monohydrate 1				Monohydrate 2			
Atom	X	Y	Z	Atom	X	Y	Z
O	0.898	-2.026	0.000	O	1.089	-1.082	0.215
C	0.724	-0.678	0.000	C	-0.020	-0.299	0.088
C	1.835	0.154	0.000	C	-0.003	1.090	0.063
C	1.625	1.531	0.000	C	-1.219	1.761	-0.055
C	0.347	2.061	0.000	C	-2.413	1.067	-0.139
C	-0.758	1.221	-0.001	C	-2.421	-0.319	-0.107
C	-0.566	-0.149	0.000	C	-1.224	-1.001	0.006
O	-1.572	-1.067	-0.001	O	-1.214	-2.357	0.037
H	-2.439	-0.633	0.000	H	-0.296	-2.636	0.101
H	-1.764	1.621	-0.001	H	-3.341	-0.883	-0.170
H	0.204	3.133	0.000	H	-3.346	1.606	-0.228
H	2.483	2.191	0.000	H	-1.220	2.843	-0.077
C	3.211	-0.445	0.001	C	1.296	1.839	0.168
H	3.364	-1.075	0.878	H	1.836	1.566	1.078
H	3.972	0.333	-0.003	H	1.117	2.912	0.196
H	3.362	-1.081	-0.873	H	1.952	1.631	-0.680
H	0.024	-2.429	0.000	H	1.918	-0.614	0.039
O	-4.124	0.091	0.001	O	3.745	-0.339	-0.297
H	-4.664	-0.110	-0.764	H	4.242	0.153	0.358
H	-4.664	-0.110	0.766	H	4.202	-1.175	-0.399

Table F.9. Cartesian coordinates for the dihydrate species optimized at the ωB97XD/Jun-cc-pVTZ level of theory

Atom	X	Y	Z
O	1.156	2.030	0.373
C	0.910	0.778	-0.086
C	1.876	-0.211	0.065
C	1.580	-1.490	-0.396
C	0.365	-1.776	-1.001
C	-0.588	-0.777	-1.156
C	-0.319	0.499	-0.684
O	-1.195	1.537	-0.760
H	-2.099	1.204	-0.597
H	-1.540	-0.976	-1.629
H	0.160	-2.773	-1.364
H	2.321	-2.271	-0.284
C	3.185	0.123	0.717
H	3.035	0.523	1.720
H	3.718	0.888	0.151
H	3.819	-0.759	0.786
H	0.368	2.554	0.193
O	-3.446	0.247	0.077
H	-3.005	-0.281	0.767
H	-4.222	0.636	0.479
O	-1.786	-1.244	1.760
H	-1.271	-0.719	2.374
H	-1.167	-1.469	1.055

Table F.10. Cartesian coordinates for the trihydrate species optimized at the ωB97XD/Jun-cc-pVTZ level of theory

Atom	X	Y	Z
O	1.516	-1.739	-1.143
C	1.204	-0.825	-0.190
C	2.118	0.170	0.132
C	1.755	1.104	1.101
C	0.521	1.041	1.732
C	-0.383	0.037	1.405
C	-0.044	-0.893	0.437
O	-0.847	-1.902	0.027
H	-1.785	-1.696	0.231
H	-1.348	-0.026	1.889
H	0.262	1.769	2.488
H	2.456	1.884	1.365
C	3.448	0.211	-0.561
H	4.018	-0.698	-0.365
H	4.033	1.065	-0.226
H	3.328	0.277	-1.644
H	0.759	-2.329	-1.228
O	-3.366	-1.046	0.443
H	-4.084	-1.537	0.044
H	-3.335	-0.184	-0.022
O	-3.106	1.308	-0.888
H	-2.178	1.565	-1.050
H	-3.551	2.103	-0.597
O	-0.477	2.049	-1.294
H	-0.019	1.891	-0.458
H	-0.019	1.490	-1.924

Table F.11. Cartesian coordinates for the tetrahydrate species optimized at the ωB97XD/Jun-cc-pVTZ level of theory

Atom	X	Y	Z
O	-1.365	0.330	1.864
C	-1.029	-0.439	0.779
C	-1.952	-0.641	-0.235
C	-1.538	-1.377	-1.345
C	-0.252	-1.889	-1.427
C	0.656	-1.686	-0.396
C	0.265	-0.954	0.712
O	1.057	-0.674	1.773
H	2.005	-0.704	1.509
H	1.662	-2.078	-0.448
H	0.046	-2.458	-2.296
H	-2.239	-1.548	-2.150
C	-3.330	-0.055	-0.133
H	-3.297	1.035	-0.159
H	-3.953	-0.395	-0.957
H	-3.808	-0.340	0.805
H	-0.605	0.298	2.459
O	3.540	-0.564	0.792
H	4.244	-0.224	1.343
H	3.395	0.107	0.087
O	2.977	1.299	-1.072
H	3.412	1.300	-1.924
H	2.019	1.403	-1.264
O	-1.224	2.741	0.344
H	-0.914	3.521	0.803
H	-1.336	2.054	1.018
O	0.350	1.563	-1.674
H	-0.047	0.691	-1.753
H	-0.188	2.023	-1.006

Table F.12. Cartesian coordinates for the pentahydrate species optimized at the ωB97XD/Jun-cc-pVTZ level of theory

Atom	X	Y	Z
O	1.316	1.055	-1.675
C	1.254	-0.046	-0.872
C	2.308	-0.306	-0.007
C	2.211	-1.420	0.823
C	1.099	-2.247	0.788
C	0.050	-1.974	-0.079
C	0.126	-0.864	-0.903
O	-0.859	-0.492	-1.768
H	-1.692	-0.960	-1.541
H	-0.826	-2.606	-0.113
H	1.046	-3.112	1.434
H	3.025	-1.640	1.502
C	3.493	0.613	0.025
H	3.209	1.609	0.370
H	4.259	0.230	0.695
H	3.925	0.732	-0.969
H	0.547	1.045	-2.253
O	0.230	2.711	0.604
H	0.859	2.492	-0.091
H	-0.635	2.630	0.162
O	-2.165	1.940	-0.629
H	-1.788	1.232	-1.164
H	-2.562	1.471	0.119
O	-3.116	-1.495	-0.720
H	-3.966	-1.290	-1.110
H	-3.075	-1.004	0.125
O	-2.748	0.102	1.481
H	-1.814	0.209	1.804
H	-3.309	0.165	2.253
O	-0.260	0.562	2.255
H	0.024	1.340	1.732
H	0.350	-0.143	2.015

Rotational Transition Frequencies for Experimental Conformer

Table F.13. Assigned rotational transitions of Monohydrate 1

J'	K_a'	K_c'	J"	K_a"	K_c"	ν_{Exp} / MHz	$\Delta\nu^a$ / MHz	Type
Ortho								
1	0	1	0	0	0	1364.897	-0.010	A
1	0	1	0	0	0	1364.897	0.005	E
2	1	2	1	1	1	2535.396	0.003	A
2	1	2	1	1	1	2537.043	0.003	E
2	0	2	1	0	1	2712.170	0.005	A
2	0	2	1	0	1	2712.129	-0.005	E
2	1	1	1	1	0	2924.227	0.001	A
2	1	1	1	1	0	2922.547	0.002	E
3	1	3	2	1	2	3792.506	-0.012	A
3	1	3	2	1	2	3792.923	0.004	E
3	0	3	2	0	2	4025.096	0.024	A
3	0	3	2	0	2	4024.989	-0.030	E
3	2	2	2	2	1	4094.702	-0.001	A
3	2	2	2	2	1	4112.654	0.003	E
3	2	1	2	2	0	4164.342	0.000	A
3	2	1	2	2	0	4146.361	0.002	E
3	1	2	2	1	1	4374.758	0.000	A
3	1	2	2	1	1	4374.296	0.001	E
4	1	4	3	1	3	5038.306	-0.001	A
4	1	4	3	1	3	5038.448	0.002	E
4	0	4	3	0	3	5291.260	0.001	A
4	0	4	3	0	3	5291.177	0.001	E
4	2	3	3	2	2	5445.842	-0.002	A
4	2	3	3	2	2	5456.968	0.002	E
4	3	2	3	3	1	5492.046	0.000	A
4	3	2	3	3	1	5494.985	-0.070	E
4	3	1	3	3	0	5498.049	-0.001	A
4	3	1	3	3	0	5495.056	0.072	E
4	2	2	3	2	1	5614.143	-0.001	A
4	2	2	3	2	1	5602.986	0.001	E
5	0	5	4	1	4	5665.828	-0.001	A
5	0	5	4	1	4	5666.378	-0.001	E
4	1	3	3	1	2	5809.959	-0.001	A
4	1	3	3	1	2	5809.723	0.000	E
5	0	5	4	0	4	6508.351	-0.001	A
5	0	5	4	0	4	6508.240	0.001	E
5	2	4	4	2	3	6785.295	-0.003	A
5	2	4	4	2	3	6789.291	0.000	E
5	3	3	4	3	2	6875.252	-0.001	A
5	3	3	4	3	2	6884.505	0.001	E
5	3	2	4	3	1	6896.024	0.000	A
5	3	2	4	3	1	6886.710	0.000	E
5	2	3	4	2	2	7101.058	-0.002	A
5	2	3	4	2	2	7097.027	0.001	E
5	1	4	4	1	3	7222.354	-0.001	A
5	1	4	4	1	3	7222.166	-0.001	E
6	1	6	5	1	5	7490.484	0.000	A
6	1	6	5	1	5	7490.484	0.007	E
6	0	6	5	0	5	7686.660	-0.001	A
6	0	6	5	0	5	7686.529	0.003	E
7	0	7	6	0	6	8843.620	0.001	A
7	0	7	6	0	6	8843.482	0.008	E
8	0	8	7	0	7	9994.338	-0.005	A
8	0	8	7	0	7	9994.198	-0.002	E
Para								
2	1	2	1	1	1	2535.126	0.001	A
2	1	2	1	1	1	2536.780	0.003	E
2	0	2	1	0	1	2711.949	0.008	A
2	0	2	1	0	1	2711.902	-0.009	E
2	1	1	1	1	0	2923.972	-0.005	A
2	1	1	1	1	0	2922.288	-0.003	E
3	1	3	2	1	2	3792.137	0.001	A
3	1	3	2	1	2	3792.554	0.017	E

3	0	3	2	0	2	4024.851	0.034	A
3	0	3	2	0	2	4024.736	-0.028	E
3	2	2	2	2	1	4094.312	-0.001	A
3	2	2	2	2	1	4112.268	-0.001	E
3	2	1	2	2	0	4163.817	-0.001	A
3	2	1	2	2	0	4145.829	0.001	E
3	1	2	2	1	1	4374.401	-0.005	A
3	1	2	2	1	1	4373.939	-0.004	E
4	1	4	3	1	3	5037.831	0.001	A
4	1	4	3	1	3	5037.972	0.004	E
4	0	4	3	0	3	5291.043	0.001	A
4	0	4	3	0	3	5290.960	0.000	E
4	2	3	3	2	2	5445.348	-0.002	A
4	2	3	3	2	2	5456.511	-0.001	E
4	3	2	3	3	1	5491.467	0.003	A
4	3	2	3	3	1	5494.466	0.004	E
4	3	1	3	3	0	5497.445	0.002	A
4	3	1	3	3	0	5494.391	0.001	E
4	2	2	3	2	1	5613.344	-0.002	A
4	2	2	3	2	1	5602.150	0.000	E
5	0	5	4	1	4	5662.772	-0.011	A
5	0	5	4	1	4	5663.340	0.004	E
4	1	3	3	1	2	5809.534	-0.005	A
4	1	3	3	1	2	5809.298	-0.005	E
5	2	4	4	2	3	6784.721	-0.002	A
5	2	4	4	2	3	6788.736	0.000	E
5	3	3	4	3	2	6874.512	-0.003	A
5	3	3	4	3	2	6883.746	0.008	E
5	3	2	4	3	1	6895.211	0.009	A
5	3	2	4	3	1	6885.925	0.005	E
5	2	3	4	2	2	7099.985	0.003	A
5	2	3	4	2	2	7095.933	0.001	E
5	1	4	4	1	3	7221.917	-0.002	A
5	1	4	4	1	3	7221.730	-0.003	E
6	1	6	5	1	5	7489.864	-0.001	A
6	1	6	5	1	5	7489.864	0.005	E
6	0	6	5	0	5	7686.529	-0.014	A
6	0	6	5	0	5	7686.408	0.001	E
8	0	8	7	0	7	9994.040	-0.003	A
8	0	8	7	0	7	9993.899	-0.001	E

[a] Δν is the difference between measured and calculated frequencies.

Table F.14. Assigned rotational transitions of Monohydrate 2

J'	K_a'	K_c'	J"	K_a"	K_c"	ν_{Exp} / MHz	$\Delta\nu^a$ / MHz
2	1	2	1	1	1	2756.292	0.004
2	0	2	1	0	1	2990.782	-0.002
2	1	1	1	1	0	3340.675	0.002
3	1	3	2	1	2	4101.329	0.001
3	0	3	2	0	2	4355.387	-0.001
3	2	1	2	2	0	4790.025	-0.012
3	1	2	2	1	1	4970.614	0.001
4	1	4	3	1	3	5415.792	0.001
4	0	4	3	0	3	5618.915	-0.001
4	1	4	3	0	3	5876.477	-0.001
4	2	3	3	2	2	6051.629	0.007
4	2	2	3	2	1	6528.897	0.002
4	1	3	3	1	2	6541.985	0.001
5	0	5	4	0	4	6829.916	-0.003

[a] Δν is the difference between measured and calculated frequencies.

Table F.15. Assigned rotational transitions of Dihydrate

J'	K_a'	K_c'	J"	K_a"	K_c"	ν_{Exp} / MHz	$\Delta\nu^a$ / MHz	Type
Ortho								
2	1	2	1	0	1	3200.511	-0.004	A
5	3	3	5	2	3	3327.329	-0.001	A
4	3	2	4	2	2	3472.376	0.008	A
4	3	1	4	2	2	3478.250	0.009	A
2	1	1	1	0	1	3523.733	-0.007	A
3	3	1	3	2	1	3553.305	0.002	A
3	3	0	3	2	1	3554.144	-0.003	A
3	2	2	2	2	1	3961.553	-0.001	A
3	2	1	2	2	0	4008.683	-0.002	A
3	1	2	2	1	1	4115.139	-0.002	A
3	1	3	2	0	2	4364.262	0.001	A
2	2	1	1	1	0	4750.410	0.001	A
2	2	0	1	1	0	4762.432	0.000	A
2	2	1	1	1	1	4858.149	-0.001	A
2	2	0	1	1	1	4870.172	-0.001	A
4	1	4	3	1	3	5044.686	-0.009	A
4	0	4	3	0	3	5169.703	0.004	A
4	2	3	3	2	2	5272.572	-0.010	A
3	2	2	2	1	1	5963.174	-0.002	A
3	2	1	2	1	1	6022.328	-0.003	A
5	1	5	4	1	4	6288.287	-0.007	A
6	1	5	5	2	3	6333.496	0.001	A
5	0	5	4	0	4	6396.717	-0.007	A
5	2	4	4	2	3	6575.596	0.010	A
5	1	5	4	0	4	6613.180	-0.008	A
2	1	2	1	0	1	3199.963	0.002	E
5	3	3	5	2	3	3300.315	-0.014	E
4	3	2	4	2	2	3436.663	-0.001	E
2	1	1	1	0	1	3524.004	-0.001	E
4	1	3	3	2	1	3556.095	0.004	E
3	0	3	2	0	2	3914.253	0.005	E
3	2	2	2	2	1	3971.598	0.003	E
3	2	1	2	2	0	3998.629	0.012	E
3	1	2	2	1	1	4114.912	0.002	E
3	1	3	2	0	2	4363.996	0.004	E
2	2	1	1	1	0	4730.721	0.005	E
2	2	1	1	1	1	4840.941	0.003	E
5	1	4	4	2	2	4985.960	-0.013	E
4	1	4	3	1	3	5044.883	-0.002	E
4	0	4	3	0	3	5169.460	0.005	E
4	2	3	3	2	2	5277.515	-0.007	E
3	2	2	2	1	1	5954.365	0.005	E
3	2	1	2	1	1	6029.328	-0.016	E
5	1	5	4	1	4	6288.658	0.004	E
6	1	5	5	2	3	6332.489	-0.004	E
5	0	5	4	0	4	6396.230	0.012	E
5	2	4	4	2	3	6577.230	0.016	E
5	1	5	4	0	4	6613.834	0.006	E
Para								
2	1	2	1	1	1	2533.383	0.003	A
2	0	2	1	0	1	2629.068	-0.006	A
2	1	2	1	0	1	3200.679	-0.004	A
4	3	2	4	2	2	3472.819	0.001	A
4	3	1	4	2	2	3478.685	-0.001	A
2	1	1	1	0	1	3523.848	-0.001	A
3	0	3	2	0	2	3914.473	0.000	A
3	1	2	2	1	1	4115.210	0.004	A
3	1	3	2	0	2	4364.487	0.002	A
4	0	4	3	1	3	4719.857	0.000	A
2	2	1	1	1	0	4750.718	0.002	A
2	2	0	1	1	0	4762.734	0.000	A
2	2	1	1	1	1	4858.438	0.000	A
2	2	0	1	1	1	4870.457	0.001	A
4	0	4	3	0	3	5169.869	0.000	A

4	2	3	3	2	2	5272.713	0.003	A
4	3	2	3	3	1	5303.894	-0.002	A
4	3	1	3	3	0	5308.922	0.002	A
4	1	3	3	1	2	5470.747	-0.002	A
3	2	2	2	1	1	5963.536	0.001	A
3	2	1	2	1	1	6022.661	-0.002	A
5	0	5	4	1	4	6071.955	0.000	A
3	2	2	2	1	2	6286.700	-0.001	A
5	1	5	4	1	4	6288.517	0.000	A
5	0	5	4	0	4	6396.962	0.000	A

[a] Δν is the difference between measured and calculated frequencies.

Table F.16. Assigned rotational transitions of Trihydrate

J'	K_a'	K_c'	J"	K_a"	K_c"	ν_{Exp} / MHz	$\Delta\nu^a$ / MHz	Type
2	1	2	1	0	1	2498.675	0.022	A
3	1	3	2	1	2	2932.618	0.004	A
3	2	2	2	2	1	3037.340	0.000	A
3	2	1	2	2	0	3060.728	0.004	A
3	1	2	2	1	1	3134.642	0.000	A
3	1	3	2	0	2	3412.296	0.009	A
2	2	1	1	1	0	3715.951	-0.014	A
2	2	0	1	1	1	3789.322	-0.015	A
4	1	4	3	1	3	3903.956	0.005	A
4	0	4	3	0	3	3993.140	0.005	A
4	2	3	3	2	2	4045.167	0.008	A
4	3	2	3	3	1	4060.690	-0.002	A
4	3	1	3	3	0	4062.632	-0.008	A
4	2	2	3	2	1	4101.782	-0.005	A
4	1	3	3	1	2	4171.808	0.001	A
4	1	4	3	0	3	4302.289	0.010	A
5	0	5	4	1	4	4646.330	0.013	A
3	2	2	2	1	1	4660.945	-0.009	A
5	1	5	4	1	4	4870.865	0.005	A
3	2	1	2	1	2	4892.618	0.006	A
5	0	5	4	0	4	4955.466	0.005	A
5	2	4	4	2	3	5049.050	0.004	A
5	3	3	4	3	2	5079.328	-0.004	A
5	2	3	4	2	2	5155.658	-0.007	A
5	1	5	4	0	4	5180.015	0.012	A
5	1	4	4	1	3	5201.371	0.005	A
4	2	3	3	1	2	5571.462	-0.009	A
6	0	6	5	1	5	5679.571	0.002	A
6	1	6	5	1	5	5833.207	0.005	A
6	0	6	5	0	5	5904.120	0.008	A
3	3	1	2	2	0	5909.620	0.012	A
3	3	0	2	2	1	5915.870	0.015	A
6	2	5	5	2	4	6048.110	0.009	A
6	1	6	5	0	5	6057.755	0.010	A
4	2	2	3	1	3	6061.793	0.009	A
6	3	4	5	3	3	6098.797	0.002	A
6	3	3	5	3	2	6116.436	0.015	A
6	2	4	5	2	3	6218.061	-0.003	A
6	1	5	5	1	4	6220.270	0.005	A
5	2	4	4	1	3	6448.715	0.006	A
7	1	7	6	1	6	6791.281	0.022	A
7	0	7	6	0	6	6844.872	0.006	A
2	1	2	1	0	1	2497.850	0.001	E
3	1	3	2	1	2	2933.007	-0.004	E
3	2	2	2	2	1	3045.192	-0.004	E
3	2	1	2	2	0	3052.838	-0.001	E
3	1	2	2	1	1	3134.263	-0.001	E
3	1	3	2	0	2	3411.932	-0.003	E
2	2	1	1	1	0	3692.164	-0.004	E
2	2	0	1	1	1	3812.334	-0.020	E
4	1	4	3	1	3	3904.208	-0.002	E
4	0	4	3	0	3	3992.911	-0.002	E
4	2	3	3	2	2	4052.474	-0.003	E
4	2	2	3	2	1	4094.438	0.000	E

4	1	3	3	1	2	4171.626	0.001	E
4	1	4	3	0	3	4302.289	-0.010	E
5	0	5	4	1	4	4645.640	0.003	E
5	1	5	4	1	4	4871.222	-0.005	E
3	2	1	2	1	2	4906.372	0.013	E
5	0	5	4	0	4	4955.016	-0.007	E
5	2	4	4	2	3	5052.361	-0.001	E
5	3	2	4	3	1	5082.801	-0.013	E
5	2	3	4	2	2	5152.312	-0.009	E
5	1	5	4	0	4	5180.604	-0.009	E
5	1	4	4	1	3	5201.232	-0.001	E
4	2	3	3	1	2	5564.597	-0.017	E
6	0	6	5	1	5	5677.647	-0.009	E
6	1	6	5	1	5	5833.923	-0.007	E
6	0	6	5	0	5	5903.235	-0.011	E
6	2	5	5	2	4	6049.450	0.004	E
6	1	6	5	0	5	6059.511	-0.009	E
4	2	2	3	1	3	6067.785	-0.002	E
6	3	4	5	3	3	6105.671	-0.011	E
6	1	5	5	1	4	6220.124	-0.003	E
5	2	4	4	1	3	6445.356	0.006	E
7	1	7	6	1	6	6792.757	-0.014	E
7	0	7	6	0	6	6843.153	-0.017	E

[a] Δν is the difference between measured and calculated frequencies.

Table F.17. Assigned rotational transitions of Tetrahydrate

J'	K_a'	K_c'	J"	K_a"	K_c"	ν_{Exp} / MHz	$\Delta\nu^a$ / MHz	
3	1	3	2	1	2	2736.935	0.003	A
2	2	1	1	1	0	2800.279	-0.007	A
3	1	2	2	1	1	2835.353	-0.006	A
2	2	0	1	1	1	2835.662	-0.005	A
3	1	3	2	0	2	3009.594	0.002	A
4	0	4	3	1	3	3460.659	-0.001	A
4	1	4	3	1	3	3646.555	-0.005	A
4	0	4	3	0	3	3692.538	0.000	A
3	2	1	2	1	1	3709.228	0.007	A
4	2	3	3	2	2	3714.998	0.003	A
4	2	2	3	2	1	3739.428	0.004	A
4	1	3	3	1	2	3777.232	0.006	A
3	2	1	2	1	2	3807.773	0.000	A
4	1	4	3	0	3	3878.434	-0.005	A
4	1	3	3	0	3	4206.088	0.004	A
3	3	1	2	2	0	4383.757	0.000	A
3	3	0	2	2	0	4383.887	0.008	A
3	3	1	2	2	1	4386.286	0.000	A
3	3	0	2	2	1	4386.409	0.000	A
5	0	5	4	1	4	4413.697	-0.008	A
5	1	5	4	1	4	4554.236	0.007	A
4	2	3	3	1	2	4576.316	0.007	A
5	2	4	4	2	3	4640.582	0.001	A
5	3	3	4	3	2	4653.668	-0.002	A
5	3	2	4	3	1	4656.205	0.002	A
5	2	3	4	2	2	4687.147	0.001	A
5	1	4	4	1	3	4715.926	-0.006	A
4	2	2	3	1	3	4810.264	-0.001	A
4	3	2	3	2	1	5307.681	0.000	A
4	3	1	3	2	1	5308.534	0.001	A
4	3	1	3	2	2	5321.080	-0.001	A
5	2	4	4	1	3	5439.666	0.001	A
6	1	6	5	1	5	5459.828	0.005	A
6	2	5	5	2	4	5564.091	-0.003	A
6	3	3	5	3	2	5592.806	-0.002	A
6	2	4	5	2	3	5639.578	0.002	A
6	1	5	5	1	4	5650.248	0.006	A
4	4	1	3	3	0	5953.124	0.000	A
4	4	0	3	3	1	5953.250	-0.001	A
5	3	3	4	2	2	6221.926	-0.001	A

5	3	2	4	2	3	6262.286	-0.004	A
3	1	3	2	1	2	2737.200	-0.003	E
3	1	2	2	1	1	2835.076	0.003	E
3	1	3	2	0	2	3009.275	0.003	E
4	0	4	3	1	3	3460.920	-0.002	E
4	2	2	3	2	1	3734.733	0.002	E
4	1	3	3	1	2	3777.097	0.004	E
4	1	4	3	0	3	3878.245	-0.007	E
4	1	3	3	0	3	4206.224	-0.003	E
5	0	5	4	1	4	4413.822	-0.002	E
6	1	5	5	1	4	5650.156	-0.003	E
4	2	3	3	2	2	3719.673	0.001	E
3	2	1	2	1	2	3817.951	-0.002	E
4	2	3	3	1	2	4570.709	-0.004	E

[a]Δν is the difference between measured and calculated frequencies.

Table F.18. Assigned rotational transitions of Pentahydrate

J'	K_a'	K_c'	J"	K_a"	K_c"	ν_{Exp} / MHz	$\Delta\nu^a$ / MHz	Type
4	1	4	3	0	3	3384.724	0.009	A
5	1	5	4	0	4	4139.360	-0.007	A
6	1	6	5	0	5	4900.887	-0.007	A
7	1	7	6	0	6	5671.765	-0.001	A
8	1	8	7	0	7	6450.403	0.013	A
4	0	4	3	1	3	3153.424	0.009	A
5	0	5	4	1	4	3992.216	-0.009	A
6	0	6	5	1	5	4814.882	0.017	A
7	0	7	6	1	6	5624.599	-0.003	A
4	1	3	3	1	2	3435.881	0.005	A
5	1	4	4	1	3	4277.751	-0.001	A
6	1	5	5	1	4	5105.696	0.000	A
7	1	6	6	1	5	5916.767	-0.004	A
4	1	4	3	1	3	3245.358	0.003	A
5	1	5	4	1	4	4047.423	-0.004	A
7	1	7	6	1	6	5640.935	-0.005	A
4	2	3	3	2	2	3349.158	0.005	A
4	2	2	3	2	1	3410.861	0.006	A
5	2	4	4	2	3	4177.908	0.003	A
5	2	3	4	2	2	4286.524	0.003	A
6	2	5	5	2	4	5001.278	0.004	A
6	2	4	5	2	3	5161.360	-0.001	A
5	3	3	4	3	2	4211.017	0.006	A
5	3	2	4	3	1	4223.380	-0.005	A
6	3	4	5	3	3	5054.887	0.004	A
6	3	3	5	3	2	5086.073	-0.016	A
7	3	5	6	3	4	5896.576	-0.008	A
3	2	2	2	1	1	3209.680	0.017	A
4	2	3	3	1	2	3974.756	0.005	A
5	2	4	4	1	3	4716.788	0.008	A
6	2	5	5	1	4	5440.306	0.003	A
3	3	1	2	2	0	3790.675	-0.005	A
4	3	2	3	2	1	4614.777	-0.003	A
5	3	3	4	2	2	5414.934	-0.002	A
6	3	4	5	2	3	6183.296	-0.002	A
3	3	0	2	2	1	3798.161	-0.003	A
4	3	1	3	2	2	4652.513	-0.003	A
5	3	2	4	2	3	5526.748	0.001	A
4	4	1	3	3	0	5143.916	-0.001	A
5	4	2	4	3	1	5982.054	0.005	A
4	4	0	3	3	1	5144.577	0.000	A
5	4	1	4	3	2	5986.710	-0.001	A
4	1	4	3	1	3	3245.358	-0.011	E
5	1	5	4	1	4	4047.423	0.000	E
7	1	7	6	1	6	5640.935	0.005	E
4	1	3	3	1	2	3435.753	-0.003	E
5	1	4	4	1	3	4277.621	-0.004	E
6	1	5	5	1	4	5105.578	-0.006	E
4	1	4	3	0	3	3384.673	-0.013	E
5	1	5	4	0	4	4139.360	0.003	E

6	1	6	5	0	5	4900.887	-0.003	E
7	1	7	6	0	6	5671.765	-0.001	E
8	1	8	7	0	7	6450.403	0.001	E
4	2	3	3	2	2	3350.940	-0.002	E
4	2	2	3	2	1	3409.021	0.002	E
5	2	4	4	2	3	4178.434	-0.003	E
5	2	3	4	2	2	4285.922	0.003	E
6	2	5	5	2	4	5001.436	-0.005	E
6	2	4	5	2	3	5161.074	-0.002	E
5	3	3	4	3	2	4215.342	0.010	E
5	3	2	4	3	1	4218.988	-0.002	E
6	3	4	5	3	3	5059.580	0.002	E
6	3	3	5	3	2	5081.317	0.011	E
7	3	5	6	3	4	5898.955	-0.004	E
4	2	3	3	1	2	3973.523	-0.003	E
5	2	4	4	1	3	4716.203	-0.005	E
6	2	5	5	1	4	5440.022	-0.002	E
4	3	2	3	2	1	4598.349	-0.002	E
5	3	3	4	2	2	5404.665	0.002	E
6	3	4	5	2	3	6178.324	0.000	E
3	3	0	2	2	1	3820.574	0.001	E
4	3	1	3	2	2	4668.597	-0.001	E
5	3	2	4	2	3	5536.648	0.003	E

Rotational Transition Frequencies for Isotopologues

Table F.19. Assigned rotational transitions of the ^{13}C isotopologues of Monohydrate 1

Atom	J'	K_a'	K_c'	J"	K_a"	K_c"	ν_{Exp}/ MHz	Δν/ MHz	Type
$^{13}C1$	3	1	3	2	1	2	3788.688	-0.009	A
	3	1	3	2	1	2	3789.095	-0.001	E
	3	0	3	2	0	2	4021.076	-0.009	E
	3	0	3	2	0	2	4021.140	0.003	A
	3	2	2	2	2	1	4090.945	-0.004	A
	3	2	2	2	2	1	4108.860	0.000	E
	3	1	2	2	1	1	4370.554	0.002	E
	3	1	2	2	1	1	4371.011	0.002	A
	4	1	4	3	1	3	5033.165	0.000	A
	4	1	4	3	1	3	5033.305	0.002	E
	4	0	4	3	0	3	5285.759	-0.001	E
	4	0	4	3	0	3	5285.836	-0.004	A
	4	2	3	3	2	2	5440.795	-0.004	A
	4	2	3	3	2	2	5451.828	-0.001	E
	4	2	2	3	2	1	5598.448	-0.001	E
	4	2	2	3	2	1	5609.513	0.002	A
	4	1	3	3	1	2	5804.663	0.001	E
	4	1	3	3	1	2	5804.897	0.003	A
	5	1	5	4	1	4	6264.574	0.001	A
	5	1	5	4	1	4	6264.625	0.009	E
	5	0	5	4	0	4	6501.294	0.005	E
	5	0	5	4	0	4	6501.398	-0.003	A
	5	2	4	4	2	3	6782.879	-0.001	E
$^{13}C2$	3	1	3	2	1	2	3776.328	-0.009	A
	3	1	3	2	1	2	3776.748	0.007	E
	3	0	3	2	0	2	4007.356	-0.007	E
	3	0	3	2	0	2	4007.412	-0.002	A
	3	2	1	2	2	0	4126.156	-0.003	E
	3	2	1	2	2	0	4143.973	-0.012	A
	3	1	2	2	1	1	4352.901	0.003	E
	3	1	2	2	1	1	4353.363	0.004	A
	4	1	4	3	1	3	5017.067	-0.002	A
	4	1	4	3	1	3	5017.209	0.000	E
	4	0	4	3	0	3	5268.983	-0.002	E
	4	0	4	3	0	3	5269.063	-0.001	A
	4	2	3	3	2	2	5420.769	0.001	A
	4	2	3	3	2	2	5431.960	-0.001	E

	4	2	2	3	2	1	5574.700	0.002	E
	4	2	2	3	2	1	5585.924	0.003	A
	4	1	3	3	1	2	5781.675	-0.001	E
	4	1	3	3	1	2	5781.911	0.003	A
	5	1	5	4	1	4	6244.980	0.005	A
	5	1	5	4	1	4	6245.024	0.004	E
	5	0	5	4	0	4	6482.122	0.003	E
	5	0	5	4	0	4	6482.228	-0.002	A
$^{13}C3$	3	1	3	2	1	2	3772.263	-0.003	A
	3	1	3	2	1	2	3772.660	0.006	E
	3	0	3	2	0	2	4004.185	-0.006	E
	3	0	3	2	0	2	4004.243	0.001	A
	3	2	2	2	2	1	4074.921	-0.003	A
	3	2	2	2	2	1	4127.727	0.002	E
	3	1	2	2	1	1	4354.659	0.002	E
	3	1	2	2	1	1	4355.109	0.004	A
	4	1	4	3	1	3	5011.043	-0.003	A
	4	1	4	3	1	3	5011.177	-0.003	E
	4	0	4	3	0	3	5262.416	-0.002	E
	4	0	4	3	0	3	5262.498	-0.001	A
	4	2	3	3	2	2	5419.256	0.001	A
	4	2	3	3	2	2	5430.036	0.001	E
	4	2	2	3	2	1	5579.130	-0.001	E
	4	2	2	3	2	1	5589.940	-0.001	A
	4	1	3	3	1	2	5783.132	-0.002	E
	4	1	3	3	1	2	5783.364	0.000	A
	5	1	5	4	1	4	6236.648	-0.001	A
	5	1	5	4	1	4	6236.695	0.005	E
	5	0	5	4	0	4	6471.279	0.003	E
	5	0	5	4	0	4	6471.387	0.000	A
$^{13}C4$	2	0	2	1	0	1	2704.871	-0.004	E
	2	0	2	1	0	1	2704.916	0.009	A
	3	1	3	2	1	2	3778.262	-0.003	A
	3	1	3	2	1	2	3778.642	-0.001	E
	3	0	3	2	0	2	4011.738	-0.002	E
	3	0	3	2	0	2	4011.795	0.001	A
	3	2	2	2	2	1	4103.324	-0.003	E
	3	1	2	2	1	1	4368.554	0.002	E
	3	1	2	2	1	1	4368.992	0.000	A
	4	1	4	3	1	3	5018.335	-0.003	A
	4	1	4	3	1	3	5018.470	0.003	E
	4	0	4	3	0	3	5269.704	-0.003	E
	4	0	4	3	0	3	5269.787	-0.003	A
	4	2	3	3	2	2	5432.557	0.000	A
	4	2	3	3	2	2	5442.986	0.003	E
	4	2	2	3	2	1	5599.366	0.001	E
	4	2	2	3	2	1	5609.827	0.000	A
	4	1	3	3	1	2	5800.609	-0.001	E
	4	1	3	3	1	2	5800.837	-0.002	A
	5	0	5	4	0	4	6477.255	0.006	E
	5	0	5	4	0	4	6477.360	-0.002	A
$^{13}C5$	3	1	3	2	1	2	3784.913	-0.001	A
	3	1	3	2	1	2	3785.302	-0.007	E
	3	0	3	2	0	2	4017.530	-0.001	E
	3	0	3	2	0	2	4017.580	-0.004	A
	3	1	2	2	1	1	4368.812	0.000	E
	3	1	2	2	1	1	4369.271	0.005	A
	4	1	4	3	1	3	5027.887	0.000	A
	4	1	4	3	1	3	5028.025	0.001	E
	4	0	4	3	0	3	5280.107	-0.001	E
	4	0	4	3	0	3	5280.189	-0.001	A
	4	2	3	3	2	2	5437.128	-0.001	A
	4	2	3	3	2	2	5448.055	0.002	E
	4	2	2	3	2	1	5597.057	0.001	E
	4	2	2	3	2	1	5608.013	0.001	A
	4	1	3	3	1	2	5801.990	-0.003	E
	4	1	3	3	1	2	5802.225	0.000	A
	5	1	5	4	1	4	6257.663	-0.001	A
	5	1	5	4	1	4	6257.711	0.005	E
	5	0	5	4	0	4	6493.219	0.007	E

	5	0	5	4	0	4	6493.321	-0.003	A
	5	2	4	4	2	3	6774.038	-0.002	A
	5	2	4	4	2	3	6777.928	-0.002	E
$^{13}C6$	3	1	3	2	1	2	3791.014	-0.007	A
	3	1	3	2	1	2	3791.416	-0.005	E
	3	0	3	2	0	2	4023.381	-0.004	E
	3	0	3	2	0	2	4023.437	-0.003	A
	3	2	2	2	2	1	4092.956	0.003	A
	3	2	2	2	2	1	4110.879	-0.005	E
	3	1	2	2	1	1	4372.330	0.001	E
	3	1	2	2	1	1	4372.795	0.003	A
	4	1	4	3	1	3	5036.332	-0.003	A
	4	1	4	3	1	3	5036.476	0.002	E
	4	0	4	3	0	3	5289.114	0.000	E
	4	0	4	3	0	3	5289.196	0.000	A
	4	2	3	3	2	2	5443.526	-0.006	A
	4	2	3	3	2	2	5454.657	0.003	E
	4	2	2	3	2	1	5600.402	-0.001	E
	4	2	2	3	2	1	5611.564	0.002	A
	4	1	3	3	1	2	5807.145	0.001	E
	4	1	3	3	1	2	5807.382	0.000	A
	5	1	5	4	1	4	6268.638	0.005	A
	5	1	5	4	1	4	6268.681	0.005	E
	5	0	5	4	0	4	6505.800	0.003	E
	5	0	5	4	0	4	6505.907	-0.002	A
$^{13}C7$	3	1	3	2	1	2	3742.980	-0.001	A
	3	1	3	2	1	2	3743.390	-0.005	E
	3	0	3	2	0	2	3971.013	-0.001	E
	3	0	3	2	0	2	3971.058	-0.005	A
	3	2	1	2	2	0	4084.851	0.001	E
	3	2	1	2	2	0	4102.443	-0.012	A
	3	1	2	2	1	1	4309.207	0.003	E
	3	1	2	2	1	1	4309.673	0.003	A
	4	1	4	3	1	3	4973.244	-0.002	A
	4	1	4	3	1	3	4973.394	0.002	E
	4	0	4	3	0	3	5223.126	-0.003	E
	4	0	4	3	0	3	5223.205	-0.001	A
	4	2	3	3	2	2	5380.828	0.003	E
	4	2	2	3	2	1	5516.975	0.000	E
	4	2	2	3	2	1	5528.463	0.003	A
	4	1	3	3	1	2	5724.342	0.000	E
	4	1	3	3	1	2	5724.578	0.004	A
	5	1	5	4	1	4	6191.103	0.004	A
	5	1	5	4	1	4	6191.153	0.006	E
	5	0	5	4	0	4	6428.078	0.000	A
	5	2	4	4	2	3	6695.162	-0.005	E
$^{18}O_{\alpha}$	2	1	2	1	1	1	2429.491	0.001	A
	2	0	2	1	0	1	2592.689	0.005	A
	2	1	1	1	1	0	2784.812	0.001	A
	3	1	3	2	1	2	3635.528	-0.002	A
	3	0	3	2	0	2	3853.480	0.003	A
	3	2	2	2	2	1	3910.714	0.001	A
	3	2	1	2	2	0	3967.957	-0.002	A
	3	1	2	2	1	1	4167.770	0.000	A
	4	1	4	3	1	3	4832.121	-0.002	A
	4	0	4	3	0	3	5075.043	0.001	A
	4	2	3	3	2	2	5203.005	-0.001	A
	4	3	2	3	3	1	5241.103	-0.001	A
	4	3	1	3	3	0	5245.521	0.000	A
	4	2	2	3	2	1	5342.219	0.000	A
	4	1	3	3	1	2	5538.340	0.000	A
	5	1	5	4	1	4	6017.669	-0.004	A
	5	0	5	4	0	4	6253.554	-0.001	A
	5	2	4	4	2	3	6485.700	-0.002	A
	5	3	3	4	3	2	6560.232	-0.002	A
	5	3	2	4	3	1	6575.549	-0.001	A
	5	2	3	4	2	2	6749.742	0.001	A
	5	1	4	4	1	3	6890.641	0.000	A
	6	1	6	5	1	5	7191.668	0.003	A
	6	0	6	5	0	5	7395.193	-0.001	A

	2	0	2	1	0	1	2592.650	-0.006	E
	3	1	3	2	1	2	3635.974	0.000	E
	3	0	3	2	0	2	3853.426	-0.004	E
	3	1	2	2	1	1	4167.273	0.001	E
	4	1	4	3	1	3	4832.281	0.000	E
	4	0	4	3	0	3	5074.969	-0.002	E
	4	1	3	3	1	2	5538.097	0.000	E
	5	1	5	4	1	4	6017.731	0.002	E
	5	0	5	4	0	4	6253.456	0.000	E
	5	1	4	4	1	3	6890.462	0.000	E
	6	0	6	5	0	5	7395.074	0.004	E
	2	1	2	1	1	1	2431.293	0.002	E
	3	2	2	2	2	1	3927.368	0.000	E
	3	2	1	2	2	0	3951.273	0.001	E
	4	2	3	3	2	2	5215.289	0.000	E
	4	3	2	3	3	1	5243.340	0.001	E
	4	3	1	3	3	0	5243.234	0.000	E
	4	2	2	3	2	1	5329.903	0.000	E
	5	2	4	4	2	3	6490.501	0.000	E
	5	3	3	4	3	2	6567.326	0.000	E
	5	3	2	4	3	1	6568.401	0.001	E
	5	2	3	4	2	2	6744.907	0.001	E
Para									
^{13}C1	3	1	3	2	1	2	3788.319	-0.003	A
	3	0	3	2	0	2	4020.824	-0.007	E
	3	0	3	2	0	2	4020.879	-0.005	A
	3	1	2	2	1	1	4370.202	0.003	E
	4	1	4	3	1	3	5032.690	-0.006	A
	4	1	4	3	1	3	5032.833	0.002	E
	4	0	4	3	0	3	5285.538	-0.006	E
	4	0	4	3	0	3	5285.622	-0.002	A
	4	1	3	3	1	2	5804.231	-0.003	E
	4	1	3	3	1	2	5804.470	0.005	A
	5	1	5	4	1	4	6264.023	-0.002	A
	5	1	5	4	1	4	6264.077	0.011	E
	5	0	5	4	0	4	6501.148	0.008	E
	5	0	5	4	0	4	6501.249	-0.002	A
^{13}C2	3	1	3	2	1	2	3775.960	-0.001	A
	3	1	3	2	1	2	3776.367	0.000	E
	3	0	3	2	0	2	4007.144	-0.015	A
	3	1	2	2	1	1	4352.538	-0.001	E
	3	1	2	2	1	1	4353.010	0.006	A
	4	1	4	3	1	3	5016.595	-0.002	A
	4	1	4	3	1	3	5016.736	-0.002	E
	4	0	4	3	0	3	5268.762	-0.003	E
	4	0	4	3	0	3	5268.841	-0.006	A
	4	1	3	3	1	2	5781.249	0.002	E
	4	1	3	3	1	2	5781.484	0.001	A
	5	1	5	4	1	4	6244.432	0.008	A
	5	1	5	4	1	4	6244.468	-0.001	E
	5	0	5	4	0	4	6481.970	0.005	E
	5	0	5	4	0	4	6482.079	0.003	A
^{13}C3	3	1	3	2	1	2	3771.881	-0.006	A
	3	0	3	2	0	2	4003.968	-0.019	A
	3	1	2	2	1	1	4354.307	0.003	E
	3	1	2	2	1	1	4354.750	0.001	A
	4	1	4	3	1	3	5010.558	-0.013	A
	4	0	4	3	0	3	5262.191	-0.009	E
	4	0	4	3	0	3	5262.282	0.003	A
	4	1	3	3	1	2	5782.709	-0.002	E
	4	1	3	3	1	2	5782.942	0.006	A
	5	1	5	4	1	4	6236.103	0.009	A
	5	1	5	4	1	4	6236.146	0.010	E
	5	0	5	4	0	4	6471.119	0.001	E
	5	0	5	4	0	4	6471.232	0.004	A
^{13}C4	3	1	3	2	1	2	3777.885	-0.006	A
	3	0	3	2	0	2	4011.486	-0.006	E
	3	0	3	2	0	2	4011.538	-0.005	A
	3	1	2	2	1	1	4368.199	-0.002	E
	3	1	2	2	1	1	4368.642	0.006	A

	4	1	4	3	1	3	5017.869	-0.001	A
	4	1	4	3	1	3	5017.997	-0.004	E
	4	0	4	3	0	3	5269.497	0.000	E
	4	0	4	3	0	3	5269.577	0.000	A
	4	1	3	3	1	2	5800.194	0.001	E
	5	1	5	4	1	4	6244.269	0.003	A
	5	1	5	4	1	4	6244.313	0.008	E
	5	0	5	4	0	4	6477.109	0.009	E
	5	0	5	4	0	4	6477.203	-0.008	A
$^{13}C5$	3	1	2	2	1	1	4368.454	0.000	E
	3	1	2	2	1	1	4368.909	-0.002	A
	4	1	4	3	1	3	5027.409	-0.005	A
	4	1	4	3	1	3	5027.550	-0.005	E
	4	0	4	3	0	3	5279.894	0.002	E
	4	0	4	3	0	3	5279.968	-0.004	A
	4	2	3	3	2	2	5436.636	0.002	A
	4	1	3	3	1	2	5801.567	-0.003	E
	4	1	3	3	1	2	5801.805	0.005	A
	5	1	5	4	1	4	6257.111	-0.001	A
	5	1	5	4	1	4	6257.165	0.009	E
	5	0	5	4	0	4	6493.064	0.007	E
	5	0	5	4	0	4	6493.163	-0.006	A
$^{13}C6$	3	1	2	2	1	1	4371.979	-0.005	E
	4	1	4	3	1	3	5035.873	0.012	A
	4	1	4	3	1	3	5035.987	-0.004	E
	4	0	4	3	0	3	5288.893	0.002	E
	4	0	4	3	0	3	5288.973	-0.005	A
	4	1	3	3	1	2	5806.724	0.004	E
	5	1	5	4	1	4	6268.108	-0.006	E
	5	0	5	4	0	4	6505.646	0.007	E
	5	0	5	4	0	4	6505.747	-0.006	A
$^{13}C7$	3	0	3	2	0	2	3970.754	-0.003	E
	3	0	3	2	0	2	3970.805	-0.004	A
	3	1	2	2	1	1	4308.858	0.000	E
	3	1	2	2	1	1	4309.330	0.002	A
	4	1	4	3	1	3	4972.777	-0.005	A
	4	1	4	3	1	3	4972.922	-0.004	E
	4	0	4	3	0	3	5222.901	0.001	E
	4	0	4	3	0	3	5222.978	0.000	A
	4	1	3	3	1	2	5723.924	-0.001	E
	4	1	3	3	1	2	5724.162	0.001	A
	5	1	5	4	1	4	6190.553	0.000	A
	5	1	5	4	1	4	6190.608	0.009	E
$^{18}O_{\alpha}$	2	0	2	1	0	1	2592.447	0.006	A
	2	1	1	1	1	0	2784.546	0.004	A
	3	1	3	2	1	2	3635.133	-0.001	A
	3	0	3	2	0	2	3853.186	0.005	A
	3	2	2	2	2	1	3910.306	0.000	A
	3	2	1	2	2	0	3967.438	-0.002	A
	3	1	2	2	1	1	4167.386	0.000	A
	4	1	4	3	1	3	4831.621	-0.002	A
	4	0	4	3	0	3	5074.758	0.002	A
	4	2	3	3	2	2	5202.484	-0.001	A
	4	3	2	3	3	1	5240.510	-0.002	A
	4	3	1	3	3	0	5244.909	-0.002	A
	4	2	2	3	2	1	5341.444	0.001	A
	4	1	3	3	1	2	5537.871	0.001	A
	5	1	5	4	1	4	6017.080	-0.005	A
	5	0	5	4	0	4	6253.314	0.000	A
	5	2	4	4	2	3	6485.084	-0.003	A
	5	3	3	4	3	2	6559.482	-0.003	A
	5	3	2	4	3	1	6574.741	0.001	A
	5	2	3	4	2	2	6748.690	0.001	A
	5	1	4	4	1	3	6890.128	0.000	A
	6	1	6	5	1	5	7191.002	0.002	A
	6	0	6	5	0	5	7394.977	-0.004	A
	2	0	2	1	0	1	2592.408	-0.005	E
	3	0	3	2	0	2	3853.133	-0.002	E
	3	1	2	2	1	1	4166.889	0.000	E
	4	1	4	3	1	3	4831.783	0.001	E

4	0	4	3	0	3	5074.683	-0.001	E
4	1	3	3	1	2	5537.626	-0.001	E
5	1	5	4	1	4	6017.142	0.002	E
5	0	5	4	0	4	6253.215	0.001	E
5	1	4	4	1	3	6889.949	0.000	E
6	0	6	5	0	5	7394.862	0.004	E
2	1	1	1	1	0	2782.709	0.001	E
3	1	3	2	1	2	3635.585	0.006	E
3	2	2	2	2	1	3926.961	0.001	E
3	2	1	2	2	0	3950.755	0.000	E
4	2	3	3	2	2	5214.804	0.001	E
4	3	2	3	3	1	5242.739	0.001	E
4	3	1	3	3	0	5242.632	-0.001	E
4	2	2	3	2	1	5329.092	0.000	E
5	2	4	4	2	3	6489.906	-0.002	E
5	3	3	4	3	2	6566.557	0.003	E
5	3	2	4	3	1	6567.612	-0.003	E
5	2	3	4	2	2	6743.835	0.002	E

[a] Δν is the difference between measured and calculated frequencies.

Table F.20. Assigned rotational transitions of the ^{18}O isotopologue of Monohydrate 2

J'	K_a'	K_c'	J"	K_a"	K_c"	ν_{Exp}/ MHz	Δν/ MHz
2	0	2	1	0	1	2865.413	0.004
3	1	3	2	1	2	3940.022	0.001
3	0	3	2	0	2	4189.163	-0.001
3	2	1	2	2	0	4548.498	-0.006
4	1	4	3	1	3	5209.188	-0.001
4	0	4	3	0	3	5421.559	-0.002
4	2	3	3	2	2	5788.144	0.006
4	2	2	3	2	1	6191.197	0.001
4	1	3	3	1	2	6248.908	-0.001
5	0	5	4	0	4	6597.715	-0.001

Table F.21. Assigned rotational transitions of the ^{18}O isotopologues of dihydrate conformer

Species	J'	K_a'	K_c'	J"	K_a"	K_c"	ν_{Exp}/ MHz	[a]Δν/ MHz	Type
$^{18}O_\alpha{}^{16}O_\beta$	3	0	3	2	0	2	3798.915	-0.004	A
	4	0	4	3	0	3	5021.625	-0.002	A
	5	0	5	4	0	4	6217.877	0.015	A
	3	1	3	2	1	2	3681.333	-0.008	A
	4	1	4	3	1	3	4897.670	-0.004	A
	5	1	5	4	1	4	6106.550	0.001	A
	3	1	2	2	1	1	3985.221	-0.010	A
	4	1	3	3	1	2	5299.767	-0.001	A
	3	2	2	2	2	1	3839.853	-0.010	A
	3	2	1	2	2	0	3880.730	-0.015	A
	4	2	3	3	2	2	5111.597	-0.005	A
	4	2	2	3	2	1	5209.560	-0.007	A
	5	2	4	4	2	3	6376.386	0.005	A
	5	2	3	4	2	2	6557.600	0.002	A
	4	3	2	3	3	1	5138.741	-0.004	A
	4	3	1	3	3	0	5142.723	-0.012	A
	5	3	3	4	3	2	6428.827	-0.005	A
	5	3	2	4	3	1	6442.584	-0.010	A
	3	0	3	2	1	2	3199.925	-0.014	A
	4	0	4	3	1	3	4540.215	-0.011	A
	5	0	5	4	1	4	5860.416	0.002	A
	2	1	2	1	0	1	3148.490	0.000	A
	3	1	3	2	0	2	4280.319	-0.003	A
	4	1	4	3	0	3	5379.074	-0.002	A
	5	1	5	4	0	4	6463.998	0.002	A
	2	2	1	1	1	0	4731.697	-0.001	A
	3	2	2	2	1	1	5910.127	0.002	A
	2	2	0	1	1	1	4843.614	0.000	A
	3	2	1	2	1	2	6265.968	0.006	A

	2	1	1	1	0	1	3453.042	-0.006	A
	3	1	2	2	0	2	4888.768	-0.002	A
	2	2	0	1	1	0	4742.097	0.002	A
	2	2	1	1	1	1	4833.223	0.006	A
	3	2	1	2	1	1	5961.402	-0.002	A
	3	2	2	2	1	2	6214.693	0.011	A
	3	0	3	2	0	2	3798.817	-0.009	E
	3	1	3	2	1	2	3681.580	0.004	E
	4	1	4	3	1	3	4897.848	0.017	E
	3	1	2	2	1	1	3984.989	-0.001	E
	4	1	3	3	1	2	5299.651	0.009	E
	3	2	2	2	2	1	3849.570	-0.006	E
	3	2	1	2	2	0	3870.998	-0.004	E
	4	2	3	3	2	2	5117.023	0.006	E
	4	2	2	3	2	1	5204.133	0.011	E
	5	2	4	4	2	3	6378.266	0.023	E
	5	2	3	4	2	2	6555.726	0.020	E
	4	3	2	3	3	1	5140.710	-0.013	E
	4	3	1	3	3	0	5140.710	0.002	E
	2	1	2	1	0	1	3147.902	-0.005	E
	3	1	3	2	0	2	4280.028	0.010	E
	2	2	1	1	1	0	4711.358	-0.005	E
	3	2	2	2	1	1	5900.380	-0.004	E
	2	1	1	1	0	1	3453.333	-0.003	E
	3	1	2	2	0	2	4888.875	0.015	E
	2	2	0	1	1	0	4758.839	-0.009	E
	2	2	1	1	1	1	4815.489	-0.010	E
	3	2	1	2	1	1	5969.284	-0.009	E
	3	2	2	2	1	2	6205.815	0.003	E
$^{16}O_{\alpha}{}^{18}O_{\beta}$	3	0	3	2	0	2	3858.062	0.003	A
	4	0	4	3	0	3	5096.883	-0.002	A
	5	0	5	4	0	4	6308.544	-0.012	A
	3	1	3	2	1	2	3741.158	0.004	A
	4	1	4	3	1	3	4976.460	0.000	A
	5	1	5	4	1	4	6203.789	-0.011	A
	3	1	2	2	1	1	4050.424	-0.005	A
	4	1	3	3	1	2	5385.132	-0.007	A
	5	1	4	4	1	3	6704.226	-0.010	A
	3	2	2	2	2	1	3903.040	0.001	A
	3	2	1	2	2	0	3947.955	-0.004	A
	4	2	3	3	2	2	5195.000	-0.008	A
	4	2	2	3	2	1	5301.930	-0.012	A
	5	2	4	4	2	3	6479.329	0.001	A
	4	3	2	3	3	1	5224.755	0.001	A
	4	3	1	3	3	0	5229.516	0.004	A
	2	1	2	1	0	1	3143.501	0.012	A
	3	1	3	2	0	2	4294.079	0.004	A
	4	1	4	3	0	3	5412.482	0.006	A
	5	1	5	4	0	4	6519.386	-0.005	A
	3	0	3	2	1	2	3305.132	-0.007	A
	4	0	4	3	1	3	4660.860	-0.009	A
	2	2	1	1	1	0	4639.812	0.001	A
	3	2	2	2	1	1	5837.465	0.006	A
	2	2	0	1	1	1	4754.622	-0.003	A
	2	1	1	1	0	1	3453.555	-0.006	A
	3	1	2	2	0	2	4913.417	-0.005	A
	2	2	0	1	1	0	4651.267	0.000	A
	2	2	1	1	1	1	4743.168	-0.001	A
	3	2	1	2	1	1	5893.837	0.002	A
	3	2	2	2	1	2	6147.541	0.010	A
	4	3	2	4	2	3	3518.890	-0.005	A
	5	3	3	5	2	4	3576.136	0.000	A
	3	0	3	2	0	2	3857.948	-0.008	E
	3	1	3	2	1	2	3741.401	0.023	E
	3	1	2	2	1	1	4050.206	0.007	E

	4	1	3	3	1	2	5385.020	0.008	E
	5	1	4	4	1	3	6704.124	0.003	E
	3	2	2	2	2	1	3912.751	0.006	E
	3	2	1	2	2	0	3938.231	0.009	E
	4	2	3	3	2	2	5199.865	0.010	E
	4	2	2	3	2	1	5297.069	0.007	E
	5	2	4	4	2	3	6480.947	0.018	E
	4	3	2	3	3	1	5227.098	0.007	E
	4	3	1	3	3	0	5227.098	-0.025	E
	2	1	2	1	0	1	3142.959	0.009	E
	2	2	1	1	1	0	4620.633	-0.002	E
	3	2	2	2	1	1	5828.810	0.001	E
	2	2	0	1	1	1	4772.880	-0.007	E
	2	1	1	1	0	1	3453.823	-0.004	E
	3	1	2	2	0	2	4913.526	0.019	E
	2	2	0	1	1	0	4667.095	-0.003	E
	2	2	1	1	1	1	4726.411	-0.013	E
	3	2	1	2	1	1	5900.745	-0.004	E
	3	2	2	2	1	2	6139.692	0.007	E
$^{18}O_{\alpha}{}^{18}O_{\beta}$	2	0	2	1	0	1	2514.381	-0.006	A
	3	0	3	2	0	2	3747.281	-0.005	A
	4	0	4	3	0	3	4954.557	-0.006	A
	5	0	5	4	0	4	6136.382	-0.007	A
	2	1	2	1	1	1	2426.716	-0.003	A
	3	1	3	2	1	2	3634.075	-0.006	A
	4	1	4	3	1	3	4835.093	-0.006	A
	5	1	5	4	1	4	6028.952	-0.007	A
	2	1	1	1	1	0	2621.997	-0.007	A
	3	1	2	2	1	1	3926.361	-0.010	A
	4	1	3	3	1	2	5221.860	-0.008	A
	5	1	4	4	1	3	6504.048	0.002	A
	3	2	1	2	2	0	3825.705	-0.009	A
	4	2	3	3	2	2	5040.827	-0.003	A
	4	2	2	3	2	1	5134.742	-0.010	A
	5	2	4	4	2	3	6288.458	0.002	A
	5	2	3	4	2	2	6462.266	-0.006	A
	3	2	2	2	2	1	3786.537	0.006	A
	4	3	2	3	3	1	5066.850	-0.002	A
	5	3	3	4	3	2	6338.747	0.000	A
	5	3	2	4	3	1	6351.887	-0.002	A
	2	1	2	1	0	1	3093.059	-0.003	A
	3	1	3	2	0	2	4212.752	-0.003	A
	4	1	4	3	0	3	5300.565	-0.004	A
	5	1	5	4	0	4	6374.959	-0.006	A
	3	0	3	2	1	2	3168.601	-0.010	A
	4	0	4	3	1	3	4489.082	-0.011	A
	5	0	5	4	1	4	5790.375	-0.008	A
	2	2	1	1	1	0	4621.018	0.000	A
	3	2	2	2	1	1	5785.544	0.000	A
	4	2	3	3	1	2	6900.008	0.005	A
	2	2	0	1	1	1	4728.620	-0.005	A
	3	2	1	2	1	2	6127.623	0.004	A
	2	1	1	1	0	1	3385.982	-0.008	A
	3	1	2	2	0	2	4797.968	-0.007	A
	4	1	3	3	0	3	6272.557	0.001	A
	2	2	1	1	1	1	4718.657	-0.004	A
	3	2	2	2	1	2	6078.472	0.000	A
	2	2	0	1	1	0	4630.981	-0.001	A
	3	2	1	2	1	1	5834.689	-0.002	A
	3	3	1	3	2	1	3532.513	0.006	A
	4	3	2	4	2	2	3464.622	0.014	A
	5	3	3	5	2	3	3341.096	0.013	A
	4	3	1	4	2	3	3612.129	0.002	A
	4	3	1	4	2	2	3469.069	0.011	A
	3	3	0	3	2	1	3533.154	0.007	A

3	3	1	3	2	2	3581.661	0.006	A
4	3	2	4	2	3	3607.676	-0.001	A
5	3	3	5	2	4	3657.965	-0.004	A
6	4	2	6	3	3	4928.596	0.008	A
5	4	1	5	3	2	4966.476	0.007	A
6	4	3	6	3	4	4978.752	-0.002	A
5	4	2	5	3	3	4983.755	0.000	A
6	4	2	6	3	4	4980.270	0.003	A
8	4	4	8	3	5	4746.604	0.019	A
5	3	2	5	2	3	3358.685	0.011	A
6	3	3	6	2	4	3205.106	0.002	A
2	0	2	1	0	1	2514.336	-0.006	E
3	0	3	2	0	2	3747.180	-0.011	E
4	0	4	3	0	3	4954.349	-0.024	E
3	1	3	2	1	2	3634.320	0.008	E
4	1	4	3	1	3	4835.282	0.023	E
3	1	2	2	1	1	3926.135	0.002	E
4	1	3	3	1	2	5221.749	0.006	E
5	1	4	4	1	3	6503.953	0.013	E
3	2	1	2	2	0	3816.284	-0.005	E
4	2	3	3	2	2	5046.132	0.009	E
4	2	2	3	2	1	5129.428	0.003	E
5	2	4	4	2	3	6290.299	0.016	E
5	2	3	4	2	2	6460.424	0.012	E
3	2	2	2	2	1	3795.927	0.002	E
4	3	2	3	3	1	5068.742	0.001	E
4	3	1	3	3	0	5068.742	0.019	E
5	3	3	4	3	2	6344.400	0.012	E
5	3	2	4	3	1	6346.207	0.015	E
2	1	2	1	0	1	3092.497	-0.002	E
3	1	3	2	0	2	4212.484	0.015	E
3	0	3	2	1	2	3169.016	-0.019	E
2	2	1	1	1	0	4601.228	-0.012	E
3	2	2	2	1	1	5776.014	-0.008	E
4	2	3	3	1	2	6896.020	0.009	E
2	2	0	1	1	1	4747.484	-0.008	E
2	1	1	1	0	1	3386.275	-0.003	E
3	1	2	2	0	2	4798.077	0.008	E
4	1	3	3	0	3	6272.649	0.028	E
2	2	1	1	1	1	4701.431	-0.013	E
3	2	2	2	1	2	6069.795	-0.007	E
2	2	0	1	1	0	4647.282	-0.006	E
3	2	1	2	1	1	5842.427	-0.008	E
4	3	1	4	2	2	3496.482	-0.016	E
3	3	0	3	2	1	3557.176	-0.024	E
3	3	1	3	2	2	3556.109	-0.012	E
4	3	2	4	2	3	3578.716	-0.023	E
5	3	2	5	2	3	3382.265	-0.013	E
6	3	3	6	2	4	3219.802	-0.005	E
4	0	4	3	1	3	4489.109	0.014	E

[a] Δν is the difference between measured and calculated frequencies.

Table F.22. Assigned rotational transitions of the ^{18}O isotopologues of trihydrate conformer

Species	J'	K_a'	K_c'	J"	K_a"	K_c"	ν_{Exp}/ MHz	[a]Δν/ MHz	Type
$^{18}O_\alpha{}^{16}O_\beta{}^{16}O_\gamma$	3	0	3	2	0	2	2944.880	-0.005	E
	3	0	3	2	0	2	2944.993	0.006	A
	3	1	2	2	1	1	3060.777	-0.003	E
	3	1	2	2	1	1	3061.156	-0.011	A
	4	1	4	3	1	3	3814.781	-0.002	A
	4	1	4	3	1	3	3815.024	-0.009	E
	4	0	4	3	0	3	3902.603	-0.008	E
	4	0	4	3	0	3	3902.807	-0.003	A

	4	2	2	3	2	1	3996.751	-0.004	E
	4	2	2	3	2	1	4004.194	-0.002	A
	4	1	3	3	1	2	4074.231	0.002	E
	4	1	3	3	1	2	4074.410	0.000	A
	5	0	5	4	1	4	4523.782	0.009	E
	5	0	5	4	1	4	4524.348	0.010	A
	5	1	5	4	1	4	4759.963	-0.002	A
	5	1	5	4	1	4	4760.283	-0.012	E
	5	0	5	4	0	4	4844.199	0.025	E
	5	0	5	4	0	4	4844.558	-0.005	A
	5	2	4	4	2	3	4932.322	0.006	A
	5	2	4	4	2	3	4935.815	-0.006	E
	5	2	3	4	2	2	5028.670	-0.002	E
	5	2	3	4	2	2	5032.199	-0.003	A
	5	1	4	4	1	3	5080.515	0.002	E
	5	1	4	4	1	3	5080.642	0.000	A
	6	0	6	5	1	5	5535.579	-0.011	E
	6	0	6	5	1	5	5537.256	0.014	A
	6	0	6	5	0	5	5772.869	0.000	A
	3	3	1	2	2	0	5866.112	0.006	A
	3	3	0	2	2	1	5871.898	-0.004	A
$^{16}O_{\alpha}{}^{18}O_{\beta}{}^{16}O_{\gamma}$	3	0	3	2	0	2	2946.074	-0.004	E
	3	0	3	2	0	2	2946.196	0.009	A
	3	1	2	2	1	1	3062.766	0.000	A
	4	1	4	3	1	3	3816.335	0.004	A
	4	1	4	3	1	3	3816.578	-0.006	E
	4	0	4	3	0	3	3903.957	-0.003	E
	4	0	4	3	0	3	3904.171	-0.002	A
	4	2	3	3	2	2	3953.244	0.007	A
	4	2	3	3	2	2	3960.506	-0.009	E
	4	2	2	3	2	1	3999.314	-0.007	E
	4	2	2	3	2	1	4006.628	-0.001	A
	4	1	3	3	1	2	4076.276	0.002	E
	4	1	3	3	1	2	4076.457	0.003	A
	5	0	5	4	1	4	4529.271	0.007	E
	5	0	5	4	1	4	4529.908	0.008	A
	5	1	5	4	1	4	4761.823	0.004	A
	5	1	5	4	1	4	4762.158	-0.009	E
	5	0	5	4	0	4	4845.573	-0.008	E
	5	0	5	4	0	4	4846.002	0.007	A
	5	2	4	4	2	3	4934.585	0.005	A
	5	2	4	4	2	3	4937.966	-0.002	E
	5	2	3	4	2	2	5032.010	-0.005	E
	5	2	3	4	2	2	5035.428	-0.004	A
	5	1	4	4	1	3	5083.038	0.000	A
	6	1	6	5	1	5	5702.948	0.006	A
	6	0	6	5	0	5	5773.566	-0.008	E
	6	0	6	5	0	5	5774.388	0.003	A
	3	3	1	2	2	0	5846.606	-0.003	A
	3	3	0	2	2	1	5852.479	0.005	A
$^{16}O_{\alpha}{}^{16}O_{\beta}{}^{18}O_{\gamma}$	3	1	3	2	1	2	2910.830	-0.001	A
	3	1	3	2	1	2	2911.199	-0.007	E
	3	0	3	2	0	2	2992.985	0.001	E
	3	0	3	2	0	2	2993.108	0.004	A
	3	1	2	2	1	1	3118.341	-0.008	E
	3	1	2	2	1	1	3118.713	0.013	A
	4	1	4	3	1	3	3874.321	0.003	A
	4	1	4	3	1	3	3874.578	-0.008	E
	4	0	4	3	0	3	3962.760	-0.005	E
	4	0	4	3	0	3	3963.012	0.004	A
	4	2	3	3	2	2	4020.046	0.000	A
	4	2	3	3	2	2	4026.923	-0.006	E
	4	2	2	3	2	1	4075.248	-0.007	E
	4	2	2	3	2	1	4082.161	-0.004	A
	4	1	3	3	1	2	4149.515	0.003	E

	4	1	3	3	1	2	4149.691	0.007	A
	4	1	4	3	0	3	4245.871	0.001	A
	4	1	4	3	0	3	4245.946	-0.005	E
	5	0	5	4	1	4	4631.512	0.006	E
	5	0	5	4	1	4	4632.325	0.003	A
	5	1	5	4	1	4	4833.021	-0.006	A
	5	0	5	4	0	4	4914.687	-0.005	E
	5	0	5	4	0	4	4915.185	0.002	A
	5	2	4	4	2	3	5019.801	-0.002	E
	5	1	5	4	0	4	5115.894	0.006	A
	5	1	5	4	0	4	5116.633	0.007	E
	5	2	3	4	2	2	5130.028	-0.001	E
	5	2	3	4	2	2	5132.967	0.002	A
	6	0	6	5	1	5	5653.069	0.002	A
	6	1	6	5	1	5	2803.755	0.001	A
$^{18}O_{\alpha}{}^{18}O_{\beta}{}^{16}O_{\gamma}$	3	1	3	2	1	2	2803.755	0.001	A
	3	0	3	2	0	2	2881.643	-0.004	E
	3	0	3	2	0	2	2881.749	0.003	A
	3	1	2	2	1	1	2994.604	0.000	A
	4	1	4	3	1	3	3732.816	0.003	A
	4	1	4	3	1	3	3733.051	-0.004	E
	4	0	4	3	0	3	3819.374	-0.006	E
	4	0	4	3	0	3	3819.574	0.003	A
	4	2	3	3	2	2	3865.856	0.003	A
	4	2	3	3	2	2	3873.186	-0.004	E
	4	2	2	3	2	1	3908.838	-0.005	E
	4	2	2	3	2	1	3916.203	-0.005	A
	4	1	3	3	1	2	3985.841	-0.002	E
	4	1	3	3	1	2	3986.022	-0.001	A
	5	0	5	4	1	4	4416.487	0.004	E
	5	0	5	4	1	4	4417.021	0.008	A
	5	1	5	4	1	4	4657.882	0.006	A
	5	1	5	4	1	4	4658.187	-0.003	E
	5	0	5	4	0	4	4741.511	-0.006	E
	5	0	5	4	0	4	4741.891	0.005	A
	5	2	4	4	2	3	4825.767	0.005	A
	5	2	4	4	2	3	4829.294	-0.007	E
	5	3	3	4	3	2	4852.718	-0.005	A
	5	3	3	4	3	2	4855.406	-0.012	E
	5	3	2	4	3	1	4855.562	-0.009	E
	5	3	2	4	3	1	4858.311	-0.007	A
	5	2	3	4	2	2	4917.614	-0.005	E
	5	2	3	4	2	2	4921.180	-0.004	A
	5	1	4	4	1	3	4970.685	0.005	E
	5	1	4	4	1	3	4970.809	0.002	A
	5	1	5	4	0	4	4982.750	0.000	A
	5	1	5	4	0	4	4983.210	-0.014	E
	6	0	6	5	1	5	5408.574	-0.004	E
	6	0	6	5	1	5	5410.146	0.012	A
	6	1	6	5	1	5	5578.773	0.008	A
	6	1	6	5	1	5	5579.358	0.000	E
	6	0	6	5	0	5	5650.274	-0.011	E
	6	0	6	5	0	5	5651.005	0.008	A
	6	2	5	5	2	4	5781.391	0.008	A
	3	3	1	2	2	0	5800.090	0.004	A
	3	3	0	2	2	1	5805.594	0.000	A
	6	1	6	5	0	5	5819.635	0.007	A
	6	1	6	5	0	5	5821.062	-0.002	E
	6	1	5	5	1	4	5946.205	0.007	E
	6	1	5	5	1	4	5946.332	0.008	A
$^{18}O_{\alpha}{}^{16}O_{\beta}{}^{18}O_{\gamma}$	3	1	3	2	1	2	2844.650	0.007	A
	3	1	3	2	1	2	2845.019	-0.001	E
	3	0	3	2	0	2	2925.166	-0.007	E
	3	0	3	2	0	2	2925.280	0.000	A
	3	1	2	2	1	1	3046.059	-0.005	E

	3	1	2	2	1	1	3046.422	0.000	A
	3	1	3	2	0	2	3305.813	-0.008	E
	3	1	3	2	0	2	3306.159	0.007	A
	4	0	4	3	1	3	3493.388	0.012	A
	4	0	4	3	1	3	3493.388	0.006	E
	4	1	4	3	1	3	3786.494	0.007	A
	4	1	4	3	1	3	3786.734	-0.006	E
	4	0	4	3	0	3	3874.025	-0.005	E
	4	0	4	3	0	3	3874.246	0.000	A
	4	2	3	3	2	2	3927.709	0.000	A
	4	2	3	3	2	2	3934.710	-0.009	E
	4	3	2	3	3	1	3943.687	-0.004	A
	4	2	2	3	2	1	3978.874	-0.004	E
	4	2	2	3	2	1	3985.908	-0.006	A
	4	1	3	3	1	2	4053.743	-0.002	E
	4	1	3	3	1	2	4053.916	0.000	A
	5	0	5	4	1	4	4512.416	0.002	E
	5	0	5	4	1	4	4513.094	0.003	A
	5	1	5	4	1	4	4723.817	0.003	A
	5	1	5	4	1	4	4724.172	-0.007	E
	5	0	5	4	0	4	4805.764	-0.008	E
	5	0	5	4	0	4	4806.208	0.005	A
	5	2	4	4	2	3	4902.011	0.003	A
	5	2	4	4	2	3	4905.078	-0.005	E
	5	3	3	4	3	2	4933.119	-0.005	A
	5	3	2	4	3	1	4940.282	-0.009	A
	5	2	3	4	2	2	5008.134	-0.006	E
	5	2	3	4	2	2	5011.232	-0.006	A
	5	1	5	4	0	4	5016.933	0.008	A
	5	1	5	4	0	4	5017.528	-0.009	E
	5	1	4	4	1	3	5053.394	0.003	E
	5	1	4	4	1	3	5053.519	0.002	A
	6	0	6	5	1	5	5512.060	-0.004	E
	6	0	6	5	1	5	5513.977	0.008	A
	6	1	6	5	1	5	5656.518	0.006	A
	6	1	6	5	1	5	5657.241	-0.005	E
	6	0	6	5	0	5	5723.820	-0.009	E
	3	3	1	2	2	0	5729.255	0.004	A
	3	3	0	2	2	1	5735.700	0.000	A
	6	1	6	5	0	5	5867.237	0.003	A
	6	2	5	5	2	4	5871.345	0.011	A
	6	2	5	5	2	4	5872.575	0.002	E
	6	1	5	5	1	4	6041.912	0.006	E
	6	1	5	5	1	4	6042.046	0.006	A
	6	2	4	5	2	3	6043.439	-0.008	E
	6	2	4	5	2	3	6044.717	0.013	A
$^{16}O_{\alpha}{}^{18}O_{\beta}{}^{18}O_{\gamma}$	3	1	3	2	1	3	2846.072	-0.002	A
	3	1	3	2	1	3	2846.439	-0.007	E
	3	0	3	2	0	3	2926.550	0.000	E
	3	0	3	2	0	3	2926.667	0.003	A
	3	1	2	2	1	3	3047.688	-0.002	E
	3	1	2	2	1	3	3048.041	-0.001	A
	4	1	4	3	1	4	3788.358	0.003	A
	4	1	4	3	1	4	3788.607	-0.005	E
	4	0	4	3	0	4	3875.698	-0.004	E
	4	0	4	3	0	4	3875.931	0.001	A
	4	2	3	3	2	4	3929.750	0.004	A
	4	2	3	3	2	4	3936.623	-0.010	E
	4	2	2	3	2	4	3981.425	0.003	E
	4	2	2	3	2	4	3988.340	0.001	A
	4	1	3	3	1	4	4055.842	0.000	E
	4	1	3	3	1	4	4056.014	0.002	A
	4	1	4	3	0	4	4166.269	0.006	A
	4	1	4	3	0	4	4166.333	0.009	E
	5	0	5	4	1	5	4517.064	0.007	E

	5	0	5	4	1	5	4517.812	0.011	A
	5	1	5	4	1	5	4726.096	0.004	A
	5	1	5	4	1	5	4726.472	-0.005	E
	5	0	5	4	0	5	4807.672	-0.007	E
	5	0	5	4	0	5	4808.139	0.003	A
	5	2	4	4	2	5	4904.506	0.007	A
	5	2	4	4	2	5	4907.482	-0.006	E
	5	2	3	4	2	5	5011.369	0.001	E
	5	2	3	4	2	5	5014.383	-0.001	A
	5	1	5	4	0	5	5016.422	-0.004	A
	5	1	4	4	1	5	5055.890	-0.004	E
	5	1	4	4	1	5	5056.026	0.003	A
	6	0	6	5	1	6	5516.566	-0.003	E
	6	0	6	5	1	6	5518.619	0.007	A
	6	1	6	5	1	6	5659.189	0.003	A
	6	1	6	5	1	6	5659.951	-0.015	E
	3	3	1	2	2	3	5715.996	-0.002	A
	3	3	0	2	2	3	5722.494	-0.001	A
	6	0	6	5	0	6	5725.979	-0.010	E
	6	0	6	5	0	6	5726.907	0.004	A
	3	3	0	2	2	3	5776.736	0.003	E
	6	1	6	5	0	6	5867.480	0.004	A
	6	2	5	5	2	6	5874.254	0.008	A
	6	2	5	5	2	6	5875.443	-0.003	E
	6	1	5	5	1	6	6044.717	0.000	E
	6	1	5	5	1	6	6044.859	0.005	A
	6	2	4	5	2	6	6047.269	-0.008	E
	6	2	4	5	2	6	6048.496	-0.003	A
	7	1	7	6	1	7	6587.963	0.000	A
$^{18}O_{\alpha}{}^{18}O_{\beta}{}^{18}O_{\gamma}$	3	1	3	2	1	2	2784.078	-0.001	A
	3	1	3	2	1	2	2784.442	-0.011	E
	3	0	3	2	0	2	2863.135	-0.005	E
	3	0	3	2	0	2	2863.247	0.002	A
	3	1	2	2	1	1	2980.606	-0.003	E
	3	1	2	2	1	1	2980.967	0.002	A
	3	1	3	2	0	2	3248.308	0.010	A
	4	0	4	3	1	3	3407.658	0.005	A
	4	0	4	3	1	3	3407.658	-0.011	E
	4	1	4	3	1	3	3706.030	0.001	A
	4	1	4	3	1	3	3706.267	-0.008	E
	4	0	4	3	0	3	3792.507	0.008	E
	4	0	4	3	0	3	3792.705	-0.001	A
	4	2	3	3	2	2	3843.677	-0.001	A
	4	2	3	3	2	2	3850.639	-0.009	E
	4	2	2	3	2	1	3892.162	-0.003	E
	4	2	2	3	2	1	3899.159	-0.003	A
	4	1	3	3	1	2	3966.880	-0.001	E
	4	1	3	3	1	2	3967.052	0.001	A
	4	1	4	3	0	3	4091.089	0.006	A
	5	0	5	4	1	4	4406.701	0.005	E
	5	0	5	4	1	4	4407.341	0.006	A
	5	1	5	4	1	4	4623.650	0.002	A
	5	1	5	4	1	4	4623.986	-0.009	E
	5	0	5	4	0	4	4705.296	-0.007	E
	5	0	5	4	0	4	4705.716	0.003	A
	5	2	4	4	2	3	4797.343	0.004	A
	5	2	4	4	2	3	4800.452	-0.005	E
	5	2	3	4	2	2	4898.598	-0.003	E
	5	2	3	4	2	2	4901.741	-0.002	A
	5	1	5	4	0	4	4922.027	0.003	A
	5	1	4	4	1	3	4945.548	0.001	E
	5	1	4	4	1	3	4945.676	0.004	A
	6	0	6	5	1	5	5387.313	0.001	E
	6	0	6	5	1	5	5389.119	0.006	A
	6	1	6	5	1	5	5536.805	0.002	A

6	1	6	5	1	5	5537.476	-0.016	E
6	0	6	5	0	5	5604.603	-0.009	E
6	0	6	5	0	5	5605.429	0.005	A
3	3	1	2	2	0	5613.483	-0.024	E
3	3	1	2	2	0	5668.945	0.023	A
3	3	0	2	2	1	5675.070	0.023	A
3	3	0	2	2	1	5729.254	-0.024	E
6	2	5	5	2	4	5746.275	0.009	A
6	2	5	5	2	4	5747.529	0.002	E
6	1	6	5	0	5	5753.120	0.005	A
6	2	4	5	2	3	5911.277	-0.003	E
6	2	4	5	2	3	5912.562	0.000	A
6	1	5	5	1	4	5913.700	0.004	E
6	1	5	5	1	4	5913.833	0.007	A
7	0	7	6	1	6	6345.740	0.001	E
7	0	7	6	1	6	6349.833	0.003	A
7	0	7	6	0	6	6495.912	-0.007	E
7	0	7	6	0	6	6497.526	0.006	A

[a] Δν is the difference between measured and calculated frequencies.

Complete Crest Results - ωB97XD

Table F.23 ωB97XD/Jun-cc-pVTZ refined CREST results of the monohydrate.

	ΔE_0 /kJ mol^{-1}	**A /MHz**	**B /MHz**	**C /MHz**	**μ_a /D**	**μ_b /D**	**μ_c /D**	**[a]ΔA /%**	**[a]ΔB /%**	**[a]ΔC /%**	**[b]ΔA /%**	**[b]ΔB /%**	**[b]ΔC /%**
1	0.0	2314.29	790.45	592.97	5.0	0.1	0.0	1.3	1.4	1.3	24.6	-13.0	-3.7
2	4.6	1882.93	935.74	633.09	5.1	0.7	0.5	-17.6	20.0	8.2	1.4	3.0	2.8
3	5.3	1506.02	1176.02	818.64	2.0	0.2	2.2	-34.1	50.8	39.9	-18.9	29.5	32.9
4	5.8	1916.73	992.81	660.10	0.6	2.6	1.4	-16.1	27.3	12.8	3.2	9.3	7.2
5	6.3	1671.81	1120.36	773.49	0.2	0.1	1.8	-26.8	43.7	32.2	-10.0	23.4	25.6
6	7.0	1921.93	987.26	659.11	0.9	3.4	1.4	-15.9	26.6	12.6	3.5	8.7	7.0
7	7.1	1684.23	1111.78	773.60	0.3	1.0	1.9	-26.3	42.6	32.2	-9.3	22.4	25.6
8	9.1	1329.87	1177.08	988.95	1.1	1.9	1.4	-41.8	51.0	69.0	-28.4	29.6	60.5
9	10.0	1584.23	1049.44	732.31	4.0	1.1	0.4	-30.6	34.6	25.1	-14.7	15.5	18.9
10	10.0	1307.39	1194.52	981.44	1.5	0.6	2.0	-42.8	53.2	67.7	-29.6	31.5	59.3
11	10.2	1735.33	961.09	662.44	2.6	0.9	1.4	-24.0	23.3	13.2	-6.6	5.8	7.5
12	10.3	2296.59	789.87	591.26	4.2	1.6	1.3	0.5	1.3	1.0	23.6	-13.0	-4.0
13	11.9	1928.86	960.87	645.60	4.6	1.2	0.1	-15.6	23.2	10.3	3.8	5.8	4.8
14	19.1	2319.86	779.08	586.94	2.1	0.2	0.0	1.6	-0.1	0.3	24.9	-14.2	-4.7
15	23.6	1862.35	918.89	646.25	3.8	0.6	0.6	-18.5	17.9	10.4	0.3	1.2	4.9

[a(b)]Percent differences between the theoretical rotational constants and the experimentally assigned rotational constants for monohydrate 1(2).

Table F.24. ωB97XD/Jun-cc-pVTZ refined CREST results of the dihydrate.

	ΔE_0 /kJ mol^{-1}	**A /MHz**	**B /MHz**	**C /MHz**	**μ_a /D**	**μ_b /D**	**μ_c /D**	**[a]ΔA /%**	**[a]ΔB /%**	**[a]ΔC /%**
1	0.0	1376.27	734.18	620.09	0.8	1.9	0.7	-0.4	2.8	2.3
2	0.2	1412.22	726.32	619.39	1.0	0.4	1.7	2.2	1.7	2.1
3	1.1	1448.79	693.19	577.20	2.0	2.0	1.2	4.9	-2.9	-4.8
4	5.2	1208.78	841.42	611.51	0.5	1.7	1.3	-12.5	17.8	0.8
5	5.5	1229.05	854.32	653.18	0.7	0.0	2.2	-11.0	19.6	7.7
6	9.6	1673.97	564.13	475.14	2.1	0.3	0.7	21.2	-21.0	-21.6
7	14.8	1380.37	712.70	499.55	0.8	0.7	0.6	-0.1	-0.2	-17.6
8	15.9	1502.93	657.01	506.52	0.0	0.9	1.0	8.8	-8.0	-16.5
9	16.6	1509.84	654.30	506.30	0.1	2.8	0.2	9.3	-8.4	-16.5
10	16.7	1346.86	737.53	529.80	2.3	1.8	2.4	-2.5	3.3	-12.6

11	16.8	1092.35	808.87	503.52	1.8	2.3	0.6	-20.9	13.3	-17.0
12	18.0	1496.85	653.19	495.80	1.3	2.5	0.2	8.4	-8.5	-18.2
13	20.7	1289.49	640.26	495.71	6.4	0.9	0.3	-6.6	-10.3	-18.3
14	20.9	1271.47	607.15	430.96	5.4	0.8	1.2	-7.9	-15.0	-28.9
15	22.2	1032.98	860.59	812.93	4.4	1.1	0.2	-25.2	20.5	34.1
16	22.7	1071.70	868.76	782.23	1.3	1.0	2.4	-22.4	21.7	29.0
17	22.8	1073.19	866.03	783.50	1.4	1.2	2.4	-22.3	21.3	29.2
18	23.0	1066.00	857.96	782.10	6.0	0.5	0.0	-22.8	20.1	29.0
19	23.2	1051.92	861.81	782.95	6.0	0.3	0.1	-23.8	20.7	29.1
20	23.3	1055.80	862.53	785.93	6.0	0.4	0.1	-23.6	20.8	29.6
21	24.5	1313.77	726.91	632.39	2.8	1.7	0.4	-4.9	1.8	4.3
22	25.0	1369.44	598.15	469.41	3.5	2.0	0.1	-0.9	-16.2	-22.6
23	26.0	1379.09	602.20	472.18	4.0	1.9	0.1	-0.2	-15.7	-22.1
24	27.6	1033.57	855.93	820.77	1.0	0.3	5.0	-25.2	19.9	35.4
25	27.9	1291.48	738.98	528.83	1.2	4.8	2.0	-6.5	3.5	-12.8
26	30.0	1467.03	613.91	502.03	4.4	2.7	2.1	6.2	-14.0	-17.2
27	35.2	1651.32	490.00	390.93	0.9	0.8	1.2	19.6	-31.4	-35.5

[a]Percent differences between the theoretical rotational constants and the experimentally assigned rotational constants of the dihydrate.

Table F.25. ωB97XD/Jun-cc-pVTZ refined CREST results of the trihydrate.

	ΔE_0 /kJ mol^{-1}	A /MHz	B /MHz	C /MHz	μ_a /D	μ_b /D	μ_c /D	[a]ΔA /%	[a]ΔB /%	[a]ΔC /%
1	0.0	1093.47	555.13	485.62	1.4	1.3	0.4	1.1	2.8	2.8
2	1.3	1101.71	560.72	483.25	1.3	1.5	0.1	1.9	3.8	2.3
3	1.4	863.20	763.06	599.22	1.2	0.7	0.5	-20.2	41.3	26.8
4	1.8	928.78	621.97	563.29	1.7	1.6	0.3	-14.1	15.2	19.2
5	2.1	913.91	717.43	594.66	0.1	0.3	0.4	-15.5	32.9	25.9
6	2.2	875.44	751.50	602.66	1.2	1.3	0.2	-19.0	39.2	27.5
7	2.3	937.24	695.02	581.92	1.3	1.4	0.6	-13.3	28.7	23.2
8	2.9	935.84	698.45	588.67	0.1	2.0	0.2	-13.4	29.4	24.6
9	2.9	875.28	751.90	605.98	0.3	0.9	0.4	-19.0	39.3	28.3
10	3.3	1085.76	526.67	468.96	1.7	1.5	0.5	0.4	-2.5	-0.7
11	3.3	1088.37	525.06	467.47	1.7	1.5	0.5	0.7	-2.8	-1.1
12	3.4	938.87	631.55	567.65	2.0	1.9	0.3	-13.2	17.0	20.1
13	3.7	1063.15	574.76	524.27	0.2	0.1	0.6	-1.7	6.4	11.0
14	3.9	892.38	749.45	662.81	0.4	1.8	0.4	-17.5	38.8	40.3
15	4.7	1124.93	579.28	496.31	0.2	0.0	0.2	4.1	7.3	5.0
16	5.2	1321.82	430.35	387.87	2.5	0.2	0.3	22.3	-20.3	-17.9
17	5.2	1339.69	440.79	407.91	1.5	1.5	0.2	23.9	-18.4	-13.7
18	5.5	879.04	621.31	588.45	1.6	0.1	0.7	-18.7	15.1	24.5
19	5.7	950.43	700.36	644.20	0.2	1.0	0.1	-12.1	29.7	36.3
20	5.8	1345.88	412.44	358.75	2.3	0.3	0.3	24.5	-23.6	-24.1
21	6.3	867.78	669.56	494.45	1.4	0.8	1.5	-19.7	24.0	4.6
22	6.4	1006.35	587.63	488.46	0.3	0.3	1.7	-6.9	8.8	3.4
23	6.5	1235.18	469.79	416.26	2.8	0.1	0.1	14.3	-13.0	-11.9
24	6.8	1119.17	521.69	385.90	2.9	1.2	0.6	3.5	-3.4	-18.3
25	7.1	1170.98	494.43	399.04	2.7	0.4	0.1	8.3	-8.4	-15.5
26	7.2	1225.06	463.13	368.39	2.8	0.0	0.5	13.3	-14.2	-22.0
27	7.3	1331.82	480.07	422.35	1.7	0.2	2.2	23.2	-11.1	-10.6
28	7.3	1128.88	511.77	407.48	1.5	0.8	1.5	4.4	-5.2	-13.8
29	7.5	1168.16	495.64	399.57	2.7	0.4	0.0	8.1	-8.2	-15.4
30	7.6	982.75	662.83	584.42	0.0	0.5	1.2	-9.1	22.8	23.7
31	7.6	1214.58	480.41	424.89	3.1	0.1	0.2	12.3	-11.0	-10.1
32	7.7	967.58	604.51	576.49	1.9	0.8	1.5	-10.5	12.0	22.0
33	7.9	1111.00	536.11	420.42	1.9	0.0	0.9	2.8	-0.7	-11.0
34	7.9	1325.49	482.33	423.56	1.5	1.3	2.2	22.6	-10.7	-10.4
35	7.9	1219.37	476.53	422.51	2.2	2.0	0.2	12.8	-11.7	-10.6
36	8.0	1134.68	526.60	415.93	2.6	0.9	0.7	5.0	-2.5	-12.0
37	8.8	1322.82	437.37	398.55	2.9	0.1	0.1	22.4	-19.0	-15.7
38	9.1	1136.69	530.54	447.22	1.9	0.8	0.7	5.1	-1.7	-5.3
39	9.2	1227.95	473.48	419.82	3.1	0.2	0.0	13.6	-12.3	-11.1
40	9.4	1096.46	562.53	459.87	2.1	0.6	0.6	1.4	4.2	-2.7
41	9.8	903.61	605.84	546.76	0.6	0.2	0.2	-16.4	12.2	15.7
42	10.0	902.57	612.20	540.61	0.4	0.6	0.3	-16.5	13.4	14.4
43	10.2	1115.82	522.28	384.03	4.2	1.6	2.0	3.2	-3.3	-18.7
44	10.2	1080.98	572.51	473.97	0.8	0.3	2.4	0.0	6.0	0.3
45	10.2	924.87	593.00	536.73	0.4	0.1	0.1	-14.5	9.8	13.6
46	10.2	1106.84	546.42	459.46	0.4	1.2	2.6	2.4	1.2	-2.8
47	10.6	916.34	613.25	538.90	0.6	0.3	0.6	-15.2	13.6	14.1

48	11.0	1138.32	510.11	380.71	2.5	1.3	1.0	5.3	-5.5	-19.4
49	12.2	893.04	605.69	553.43	1.4	0.8	1.4	-17.4	12.2	17.1
50	12.4	1126.12	517.51	400.48	1.6	0.3	0.6	4.2	-4.2	-15.2
51	12.6	922.70	609.51	526.37	1.2	0.9	1.8	-14.7	12.9	11.4
52	12.7	1311.60	485.41	426.98	1.0	1.3	2.7	21.3	-10.1	-9.6
53	13.5	1156.60	501.50	386.64	1.1	1.1	1.8	7.0	-7.1	-18.2
54	13.8	828.17	721.94	496.29	0.1	0.6	0.2	-23.4	33.7	5.0
55	13.9	1099.78	559.53	464.53	1.4	0.5	1.6	1.7	3.6	-1.7
56	14.3	870.10	712.04	571.77	1.4	0.7	1.2	-19.5	31.9	21.0
57	14.4	1137.01	506.01	376.17	1.3	1.0	1.6	5.2	-6.3	-20.4
58	14.8	1139.91	505.27	375.42	0.1	0.4	0.2	5.4	-6.4	-20.5
59	15.0	1199.26	471.54	376.49	2.2	1.1	2.1	10.9	-12.7	-20.3
60	15.2	1048.22	641.97	563.56	2.9	0.6	1.1	-3.0	18.9	19.3
61	15.4	970.51	655.56	601.52	3.5	0.6	0.4	-10.2	21.4	27.3
62	15.5	1271.59	484.13	405.33	3.7	0.2	0.3	17.6	-10.3	-14.2
63	15.8	794.26	711.59	451.17	1.0	2.5	0.4	-26.5	31.8	-4.5
64	16.1	908.64	665.29	603.31	0.9	0.5	0.6	-16.0	23.2	27.7
65	16.3	1232.17	453.48	358.53	0.8	0.9	0.1	14.0	-16.0	-24.1
66	16.4	1223.50	456.04	360.63	2.3	1.1	1.7	13.2	-15.5	-23.7
67	17.2	1187.09	487.54	349.89	0.4	0.7	0.5	9.8	-9.7	-25.9
68	17.8	1126.04	511.68	371.40	1.1	1.0	1.4	4.2	-5.2	-21.4
69	18.9	1218.48	447.04	411.49	3.1	1.9	0.5	12.7	-17.2	-12.9
70	19.3	1105.09	558.76	458.07	0.9	0.5	0.8	2.2	3.5	-3.1
71	19.3	1347.14	382.82	341.39	3.8	0.7	0.7	24.6	-29.1	-27.7
72	20.2	1134.14	530.27	440.56	2.5	1.8	0.9	4.9	-1.8	-6.8
73	20.9	1305.80	467.79	409.97	0.3	0.1	0.9	20.8	-13.4	-13.2
74	21.0	1327.26	453.97	399.43	0.8	2.5	1.3	22.8	-15.9	-15.5
75	21.3	1069.76	535.48	416.15	0.1	0.9	0.4	-1.0	-0.8	-11.9
76	21.4	1311.40	461.13	405.32	0.1	0.8	1.0	21.3	-14.6	-14.2
77	21.8	923.90	652.57	618.72	4.3	1.9	1.4	-14.5	20.9	30.9
78	22.1	953.52	635.99	599.76	2.8	0.8	0.2	-11.8	17.8	26.9
79	23.0	1008.65	622.37	459.60	0.5	1.4	0.4	-6.7	15.3	-2.7
80	23.1	955.05	636.63	591.15	2.8	1.0	0.0	-11.7	17.9	25.1
81	23.1	968.14	636.79	588.30	5.2	0.2	1.8	-10.4	17.9	24.5
82	23.1	1194.40	514.43	401.01	2.3	1.2	2.8	10.5	-4.7	-15.1
83	23.4	1117.33	493.64	401.29	2.9	0.3	3.4	3.4	-8.6	-15.1
84	23.7	946.05	637.09	441.74	0.0	0.9	0.5	-12.5	18.0	-6.5
85	24.0	985.88	601.22	402.84	2.7	3.5	0.2	-8.8	11.3	-14.7
86	25.8	897.97	569.95	387.89	2.7	1.8	0.1	-16.9	5.6	-17.9
87	25.9	1041.81	602.55	514.34	3.7	0.9	0.1	-3.6	11.6	8.9
88	26.0	1161.21	528.10	420.10	1.7	1.5	2.4	7.4	-2.2	-11.1
89	26.2	1212.70	464.92	376.74	3.7	2.1	1.8	12.2	-13.9	-20.3
90	26.2	1329.63	388.86	334.42	5.4	0.0	0.1	23.0	-28.0	-29.2
91	26.4	1167.00	419.11	392.87	0.1	0.1	0.0	7.9	-22.4	-16.9
92	27.1	1229.21	496.52	407.26	2.6	1.6	2.3	13.7	-8.0	-13.8
93	27.4	737.28	675.74	380.14	3.7	0.1	0.3	-31.8	25.1	-19.5
94	31.6	1284.66	446.19	359.00	1.0	2.8	0.3	18.8	-17.4	-24.0
95	32.0	880.58	710.85	610.69	3.0	2.3	0.0	-18.5	31.7	29.2
96	32.3	1361.93	377.37	323.51	1.6	0.7	0.0	26.0	-30.1	-31.5
97	32.6	1455.98	396.85	336.97	2.1	3.1	0.1	34.7	-26.5	-28.7
98	32.7	1315.42	388.47	334.39	3.9	0.5	0.4	21.7	-28.1	-29.2
99	32.9	1322.05	386.31	332.31	3.8	0.6	0.3	22.3	-28.5	-29.7
100	33.0	935.00	588.91	562.96	0.6	1.4	1.8	-13.5	9.1	19.1

[a]Percent differences between the theoretical rotational constants and the experimentally assigned rotational constants of the trihydrate.

Table F.26. ωB97XD/Jun-cc-pVTZ refined CREST results of the tetrahydrate.

	ΔE_0 /kJ mol^{-1}	**A /MHz**	**B /MHz**	**C /MHz**	**μ_a /D**	**μ_b /D**	**μ_c /D**	**[a]ΔA /%**	**[a]ΔB /%**	**[a]ΔC /%**
1	0.0	791.67	495.15	461.48	0.7	0.6	0.4	1.0	2.9	3.0
2	0.2	797.34	495.64	458.65	1.1	1.0	0.6	1.7	3.0	2.3
3	0.9	790.80	493.29	466.52	0.8	0.3	0.6	0.9	2.5	4.1
4	1.1	797.02	490.71	467.91	0.8	0.6	0.2	1.7	2.0	4.4
5	1.5	858.91	525.35	453.42	1.1	2.0	0.6	9.6	9.2	1.2
6	1.6	702.14	620.95	541.60	0.7	0.1	1.1	-10.4	29.1	20.8
7	1.7	825.63	537.01	491.44	2.0	0.2	0.8	5.3	11.6	9.6
8	2.0	795.94	550.30	514.56	0.3	0.4	2.3	1.5	14.4	14.8
9	2.0	829.69	558.82	469.92	0.2	3.3	0.5	5.8	16.2	4.8
10	2.7	854.45	525.96	452.97	0.5	1.9	1.1	9.0	9.3	1.1
11	2.8	884.23	471.41	437.86	0.4	0.8	1.3	12.8	-2.0	-2.3

12	3.0	854.23	535.82	458.48	1.2	2.3	0.6	9.0	11.4	2.3
13	3.0	954.29	411.35	397.23	0.5	0.1	1.6	21.7	-14.5	-11.4
14	3.2	945.01	428.66	396.55	0.2	0.0	1.5	20.5	-10.9	-11.5
15	3.4	881.36	467.58	437.77	0.3	0.7	1.2	12.4	-2.8	-2.3
16	3.7	875.40	479.77	444.65	0.9	0.5	0.3	11.7	-0.3	-0.8
17	3.8	739.60	574.57	560.33	0.7	0.4	1.7	-5.7	19.4	25.0
18	4.2	809.80	543.93	499.82	1.9	0.3	0.5	3.3	13.1	11.5
19	4.6	804.67	523.20	483.09	2.2	0.6	0.1	2.6	8.8	7.8
20	4.6	801.31	523.10	495.43	1.2	0.4	2.3	2.2	8.7	10.5
21	4.7	855.14	530.95	454.01	0.2	2.4	1.1	9.1	10.4	1.3
22	5.5	787.10	531.18	484.25	1.2	1.0	1.7	0.4	10.4	8.0
23	5.7	947.62	418.89	406.47	1.6	1.1	0.9	20.9	-12.9	-9.3
24	6.2	904.89	471.85	454.94	2.8	1.3	1.2	15.4	-1.9	1.5
25	6.7	847.19	429.49	350.13	1.9	1.1	0.5	8.1	-10.7	-21.9
26	7.1	852.39	389.61	339.40	1.6	0.5	0.1	8.7	-19.0	-24.3
27	7.1	654.18	556.56	428.04	1.5	2.1	0.3	-16.6	15.7	-4.5
28	7.4	872.37	455.37	373.08	0.4	2.0	0.6	11.3	-5.3	-16.8
29	7.8	911.42	350.44	300.84	1.7	0.1	0.1	16.3	-27.2	-32.9
30	8.0	786.82	530.74	410.30	1.3	0.6	1.2	0.4	10.3	-8.5
31	8.1	878.98	451.89	370.60	1.1	1.1	0.6	12.1	-6.1	-17.3
32	8.2	850.79	477.74	437.36	1.4	1.7	0.0	8.5	-0.7	-2.4
33	8.3	1023.53	376.77	318.62	3.1	0.1	0.3	30.6	-21.7	-28.9
34	8.4	642.45	566.48	441.56	1.8	1.6	0.2	-18.1	17.8	-1.5
35	8.5	804.31	593.80	481.51	0.9	0.9	3.1	2.6	23.4	7.4
36	8.6	845.28	430.52	358.03	2.7	2.0	0.7	7.8	-10.5	-20.1
37	9.0	853.96	505.90	452.50	4.3	0.3	0.9	8.9	5.2	1.0
38	9.1	890.26	443.77	368.99	0.1	2.1	0.5	13.6	-7.7	-17.7
39	9.1	787.98	450.18	395.98	0.8	0.7	0.3	0.5	-6.4	-11.7
40	9.4	872.61	363.68	359.94	2.3	1.0	0.1	11.3	-24.4	-19.7
41	9.5	1014.97	446.84	373.69	1.8	1.4	0.6	29.5	-7.1	-16.6
42	9.6	868.04	365.81	362.40	2.3	1.0	0.0	10.7	-24.0	-19.1
43	9.6	892.60	364.56	295.23	2.2	0.5	0.3	13.9	-24.2	-34.1
44	10.0	1027.92	438.54	367.75	2.0	1.2	0.3	31.1	-8.8	-17.9
45	10.5	963.41	349.01	334.90	2.2	1.6	0.2	22.9	-27.4	-25.3
46	10.6	1020.57	374.78	318.58	2.9	0.4	0.0	30.2	-22.1	-28.9
47	10.8	803.31	473.20	362.17	1.1	1.3	1.3	2.5	-1.6	-19.2
48	10.9	797.10	448.46	398.75	1.4	0.8	0.9	1.7	-6.8	-11.0
49	10.9	886.67	397.84	343.84	1.0	1.3	0.7	13.1	-17.3	-23.3
50	11.1	1025.81	435.58	368.35	2.7	1.0	2.2	30.8	-9.5	-17.8
51	11.3	831.30	506.50	411.27	0.4	0.8	4.2	6.0	5.3	-8.2
52	11.4	1083.21	382.03	338.81	1.1	1.3	3.0	38.2	-20.6	-24.4
53	11.6	814.58	460.65	353.29	0.1	0.1	0.3	3.9	-4.2	-21.2
54	11.8	1061.31	306.41	288.33	2.0	0.4	0.8	35.4	-36.3	-35.7
55	11.9	1021.57	324.43	268.32	1.6	0.4	0.9	30.3	-32.6	-40.1
56	12.0	780.59	475.66	361.28	0.9	2.4	1.8	-0.4	-1.1	-19.4
57	12.1	798.54	414.63	331.09	0.9	0.4	1.8	1.9	-13.8	-26.1
58	12.2	833.76	499.80	412.50	1.3	1.0	0.6	6.3	3.9	-8.0
59	12.2	818.98	489.95	393.20	0.9	1.4	1.3	4.5	1.9	-12.3
60	12.3	857.47	488.74	402.79	2.0	1.3	2.9	9.4	1.6	-10.1
61	12.5	1049.41	316.35	260.01	1.3	0.1	1.0	33.9	-34.2	-42.0
62	12.6	816.85	443.66	385.48	2.0	1.1	0.4	4.2	-7.8	-14.0
63	12.7	1065.65	404.49	351.23	0.9	3.0	0.3	35.9	-15.9	-21.6
64	12.8	836.90	415.99	351.02	1.6	1.2	0.2	6.7	-13.5	-21.7
65	13.0	727.50	584.19	450.81	0.0	0.1	2.5	-7.2	21.4	0.6
66	13.1	959.59	385.17	359.57	0.4	2.4	1.9	22.4	-19.9	-19.8
67	13.2	1070.28	396.50	351.24	0.6	1.4	1.6	36.5	-17.6	-21.6
68	13.3	812.08	485.97	411.66	0.1	0.3	1.0	3.6	1.0	-8.2
69	13.7	1085.09	304.26	246.60	2.2	0.1	2.1	38.4	-36.8	-45.0
70	13.7	1100.16	374.76	323.35	1.1	1.6	1.1	40.3	-22.1	-27.9
71	13.8	933.13	342.73	270.68	2.6	0.2	0.0	19.0	-28.8	-39.6
72	13.8	903.84	452.81	359.05	3.6	0.7	1.6	15.3	-5.9	-19.9
73	13.9	865.21	496.39	434.40	2.8	1.7	0.2	10.4	3.2	-3.1
74	13.9	963.99	418.87	380.43	2.1	0.7	0.3	23.0	-12.9	-15.1
75	14.0	807.68	535.91	462.50	1.6	1.1	1.3	3.0	11.4	3.2
76	14.2	1093.73	352.57	316.13	3.6	1.3	1.9	39.5	-26.7	-29.5
77	14.6	974.23	397.09	317.77	1.1	1.1	0.8	24.3	-17.5	-29.1
78	14.7	943.39	383.18	302.10	2.2	0.6	2.3	20.3	-20.3	-32.6
79	14.9	905.65	441.21	411.61	2.8	2.7	1.3	15.5	-8.3	-8.2
80	15.0	712.36	478.56	436.09	0.7	1.3	1.0	-9.1	-0.5	-2.7
81	15.5	1117.67	340.50	296.13	2.5	0.4	2.8	42.6	-29.2	-33.9

82	16.1	830.42	469.82	375.78	1.0	0.0	0.8	5.9	-2.3	-16.2
83	16.3	1172.82	310.92	282.48	1.1	1.6	2.5	49.6	-35.4	-37.0
84	16.3	1143.77	343.72	300.38	2.3	1.1	3.1	45.9	-28.5	-33.0
85	16.4	785.30	502.67	389.22	4.2	0.5	1.6	0.2	4.5	-13.2
86	16.6	828.66	517.44	441.31	2.2	0.6	3.4	5.7	7.6	-1.5
87	16.7	887.09	452.76	376.24	1.3	0.8	1.5	13.2	-5.9	-16.1
88	16.9	800.72	548.49	457.01	1.4	1.7	1.5	2.1	14.0	2.0
89	16.9	724.54	588.62	526.44	4.2	0.3	0.6	-7.6	22.4	17.5
90	17.0	718.42	593.24	530.55	4.5	0.3	0.3	-8.4	23.3	18.4
91	17.1	964.45	389.42	335.19	3.6	0.5	1.9	23.0	-19.0	-25.2
92	17.1	830.02	435.28	305.03	2.8	0.1	0.1	5.9	-9.5	-31.9
93	17.1	1175.73	310.96	284.65	2.5	0.3	3.1	50.0	-35.4	-36.5
94	17.2	1135.49	333.70	291.71	3.0	0.2	3.0	44.8	-30.6	-34.9
95	18.8	847.40	480.25	431.83	2.0	1.3	2.7	8.1	-0.2	-3.7
96	19.0	815.17	464.04	375.20	0.8	0.1	0.5	4.0	-3.5	-16.3
97	19.0	988.78	445.44	366.69	1.4	2.6	2.1	26.1	-7.4	-18.2
98	19.1	874.77	485.18	430.91	1.9	1.0	0.5	11.6	0.9	-3.9
99	19.2	868.26	486.95	434.72	1.9	1.4	0.5	10.7	1.2	-3.0
100	19.3	854.13	431.53	364.57	1.0	2.0	1.0	8.9	-10.3	-18.7
101	19.4	885.49	479.28	422.80	2.9	0.9	1.2	12.9	-0.4	-5.7
102	19.4	1189.60	319.89	288.77	4.3	0.7	1.3	51.7	-33.5	-35.6
103	19.5	766.52	596.06	505.54	0.3	1.1	0.9	-2.2	23.9	12.8
104	19.6	827.09	519.77	445.36	3.2	2.2	1.9	5.5	8.0	-0.6
105	19.6	994.37	379.70	326.30	4.0	0.9	1.5	26.8	-21.1	-27.2
106	20.0	1018.64	393.08	327.43	0.7	0.4	0.9	29.9	-18.3	-26.9
107	20.2	881.92	478.63	423.68	3.0	1.4	1.3	12.5	-0.5	-5.5
108	20.6	671.25	536.03	432.52	1.8	0.4	0.3	-14.4	11.4	-3.5
109	20.7	852.07	436.35	368.86	1.2	2.2	1.1	8.7	-9.3	-17.7
110	20.8	960.89	377.30	319.16	1.5	3.2	0.8	22.6	-21.6	-28.8
111	21.0	944.61	351.06	286.41	0.7	1.1	2.9	20.5	-27.0	-36.1
112	21.3	1053.38	321.54	266.80	0.7	2.4	0.4	34.4	-33.2	-40.5
113	21.4	927.78	345.83	317.47	2.3	1.3	0.1	18.3	-28.1	-29.2
114	21.7	953.94	389.83	328.36	0.1	3.4	0.5	21.7	-19.0	-26.7
115	21.7	978.51	367.00	310.34	0.8	3.7	1.3	24.8	-23.7	-30.8
116	22.0	961.17	428.27	372.97	3.6	0.5	0.6	22.6	-11.0	-16.8
117	22.0	909.17	393.52	352.53	3.4	1.2	0.2	16.0	-18.2	-21.3
118	22.8	919.07	341.24	321.75	0.1	0.1	0.8	17.2	-29.1	-28.2
119	23.9	877.40	416.31	338.41	1.6	0.1	0.6	11.9	-13.5	-24.5
120	24.3	1171.84	287.02	264.76	0.9	0.9	1.5	49.5	-40.3	-40.9
121	25.7	847.80	482.89	426.16	1.3	1.2	0.3	8.1	0.4	-4.9
122	26.1	903.45	337.75	292.67	3.5	0.2	1.4	15.2	-29.8	-34.7
123	26.2	885.60	346.50	297.46	3.0	1.5	2.2	13.0	-28.0	-33.6
124	26.3	1057.10	357.00	289.11	4.0	0.4	0.3	34.8	-25.8	-35.5
125	26.9	837.47	483.94	428.95	1.2	1.3	0.2	6.8	0.6	-4.3
126	27.0	961.33	386.75	344.77	1.7	0.6	0.7	22.6	-19.6	-23.1
127	27.3	900.05	413.77	387.48	2.0	0.5	2.0	14.8	-14.0	-13.5
128	29.8	718.47	459.35	317.22	2.2	1.4	0.6	-8.4	-4.5	-29.2
129	33.4	730.20	392.13	287.61	2.6	1.4	1.0	-6.9	-18.5	-35.8
130	36.8	778.04	464.22	451.66	4.2	1.2	0.5	-0.8	-3.5	0.8

[a]Percent differences between the theoretical rotational constants and the experimentally assigned rotational constants of the tetrahydrate.

Table F.27. ωB97XD/Jun-cc-pVTZ refined CREST results of the pentahydrate.

	ΔE_0 /kJ mol^{-1}	A /MHz	B /MHz	C /MHz	μ_a /D	μ_b /D	μ_c /D	[a]ΔA /%	[a]ΔB /%	[a]ΔC /%
1	0.0	691.99	458.59	408.54	1.5	2.5	0.1	2.5	3.4	3.4
2	3.6	655.46	444.84	381.00	3.2	0.8	1.1	-2.9	0.3	-3.6
3	3.7	586.51	499.62	415.70	1.5	2.0	0.3	-13.1	12.6	5.2
4	4.0	581.53	502.27	415.57	0.6	1.4	2.2	-13.8	13.2	5.2
5	4.4	667.73	457.18	421.08	2.8	0.4	1.0	-1.1	3.1	6.6
6	5.3	682.64	435.22	391.83	2.4	1.1	2.4	1.2	-1.9	-0.8
7	5.4	680.58	439.86	390.59	3.2	1.8	0.8	0.9	-0.8	-1.1
8	5.5	708.77	446.92	413.46	1.7	3.4	0.8	5.0	0.8	4.7
9	5.8	590.17	498.34	421.41	1.4	0.8	0.2	-12.5	12.3	6.7
10	6.3	706.41	448.75	411.32	1.7	3.9	0.4	4.7	1.2	4.1
11	6.8	687.19	432.46	385.02	3.2	1.4	0.8	1.8	-2.5	-2.5
12	6.9	718.39	409.30	360.04	0.2	1.5	1.3	6.5	-7.7	-8.9

13	6.9	731.35	381.16	318.19	0.7	2.2	0.0	8.4	-14.1	-19.5
14	7.1	732.64	399.90	347.53	3.5	1.2	2.5	8.6	-9.8	-12.0
15	7.1	613.09	479.15	405.77	0.9	1.7	0.9	-9.1	8.0	2.7
16	7.1	735.42	397.82	350.98	4.1	0.1	1.3	9.0	-10.3	-11.2
17	7.4	717.55	412.03	357.11	0.3	0.3	0.2	6.3	-7.1	-9.6
18	7.5	830.50	370.04	351.80	2.8	2.4	0.5	23.1	-16.6	-10.9
19	7.6	596.77	494.44	421.44	1.6	1.6	1.9	-11.6	11.5	6.7
20	7.9	688.49	459.70	400.06	1.0	0.3	4.1	2.0	3.6	1.3
21	8.2	606.38	482.00	410.91	0.6	2.1	0.8	-10.1	8.7	4.0
22	8.2	692.43	455.90	399.72	0.2	1.5	3.3	2.6	2.8	1.2
23	8.4	662.65	447.23	399.56	1.1	2.3	3.2	-1.8	0.8	1.1
24	8.4	718.52	404.04	348.35	1.2	2.7	0.6	6.5	-8.9	-11.8
25	8.8	727.51	393.44	346.87	1.7	0.6	2.4	7.8	-11.3	-12.2
26	8.9	824.45	368.45	349.14	2.8	2.1	0.4	22.2	-16.9	-11.6
27	9.0	741.47	384.58	355.03	0.5	1.4	1.1	9.9	-13.3	-10.1
28	9.1	703.63	407.35	345.69	2.1	0.7	1.7	4.3	-8.2	-12.5
29	9.5	746.39	418.04	348.05	2.0	1.1	0.5	10.6	-5.8	-11.9
30	9.6	589.06	408.21	364.39	0.8	0.8	0.4	-12.7	-8.0	-7.8
31	9.7	745.99	382.39	320.27	0.8	1.7	1.3	10.5	-13.8	-18.9
32	9.8	625.03	449.80	396.88	0.8	1.5	2.5	-7.4	1.4	0.5
33	9.8	637.33	447.80	380.51	0.5	0.2	0.5	-5.6	1.0	-3.7
34	9.9	687.56	467.24	404.86	1.1	0.1	2.7	1.9	5.3	2.5
35	10.0	718.13	386.31	368.07	1.1	0.5	2.6	6.4	-12.9	-6.8
36	10.2	589.18	406.05	361.56	0.5	0.6	0.7	-12.7	-8.5	-8.5
37	10.2	713.62	430.06	402.58	2.0	2.5	2.8	5.7	-3.0	1.9
38	10.3	697.03	412.72	350.62	3.7	1.0	1.0	3.3	-7.0	-11.2
39	10.6	626.06	462.51	368.81	1.2	3.2	0.9	-7.2	4.3	-6.6
40	10.7	683.38	379.64	347.64	1.0	0.4	0.7	1.3	-14.4	-12.0
41	10.7	824.65	374.70	345.15	2.2	0.9	1.3	22.2	-15.5	-12.6
42	10.9	625.27	461.29	389.94	0.3	0.2	0.2	-7.3	4.0	-1.3
43	11.1	793.21	345.04	311.07	1.4	0.8	0.8	17.5	-22.2	-21.3
44	11.5	578.73	433.55	362.46	1.5	0.1	1.0	-14.2	-2.3	-8.2
45	11.6	734.17	423.67	356.91	1.4	2.1	1.0	8.8	-4.5	-9.7
46	11.9	728.58	385.21	320.59	0.5	2.5	0.1	8.0	-13.2	-18.8
47	12.0	744.02	385.01	332.94	3.3	1.1	0.1	10.3	-13.2	-15.7
48	12.0	601.56	485.17	356.68	0.6	2.3	0.6	-10.9	9.4	-9.7
49	12.3	698.77	404.20	347.86	4.1	0.4	0.2	3.5	-8.9	-11.9
50	12.3	651.48	406.83	354.13	2.2	0.3	0.8	-3.5	-8.3	-10.4
51	12.4	583.07	440.60	422.99	0.6	0.7	0.5	-13.6	-0.7	7.1
52	12.5	605.35	464.28	391.73	0.0	0.8	2.4	-10.3	4.7	-0.8
53	12.7	721.70	380.48	366.00	0.8	0.4	1.0	6.9	-14.2	-7.4
54	12.8	807.07	367.70	331.55	2.7	0.8	3.1	19.6	-17.1	-16.1
55	12.9	583.23	448.56	422.27	1.9	0.4	1.2	-13.6	1.1	6.9
56	12.9	629.78	416.56	393.52	3.0	0.7	0.7	-6.7	-6.1	-0.4
57	13.1	650.61	434.03	360.66	2.0	0.4	1.6	-3.6	-2.2	-8.7
58	13.3	813.94	339.43	270.01	3.1	0.9	1.0	20.6	-23.5	-31.7
59	13.5	664.59	451.35	414.28	1.4	1.6	2.9	-1.5	1.8	4.9
60	13.5	594.39	416.67	357.99	0.2	0.9	2.2	-11.9	-6.1	-9.4
61	13.5	817.50	338.09	269.17	3.2	0.7	1.0	21.1	-23.8	-31.9
62	13.5	601.76	385.53	364.56	1.1	0.6	0.7	-10.8	-13.1	-7.7
63	13.6	823.56	363.54	343.00	1.3	4.2	2.9	22.0	-18.0	-13.2
64	13.7	760.65	377.49	344.31	1.4	1.3	1.0	12.7	-14.9	-12.8
65	13.8	560.22	522.46	361.33	1.4	1.8	1.9	-17.0	17.8	-8.5
66	13.8	695.70	409.17	344.52	2.0	1.3	1.3	3.1	-7.8	-12.8
67	13.9	859.15	341.04	293.30	1.5	1.8	2.2	27.3	-23.1	-25.8
68	14.1	628.81	495.48	374.92	3.0	0.5	2.2	-6.8	11.7	-5.1
69	14.3	744.45	368.83	335.56	0.5	0.9	2.5	10.3	-16.9	-15.1
70	14.3	750.58	393.45	329.42	2.0	0.1	1.8	11.2	-11.3	-16.6
71	14.4	731.40	396.47	316.00	2.1	2.7	0.5	8.4	-10.6	-20.0
72	14.5	913.56	298.33	280.02	2.8	0.4	1.5	35.4	-32.7	-29.1
73	14.6	679.77	387.34	360.32	3.6	0.2	0.4	0.7	-12.7	-8.8
74	14.6	711.50	400.47	360.77	3.6	0.1	0.4	5.4	-9.7	-8.7
75	14.7	697.80	395.29	339.19	4.0	0.8	0.1	3.4	-10.9	-14.1
76	14.8	591.32	429.73	310.36	0.2	0.6	0.8	-12.4	-3.1	-21.4
77	14.8	685.63	390.57	371.77	1.2	1.0	0.5	1.6	-12.0	-5.9
78	14.8	696.29	403.94	324.94	3.0	1.2	1.4	3.2	-8.9	-17.7
79	15.0	630.45	396.52	295.95	1.2	0.6	0.1	-6.6	-10.6	-25.1
80	15.0	677.62	376.36	367.79	1.2	0.8	2.6	0.4	-15.2	-6.9
81	15.1	924.14	297.87	277.12	3.0	1.3	0.3	36.9	-32.8	-29.9
82	15.1	701.01	379.26	323.81	0.2	0.5	2.3	3.9	-14.5	-18.0

83	15.1	575.51	503.65	364.95	0.4	1.4	2.9	-14.7	13.5	-7.6
84	15.2	717.10	435.59	407.16	0.5	3.7	0.8	6.3	-1.8	3.1
85	15.3	632.67	401.17	352.21	0.4	1.8	2.0	-6.2	-9.6	-10.8
86	15.4	570.68	521.22	414.52	0.5	0.9	0.6	-15.4	17.5	4.9
87	15.4	693.31	395.69	300.12	0.7	1.0	0.8	2.7	-10.8	-24.0
88	15.5	765.10	382.78	366.55	1.3	1.9	0.5	13.4	-13.7	-7.2
89	15.5	645.08	395.86	313.35	0.1	1.8	0.8	-4.4	-10.8	-20.7
90	15.6	727.18	379.90	371.49	0.1	0.0	1.7	7.8	-14.4	-6.0
91	15.8	835.24	334.70	289.95	3.2	1.5	3.0	23.8	-24.5	-26.6
92	15.9	604.72	455.34	410.62	0.5	0.6	2.4	-10.4	2.7	3.9
93	15.9	681.09	422.32	382.98	0.5	1.0	0.5	0.9	-4.8	-3.1
94	16.0	640.96	409.45	326.60	1.8	1.6	1.9	-5.0	-7.7	-17.3
95	16.0	704.13	393.09	322.06	0.6	0.8	2.4	4.3	-11.4	-18.5
96	16.0	622.24	398.34	303.78	0.2	0.5	1.6	-7.8	-10.2	-23.1
97	16.1	794.25	335.04	293.48	0.3	1.0	2.0	17.7	-24.5	-25.7
98	16.2	736.11	394.91	362.97	1.0	0.6	0.3	9.1	-11.0	-8.1
99	16.4	638.87	434.24	367.91	1.7	0.8	3.1	-5.3	-2.1	-6.9
100	16.4	830.60	328.04	295.06	0.4	1.4	3.2	23.1	-26.0	-25.3
101	16.6	807.09	334.94	301.94	0.2	2.8	0.9	19.6	-24.5	-23.6
102	16.6	905.23	290.08	281.07	0.9	1.7	0.7	34.1	-34.6	-28.9
103	16.8	651.79	410.58	332.57	1.6	0.6	1.3	-3.4	-7.4	-15.8
104	16.8	706.30	397.74	323.32	0.6	0.3	2.1	4.7	-10.3	-18.2
105	17.1	899.16	282.59	253.62	1.3	2.3	1.7	33.2	-36.3	-35.8
106	17.1	642.63	436.45	375.72	1.6	0.9	0.9	-4.8	-1.6	-4.9
107	17.2	595.81	412.83	305.05	0.5	1.1	2.3	-11.7	-6.9	-22.8
108	17.2	571.11	447.15	390.43	1.1	0.3	2.2	-15.4	0.8	-1.2
109	17.2	838.47	332.55	315.52	0.5	0.9	2.4	24.3	-25.0	-20.1
110	17.3	732.12	423.30	342.68	1.3	2.2	0.0	8.5	-4.6	-13.3
111	17.3	729.16	401.83	369.95	0.3	1.5	2.4	8.1	-9.4	-6.4
112	17.4	582.37	526.77	421.06	1.1	1.1	3.3	-13.7	18.8	6.6
113	17.4	750.28	385.98	348.74	3.2	0.7	1.4	11.2	-13.0	-11.7
114	17.5	976.51	272.08	249.54	3.6	1.2	0.1	44.7	-38.7	-36.8
115	17.5	685.23	438.63	386.51	0.7	0.4	1.1	1.5	-1.1	-2.2
116	17.7	705.81	387.11	286.10	1.8	0.6	2.1	4.6	-12.7	-27.6
117	17.7	738.95	324.81	277.81	3.6	0.6	0.8	9.5	-26.8	-29.7
118	17.8	797.74	342.24	320.26	1.3	1.0	0.3	18.2	-22.8	-18.9
119	17.8	791.14	348.21	275.59	0.6	0.8	2.3	17.2	-21.5	-30.2
120	17.9	717.44	373.16	281.56	2.5	1.7	1.9	6.3	-15.9	-28.7
121	17.9	789.00	346.52	337.12	3.5	0.2	2.2	16.9	-21.9	-14.7
122	17.9	676.07	416.99	388.78	1.1	0.1	0.1	0.2	-6.0	-1.6
123	18.0	739.68	328.00	284.50	2.2	1.4	2.2	9.6	-26.1	-28.0
124	18.1	935.57	298.56	278.39	1.6	1.5	0.6	38.6	-32.7	-29.5
125	18.1	866.48	289.92	271.39	4.3	2.5	1.7	28.4	-34.6	-31.3
126	18.2	893.23	297.58	280.64	0.3	2.8	0.5	32.4	-32.9	-29.0
127	18.2	828.77	326.05	292.86	3.0	0.9	2.2	22.8	-26.5	-25.9
128	18.2	571.51	391.60	249.78	0.6	0.3	0.1	-15.3	-11.7	-36.8
129	18.3	873.02	296.55	260.23	0.3	0.5	1.9	29.4	-33.1	-34.1
130	18.3	560.12	422.76	279.22	1.3	0.8	0.3	-17.0	-4.7	-29.3
131	18.3	793.14	340.52	325.73	1.6	1.6	3.1	17.5	-23.2	-17.5
132	18.3	569.85	400.13	278.80	0.9	1.2	0.7	-15.6	-9.8	-29.4
133	18.5	510.97	416.74	255.34	0.5	0.4	0.1	-24.3	-6.1	-35.4
134	18.6	587.82	466.75	361.41	0.2	2.2	0.3	-12.9	5.2	-8.5
135	18.7	757.96	329.19	305.90	1.5	2.5	1.9	12.3	-25.8	-22.6
136	18.8	792.49	338.22	297.37	0.3	3.5	0.1	17.4	-23.8	-24.7
137	18.9	931.54	273.78	253.92	3.5	1.1	3.1	38.0	-38.3	-35.7
138	18.9	660.21	412.94	336.17	1.9	1.3	2.1	-2.2	-6.9	-14.9
139	19.0	688.97	348.90	280.18	0.4	0.5	1.6	2.1	-21.3	-29.1
140	19.1	824.59	330.70	267.94	0.1	1.1	1.1	22.2	-25.4	-32.2
141	19.1	756.93	352.30	281.93	2.4	2.0	0.3	12.2	-20.6	-28.6
142	19.2	674.64	413.23	381.54	0.1	0.4	1.0	0.0	-6.8	-3.4
143	19.3	668.55	405.96	300.33	2.1	0.4	0.1	-0.9	-8.5	-24.0
144	19.3	735.16	263.89	253.20	2.5	0.3	1.9	8.9	-40.5	-35.9
145	19.3	724.04	307.53	233.68	0.2	0.7	0.4	7.3	-30.7	-40.8
146	19.4	761.42	335.10	309.09	1.9	3.0	0.4	12.8	-24.5	-21.8
147	19.5	857.20	284.65	254.57	0.4	1.8	0.3	27.0	-35.8	-35.6
148	19.6	636.47	390.49	292.03	2.5	1.8	2.5	-5.7	-12.0	-26.1
149	19.6	894.14	297.77	257.52	5.5	1.4	2.0	32.5	-32.9	-34.8
150	19.7	628.05	360.56	260.60	0.9	0.2	0.7	-6.9	-18.7	-34.0
151	19.8	616.95	321.98	314.75	0.8	1.1	0.2	-8.6	-27.4	-20.3
152	19.8	562.25	398.64	275.46	0.2	0.6	1.3	-16.7	-10.1	-30.3

153	19.8	689.86	422.11	371.47	0.6	0.4	1.7	2.2	-4.8	-6.0
154	19.9	990.66	230.89	220.37	1.8	1.4	2.9	46.8	-47.9	-44.2
155	19.9	610.74	423.40	319.23	3.4	0.7	2.0	-9.5	-4.5	-19.2
156	20.0	1127.72	244.98	223.60	0.5	0.4	0.9	67.1	-44.8	-43.4
157	20.1	718.42	368.57	280.79	2.6	0.8	1.8	6.5	-16.9	-28.9
158	20.3	1116.84	244.68	223.28	0.4	0.1	0.9	65.5	-44.8	-43.5
159	20.5	840.06	308.58	257.96	3.2	0.2	0.4	24.5	-30.4	-34.7
160	20.5	906.96	277.33	253.21	1.7	1.1	0.6	34.4	-37.5	-35.9
161	20.7	775.02	347.53	339.49	0.6	2.0	2.4	14.8	-21.7	-14.1
162	20.8	690.97	388.13	290.08	0.8	0.3	1.3	2.4	-12.5	-26.6
163	20.9	968.31	220.41	211.31	3.6	2.2	1.1	43.5	-50.3	-46.5
164	20.9	729.39	396.17	367.64	0.6	0.0	1.5	8.1	-10.7	-6.9
165	21.0	713.07	404.54	367.84	0.4	2.4	1.6	5.7	-8.8	-6.9
166	21.1	619.55	318.54	310.22	2.6	0.8	1.1	-8.2	-28.2	-21.5
167	21.1	715.59	346.48	267.29	0.3	2.2	1.2	6.0	-21.9	-32.3
168	21.2	650.00	442.75	413.81	0.8	0.7	0.1	-3.7	-0.2	4.7
169	21.3	800.63	308.46	283.59	0.4	1.5	0.1	18.6	-30.5	-28.2
170	21.3	740.73	395.59	330.72	1.1	2.6	2.2	9.8	-10.8	-16.3
171	21.4	975.73	260.03	232.02	4.5	2.1	0.3	44.6	-41.4	-41.3
172	21.5	865.04	295.58	258.24	4.9	1.7	2.0	28.2	-33.4	-34.6
173	21.5	569.49	413.02	277.38	1.4	0.9	0.3	-15.6	-6.9	-29.8
174	21.6	670.92	397.69	296.64	1.8	1.8	0.4	-0.6	-10.3	-24.9
175	21.6	892.97	323.11	278.90	1.8	1.6	1.0	32.3	-27.2	-29.4
176	21.7	754.73	367.63	306.96	2.3	2.1	2.2	11.8	-17.1	-22.3
177	21.8	622.49	464.55	394.54	2.8	1.6	0.5	-7.8	4.7	-0.1
178	21.8	898.52	257.66	236.70	2.8	0.6	2.4	33.1	-41.9	-40.1
179	21.8	715.13	400.06	368.34	0.8	1.3	0.1	6.0	-9.8	-6.8
180	21.9	896.22	321.74	277.94	1.8	2.2	1.1	32.8	-27.5	-29.6
181	21.9	916.14	278.94	254.61	2.8	2.7	3.1	35.8	-37.1	-35.5
182	21.9	825.03	335.17	282.90	1.1	1.1	2.3	22.3	-24.4	-28.4
183	22.0	724.10	404.34	365.33	0.9	1.4	0.2	7.3	-8.8	-7.5
184	22.0	781.06	300.76	266.17	0.9	1.0	1.7	15.7	-32.2	-32.6
185	22.1	532.36	479.81	308.90	0.8	1.1	0.4	-21.1	8.2	-21.8
186	22.2	668.61	425.92	354.06	2.7	1.1	2.3	-0.9	-4.0	-10.4
187	22.3	864.92	313.37	282.05	0.9	1.6	3.3	28.2	-29.4	-28.6
188	22.4	864.25	287.26	255.44	1.2	2.8	1.8	28.1	-35.2	-35.3
189	22.5	758.26	319.45	276.70	0.7	0.2	1.4	12.4	-28.0	-30.0
190	22.7	718.08	352.06	303.57	2.3	3.2	0.7	6.4	-20.6	-23.2
191	22.7	707.16	353.76	310.78	1.3	2.4	2.6	4.8	-20.2	-21.3
192	22.7	1117.06	237.76	217.18	3.8	2.1	2.4	65.5	-46.4	-45.0
193	22.8	803.91	349.27	321.39	1.0	0.8	0.9	19.1	-21.3	-18.6
194	22.9	799.09	298.33	263.65	1.1	2.2	3.1	18.4	-32.7	-33.3
195	23.0	919.50	274.81	237.22	2.6	2.7	0.5	36.3	-38.0	-40.0
196	23.1	683.26	393.13	322.69	0.1	1.7	1.4	1.3	-11.4	-18.3
197	23.2	962.21	260.67	248.34	0.2	0.4	1.9	42.6	-41.2	-37.1
198	23.3	787.94	293.24	268.35	0.8	1.6	0.3	16.8	-33.9	-32.1
199	23.4	790.01	299.04	266.20	0.2	0.3	3.4	17.1	-32.6	-32.6
200	23.4	997.13	222.47	217.47	1.7	1.9	0.8	47.8	-49.8	-45.0
201	23.5	770.61	355.72	331.80	1.6	1.3	2.4	14.2	-19.8	-16.0
202	23.6	942.70	277.61	245.92	0.5	1.5	0.4	39.7	-37.4	-37.7
203	23.8	871.22	330.88	283.57	2.4	2.0	2.2	29.1	-25.4	-28.2
204	23.9	756.12	340.81	277.18	2.5	1.4	1.0	12.0	-23.2	-29.8
205	23.9	866.73	257.76	242.59	4.7	2.5	1.5	28.4	-41.9	-38.6
206	24.0	880.38	298.39	271.65	1.5	2.4	3.1	30.5	-32.7	-31.2
207	24.1	778.29	342.69	285.52	2.2	3.7	0.0	15.3	-22.7	-27.7
208	24.1	605.97	475.48	409.12	0.6	0.3	4.0	-10.2	7.2	3.6
209	24.1	648.76	420.30	317.84	0.8	1.5	2.1	-3.9	-5.2	-19.5
210	24.2	811.25	292.47	265.26	1.7	1.2	2.9	20.2	-34.1	-32.9
211	24.2	898.62	292.63	252.75	2.6	2.3	0.3	33.2	-34.0	-36.0
212	24.4	735.41	369.89	278.89	0.0	2.1	1.2	9.0	-16.6	-29.4
213	24.6	677.38	394.51	322.40	0.4	1.4	1.5	0.4	-11.1	-18.4
214	24.7	548.79	434.14	286.96	2.1	1.8	0.0	-18.7	-2.1	-27.4
215	24.9	840.59	302.52	256.62	0.8	0.4	1.5	24.6	-31.8	-35.0
216	25.1	850.48	313.88	269.46	1.8	1.7	1.6	26.0	-29.2	-31.8
217	25.3	650.38	387.68	277.63	3.8	1.5	0.8	-3.6	-12.6	-29.7
218	25.5	912.75	266.77	241.65	1.0	1.4	2.1	35.3	-39.9	-38.8
219	25.5	838.82	256.87	238.83	3.8	0.6	0.5	24.3	-42.1	-39.5
220	25.6	780.71	342.85	309.38	1.2	0.9	3.3	15.7	-22.7	-21.7
221	25.6	919.99	262.54	230.21	2.6	4.3	0.2	36.3	-40.8	-41.7
222	25.7	849.37	290.77	240.64	1.6	2.5	1.8	25.9	-34.4	-39.1

223	25.8	632.17	436.54	397.52	3.0	0.9	0.5	-6.3	-1.6	0.6
224	25.8	588.93	473.91	338.45	0.8	1.3	2.4	-12.7	6.8	-14.3
225	26.0	1104.60	240.59	219.15	3.3	2.3	2.4	63.7	-45.8	-44.5
226	26.1	894.03	315.28	265.25	1.6	3.6	0.8	32.5	-28.9	-32.9
227	26.3	698.04	386.04	286.29	1.7	3.3	0.3	3.4	-13.0	-27.5
228	26.4	846.03	291.36	241.04	3.1	2.9	0.5	25.4	-34.3	-39.0
229	26.4	1006.10	259.21	225.42	2.8	1.4	0.1	49.1	-41.6	-42.9
230	26.5	763.35	304.35	263.06	0.5	3.4	0.7	13.1	-31.4	-33.4
231	27.1	826.24	330.74	284.32	4.8	1.0	0.2	22.4	-25.4	-28.0
232	27.2	791.72	303.08	258.75	0.5	3.3	2.8	17.3	-31.7	-34.5
233	27.2	835.15	328.12	280.61	0.4	4.0	0.3	23.8	-26.0	-29.0
234	28.0	815.14	337.36	285.05	0.9	0.3	4.1	20.8	-23.9	-27.8
235	28.1	755.19	357.59	288.13	0.0	0.0	2.2	11.9	-19.4	-27.1
236	28.7	801.53	304.95	262.52	1.3	3.0	0.7	18.8	-31.3	-33.5
237	28.8	723.66	388.60	296.52	1.6	2.0	2.4	7.2	-12.4	-24.9
238	28.8	1005.45	254.82	224.39	0.8	2.2	3.0	49.0	-42.6	-43.2
239	29.9	759.00	348.60	284.11	0.7	2.0	3.3	12.5	-21.4	-28.1
240	30.6	819.00	289.31	244.26	5.2	1.0	0.2	21.4	-34.8	-38.2
241	30.9	726.50	327.61	255.03	2.5	0.1	1.4	7.7	-26.1	-35.4
242	31.7	710.88	364.68	302.87	2.4	2.2	1.4	5.3	-17.8	-23.3
243	32.0	981.37	273.28	241.09	1.5	0.9	0.2	45.4	-38.4	-39.0
244	33.7	701.69	329.44	290.78	1.4	2.4	2.5	4.0	-25.7	-26.4
245	34.1	1045.23	251.61	224.78	2.1	1.4	0.7	54.9	-43.3	-43.1

[a]Percent differences between the theoretical rotational constants and the experimentally assigned rotational constants of the pentahydrate.

Complete Crest Results – B3LYPD3BJ

Table F.28. B3LYP-D3BJ/def2-TZVP refined CREST results of the monohydrate.

	ΔE_0 /kJ mol^{-1}	A /MHz	B /MHz	C /MHz	μ_a /D	μ_b /D	μ_c /D	[a]ΔA /%	[a]ΔB /%	[a]ΔC /%	[b]ΔA /%	[b]ΔB /%	[b]ΔC /%
1	0.0	2298.63	792.57	593.16	5.4	0.2	0.0	0.6	1.7	1.4	23.8	-12.7	-3.7
2	4.6	1885.03	1004.80	667.27	0.6	2.7	1.5	-17.5	28.9	14.0	1.5	10.6	8.3
3	5.1	1803.45	955.70	649.05	5.5	0.3	0.3	-21.0	22.6	10.9	-2.9	5.2	5.4
4	6.2	1504.52	1171.26	813.05	2.1	0.0	2.4	-34.1	50.2	38.9	-19.0	29.0	32.0
5	6.3	1688.86	1109.02	765.53	0.2	1.1	1.9	-26.1	42.2	30.8	-9.1	22.1	24.3
6	6.6	1887.60	1000.07	666.96	1.0	3.3	1.5	-17.4	28.3	14.0	1.6	10.1	8.3
7	10.7	1922.62	957.46	643.27	4.7	1.2	0.0	-15.8	22.8	9.9	3.5	5.4	4.4
8	11.0	1470.97	1140.02	804.56	4.1	0.6	0.3	-35.6	46.2	37.5	-20.8	25.5	30.6
9	11.1	1322.93	1193.43	984.93	1.6	0.5	2.1	-42.1	53.1	68.3	-28.8	31.4	59.9
10	11.3	1342.74	1182.52	991.39	1.2	1.7	1.4	-41.2	51.7	69.4	-27.7	30.2	60.9
11	11.4	1720.52	963.07	663.21	2.8	0.7	1.5	-24.7	23.5	13.3	-7.4	6.0	7.7
12	11.4	1718.07	964.96	664.67	2.8	0.8	1.5	-24.8	23.8	13.6	-7.5	6.2	7.9
13	12.1	2274.62	791.18	591.25	4.5	1.5	1.3	-0.4	1.5	1.0	22.5	-12.9	-4.0
14	20.2	2304.75	781.16	587.18	2.5	0.2	0.0	0.9	0.2	0.3	24.1	-14.0	-4.7
15	24.2	2266.72	597.53	475.29	4.0	0.4	0.0	-0.8	-23.4	-18.8	22.0	-34.2	-22.8
16	25.2	1661.61	1057.86	731.65	3.6	0.7	1.5	-27.3	35.7	25.0	-10.5	16.5	18.8

[a(b)]Percent differences between the theoretical rotational constants and the experimentally assigned rotational constants for monohydrate 1(2).

Table F.29. B3LYP-D3BJ/def2-TZVP refined CREST results of the dihydrate.

	ΔE_0 /kJ mol^{-1}	A /MHz	B /MHz	C /MHz	μ_a /D	μ_b /D	μ_c /D	[a]ΔA /%	[a]ΔB /%	[a]ΔC /%
1	0.0	1423.72	716.28	603.88	1.2	0.3	1.9	3.1	0.3	-0.4
2	0.8	1451.37	690.72	571.41	2.1	2.0	1.3	5.1	-3.3	-5.8
3	3.0	1217.05	831.02	606.25	0.5	1.8	1.4	-11.9	16.4	0.0
4	3.5	1230.13	841.72	636.23	0.6	0.2	2.5	-10.9	17.9	4.9
5	5.2	1633.39	610.30	522.66	2.0	0.4	0.5	18.3	-14.5	-13.8
6	8.6	1680.29	563.02	475.28	2.2	0.3	0.7	21.7	-21.2	-21.6
7	13.9	1360.81	731.37	523.78	1.0	0.6	0.9	-1.5	2.4	-13.6
8	14.6	1491.47	660.72	507.12	0.1	1.0	1.0	8.0	-7.5	-16.4
9	15.1	1499.26	657.41	506.18	0.0	3.0	0.2	8.5	-7.9	-16.5
10	15.4	1332.22	753.57	546.93	2.6	2.0	2.3	-3.5	5.5	-9.8

11	16.5	1483.71	657.51	495.87	1.5	2.6	0.2	7.4	-7.9	-18.2
12	16.6	1081.56	816.27	507.32	1.9	2.3	0.6	-21.7	14.3	-16.3
13	22.3	1291.19	647.86	508.79	6.6	1.1	0.4	-6.5	-9.3	-16.1
14	23.2	1275.89	608.09	434.19	5.8	0.6	1.1	-7.6	-14.8	-28.4
15	23.7	1023.19	868.77	820.74	4.5	1.0	0.3	-25.9	21.7	35.3
16	24.2	1087.35	853.27	702.20	2.8	2.1	2.3	-21.3	19.5	15.8
17	24.3	1060.57	861.95	785.27	6.2	0.6	0.1	-23.2	20.7	29.5
18	27.8	1282.73	754.11	548.39	0.5	4.9	2.2	-7.1	5.6	-9.6
19	28.3	1337.63	715.61	618.78	2.8	1.7	0.6	-3.2	0.2	2.0
20	28.5	1039.63	858.11	827.52	0.7	1.8	5.1	-24.7	20.2	36.5
21	28.6	1285.58	655.75	510.36	3.9	2.0	0.0	-6.9	-8.2	-15.8
22	28.7	883.32	786.58	418.78	3.5	0.1	0.0	-36.0	10.1	-30.9
23	32.4	1466.41	613.11	499.22	4.7	2.8	2.2	6.2	-14.1	-17.7
24	38.4	1625.10	505.50	402.94	1.0	1.1	1.1	17.7	-29.2	-33.6

[a]Percent differences between the theoretical rotational constants and the experimentally assigned rotational constants of the dihydrate.

Table F.30. B3LYP-D3BJ/def2-TZVP refined CREST results of the trihydrate.

	ΔE_0 /kJ mol^{-1}	A /MHz	B /MHz	C /MHz	μ_a /D	μ_b /D	μ_c /D	[a]ΔA /%	[a]ΔB /%	[a]ΔC /%
1	0.0	1089.05	553.95	484.83	1.6	1.4	0.5	0.7	2.6	2.6
2	0.4	854.20	770.64	597.12	1.4	0.6	0.6	-21.0	42.7	26.4
3	1.0	1097.58	558.22	483.32	1.4	1.5	0.0	1.5	3.4	2.3
4	1.2	949.82	683.43	574.94	1.2	1.6	0.7	-12.1	26.6	21.7
5	1.3	868.32	757.59	606.03	0.1	1.0	0.4	-19.7	40.3	28.3
6	1.7	865.16	758.15	600.45	1.5	1.4	0.2	-20.0	40.4	27.1
7	1.7	948.43	685.77	582.38	0.2	2.3	0.1	-12.3	27.0	23.3
8	2.3	913.21	620.16	566.98	1.8	1.6	0.3	-15.5	14.9	20.0
9	3.2	929.50	631.05	568.37	2.1	1.9	0.2	-14.0	16.9	20.3
10	3.3	1354.15	428.07	398.11	1.6	1.5	0.1	25.3	-20.7	-15.7
11	3.4	895.82	748.79	660.85	0.4	1.9	0.4	-17.1	38.7	39.9
12	3.5	1224.24	465.08	372.80	2.9	0.0	0.4	13.2	-13.9	-21.1
13	3.5	1234.16	464.40	408.04	1.2	0.8	1.0	14.2	-14.0	-13.6
14	3.5	1230.96	466.00	409.31	1.1	0.8	1.0	13.9	-13.7	-13.4
15	3.7	1118.64	522.03	389.14	3.0	1.2	0.6	3.5	-3.3	-17.6
16	3.8	1107.23	513.57	458.29	1.9	1.4	0.6	2.4	-4.9	-3.0
17	3.9	1325.74	429.46	383.69	2.6	0.2	0.4	22.6	-20.5	-18.8
18	4.2	1191.55	486.71	398.16	2.7	0.3	0.2	10.2	-9.9	-15.7
19	4.2	1121.20	516.73	412.75	1.5	0.8	1.6	3.7	-4.3	-12.6
20	4.3	1329.59	482.60	423.55	1.8	0.3	2.3	23.0	-10.6	-10.4
21	4.4	953.83	699.39	641.53	0.3	1.0	0.2	-11.8	29.5	35.8
22	4.4	1338.80	416.76	363.40	2.5	0.4	0.3	23.8	-22.8	-23.1
23	4.5	1324.40	484.22	424.42	1.6	1.5	2.3	22.5	-10.3	-10.2
24	4.7	865.76	673.20	495.47	1.5	0.8	1.6	-19.9	24.7	4.9
25	4.8	970.76	607.74	571.04	2.0	0.7	1.6	-10.2	12.6	20.9
26	4.8	1001.33	585.27	478.27	0.4	0.4	1.8	-7.4	8.4	1.2
27	4.9	1120.46	531.09	421.36	2.0	0.1	0.8	3.6	-1.6	-10.8
28	6.1	985.89	663.96	578.23	0.0	0.6	1.2	-8.8	23.0	22.4
29	6.6	1218.49	474.58	417.27	2.2	1.7	0.7	12.7	-12.1	-11.7
30	6.7	1300.67	434.29	390.40	1.5	1.0	0.0	20.3	-19.6	-17.4
31	6.7	1125.62	540.02	450.76	2.1	0.6	1.1	4.1	0.0	-4.6
32	6.8	1090.30	570.20	463.48	2.1	0.7	1.0	0.9	5.6	-1.9
33	7.1	911.89	610.14	538.58	0.4	0.6	0.2	-15.7	13.0	14.0
34	7.2	1221.06	470.27	416.20	2.3	1.9	0.3	12.9	-12.9	-11.9
35	7.3	1215.26	475.59	419.23	3.2	0.0	0.1	12.4	-11.9	-11.3
36	7.5	1097.01	555.92	464.40	0.3	1.0	3.0	1.5	3.0	-1.7
37	7.6	1076.87	579.07	477.24	0.7	0.2	2.8	-0.4	7.2	1.0
38	7.9	923.52	609.82	535.59	0.5	0.4	0.5	-14.6	12.9	13.4
39	8.0	1124.24	517.99	385.46	4.3	1.8	2.2	4.0	-4.1	-18.4
40	8.5	1235.05	465.49	413.25	3.1	0.1	0.2	14.2	-13.8	-12.5
41	9.6	1127.91	518.12	388.40	2.8	1.2	1.0	4.3	-4.0	-17.8
42	9.8	909.80	601.52	543.96	1.7	0.8	1.5	-15.8	11.4	15.1
43	10.1	929.04	607.84	527.38	1.4	1.0	1.7	-14.1	12.6	11.6
44	10.4	1315.22	488.47	428.16	1.0	1.4	3.0	21.7	-9.5	-9.4
45	10.8	1221.08	467.45	367.36	3.0	0.2	0.4	12.9	-13.4	-22.3
46	12.2	1143.48	510.47	399.17	1.1	1.1	2.0	5.8	-5.5	-15.5
47	13.4	1114.41	518.56	387.36	1.4	1.0	1.7	3.1	-4.0	-18.0

48	13.5	1119.98	516.69	385.81	0.1	0.3	0.1	3.6	-4.3	-18.3
49	13.7	1160.20	491.21	392.50	2.2	1.0	2.2	7.3	-9.0	-16.9
50	14.2	867.81	712.92	560.38	1.4	0.5	1.4	-19.7	32.0	18.6
51	14.3	1068.44	644.98	555.56	3.1	0.6	1.3	-1.2	19.5	17.6
52	14.8	825.24	726.24	495.68	0.2	0.6	0.1	-23.7	34.5	4.9
53	15.7	1190.34	472.05	373.23	0.5	0.9	0.3	10.1	-12.6	-21.0
54	16.1	914.08	665.78	611.12	0.9	0.4	0.7	-15.4	23.3	29.3
55	16.2	947.11	662.29	600.71	3.6	0.5	0.5	-12.4	22.7	27.1
56	16.3	1272.89	483.18	404.53	3.9	0.3	0.3	17.7	-10.5	-14.4
57	16.3	1171.02	493.57	354.99	0.2	0.9	0.2	8.3	-8.6	-24.9
58	16.7	1091.84	529.98	385.34	1.1	1.0	1.5	1.0	-1.8	-18.4
59	16.8	793.93	711.66	447.95	1.3	2.5	0.5	-26.6	31.8	-5.2
60	17.4	809.25	737.62	491.63	1.5	1.6	2.0	-25.1	36.6	4.0
61	17.6	1334.61	464.03	411.18	1.8	2.8	0.4	23.4	-14.1	-13.0
62	17.7	1113.84	555.32	458.03	0.8	0.6	0.6	3.0	2.8	-3.1
63	18.6	1299.94	469.17	410.35	0.2	1.9	1.4	20.2	-13.1	-13.2
64	18.9	1121.44	516.41	470.50	0.2	0.6	0.6	3.7	-4.4	-0.4
65	19.0	1130.91	533.43	443.35	2.5	1.8	0.8	4.6	-1.2	-6.2
66	19.2	800.84	698.88	438.91	3.4	2.2	1.8	-25.9	29.4	-7.1
67	19.4	1181.97	516.70	420.62	0.5	2.2	0.0	9.3	-4.3	-11.0
68	19.9	1315.61	460.00	404.89	0.6	2.6	1.5	21.7	-14.8	-14.3
69	21.5	871.97	702.77	453.69	0.8	1.8	0.7	-19.3	30.2	-4.0
70	21.8	925.10	651.90	620.24	4.4	2.2	1.3	-14.4	20.7	31.3
71	22.2	1315.10	463.18	379.36	2.3	0.3	2.8	21.6	-14.2	-19.7
72	22.4	871.48	684.37	435.08	0.6	0.1	0.5	-19.4	26.7	-7.9
73	22.5	1007.85	616.51	451.63	0.5	1.5	0.5	-6.8	14.2	-4.4
74	22.8	1068.57	540.40	418.78	0.2	0.9	0.4	-1.2	0.1	-11.4
75	23.0	955.56	630.70	438.38	0.1	0.9	0.5	-11.6	16.8	-7.2
76	23.1	1083.43	523.51	374.64	3.8	1.8	0.2	0.2	-3.0	-20.7
77	23.4	1009.09	572.48	403.33	0.4	0.7	0.4	-6.7	6.0	-14.6
78	23.6	916.01	757.57	631.36	1.3	0.4	0.2	-15.3	40.3	33.6
79	24.3	942.80	643.06	597.01	2.7	1.0	0.1	-12.8	19.1	26.4
80	24.4	942.57	638.16	598.10	2.7	0.6	0.1	-12.8	18.2	26.6
81	24.7	1056.54	639.13	508.21	1.3	2.6	1.2	-2.3	18.4	7.6
82	25.8	1161.31	528.76	419.43	1.9	1.5	2.6	7.4	-2.1	-11.2
83	26.1	878.71	727.57	640.27	4.3	3.5	2.7	-18.7	34.7	35.5
84	26.3	1430.64	344.06	322.67	4.2	0.1	1.6	32.3	-36.3	-31.7
85	26.3	1441.09	344.74	322.43	4.3	0.0	1.5	33.3	-36.2	-31.8
86	26.7	1223.64	499.38	408.69	2.6	1.6	2.5	13.2	-7.5	-13.5
87	26.8	1097.03	539.36	517.84	3.6	2.0	0.5	1.5	-0.1	9.6
88	27.0	1346.79	395.26	336.90	4.9	0.1	0.1	24.6	-26.8	-28.7
89	27.2	1206.88	468.98	378.89	3.7	2.3	1.8	11.6	-13.1	-19.8
90	27.8	1174.12	422.70	394.20	0.0	0.1	0.0	8.6	-21.7	-16.6
91	27.9	1045.19	598.06	512.57	3.6	0.4	0.1	-3.3	10.8	8.5
92	28.0	1155.93	541.90	435.38	0.6	2.9	0.0	6.9	0.4	-7.9
93	28.0	1026.88	606.84	520.77	3.6	0.8	0.1	-5.0	12.4	10.2
94	28.2	1325.32	389.42	334.69	5.3	0.1	0.6	22.6	-27.9	-29.2
95	28.4	1041.83	518.14	447.14	0.6	2.0	0.0	-3.6	-4.0	-5.4
96	29.1	1248.30	440.74	356.28	3.0	2.8	1.8	15.5	-18.4	-24.6
97	29.2	737.32	679.64	383.18	3.9	0.3	0.5	-31.8	25.9	-18.9
98	30.8	1170.29	462.74	380.44	1.3	0.5	1.1	8.2	-14.3	-19.5
99	31.4	1286.70	446.61	359.21	0.9	2.9	0.4	19.0	-17.3	-24.0
100	31.8	879.84	704.74	606.05	2.8	2.1	0.2	-18.6	30.5	28.3
101	32.1	884.29	705.17	604.78	3.1	2.3	0.1	-18.2	30.6	28.0
102	33.1	1454.87	399.91	338.56	1.9	3.2	0.2	34.6	-25.9	-28.3
103	33.5	895.51	678.12	616.88	3.7	1.5	0.9	-17.2	25.6	30.6
104	35.2	1293.38	393.18	338.16	3.9	0.4	0.3	19.6	-27.2	-28.4
105	35.6	1330.28	383.69	328.03	1.5	0.7	0.6	23.0	-28.9	-30.6
106	35.7	1321.66	385.30	330.82	1.5	0.8	0.6	22.3	-28.6	-30.0
107	35.9	1270.03	407.89	351.82	2.0	0.3	0.6	17.5	-24.5	-25.5

[a]Percent differences between the theoretical rotational constants and the experimentally assigned rotational constants of the trihydrate.

Table F.31. B3LYP-D3BJ/def2-TZVP refined CREST results of the tetrahydrate.

	ΔE_0 /kJ mol^{-1}	A /MHz	B /MHz	C /MHz	μ_a /D	μ_b /D	μ_c /D	[a]ΔA /%	[a]ΔB /%	[a]ΔC /%
1	0.0	702.85	620.00	542.97	0.8	0.0	1.2	10.3	28.9	21.1
2	0.2	865.30	521.45	450.46	1.3	2.0	0.6	10.4	8.4	0.5
3	0.3	698.65	622.22	542.76	0.8	0.2	1.3	10.9	29.3	21.1
4	0.7	790.88	495.70	462.36	0.6	0.8	0.3	0.9	3.0	3.2
5	1.0	797.35	495.94	459.69	1.2	1.2	0.7	1.7	3.1	2.6
6	1.0	816.24	538.86	497.80	2.1	0.2	0.7	4.1	12.0	11.1
7	1.4	778.91	556.09	528.59	0.2	0.5	2.3	0.6	15.6	17.9
8	1.5	790.34	493.64	466.63	0.8	0.6	0.5	0.8	2.6	4.1
9	1.7	860.91	521.60	449.81	0.7	1.9	1.3	9.8	8.4	0.4
10	1.9	796.78	491.00	468.91	1.0	0.9	0.3	1.6	2.1	4.6
11	2.0	830.67	557.61	468.36	0.4	3.4	0.5	6.0	15.9	4.5
12	2.3	857.25	533.42	456.36	1.5	2.3	0.5	9.3	10.9	1.8
13	2.8	723.10	582.96	568.16	0.7	1.3	1.2	7.8	21.2	26.8
14	3.2	958.16	437.89	386.02	0.5	2.2	1.3	22.2	9.0	13.9
15	3.2	900.37	456.62	426.06	0.3	0.7	1.3	14.8	5.1	4.9
16	3.5	808.06	545.03	500.87	2.1	0.3	0.5	3.1	13.3	11.8
17	3.7	898.79	453.88	425.01	0.5	0.8	1.3	14.6	5.6	5.2
18	3.7	857.77	529.04	452.03	0.4	2.4	1.3	9.4	10.0	0.9
19	3.7	953.18	413.47	399.59	0.4	0.1	1.6	21.6	14.0	10.8
20	3.9	889.37	466.19	434.41	1.1	0.7	0.5	13.4	3.1	3.1
21	4.5	952.73	420.34	392.83	0.2	0.0	1.4	21.5	12.6	12.4
22	4.6	960.21	411.88	396.41	0.8	1.1	0.0	22.5	14.4	11.6
23	4.9	800.67	521.61	495.57	1.1	0.3	2.4	2.1	8.4	10.6
24	4.9	805.16	522.75	483.66	2.5	0.6	0.1	2.7	8.7	7.9
25	5.7	790.11	528.50	484.54	1.5	1.0	1.8	0.8	9.9	8.1
26	6.5	757.06	512.18	398.11	0.4	0.8	0.7	3.4	6.5	11.2
27	6.8	930.63	448.63	429.04	0.2	1.9	1.6	18.7	6.7	4.3
28	7.3	891.43	368.71	300.76	2.4	0.5	0.2	13.7	23.4	32.9
29	7.7	769.03	526.97	425.95	2.1	2.1	0.0	1.9	9.5	5.0
30	7.9	914.82	459.26	442.42	3.2	1.1	1.5	16.7	4.5	1.3
31	7.9	869.48	454.17	369.87	0.4	2.0	0.7	10.9	5.6	17.5
32	8.0	864.89	378.01	327.92	1.7	0.1	0.0	10.3	21.4	26.8
33	8.2	909.74	459.67	452.83	2.9	0.0	1.4	16.0	4.4	1.0
34	8.3	790.47	519.96	403.78	1.3	0.7	1.1	0.8	8.1	9.9
35	8.5	862.89	519.54	464.68	4.6	0.0	1.1	10.1	8.0	3.7
36	8.5	661.53	551.44	431.11	1.5	2.3	0.4	15.6	14.6	3.8
37	8.7	1011.45	446.39	372.96	2.0	1.4	0.6	29.0	7.2	16.8
38	8.8	876.56	449.83	365.74	1.3	1.1	0.6	11.8	6.5	18.4
39	8.8	649.66	558.17	434.84	1.4	2.1	0.3	17.1	16.0	3.0
40	8.9	807.31	588.78	478.54	0.7	0.8	3.3	3.0	22.4	6.8
41	8.9	1030.29	371.56	314.19	3.3	0.2	0.1	31.4	22.8	29.9
42	9.0	846.76	424.13	351.18	2.0	1.1	0.5	8.0	11.8	21.6
43	9.1	858.78	474.95	433.38	1.4	1.7	0.1	9.5	1.3	3.3
44	9.2	1024.21	439.85	368.66	2.1	1.2	0.3	30.6	8.6	17.7
45	9.2	793.80	453.31	403.10	0.0	0.8	0.4	1.3	5.8	10.1
46	9.4	890.52	441.09	365.78	0.2	2.1	0.5	13.6	8.3	18.4
47	9.6	849.77	485.87	414.83	3.0	0.1	0.1	8.4	1.0	7.4
48	9.8	851.90	524.43	442.04	0.7	4.4	1.6	8.7	9.0	1.4
49	10.0	983.26	436.22	377.78	2.6	3.4	1.8	25.4	9.3	15.7
50	10.0	852.10	392.16	342.31	1.7	0.5	0.2	8.7	18.5	23.6
51	10.1	843.10	387.19	380.91	2.4	0.8	0.2	7.5	19.5	15.0
52	10.2	880.90	401.49	346.52	1.2	1.3	0.8	12.4	16.5	22.7
53	10.5	836.95	497.06	403.47	0.6	0.7	4.7	6.8	3.3	10.0
54	10.5	836.16	481.47	390.08	1.0	1.6	1.2	6.7	0.1	13.0
55	10.8	850.09	512.34	458.36	4.6	0.4	1.2	8.4	6.5	2.3
56	10.9	1069.60	389.35	345.01	1.7	2.5	1.5	36.4	19.1	23.0
57	11.0	861.83	516.97	436.92	1.4	4.6	0.3	9.9	7.5	2.5
58	11.1	809.16	468.53	358.80	1.2	1.4	1.4	3.2	2.6	19.9
59	11.1	870.18	476.88	394.79	2.4	1.5	3.1	11.0	0.9	11.9
60	11.1	842.06	490.82	404.71	1.3	1.0	0.4	7.4	2.0	9.7
61	11.3	791.24	455.84	404.36	1.4	0.8	0.8	0.9	5.2	9.8
62	11.4	820.91	458.87	355.85	0.2	0.3	0.4	4.7	4.6	20.6
63	11.4	818.34	445.71	387.10	2.2	1.3	0.5	4.4	7.3	13.6
64	11.4	1026.76	371.31	315.77	3.1	0.5	0.0	31.0	22.8	29.5
65	11.6	1029.88	435.50	366.17	3.0	0.9	2.3	31.4	9.5	18.3
66	11.8	843.87	434.31	359.84	2.9	2.2	0.9	7.6	9.7	19.7
67	12.0	931.26	385.09	338.16	1.8	0.2	1.0	18.8	19.9	24.6
68	12.1	929.45	405.98	366.44	0.8	0.3	3.1	18.6	15.6	18.2

69	12.3	1073.29	386.18	342.27	1.2	1.3	3.2	36.9	19.7	23.6
70	12.5	843.93	411.83	350.05	1.8	1.3	0.3	7.6	14.4	21.9
71	12.5	813.06	482.22	406.43	0.2	0.2	1.0	3.7	0.2	9.3
72	12.7	957.51	437.86	380.93	3.0	1.7	2.9	22.1	9.0	15.0
73	12.8	1015.03	330.19	272.39	1.7	0.5	0.9	29.5	31.4	39.2
74	12.8	1049.67	319.08	261.65	1.4	0.1	1.0	33.9	33.7	41.6
75	13.1	954.25	426.25	385.31	2.2	3.2	1.7	21.7	11.4	14.0
76	13.1	901.10	410.54	374.40	0.8	0.5	1.4	14.9	14.7	16.5
77	13.1	962.85	344.46	307.66	2.2	1.0	0.9	22.8	28.4	31.4
78	13.2	881.05	459.83	367.25	3.6	0.7	2.0	12.4	4.4	18.1
79	13.3	1100.55	372.79	321.64	1.3	1.6	1.3	40.4	22.5	28.2
80	13.5	858.38	455.17	399.89	0.5	0.1	1.0	9.5	5.4	10.8
81	13.7	808.76	410.12	328.97	1.1	0.5	1.9	3.2	14.7	26.6
82	13.8	734.29	582.34	446.76	0.2	0.1	2.7	6.3	21.1	0.3
83	13.9	1063.81	405.85	351.45	0.8	3.2	0.3	35.7	15.6	21.6
84	14.0	880.14	476.36	414.12	2.2	2.2	0.1	12.3	1.0	7.6
85	14.1	980.56	392.84	318.09	1.2	1.2	1.0	25.1	18.3	29.0
86	14.2	871.79	488.32	426.04	2.9	1.9	0.2	11.2	1.5	4.9
87	14.2	973.87	429.39	383.18	2.0	0.1	4.2	24.2	10.7	14.5
88	14.5	908.47	356.94	281.99	3.9	0.1	1.4	15.9	25.8	37.1
89	14.7	1069.40	395.48	349.11	0.5	1.4	1.6	36.4	17.8	22.1
90	14.9	1083.83	354.41	316.21	3.8	1.4	2.2	38.2	26.3	29.4
91	15.3	954.72	380.82	299.58	2.4	0.6	2.4	21.8	20.8	33.2
92	15.4	788.62	462.56	356.14	1.1	2.5	1.8	0.6	3.8	20.5
93	15.5	721.74	472.54	433.28	0.8	1.4	0.9	7.9	1.8	3.3
94	16.0	960.46	388.58	335.23	3.9	0.3	2.0	22.5	19.2	25.2
95	16.3	814.40	531.14	461.51	1.9	1.2	1.4	3.9	10.4	3.0
96	16.7	778.03	483.32	368.83	0.3	0.5	0.7	0.8	0.5	17.7
97	16.7	960.98	420.41	380.71	2.3	0.8	0.3	22.6	12.6	15.1
98	16.7	867.89	416.86	326.58	2.4	1.5	1.5	10.7	13.3	27.1
99	16.8	1223.92	269.35	247.45	2.7	1.5	1.0	56.1	44.0	44.8
100	16.8	813.17	408.44	297.00	0.9	0.8	0.5	3.7	15.1	33.7
101	17.0	823.85	477.61	380.19	1.1	0.0	0.8	5.1	0.7	15.2
102	17.1	1123.81	337.71	294.25	2.7	0.5	3.0	43.3	29.8	34.3
103	17.1	773.31	487.33	368.63	0.2	1.4	1.5	1.4	1.3	17.8
104	17.2	971.37	381.73	298.54	1.9	1.0	0.4	23.9	20.6	33.4
105	17.3	888.93	447.24	418.54	3.0	2.9	1.4	13.4	7.0	6.6
106	17.4	719.69	592.32	526.64	4.4	0.2	0.8	8.2	23.1	17.5
107	17.5	804.45	545.24	452.08	1.3	1.8	1.4	2.6	13.3	0.9
108	17.5	886.64	457.36	379.89	1.4	0.7	1.6	13.1	4.9	15.2
109	17.6	1166.69	314.10	284.58	1.2	1.7	2.6	48.8	34.7	36.5
110	17.7	710.01	597.99	532.87	4.5	0.1	0.4	9.4	24.3	18.9
111	18.0	829.73	517.93	440.85	2.6	0.6	3.6	5.8	7.7	1.6
112	18.1	901.24	445.07	407.95	1.6	2.6	1.3	15.0	7.5	9.0
113	18.1	850.96	435.11	366.81	0.9	2.0	1.0	8.5	9.5	18.2
114	18.3	879.47	411.11	320.88	3.9	1.1	0.0	12.2	14.5	28.4
115	18.5	1053.13	357.69	311.68	4.2	3.2	0.1	34.3	25.6	30.5
116	18.6	1173.50	311.30	284.45	2.8	0.2	3.2	49.7	35.3	36.5
117	18.7	834.23	434.89	305.14	3.1	0.1	0.0	6.4	9.6	31.9
118	18.7	982.64	381.12	327.90	4.1	0.8	2.0	25.3	20.8	26.8
119	18.8	917.53	389.11	293.67	2.8	0.2	2.6	17.0	19.1	34.5
120	19.0	781.23	454.32	332.34	1.5	2.6	0.4	0.4	5.6	25.8
121	19.2	791.89	558.68	470.27	1.3	1.6	1.7	1.0	16.1	4.9
122	19.2	856.76	469.10	419.24	2.4	1.3	2.8	9.3	2.5	6.5
123	19.5	761.80	599.74	507.77	0.5	1.0	0.9	2.8	24.7	13.3
124	20.0	846.91	439.15	370.94	1.1	2.2	1.1	8.0	8.7	17.2
125	20.3	1166.87	319.66	284.48	4.7	0.7	1.3	48.8	33.5	36.5
126	20.3	1017.16	395.98	330.47	0.8	0.5	1.0	29.7	17.7	26.3
127	20.3	783.98	504.00	392.64	4.6	0.5	1.7	0.0	4.8	12.4
128	20.4	1184.73	320.48	288.61	4.7	0.7	1.2	51.1	33.4	35.6
129	20.5	1221.23	273.51	250.02	3.9	2.6	0.1	55.8	43.1	44.2
130	20.7	959.63	429.34	374.23	3.7	0.5	0.8	22.4	10.7	16.5
131	20.8	833.28	524.81	456.07	2.9	0.2	0.4	6.3	9.1	1.8
132	20.8	950.58	357.18	288.61	0.4	1.0	1.2	21.2	25.7	35.6
133	21.0	822.02	523.86	448.22	3.2	2.5	2.0	4.9	8.9	0.0
134	21.4	954.39	386.90	326.27	1.5	3.1	0.9	21.7	19.6	27.2
135	21.5	939.53	356.01	297.25	0.8	1.2	3.3	19.8	26.0	33.7
136	21.7	854.31	493.13	441.60	1.7	1.0	0.5	9.0	2.5	1.5
137	21.7	837.37	494.16	448.50	1.6	1.3	0.4	6.8	2.7	0.1
138	22.0	1078.92	318.79	263.87	0.6	2.4	0.5	37.6	33.7	41.1

139	22.4	859.76	483.92	432.51	3.0	1.4	1.3	9.7	0.6	3.5
140	22.8	952.91	393.99	331.02	0.1	3.6	0.7	21.5	18.1	26.1
141	23.2	976.09	450.51	368.89	2.1	3.2	2.0	24.5	6.3	17.7
142	24.3	930.34	410.71	388.74	3.8	1.8	0.4	18.7	14.6	13.3
143	24.3	675.03	539.48	436.96	2.0	0.4	0.4	13.9	12.1	2.5
144	24.4	921.57	345.78	318.46	2.4	1.4	0.2	17.5	28.1	28.9
145	24.5	924.20	342.13	325.43	0.2	0.2	0.9	17.9	28.9	27.4
146	24.7	886.94	413.31	337.56	1.9	0.1	0.5	13.1	14.1	24.7
147	25.0	774.29	520.25	485.50	0.0	0.6	1.3	1.2	8.1	8.3
148	25.5	923.80	386.99	348.81	3.8	1.4	0.4	17.8	19.6	22.2
149	25.6	766.18	509.21	378.35	0.1	0.8	1.0	2.3	5.9	15.6
150	26.2	1057.81	355.87	315.55	2.8	2.8	0.4	34.9	26.0	29.6
151	26.5	730.07	499.04	342.25	0.2	0.6	1.5	6.9	3.7	23.6
152	26.7	672.02	605.01	565.22	4.1	0.5	0.7	14.3	25.8	26.1
153	27.3	668.70	598.88	549.53	1.7	1.4	1.7	14.7	24.5	22.6
154	27.9	1043.24	366.60	297.65	4.2	0.2	0.1	33.1	23.8	33.6
155	28.3	979.76	409.73	319.38	0.5	3.5	0.3	25.0	14.8	28.7
156	28.4	1173.35	284.76	261.73	1.1	0.9	1.5	49.7	40.8	41.6
157	28.7	808.62	427.53	311.61	4.2	0.8	1.5	3.1	11.1	30.5
158	29.1	746.06	514.30	347.48	0.4	1.0	0.1	4.8	6.9	22.5
159	29.4	851.58	476.67	420.16	1.2	1.1	0.4	8.6	0.9	6.3
160	29.7	1041.76	306.24	271.58	2.7	0.1	0.1	32.9	36.3	39.4
161	29.7	957.69	342.46	323.41	4.4	1.1	0.3	22.2	28.8	27.8
162	29.8	956.40	341.00	297.52	3.0	2.0	1.2	22.0	29.1	33.6
163	30.4	907.30	337.25	292.37	3.6	0.0	1.4	15.7	29.9	34.8
164	31.3	729.59	459.17	325.37	2.3	1.5	0.8	6.9	4.5	27.4
165	31.7	875.81	411.68	391.78	1.9	0.6	2.2	11.7	14.4	12.6
166	31.7	800.85	450.98	424.00	1.7	0.1	1.8	2.2	6.3	5.4
167	32.2	870.87	452.45	355.20	0.7	1.8	0.8	11.1	5.9	20.7
168	32.9	1027.53	309.53	274.39	2.4	0.3	0.1	31.1	35.7	38.8
169	34.4	1014.48	337.59	293.86	2.5	0.4	0.4	29.4	29.8	34.4
170	35.0	1011.72	336.14	293.47	4.7	1.3	0.6	29.0	30.1	34.5
171	35.2	1017.22	335.04	292.17	4.5	1.3	0.6	29.7	30.4	34.8
172	36.2	893.57	419.19	313.46	0.4	0.1	2.6	14.0	12.9	30.1
173	37.2	1139.18	258.43	221.56	2.5	1.3	0.0	45.3	46.3	50.6
174	40.4	772.13	469.18	452.33	4.2	1.1	0.7	1.5	2.5	0.9

[a]Percent differences between the theoretical rotational constants and the experimentally assigned rotational constants of the tetrahydrate.

Table F.32. B3LYP-D3BJ/def2-TZVP refined CREST results of the pentahydrate.

	ΔE_0 /kJ mol^{-1}	A /MHz	B /MHz	C /MHz	μ_a /D	μ_b /D	μ_c /D	[a]ΔA /%	[a]ΔB /%	[a]ΔC /%
1	0.0	691.99	458.59	408.54	1.5	2.5	0.1	2.5	3.4	3.4
2	3.6	655.46	444.84	381.00	3.2	0.8	1.1	-2.9	0.3	-3.6
3	3.7	586.51	499.62	415.70	1.5	2.0	0.3	-13.1	12.6	5.2
4	4.0	581.53	502.27	415.57	0.6	1.4	2.2	-13.8	13.2	5.2
5	4.4	667.73	457.18	421.08	2.8	0.4	1.0	-1.1	3.1	6.6
6	5.3	682.64	435.22	391.83	2.4	1.1	2.4	1.2	-1.9	-0.8
7	5.4	680.58	439.86	390.59	3.2	1.8	0.8	0.9	-0.8	-1.1
8	5.5	708.77	446.92	413.46	1.7	3.4	0.8	5.0	0.8	4.7
9	5.8	590.17	498.34	421.41	1.4	0.8	0.2	-12.5	12.3	6.7
10	6.3	706.41	448.75	411.32	1.7	3.9	0.4	4.7	1.2	4.1
11	6.8	687.19	432.46	385.02	3.2	1.4	0.8	1.8	-2.5	-2.5
12	6.9	718.39	409.30	360.04	0.2	1.5	1.3	6.5	-7.7	-8.9
13	6.9	731.35	381.16	318.19	0.7	2.2	0.0	8.4	-14.1	-19.5
14	7.1	732.64	399.90	347.53	3.5	1.2	2.5	8.6	-9.8	-12.0
15	7.1	613.09	479.15	405.77	0.9	1.7	0.9	-9.1	8.0	2.7
16	7.1	735.42	397.82	350.98	4.1	0.1	1.3	9.0	-10.3	-11.2
17	7.4	717.55	412.03	357.11	0.3	0.3	0.2	6.3	-7.1	-9.6
18	7.5	830.50	370.04	351.80	2.8	2.4	0.5	23.1	-16.6	-10.9
19	7.6	596.77	494.44	421.44	1.6	1.6	1.9	-11.6	11.5	6.7
20	7.9	688.49	459.70	400.06	1.0	0.3	4.1	2.0	3.6	1.3
21	8.2	606.38	482.00	410.91	0.6	2.1	0.8	-10.1	8.7	4.0
22	8.2	692.43	455.90	399.72	0.2	1.5	3.3	2.6	2.8	1.2
23	8.4	662.65	447.23	399.56	1.1	2.3	3.2	-1.8	0.8	1.1
24	8.4	718.52	404.04	348.35	1.2	2.7	0.6	6.5	-8.9	-11.8

25	8.8	727.51	393.44	346.87	1.7	0.6	2.4	7.8	-11.3	-12.2
26	8.9	824.45	368.45	349.14	2.8	2.1	0.4	22.2	-16.9	-11.6
27	9.0	741.47	384.58	355.03	0.5	1.4	1.1	9.9	-13.3	-10.1
28	9.1	703.63	407.35	345.69	2.1	0.7	1.7	4.3	-8.2	-12.5
29	9.5	746.39	418.04	348.05	2.0	1.1	0.5	10.6	-5.8	-11.9
30	9.6	589.06	408.21	364.39	0.8	0.8	0.4	-12.7	-8.0	-7.8
31	9.7	745.99	382.39	320.27	0.8	1.7	1.3	10.5	-13.8	-18.9
32	9.8	625.03	449.80	396.88	0.8	1.5	2.5	-7.4	1.4	0.5
33	9.8	637.33	447.80	380.51	0.5	0.2	0.5	-5.6	1.0	-3.7
34	9.9	687.56	467.24	404.86	1.1	0.1	2.7	1.9	5.3	2.5
35	10.0	718.13	386.31	368.07	1.1	0.5	2.6	6.4	-12.9	-6.8
36	10.2	589.18	406.05	361.56	0.5	0.6	0.7	-12.7	-8.5	-8.5
37	10.2	713.62	430.06	402.58	2.0	2.5	2.8	5.7	-3.0	1.9
38	10.3	697.03	412.72	350.62	3.7	1.0	1.0	3.3	-7.0	-11.2
39	10.6	626.06	462.51	368.81	1.2	3.2	0.9	-7.2	4.3	-6.6
40	10.7	683.38	379.64	347.64	1.0	0.4	0.7	1.3	-14.4	-12.0
41	10.7	824.65	374.70	345.15	2.2	0.9	1.3	22.2	-15.5	-12.6
42	10.9	625.27	461.29	389.94	0.3	0.2	0.2	-7.3	4.0	-1.3
43	11.1	793.21	345.04	311.07	1.4	0.8	0.8	17.5	-22.2	-21.3
44	11.5	578.73	433.55	362.46	1.5	0.1	1.0	-14.2	-2.3	-8.2
45	11.6	734.17	423.67	356.91	1.4	2.1	1.0	8.8	-4.5	-9.7
46	11.9	728.58	385.21	320.59	0.5	2.5	0.1	8.0	-13.2	-18.8
47	12.0	744.02	385.01	332.94	3.3	1.1	0.1	10.3	-13.2	-15.7
48	12.0	601.56	485.17	356.68	0.6	2.3	0.6	-10.9	9.4	-9.7
49	12.3	698.77	404.20	347.86	4.1	0.4	0.2	3.5	-8.9	-11.9
50	12.3	651.48	406.83	354.13	2.2	0.3	0.8	-3.5	-8.3	-10.4
51	12.4	583.07	440.60	422.99	0.6	0.7	0.5	-13.6	-0.7	7.1
52	12.5	605.35	464.28	391.73	0.0	0.8	2.4	-10.3	4.7	-0.8
53	12.7	721.70	380.48	366.00	0.8	0.4	1.0	6.9	-14.2	-7.4
54	12.8	807.07	367.70	331.55	2.7	0.8	3.1	19.6	-17.1	-16.1
55	12.9	583.23	448.56	422.27	1.9	0.4	1.2	-13.6	1.1	6.9
56	12.9	629.78	416.56	393.52	3.0	0.7	0.7	-6.7	-6.1	-0.4
57	13.1	650.61	434.03	360.66	2.0	0.4	1.6	-3.6	-2.2	-8.7
58	13.3	813.94	339.43	270.01	3.1	0.9	1.0	20.6	-23.5	-31.7
59	13.5	664.59	451.35	414.28	1.4	1.6	2.9	-1.5	1.8	4.9
60	13.5	594.39	416.67	357.99	0.2	0.9	2.2	-11.9	-6.1	-9.4
61	13.5	817.50	338.09	269.17	3.2	0.7	1.0	21.1	-23.8	-31.9
62	13.5	601.76	385.53	364.56	1.1	0.6	0.7	-10.8	-13.1	-7.7
63	13.6	823.56	363.54	343.00	1.3	4.2	2.9	22.0	-18.0	-13.2
64	13.7	760.65	377.49	344.31	1.4	1.3	1.0	12.7	-14.9	-12.8
65	13.8	560.22	522.46	361.33	1.4	1.8	1.9	-17.0	17.8	-8.5
66	13.8	695.70	409.17	344.52	2.0	1.3	1.3	3.1	-7.8	-12.8
67	13.9	859.15	341.04	293.30	1.5	1.8	2.2	27.3	-23.1	-25.8
68	14.1	628.81	495.48	374.92	3.0	0.5	2.2	-6.8	11.7	-5.1
69	14.3	744.45	368.83	335.56	0.5	0.9	2.5	10.3	-16.9	-15.1
70	14.3	750.58	393.45	329.42	2.0	0.1	1.8	11.2	-11.3	-16.6
71	14.4	731.40	396.47	316.00	2.1	2.7	0.5	8.4	-10.6	-20.0
72	14.5	913.56	298.33	280.02	2.8	0.4	1.5	35.4	-32.7	-29.1
73	14.6	679.77	387.34	360.32	3.6	0.2	0.4	0.7	-12.7	-8.8
74	14.6	711.50	400.47	360.77	3.6	0.1	0.4	5.4	-9.7	-8.7
75	14.7	697.80	395.29	339.19	4.0	0.8	0.1	3.4	-10.9	-14.1
76	14.8	591.32	429.73	310.36	0.2	0.6	0.8	-12.4	-3.1	-21.4
77	14.8	685.63	390.57	371.77	1.2	1.0	0.5	1.6	-12.0	-5.9
78	14.8	696.29	403.94	324.94	3.0	1.2	1.4	3.2	-8.9	-17.7
79	15.0	630.45	396.52	295.95	1.2	0.6	0.1	-6.6	-10.6	-25.1
80	15.0	677.62	376.36	367.79	1.2	0.8	2.6	0.4	-15.2	-6.9
81	15.1	924.14	297.87	277.12	3.0	1.3	0.3	36.9	-32.8	-29.9
82	15.1	701.01	379.26	323.81	0.2	0.5	2.3	3.9	-14.5	-18.0
83	15.1	575.51	503.65	364.95	0.4	1.4	2.9	-14.7	13.5	-7.6
84	15.2	717.10	435.59	407.16	0.5	3.7	0.8	6.3	-1.8	3.1
85	15.3	632.67	401.17	352.21	0.4	1.8	2.0	-6.2	-9.6	-10.8
86	15.4	570.68	521.22	414.52	0.5	0.9	0.6	-15.4	17.5	4.9
87	15.4	693.31	395.69	300.12	0.7	1.0	0.8	2.7	-10.8	-24.0
88	15.5	765.10	382.78	366.55	1.3	1.9	0.5	13.4	-13.7	-7.2
89	15.5	645.08	395.86	313.35	0.1	1.8	0.8	-4.4	-10.8	-20.7
90	15.6	727.18	379.90	371.49	0.1	0.0	1.7	7.8	-14.4	-6.0
91	15.8	835.24	334.70	289.95	3.2	1.5	3.0	23.8	-24.5	-26.6
92	15.9	604.72	455.34	410.62	0.5	0.6	2.4	-10.4	2.7	3.9
93	15.9	681.09	422.32	382.98	0.5	1.0	0.5	0.9	-4.8	-3.1
94	16.0	640.96	409.45	326.60	1.8	1.6	1.9	-5.0	-7.7	-17.3

95	16.0	704.13	393.09	322.06	0.6	0.8	2.4	4.3	-11.4	-18.5
96	16.0	622.24	398.34	303.78	0.2	0.5	1.6	-7.8	-10.2	-23.1
97	16.1	794.25	335.04	293.48	0.3	1.0	2.0	17.7	-24.5	-25.7
98	16.2	736.11	394.91	362.97	1.0	0.6	0.3	9.1	-11.0	-8.1
99	16.4	638.87	434.24	367.91	1.7	0.8	3.1	-5.3	-2.1	-6.9
100	16.4	830.60	328.04	295.06	0.4	1.4	3.2	23.1	-26.0	-25.3
101	16.6	807.09	334.94	301.94	0.2	2.8	0.9	19.6	-24.5	-23.6
102	16.6	905.23	290.08	281.07	0.9	1.7	0.7	34.1	-34.6	-28.9
103	16.8	651.79	410.58	332.57	1.6	0.6	1.3	-3.4	-7.4	-15.8
104	16.8	706.30	397.74	323.32	0.6	0.3	2.1	4.7	-10.3	-18.2
105	17.1	899.16	282.59	253.62	1.3	2.3	1.7	33.2	-36.3	-35.8
106	17.1	642.63	436.45	375.72	1.6	0.9	0.9	-4.8	-1.6	-4.9
107	17.2	595.81	412.83	305.05	0.5	1.1	2.3	-11.7	-6.9	-22.8
108	17.2	571.11	447.15	390.43	1.1	0.3	2.2	-15.4	0.8	-1.2
109	17.2	838.47	332.55	315.52	0.5	0.9	2.4	24.3	-25.0	-20.1
110	17.3	732.12	423.30	342.68	1.3	2.2	0.0	8.5	-4.6	-13.3
111	17.3	729.16	401.83	369.95	0.3	1.5	2.4	8.1	-9.4	-6.4
112	17.4	582.37	526.77	421.06	1.1	1.1	3.3	-13.7	18.8	6.6
113	17.4	750.28	385.98	348.74	3.2	0.7	1.4	11.2	-13.0	-11.7
114	17.5	976.51	272.08	249.54	3.6	1.2	0.1	44.7	-38.7	-36.8
115	17.5	685.23	438.63	386.51	0.7	0.4	1.1	1.5	-1.1	-2.2
116	17.7	705.81	387.11	286.10	1.8	0.6	2.1	4.6	-12.7	-27.6
117	17.7	738.95	324.81	277.81	3.6	0.6	0.8	9.5	-26.8	-29.7
118	17.8	797.74	342.24	320.26	1.3	1.0	0.3	18.2	-22.8	-18.9
119	17.8	791.14	348.21	275.59	0.6	0.8	2.3	17.2	-21.5	-30.2
120	17.9	717.44	373.16	281.56	2.5	1.7	1.9	6.3	-15.9	-28.7
121	17.9	789.00	346.52	337.12	3.5	0.2	2.2	16.9	-21.9	-14.7
122	17.9	676.07	416.99	388.78	1.1	0.1	0.1	0.2	-6.0	-1.6
123	18.0	739.68	328.00	284.50	2.2	1.4	2.2	9.6	-26.1	-28.0
124	18.1	935.57	298.56	278.39	1.6	1.5	0.6	38.6	-32.7	-29.5
125	18.1	866.48	289.92	271.39	4.3	2.5	1.7	28.4	-34.6	-31.3
126	18.2	893.23	297.58	280.64	0.3	2.8	0.5	32.4	-32.9	-29.0
127	18.2	828.77	326.05	292.86	3.0	0.9	2.2	22.8	-26.5	-25.9
128	18.2	571.51	391.60	249.78	0.6	0.3	0.1	-15.3	-11.7	-36.8
129	18.3	873.02	296.55	260.23	0.3	0.5	1.9	29.4	-33.1	-34.1
130	18.3	560.12	422.76	279.22	1.3	0.8	0.3	-17.0	-4.7	-29.3
131	18.3	793.14	340.52	325.73	1.6	1.6	3.1	17.5	-23.2	-17.5
132	18.3	569.85	400.13	278.80	0.9	1.2	0.7	-15.6	-9.8	-29.4
133	18.5	510.97	416.74	255.34	0.5	0.4	0.1	-24.3	-6.1	-35.4
134	18.6	587.82	466.75	361.41	0.2	2.2	0.3	-12.9	5.2	-8.5
135	18.7	757.96	329.19	305.90	1.5	2.5	1.9	12.3	-25.8	-22.6
136	18.8	792.49	338.22	297.37	0.3	3.5	0.1	17.4	-23.8	-24.7
137	18.9	931.54	273.78	253.92	3.5	1.1	3.1	38.0	-38.3	-35.7
138	18.9	660.21	412.94	336.17	1.9	1.3	2.1	-2.2	-6.9	-14.9
139	19.0	688.97	348.90	280.18	0.4	0.5	1.6	2.1	-21.3	-29.1
140	19.1	824.59	330.70	267.94	0.1	1.1	1.1	22.2	-25.4	-32.2
141	19.1	756.93	352.30	281.93	2.4	2.0	0.3	12.2	-20.6	-28.6
142	19.2	674.64	413.23	381.54	0.1	0.4	1.0	0.0	-6.8	-3.4
143	19.3	668.55	405.96	300.33	2.1	0.4	0.1	-0.9	-8.5	-24.0
144	19.3	735.16	263.89	253.20	2.5	0.3	1.9	8.9	-40.5	-35.9
145	19.3	724.04	307.53	233.68	0.2	0.7	0.4	7.3	-30.7	-40.8
146	19.4	761.42	335.10	309.09	1.9	3.0	0.4	12.8	-24.5	-21.8
147	19.5	857.20	284.65	254.57	0.4	1.8	0.3	27.0	-35.8	-35.6
148	19.6	636.47	390.49	292.03	2.5	1.8	2.5	-5.7	-12.0	-26.1
149	19.6	894.14	297.77	257.52	5.5	1.4	2.0	32.5	-32.9	-34.8
150	19.7	628.05	360.56	260.60	0.9	0.2	0.7	-6.9	-18.7	-34.0
151	19.8	616.95	321.98	314.75	0.8	1.1	0.2	-8.6	-27.4	-20.3
152	19.8	562.25	398.64	275.46	0.2	0.6	1.3	-16.7	-10.1	-30.3
153	19.8	689.86	422.11	371.47	0.6	0.4	1.7	2.2	-4.8	-6.0
154	19.9	990.66	230.89	220.37	1.8	1.4	2.9	46.8	-47.9	-44.2
155	19.9	610.74	423.40	319.23	3.4	0.7	2.0	-9.5	-4.5	-19.2
156	20.0	1127.72	244.98	223.60	0.5	0.4	0.9	67.1	-44.8	-43.4
157	20.1	718.42	368.57	280.79	2.6	0.8	1.8	6.5	-16.9	-28.9
158	20.3	1116.84	244.68	223.28	0.4	0.1	0.9	65.5	-44.8	-43.5
159	20.5	840.06	308.58	257.96	3.2	0.2	0.4	24.5	-30.4	-34.7
160	20.5	906.96	277.33	253.21	1.7	1.1	0.6	34.4	-37.5	-35.9
161	20.7	775.02	347.53	339.49	0.6	2.0	2.4	14.8	-21.7	-14.1
162	20.8	690.97	388.13	290.08	0.8	0.3	1.3	2.4	-12.5	-26.6
163	20.9	968.31	220.41	211.31	3.6	2.2	1.1	43.5	-50.3	-46.5
164	20.9	729.39	396.17	367.64	0.6	0.0	1.5	8.1	-10.7	-6.9

165	21.0	713.07	404.54	367.84	0.4	2.4	1.6	5.7	-8.8	-6.9
166	21.1	619.55	318.54	310.22	2.6	0.8	1.1	-8.2	-28.2	-21.5
167	21.1	715.59	346.48	267.29	0.3	2.2	1.2	6.0	-21.9	-32.3
168	21.2	650.00	442.75	413.81	0.8	0.7	0.1	-3.7	-0.2	4.7
169	21.3	800.63	308.46	283.59	0.4	1.5	0.1	18.6	-30.5	-28.2
170	21.3	740.73	395.59	330.72	1.1	2.6	2.2	9.8	-10.8	-16.3
171	21.4	975.73	260.03	232.02	4.5	2.1	0.3	44.6	-41.4	-41.3
172	21.5	865.04	295.58	258.24	4.9	1.7	2.0	28.2	-33.4	-34.6
173	21.5	569.49	413.02	277.38	1.4	0.9	0.3	-15.6	-6.9	-29.8
174	21.6	670.92	397.69	296.64	1.8	1.8	0.4	-0.6	-10.3	-24.9
175	21.6	892.97	323.11	278.90	1.8	1.6	1.0	32.3	-27.2	-29.4
176	21.7	754.73	367.63	306.96	2.3	2.1	2.2	11.8	-17.1	-22.3
177	21.8	622.49	464.55	394.54	2.8	1.6	0.5	-7.8	4.7	-0.1
178	21.8	898.52	257.66	236.70	2.8	0.6	2.4	33.1	-41.9	-40.1
179	21.8	715.13	400.06	368.34	0.8	1.3	0.1	6.0	-9.8	-6.8
180	21.9	896.22	321.74	277.94	1.8	2.2	1.1	32.8	-27.5	-29.6
181	21.9	916.14	278.94	254.61	2.8	2.7	3.1	35.8	-37.1	-35.5
182	21.9	825.03	335.17	282.90	1.1	1.1	2.3	22.3	-24.4	-28.4
183	22.0	724.10	404.34	365.33	0.9	1.4	0.2	7.3	-8.8	-7.5
184	22.0	781.06	300.76	266.17	0.9	1.0	1.7	15.7	-32.2	-32.6
185	22.1	532.36	479.81	308.90	0.8	1.1	0.4	-21.1	8.2	-21.8
186	22.2	668.61	425.92	354.06	2.7	1.1	2.3	-0.9	-4.0	-10.4
187	22.3	864.92	313.37	282.05	0.9	1.6	3.3	28.2	-29.4	-28.6
188	22.4	864.25	287.26	255.44	1.2	2.8	1.8	28.1	-35.2	-35.3
189	22.5	758.26	319.45	276.70	0.7	0.2	1.4	12.4	-28.0	-30.0
190	22.7	718.08	352.06	303.57	2.3	3.2	0.7	6.4	-20.6	-23.2
191	22.7	707.16	353.76	310.78	1.3	2.4	2.6	4.8	-20.2	-21.3
192	22.7	1117.06	237.76	217.18	3.8	2.1	2.4	65.5	-46.4	-45.0
193	22.8	803.91	349.27	321.39	1.0	0.8	0.9	19.1	-21.3	-18.6
194	22.9	799.09	298.33	263.65	1.1	2.2	3.1	18.4	-32.7	-33.3
195	23.0	919.50	274.81	237.22	2.6	2.7	0.5	36.3	-38.0	-40.0
196	23.1	683.26	393.13	322.69	0.1	1.7	1.4	1.3	-11.4	-18.3
197	23.2	962.21	260.67	248.34	0.2	0.4	1.9	42.6	-41.2	-37.1
198	23.3	787.94	293.24	268.35	0.8	1.6	0.3	16.8	-33.9	-32.1
199	23.4	790.01	299.04	266.20	0.2	0.3	3.4	17.1	-32.6	-32.6
200	23.4	997.13	222.47	217.47	1.7	1.9	0.8	47.8	-49.8	-45.0
201	23.5	770.61	355.72	331.80	1.6	1.3	2.4	14.2	-19.8	-16.0
202	23.6	942.70	277.61	245.92	0.5	1.5	0.4	39.7	-37.4	-37.7
203	23.8	871.22	330.88	283.57	2.4	2.0	2.2	29.1	-25.4	-28.2
204	23.9	756.12	340.81	277.18	2.5	1.4	1.0	12.0	-23.2	-29.8
205	23.9	866.73	257.76	242.59	4.7	2.5	1.5	28.4	-41.9	-38.6
206	24.0	880.38	298.39	271.65	1.5	2.4	3.1	30.5	-32.7	-31.2
207	24.1	778.29	342.69	285.52	2.2	3.7	0.0	15.3	-22.7	-27.7
208	24.1	605.97	475.48	409.12	0.6	0.3	4.0	-10.2	7.2	3.6
209	24.1	648.76	420.30	317.84	0.8	1.5	2.1	-3.9	-5.2	-19.5
210	24.2	811.25	292.47	265.26	1.7	1.2	2.9	20.2	-34.1	-32.9
211	24.2	898.62	292.63	252.75	2.6	2.3	0.3	33.2	-34.0	-36.0
212	24.4	735.41	369.89	278.89	0.0	2.1	1.2	9.0	-16.6	-29.4
213	24.6	677.38	394.51	322.40	0.4	1.4	1.5	0.4	-11.1	-18.4
214	24.7	548.79	434.14	286.96	2.1	1.8	0.0	-18.7	-2.1	-27.4
215	24.9	840.59	302.52	256.62	0.8	0.4	1.5	24.6	-31.8	-35.0
216	25.1	850.48	313.88	269.46	1.8	1.7	1.6	26.0	-29.2	-31.8
217	25.3	650.38	387.68	277.63	3.8	1.5	0.8	-3.6	-12.6	-29.7
218	25.5	912.75	266.77	241.65	1.0	1.4	2.1	35.3	-39.9	-38.8
219	25.5	838.82	256.87	238.83	3.8	0.6	0.5	24.3	-42.1	-39.5
220	25.6	780.71	342.85	309.38	1.2	0.9	3.3	15.7	-22.7	-21.7
221	25.6	919.99	262.54	230.21	2.6	4.3	0.2	36.3	-40.8	-41.7
222	25.7	849.37	290.77	240.64	1.6	2.5	1.8	25.9	-34.4	-39.1
223	25.8	632.17	436.54	397.52	3.0	0.9	0.5	-6.3	-1.6	0.6
224	25.8	588.93	473.91	338.45	0.8	1.3	2.4	-12.7	6.8	-14.3
225	26.0	1104.60	240.59	219.15	3.3	2.3	2.4	63.7	-45.8	-44.5
226	26.1	894.03	315.28	265.25	1.6	3.6	0.8	32.5	-28.9	-32.9
227	26.3	698.04	386.04	286.29	1.7	3.3	0.3	3.4	-13.0	-27.5
228	26.4	846.03	291.36	241.04	3.1	2.9	0.5	25.4	-34.3	-39.0
229	26.4	1006.10	259.21	225.42	2.8	1.4	0.1	49.1	-41.6	-42.9
230	26.5	763.35	304.35	263.06	0.5	3.4	0.7	13.1	-31.4	-33.4
231	27.1	826.24	330.74	284.32	4.8	1.0	0.2	22.4	-25.4	-28.0
232	27.2	791.72	303.08	258.75	0.5	3.3	2.8	17.3	-31.7	-34.5
233	27.2	835.15	328.12	280.61	0.4	4.0	0.3	23.8	-26.0	-29.0
234	28.0	815.14	337.36	285.05	0.9	0.3	4.1	20.8	-23.9	-27.8

235	28.1	755.19	357.59	288.13	0.0	0.0	2.2	11.9	-19.4	-27.1
236	28.7	801.53	304.95	262.52	1.3	3.0	0.7	18.8	-31.3	-33.5
237	28.8	723.66	388.60	296.52	1.6	2.0	2.4	7.2	-12.4	-24.9
238	28.8	1005.45	254.82	224.39	0.8	2.2	3.0	49.0	-42.6	-43.2
239	29.9	759.00	348.60	284.11	0.7	2.0	3.3	12.5	-21.4	-28.1
240	30.6	819.00	289.31	244.26	5.2	1.0	0.2	21.4	-34.8	-38.2
241	30.9	726.50	327.61	255.03	2.5	0.1	1.4	7.7	-26.1	-35.4
242	31.7	710.88	364.68	302.87	2.4	2.2	1.4	5.3	-17.8	-23.3
243	32.0	981.37	273.28	241.09	1.5	0.9	0.2	45.4	-38.4	-39.0
244	33.7	701.69	329.44	290.78	1.4	2.4	2.5	4.0	-25.7	-26.4
245	34.1	1045.23	251.61	224.78	2.1	1.4	0.7	54.9	-43.3	-43.1

[a]Percent differences between the theoretical rotational constants and the experimentally assigned rotational constants of the pentahydrate.